Reconstructing modern and past weathering regimes using boron isotopes in river sediments

Christian Ercolani

UNIVERSITÉ DE STRASBOURG

École Doctorale des Sciences de la Terre et de l'Environnement

Laboratoire d'Hydrologie et de Géochimie de Strasbourg (LHyGeS)

THÈSE

présentée par :

Christian ERCOLANI

soutenue le : **25 septembre 2018**

pour obtenir le grade de : **Docteur de l'université de Strasbourg**

Discipline/ Spécialité : Géochimie

Reconstruction des régimes d'altération actuels et passés à partir des isotopes du bore dans les sédiments de rivière

THÈSE dirigée par :

LEMARCHAND Damien	MCF, HDR, Université de Strasbourg
DOSSETO Anthony	Associate Professor, University of Wollongong

RAPPORTEURS :

NÄGLER Thomas	Professor, Universität Bern
PUCÉAT Emmanuelle	MCF, HDR, Université de Bourgogne

EXAMINATEURS :

CHABAUX François	Professeur, Université de Strasbourg
VIGIER Nathalie	DR., Laboratoire d'Océanographie de Villefranche

INVITÉ

PARIS Guillaume	CR., Centre de Recherche Pétrographiques et Géochimiques, Nancy

UNIVERSITY
OF WOLLONGONG
AUSTRALIA

Reconstruction of modern and past weathering regimes using boron isotopes in river sediments

Christian Paul Ercolani

Supervisors:
Dr. Anthony Dosseto
Dr. Damien Lemarchand

This thesis is presented as part of the requirement for the conferral of the degree:
Doctor of Philosophy

The University of Wollongong

School of Earth and Environmental Science

November 2018

Christian ERCOLANI

Reconstruction of modern and past weathering regimes using boron isotopes in river sediments

Résumé

Cette thèse a les objectifs suivants :

1. Mieux comprendre comment les isotope du bore dans les sédiments fluviaux modernes enregistrent le régime d'altération à la échelle du bassin versant.

2. Mieux comprendre comment le « signal » d'altération porté par les sédiments fluviaux est transféré des zones sources vers l'environnement de dépôt.

3. Déterminer si les isotopes du B dans les dépôts sédimentaires (paléo-canaux) peuvent être utilisés pour reconstituer les conditions paléo-climatiques et paléo-environnementales et ainsi révéler comment l'altération continentale au sens large (production et transport de sédiments) a réagi à la variabilité climatique au cours du dernier cycle glaciaire-interglaciaire (derniers 100 ka).

Ces objectifs ont été examinés en étudiant les matériaux fluviaux des fleuves Gandak (Himalaya) et Murrumbidgee (NSW, Australie) et des dépôts de sédiments fluviaux de la Riverine Plain (bassin versant de Murrumbidgee, Australie). La connaissance des paramètres qui contrôlent le fractionnement isotopique du bore des sédiments fluviaux au cours de la formation et du transport a d'abord été acquise dans les systèmes modernes, puis appliquée à d'anciens dépôts de paléochenaux.

Résumé en anglais

This thesis has the following objectives:

1. To better understand how boron isotopes in modern fluvial sediments record the weathering regime at the catchment scale.

2. To better understand how the weathering "signal" carried by river sediments is transferred from source areas to the depositional environment.

3. To determine if boron isotopes in sediment deposits (paleochannels) can be used to reconstruct paleo-weathering and paleo-environmental conditions and reveal how continental weathering at large (production and sediment transport) responds to climatic variability over the last glacial-interglacial cycle (approximately the last 100 ka).

These objectives were addressed by studying fluvial material from the Gandak (Himalayas) and Murrumbidgee (NSW, Australia) Rivers and fluvial sediment deposits from the Riverine Plain (Murrumbidgee catchment, Australia). Knowledge of the parameters that control boron isotope fractionation of river sediment during formation and transport was first gained in the modern systems and then applied to ancient paleochannel deposits.

ABSTRACT

Chemical weathering coupled with carbonate precipitation in the oceans is largely responsible for the sequestration of atmospheric CO_2, which balances CO_2 inputs into the atmosphere from mantle degassing and thus participates in the global climate regulation at the geological time scale. Despite the importance of chemical weathering in maintaining habitable conditions on the Earth's surface, quantification of past and present chemical weathering remains difficult. The intensity of modern chemical weathering is generally determined from the geochemistry of solutes and sediments transported by rivers. However, this approach suffers from the lithological control on the composition of the dissolved load and granulometric/mineralogical sorting during sediment transport. Alternatively, boron (B) isotopes have physicochemical properties suitable to study of water-rock interactions, including those involving a biological component. The processes responsible for B isotope fractionation are adsorption on clay and detrital particles, precipitation in secondary phases, and recycling through vegetation. While several studies have used B isotopes as a proxy to quantify chemical weathering reactions in the dissolved load of rivers, few have focused on river sediments. As a result, the parameters that control B isotope behavior during the production of secondary products and subsequent transport from source areas to the deposition environment are not fully understood. Additionally, the use of B isotopes as potential proxy for paleo-weathering and paleo-environment reconstruction is relatively unknown. In the Gandak River (Himalayas) suspended and river bank sediments were collected along the course of the river in order to better understand the parameters that control B isotope fractionation in sediments transported by rivers. Grain size fractions were analyzed for B isotopes and major and trace element concentrations. Boron isotopes in the clay fraction (<2 μm) are highly fractionated with respect to the primary minerals, represented by the sand fraction (63 μm - 2 mm), and evolve downstream, while all other size fractions have a constant composition. The downstream evolution of B isotope compositions and concentrations in the clay fraction reflect differences in the weathering regime; dissolution reactions are dominant in the headwaters, while secondary phase precipitation reactions dominate downstream. Similarly, bank sediments and the dissolved load of the Murrumbidgee River and its tributaries (NSW, Australia) were analyzed to assess the role of lithology, climate, and geomorphology on B isotope fractionation in weathering products and their transport from source areas to the depositional environment.

Boron isotopes in the clay fraction of bank sediments also show an increase in isotope ratios downstream in the watershed, a behavior attributed to changes in the weathering regime in sediment production areas. The B isotope composition of clay fractions is disconnected from that of the dissolved load of the river, which reflects both an absence of isotopic exchange during transport and a disconnection between the fluid that produces the clay and the fluid that composes the dissolved phase of the river. A mass balance model reveals that the composition of the clay fraction represents a mixture of sediment sources throughout the watershed. Therefore, no chemical or isotopic evolution of the sediments was observed during transport. Paleochannel sediments in the Murrumbidgee catchment were also analyzed for boron and neodymium (Nd) isotopes, major and trace element concentrations, and sediment mineralogy. After identification and removal of samples which were affected by post-depositional alteration, distinct B isotope variations between paleochannel systems can be made. This B isotope record in the paleochannels correlates with a sea surface temperature (SST) and vegetation cover records over the last 100 ka indicating that clay formation in source areas has responded to climatic variability, particularly temperature and vegetation cover. During warmer and wetter periods (Marine Isotope Stages 1, 3, and 5), the role of vegetation on pedogenesis is greater than during colder periods (Marine Isotope Stage 2). Finally, Nd isotopes in the clay fraction show that there has been no significant change in sediment provenance for the last 100 ka. These results highlight the potential for the use of B isotopes to quantify modern and past weathering regimes, including their use in sediment deposits as a proxy to reconstruct paleo-weathering and paleo-environmental conditions.

ACKNOWLEDGEMENTS

The opportunity to earn a doctoral degree comes but once in a life time. Success is not measured by how much you achieve, but rather how many times you attempt to achieve success. Hardships and mishaps are just part of the experience, which in the end, often lead to much better and interesting results. Patience and perseverance are two skills I learned through the undertaking of this degree; skills I will use the rest of my life. I would like to thank my PhD supervisors, Drs. Anthony Dosseto and Damien Lemarchand for their continual guidance, wisdom, and support they have given me throughout every step of this process. Without their oversight and encouragement, this project would not have reached its full potential. Likewise, my potential as a scientist may not have been realized.

I would like to thank both the University of Wollongong and the Université de Strasbourg for providing matching post-graduate scholarships which made this research possible. I would also like to thank both institutions for hosting me and giving access to their fine laboratory equipment and space. This includes the assistance from lab technicians Lili Yu, José Abrantes, Thierry Perrone, Mathieu Granet, René Boutin and Professors Brian Jones and Tim Cohen.

I would like to thank my PhD colleagues who have helped with my work, both in the field and lab, including Philippe Roux, Leo Rothacker, Ashley Martin, and Gabriel Enge.

I also give many thanks to my family, especially my parents, who have provided continual love and support, not only through this process but throughout my life. They taught me to make my dreams a reality, which is what I did.

I would like to thank my colleagues and friends I've made along this journey for their support, encouragement, and guidance during this difficult time. It was great to have these wonderful people in my life.

Finally, I truly may not have made it without the endless love and support of my partner, Andrew, who undertook this adventure with me. With you by my side, I know anything is possible. You are my rock.

TABLE OF CONTENTS

TABLE OF FIGURES

TABLE OF TABLES

Chapter 1

INTRODUCTION

1.1 Introduction to chemical weathering

The study of chemical weathering has been a topic of scientific exploration and advancement dating back to the 1800s with various implications in a wide range of fields such as geology, biology, chemistry, and more recently, global climate. Chemical weathering of rocks forms part of the geologic cycle in which rocks are continuously formed, broken down, and recycled, thereby shaping the surface of the Earth. Chemical weathering occurs because silicate rocks and minerals are formed under very different conditions deep in the Earth than those that are present on the surface. Examples of these differences include changes in temperature, pressure, oxygen availability, and water content (Livingstone, 1972). The process is initiated when primary minerals formed at high temperature and pressure deep in the Earth's interior are transported to the surface via uplift or erosion and exposed to circulating water on or near the surface. Surface processes that have the greatest influence on silicate weathering are associated with the chemistry and flow patterns of water and the term "weathering" implies strong dependency on processes associated with the hydrosphere, atmosphere, and biosphere. Exposure to increased water content, lower temperature and pressure, and increased atmospheric oxygen causes exposed rocks and minerals to become thermodynamically unstable in ambient conditions at the Earth's surface (Garrels, 1988). During this process, minerals in rocks are dissolved primarily by water and other solutes releasing various elemental constituents to the soil. This in turn provides raw material needed for soil development and formation, nutrients for living organisms, and defines the chemical composition of soil solutions and rivers. The biogeochemical cycle of nearly every element is affected by chemical weathering.

During chemical weathering protons are the primary weathering agent, commonly derived from the dissolution of carbon dioxide gas in water (1-1). Protons can also be derived through chemical reactions such as the oxidation of sulphide minerals and organic matter. Acid hydrolysis occurs when a mineral react with protons in water which changes the chemical composition of the mineral. Examples of this reaction involving a silicate (anorthite) and a carbonate (calcite) are shown in Equations 1-2 and 1-3, respectively.

$$CO_{2\,(g)} + H_2O_{(l)} \rightleftharpoons H_2CO_{3\,(ag)} \rightleftharpoons HCO^-_{3\,(aq)} + H^+_{(aq)} \qquad (1\text{-}1)$$

$$CaAl_2Si_2O_{8\,(s)} + 2CO_{2(g)} + 3H_2O_{(l)} \rightleftharpoons H_4Al_2Si_2O_{9\,(s)} + Ca^{2+}_{(aq)} + 2HCO^-_{3\,(aq)} \quad (1\text{-}2)$$

$$CaCO_{3\,(s)} + H_2O_{(l)} + CO_{2\,(g)} \rightleftarrows Ca^{2+}_{(aq)} + 2HCO^-_{(aq)} \quad (1\text{-}3)$$

In Equation 1-1, the combination of $C0_2$ and H_2O produces carbonic acid, which dissociates into bicarbonate (HCO_3^-) and a hydrogen ion (H^+), both active weathering agents. Notice the difference between the silicate (1-2) and carbonate (1-3) examples. Unlike the carbonate reaction, the weathering of silicates rarely results in the total dissolution of the initial mineral, leading to the production of secondary minerals, kaolinite ($H_4Al_2Si_2O_9$), in the example used in Equation 1-2. This reaction holds true regardless of the type of silicate mineral, as weathering results in the release of cations and bicarbonate into the environment, coupled to the consumption of atmospheric CO_2 (White and Brantley, 1995). As shown in Equations 1-2 and 1-3, chemical weathering of silicate and carbonate minerals is associated with the conversion of atmospheric CO_2 to HCO_3^- in an aqueous solution. By this mechanism, mineral weathering consumes CO_2 and the rate of mineral dissolution reactions therefore determines the importance of mineral weathering as a sink for atmospheric CO_2 (Jenny, 1941). The release of the bicarbonate ions from this reaction into solution will be transported across Earth's surface by the rivers that eventually flow to the ocean. During this process, silicate weathering supplies cations (Ca^{2+} and Mg^{2+}) to the oceans where they react with carbonate ions and precipitate Ca-Mg carbonate minerals. The weathering of silicate minerals followed by the deposition of carbonate minerals in the ocean to form carbonates and eventually sedimentary rocks is the main process by which carbon dioxide is transferred from the atmosphere back to solid earth (Figure 1-1) (Berner, 1992, 2003; Siever, 1968). The deep burial and thermal decomposition of carbonates releases carbon dioxide back into the atmosphere. After burial, carbon is recycled in the crustal material through plate subduction, where rocks under extreme temperature and pressure melt and recombine into silicate mineral. Finally, upon volcanic eruption, CO_2 is released back into the atmosphere where it can once again bind with water molecules to form carbonic acid, react with silicate minerals when precipitated, and ultimately be consumed via silicate weathering (right side) or photosynthesis (left side), shown in Figure 1-1. In the case of photosynthesis uptake of CO_2, carbon would be transferred to organic material; upon death and burial, it will be transformed into organic carbon in sediments and eventually hydrocarbons. Oxidation or burning of organic matter / hydrocarbons releases CO_2 to

the atmosphere, while deep burial and plate subduction returns carbon to the mantle where it is recycled (Berner, 2003).

Silicate weathering is governed by the rate of dissolution reactions which should depend mineralogy of the rocks and their characteristics (i.e. supply, exposed surface area, reactivity, etc.), availability of water and its residence time in the soil, soil pH, presence of vegetation (i.e. increasing production of organic acids and humic matter), and Arrhenius' rate law which describes the temperature-dependency of the weathering reaction (Kump et al., 2000; Lasaga et al., 1994; Jackson, 1975). The temperature-dependence of this reaction on Earth's surface

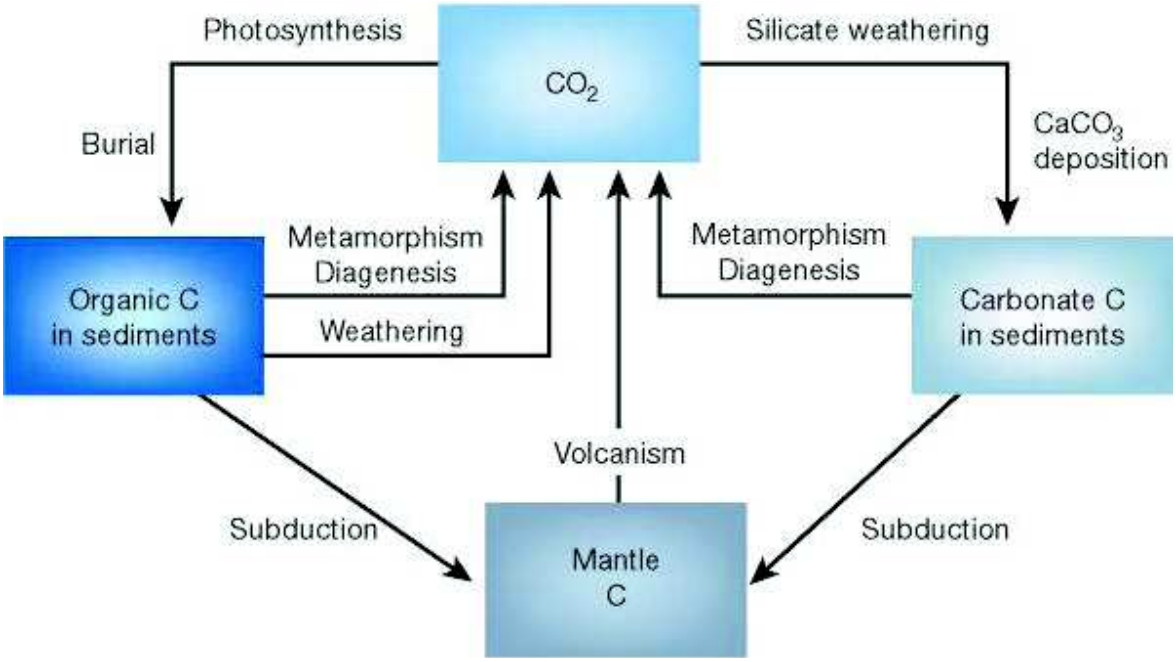

Figure 1-1. A model of the long-term carbon cycle. Source: Berner (2003).

has been proposed to provide the feedback mechanism that regulates climate over geologic timescales (Berner et al., 1983; Walker et al., 1981) and maintains relative climatic stability over Earth's history. This hypothesis and other competing hypotheses regarding the chemical weathering – climate relationship will be further discussed in the next section (Section 1.2).

If temperature plays a crucial role in silicate weathering and thus promoting stable climatic conditions on Earth, being able to distinguish the role of the temperature from other factors that influence mineral dissolution reactions is vital. However, isolating the effect of temperature from other variables influencing chemical weathering such as precipitation, geomorphology, vegetation, and lithology has proven to be a difficult task (West et al., 2005).

There are two general approaches that are used to investigate the role of temperature on chemical weathering: laboratory experiments that focus on the mineral dissolution (rate-dependencies) as a function of temperature; and natural field experiments on various scales (individual rock types, soil profiles, and small and large catchments) typically measuring solute discharges. Field experiments are often used in combination with laboratory experiments to ground-truth laboratory results (Velbel, 1993a). Decades of laboratory experiments have focused on systematically defining the rate-dependency of silicate weathering reactions and mineral dissolution on these controlling factors, including temperature and solution chemical composition. The effects of temperature on the weathering rates of certain silicate minerals such as feldspars (Blum and Stillings, 1995), granites (White et al., 1999), quartz (Dove, 1995), and pyroxenes and amphiboles (Brantley and Chen, 1995) have been well established. These studies indicate that an increase in temperature from 0 – 25°C should increase weathering rates by approximately an order of magnitude (based on average experimental dissolution activation energies of 50 – 80 kJ/mol); an effect that is observable in natural environments. The activation energy is the energy that must be available for the chemical reaction to occur (Brady and Carroll, 1994). The effect of temperature on chemical weathering was also investigated both experimentally and in the field on fresh and weathered granitoid rocks, showing that increasing temperature correlates with an increase in Si dissolution, measured at four different sites (White et al., 1999) (Figure 1-2). Temperature trends for Si effluents are parallel for fresh and weathering paired granitoids, indicating that their sensitivity to temperature changes are similar regardless if they have experienced natural weathering. This implies that the nature of the weathering reactions are also similar. However, at any temperature, Si effluent concentrations from weathered rocks are lower than effluents taken from pristine rocks. White et al. (1999) also found similar relationships between the dissolution of Na and K in both fresh and weathered granitoids as a function of temperature (not shown). Additionally, a coupled temperature-precipitation model (White et al., 1999) produced apparent activation energies for Si which were comparable to those derived in the experimental field sites. This finding reinforces the fact that temperature significantly impacts natural silicate weathering rates. Several other studies have also shown the effects of temperature on the weathering and dissolution of various silicate minerals (e.g. anorthite, augite, kaolinite, smectite), demonstrating than in most cases an increase in temperature positively correlates with the rates of silicate mineral dissolution (e.g. Bauer and Berger, 1998; Brady and Carroll, 1994, among others). However,

silicate dissolution rates between laboratories are often inconsistent (within two orders of magnitude) and therefore generally considered to be not well-constrained (Brantley and Chen, 1995).

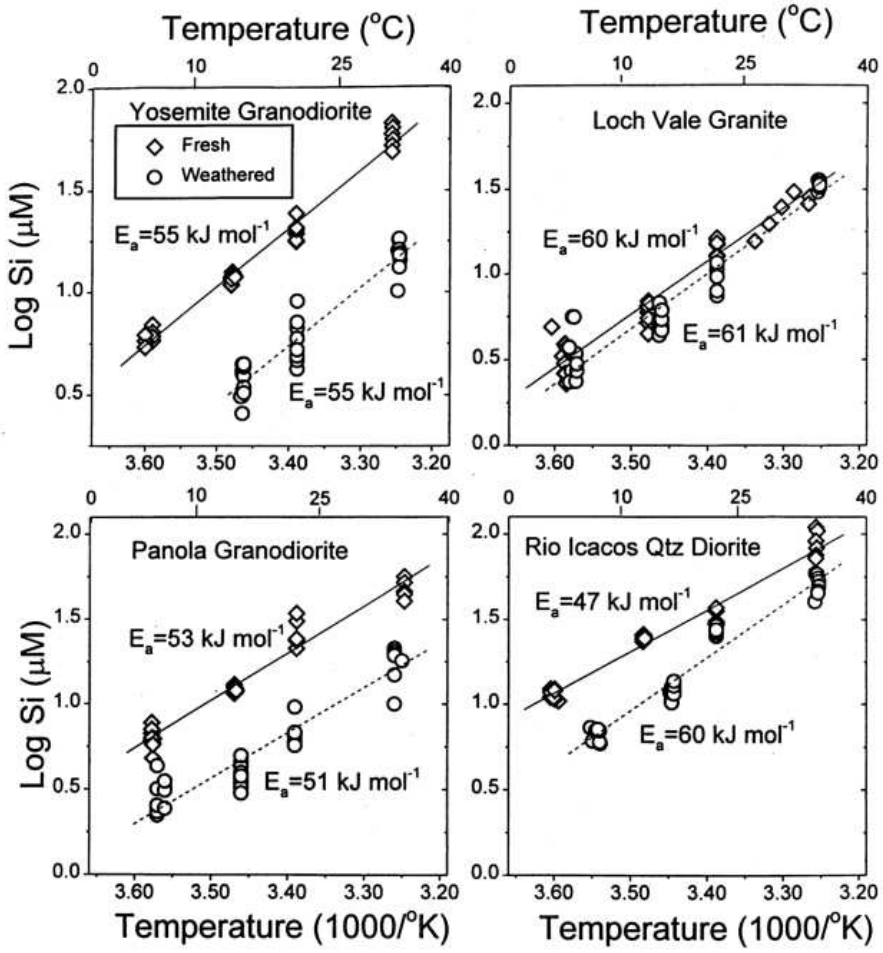

Figure 1-2. Arrhenius diagrams of the log Si effluent concentrations from both fresh and weathered granitoid rocks. The inverse of absolute temperature is displayed in the lower x-axis and the nonlinear scale to the temperature increase (°C) on the upper x-axis. Solid and dashed lines both correspond to linear fits of the effluent measurements of fresh and weathered granitoid rocks. Source: White et al. (1999).

Long term, direct observations in natural systems is the alternative approach to derive mineral weathering rates. Although this approach is a more direct way to study the relationship between temperature and weathering, it proves to be difficult because chemical, biological, and physical conditions, i.e. mineral compositions, temperature, surface area, fluid residence times and pathways, are generally not well-constrained. In addition, the time scale on which natural

weathering occurs is rarely able to be duplicated in experimental studies, accounting for and possibly explaining contradictions in silicate weathering rates among studies (White and Hochella, 1992). In general, as the scale in which we study weathering processes increases, our ability to detect and isolate a temperature signal decreases. This is mainly due to the complexity of interacting factors in larger systems and may explain why the comparison of solute concentrations and fluxes in the world's largest rivers systems often fail to detect a temperature effect that is independent from other factors (Huh et al., 1998; Edmond et al., 1995). However, there have been a relatively small number of studies that have successfully isolated the effects of temperature from other factors. For example, estimated elevation-dependent temperature differences on the weathering of plagioclase minerals was determined in the Coweeta watershed (North Carolina) with a calculated activation energy of 77 kJ mol^{-1} by Velbel (1993b) while Dorn and Brady (1995) used plagioclase porosity in Hawaiian basaltic flows sampled at different temperatures/elevations to calculate an activation energy of 109 kJ mol^{-1}. In contrast, the study of weathering as function of temperature on the smaller scale has proved to be more rewarding. A compilation of works illustrating the impact of mean annual air temperature on weathering rates from various small granitoid catchments worldwide has been compiled by White and Brantley (1995) which collectively point to increased temperature and precipitation as a means to explain rapid weathering rates in various geographical settings (White et al., 1999). These efforts have significantly assisted weathering and kinetic models, for example, by providing rate constants for the dissolution of primary minerals (Brantley and Olsen, 2013; Hilley et al., 2010; White and Brantley, 1995). The positive correlations between dissolution rates of various minerals and rocks as a function of temperature both in the field and laboratory have provided support for the linkage between climate and silicate weathering on Earth's surface.

Lithology is considered to be a major control on chemical denudation and weathering rates by controlling the composition of minerals involved in water-rock interactions and their susceptibility to weathering (Bluth and Kump, 1994; Meybeck, 1987; Peters, 1982; Garrels and Mackenzie, 1971). For example, mafic silicates in basalts such as olivine and pyroxene tend to be more reactive and weather much faster than felsic minerals in granites like quartz and feldspar. Meybeck (1987) reported a relative index of chemical weathering rates for common continental rocks ranging from 1–80: granites and gneisses being the lowest (1 - least likely to weather); limestones (12 – low to

intermediate) and saltrocks (80 - easier to weathering). This is because different minerals are composed of different elemental compounds which have different degrees of solubility in water. Generally, field studies that have sought to estimate the supply of major ions coming from specific lithologies often have had difficulties because the mobility of elements is dependent upon the parent rock composition (mineral composition, grain size, joints/fractures) and not geochemical processes alone (Sayyed, 2014). This problem became apparent in early studies that investigated the controls of stream chemistry at the watershed scale, i.e. (Peters, 1982; Garrels and Mackenzie, 1971), who found that the rates of dissolution and dissolved load chemistry are directly related to catchment lithology and the permeability of soils and bedrock material. The study of dissolved load chemistry at the basin scale, such as the Amazon, was undertaken by Stallard and Edmond (1983). The objective of this study was to determine the relationship between the major dissolved species in Amazonian rivers and factors such geology, topography, and the role of catchment soils. Results from this study also revealed that substrate catchment lithology and associated erosional regime were the major controls on the chemistry of surface waters within a catchment. For example, rivers that drained siliceous lithologies were relatively high in silica content and low in total dissolved cations; rivers draining carbonates were found to be high in alkalinity and intermediate levels of total cations. These results are consistent with mineral susceptibility trends for minerals in tropical environments such as the Amazon. More recent studies focusing on determining the global weathering rates and budgets by analyzing the dissolved load and suspended loads in large river systems (i.e. Bluth and Kump, 1994b; Gaillardet et al., 1999a) also report the dominant control lithology has on stream chemistry. Gaillardet et al. (1999a) reports that the chemical weathering (and possibly climate) signals carried by the rivers was also found to be dependent on and obscured by effects from parent lithology. The observation of the dependency of silicate weathering rates and intensities on parent lithology is not unique to studies focusing on large catchments nor to studies only using major and trace element as proxies for chemical weathering. For example, the chemical and isotopic compositions of dissolved load and solid phases carried by the river in small catchments may also be affected. A recent study of detrital material in stream sediments points to the strong control lithology has on the lithium (Li) isotopic composition of the clay fraction and therefore correct for it by subtracting the composition of bedrock from that of the sediment clay fraction before making any chemical weathering interpretations (Dellinger et al., 2017). Due to the inherent problem lithology often causes when

trying to get estimates of silicate weathering rates and access to the weathering regime in the field, many find it preferable to perform laboratory experiments on specific minerals (e.g. illites or smectites) (Williams et al. 2001a), or rock types such as basalts or granites (e.g. White and Brantley, 1995) and field experiments in small watersheds where monolithological units can be identified and studied (e.g. Dessert et al., 2003; Meybeck, 1987; Nesbit and Wilson, 1992).

The contributions of cations provided to streams and rivers by silicate weathering is to a large extent influenced by watershed hydrology and surface runoff and ultimately control the total dissolved yield in rivers (Garrels and Mackenzie, 1971). Additionally, the rates at which silicate weathering occur are thought to be a function of hydrology (Lasaga et al., 1994; Berner, 1978). Generally, the dissolution of minerals in water-saturated rocks, soils, and sediments are expected to rise with increasing flushing/flow rates up to a certain threshold where increased flow rates have no effect on dissolution (Berner, 1978); beyond the threshold, weathering reactions are no longer transport-controlled and become surface reaction-controlled. Therefore, one could expect weathering to be transport-limited at low flushing rates and surface-reaction controlled, also referred to as interface-limited, at high flushing rates. Holland (1978) reported TDS data from rivers worldwide as a function of runoff (Figure 1-3) which show that increasing flushing rates above a critical value do not increase the dissolve solid concentration in rivers throughout the world, but rather dilute them; a theory that is in agreement with Berner (1978). According to Schnoor (1990), lower flushing rates of field systems can account for the lower Si release rates observed in natural systems. Although this is the first order relationship between total dissolved solids (TDS) concentrations and runoff, other hydrological factors may also take part in this relationship to a lesser degree such as the activation of alternative flow ways and increasing drainage area during large storm events (Burns et al., 2001).

1.2 Chemical weathering and climate

Our current understanding of Earth's climate system from Quaternary geology, including sedimentary, isotopic, and glaciological records, is that the climate system appears to be extremely sensitive to perturbations, particularly near critical thresholds between glacial and interglacial conditions (e.g. Rasmussen et al., 2014; Clement and Peterson, 2008; Ganopolski and Rahmstorf, 2001) . However, on longer time scales (millions to billions of years), we find a climate system

that is relatively stable and resilient to external forcing (Kasting, 1993). This would indicate that the processes affecting climate on shorter, millennial time scales may be components of positive feedbacks (where an initial change in the climate system leads to a secondary change which in turn enhances or magnifies the initial change) and those affecting climate on longer geologic time scales most often create negative feedbacks (where an initial change in the climate system leads to a secondary change which acts to reverse that initial

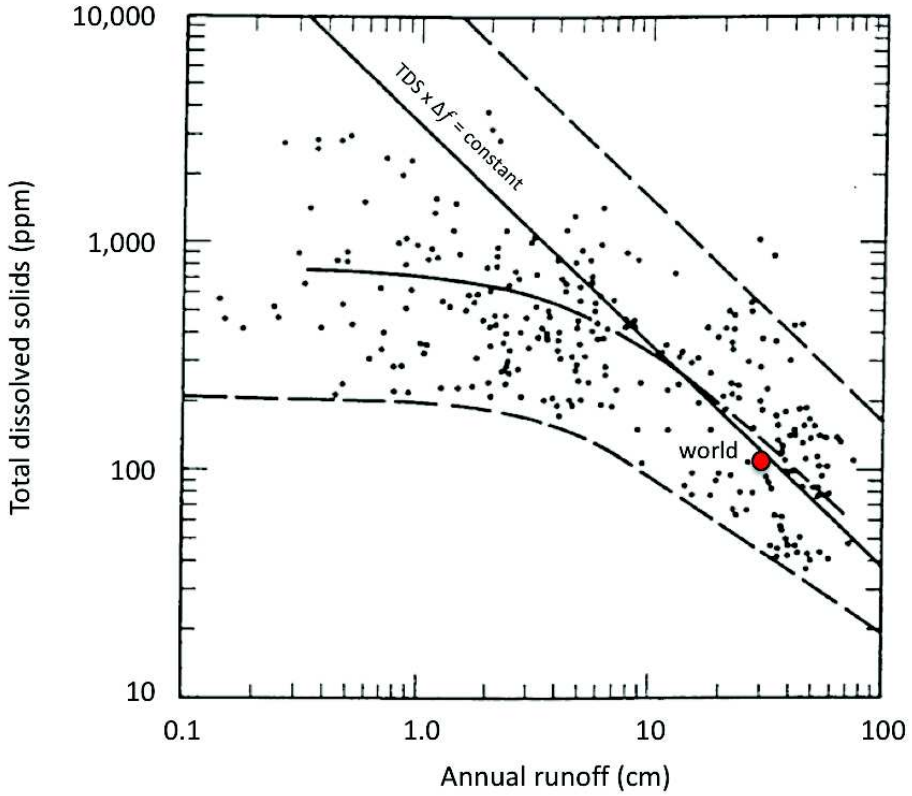

Figure 1-3. Total dissolved solids vs. runoff for rivers worldwide. The solid curve shows the general trend between TDS and annual runoff; solid line shows the dilution trend. The red dot shows the average values for the rivers worldwide. This figure demonstrates that past a critical threshold, increased runoff dilutes rather than increases TDS. Source: Holland (1978).

change) (Kump et al., 2000). Through positive feedbacks, subtle changes within the climate system can be detected and amplified (e.g. Curry et al., 1995), while the long-term response of the climate system acts within stable bounds through negative feedbacks (Walker et al., 1981). In the following, the current state of knowledge regarding potential drivers of chemical weathering and its relation to climate variability over both millennial and geologic timescales will be discussed.

1.2.1 Chemical weathering over geological timescales

Using the stratigraphic record, we can roughly estimate climatic conditions on Earth's surface for the last 2.4 billion years, with more coherent estimates over the last 700 million years (Hambrey and Harland, 1981). Over the last 570 million years, four major glaciation events are recognized: Late Precambrian (1st); Ordovician-Silurian boundary (2nd); Permo-Carboniferous (3rd); and, the present Cenozoic Era (4th) (Harland, 1981). The first, third, and fourth events are spaced roughly 300 million years apart and occur during times of continually low sea level (Vail et al., 1977). In contrast, the time period between the 1st and 3rd glaciations (Early- and Mid-Paleozoic), including the 2nd glaciation, corresponds to a general period of high sea levels and is similar climatically to the Mesozoic. Prior to Phanerozoic glaciations, there are several approximately known intervals of glaciation in the Proterozoic, with the oldest being in the Early Proterozoic (2.5 – 2.1 Ga ago) and several intervals in the Middle to Late Proterozoic (1.0 – 0.57 Ga) (Christie-Blick, 1982).

Significant climatic oscillations between greenhouse and icehouse states indicate that the mechanism(s) responsible for climatic regulation on Earth's surface is (are) not perfect. However, they are able to correct for large climatic variations, thus promoting climatic stability over geological timescales and have not allowed the Earth to become locked into an inescapable Snowball Earth state (Caldeira and Kasting, 1992). Although some of the original energy-balance climate models such as those by Budyko (1969) and Sellers (1969) have predicted that a slight (2-5%) decrease in solar output could lead to a runaway glaciation, we now know that solar fluxes were 25-30% lower than present (Gough, 1981; Sagan and Mullen, 1972) and did not lead to irreversible freezing on Earth's surface. Hence, the stability of Earth's climate therefore requires a negative feedback between chemical weathering and climate and a mechanism allowing the extent of regulation or strength of the feedback to vary (Ruddiman, 1997).

Principle components of climate, i.e. temperature and precipitation, have been proposed to be responsible for controlling the rates of surficial silicate weathering and balancing the rates of atmospheric CO_2 production, thereby producing stable climatic conditions on Earth (Broecker and Sanyal, 1998; Berner and Berner, 1997; Walker et al., 1981). Walker et al. (1981) suggested that the partial pressure of carbon dioxide in the atmosphere is buffered by a negative feedback

mechanism where the rate of weathering of silicate minerals, and subsequent deposition of carbonate minerals, is controlled by surface temperature, and surface temperature, in turn, depends on the carbon dioxide partial pressure via the greenhouse effect. If this hypothesis is correct, a link must exist between climate and tectonics in which a balance must be reached between planetary degassing of CO_2 and the supply of CaO derived from the chemical weathering of silicates. In theory, if the supply of CaO to the oceans were too small to match the input of CO_2 to the ocean-atmosphere system, then the CO_2 content of the atmosphere would rise, thereby increasing the rate of chemical weathering until the system was balanced. On the contrary, if the rate of CaO supplied to the oceans were larger than the amount of CO_2 inputted to the ocean-atmosphere system, then the atmosphere's CO_2 content would be drawn down causing the planet to cool and thereby reducing the rate of chemical weathering. Although the quantitative estimates of this mechanism were crude, they were considered reasonable in partially explaining the stabilization of Earth's surface temperature against the continuous increase in solar luminosity. Several subsequent studies (e.g. Broecker and Sanyal, 1998; Berner and Caldeira, 1997; Berner and Kothavala, 1994; Lasaga et al., 1985; Berner et al., 1983) have agreed with the hypothesis proposed by Walker et al. (1981).

For example, Berner et al. (1983) reconstructed the CO_2 content of the atmosphere over the last 100 Myr using a series of assumptions based on carbon cycling and geologic processes. Model outputs indicate that the CO_2 content of the atmosphere is highly sensitive to changes in rates of seafloor spreading and continental land area. Accordingly, this study reports that plate tectonics may have a major control on world climate. By calculating the changes in the carbonate chemistry of the modern surface ocean as function of varying amounts of CaO and calcite, Broecker and Sanyal (1998) conclude that the most likely mechanism to "police" or stabilize Earth's climate is the CO_2 content of the atmosphere because it controls silicate weathering rates. Berner and Caldeira (1997) found through a series of carbon mass balance equations that in the absence of a negative feedback mechanism, atmospheric CO_2 levels would highly fluctuate. Important conclusions were drawn from this study that support the now-accepted "Walker hypothesis":

- Carbon inputs and outputs to and from the oceans, atmosphere, and biosphere are closely balanced over geological time scales
- A negative feedback related to atmospheric CO_2 levels is required to maintain this

balance

- Silicate weathering response to climatic variability is sufficient to provide this negative feedback
- The rate of CO_2 supply to the surficial system along with imbalances in the organic carbon cycle control long-term global weathering rates

However, the CO_2 policing mechanism proposed by Walker et al. (1981) and agreed on by others (e.g. Berner and Kothavala, 1994; Lasaga et al., 2013) did not go unchallenged by the scientific community. Raymo et al. (1988) and Raymo and Ruddiman (1992) were the first to challenge this concept which lead to a significant amount of controversy regarding the role of chemical weathering in regulating the atmospheric partial pressure of CO_2, thus the extent and strength of the greenhouse effect and global climate (Kump et al., 2000). Arguments in the literature generally center around the sensitivity of chemical weathering to various climatic factors, particularly temperature and to a lesser extent precipitation. Those that do not accept the climate-continental silicate weathering-atmospheric CO_2 relationship proposed by Walker et al. (1981) not only question the effect of surface temperature on chemical weathering, but also point to other drivers of long-term control on atmospheric CO_2 such as tectonic uplift, denudation, and erosion (Raymo et al., 1988), a combination of both tectonic uplift and climate (West et al., 2005), and global climate change (Molnar and England, 1990). Most notably, the hypothesis first proposed by Raymo et al. (1988) is likely the strongest opponent of the "Walker hypothesis" and is the center of controversy in the literature because it fundamentally challenges the idea that the Earth's "thermostat" is controlled by balancing the rates of CO_2 production via silicate weathering and carbonate deposition which is ultimately a function of climate. The challenging "Raymo hypothesis" proposes that episodes of orogenic activity, i.e. tectonic uplift and erosion, may have caused increases in chemical weathering rates which resulted in a decrease of atmospheric CO_2 concentration over the last 40 million years (Myr). This argument stems from the suggestion that the rapid uplift of the Himalayan-Tibetan plateau region and the Andes in the late Cenozoic had a significant impact on atmospheric circulation (Ruddiman et al., 1988). Using ocean box models of the geochemical cycles of strontium (Sr), calcium (Ca), and carbon (C) in marine sediments, Raymo et al. (1988) showed that the their record of carbonate sedimentation, calcite compensation depth, $\delta^{87}Sr$, and $\delta^{13}C$ indicate increasing fluxes of weathering products to the sea over the past 5

Myr. It is proposed that this increase in chemical weathering rates over that time period caused a drawdown of atmospheric CO_2 and therefore may have caused global cooling. By pairing their marine record data with evidence of substantial mountain building throughout the world, enhanced uplift rates, and an apparent increase in global erosion, Raymo et al. (1988) conclude that chemical weathering rates and dissolved fluxes to the sea would increase stating the following reasons:

- rapid mechanical breakdown of rocks in areas experiencing rapid uplift would enhance exposure of primary minerals to chemical weathering, while abrasion of mountain stream would remove the iron-oxide coating that inhibits and slows weathering reactions (Stallard and Edmond, 1983)
- dissolved load of rivers are highest in areas that drain easily-eroded sedimentary rocks, a characteristic that is found in highly tectonic areas (Stallard and Edmond, 1983)
- Chemical and physical weathering rates increase with runoff which is often highest in mountainous regions because of the orographic effects of mountain ranges on precipitation patterns

The hypothesis that rapid uplift of the Himalayas and Tibet has the potential to change Earth's atmosphere and climate over the Cenozoic period, proposed by Raymo et al. (1988), Raymo and Ruddiman (1992), and Ruddiman (1997), has found support of subsequent studies such as Hilley et al. (2010); and Hilley and Porder (2008). In an effort to shed light on how tectonics, climate, and rock-type influence silicate weathering and drive global rates, Hilley and Porder (2008) developed a model that considers whether local erosion rates, GCM-derived dust fluxes, temperature, and water balance can adequately capture global variation in silicate weathering. The model predicts that 50% of the atmospheric CO_2 drawdown via silicate weathering occurs in active mountain belts worldwide (20% within the Indo-Asian mountains) which lend support to the hypothesis that the continual uplift of the Himalayas over the late Cenozoic played a major role in regulating climate proposed by Raymo and Ruddiman (1992).

Hilley et al. (2010) then attempts to clarify the relative role that mineral supply and reaction may play on a select group of various mineral phases by modeling denudation and reaction kinetics. Laboratory and field measurement values of silicate weathering kinetic constants, observed weathering zone thicknesses, and denudation rates inferred from topography, were used

in the model. The study concludes that fresh mineral supply plays a dominant role in moderation silicate weathering fluxes for the minerals considered which suggests that the concentration of atmospheric CO_2, which is regulated by silicate weathering over geological timescales, may depend on those factors that control long-term erosion rates.

Another competing hypothesis to Walker et al. (1981) and Raymo et al. (1988) which essentially stems from the "Raymo hypothesis" is that proposed by Molnar and England (1990). In this case, the recent uplift of most mountain ranges documented by increased denudation and sedimentation rates, along with paleo-botanical evidence suggesting a shift to colder climatic conditions, are proposed to be the result of late Cenozoic climate change

In essence, they support the finding that erosion is controlled by climate (Wilson, 1973; Fournier, 1960), i.e. sediment yield is directly related to precipitation, and propose that increasing precipitation rapidly enhances erosion which causes isostatic rebound and uplift of the landscape. However, they argue that the mean elevation of the Himalayas perhaps did not rapidly accelerate over the Cenozoic, when accounting for both erosion and isostatic compensation of the landscape but that climate change, weathering, erosion, and isostatic rebound might interact in a system of positive feedback causing further global cooling. A more recent study (Willenbring and von Blanckenburg, 2010) has provided evidence of long-term stability of global weathering and erosion rates over the Cenozoic which partly contradicts the hypothesis proposed by Molnar and England (1990). Using the ocean dissolved $^{10}Be/^{9}Be$ record as a proxy for chemical weathering, stable weathering fluxes are observed over the past 12 Myr. Results from this study question whether the apparent fourfold increase in global sedimentation rates (driven by increased precipitation) proposed by studies such as Hay et al.(1988) has actually occurred. These results agree with other studies (e.g. Derry and France-Lanord, 1996) which suggest that an increase in burial of young organic matter (which would accompany increased sedimentation) is not apparent. Accordingly, the conclusions from this work are that neither global erosion nor weathering have increased as a results of climate change over the timescale of analyses (4 Mya) in spite of pulses of mountain building.

1.2.2 Chemical weathering over glacial-interglacial timescales

Over the last 420 ka, we observe four distinct glacial-interglacial sequences (Petit et al., 1999) (Figure 1-4); interglacial periods are characterized by a thicker greenhouse atmosphere (higher atmospheric CO_2 and CH_4 content), higher atmospheric temperatures, greater June insolation (at 65°N), and more positive $\delta^{18}O$ values in the atmosphere; during glacial periods we observe the opposite. The pattern of climate variability observed in the ice core can be described as 'sawtooth' during warm inter-glacial periods (stages 11.3, 9.3, 7.5 and 5.5), followed by increasingly colder interstadial events which end with a rapid return towards the following interglacial period (Petit et al., 1999). The coldest part of each glacial cycle occurs immediately before glacial termination and return to interglacial conditions, except in the third glacial cycle (225,000 to 325,000 yr BP), which according to Petit et al. (1999) may reflect a greater influence from the June 65°N insolation minimum prior to the transition. The ice core record presented by Petit et al. (1999), and others from Antarctica (Augustin et al., 2004) and Greenland (Andersen et al., 2004), have shown that the climate of the Earth over short timescales is sensitive to perturbations while oscillating within a stable bound between glacial and interglacial conditions.

Over 60 years have passed since the discovery of glacial-interglacial cycles via $\delta^{18}O$ measurements in carbonates (Emiliani, 1955) and nearly 20 years since they have been thoroughly investigated using ice cores. Nevertheless, our current understanding of how silicate weathering has or will respond to climatic variability remains limited. This is primarily because until very recent times, the role of chemical weathering was thought to be slowly reactive to climate change and therefore only considered in studies investigating geologic climate variability (e.g. Livingstone, 1972). However, recent modeling efforts (Beaulieu et al., 2012) have shown that the weathering regime can respond very quickly (<100 yr) to changes in climate and may regulate atmospheric CO_2 levels over short time periods. Although the role of climate on chemical weathering is still debated, several studies (Bastian et al., 2017; Dosseto et al., 2015; Gislason et al., 2009) have challenged the notion that chemical weathering responds slowly to climate change and have shown that climate (temperature and precipitation) does play a role in determining chemical weathering regimes over glacial-

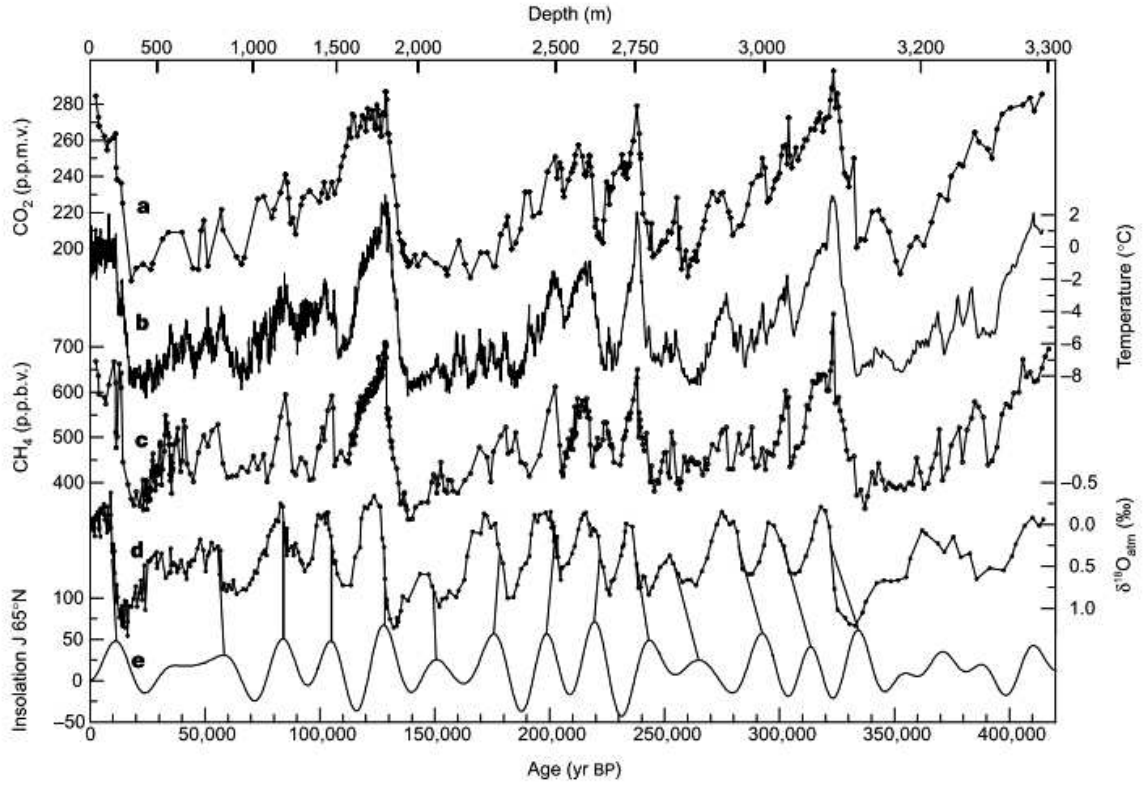

Figure 1-4. Ice core data from Vostok (Antarctica); time series (lower axis) and insolation, with corresponding depth in the ice core on the top axis. A) CO_2; B) isotopic temperature of the atmosphere (see text); C) CH_4; D) $\delta^{18}O_{atm}$; and E) mid-June insolation at 65°N (in Wm^{-2}) (Berger, 1978). CO_2, isotopic temperature of the atmosphere, CH_4, and $\delta^{18}O_{atm}$ data all taken from Petit et al. (1999). Source: Petit et al. (1999).

interglacial timescales. For example, Gislason et al. (2009) reported a rapid increase (up to 30% over four decades) in the chemical weathering flux in Iceland attributed to high latitude climate change. Here, ice melt is attributed to increasing temperatures which increased the liquid water available for chemical weathering. Others report that climate can affect chemical weathering rates by increasing soil respiration and cause perturbations in net primary production (i.e. Zhao and Running, 2010), which in turn can change soil acidity and impact chemical weathering rates. A strong link between physical erosion, runoff, and chemical weathering was observed by Dosseto et al. (2015) in the clay composition of Himalayan terrace sediments. In this work, temperature was shown to play a secondary role to both runoff and physical erosion, which acted to retard chemical weathering by accelerating sediment transport in the system, hence controlling the feedback between chemical weathering and atmospheric carbon dioxide.

Foster and Vance (2006) investigated the relationship between climatic variability and chemical weathering rates over a long timescale (550 ka) by coupling lead (Pb) isotope compositions of ferromanganese crusts which precipitated directly from seawater in the North Atlantic to a quantitative model of the changes in the Pb isotope composition of the North Atlantic Deep Water (NADW) in response to continental chemical weathering rates. Agreeing with previous studies, they find negligible variation in chemical weathering rates during glacial-interglacial cycles. Foster and Vance (2006) report that during glacial periods, a two to three times lower chemical weathering regime is observed on continental landmasses compared to interglacial times, however this decrease is nearly balanced by chemical weathering of the exposed continental shelves, resulting in nearly constant chemical weathering regimes in warm and cold periods alike.

Later, Vance et al. (2009) contend that an increase in chemical weathering is inevitable during deglaciation periods such as that which followed the last glacial maximum (LGM) 18 ka ago. They hypothesized that weathering rates would rise rapidly as pristine parent minerals would be exposed after the retreat of the ice-sheet and then rates would slowly decay over the duration of the subsequent interglacial. Applied to Sr isotopes and the ocean budget, this weathering scenario would suggest that there are indeed cyclic patterns in chemical weathering related to glacial-interglacial cycles. However, Vance et al. (2009) conclude that these variations are not observed in the oceans over the past 400 kyr (Henderson et al., 1994) because Sr (and various other elements) have oceanic residences times that are longer than Quaternary glacial-interglacial cycles. Here, they stress the importance of temporal variability in riverine fluxes to the oceans as they likely play a critical role in reconciling the long-standing chemical and mass imbalance problems in the oceans.

1.3 Budget and rates of chemical weathering

Rock weathering and sediment transport by rivers to the ocean is one of the most important processes controlling landscape evolution, biogeochemical cycles, and ultimately Earth's climate over geological and possibly millennial timescales. Proposed by the works of e.g. Berner et al. (1983) and Walker et al. (1981), silicate weathering regulates ocean alkalinity and thus is a major long-term sink of atmospheric CO_2 and hence acts to regulate the greenhouse effect. Accordingly, as chemical weathering rates increase with temperature, this should create a negative feedback

which buffers Earth's climate from increasing solar luminosity. However, chemical weathering rates are also dependent on physical erosion and vice versa. Simply, chemical weathering rates depend on the availability of fresh mineral surfaces which tend to increase with physical erosion rates via the physical breakdown of rock (West et al., 2005; Riebe et al., 2003). From this relationship, increased physical erosion will then drive chemical rates, followed by an increase in atmospheric CO_2 consumption, leading to global cooling (Raymo et al., 1988). As the hypotheses of both Raymo et al. (1988) and Walker et al. (1981) illustrate, there is a need to better understanding the factors, i.e. temperature, runoff, relief, controlling both silicate weathering and denudation in order to access the extent of their influence on past, present, and future climates.

There are different scales in which to study the controls on continental denudation in nature and derive chemical weathering rates, budgets and fluxes: soil profile scale; small catchment scale; and the global scale. Although the experimental approach in the laboratory is another possibility, most attempts to mimic natural conditions have failed and therefore the results are less conclusive and applicable to natural systems (Lasaga et al., 1994). The study of in-situ chemical weathering reactions via soil profiles, e.g. Nesbit and Wilson (1992), are the classic way to derive chemical weathering rates in nature by comparing mass loss of mobile vs. immobile elements in soil compared to parent material. Data from this approach is more straightforward to interpret as weathering product form in situ, however physical erosion and continual soil development often complicate the quantification of weathering rates. Additionally, soil profiles have been used to determine factors influencing climate. For example, Fedo et al. (1995) determined paleo-weathering regimes using the major element geochemistry and minerology of bulk siliclastic soils, while Curtis (1990) showed that climate influences clay mineralogy and the geochemistry of soils, palaeosols and clastic sedimentary rocks. Smaller scale studies on monolithological watersheds, e.g. Louvat and Allègre (1997); White and Blum (1995); Bluth and Kump (1994); Velbel (1993b), have also been able to discern the interconnection between climate and chemical weathering. Data from these studies tends to be of better quality than larger-scale studies because hydrology and solute budgets are better defined. Possibly the most successful of these approaches, capable of deriving global laws on the controls of continental denudation as well as global budget and chemical weathering fluxes is the global approach via the study of the dissolved load of the world's largest rivers (e.g. Gaillardet et al., 1999; Meybeck, 1987; Moon et al., 2014). Although lithology is dominant control on the river water composition, several studies have been made to reasonably

correct for lithological effects with success (Berner et al., 1983; Gaillardet et al., 1999; Holland, 1978). Additionally, there have been successes at quantifying the weathering regime by analyzing the suspended load (Bouchez et al., 2012; Dellinger et al., 2014; Gaillardet et al., 1999) and more recently weathering products of riverine material such as clay fractions (Dellinger et al., 2017; Dosseto et al., 2015; Cividini et al., 2010) using a variety of chemical weathering proxies from traditional chemical mass balance approaches based on elemental loss to non-traditional stable isotopes.

Commonly used approaches in gaining insight to both physical denudation and chemical weathering processes which shape the landscape, control biogeochemical cycles, and control the evolution of climate will be discussed below.

1.3.1 Chemical mass budget approach

1.3.1.1 Soil profile and sediment deposits

Chemical weathering rates over long-term time scales have traditionally been measured on the soil scale using soil mass balance techniques to quantify the total mass of an element that is removed when a known volume of pristine parent material is converted to soil (Brimhall Jr. and Dietrich, 1987; April et al., 1986). However, mass loss can be attributed solely to chemical weathering only if physical erosion has been negligible over the time the soil has been forming. If the age of the soil is known, it can be used to average the mass loss over the soil formation time (Taylor and Blum, 1995). This scenario is unlikely because in nature non-eroding soils are rare; hence most quantifications of chemical weathering using this method will involve some comparison of physical erosion or denudation to chemical weathering. Examples of where physical erosion in soil profiles may be negligible would include flat-topped moraines (Taylor and Blum, 1995) and fluvial terraces (Bain et al., 1993). In these rare cases, measurements of immobile element enrichment provide estimates of mass loss that can be attributed directly to chemical weathering rates. However in mountainous settings, most soils are actively being eroded and the age of the soil is difficult to determine, mainly because of the continual renewal of fresh material that replaces weathered material removed by physical erosion (Riebe et al., 2003). Alternatively, soil residence times can be paired to mass loss to infer chemical weathering rates (White et al.,

1999). The use of cosmogenic isotopes, i.e. beryllium isotopes (^{10}Be), to measure long-term chemical weathering rates of eroding catchments and soils will be discussed in the next section (section 1.3.2).

To determine chemical weathering rates in eroding soils using immobile element enrichments, a conservation of mass assumption must apply where the mass of weathered material in storage on the landscape is approximately constant over time. This assumption implies that the rate of transformation from bedrock to weathering products is equal to total denudation rate, which is defined as the sum rates of chemical weathering and physical erosion (Riebe et al., 2003; Brimhall Jr. and Dietrich, 1987):

$$R = D = E + W \tag{1-4}$$

where R is the conversion rate of bedrock to weathered material; D is the total denudation flux; E is the physical erosion flux of weathered material; and, W is the chemical weathering flux. All fluxes in Equation 1-4 are expressed as mass per area per time. Accordingly, rock and soil densities are not necessary in this expression. However, if using data from the literature that reports denudation rates in units of length per time, knowledge of the material density is necessary to yield a denudation flux which can then be used in Equation 1-4. The conservation of mass equation above can be written for individual elements in the rock and soil as such:

$$D \cdot [X]_{rock} = E \cdot [X]_{soil} + W_x \tag{1-5}$$

where $[X]_{rock}$ and $[X]_{soil}$ are the concentrations of the element of interest in the rock and soil, respectively, and W_x is the chemical weathering rate of that element. In the case of an immobile element, (e.g. Zr, Al, Ti), the W_x term is zero and can be ignored and one obtains:

$$D \cdot [Zr]_{rock} = E \cdot [Zr]_{soil} \tag{1-6}$$

where zirconium (Zr) is used as an example of an immobile element. Then rearranging Equations 1-4 and 1-5 one obtains:

$$W = D\left(1 - \frac{[Zr]_{rock}}{[Zr]_{soil}}\right) \tag{1-7}$$

Here, the chemical weathering rate is expressed as a fraction of the total denudation rate that is accounted for by chemical weathering, also referred to the chemical depletion factor (CDF) (Riebe

et al., 2003). The bulk chemical weathering rate in the soil in Equation 1-6 can then be partitioned into weathering rates of specific elements by rearranging Equations 1-5 and 1-6 which yields:

$$W_x = D\left([X]_{rock} - [X]_{soil}\frac{[Zr]_{rock}}{[Zr]_{soil}}\right) \quad (1\text{-}8)$$

By normalizing W_x to the total rate of denudation of element X, one is able to obtain the negative mass transfer coefficient for any element considered to be mobile during weathering reactions, which directly corresponds to those calculated by Brimhall Jr. and Dietrich (1987):

$$\frac{W_x}{D\cdot[X]_{rock}} = \left(1 - \frac{[X]_{soil}}{[X]_{rock}} \cdot \frac{[Zr]_{rock}}{[Zr]_{soil}}\right) = CDF_x \quad (1\text{-}9)$$

Equation 1-9 is similar to the expression in Equation 1-7, however it expresses chemical weathering rates as a fraction of the total denudation for individual elements, rather than the bulk soil as a whole.

This mass balance approach can also be used to determine weathering rates of individual soil units within a weathering profile and regolith as a whole. For example, in the case of regolith composed of saprolite which is overlain by soil, as in the case of the Rio Icacos watershed in Puerto Rico (Riebe et al., 2003): if we respect the law of mass conservation, that is to state that the conversion of rock to saprolite is balanced by chemical weathering in the saprolite and physical conversion of saprolite to soil, then the mass of the saprolite remains constant through time. This can be expressed as in two ways: saprolite as a whole (Equation 1-10) and for individual elements of interest within it (Equation 1-11):

$$W_{saprolite} = D\left(1 - \frac{[Zr]_{rock}}{[Zr]_{saprolite}}\right) \quad (1\text{-}10)$$

$$W_{x,saprolite} = D\left([X]_{rock} - [X]_{saprolite}\frac{[Zr]_{rock}}{[Zr]_{saprolite}}\right) \quad (1\text{-}11)$$

where $W_{saprolite}$ and $W_{x,saprolite}$ are the chemical weathering rates for the whole saprolite and for an individual element X within the saprolite, respectively; $[X]_{saprolite}$ and $[Zr]_{saprolite}$ are element X in the saprolite and the concentration of an immobile element in the saprolite (Zr in this example). The partitions of chemical weathering rates from an entire profile to the scale of

individual contributions from soil and saprolite weathering, allows quantification of the weathering regime within regolith profile.

Apart from mass transfer coefficients, there are several other commonly used chemical weathering indices or indices of alteration for characterizing chemical weathering in soil profiles and watersheds. Weathering indices essentially measure the degree of mobile element depletion relative to immobile elements during chemical weathering. Each index typically incorporates the bulk major element oxide chemistry into a single value, allowing comparisons between samples (typically as a function of depth within a profile). Changes in the bulk chemistry with depth within the profile are then attributed to the weathering regime of the parent material. Often these changes are gradual, steady, and continuous for homogenous rocks like granite (Sutton and Maynard, 1992) which reflect the continuous leaching of elements on homogenous host material. However, weathering profiles developed on heterogeneous, i.e. metamorphic, parent rocks often does not yield systematic trends of elemental change throughout the profile and highly complicates the interpretation of chemical weathering in the vertical profile (Price and Velbel, 2003). In this case, changes in major element concentrations between the parent rock and the soil or sediment could simply be attributed to variations in parent rock chemistry and minerology, and not the degree of weathering.

Examples of these indices of chemical weathering include the Weathering Index of Parker (WIP) (Parker, 1970), Chemical Index of Alteration (CIA) (Nesbitt and Young, 1982), Chemical Index of Weathering (CIW) (Harnois, 1988), and the Plagioclase Index of Alteration (PIA) (Fedo et al., 1995). The WIP is based on the proportions of alkali and alkaline earth metals present, as these are considered to be the most mobile of the major elements. Here, the bond strengths of major elements to oxygen are used as weighing factors, which measures the degree intensity of rock weathering with respect to the parent material and also its susceptibility to weathering. Since this index only includes highly mobile elements, it yields values that are significantly different than the parent rock. Hence, this proxy is most appropriate to use on profiles developed on heterogeneous bedrock.

Nesbitt and Young (1982) were the first to propose the CIA in an attempt to reconstruct paleoclimate from Early Proterozoic sediments north of Lake Huron (Canada). Since then, it has been widely used as a proxy of chemical weathering intensity in weathering profiles (e.g. Braun

et al., 2009), and in drainage basins (e.g. Li and Yang, 2010; Vital and Stattegger, 2000). The CIA is defined as:

$$CIA = \frac{Al_2O_3}{(Al_2O_3 + CaO^* + Na_2O + K_2O)} \times 100 \quad (1\text{-}12)$$

where all terms are molar contents, with CaO^* being the CaO content in the silicate fraction of the sample. The CIA values are typically interpreted as the extent to which feldspar has converted to clays (Fedo et al., 1995; Nesbitt and Young, 1982). McLennan (1993) first
calculated CIA values in the suspended load of rivers worldwide and found there to be a negative correlation between weathering history and sediment yield. More recently, Li and Yang (2010) re-calculated the CIA values of 44 rivers worldwide and suggested globally that the CIA is sensitive to land surface temperature, latitude of the river mouths and soil depth in the watershed, reflecting the integrated weathering history.

The CIW proposed by Harnois (1988) which is generally applied to modern soils and paleosols is very similar to the CIA, however K_2O is not part of the expression; it is defined as:

$$CIW = \frac{Al_2O_3}{(Al_2O_3 + CaO^* + Na_2O)} \times 100 \quad (1\text{-}13)$$

Here, all elements are in molar proportions and Al_2O_3 is used as the immobile element while CaO and Na_2O are the mobile elements that are readily leached during weathering reactions. The CIW does not include K_2O because most paleosols are enriched in potassium, which may be a diagenetic effect (Retallack, 1986). In solution, K^+ can be incorporated into K-minerals, preferentially absorbed on clays particles via ion exchange compared to Na^+ and Ca^{2+} which have lower exchange capacities than K^+ (Kronberg et al., 1987), or previously leached out and removed by soil solutions (Harnois, 1988). As other indices (e.g. CIA; WIP) use K_2O as a mobile component, this would limit their ability to interpret chemical weathering in paleosols and soils. Harnois (1988) argues that in order for a chemical weathering index to truly and accurately quantify the amount of chemical weathering in a sample (relative to the parent material) it should: 1) only include elements that have consistent geochemical behavior during weathering, 2) be independent of the state of oxidation of the weathered material, 3) only involve elements that are commonly reported in the literature, and 4) be simple and straightforward to use. Hence, in this view, this proxy is seen as a better estimate of the degree of weathering of a material relative to its source rock.

In the case where the plagioclase weathering alone needs to be monitored, the Plagioclase Index of Alteration (PIA) can be used:

$$PIA = \frac{(Al_2O_3 - K_20)}{(Al_2O_3 + CaO^* + Na_2 - K_20)} \times 100 \quad (1\text{-}14)$$

This equation is simply a modification of the CIA and CIW formulas. As stated earlier, there can be problems including K_20 in the weathering calculation (in the case of the CIA), as K is often enriched in certain materials, and leaving it out of the equation (in the case of the CIW) neglects the contribution of aluminum associated with K-feldspar. A comparison of the CIA, CIW, and PIA methods in a weathering profile of bedrock and saprolite is shown in Figure 1-5.

1.3.1.2 Dissolved and suspended loads

In addition to obtaining long-term weathering rates and intensities in weathering profiles using chemical mass balance techniques, modern silicate weathering rates can be studied in a similar manner by analyzing the major and trace elemental composition of riverine material and the dissolved load. River geochemistry can provide an enormous amount of data on various scales by integrating factors such as climatic, lithologic, and weathering. To model the global carbon cycle and better understand how atmospheric CO_2 has varied in the past, we first need to understand and be able to quantify the current global silicate weathering rate (Berner and Kothavala, 1994; Walker et al., 1981). In this effort, studies generally focus on large rivers with large drainage areas and floodplains such as rivers in the Amazon, Congo, Canadian Shield, and Himalayas (Dessert et al., 2003; Edmond et al., 1995; Gaillardet et al., 1995;1999; Lupker et al., 2012; Millot et al., 2002; Moon et al., 2014; Stallard and Edmond, 1983; Vital and Stattegger, 2000) and on the factors that control silicate weathering rates (West et al., 2005; Millot et al., 2002; White and Blum, 1995).

Chemical weathering rates at the catchment scale are typically quantified by measuring chemical fluxes in the dissolved load. These fluxes are calculated as the product of discharge and the concentrations of major elements. The concentrations of the ‘grab’ or ‘spot’ samples, (that is samples which are taken at a selected location, depth, and time) are then multiplied by mean annual precipitation and runoff values or temporally-averaged discharge values from gauging stations (Huh et al., 1998; Edmond et al., 1995). However, to accurately quantify silicate weathering rates,

high-temporal resolution sampling is needed of river chemistry and discharge in order to capture the overall variation of chemical fluxes and discharge regimes

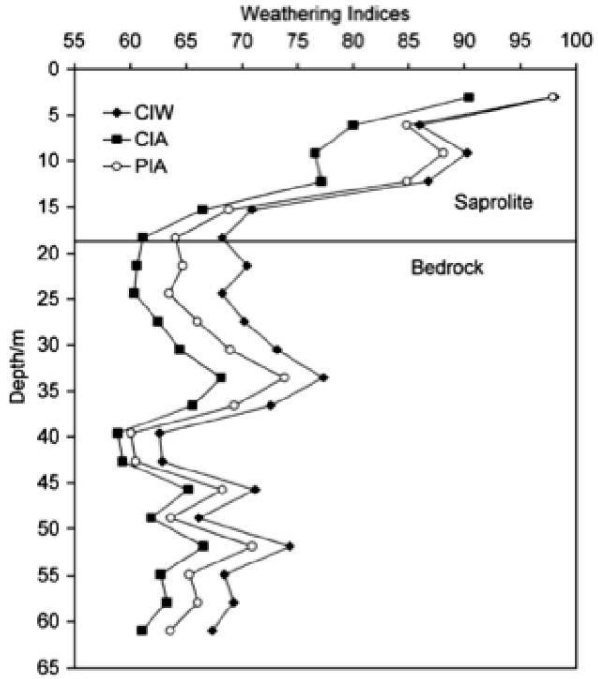

Figure 1-5. Chemical Index of Weathering (CIW), Chemical Index of Alteration (CIA), and Plagioclase Index of Alteration (PIA) taken from a weathering profile consisting of bedrock and saprolite. Source: Price and Velbel (2003).

(e.g. Moon et al., 2014). Additionally, chemical elements in the river may derive from various sources such as silicate and carbonate weathering, atmospheric inputs, evaporite dissolution, and anthropogenic sources. The identification and partitioning of sources is necessary to isolate the contribution of silicate weathering from the total dissolved load flux of the river (Meybeck, 1987; Garrels and Mackenzie, 1971).

There are two standard approaches to differentiate silicate vs. non-silicate chemical sources: forward and inverse models. Although both models use the composition of silicates to calculate the relative contribution of silicate weathering in the chemical fluxes, each take a different approach in determining the composition of silicates and calculating the contribution from each source. The forward method calculates the contribution of each source sequentially, by subtracting a pre-determined composition for each element from their measured concentration. The silicate fraction is then determined based on the corrected Na concentration and pre-

determined Ca/Na and Mg/Na ratio values for weathering of silicate rocks, which are taken from the underlying bedrock or from small catchments that drain exclusively silicate rocks (Moon et al., 2014).

Using this approach, Edmond et al. (1995) measured major element concentrations and found a clear chemical expression in the dissolved load derived from the primary weathering of bedrock in the Guayana Shield. by combining the dissolved load data in this study with the discharge and suspended load data from Meade et al. (1990), estimates of the chemical and mechanical weathering yield were made. Total denudation rates found to be extremely low (~10 m per Mya), with equal contributions from the dissolved and suspended loads. The relationship between elevation and weathering is not pronounced, with little difference in weathering rates between highland and lowlands. Here, continual recycling of sediment and little production of "new" sediment by actively eroding margins leads to a relatively small consumption of atmospheric CO_2.

Galy and France-Lanord (1999) took this approach and characterized the weathering reactions in different regions within the Ganges–Brahmaputra (G–B) Basin, spanning from Tibet to the Gangetic plain. Major element concentrations were measured in the dissolved load of stream waters within the Narayani basin in Nepalese Himalaya and in the G–B in Bangladesh with the goal of refining the budget of silicate weathering in the Himalayas. Carbonate dissolution was found to represent 80-90% of the total cationic charge in all of areas of their study basin, making it the lithological control on the chemical signature of rivers flowing north to south. Taken together with the fact that most Himalayan silicate rocks have alkaline compositions, this implies that the overall long-term CO_2 uptake related to modern Himalayan erosion seems to be minor on the global scale, similar to the findings of Edmond et al. (1995).

The other method to differentiate silicate from non-silicate sources is via the inverse model which calculates the contributions from chemical sources based on mass balance equations of Na-normalized elemental ratios of major elements (Garrels and Mackenzie, 1967). The mass balance equations can be written as:

$$\left(\frac{X}{Na}\right)_{dissolved\ load} = \sum_i \left(\frac{X}{Na}\right)_i \propto_{i,Na} \quad (1\text{-}15)$$

where the subscript i indicates a chemical source endmember, i.e. silicate, carbonate, precipitation, evaporite; X denotes the element of interest, i.e. Mg, Ca, Cl. The $\left(\frac{X}{Na}\right)_i$ ratio is the Na-normalized elemental ratios of the various source end-members; and $\propto_{i,Na}$ represents the mixing proportions of the end-members. Here, the sum of $\propto_{i,Na}$ values = 1. All data points will share the same $(X/Na)_i$ value, however each will have a different a $\propto_{i,Na}$ value. Starting from a range of *a priori* ranges of $(X/Na)_{i,}$, the model determines the best *a posteriori* value of both $(X/Na)_i$ and $\propto_{i,Na}$ (Moon et al., 2014). This model differs from the forward model in that it does not assign input ratio values from known sources but rather finds the best fit values for the chemical sources from observed datasets within an *a priori* range of values. This approach is favorable when the chemical compositions from monolithological silicate catchments is not known or trace inputs of calcite are suspected.

In the Congo, Négrel et al. (1993) used this approach to determine erosional sources by measuring Cl, Na, Mg, Ca, and Sr concentrations in the dissolved load in combination with Sr isotope compositions as a source tracer (Dasch, 1969). Here, dissolved Na inputs are dominated by silicate weathering, while both dissolved Ca and Mg inputs come from carbonate sources which even though are poorly exposed, significantly influence river geochemistry. Additionally, rainwater inputs to all river systems in the study have an impact on Ca, Mg, and Sr concentrations in the dissolved load.

This approach was also used by Gaillardet et al. (1999) in calculating global silicate weathering rates and CO_2 from sixty of the world's largest river systems. Here, weathering rates were calculated using Na-normalized ratios and source data from large rivers worldwide. Regarding sources of dissolved solutes, Gaillardet et al., (1999) finds that: 1) contribution of silicate weathering to the dissolved load of rivers never exceeds 40%; 2) all rivers are influenced to some extent by carbonate dissolution; and 3) for most large rivers, rain inputs are negligible. A good correlation is observed between 1) cationic silicate weathering fluxes and the total silicate weathering fluxes (Figure 1-6a) and 2) the flux of CO_2 removed from the atmosphere via weathering of aluminosilicates (Figure 1-6b). The cationic weathering rates (either total: Na+ K+ Ca+ Mg; or derived from Ca-Mg silicates: Ca + Mg) are given because for some rivers, dissolved silica represents the major component of the TDS coming from silicate weathering. Rivers that are rich in silica (Amazon, Zaire, Orinoco, Niger, Zambese) somewhat deviate from these global

trends. These important findings then suggest that the time frame in which silicate weathering can influence atmospheric CO_2 may be much shorter than originally proposed by Berner et al. (1983).

In the Mackenzie River basin (Canada), Millot et al. (2003) used the inverse approach, similar to both Négrel et al. (1993) and Gaillardet et al. (1999), on Sr isotopes and chemical ratios of the suspended and dissolved loads of the Mackenzie River and its tributaries to distinguish between the weathering of silicate and carbonate fractions. The overall aim of this study was to determine the erosion rates of rocks under cold climatic conditions. Results from both (chemical ratio and Sr isotopes) inversions show that the chemistry of Mackenzie Basin rivers is derived primarily from the weathering of sedimentary rocks. The Sr isotope compositions of the dissolved load reveal that the presence of unradiogenic carbonate rocks can explain the gradual decrease of the Sr isotope ratio from the headwaters out to the ocean, confirming the extreme sensitivity of Sr isotopes to lithology types. A surprising but important finding of this study was that chemical denudation rate of silicate minerals was much higher (3 or 4 times) in the lowlands (Interior Platform) than compared to those in the Rocky and Mackenzie Mountains. This result contradicts the "Raymo hypothesis" (Raymo and Ruddiman, 1992) that states that mountains are the place where erosion and chemical weathering is accelerated (see earlier discussion in Section 1.2.1). Reasons for higher chemical denudation and weathering in low-lying areas was attributed to poorly lithified sediments and the contributions of local factors such as organic material which can enhance weathering yields even at low temperatures.

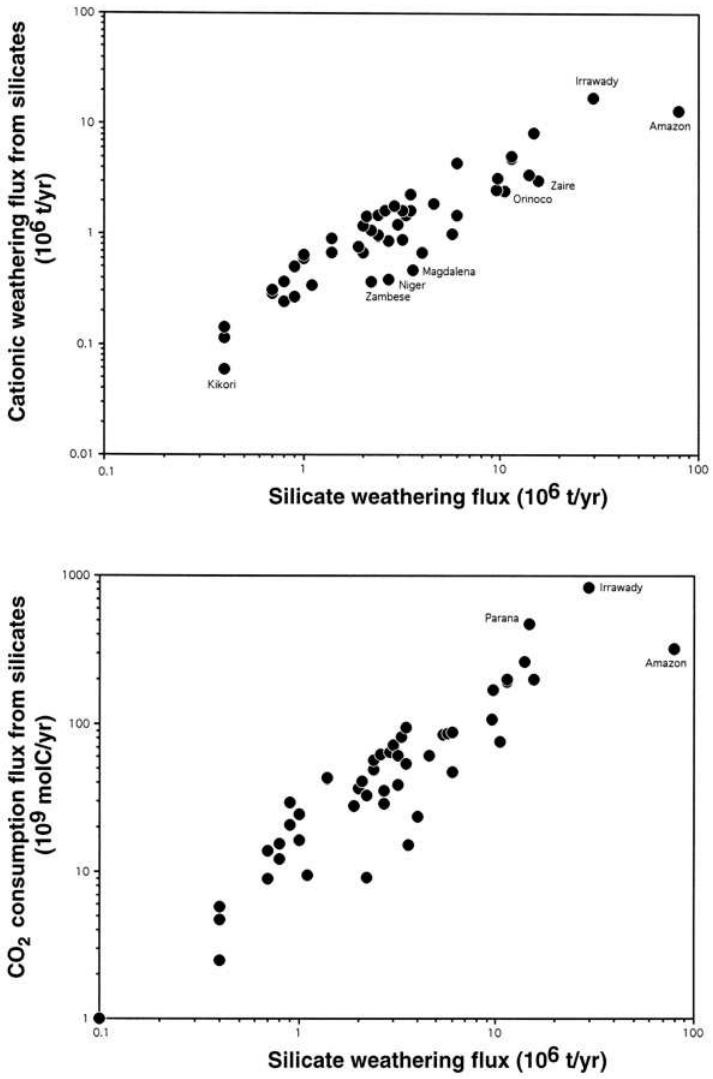

Figure 1-6. Relationships between the fluxes of material coming from chemical weathering of silicates and a) the fluxes of cations from the weathering of silicate material and b) the flux of CO_2 removed from the atmosphere from weathering attributed to aluminosilicate weathering. Source: Gaillardet et al. (1999)

1.3.1.3 River sediments

As shown in the studies above, modern denudation and weathering rates are often derived from river solute and suspended load fluxes in some of the world's largest river systems, providing reasonable estimates of CO_2 consumption via the weathering of silicates.

However, studies that focus on solid phases such as the suspended load, bedload, and detrital material, e.g. Bouchez et al. (2012); Gaillardet et al. (1999b); Gislason et al. (2006), have received

much less attention possibly because of the difficulties in integrating temporal and spatial variability of detrital sediments. An example of a novel study that used the sediment record in the Ganga fluvial system to understand and quantify the link between chemical weathering and the chemical composition of river sediment is Lupker et al. (2012). They argue that although this Himalayan system has gained much attention in the literature (e.g. Galy and France-Lanord, 1999; France-Lanord and Derry, 1997; Raymo et al., 1988) regarding the role mountain uplift plays in promoting physical erosion, chemical weathering, and ultimately atmospheric CO_2 consumption, the budget and '*locus'* (meaning location or place) of weathering within the entire Himalayan basin has not been established. Although, Galy and France-Lanord (1999) and West et al. (2005) both point to the floodplain as a key component in the weathering budget. From Galy and France-Lanord, (2001), major elements (K, Fe, Na, Si, Al), carbonate content, and sediment hydration were measured in the suspended and bedload sediments to characterize the weathering regime. To remove mineralogical sorting effects from the chemical weathering signal (and possible downstream evolution), element concentrations are normalized to silicon (Si) content to exclude dilution effects (Galy and France-Lanord, 2001) and plotted as function of their Al/Si molar ratio (see example in Figure 1-8 from Bouchez et al., 2012). The Al/Si ratio is used as proxy of mineral sorting (linked to grain size), as coarse-grained material will be enriched in quartz having a low Al/Si ratio and finer-grained material enriched in phyllosilicates/clay minerals that tend to have higher Al/Si ratios. To determine the role the floodplain in chemical weathering of sediments, the weathering regime is characterized and quantified from source to sink. For a select grain size fraction, the loss or gain of the mobile element, X, relative to Si $(\Delta X/Si)^i$ can be calculated from the difference in X/Si composition between upstream and downstream river sediment samples:

$$(\Delta X/Si)^i = \left(\frac{X}{Si}\right)^i_{upstream} - \left(\frac{X}{Si}\right)^i_{downstream} \quad (1\text{-}16)$$

The average loss of mobile elements ($\Delta\overline{X/Si}$) for a given river reach can also be determined if the average Al/Si ratio of the transported sediment is known:

$$\Delta\overline{X/Si} = \left(\overline{X/Si}_{upstream} - \overline{X/Si}_{downstream}\right) \quad (1\text{-}17)$$

To determine where in the system mobile elements are being lost, Lupker et al. (2012) divide the Himalayas into three sub-regions (Himalayan Range; Floodplain North, and Floodplain South) in order to partition the loss of mobile elements occurring throughout the range. The average mobile element loss (relative to Si) in each sub-region was then determined by subtracting the average element loss from the sub-region directly upstream. Results from their dataset and analyses show that by using the relationship between silicon-normalized mobile element concentration and Al/Si ratios it is possible to determine the average chemical composition of a targeted river reach and hence trace its evolution downstream. Spatial analysis, combined with temporal discharge data allow the loss of chemical elements in the sediment to be budgeted. Lupker et al. (2012) show that 1) sediment undergo significant major element loss accompanied by a gain in hydration during floodplain transfer;

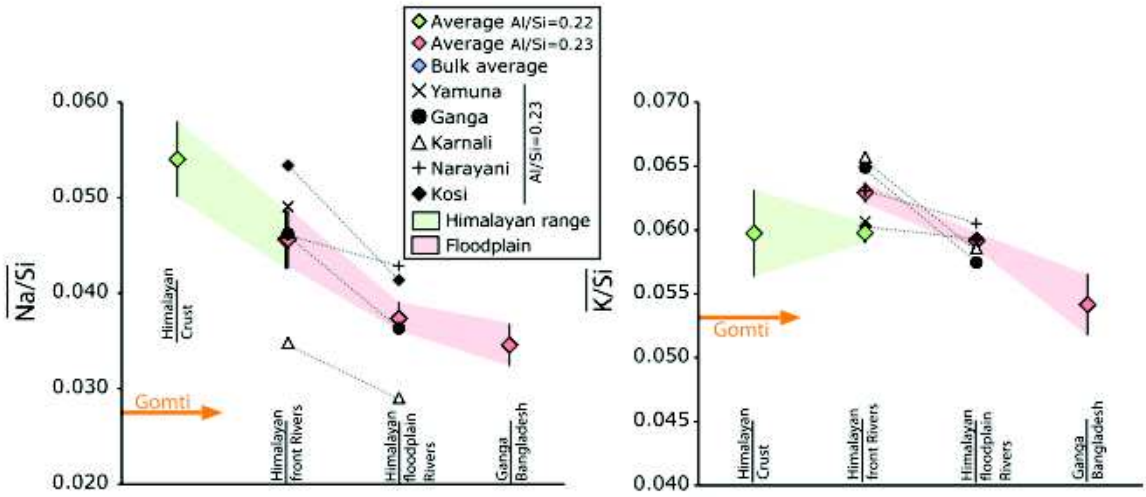

Figure 1-7. Evolution of the normalized mobile elements composition (relative to Si) of Himalayan sediments. Green shading represents the weathering in the Himalayan range; red shading represents weathering in the floodplain. Source: Lupker et al. (2012).

2) weathering on the floodplain is significant; and 3) carbonate dissolution accounts for most of the weathering which ultimately makes the floodplain a relatively limited carbon sink. In agreement with other studies (e.g. Millot et al., 2003), these results then suggests that weathering not only occurs in uplifted, erosion-prone areas, but also in the lowlands.

Following a similar approach as Lupker et al. (2012), Bouchez et al. (2012) analyzed major chemical elements (Na, K, Mg, Ca) of the suspended load in river depth profiles taken at various locations in the Amazon River basin. Here, weathering intensities were calculated based on the

loss of major elements derived from weathering reactions during transport, in three different tributary reaches (two in the headwaters and one on the floodplain). Water discharge data in this study was provided by Moquet et al. (2011). To determine the loss or gain of soluble elements in the sediment composition between two points in the river, a steady-state mass balance is written in regard to each sediment grain size, by using the Al/Si ratio, which states that the sum of the particulate flux of a mobile element at the mouth of the river is equal to sum of the particulate flux coming from tributary inputs minus the flux from sediment deposition from the channel to the floodplain, plus the flux of floodplain sediment incorporation to the channel. They consider no imbalance between deposition and incorporation of sediment into the channel, but that a gain or loss of mobile elements may occur in sediments that are stored in the floodplain. Sediments are then analyzed based on their Al/Si and X/Al ratios. As explained earlier, the Al/Si ratio is proxy for grain size, where coarse material have lower Al/Si values due to increased content of Si and fine material are Al-rich; intermediate sediments represent a mixture of each end-member. The X/Al ratio is considered a weathering proxy because major elements like Na, K, Mg, and Ca are soluble during weathering reactions; Al is considered a major insoluble element, not preferentially carried by any accessory minerals (Bouchez et al., 2011; Dupré et al., 1996), and can be used to correct for the dilution of quartz. Using both X/Al and Al/Si proxies then allows a weathering characterization which is corrected for grain-size sorting. Conceptually, this is shown in Figure 1-8. The brown star represents the fine grained end-member of sediment carried by the river, typical of a sample at that channel surface, and the yellow star is the coarse grained end-member, typical of a sample at the bottom of channel. All samples taken at intermediate depths are a mixture of each end-member that depend on sorting/mixing processes. In this example, weathering induces a change in the X/Al ratio during transport between upstream and downstream locations; for example mineral dissolution would cause a decrease in the X/Al ratio. Here, Si loss due to weathering processes was found to be negligible and therefore can be ignored. On the contrary, incorporation of soluble elements into the clay fraction will lead to an upward shirt in the diagram if the source(s) are external to the catchment (not shown). Results from this study show that the chemistry of sediment does not dramatically change downstream and therefore changes in chemical composition associated with chemical weathering in floodplains are small. However, due to the overall smaller fluxes carried by the dissolved load, changes of chemical weathering on the floodplain should be more strongly expressed in the dissolved load.

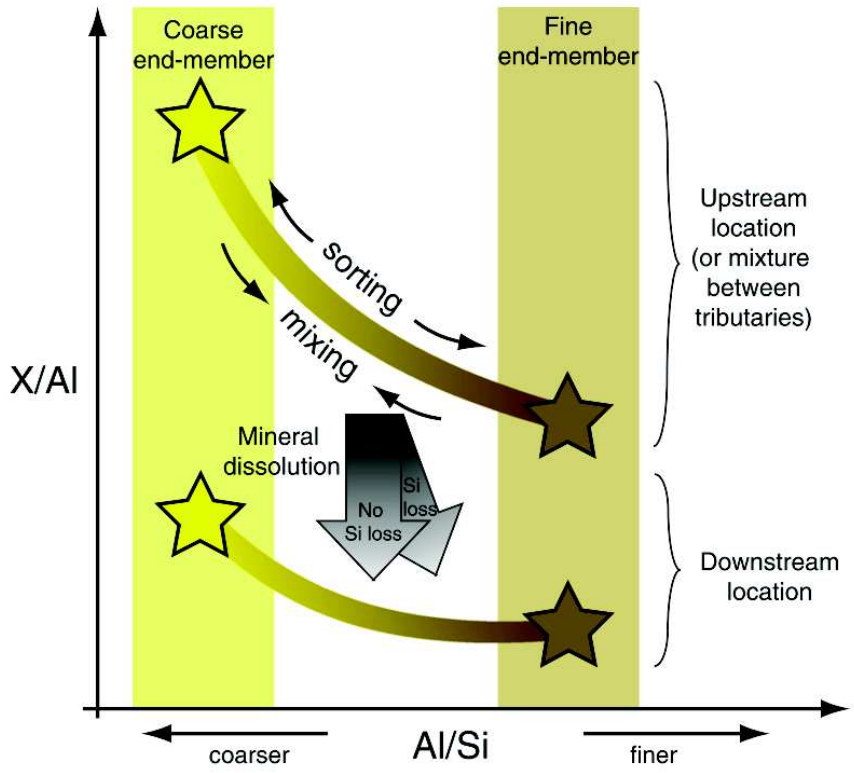

Figure 1-8. Conceptual diagram of an Al-normalized soluble element concentration (X/Al) used as a weathering index, as function of Al/Si, used as a grain size proxy. The brown star represents the fine grained end-member (channel surface) of sediment carried by the river and the yellow star is the coarse grained end-member (bottom of channel). All samples taken at intermediate depths are a mixture of each end-member that depend on sorting/mixing processes. In this example, weathering indices a changes in the X/Al ratio during transport between upstream and downstream locations; an example being that mineral dissolution would cause a decrease in the X/Al ratio. Here, Si loss due to weathering processes can be ignored. Source: Bouchez et al. (2012).

As demonstrated above, the use of mobile and immobile elements as weathering proxies can be a very tool in quantifying the weathering regime in a variety of environments including soil profiles and rivers. For example, in soil profiles, mass balance approaches to determine element loss using mass transfer coefficients and chemical weathering proxies such as the CIW, CIA, and PIA are very useful in deriving chemical weathering rates (e.g. Price and Velbel, 2003; Brimhall Jr. and Dietrich, 1987). In rivers, major and trace element analyses of the dissolved and suspended loads can provide an enormous amount of information as rivers integrates factors such as lithology, climate, and weathering. When study the world's largest rivers (e.g. Moon et al., 2014; Gaillardet et al., 1999b), modern global silicate weathering rates can be estimated, which

can then be used to model the global carbon cycle and associated CO_2 consumption rates. Although harder to interpret than the dissolved load, the use of river sediments and transported detrital material have proven very useful in estimating weathering fluxes and the 'lotus' or place of chemical weathering in the watershed (Bouchez et al., 2012; Lupker et al., 2012). However, the use of elemental concentrations in deriving weathering fluxes, whether in soil profiles, dissolved load of rivers, or river sediments, suffers from the dominant control lithology plays on sediment and dissolved load compositions. Additionally, sediment sorting in rivers also adds to the difficulty in quantifying weathering reactions at the catchment scale.

1.3.2 Radiogenic and cosmogenic isotope approach

The use of radiogenic (e.g. U-series) and cosmogenic (e.g. ^{10}Be, ^{26}Al) isotopes to study erosion and weathering are an alternative and often complimentary approach to the use of major and trace elements. They are an integral part in the effort of refining the geologic timescale, calibrating events in Earth's history, and provide quantitative information about rates of landscape evolution.

1.3.2.1 Soil Profiles

Analytical advancements in the precise measurement of U-series nuclides (^{238}U– ^{234}U–^{230}Th) in geological material have recently (40 – 50 years) led to the study of U-series nuclides in weathering profiles and soils and the ability to quantify regolith production along weathering profiles (e.g. Ackerer et al., 2016; Chabaux, 2003; Dosseto et al., 2008; Ma et al., 2010). The use of U-series nuclides is primarily based on the ($^{234}U/^{238}U$) and ($^{230}Th/^{234}U$) activity ratios which provide estimates of regolith and soil production rates and timescales of chemical weathering. The ability to use the U-series radioactive disequilibria as both a tracer and chronometer of weathering processes stems from the dual property of the nuclides series in which: a) fractionation occurs during water-rock interaction and b) nuclides have radioactive periods of the same order of magnitude as the time constants of most weathering processes and subsequent transfers to ground and river waters (Chabaux, 2003). During chemical weathering, ^{234}U is preferentially lost from minerals compared to ^{238}U, resulting from recoil and preferential leaching (Carroll, 1970). The

loss of ^{234}U continues through time since the weathering reaction began, referred to as the 'weathering age' (Dosseto et al., 2014), which results in a lower $^{234}U/^{238}U$ ratio. This ratio is expressed as $\delta^{234}U$, where $\delta^{234}U = (\lambda_{234} \cdot N_{234} / (\lambda_{238} \cdot N_{238} - 1)$ x 1000; units are in parts per thousand (‰). Here, λ represents the decay constant (yr^{-1}); N the number of atoms for each isotope; and the subscripts 234 and 238 represent the ^{234}U and ^{238}U isotopes, respectively. In soil profiles, $\delta^{234}U$ values are expected to decrease with depth as the weathering age increase (Rothacker et al., 2018).

An example of the application of U-series isotopes to quantify regolith formation rates on shale lithology was performed by Ma et al. (2010) in three weathering profiles on a hillslope at the Susquehanna/Shale Hills Observatory in central Pennsylvania. All profiles displayed significant $^{234}U - ^{238}U$ disequilibria whose activity ratios are consistent with U-series isotope fractionation during chemical weathering and relative element mobility which decrease in the following order: $^{234}U > ^{238}U > ^{230}Th$. Depth profiles can be explained by a) loss of U-series isotopes during water-rock interactions and b) re-deposition of these U-series isotopes downslope. Here, regolith production rates calculated using U-series isotopes systematically decrease from 45 m/Myr to 17 m/Myr with increasing regolith thickness from the ridge to the valley floor. The apparent equivalent regolith residence times increase from 7 to 40 kyr with increasing distance from the ridge to the valley floor. Considering peri-glacial climatic conditions and an average erosion rate ~15 m/Myr, it was concluded that the hillslope retains the regolith formed before the peri-glacial conditions and geomorphologically is not at steady state. This research demonstrates the use of U-series isotopes in constraining chemical weathering timescales and regolith production rates.

The application of cosmogenic ^{10}Be and ^{26}Al measurements in depth profiles have enabled the estimation of exposure ages, mean denudation rates, and soil production rates (Braucher et al., 2003; Heimsath et al., 2000; Brown et al., 1995; McKean et al., 1993). In-situ ^{10}Be and ^{26}Al isotopes have also been used to determine regolith denudation rates (Ferrier and Kirchner, 2008; Small et al., 1999) and to constrain the age of depositional landscape features such as alluvial terraces and fans (Schaller et al., 2002; Anderson et al., 1996). In the case of cosmogenic isotopes such as ^{10}Be and ^{26}Al, cosmic rays induce in-situ nuclear reactions which produce rare nuclides within mineral grains in soils and rocks which accumulate at or immediately below Earth's surface. To quantify erosion or exposure time, it is essential to know how their production varies with depth with the profile. Since the production rates of most cosmogenic nuclides decrease exponentially

with depth, their concentrations in substrates are directly linked to the time of surface or near-surface exposure (Brown et al., 1991; Lal, 1991). These properties make it a powerful tool to trace and date transported sediment. However, to be able to use in situ nuclides for the study of erosional histories of sediments, one must first have knowledge of production rates under different irradiation conditions such as latitude, altitude, irradiation geometry, and shielding (Lal, 1991).

Recently, Ackerer et al. (2016) used U-series isotopes and in-situ ^{10}Be together to independently constrain production and denudation rates of regolith in a weathering profile in the Strengbach catchment (France). The mean production rate of regolith using U-series isotopes was estimated using a system of equations that describe the radioactive decay and loss and gain constants over time between a reference weathering state and the sample's current state (for review see Dosseto et al., 2008). The depth variations of in-situ ^{10}Be concentrations within the weathering profile were determined using the method described by Braucher et al. (2003). The denudation rates determined by cosmogenic nuclides were then used in combination with geochemical mass balance approach of the chemical depletion factor (CDF) described by Riebe et al. (2003) allowing them to distinguish the chemical and physical components of the total denudation as well as estimating the long-term weathering fluxes along the regolith profile. Results from this combined proxy approach suggest that the long-term evolution of the regolith in the Strengbach catchment is relatively close to steady- state and that physical erosion is the dominant process of regolith loss in the catchment.

1.3.2.2 Sediments transported by rivers

Uranium-series and ^{10}Be isotopes have also been used in river material to trace and determine quantitative time constraints on the transfer of erosion products from source to sink (i.e. Brown et al., 1988; Dosseto et al., 2014, 2010; Handley et al., 2013), providing a better understanding of sediment transport processes and ultimately the long-term evolution of Earth's surface. For example, Schaller et al. (2002) measured cosmogenic ^{10}Be in river-borne quartz sands in fluvial terraces in France (Allier and Dore catchments) and the Netherlands (Meuse River) to derived paleo-erosion rates. After correction for post-depositional effects on the ^{10}Be concentrations of quartz grains, palao-erosion rates in the terraces along the Allier River varied between 40 and 70 mm/kyr where the highest value occurred during the Pleistocene-Holocene

transition, while those from the Dore terraces varied between 48 and 53 mm/kyr and remained relatively constant over time (within error between ~15 kyr and 5 kyr). Differences between catchments were attributed to possible differences in glaciation history and relief. Their method was independently verified by comparing their ^{10}Be-derived paleo-erosion rates with a study that estimated paleo-erosion rates in nearby lake deposits within the same (Allier) catchment (Macaire et al., 1997) and erosion rates between the two studies are in good agreement. In the Meuse terraces, paleo-erosion rates decreased steadily from 81 mm/kyr in the late Pleistocene to 31 mm/kyr in the Holocene, with enhanced erosion rates during the last glacial maximum (LGM) when peri-glacial processes prevailed in the catchment. The estimates of paleo-erosion using modern river sediments agree well with the Holocene estimation taken from the river terraces.

Recently Dosseto et al. (2014) applied U-series isotopes to riverine material in two spatial distinct small granitic catchments: Nunnock River catchment (SE Australia) and Puerto Rico in order to determine the controls the U-series isotope composition of river material and to understand how erosion products acquire their geochemical compositions. Here, thorium (Th) isotopes record the origin of sediments and the dissolved load; stream solutes mainly derive from the deepest part of the weathering profile; and stream sediment originate from shallower horizons. These observations suggest solute and sediments have distinct origins in environments where thick weathering profiles have developed. The weathering ages of sediments were modeled using the method in Dosseto et al. (2008) and reveal much older weathering ages in Australian stream sediments (between 346 kyr and 1.8 Myr) compared to Puerto Rican (between 5 and 19 kyr) reflecting the type of erosion in each catchment. The old ages likely reflect shallow erosion of sediment mobilized by near-surface soil transport, while the younger weathering ages in Puerto Rico likely reflect sediments derived from less weathered, deeper profiles mobilized by landslides. In this study, U-series-derived weathering ages were also used to calculate catchment-wide weathering rates, demonstrating the usefulness of U-series isotopes in not only constraining weathering ages of eroded sediment but also in estimating weathering rates in small catchments.

Although there are others, these studies illustrate the ability of both of radiogenic and cosmogenic isotopes to resolve issues regarding the rates of regolith and sediment production, style and rates of erosion, timescales of sedimentary processes, and depositional characteristic of sediment on the landscape from source to sink. Ultimately, the use of radiogenic (and cosmogenic)

isotopes enables a better understanding of the relationships between tectonics, climate, and landscape evolution, and enhance the use of geochronology (DePaolo et al., 2006).

1.3.3 Non-traditional stable isotope approach

The chemical composition of the components in the weathering zone (i.e. unweathered substrate, bulk saprolite, soil and sediments, organic matter, soil and river water, etc.) is controlled by the partitioning of elements during various weathering reactions (Bouchez et al., 2013). However, the use of elemental concentrations and ratios to quantify and trace physico-chemical processes in the weathering zone suffer from a variety of problems such as the dominant control lithological plays on the weathering regime and mineral sorting effects. As such, estimates of chemical weathering using major and trace element ratios may be crude. Alternatively, the mass-dependent fractionation of "non-traditional" stable isotopes of metals and metalloids (e.g. Li, B, Ca, Mg, Sr) imprints a strong signal on material in the weathering zone which can be used to track elemental fluxes. The composition of this signal depends on specific physico-chemical processes that induce a characteristic shift in the isotope ratios of the elements involved. In spite of the years of progress in the field, pinpointing the exact processes that result in isotopic shifts remains difficult. Hence, much is still to be learned in this relatively new field. A conceptual and mathematical framework which to interpret these isotope ratios was provided by Bouchez et al. (2013) who takes a steady-state elemental and isotopic mass balance approach to model the various components in the weathering zone, designed to be applicable to any element affected by stable isotope fractionation. This model 1) links novel stable ratios with weathering processes through the use of element fluxes, 2) presents a diverse spatial-scale approach (from the soil profile to large rivers to entire continents), and 3) enables the calibration of isotope fractionation factors based on field measurements. The conceptual diagram of this model and summary of symbols are shown in Figure 1-9. Five compartments are represented in the weathering zone, regardless of geomorphological setting. The saprolite and soil are lumped into one term regolith, which is then divided into three compartments based on their mineralogical and structural composition, and their process: a) unweathered primary minerals, b) secondary solid weathering products which include elements adsorbed onto mineral surfaces, precipitates, clays, oxi-hydroxides, and c) solid organic material comprised of litter fall or dead roots. Water passing through the regolith is termed 'soil water' which includes dissolved inorganic and organic species. Plants take up their nutrients from

this compartment and secondary weathering products are precipitated. In this case, the weathering zones is treated as a 'batch reactor' indicating that all compartments interact with one another in their entirety (Bouchez et al., 2013). The use and premise of this model assumes a steady state, implying that within each box or component, over some time scale, incoming mass fluxes balance outgoing fluxes for each and every isotope or element considered.

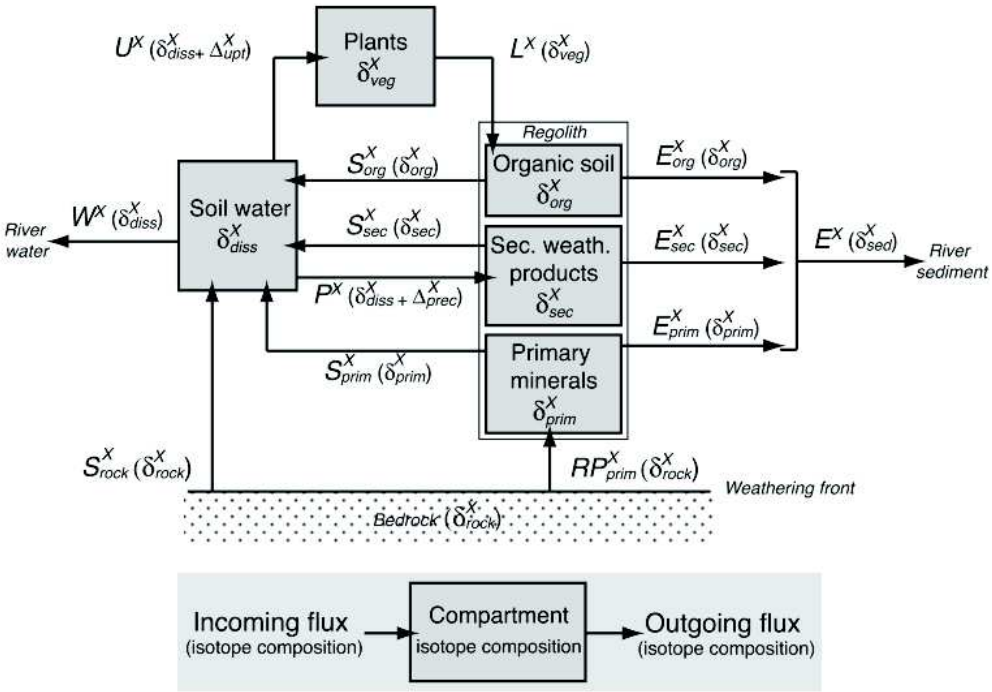

Figure 1-9. Schematic diagram of the weathering zone model. Source: Bouchez et al. (2013).

Table 1-1. Summary of symbols corresponding to Figure 1-9. Source: Bouchez et al. (2013).

Summary of symbols

	Total mass fluxes (for example in kg m^{-2} yr^{-1})
RP	Regolith production [$RP = D$ at steady-state]
E	Erosion
W	Weathering
D	Denudation [$D = E + W$ at steady-state]
	Dimensional elemental fluxes F^X (for example in mol_X m^{-2} yr^{-1})
S^X_{rock}	Dissolution ("solubilization") of X from primary minerals at the weathering front
RP^X_{prim}	Transfer of X in primary minerals from bedrock to regolith at the weathering front
W^X	Dissolved export of X ("weathering")
E^X	Particulate export of X ("erosion") [$E^X = E^X_{prim} + E^X_{sec} + E^X_{org}$ by definition]
U^X	Uptake of X by plants [$U^X = L^X$ at steady-state]
L^X	Flux of X from plants to soil through litter fall
P^X	Incorporation of X into secondary weathering products (including adsorption)
S^X_{prim}	Dissolution of X ("solubilization") from primary minerals in the regolith
E^X_{prim}	Erosion of X contained in primary minerals [$E^X_{prim} = RP^X_{prim} - S^X_{prim}$ at steady-state]
S^X_{sec}	Dissolution of X ("solubilization") from secondary weathering products in the regolith
E^X_{sec}	Erosion of X contained in secondary weathering products [$E^X_{sec} = P^X - S^X_{sec}$ at steady-state]
S^X_{org}	Dissolution of X ("solubilization") from organic matter in the regolith
E^X_{org}	Erosion of X contained in organic matter [$E^X_{org} = L^X - S^X_{org}$ at steady-state]

(continued)

	Isotope composition (in ‰)
δ^X_{rock}	Isotope composition of *X* in bedrock
δ^X_{prim}	Isotope composition of *X* in regolith primary minerals
δ^X_{sec}	Isotope composition of *X* in secondary weathering products
δ^X_{org}	Isotope composition of *X* in regolith organic matter
δ^X_{veg}	Isotope composition of *X* in vegetation
δ^X_{sed}	Isotope composition of *X* in bulk top soil or rover sediment
δ^X_{diss}	Isotope composition of *X* in soil- or river water
	Isotope fractionation factor (in ‰)
Δ^X_{prec}	Isotope fractionation factor associated with precipitation of secondary weathering products (including adsorption)
Δ^X_{upt}	Isotope fractionation factor associated with uptake by plants
$\overline{\Delta}^X$	"Lumped" isotope fractionation factor [includes precipitation and uptake by plants]

1.4 Boron and boron isotopes

1.4.1 General overview of boron isotopes

Boron (B), a moderately volatile metalloid, is a relatively light (atomic number 5) and low-abundance element in the Earth's crust because of its poor stability during nucleosynthesis reactions in stars. Crystalline boron is a very hard, black material with a melting point about 2000°C, however it also exists in three other polymorphs. Boron is highly incompatible during magmatic processes which results in the continental crust being highly enriched (~10 ppm) compared to the mantle (~0.1 ppm) (Gao et al., 2004). Boron is present at Earth's surface in its more common naturally occurring compounds such as borate minerals. Boron forms covalent, rather that ionic, bonds owing to its high ionization potential. Boron has two stable isotopes, ^{10}B and ^{11}B, which make up approximately 19.82% and 80.18% of total boron, respectively. Boron isotope ratios are given in the delta notation $\delta^{11}B$ (‰) and defined as the deviation from the standard NIST-SRM 951 (Catanzaro, 1970):

$$\delta^{11}B\ (‰) = [(^{11}B/^{10}B)_{sample} / (^{11}B/^{10}B)_{NIST\text{-}SRM\ 951} - 1] \times 1000 \qquad (1\text{-}18)$$

The large relative mass difference (10%) between ^{10}B and ^{11}B leads to significant boron isotopic fractionation during geologic processes, particularly low temperature water-rock interactions (Lemarchand et al., 2002a, 2012; Schmitt et al., 2012; Muttik et al., 2011; Spivack et al., 1987; Schwarcz et al., 1969). Unlike most other stable isotope systems, but similar to lithium (Li), the heavy and odd mass isotope ^{11}B is the dominant species, such that the average $^{11}B/^{10}B$ in nature is approximately 4.05. This particular feature is due to a combination of nuclear instability in stars during nucleosynthesis and a high neutron cross section producing stable ^{11}B after capture of a neutron by the ^{10}B isotope. Boron is a very soluble element in aqueous environments and has a high geochemical reactivity. In solution, B is present as two dissolved species, boric acid and borate ion, the proportion of which is dependent on the pH of the solution (Hershey et al., 1986) (see discussion below); this leads to large isotope fractionation between these two species and produces quite diverse $\delta^{11}B$ values in different environments. In nature, strong isotope fractionations produce $\delta^{11}B$ values between –70‰ (Leeman et al., 2004) and +75‰ (Hogan and Blum, 2003). Figure 1-10 displays the $\delta^{11}B$ variation in different natural reservoirs. Due to the long residence time of boron in seawater (about 10 Ma) (Chaussidon and Albarède, 1992) modern seawater taken from offshore has a nearly constant $\delta^{11}B$ value of +39.7 ± 0.3‰ (n = 17, 2SE) (Palmer et al., 1998). The continental crust and most plutonic rocks have $\delta^{11}B$ values ranging from approximately 0‰ to –20‰ with an estimated mean value of –7‰ (Chaussidon and Albarède, 1992); in non-marine evaporitic and tourmaline minerals in the continental crust up to +60‰ in brines from salt lakes (Palmer and Swihart, 1996). The B isotope composition in rainwaters can vary significantly from –10‰ to +45‰ with an average $\delta^{11}B$ value of about +20‰. Hence, the large isotopic fractionation observed in nature makes boron suitable to investigate various Earth surface processes such as water-rock interactions, including those involving a biological component (as B is highly fractionated by vegetation) (Cividini et al., 2010) and well as in the deep crust and mantle (Leeman et al., 2004).

In silicates, boron substitutes for Si or Al which makes it part of the group of structure-forming elements. Silicate minerals display large variations in B concentrations with orders of magnitude between them in increasing order: quartz (only traces), feldspars and plagioclases (~10 ppm); phyllosilicates (~100 ppm); and secondary clay minerals displaying a very large range in B content (as high as 10 wt% in tourmaline). The concentration of B in clay minerals is highly dependent on the context in which they formed; examples include: boron content, salinity, and

water temperature of the solution from which they formed; grain size of minerals formed (fine clays are more enriched than coarser clays); and type of minerals formed (e.g. illite or mica contain more B than other mineral types) (Harder, 1970). Incorporation of B into illite, for example, occurs in two steps (Harder, 1970): 1) adsorption of boron-anion on the clay surface, occurring very quickly. This reaction is reversible, suggesting that the ionic bonds to the surface layer of illite are weak because the adsorbed B is able to be desorbed very easily. The second step of boron uptake involves the incorporation in the tetrahedral sites of the mica structure. This process occurs very slowly and the attachment bonds are very strong. Boron distribution between the crystalline structure and interlayer sites is highly variability and depends on the rate of mineral transformation (from illite to smectite) and the progression of the reaction between the mineral and contact fluid (Voinot et al., 2013; Williams, 2001). In carbonates, boron content and isotopic composition is pH-dependent and has been utilized as a proxy to reconstruct seawater paleo-pH from various marine records by several studies, (e.g. Kakihana et al. (1977); Klochko et al. (2006); Lemarchand et al. (2000); Palmer et al., (1998).

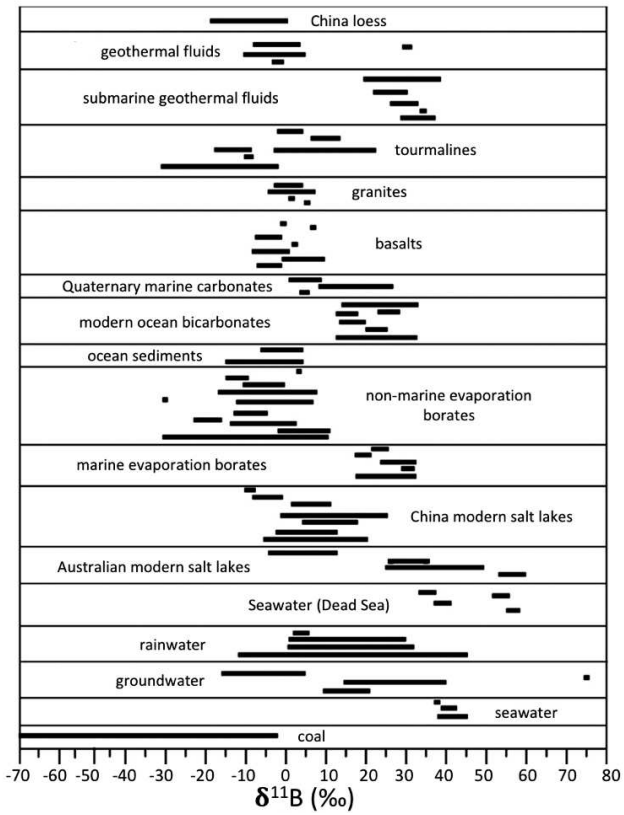

Figure 1-10. Boron isotopic compositions in nature. Source: Xiao et al., (2013).

1.4.2 Isotope fractionation processes

1.4.2.1 Adsorption of dissolved B on mineral surfaces

In aqueous solutions, dissolved boron is present as boric acid $B(OH)_3$, the borate ion $B(OH)_4^-$, polyborates and borates (i.e. $NaB(OH)_4^+$, $MgB(OH)_4^+$ and $CaB(OH)_4^+$); in seawater the dominant species are trigonal and tetrahedral forms (Hershey et al., 1986). At low concentrations, the relative proportion of the two species is mainly a function of pH, unlike high concentrations where speciation is also influenced by the formation of polyborates (Palmer et al., 1987). In solution with low pH, boron is predominately present as $B(OH)_3$ and as $B(OH)_4^-$ at high pH. The ionization of boric acid is expressed as:

$$B(OH)_3 + H_2O = B(OH)_4^- + H^+ \quad (1\text{-}19)$$

Hershey et al. (1986) and Vengosh et al. (1991) have studied the ionization of boric acid experimentally in a variety of Na-Cl-Ca-Mg solutions at 25°C; results shows that when applied to typical seawater (pK* = 8.83; pH = 8.2), the mole fractions of $B(OH)_3$ and $B(OH)_4^-$ species are calculated to be 0.81 and 0.19, respectively. In seawater for example, the two aqueous species are in a pH-dependent equilibrium which can be expressed as:

$$^{10}B(OH)_3 + [^{11}B(OH)_4]^- \leftrightarrow {}^{11}B(OH)_3 + [^{10}B(OH)^4]^- \quad (1\text{-}20)$$

The isotopic composition of the seawater is governed by B isotope exchange between the two aqueous species. Vengosh et al. (1991) proposed that the calcium carbonates preferentially uptake ^{10}B in the tetrahedral form and that the coprecipitation of different proportions of both species can explain their B concentration and isotopic compositions. Shortly after, Hemming and Hanson (1992) reported a relatively narrow range in B isotope compositions of various carboniferous species and also concluded that only the borate ion aquatic species is involved in reactions in which boron is incorporated into the carbonate structure, a finding that was also supported by Gaillardet and Allègre (1995). However, more recent works have challenged this idea (Mavromatis et al., 2015; Noireaux et al., 2015). These works report that trigonal and tetrahedral species were present in the crystallographic sites of the synthetic calcite and aragonite

samples measured which was a function of solution pH and mineralogy of the precipitated carbonate mineral. Therefore, with conflicting results from older and newer studies, the mechanism responsible for B incorporation into carbonates remains elusive and perhaps more complex than once though.

The differential uptake of the two boron species during the interaction of dissolved boron with solid phases leads to significant isotope fractionation. The adsorption of boron onto clay surfaces was first documented by Schwarcz et al. (1969) who made the preliminary observation that ^{10}B is preferentially adsorbed from solution relative to ^{11}B. However, application of this finding to natural solutions was not possible due to the experimental design. Several studies have shown the relationship between boron isotope fractionation and various factors such as boron species, temperature, pH and pressure (Vengosh et al., 1991b; Palmer et al., 1987; Spivack and Edmond, 1987; Kakihana and Kotaka, 1977). Palmer et al. (1987) for example, reported the variations of adsorption constants and isotope fractionation with pH and temperature during B adsorption from seawater onto marine clays. Here, the partition coefficient of boron exchange between the solution and clay fraction is expressed as:

$$Kd = \left(\frac{[B]_{sediment}}{[B]_{solution}}\right) \quad (1\text{-}21)$$

Here $[B]_{sediment}$ and $[B]_{solution}$ are the boron concentrations (for example, in ng g^{-1} or µg g^{-1}) of the adsorbed and dissolved species. Under experimental conditions, Keren and Mezuman (1981) demonstrate that adsorption is reversible and that the fractionation factor between the adsorbed and dissolved species can be expressed as:

$$\alpha = \left(\frac{1}{(\delta^{11}B)_f+10^3}\right) \cdot \left(\frac{(\delta^{11}B)_i+10^3)-F(\delta^{11}B)_f+10^3)}{1-F}\right) \quad (1\text{-}22)$$

where $(\delta^{11}B)_i$ is the initial $\delta^{11}B$ of the solution (here seawater was used, +39.5‰), $(\delta^{11}B)_f$ is the final $\delta^{11}B$ of the solution and F represents the ratio of the final to initial boron concentrations in the solution. In agreement with Keren and Mezuman (1981), Palmer et al. (1987) reported that Kd increases with pH over the range of pH (6.5 – 8.5) values considered in the study (Figure 1-11a) using both standard clay minerals and natural clays. The cause of the pH dependence of Kd is attributed to the speciation of dissolved boron (Figure 1-11c and d). At lower pH values (<7) Kd is low because clays have a low affinity for $B(OH)_3$; accordingly Kd increases with pH since clays have a stronger adsorption affinity for the $B(OH)_4^-$ (Palmer et al., 1987). Note that Kd decreases as a function of pH beyond the upper limits for this study due to competition for sites with OH^-

(not shown). A positive correlation between the fractionation factor and pH is also observed (Figure 1-11b), where the fractionation factors obtained at 40°C are analytically undistinguishable from those at 5°C. This demonstrates that the effect of temperature on the fractionation factor appears not to play as significant of a role as does pH. The dissolved boron speciation as a function of pH (Figure 1-11d) is likely observed because the ∝-Al_2O_3-boron complex is tetrahedrally coordinated for both species adsorbed from the solution. Therefore, the fractionation factor calculated for the trigonally coordinated $B(OH)_3$ should undergo a higher degree of fractionation during formation of the tetrahedrally coordinated boron adsorption complex than the $B(OH)_4^-$ which is already tetrahedrally coordinated (Palmer et al., 1987; Spivack and Edmond, 1987). Hence, the difference in isotope fractionation factors between both species leads to a pH dependence

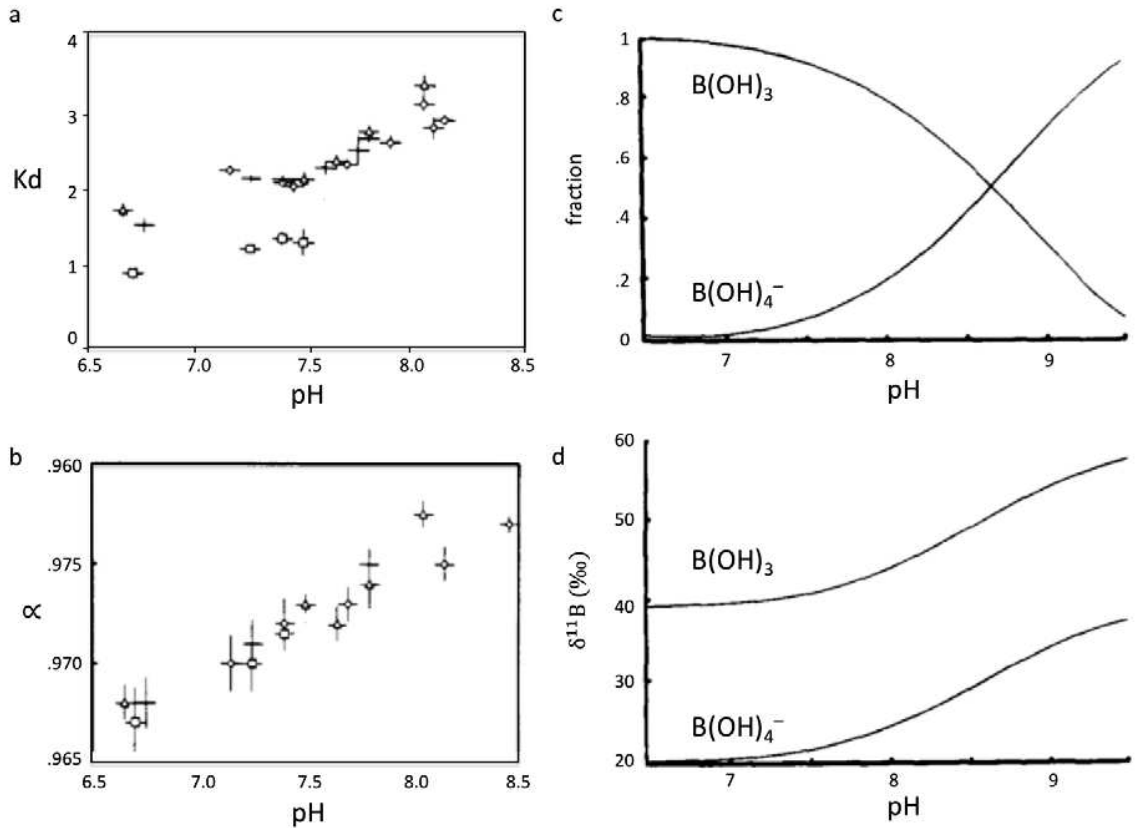

Figure 1-11. a) Boron adsorption distribution coefficient as a function of pH. (◇) 5°C (Δ) 15°C, (+) 25°C, (□) 40°C. b) Boron adsorption isotopic factor as a function of pH. c) Boron coordination at 25°C at 1 atm as function of pH (data from Hershey et al., 1986). d) Boron isotopic composition of $B(OH)_3$ and $B(OH)_4^-$ at 25°C at 1 atm as function of pH (using the theoretical fractionation factor calculated by Kakihana et al. (1977). Source: Palmer et al. (1987).

of the measured isotope fractionation, where less fractionation occurs at higher pH values. These combined results then indicate that isotope fractionation factors are the result of equilibrium processes and are not caused by a kinetic effect. A compilation of published relationships between pH and the B partition coefficient (k_d) and the B isotopic fractionation factor (α) for different geologic and synthetic material is shown in Figure 1-12 (Lemarchand et al. 2015). All material (Amberlite resin, humic acids, birnessite and goethite minerals, 'carbonates', and 'sediments') display relatively similar behavior regarding the partition coefficient as a function of pH with maximum K_d values reached between pH values of approximately 8 and 10; B isotopic fractionation factor – pH relationships in geologic and synthetic materials are also similar.

For example, the mechanisms by which dissolved boron adsorbs on solids and coprecipitates in minerals was investigated by Lemarchand et al. (2007) who focused on boron isotope fractionation during adsorption on goethite and birnessite as function of solution of pH (see Figure 1-12). Boron adsorption at the surface of goethitite was found to induce strong pH-dependent isotopic fractionation over a pH range of 8–10. Adsorption of boron on birnessite at low or neutral pH caused a lower boron isotopic fractionation compared to goethetite and decreased with increasing pH above 8 and reverses at pH = 9. Dissolved boron was reported to react as a Lewis acid with mineral surfaces forming predominately inner-sphere complexes by ligand exchange with hydroxyl groups; however Lemarchand et al. (2007) also found outer-sphere complexes to be formed on birnessite by physical adsorption. Here, boron isotope fraction is strongly dependent on the structure of the surface complexes formed. Lemarchand et al. (2007) concluded that ^{11}B enrichment should be expected in waters in equilibrium with iron or manganese oxides, which is a function of pH that changes boron speciation in solution and at solid surfaces, typically the case for soil solution and in seawater. Additionally, since boron complexation relies on protonation and deprotonation reactions (protons and hydroxides only), the absence of other cations suggests an almost independence of boron surface reactions to the ionic strength of the solution (Lemarchand et al., 2007)

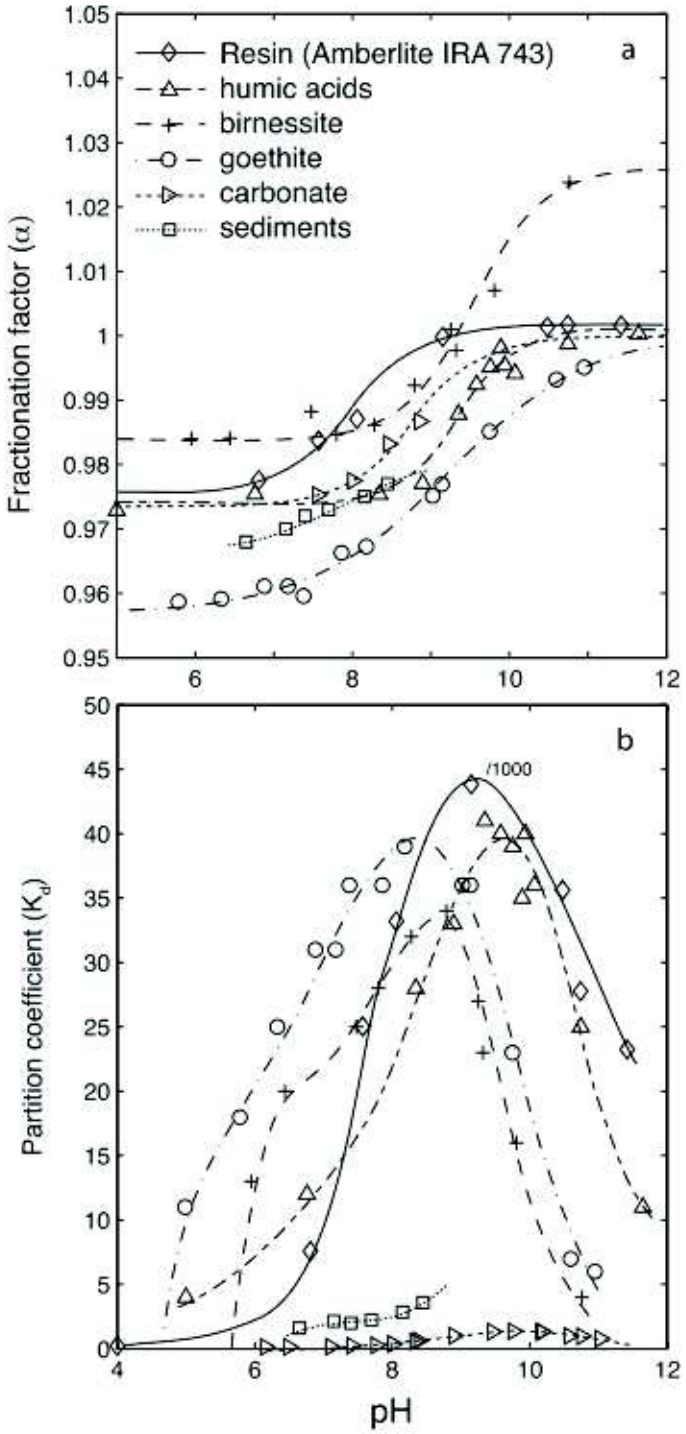

Figure 1-12. K_d – pH and α – pH relationships for different geology and synthetic material. Sources: Amberlite resin values: Lemarchand (2001); humic acids: Lemarchand et al. (2005); birnessite and goethite values: Lemarchand et al. (2007); carbonate values: Hemming et al. (1995) and Goldberg and Forster (1991); and sediment values: Spivack et al. (1987). Source of figure: Lemarchand et al. (2015).

In soil profiles and in rivers, boron has an affinity of clay minerals, metal oxides, and organic matter due to their high boron partition coefficient which is a function of specific surface area of the solid exposed to water and on the density of surface hydroxyl groups (Gaillardet and Lemarchand, 2017). The boron partition coefficient can be expressed as:

$$Kd = \left(\frac{[B]_{adsorbed}}{[B]_{solution}}\right) = \left(\frac{M_{B\ adsorbed}}{M_{solid}}\right) \Big/ \left(\frac{M_{B\ solution}}{M_{solution}}\right) \quad (1\text{-}23)$$

where $[B]_{adsorbed}$ and $[B]_{solution}$ are the concentrations (for example, in ng g^{-1} or µg g^{-1}) of the adsorbed and dissolved boron and $M_{B\ adsorbed}$, M_{solid}, $M_{B\ solution}$, and $M_{solution}$ are the mass of adsorbed boron (ng; µg), mass of solid (g), the mass boron in solution (ng; µg), and the mass of solution (g), respectively. Accordingly, solid surfaces with less surface area and fewer hydroxyl group such as tectosilicates, i.e. quartz, have very low K_d values (< 1); carbonates are intermediate (K_d ranges between 1 – 6); while organic compounds and phyllosilicates have much higher values (10 – 100) (Goldberg, 1997). The K_d maximum value of 40,000 is reached with the synthetic boron specific resin Amberlite IRA 743 (Lemarchand et al., 2002a). In soils and groundwaters with relatively low water-rock ratios (about 0.1), large K_d values of minerals, secondary phases, and organic surfaces lead boron to be largely adsorbed in the weathering zone. For example, with a partition coefficient of just 5 and water-rock ratio of 0.1, 98% of the dissolve boron will be absorbed by the clay fraction. On the contrary, boron is mostly found in the dissolved phase in rivers where the water-rock ratio is about 10,000 (Gaillardet and Lemarchand, 2017). The exchangeability of boron between solution and the solid then depends on the acid dissociation constant of both boric acid and the ligand involved, where adsorption on surfaces reflects the competition for surface reactive sites (possibly produced by variations in pH) between the two boron species, protons, and hydroxides (Pizer and Selzer, 1984).

1.4.2.2 Coprecipitation of boron into solids

The mechanism by which boron is precipitated into minerals during clay formation is less studied than adsorption processes and therefore not completely understood. Regarding precipitation, most studies have focused on boron isotope behavior of carbonates (e.g. Vengosh et

al. (1991), with a goal determining if both or only one of the boron species is incorporated into the carbonate structure. As mentioned earlier, this question is still unresolved due to new evidence provided by Mavromatis et al. (2015) and Noireaux et al. (2015) stating that both the trigonal and tetrahedral forms of boron can be incorporated into carbonate crystals, thereby challenging the hypothesis that only the borate ion is incorporated (e.g. Hemming and Hanson, 1992). Studies that have investigated the precipitation of boron into silicates remain limited. Mainly, the experimental works of Williams et al., (2001a), (2001b); and Williams and Hervig (2005) in diagenetic environments have provided sights in boron behavior during precipitation into newly formed clay minerals. Williams et al., (2001a) performed experiments to measure the isotopic fractionation of boron between illite/smectite clay minerals and water as a function of temperature and degree of illitization (Figure 1-13). Combined with the B-adsorbed on clay surfaces data at 25°C from Palmer et al. (1987) and fluid-silicate melt fractionation measurements at 300°C and 350°C (1kbar) of Hervig et al. (2002), a linear change in fractionation with reciprocal temperature is observed. Interestingly, the temperature dependence of the boron isotope fractionation factor between the clay mineral and the water appears to be similar for all silicate-water reactions considered, regardless of the conditions in which the reaction occurred (i.e. adsorption onto clay minerals, silicate melts/water, illitization of smectite to illite). Williams et al. (2001b) demonstrated that during illitization, that boron is initially adsorbed onto the newly formed clay surface at low temperature and then is incorporated into the silicate lattice by substitution of Si in the borate ion form when the experiment temperature exceeds 60°C. Because tetrahedral boron is preferentially enriched in the ^{10}B isotope, the illitization process of smectite is characterized by a preferentially incorporation of ^{10}B during the transformation, thereby producing isotopically lighter neoformed clay minerals. Without more detailed studies on B behavior during precipitation, we can only speculate that the incorporation of ^{10}B into the silicate structure proceeds in the same manner as adsorption, i.e. through the formation of surfaces complexes, followed by subsequent incorporation into the mineral lattice (Lemarchand et al., 2007).

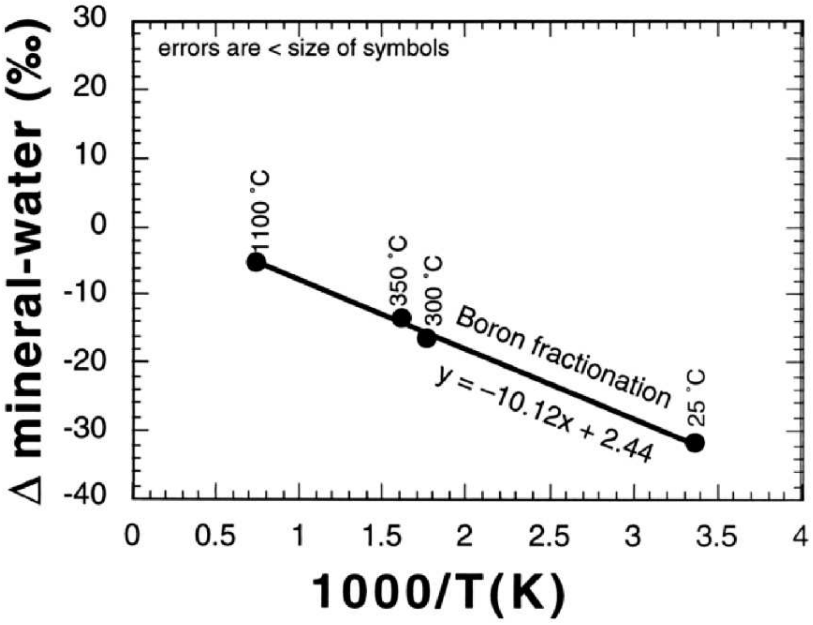

Figure 1-13. Boron isotope fractionation as a function of reciprocal temperature. Source: re-drawn from Williams et al. (2001a).

1.4.2.3 Boron uptake during biological processes

Boron is a micronutrient in plants where it is involved in many biochemical and physiological functions such as: sugar transport (Saleem et al., 2013), cell wall structure where it forms a cross-linking structure with rhamnogalacturonan-II (RG–II) units (Matoh, 1997), nitrate assimilation (Ruiz et al., 1998), and hormonal metabolism and reproduction (Blevins and Lukaszewski, 1998). The function of boron in the formation and stabilization of the primary cell wall structure have also been reported by O'Neill et al. (2001). Boron deficiency symptoms have been observed in more than 80 countries, making boron deficiency the second largest global nutritional problem in crops (Alloway, 2008). Understanding the mechanisms that control the boron transfer between vegetation and soil is therefore fundamental to the constraint of the biological cycling of this nutrient. Despite the fact that the physiological role of boron in plants is well documented, e.g. Lehto et al. (2010), very little is known about the B isotope fractionation during root absorption, and the very few studies which are published lead to contradictory conclusions. The principle reason for the lack of B isotope data stems from the difficulties in separating boron from an organic matrix; incomplete separation in the form of residual organic

material in the sample will lead to isobaric interferences when measured by mass spectrometry (Roux et al., 2015; Lemarchand et al., 2002a). Vanderpool and Johnson (1992) reported that B isotope fractionated occurs during incorporation into commercial produce however with various results (enrichments of both ^{10}B and ^{11}B dependent on the species); while Wieser et al. (2001) observed fractionation in coffee beans (with $\delta^{11}B$ values ranging from –12‰ to +19‰) but concluded that since boron was not readily translocated once bound in plant tissue, that the $\delta^{11}B$ of coffee beans represented the cumulative input of various sources. In this case, no isotope fractionation was assumed between the crop and soil. This hypothesis has been challenged by the work of Cividini et al. (2010) and Noireaux et al. (2017) who propose that although the B isotope composition of the plant/tree leaves are similar to that of the soil solution, a large isotope fractionation occurs between various compartments within the plant/tree (i.e. leaves, branches, roots, and trunk). These works suggest that no isotope fractionation occurs during boron uptake from the soil solution but that B isotope fractionation occurs via translocation within the plant biomass. In this case, boron excreted from leaves is enriched in ^{11}B compared to the woody parts of the plant that store ^{10}B. Upon abscission and decay or via throughfall, the soil solution will then become enriched in ^{11}B. By this mechanism, biological cycling is thought to induce boron isotope fractionation within the ecosystem and the extent of the ^{11}B enrichment therefore depends on the rate at which boron is cycled through the ecosystem. However, the working hypothesis behind these preliminary findings needs further exploration to clarify boron isotope behavior during biological processes.

1.4.2.4 Evaporation and condensation processes

Due to volatile nature of boron, it is partitioned between the solid, liquid, and vapor phases. One of the earliest recognitions of this phenomenon was during seawater evaporation experiments in 1959 conducted by Gast and Thomas who reported that seawater is a major source of atmospheric boron. In a later investigation of boron behavior during seawater evaporation, Vengosh et al. (1992) reported a gradual increase in $\delta^{11}B$ values of evaporated seawater (from 39‰ to 54.7‰) relative to the standard NIST 951. They find that higher $\delta^{11}B$ values of brines and lower values of coexisting precipitates ($MgSO_4$ and K-$MgSO_4$ salts with $\delta^{11}B$ that range from 11.4‰ to 36.0‰) may be attributed to selective uptake of ^{10}B by the salts. Vengosh et al. (1992)

suggested that the coprecipitation of $B(OH)_4^-$ species within the salts, and/or precipitation of Mg-borate minerals with a coordination number of 4 are the responsible mechanisms for boron isotope fractionation during evaporation of seawater. Experiments conducted at high temperatures, e.g. Spivack et al. (1990), were in agreement with the finding of Vengosh et al. (1992) and reported that in hydrothermal conditions, boron is partitioned into both the vapor and brine/solid phases where the composition of the vapor is slightly enriched in ^{11}B. However, there have been several other studies that show that the behavior of boron isotopes during seawater evaporation is highly dependent on the experimental conditions (Gaillardet et al., 2001; Xiao et al., 1997). For example, Xiao et al. (2001) performed airflow experiments and reported that the vapor phase was enriched in ^{10}B. In the natural system, Rose-Koga et al. (2006) found a similar result and proposed that boron evaporation at the seawater-atmosphere interface and boron condensation in the clouds lead to seawater-vapor kinetic fractionation of 25.5‰ where the vapor is characterized by a ^{10}B enrichment and a rain-vapor fractionation of 32‰. These contradictory findings regarding condensation and evaporation demonstrate how significant experimental conditions can be in influencing measured $\delta^{11}B$ fractionation values. Recently, Roux et al. (2017) investigated boron atmospheric inputs (dust and dissolved depositions) to continents in order to better understand the sources and processes that control the cycling of atmospheric boron. They reported $\delta^{11}B$ compositions in dust and dissolved inputs of 1‰ and 18‰, respectively. High B contents (190 – 390 $\mu g\ g^{-1}$) of dust sample were attributed to the spreading of boron-rich fertilizers. Boron isotope compositions in dissolved depositions were attributed to a Rayleigh-like evolution of the atmospheric gaseous B reservoir with limited anthropogenic contributions. These results are in opposition to the hypothesis that atmospheric boron is controlled by the dissolution of sea salts. Nevertheless, our understanding of boron isotope fractionation during these processes remains somewhat limited because of the lack of research in this field and the specific mechanisms responsible for preferential uptake of one boron species over the other are not clearly identified.

1.4.3 Boron isotopes in the weathering zone

This section will review the state of the art of the use of boron isotopes to better understand water-rock interactions in the weathering zone, the distinctive layer of Earth's surface where chemical weathering occurs. As reviewed in the previous section (section 1.4.2) boron displays

physico-chemical properties that are suitable for investigating water-rock interactions, including those that involve a biological component. Particularly the large isotope fractionations induced by adsorption on clay or organic particles, coprecipitation, vegetation cycling, and evaporation and condensation processes allow boron to trace the processes responsible for the chemical weathering of rock into soil and sediment. Boron systematics suggest that during the dissolution of the bedrock and primary minerals, no significant isotope fractionation occurs (Lemarchand et al., 2000, 2012; Rose et al., 2000; Schwarcz et al., 1969). Due to the speciation of boron in solution and affinity of the borate ion to clay particles and organic matter, large isotope fractionations occur during adsorption and coprecipitation processes. This fractionation is characterized by a ^{10}B-enrichment in the solid phase and a complimentary enrichment of ^{11}B in the solution. To the best of our knowledge, biological processes induce isotope fractionation between the leaves and the plant characterized by an ^{11}B-enrichment in the leaves and (upon abscission and/or throughfall) the soil solution, and a complimentary ^{10}B-enrichment in the plant tissue (Cividini et al., 2010; Noireaux et al. 2017). These general characteristics of boron isotope fractionation during silicate weathering and vegetation cycles are perhaps the reasons many of the following studies have chosen boron isotopes as their proxy to understand and quantify water-rock interactions at a variety of scales.

1.4.3.1 Boron isotopes in soil profiles

Very few studies have investigated the behavior of boron isotopes in soils. Taken from an 90-cm thick oxisol on the upper Orinoco (Venezuela), Spivack et al. (1987) measured the boron isotope composition of the bulk soil. They reported that boron is partially mobilized during weathering as a function of distance from the bedrock, with a slight ^{10}B-enrichment in the labile and refractory minerals. They noted that boron was lost at the bottom of the profile (behaving as a mobile element) and then conservatively upwards. This behavior should not be generalized however, as Lemarchand et al. (2012) reported a boron depletion in a temperate soil profile in northeastern France relative to the immobile element titanium (Ti) and an ^{11}B enrichment in the clay-sized fraction which was associated with the incorporation of ^{11}B into the clay fraction derived from a soil solution that was heavily impacted by vegetation. Differences in the B isotopes between the two profiles are consistent with the pedogenic processes that govern their formation. In the podzolic soil, B isotopes have are explained by a model in which pedogenesis occurs by

continuous dissolution of primary minerals and precipitation of secondary minerals. A more complex model is proposed for the brown soil where clay precipitation occurs in the deep soil horizons while being gradually dissolved in the upper layers. Therefore, the clay fraction records the nature of weathering processes that are controlling mineral transformations. Here, the effect of grain size on boron isotope geochemistry was also studied. They reported that unlike the clay fraction, coarse sand, fine sand, and silt fractions have similar boron isotope compositions and unchanging or depleted B concentrations throughout the profile and reveal information about the primary minerals, and by extension, the bedrock. On the contrary, B concentration in the clay fraction (<2 μm) increases and an isotope fractionation towards heavier values between the clay fraction and the bedrock of approximately 9‰ is observed, with an expected hydrothermal component lighter than -35‰.

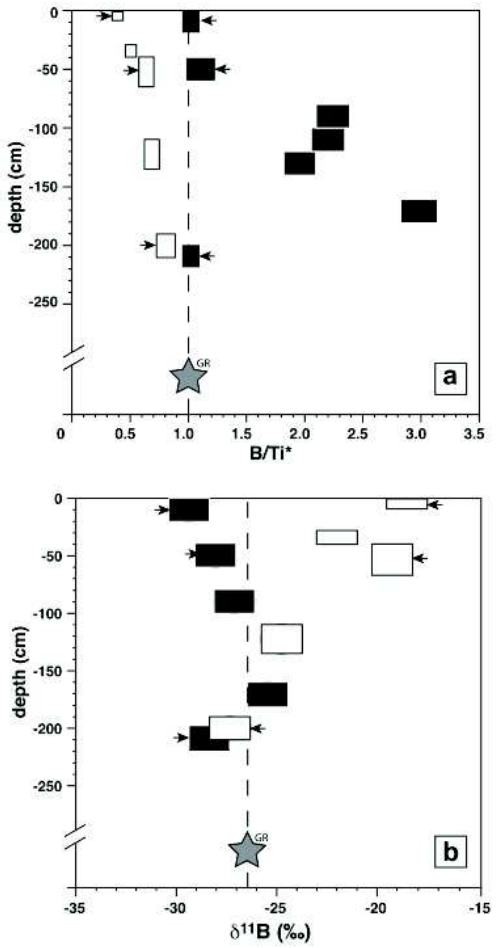

Figure 1-14. B/Ti* (a) and $\delta^{11}B$ in bulk soil samples as a function of depth taken in the Strengbach forest catchment (France). The grey star represents the value of the altered bedrock in the catchment which was used to normalize the B/Ti ratio. Open and closed symbols refer to podzolic and brown soil profiles, respectively. Source: Lemarchand et al. (2012).

At Mule Hole in southern India, Noireaux et al. (2017) reported B isotope compositions of soils in a dry tropical soil profile. In spite of the significant role vegetation cycling plays in the tropics, vegetation control on the $\delta^{11}B$ signal of the soil was not observed. In this profile, a B enrichment in the soil was observed resulting from the downward migration of boron within the profile and the fixation of B on clay-size particles. This result is different from Spivack et al. (1987) who reported boron depletions in the soil. They report that the clay fraction in this profile appears to be fractionated by approximately –50‰ with regard to the soil solution, indicating that it is very unlikely to be in equilibrium with the porewater (unless considering an unrealistic clay-fluid isotope fractionation factor). It is interesting to note here that the clay fraction is lower than the bedrock, which is contrary to the situation found in the Strengbach. The reason for this occurrence is yet to be explored. In this profile, B isotope compositions of between the bulk soil and the bedrock correlate with the Al/Si ratio, which is a grain size proxy used to discriminate between clay-rich particles and quartz-rich coarse particles (Figure 1-15). Other published values from two soil profiles in the Strengbach, France (Lemarchand et al., 2012) and Shale Hills, Pennsylvania (Noireaux et al., 2014a) are compared to the Mule Hole data. The ^{11}B enrichment observed in the Strengbach may be attributed to boron cycling through vegetation, while no isotope fractionation between the bulk soil and the bedrock was observed at Shale Hills. Although, in the Shale Hills soil profile, (Noireaux et al., 2014a) reported a loss of B along the profile, which mimics that of Al, thought to be caused by the migration of clay particles causing isotope fractionation. Studies of soil profiles consistently suggest that differences in grain size play an important role in understanding B isotope geochemistry in soil.

1.4.3.2 Boron isotopes at the catchment scale

Only in the rare cases are we able to gather data from many different components in the weathering zone at the catchment scale. Two recent examples are the previously discussed watersheds in the Strengbach catchment, France (Cividini et al., 2010) and in Mule Hole, India (Noireaux et al., 2017) where boron isotope data was gathered in Critical Zone Observatories (CZO) on throughfall, precipitation, overland flow, stream and stream water time series, groundwater, litterfall, bedrock and soils (Figure 1-16). Boron isotopes show a wide range

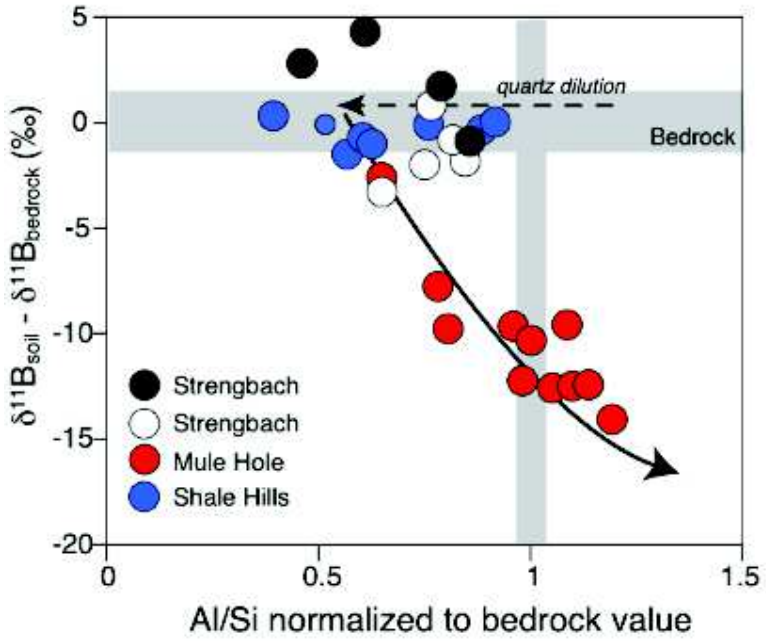

Figure 1-15. Published boron isotopes compositions in bulk soils as function of the Al/Si ratio in different soil profiles. The Al/Si ratio is proxy for grain size where low Al/Si values indicate larger grain sizes and higher ratios indicate smaller finer grain sizes. Enrichments in ^{11}B are likely caused by the incorporation of biogenic boron. Data sources: Strengbach (Lemarchand et al. 2012); Mule Hole (Noireaux et al. 2017); Shale Hills (Noireaux et al., 2014a). Source of figure: Gaillardet and Lemarchand (2017).

(80‰) of distribution. Comparison of these watersheds, particularly in regards to assessing the relative impacts of chemical weathering and vegetation cycling on boron isotope compositions in the weathering zone, highlight the potential of boron isotopes in understanding geological and biological processes at the catchment scale.

Climatically, the biggest difference between the two catchments is that the Strengbach is located in a cold temperature zone, while the Mule Hole catchment has a dry tropical climate. Regardless, both catchments show that boron isotopes behave similarly in most of the compartments, with few significant differences. In particular, vegetation in both systems is characterized by a ^{11}B enrichment; dissolved loads are significantly isotopically heavier than the bedrock; and wet atmospheric deposition inputs to the soil/vegetation system are significant. The high flux associated with vegetation cycling is a common thread between the catchments, although

different in magnitude. In the Strengbach, this flux is 5 times greater than the boron exported from the catchment by streams, while in the Mule Hole it is 10 times greater. Both studies report that the transfer of boron from the vegetation to the soil and soil solution is equally shared between litterfall and soluble boron leached from leaves by rainfall (Noireaux et al., 2017; Cividini et al., 2010). Interestingly, the biomass reported in both studies is highly enriched in ^{11}B compared to soil minerals, bedrock, and rainwater. Within the Mule Hole basin, boron derived from chemical weathering of bedrock is negligible, with the throughfall being 10-15‰ enriched in the heavy isotope compared to the rainfall and litter samples, suggesting a major boron fractionation process occurs between the plant and plant leaves (Gaillardet and Lemarchand, 2017).

In the Strengbach, Cividini et al. (2010) assessed the impact of biological and atmospheric cycling on the isotopic signature of the runoff by sampling pore water with depth in a soil profile. Here, a characteristic decrease in B concentrations in the soil solution is attributed to active plant uptake via roots in the upper soil layers (~50% of B removed in the top 10 cm where roots are most active; and 25% of the remaining portion is removed down to 30 cm). In order to assess how much boron in soil solution is derived from weathering reactions compared to that involved in vegetation cycling (investigating the large B isotopic difference between vegetation, +30-35‰, and soil minerals, -25‰) a simplistic boron budget model was created and applied to difference depths in the profile. In this model, boron in soil solution is derived from biological cycling, atmospheric inputs, and chemical weathering; mineral dissolution is assumed to release B but cause no isotope fractionation, while clay mineral formation induces a strong isotope fractionation of 30‰ by enriching the soil solution in ^{11}B. Results from the model show that the flux associated with B uptake by roots is higher than that released by the weathering of silicates in all depths in the profile, but particularly in the upper layers where leaf litter is recycled.

An important distinction between the two catchments is in regards to composition of the stream water leaving the catchment. Although both settings produce stream water that is isotopically heavier than the bedrock ($\delta^{11}B$ = 45‰ in the Strengbach and 60‰ in Mule Hole), the origin of the signature is different. In the Strengbach, about 50% of the boron in the dissolved load was calculated to be derived from water-rock interactions; while the composition of the dissolved load in Mule Hole is controlled entirely by overland flow (e.g. B derived from the cycling of vegetation).

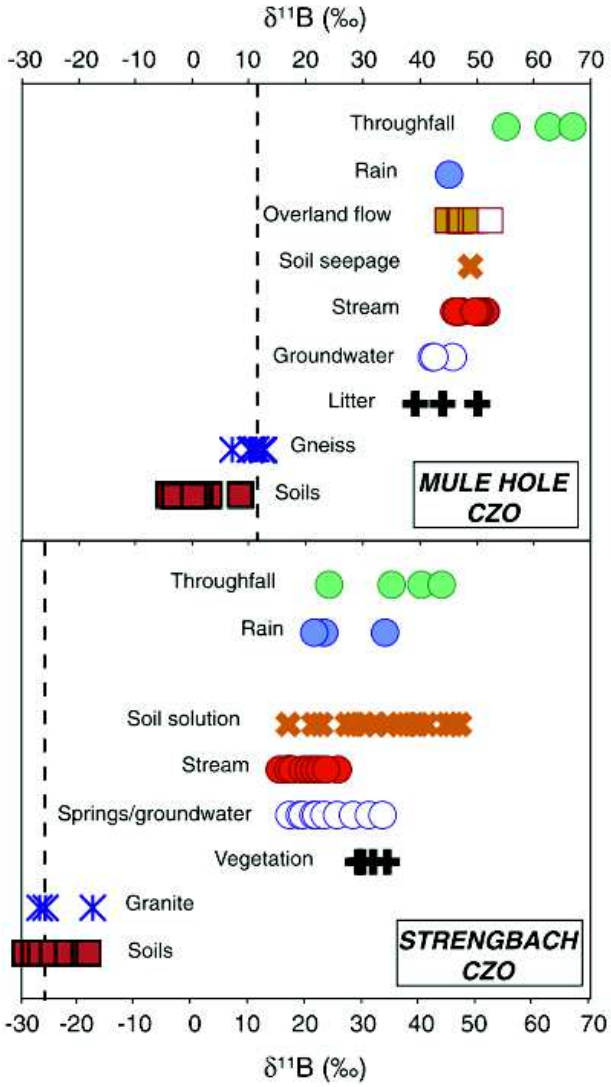

Figure 1-16. $\delta^{11}B$ values in the different compartments of two contrasted Critical Zone Observatories, Mule Hole basin, India (tropical climate) and Strengbach basin, France (temperature climate). The dashed line in both panels represents the composition of catchment bedrock. Source: Gaillardet and Lemarchand (2017).

An important finding of these works is that the boron isotope composition of both the solid and dissolved phases in a soil profile may be a function of depth. Cividini et al., (2010) explains that below the depth of B uptake by active tree roots, the control of B isotopes by biologically-mediated reactions on the composition of the porewater diminishes and its composition is then controlled by weathering reactions; therefore, the distribution of boron isotopes in deep soils is imprinted solely by weathering reactions and reflects differences in mineralogy and/or the

weathering regime. Soil solutions derived from shallower profiles should then be expected to have much heavier B isotope signatures than those derived from deeper locations where the influence of weathering reactions control their isotope compositions (Gaillardet and Lemarchand, 2017).

1.4.3.3 Boron isotopes in the dissolved phase

The study of boron isotopes in the dissolved load of rivers generally has two goals. The first is the need to reconcile the global boron oceanic budget which will help to determine how the seawater pH has evolved overtime in response to ancient pCO_2 and hence climate variability (Goddéris and François, 1996; Lasaga et al., 1985). The second is a need to better understand the mechanisms that drive silicate weathering rates and reactions and the ability to precisely quantify them, as changes in silicate weathering rates may have the potential to regulate atmospheric CO_2 (Raymo et al., 1988; Berner et al., 1983). Boron isotope compositions in large rivers worldwide have shed light on both these issues. The dissolved load of large rivers in the Himalayas (Ganges-Brahamaputra basin) (Rose et al., 2000), Mississippi (Spivack et al., 1987), Changjiang basin (Chetelat et al., 2009), Mackenzie basin (Canada) (Lemarchand and Gaillardet, 2006), and many other rivers worldwide, including the Amazon and Congo (Lemarchand et al., 2002b) displaying a very large range of $\delta^{11}B$ values from approximately –6‰ to +45‰ with an average $\delta^{11}B$ of 10‰ and a discharge-weighted mean B concentration of 10.2 ppb (Lemarchand et al., 2002b). Low concentrations in river water have historically made the analyses of boron isotopes in river waters difficult. However, a pre-concentration step developed by Lemarchand et al. (2002a) using the B-specific resin Amberlite IRA 743 has made boron isotope analyses of diluted solution much easier.

The significant boron isotope fractionation during water-rock interactions associated with B adsorption onto clay particles and organic makes $\delta^{11}B$ a good tracer for hydrographic circulation, especially in large rivers to study continental weathering (Chetelat et al., 2009; Rose et al., 2000). In the Himalayan rivers, Rose et al. (2000) found no systematic correlation between the $\delta^{11}B$ values and the major ion chemistry of the dissolved load, except that B- and Cl- rich waters have the highest $\delta^{11}B$ values, likely controlled by evaporite dissolution. Here, they report a large range of isotopic fractionation among river waters controlled by: 1) crystallization of newly formed clay minerals derived from alteration of silicate in soils, and 2) adsorption processes on suspended matter or bedload sediments in rivers. After correction for evaporate dissolution (which was a major source of B to the dissolved load), it was concluded that most of the 30‰ range of $\delta^{11}B$

values is due to processes occurring in soils where dissolved [B] in waters can be several order of magnitude higher than in the river waters and that incongruent weathering of bedrock occurs with a large boron isotope fractionation between the soil solution and clay fraction that depends on pH (Figure 1-17). This interpretation assumes that the B isotope fractionation between the neo-formed clay minerals and the soil solution is pH dependent and that only the borate species is incorporated into the clay mineral. Therefore, high $\delta^{11}B$ values of the dissolved load in Himalayan rivers can be interpreted as being influenced by a large proportion of B which have been uptaken by secondary mineral formed in high pH soils.

In the Changjiang basin, the total about of boron derived from silicate weathering varies highly (between 40% and 88%), with up to 20% of dissolved boron originating from evaporites and 20% from anthropogenic sources. Here, boron is reported to be highly mobile during silicate weathering, partitioning between the suspended (70%) and dissolved (30%) loads. A range of $\Delta^{11}B_{solid\text{-}dissolved}$ values from –19‰ to –3‰ was reported, where 'solid' and 'dissolved' refer to the boron isotope compositions of the suspended and dissolved loads, respectively, whose compositions were explained as the extent of boron leaching from bedrock dissolution relative

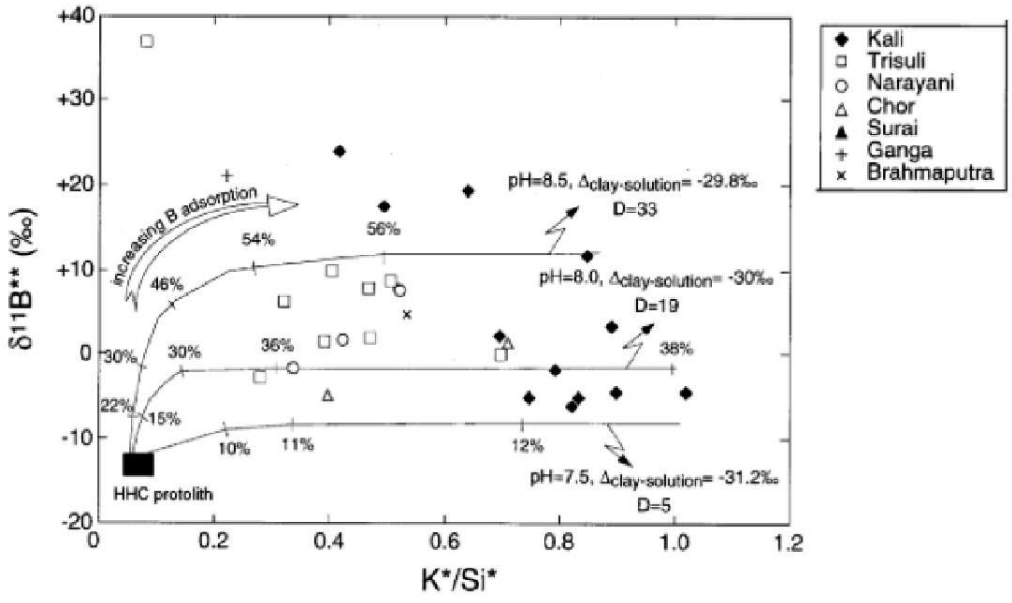

Figure 1-17. Modelled changes in B isotopes in Himalayan soil porewaters during weathering processes as a function of water pH. Increasing K*/Si* ratios relative to the HHC value (bedrock) indicate an increase in secondary clay mineral formation. At pH values ≤ 7.5, the largest changes in $\delta^{11}B$ values between clay minerals and porewater can be expected. This graph shows that $\delta^{11}B$ values of the dissolved load seem to keep a record of the pH variations at the secondary minerals formation cites. Source: Rose et al. (2000).

to boron uptake into secondary minerals. Chetelat et al. (2009) stress that leaching is characterized by a loss of boron relative to the bedrock with no apparent isotope fractionation, where the precipitation/adsorption leads to a large isotope fractionation which enriches the dissolve load in ^{11}B compared to suspended sediments.

The $\delta^{11}B$ of rivers in the Congo, French Guiana, and Niger (Lemarchand et al., 2002b) are characterized by the highest B isotope compositions (between +28‰ and +43‰) where higher $\delta^{11}B$ values are attributed to the strong impact of biological cycling; strong atmospheric inputs can also explain isotopically heavier dissolved load compositions, especially in coastal rivers where the proportion of atmospheric input is higher (Chetelat et al., 2005). In the tropical basaltic-draining rivers of Réunion Island and andesite-draining rivers of Guadeloupe (Lesser Antilles), Louvat et al. (2014, 2011) report similarly high $\delta^{11}B$ compositions (up to 48‰) in the dissolved loads as those reported by Lemarchand et al. (2002b). Here, the large variation in $\delta^{11}B$ values (1 – 48‰) are reflect mixed B-sources and water-rock interaction processes: rain ($\delta^{11}B$ = 40‰); hydrothermalism ($\delta^{11}B$ = 0‰), low temperature basalt weathering ($\delta^{11}B$ = 30‰), and cycling with soil and vegetation ($\delta^{11}B \geq 40$‰). Rivers on Réunion were characterized have two types of $\delta^{11}B$ signatures which reflect low-temperature water-rock interactions: rivers with high weathering rates (~30‰) and those in small forested catchments under low weathering rates (~45‰). The soil-vegetation cycle, although not clearly characterized, was reported to enriched soil solution in ^{11}B and therefore contribute to higher $\delta^{11}B$ values in the dissolved load of the rivers.

In Guadalupe, B isotopes in rivers and springs show a distinct contrast with non-hydrothermally impacted rivers displaying B isotope compositions between 40 – 45‰ and low B content (30 µg/L), and thermal springs between 8‰ and 15‰ with higher B content (250µg/L). A large difference between surface waters and volcanic bedrock was noted. The 40‰ difference between the average B isotope composition surface waters (40‰) compared to the bedrock (0‰) reveals either a huge isotope fractionation takes places during rock weathering, characterized by either a preferential ^{10}B incorporation into the clay fraction during clay formation or adsorption on clays during rock weathering in soil. Alternatively, the soil-vegetation cycle was reported to possibly cause such a fractionation. Results from these studies demonstrated that a wide range of $\delta^{11}B$ values could be produced in the dissolved load without being impacted by hydrothermal activity.

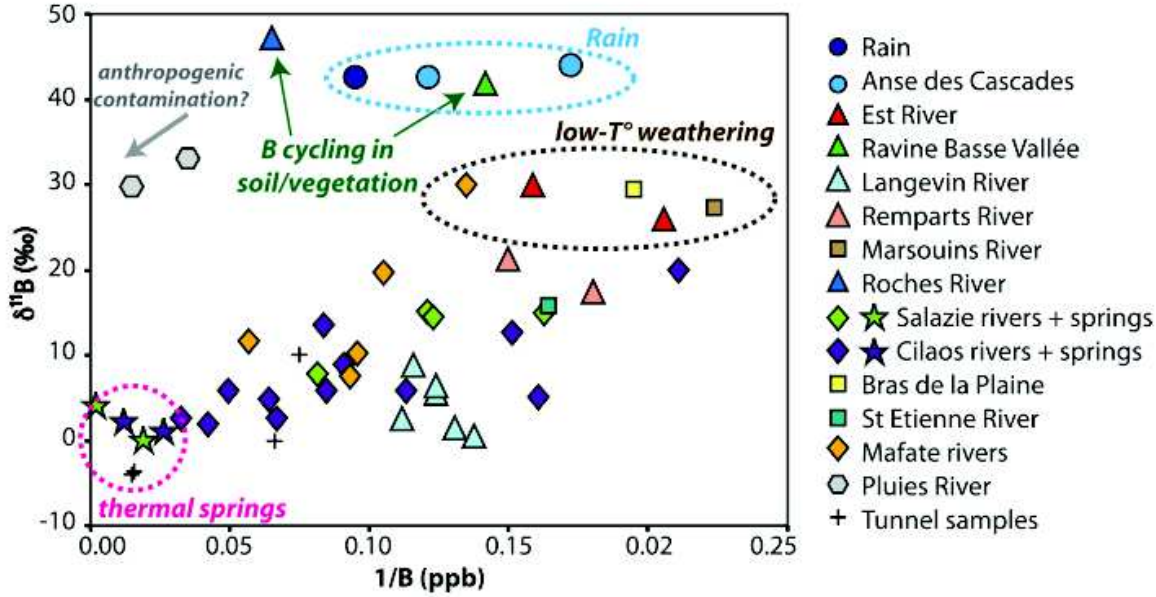

Figure 1-18. Boron isotope compositions as a function of B concentrations for Réunion Island rivers and springs. Circles represent rain-like samples, triangles represent Piton de la Fournaise rivers and springs, diamonds for Pition des Neiges's, squares for river in between the two massifs, and crosses for the tunnels. Source: Louvat et al. (2014)

In tropical southern Taiwan Liu et al. (2012) did not measure such high $\delta^{11}B$ compositions in the dissolved load. Here, mass balance calculations indicate that the major contribution of B in the dissolved load comes from silicate weathering that is characterized by low B concentrations and intermediate $\delta^{11}B$ values. Other B sources include seawater, groundwater, geothermal inputs, and anthropogenic inputs. Therefore, they conclude that the dissolved B and $\delta^{11}B$ in the river are controlled by a mixing of these sources. Similar to Louvat et al. (2014), lower $\delta^{11}B$ values and higher B concentrations in the dissolved load of the Kao-ping River were attributed to contributions from local geothermal inputs. The mobility of boron in hydrothermal systems have also been used to trace hydrothermal inputs to groundwaters (e.g. Millot et al., 2010b; Millot and Négrel, 2007). For example, using a multi-proxy approach (boron, lithium, and strontium isotopes), Millot and Négrel (2007) find that the strontium and boron isotopes compositions of various hydro- and geothermal sites in France are quite variable ($^{87}Sr/^{86}Sr$ = 0.70755 – 0.72187 and $\delta^{11}B$ = –8.3‰ to +21.6‰) and reflect a lithological control over both their signatures while $\delta^{7}Li$ values range between –0.1‰ and +10.0‰ and seem to be controlled by the temperature of hydro- and geothermal fluids. Others have also used boron isotopes as a tracer of anthropogenic

sources in groundwater and rivers (i.e. (Petelet-Giraud et al., 2009; Chetelat and Gaillardet, 2005).

Generally in unpolluted groundwater, the broad agreement is that the boron isotope composition is controlled by mineralogy of the parent bedrock and boron isotope fractionation processes such as adsorption onto solid phases (clay minerals, organic matter, etc.) and the coprecipitation of boron into secondary minerals (Gaillardet and Lemarchand, 2017; Lemarchand et al., 2015; Lemarchand and Gaillardet, 2006). During the dissolution of primary minerals, boron is partitioned between the solution and adsorbed or precipitated onto solid phases. In order to model this interaction, two basic equations govern the exchange of boron between the solution and the solid surface. The first describes when a volume of water containing dissolved boron with an initial concentration of dissolved boron $[B]_T$ equilibrates with a mineral or organic surface:

$$[B]_{sol} = \frac{\omega_R}{K_d+\omega_R} [B]_T \quad (1\text{-}24)$$

where $[B]_{sol}$ is the soluble B concentration, K_d is the boron partition coefficient and ω_R is the water rock ratio. Using a typical porosity value between 20 – 30% and a K_d value of 20, Lemarchand and Gaillardet (2006) estimate that 98% of the boron stock is absorbed. This result implies that in groundwater, the dissolved B and isotopic composition are buffered by the solid phase and that slight changes in K_d caused by changes in solution pH and/or temperature may have a dramatic effect on the composition of the dissolve load. The isotopic composition of the solution in equilibrium ($\delta^{11}B_{sol}$) can then be written as:

$$\delta^{11}B_{sol} = \frac{K_d+\omega_R}{\propto K_d+\omega_R}\delta^{11}B_T + 1000\frac{K_d(1-\propto)}{\propto K_d+\omega_R} \quad (1\text{-}25)$$

where $\propto$ is the averaged boron isotope fractionation factor between the solid and solution and $\delta^{11}B_T$ is the initial boron isotope composition of the solution (in ‰ notation).

Lemarchand and Gaillardet (2006) proposed a water-rock interaction model that aims to explain the high $\delta^{11}B$ composition of the dissolved load of the Mackenzie River and tributaries by considering variations in the residence time of water in the catchment (water advection), partition coefficient between the groundwater and clay surfaces, and weathering rates. Projections from the model show that the boron isotope composition of the river responses to changes in weathering rates and residence time of the solution. The dissolved load then evolves in two steps after an induced perturbation resulting from boron exchange and associated isotope fractionation (Figure

1-19). The first step involves ion exchange reactions which cause a retardation factor via scavenging or releasing boron on/from mineral surface with an associated isotopic fractionation. Secondly, after the perturbation front has passed through the system, a new steady state can be established where the isotopic composition of the porewaters are no longer controlled by ion exchange, but rather dissolution and precipitation reactions (Lemarchand and Gaillardet, 2006). This water-rock interaction model shows that the $\delta^{11}B$ of the groundwater can response to a perturbation, such as a B-enrichment caused by increased erosion and chemical weathering for example, given that all other parameters (e.g. source rocks, pH) remain fairly constant. The duration of the perturbation is then proportional to the chemical properties of the hosting rock together with residence time of the solution. In the case of the Mackenzie, Lemarchand and Gaillardet (2006) estimate that the groundwater residence time is about 500 years, hence the composition of the dissolved load of the catchment's rivers can be expected to be controlled by ion exchange for over 10 – 25 kyr. Measured $\delta^{11}B$ values of the dissolved load on the plain were therefore reported to represent an ancient perturbation caused by increased weathering associated with the last glaciation; the groundwater in the Mackenzie still has not reached steady state.

1.4.3.4 Boron isotopes sediments, lakes, and brines

Very few studies have focused on boron isotopes in river sediments. Boron content and isotope compositions of fluvial suspended and deep sea marine sediments were reported by Spivack et al. (1987). Here, an experimental approach was used to determine the low temperature interaction of dissolved boron with detrital sediment. Grain size separation (bulk sediment, < 64 μm, and < 4 μm) revealed that B contents increase with decreasing grain size, while the B isotope composition of the bulk and < 64 μm fraction at the river delta were 2‰ heavier than in the upstream river. The < 4μm fraction in the delta sediment was distinctly heavier (+1.9‰) than the bulk sediment (–4.3‰) at this location, similar to the range found in marine sediments in this study (between –1.2‰ and –9.0‰). The adsorption of boron from seawater onto fluvial sediment during estuarine mixing is the proposed mechanism for explaining the composition of the clay fraction at the river delta, which still being 26‰ lighter than the seawater. Additionally, the high boron content of deep sea detrital samples suggests that boron is also incorporated into authigenic silicates forming on the sea floor, thus acting a major boron sink in the oceans. In the Changjiang River basin, Chetelat et al. (2009) reports B isotope compositions of suspended particulate matter

ranging –11‰ to –6‰ where about 70% of the boron is transported by the suspended sediments and 30% by solution. Here, they show a positive correlation between $\Delta^{11}B_{\text{solid-dissolved}}$ values and Al/B ratios used as a proxy for boron mobility during weathering, which suggests that the re-incorporation of boron onto the suspended load may be controlling the isotopic composition of the dissolved load.

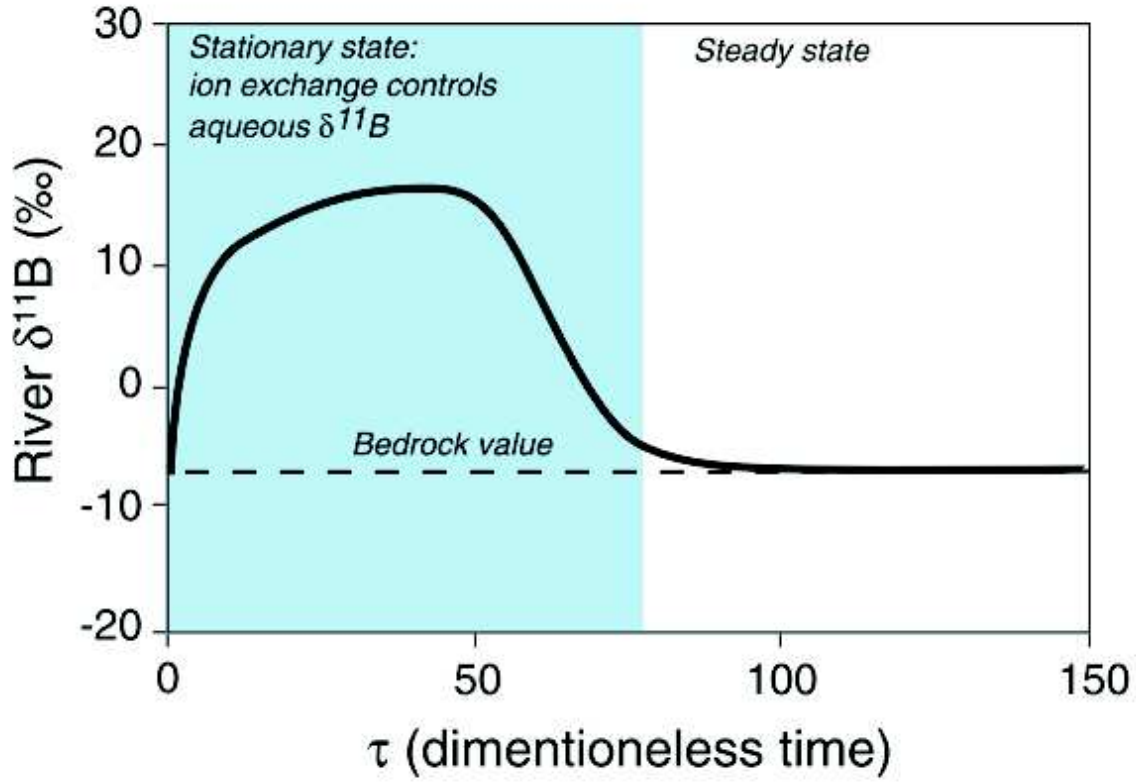

Figure 1-19. Modeled temporal evolution of the B isotope ratio in shallow groundwaters in the Mackenzie River basin in response to changes in the weathering conditions (caused by past glacial events). An isotopic composition of –7‰ is assumed for the silicate source of B. This model illustrates the competition between ion exchange reactions between groundwater and clay surfaces (fast reaction) and bedrock dissolution (slow reaction), and time, expressed as the dimensionless τ symbol (normalized to the residence time of groundwater). Higher $\delta^{11}B$ values are generated when fast ion exchange reactions occur. Source: Gaillardet and Lemarchand (2017).

The behavior of boron isotopes have also been studied in several lakes throughout the world with the goal of determining their geochemical evolution and also assessing the origin of evaporates in the sediment archives (marine or non-marine sources) (Leslie et al., 2014; Vengosh et al., 1991a, 1995; Xiao et al., 1992). Vengosh et al. (1991a) investigated brines, groundwaters, and detrital

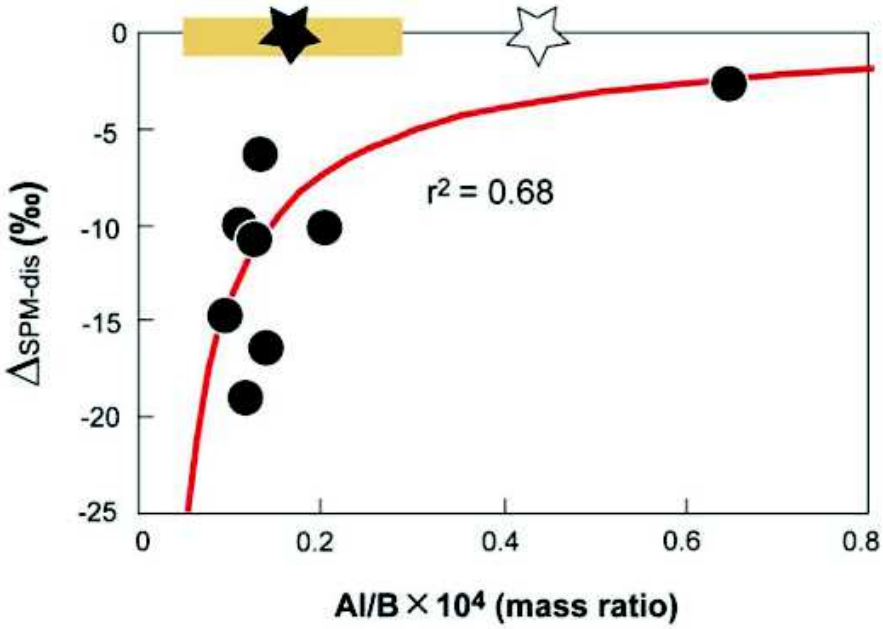

Figure 1-20. Evolution of the $\Delta^{11}B$ solid-dissolved as a function of the Al/B mass ratio measured in suspended sediments of the Changjiang basin rivers. Filled and open stars refer to the Al/B ratios of the upper continent crust used for comparison, taken from Hu and Gao (2008) and Wedepohl (1986), respectively. Source of figure: Chetelat et al. (2009).

sediment in modern Australian salt lakes and reported various B isotope compositions (Figure 1-21). Two different lakes types were characterized, both however strongly influenced by marine sources. The first was characterized by high Na/Cl molar ratios similar to that of marine water, low B/Cl indicating B depletion relative to seawater, and very high $\delta^{11}B$ values (between 54‰ and 59‰). These properties were attributed to a marine cyclic salt origin and adsorption processes on clay materials and in closed systems with low water-rock ratios. Here, a ^{10}B enrichment in the clay fraction contributes to isotopically heavier $\delta^{11}B$ values in the dissolved load. In the second type, surface brines were characterized by very high salinities, low B/Cl values and $\delta^{11}B$ values ranging from 25‰ to 35‰. Vengosh et al. (1991b) concludes that Na/Cl ratios can be used as indicators of the origin of the salt, while $\delta^{11}B$ values and B/Cl ratios are sensitive to a marine or non-marine origin, boron adsorption onto clays, and water-rock ratios.

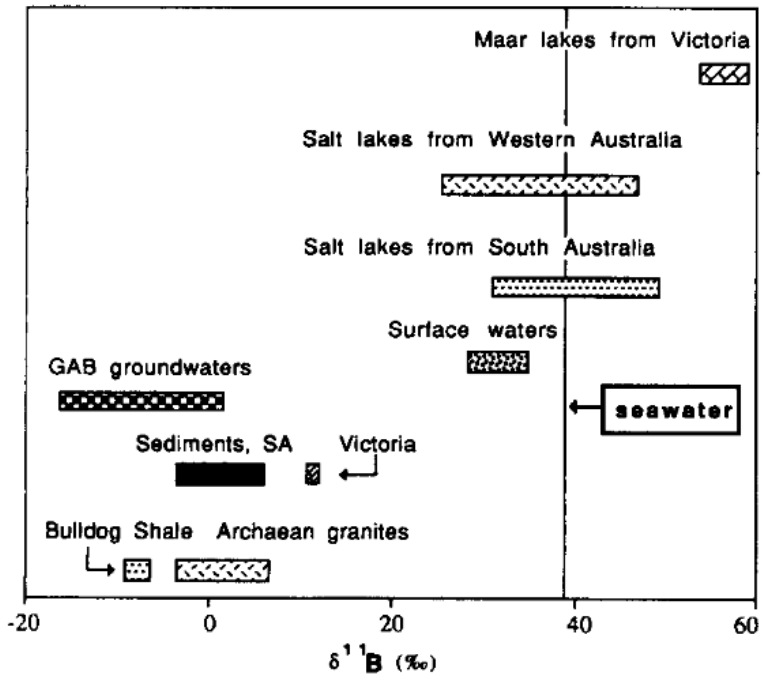

Figure 1-21. $\delta^{11}B$ compositions in some Australian brines, surface waters, groundwaters, sediments, and bedrock. Seawater value taken from Spivack et al. (1987). GAB = Great Artesian Basin. Source: (Vengosh et al., 1991a)

Xiao et al. (1992) finds a wide range of B isotope compositions between the brine, minerals, source water, and sediment in a Chinese lake which reveal the sedimentary cycle of boron isotopes. The composition of the lake is explained as a portion of boron in the lake derived from source waters which is adsorbed by the sediment on the lake floor and a portion coprecipitated into boron minerals; both processes causing enrichment of ^{11}B in the aqueous phase relative to the continental crust (–7‰). In Antarctica, Leslie et al. (2014) also reports a wide range of $\delta^{11}B$ values (between +12‰ to +51‰) which correspond to the variations from glacier meltwater streams and an in situ, hypersaline frozen lake layer. Here, the sources of B are controlled by terrestrial chemical weathering of aluminosilicates within stream channels and a marine source, either derived from marine aerosols or in the form of ancient seawater. All studies considered, the general behavior of boron isotopes in lakes, lake sediments, and brines is that boron is a mobile element in solution and is likely to be adsorbed onto clay surfaces and coprecipitated into minerals, causing an ^{10}B-enrichment in the solid phase and a complimentary ^{11}B-enrichment in the solution. The wide range of isotope compositions (0 – 60‰) and B concentrations (between 1 $\mu g\ L^{-1}$ and 0.5 $g\ L^{-1}$) reported

therefore likely reflect a mixture of different inputs to the lake and internal geochemical processes such as absorption and coprecipitation onto/into clay-sized particles and possibly organic matter.

1.5 Conclusion

The use of boron isotopes as a proxy to quantify and trace weathering reactions at Earth's surface have been demonstrated in a variety of environments such as soil profiles, groundwater, rivers, and lakes using both the dissolved and solid phases. Due to its high mobility and isotope fractionation during weathering processes, boron isotopes display great potential in exploring chemical weathering reactions on both the local and global scales, including those with a biological component. Boron isotopes are largely fractionated by absorption and coprecipitation processes (characterized by a ^{10}B enrichment in the clay-sized fraction and organic matter and a complementary ^{11}B enrichment in the solution), evaporation and condensation processes (showing both ^{10}B and ^{11}B enrichments which appear to be highly controlled by experimental conditions), and boron cycling through vegetation which appears to induce an ^{11}B enrichment on the surrounding environment and soil solutions. Boron isotope fractionation at Earth's surface can mainly be attributed to the difference in affinity of B isotopes between trigonal and tetrahedral species. Competition between boron species in solution and onto solids produces large isotope variations in nature with an observed range of approximately 70‰. The dissolved load of river, rainwater, and vegetation are typically enriched in ^{11}B, while a complimentary depletion in ^{11}B (enrichment in ^{10}B) is observed in clay minerals, with an average B isotope value of continental crust being approximately -10‰. On the ecosystem scale, chemical weathering does not induce a large flux of B. The major flux of B to the ecosystem is associated with biological recycling. On the global scale, B is added to the oceans by rivers, where the most important B sink is adsorption on clay-sized particles. This characteristic also makes boron a good proxy to reconcile the global weathering/erosion budget, including its use for reconstructing the pH of ancient seawater.

1.6 Objective of the thesis

Variations in silicate weathering rates have the potential to regulate atmospheric CO_2 concentrations and therefore climate on geological timescales (e.g. Raymo et al., 1988; Walker et al., 1981). The quantification of modern silicate weathering rates and identification of their

controls are therefore necessary to order to interpret paleo-weathering records and reconstruct past climatic changes (White and Brantley, 1995). Modern silicate weathering rates and intensities are typically derived from the dissolved load of large rivers, with few studies focusing on the solid phase (e.g. West et al., 2005; Gaillardet et al., 1999b). Recently, new isotope tracers such as Li, Ca, and Si have been developed to study to chemical weathering because they typically do not suffer from the sample limitations as other weathering proxies which use major and trace element concentrations. For example, these limitations include the dominant role lithology plays on controlling the composition of the dissolved load and weathering products (Gaillardet et al., 1999b; Bluth and Kump, 1994) and grain sizes/mineral sorting of river sediments (e.g. Garzanti et al., 2011; Galy and France-Lanord, 2001; Morton and Hallsworth, 1999). Boron isotopes in the dissolved load (e.g. Louvat et al., 2014; Lemarchand and Gaillardet, 2006; Lemarchand et al., 2002b), suspended load (e.g. Chetelat et al., 2009; Spivack et al., 1987), and soil profiles (e.g. Noireaux et al., 2017; Lemarchand et al., 2012; Cividini et al., 2010) have also been used in this regard and show great potential as a chemical weathering proxy. However, our lack of knowledge of B isotope behavior during chemical weathering remains limited, particularly during pedogenesis and subsequent transport of the weathering "signal" from source areas to the depositional environment. Additionally, no other study has investigated if B isotope in fluvial sediment deposits can be used as a proxy to reconstruct paleo-weathering and paleo-environmental conditions. As such, more research needs to be done to better understand B isotope behavior during weathering reaction and sediment transport, including its use in sediment deposits as a paleo-weathering proxy. With this in mind, this study focuses on three key aspects of B isotope behavior in the weathering zone that are currently understudied with the following objectives:

1. To gain a better understanding of the parameters than control boron isotope fractionation in modern river sediment and how these sediments record the weathering regime.

2. To understand how the weathering 'signal' carried by river sediment is transferred from sources areas of the catchment to the depositional environment.

3. To determine if boron isotopes in sediment deposits (paleochannels) can be used as a proxy to reconstruct paleo-weathering and paleo-environmental conditions and therefore reveal how pedogenesis has responded to climate variability over the last glacial-interglacial cycle.

The study of the paleochannel systems aims to determine if:

a) spatial variations exist in the chemical and isotopic signatures of the sediment clay fraction within a given channel.
b) chemical and isotope differences exist in the sediment clay fraction between channel systems that can be attributed to weathering and/or vegetation cycling in the source areas, which can be used to re-construct paleo-weathering and paleo-environmental regimes over the last glacial cycle.
c) post-depositional processes have overprinted the chemical and isotopic signature of the sediment clay fraction thereby preventing an accurate paleo weathering regime reconstruction
d) the source of the sediments have changed over the last glacial cycle

Chapter 2

SAMPLING AND ANALYTICAL TECHNIQUES

This chapter contributed to the following manuscript:

An automated chromatography procedure for the analysis of $^{143}Nd/^{144}Nd$ isotope ratios in geological materials

Christian Ercolani*[1,2,+], T. Gabriel Enge[1,+], Leo Rothacker[1], M. Paul Field[3], and Anthony Dosseto[1]

Contact: cpe877@uowmail.edu.au

Received: January 2018, Journal Analytical Atomic Spectrometry
Accepted:

Keywords: automation, ion exchange chromatography, neodymium isotopes, multi collector ICP-MS, isotope geochemistry, geology

*Corresponding Author:
Christian Ercolani
Wollongong Isotope Geochronology Laboratory
School of Earth and Environmental Sciences
University of Wollongong
Wollongong, NSW, 2522
Australia

[1] Wollongong Isotope Geochronology Laboratory, School of Earth and Environmental Sciences, University of Wollongong, Australia.

[2] Laboratoire d'Hydrologie et de Géochimie de Strasbourg, EOST, Université de Strasbourg, 1 rue Blessig, 67084 Strasbourg, France

[3] Elemental Scientific, Omaha, Nebraska, USA

[+] Authors contributed equally to the manuscript

2.1 Sample collection and processing

2.1.1 Bedrock

Bedrock samples were collected in monolithological catchments throughout the Murrumbidgee River basin. The location of the monolithological catchments and bedrock samples were predetermined by Ersi® ArcGIS 10.4 software by overlaying a lithology map (source: NSW Government, Resources & Energy), a calculated drainage basin map (Figure 2-1) which displays the location of monolithological drainage areas where bedrock samples were taken, as well as sediment and water sampling points along the tributaries and main channel. Bedrock outcrop exposures were identified in each of the 11 monolithological catchments (when possible) and were either exposed on the surface of the landscape or exposed by stream incision, giving relatively easy access to them. The outmost surface of the rock was chipped away using a hammer and then discarded because this portion has likely been exposed to weathering processes. A sub-sample was then chipped off of the inner portion of the bedrock and taken back to the laboratory for preparation at the University of Wollongong (UOW). After sample collection, the remaining weathered edges of the rocks were cut off with a diamond saw and only the inner core saved. This pristine portion of the rock was crushed to a fine power using a tungsten carbide mill (TEMA).

2.1.2 River sediment

In the modern Murrumbidgee River catchment, approximately three kilograms in total of sediment per sample were taken from the river banks and sandbar deposits along the river in an area of approximately 1 m^2 (where possible) and amalgamated (Figure 2-2). Where sandbar deposits were not present, samples were taken directly from the stream bedload. To assess site variability, particularly at sites where multiple deposits were present, two or more aliquots of sediment were taken several meters apart (Figure 2-2). Samples were scooped by hand into large plastic sample bags, sealed, labeled and transported directly back to the laboratory.

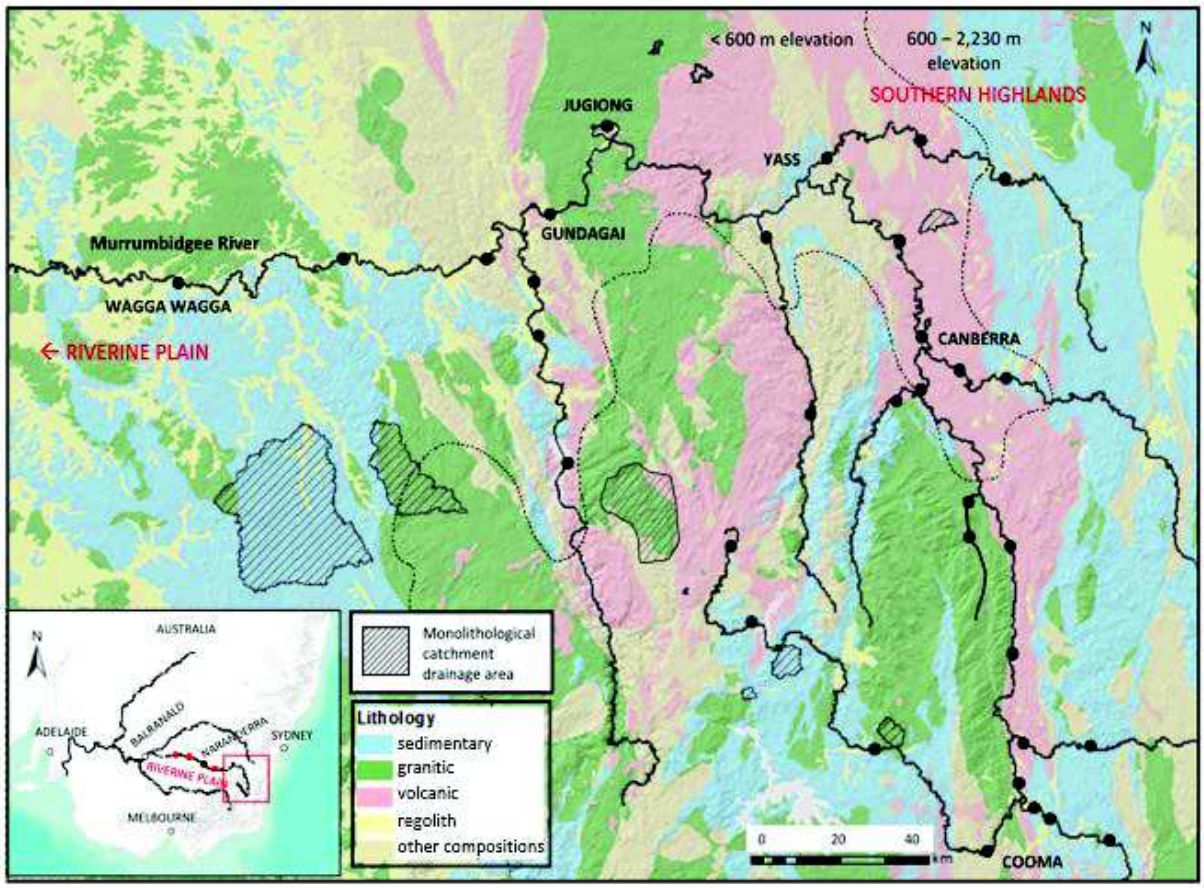

Figure 2-1. Lithology and digital elevation map (DEM) of the upper Murrumbidgee River and tributaries displaying sampling points for sediments and water (black dots) and sampling points for sediment, water, and bedrock in monolithological catchments with respective drainage catchment areas (hashed areas). The dashed line separates the upper (> 600 m elevation) and lower (< 600 m) catchments. Inset map: southeastern Australia; red rectangle shows area displayed in the main panel. Source of DEM: Geoscience Australia; source of lithology map: NSW Government; Resources and Energy; source of inset map: Esri, USGS, NOAA

In the laboratory, sediment samples were dried at 60°C for approximately one week to stop further chemical reactions and allow for proper storage. Following this, samples were wet-sieved with distilled water at 2 mm to remove gravels and organic debris, 500 µm, and 63 µm. Both the fine sand-sized (63 µm – 500 mm; termed 'sand fraction' hereafter) and < 63 µm fractions were retained. The sand fraction was wet-sieved an additional time to remove any fine particles then times to suspend remaining fine particles. The supernatant was then removed and The <63 µm fraction was transferred to a centrifuge tube and further processed by centrifugation to extract

Figure 2-2. Examples of river sediment collection on the river bank of the Murrumbidgee River. Left panel: sediment collection at the banks of the stream, displaying the location of the two aliquots taken (A and B), Right panel: sediment collection of river sand bank deposits (A and B). Two aliquots are used to assess local site variability.

the clay-sized fraction (<2 μm; termed 'clay fraction' hereafter) using the protocol established by Starkey et al. (1984). Approximately 0.25 g of $NaPO_3$ (< 1% w/w) (acting as a dispersing agent) was added to approximately 25 g of the < 63 μm fraction and suspended in 18.2 MΩ water. The slurry was then centrifuged in order to separate the clay fraction (supernatant) from the course fraction. The supernatant was then transferred to another centrifuge tube, centrifuged a second time, and the supernatant (water) poured out. The clay fraction was thoroughly rinsed with 18.2 MΩ water following grain size separation and chemical treatment. Grain size separation was verified by particle size analysis, performed on a Malvern Mastersizer 3000 particle analyzer. This procedure yielded ≥ 94% of < 2 μm material in the clay fraction. Clay and sand fractions were then oven-dried at 60°C and crushed by hand with an agate mortar prior to chemical and isotopic analyses.

2.1.3 **River water**

Water samples in the Murrumbidgee River catchment were collected in acid-washed HDPE plastic bottles in the middle of the channel when possible (Figure 2-3). Samples were filtered in the field using a Merck Millipore® portable filtration unit with 0.2 µm MCE membrane filters. The pH and the alkalinity were determined on the < 0.2 µm fraction (termed 'dissolved load' hereafter). Alkalinity was measured by titration using 0.01M HNO_3 following the method of Barnes (1964). The filtered river water was slightly acidified using Merck Ultrapur™-grade HNO_3 acid prior to storage. In the laboratory, samples were filtered an additional time and centrifuged prior to isotopic analyses. This was done as a precautionary measured to remove any solid particles remaining in the river water, however little residue remained and no precipitates were observed.

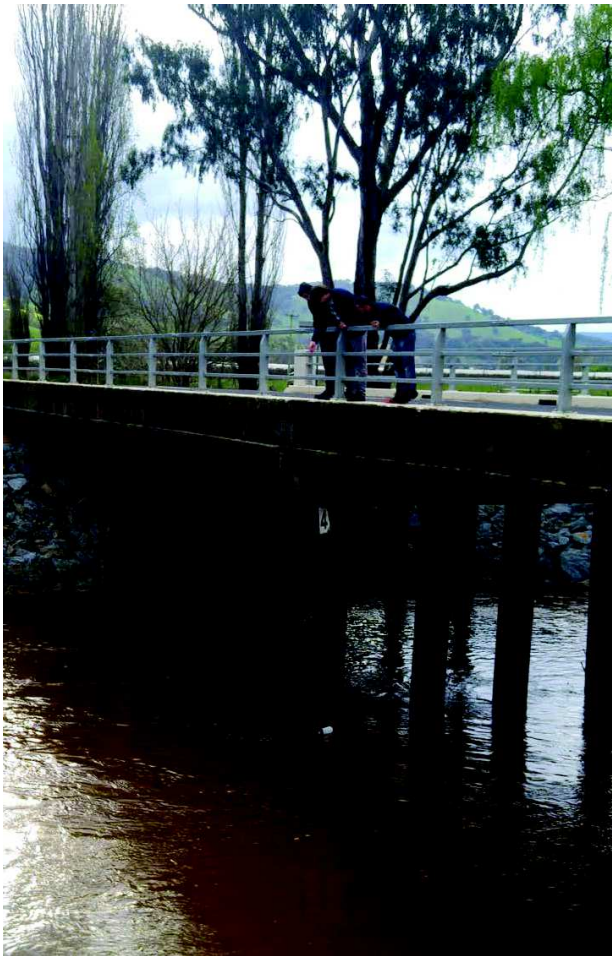

Figure 2-3. River water sample taken from the middle of the stream in a plastic HDPE bottle.

2.1.4 **Paleochannel sediment deposits**

On the alluvial plain, paleochannel sediment deposits were obtained by drilling horizontal core samples in the face of the sediment profile using a 9–cm diameter aluminum pipe, a metal core head, and a sledgehammer (Figure 2-4). Prior to coring, sediment profiles faces were 'cleaned' with a shovel, removing any visible traces of weathered material from the profile surface and exposing the most pristine inner portion of sediment, then sampled. The core pipe was forcefully removed by pulling on the opposite end, being careful not to disturb or lose the compacted sediment sample inside. Core lengths were determined by sediment compaction, solidity, and ultimately our ability to drive the core pipe into the sediment wall. Typical core lengths were approximately 50 cm. The sample was then spilt into two portions labeled 'inside' and 'outside', where inside and outside refer to the sediment furthest into the sediment profile and the sediment closest to the exposed profile surface wall respectively. By this measure, an estimate of sample variability can be made which may or may not be attributed to sample positioning relative to the exposed surface and therefore preservation integrity. It was first conceived that sediments further in the deposit would be less likely to be affected by post-deposition alteration and therefore better preserved. Both portions of the sample were sealed in plastic bags and brought back to the laboratory for analysis.

To access chemical and isotopic variability and possible post-depositional alteration of the sediment deposit, core samples were taken along the sediment profile with depth (Figure 2-4). On average 3 – 4 horizontal cores were taken at each site. The first sample was taken at the bottom of the profile, followed by the middle sample(s), and finally a sample was extracted from the top (about 30 -50 cm) of the surface. Cores were taken in this order to prevent contamination of falling sediment from above. After collection, sediment samples were treated in the same manner as described in Section 2.1.2 to obtain both sand and clay fractions.

2.2 **X-ray Diffraction**

Mineral identification of the bedrock and clay fraction of monolithological and main river sediment samples was determined by X-ray diffraction (XRD) at the University of Wollongong. Using a Phillips 1130/90 diffractometer, samples were analyzed between 4 and 70° 2-theta at 2°

Figure 2-4. Paleochannel sediment deposit profiles showing sampling strategy. Left panel: sampling profile with depth displaying 3 core locations: one at the bottom of the profile; one in the middle of the profile; and one near the surface, Right panel: bottom core sample being hammered in, displaying aluminum core pipe and metal core head.

per minute with a step size of 0.02. For both the bedrock and the clay fraction, an aliquot of powdered sample was mounted in aluminum holders and placed into the diffractometer for measurement. The clay fraction sample was mounted specifically to orientthe clay minerals based on their principle reflection. After first analyses, clay fraction samples were treated with ethylene glycol and processed a second time allowing better quantification of the expandable clay content. Traces were produced through a GBC 122 control system and a semi-quantitative analysis of the relative proportions of crystalline phases was performed using the Traces and SIROQUANT software. An example of a diffraction pattern is shown in Figure 2-5 displaying a non-glycol treated clay fraction diffraction pattern (green) overlain by a glycol-treated diffraction pattern (red) for the same sample. The red square highlights the difference between the two patterns which represents the relative amount of expandable clays in the sample. In this example approximately 20% of mixed (I/S) layer clays was identified. In Figure 2-6, an example is provided of a clay

fraction diffraction pattern which was quantified by the SIROQUANT software. Using the Traces software on the diffraction pattern (shown in Figure 2-5), the quartz peak was first shifted to 26.66. The pattern was then loaded in SIROQUANT and specific mineral phases selected. The first 5 degrees and from 44.4 – 44.6 degrees were removed from the analyses as the diffractometer causes interference in these areas and therefore cannot quantify them. The yellow pattern is the sample diffraction pattern from the diffractometer and the red pattern is the software's modelled projection based on specified mineral phases (Figure 2-6). Percent abundances were calculated using the SIROQUANT software by matching the modelled diffraction pattern (using selected mineral phases) with the observed diffraction pattern. Based on this example, a chi-squared (χ^2) value of 4.34 was obtained, which indicates the goodness-of-fit between the model and the data. For clay sample diffraction patterns, particularly those with large amorphous humps like observed in Figure 2-5, generally χ^2 values ≤ 5 indicate an acceptable quantification. The reproducibility of the mineral quantification for the bedrock and clay fraction was performed by repeated (n = 2) analyses of same sample with mixed (I/S) layer ranging from 8 – 19; kaolinite ranging from 66 – 77; and illite ranging from 7 – 11 (Table 2-1). Based on these results of sample replicates the reproducibility of biotite, chlorite, kaolinite, quartz, muscovite, orthoclase, albite, and k-feldspar is 3%, 0%, 1%, 6%, 1%, 3%, 4%, and 7% (2SD, n = 2), respectively. The reproducibility of mixed (I/S) layer, kaolinite, and illite mineral quantification for the clay fraction is 16%, 16%, and 6% (2SD, n = 2), respectively.

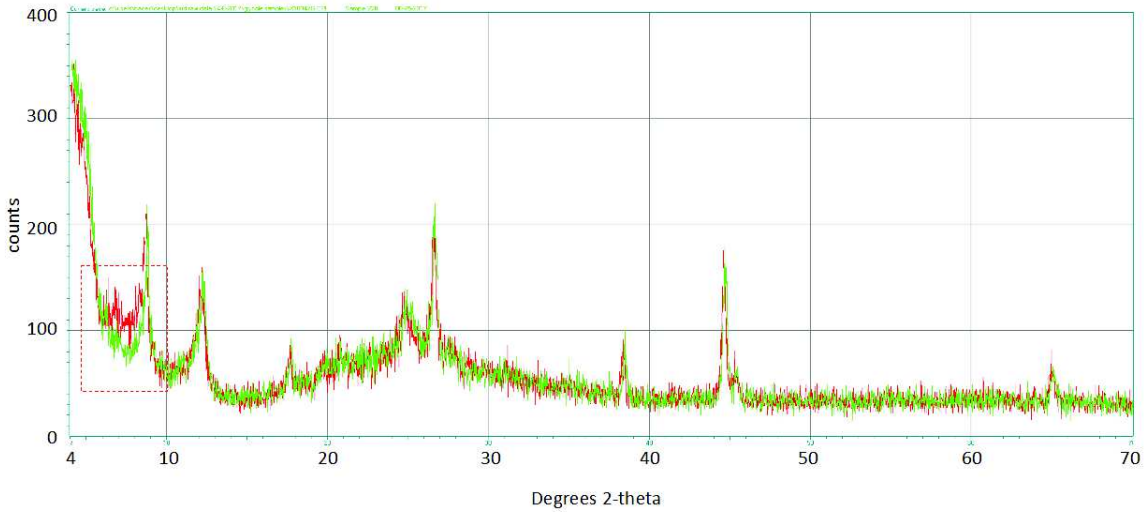

Figure 2-5. XRD diffraction pattern of a clay fraction sample showing the non-glycol (green) diffraction patter overlain by the glycol (red) diffraction patter. The difference between the two patterns represents the amount of expandable clays in the sample.

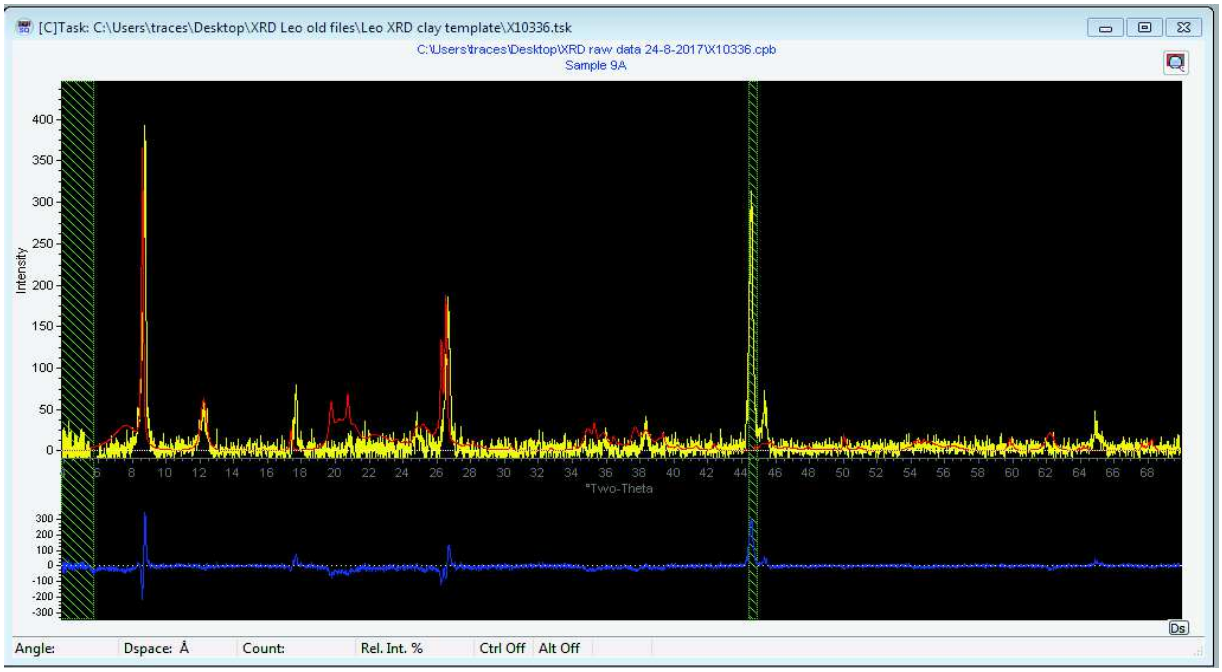

Figure 2-6. XRD diffraction pattern of a clay fraction sample being quantified by the SIROQUANT software. The yellow pattern is the sample diffraction pattern and the red line is the software match to mineral phases. In this example, the chi squared (χ^2) value = 4.34 after background subtraction, indicating the goodness-of-fit between the sample minerals and the software quantification. Large x^2 values indicate the model is poor, while smaller $\square^2$ values indicate the model is in better agreement with the data.

Table 2-1. XRD results of bedrock and clay fraction sample replicates

Bedrock Sample	Biotite (%)	Chlorite (%)	Kaolinite (%)	Quartz (%)	Muscovite (%)	Orthoclase (%)	Albite (%)	K-Feldspar (%)
Numeralla Granitic	19	0	3	45	5	5	17	0
Numeralla Granitic	17	0	2	49	4	7	20	5

Clay Sample	Mixed (I/S) layer (%)	Illite (%)	Kaolinite (%)	Quartz (%)
N. Booroorban 2	19	11	66	4
N. Booroorban 2	8	7	77	8

2.3 Major and trace elements

2.3.1 Introduction to the Q ICP-MS

Major and trace elements were measured by quadrupole inductively coupled plasma mass spectrometer (Q ICP-MS) iCAP (Thermo Scientific, Bremen, Germany) at the Wollongong

Isotope Geochronology Laboratory (WIGL) at UOW. The iCAP can be used for direct analyses of samples in liquid form. The instrument can be divided into four main components: sample introduction; interface (ion generation); ion optics (ion focusing); and, mass analyzer. The introduction system of the iCAP used at WIGL consists of a peristaltic pump, a PFA-100 microflow nebulizer (ESI, Omaha, NE, USA) with a flow rate of 90 – 150 μL min^{-1}, a cyclonic quartz spray chamber, and an ICP torch with injector; the interface consists of a Ni sample and skimmer cone (Thermo Scientific), and the extraction lens. The introduction system is where the liquid sample is pumped via the peristaltic pump to be nebulizer. The sample is transformed into an aerosol by the nebulizer and passed to the spray chamber which filters out large aerosol drops, thereby improving the signal stability. Then, the sample is carried to the interface region where it is injected into the plasma (made by partially ionizing argon gas) and ionized. The newly generated ions are brought from atmospheric pressure to the vacuum region via the sample cone and then into the mass spectrometer as an ion beam via the skimmer cone. Ions are then introduced into the quadrupole mass analyzer which filters out ions based on a specific mass to charge ratio, depending on the voltage applied to the quadrupole rods. Finally, ions are passed through the quadrupole, transferred to the dual mode secondary electron multiplier (SEM) and detected (Thermo Fisher Scientic, 2012); the electrical signal is measured in counts per second (cps).

2.3.2 **Sample preparation and concentration quantification**

All sample preparation was performed in a Class 100 cleanroom laboratory at WIGL, UOW. Perfluoroalkoxy alkane (PFA) vials were used for sediment sample digestion and to dry down solutions. Approximately 100 mg of sample powder were weighted in PFA vials and then dissolved in Ultrapur® 48% HF and Suprapur® 65% HNO_3 at 100°C for > 12 hours. After drying down, the samples were re-dissolved twice in aqua regia (made from Suprapur® reagents) at 130°C for >12 hours to drive off any fluorides. After another dry down step the samples were re-dissolved in 4 mL of Suprapur® 0.3M HNO_3 and an aliquot was diluted and used for measurement. Samples were processed alongside full procedure blanks. Geological reference materials: BCR-2, a basalt (Oregon, U.S.); GSP-2, a granodiorite (Colorado, U.S.) (both USGS reference materials); and JG-2, a granite (GSJ reference material) along with replicate samples were processed to assess external reproducibility of the concentration measurements.

Concentration measurements were performed using 50 sweeps and a dwell time of 0.01 s. Major elements (Na, Mg, Al, K, Ti, and Ca) were measured in standard mode; most trace elements (i.e. Li, Nb, Ta, Nd, Sm, Rb, Ba, La, Ce, Pr) were measured KED mode. A multi-element external calibration curve from 0.05 to 300 ppb was used to quantify elemental concentrations using a mixture of 71A and 71B multi-element standards (Inorganic Ventures, USA). To assess instrumental drift, 1 ppb and 200 ppb solutions were measured every 10 samples for trace and major elements, respectively. Instrumental drift was assessed to be < 1% (2RSE) for trace elements and approximately 2% (2RSE) for majors. Measures were corrected for blank contribution by analyzing a blank solution every 10 samples and subtracting it from the concentration measurement. The external relative analytical uncertainty (2 RSD, n = 5) of concentration measurements was obtained for major and trace elements by repeatedly measuring geological reference materials (BCR-2, JG-2, GSP-2) and assessed for major elements Na, K, Mg, Al, and Ti to be 4%, 3%, 3%, 3%, and 3%, respectively; and for trace elements Li, Nb, Ta, Sm, and Nd is 4%, 5%,7%, 6%, and 5%, respectively (Table 2-2). Sample replicates were also measured to assess the local variability within the datasets. The average 2 RSD (n = 5) calculated for major elements (Na, K, Mg, Al, and Ti) using natural sample replicates is 18%, 10%, 6%, 8%, and 9% respectively, and for trace elements (Li, Nb, Ta, Sm, and Nd) is 7%, 7%, 6%, 8%, and 9%. The larger relative errors associated with the measurement of natural samples (particularly clays) likely derives from the heterogeneity of the samples themselves; precision on presumably more homogenous reference material was therefore better, particular for major elements.

Accuracy of major and trace element concentration measurements was assessed by comparison with recommended values measured by Raczek et al. (2001) for BCR-2 and GSP-2 and Korotev, (1996) for JG-2 (Table 2-3). For BCR-2, all measured concentrations for rock standards agree with recommended values. For GSP-2, all major elements agree with recommended values except Ti, which measured 0.41 ± 0.02% compared to 0.69 ± 0.04% reported by Raczek et al. (2001). The Sm and Nd values measured in this study (23.3 ± 0.8 ppm and 181 ± 12 ppm, respectively) are also slightly less than reported values of 26.2 ± 0.4 ppm and 207 ppm. For JG-2, all measured elements except K (measured: 4.33 ± 0.3%; reported: 3.6 ± 0.3%) are in agreement with those reported by (Korotev, 1996).

Table 2-2. External reproducibility of major and trace element concentrations using reference materials BCR-2, JG-2, and GSP-2

Reference material replicate	Na (wt%)	K (wt%)	Mg (wt%)	Al (wt%)	Ti (wt%)	Li (ppm)	Nb (ppm)	Ta (ppm)	Sm (ppm)	Nd (ppm)
BCR-2	2.52	1.58	3.45	13.41	2.41	46.52	11.84	3.93	6.74	27.51
BCR-2	2.61	1.61	3.65	13.66	2.55	46.09	11.66	3.59	6.30	30.15
BCR-2	2.73	1.63	3.71	13.30	2.83	45.70	12.29	3.32	6.45	27.18
BCR-2	2.88	1.68	3.62	13.54	2.58	47.88	12.49	3.58	7.26	29.99
BCR-2	2.56	1.60	3.88	13.19	2.35	46.31	11.97	3.49	6.08	28.20
average	**2.66**	**1.62**	**3.66**	**13.42**	**2.54**	**46.50**	**12.05**	**3.58**	**6.57**	**28.61**
SD	0.15	0.04	0.16	0.19	0.19	0.83	0.34	0.22	0.46	1.39
RSD	**5.5**	**2.5**	**4.2**	**1.4**	**7.4**	**1.8**	**2.8**	**6.2**	**7.0**	**4.9**
JG-2	2.89	4.30	0.030	7.03	0.031	218.31	16.41	2.32	7.94	25.22
JG-2	2.92	4.34	0.031	6.64	0.032	228.39	14.77	2.36	9.99	27.60
JG-2	2.81	4.18	0.034	6.38	0.031	222.47	16.47	3.00	8.97	26.48
JG-2	2.94	4.36	0.031	6.65	0.032	228.95	15.58	2.24	9.44	28.54
JG-2	3.05	4.45	0.030	6.96	0.033	233.92	17.34	2.88	8.30	25.54
average	**2.92**	**4.33**	**0.03**	**6.73**	**0.032**	**226.41**	**16.11**	**2.56**	**8.93**	**26.68**
SD	0.09	0.10	0.002	0.27	0.001	6.08	0.97	0.35	0.83	1.39
RSD	**3.0**	**2.3**	**5.1**	**3.9**	**2.8**	**2.7**	**6.0**	**13.8**	**9.3**	**5.2**
GSP-2	2.38	5.06	0.92	14.16	0.42	194.41	26.34	4.01	23.70	188.46
GSP-2	2.40	5.04	0.96	14.26	0.42	197.72	29.41	4.18	23.42	175.33
GSP-2	2.21	4.63	1.01	14.63	0.39	187.18	27.20	4.02	23.50	183.93
GSP-2	2.42	5.02	0.97	14.17	0.41	198.06	30.16	4.12	23.14	185.14
GSP-2	2.35	4.93	0.90	15.00	0.41	197.11	28.78	3.89	22.65	174.04
average	**2.35**	**4.94**	**0.95**	**14.44**	**0.41**	**194.90**	**28.37**	**4.04**	**23.28**	**181.38**
SD	0.08	0.18	0.04	0.36	0.01	4.54	1.58	0.11	0.41	6.35
RSD	**3.6**	**3.6**	**4.5**	**2.5**	**3.0**	**2.3**	**5.6**	**2.8**	**1.7**	**3.5**

Table 2-3. Recommended values for BCR-2, JG-2, and GSP-2 geologic reference materials.

Standard	Na (wt%)	K (wt%)	Mg (wt%)	Al (wt%)	Ti (wt%)	Li (ppm)	Nb (ppm)	Ta (ppm)	Sm (ppm)	Nd (ppm)
BCR-2	3.08 ± 0.28	1.78 ± 0.14	3.56 ± 0.14	13.28 ± 0.4	2.26 ± 0.4	46.5 ± 0.2	12.01 ± 0.6	3.6 ± 0.6	6.57 ± 0.4	28.7 ± 0.3
JG-2	2.62	3.60	0.03	6.60	0.026	42.20	14.70	2.76	8.10	25.00
GSP-2	2.73 ± 0.22	5.42 ± 0.43	0.98 ± 0.04	14.95 ± 0.3	0.69 ± 0.04	194.90	28.37	4.04	26.2 ± 0.4	207 ± 0.0

BCR-2 and GSP-2 values were reported by Raczek et al. (2001). Li, Nb, and Ta values associated with these rock standards derive from the certificate of analysis issued with the reference material. JG-2 values were reported by Korotev (1996). Errors were not reported for JG-2 reference materials not for Li, Nb, and Ta measurement associated with the GSP-2 material. All reported errors are RSD.

Full procedure blanks were run alongside samples and standards then measured for major and trace elements (Table 2-4). For major elements Na, Mg, Al, K, and Ti, blanks ranged from 0.13 µg – 3.6 µg, 0.3 µg – 2.8 µg, 3.6 µg – 29.5 µg, 0.6 ng – 3.0 µg, and 0.014 µg – 0.9 µg, respectively. The average blank mass of Na, Mg, Al, K, and Ti is 1.4 µg, 0.4 µg, 11.7 µg, 1.9 µg, 0.5 µg, respectively, which represents an average blank contribution of < 1% for all major elements measured. Blanks for trace elements Li, Nb, Ta, Sm, and Nd range from 0.57 ng –

1.22 ng, 0.01 ng – 0.02 ng, 0.001 ng – 0.005 ng, 0.011 ng – 0.025 ng, and 0.002 ng – 0.005 ng, respectively. The average blank mass of Li, Nb, Ta, Sm, and Nd is 0.81 ng, 0.01 ng, 0.002 ng, 0.003 ng, and 0.015 ng, which represents a blank contribution of << 1% for trace elements. The local variability of natural samples was determined by individually processing separate aliquots of several samples in order to determine if blank contributions are negligible. The average measurement reproducibility (RSD) of major elements Na, K, Mg, Al, and Ti in natural sample replicates is 18%, 10%, 6%, 8%, and 9% respectively; and trace elements Li, Nb, Ta, Sm, and Nd is 7%, 7%, 6%, 8%, and 9%, respectively. Since the local sample variability is greater than the blank contribution for both major and trace elements, blank contributions are considered negligible.

Table 2-4. Full procedure blanks for both major and trace elements

Blank ID	Na (ng)	Mg (ng)	Al (ng)	K (ng)	Ti (ng)	Li (ng)	Nb (ng)	Ta (ng)	Nd (ng)	Sm (ng)
1789	383	0	10,288	2,157	319	1.22	0.01	0.005	0.020	0.003
1879	219	0	29,513	2,861	291	0.59	0.01	0.002	0.015	0.004
2481	2,613	0	13,767	1,017	894	0.57	0.01	0.002	0.012	0.003
2493	2,684	0	12,694	3,024	764	0.62	0.02	0.004	0.012	0.003
2510	3,589	0	11,982	0	811	1.02	0.01	0.001	0.025	0.004
2570	126	2755	0	3377	77	1.05	0.01	0.002	0.011	0.002
3295	412	295	3572	553	14	0.63	0.00	0.000	0.013	0.005

2.4 **Sample preparation for B isotopes and concentration**

2.4.1 **Alkali fusion**

Crushed bedrock and sediment samples were digested by alkali fusion in platinum (PtAu5%) crucibles using potassium carbonate in a 5:1 flux to sample ratio (Lemarchand et al., 2012; Tonarini et al., 1997). Routinely, 50 mg of powdered sample, corresponding to approximately 2500 ng B, is mixed with 250 mg of ground K_2CO_3, loaded into the crucible and placed in a muffle furnace at 950°C for 40 min. After cooling to room temperature the resulting fusion residue typically has a green-blue color, though other colors such as dark red and purple have been observed. Approximately 4 mL of 1M HCl (Suprapur®) is added to the crucible causing immediate outgassing of CO_2 and dissolution of carbonate phases. The crucible is then placed in an ultrasonic bath for 20 mins. The solution and the suspended material are pipetted into a centrifuge tube and diluted to 40 mL with 18.2 MΩ water. The tube is centrifuged for 20 minutes.

This procedure yields a solid residue; however it has been shown not to contain boron (Lemarchand et al., 2012).

2.4.2 **Reagents**

Reagents used in the chromatography include Merck HCl (Suprapur®), NaOH (technical grade), NaCl (technical grade), and deionized 18.2 MΩ-cm H_2O (Millipore) was used to prepare stock solutions. NaOH is B-purified by processing the commercial solution on 1.5 mL of Amberlite IRA 743 resin previously cleaned with 6M HCl. Then approximately 5 mL of NaOH is loaded onto the column and the effluent goes to the waste. After checking that the eluted solution has a basic pH, the column is then filled with NaOH and the eluent is collected in a PFA vial. NaCl is B-purified by adding dry Amberlite IRA 743 resin (approximately 10 g) to the stock solution and the pH of the solution is adjusted to 8 – 10 by adding several milliliters of B-purified NaOH. The pH of the solutions can be checked by pipetting a small amount of solution onto pH paper (not dipping it in solution). The K_2CO_3 used in the alkali fusion was 99.995% trace metals basis, powder and chunks form (Sigma Aldrich). Note: the batch of 0.5M HCl used for sample elution is the same as that used to make standard solutions and blanks when running the MC ICP-MS; this is what is meant by 0.5M HCl (precise).

2.4.3 **Ion exchange chromatography**

Boron is extracted from the supernatant by ion exchange chromatography performed under Class 100 cleanroom conditions at WIGL. Following the method of Lemarchand et al. (2012) and Roux et al. (2015), ion exchange is performed in two steps. First, a column containing 1.5 mL of BIORAD AG50W-X8 cation exchange resin is cleaned with 6M HCl by filling the column at least twice (Table 2-5). The column is then conditioned by adding 2 mL of 0.01M HCl three separate times, waiting for the solution to completely pass before proceeding to the next step. The sample is weighed and loaded onto the column, which typically consists of 5 mL of the total sample solution, corresponding to approximately 300 ng of B. The sample is passed through the column and collected into a 15 ML centrifuge tube. To ensure full sample recovery, 1 mL of 0.01M HCl is added to the column twice after the sample passes and collected. The first column is used to

remove cations from the solution, particularly K, which is added to the sample via the K_2CO_3 flux during alkali fusion. Because boron is present in acidic solutions as uncharged boric acid, $B(OH)_3$, it is not retained by the cation exchange resin. However, some other elements may not stick to the resin and also pass to the second step where they will be removed. The pH of the solution is then raised to 8 – 10, which is optimal for B adsorption on the Amberlite resin in the second step, by adding a small (~500 µL – 2000 µL) amount of purified NaOH to the sample elution.

A second column filled with 0.5 mL of crushed and sieved (100 – 200 mesh) Amberlite IRA 743 B-specific resin is then cleaned with approximately 20 mL of HCl; more (~50 mL) if the column has not been used in a long time (10 – 15 days) (Table 2-5). The column is then filled with 10 mL of Milli-Q® water to rinse all traces of acid from the resin. The resin is conditioned with 5 mL of Milli-Q® water in three steps: 1 mL, 2 mL, and 2 mL. The pH-adjusted sample is then slowly pipetted onto to the column as not to disturb the resin. There are three matrix elution steps which are accomplished by adding 2.5 mL of water, 2.5 mL of NaCl, and then 2.5 mL of water again, consecutively. Each individual step is done in three phases: 0.5 mL; 1 mL; and 1 mL. The two water steps are acting to rinse the resin, while the chloride in the NaCl solution exchanges with anions that are possibly absorbed on the Amberlite resin due to the presence of tertiary amino groups in the resin. After the three matrix elution steps, B is eluted in 5 mL of precise 0.5M HCl in three steps: 1 mL, 2 mL, and 2 mL. Ten minutes should pass between the loading of the first and second aliquots of precise 0.5M HCl during the sample elution. This is to ensure the resin becomes fully acidified and all B is desorbed from the resin.

2.5 **Boron concentration measurements by ID ICP-MS**

Boron concentrations were determined by isotopic dilution (ID ICP-MS) on the Q ICP-MS iCAP (Thermo Scientific, Bremen, Germany) at WIGL, UOW following the procedure of Roux et al. (2015). Isotope ratios were measured on the iCAP to prevent cross-contamination of ^{10}B-enriched solutions on the MC ICP-MS, which is used for isotope ratio determination of natural samples. Isotope dilution was used because it has the best analytical precision compared to other methods even at low concentrations (ng g^{-1}); provides ideal internal standardization which allows accurate correction of the measured ion currents from instrumental fluctuations (because isotope ratios are measured); and whose results are not significantly affected by sample to sample variations or the

chemical matrix (Menard et al., 2013). The isotope dilution technique consists of mixing a well-known mass of a sample solution and a ^{10}B isotopically enriched "spike" solution; NIST SRM 952, certified $^{11}B/^{10}B = 0.0532$ in this case. The measured $^{11}B/^{10}B$ ratio is then used to calculate the mass of B in the sample using Equation 2-1:

$$m_{spl}^{B} = V_{sp} \times C_{sp}^{B} \times \frac{M^{11} \times R_{spl} + M^{10}}{M^{11} \times R_{sp} + M^{10}} \times \frac{R_{meas} - R_{sp}}{R_{spl} - R_{meas}} \quad (2\text{-}1)$$

where m_{spl}^{B} is the mass of B in the sample given atomic mass units (amu); V_{sp} and C_{sp}^{B} are the volume (mL) and concentration (ppb) of the spike solution that are added to the sample, respectively; M^{11} and M^{10} are the atomic masses of ^{10}B and ^{11}B (M^{11} = 11.009305 amu and M^{10} = 10.012938 amu); R_{spl}, R_{sp}, and R_{meas} are the $^{11}B/^{10}B$ isotopic ratios of the sample, the spike, and the measured value of the mixture, respectively. As the ratios of the sample and spike need to be known independently, the accepted $^{11}B/^{10}B$ values for B isotope standards NIST SRM 951 and 952 are used for R_{spl} and R_{sp}, which are 4.0436 and 0.038, respectively.

Table 2-5. Ion exchange chromatography protocol for the separation of B from silicate materials and waters

Column	Step	Purpose	Volume (mL)	Reagent
1[#]	1	Clean column	10	6 M HCl
	2	Clean column	10	6 M HCl
	3	Condition column	6	0.01M HCl
	4	Sample load	5	
	5	Boron elution	2	0.01M HCl
2[*]	1	Clean column	20	0.5M HCl
	2	Clean column	10	H_2O
	3	Condition column	5	H_2O
	4	Load Sample at pH 9	7 – 25	
	5	Matrix elution	2.5	H_2O
	6	Matrix elution	2.5	0.5 M NaCl
	7	Matrix elution	2.5	H_2O
	8	Boron elution	5	0.5 M HCl (precise)

[#] BIORAD AG50W-X8 cation exchange resin (100 – 150 µm), 1.5 mL bed volume
[*] Amberlite IRA 743 B-specific anion exchange resin (100 – 200 µm), 0.5 mL bed volume
Column 1 (Step 4): Be sure to collect sample in PFA vial after loading onto column. Column 1 and 2 (Step 4): Sample is not loaded in a specific reagent, rather the supernatant solution from the alkali fusion process (column 1) and the sample elution from column 1 + an unspecified amount of NaOH, sufficient to raise to the pH level to 8 –10 (column 2). For water samples, the amount of sample loaded onto column 2 depends on the B concentration of the sample.

In the laboratory, the sample was typically prepared by placing a rinsed ICP vial onto the balance and weighing 1 mL of sample elution which passed both steps of ion exchange chromatography. Spike solution was then added to the vial and its weight recorded; the mixture is

isotopically homogenized by shaking and letting rest for several hours. The ideal sample to spike mixture ratio is between 0.3 and 1.5, which results in a measurement uncertainty as low as 1% (± 2 RSE) for B concentrations (Roux et al., 2015). Sample introduction is similar to that explained in Section 2.3.2, the only difference being introduction acid, which for this protocol is 0.5 M HCl (same as the sample), opposed to the 0.3 M HNO_3 used to measure major and trace elements. Intensities of both B isotopes at masses 10 and 11 were measured in a 0.5M HCl solution to establish the baseline signal before each sample and subtracted from the sample ratio (R_{meas}). The average baseline counts per second (cps) represent approximately 0.6% and 0.4% of the total B on mass 11 and 10, respectively, in the measured sample. Mass discrimination on the measurement of B isotopes by ICP-MS is significant. Measured sample ratios are therefore corrected by the classical exponential law:

$$R_{true} = R_{meas} \times \left(\frac{M^{11}}{M^{10}}\right)^{\beta} \quad (2\text{-}2)$$

where R_{true} is the true (corrected) $^{11}B/^{10}B$ isotope ratio of the sample; and β is the mass discrimination exponential factor. According to Roux et al. (2015), who performed experiments on the relationship between R_{true} and β using solutions with various $^{11}B/^{10}B$ ratios, within and between analytical sessions, β only varies slightly (< 5%) over the range of measures isotope ratios, however the β value may vary significantly from one session to the other (up to 50%) attributed to changes in instrumental settings. Hence, β must be determined each session by preparing and measuring a 10 ppb NIST SRM 951 standard solution with a known $^{11}B/^{10}B$ isotope ratio of 4.0436; all sample ratios are then corrected for mass discrimination based on the β value of the standard solution using Equation 2-2.

Geological reference materials and sample replicates were used to access the external reproducibility and accuracy of B concentration measurements (Table 2-6). The average B concentration obtained for the W-2a rock standard is 11.7 ± 0.4 ppm (2 SE, n = 6), which is in good agreement with Govindaraju (1994) who report a B concentration of 12 ± 0.3 ppm (2 SE). The 2 RSE associated with the repeated B concentration measurement of this reference material is 3% (n = 6). Three individually processed aliquots of the SDC-1 reference material were also measured for B concentration and yield an average B value of 12.6 ± 0.3 ppm (2SE, n = 3) also in agreement with the reported value Govindaraju (1994) who reported a B concentration of 13 (± n/a). A sample replicate (14B) was also measured to assess the external variability of natural

sediment samples. An average value of 15.6 ± 0.3 ppm (2SE, n = 3) was obtained for the bulk sediment, yielding a 2 RSE of 2% which is the same as that obtained for the SDC-1 reference material and slightly better than that obtained for the W-2a material. External reproducibility of all standards (W-2a and SDC-1) and sample replicate (14B) in this study is 3% (RSD).

Table 2-6. External reproducibility and accuracy of B concentration measurements of geological reference materials and sample replicates processed through the entire chemical procedure

Material	ID	Mass Sample (mg)	Mass B Sample aliquot (ng)	Mass B spike (ng)	[B] ppm measured	[B] ppm reported	2 SE
W-2a	1826	50.60	46	55	11.4	12	0.3
W-2a	1827	68.50	62	55	11.3	12	0.3
W-2a	1935	49.69	45	56	11.2	12	0.3
W-2a	1936	50.22	50	57	12.5	12	0.3
W-2a	2021	50.28	48	54	11.8	12	0.3
W-2a	2022	51.51	49	57	11.8	12	0.3
SDC-1	3326	50.80	51	54	12.6	13	0.2
SDC-1	3327	54.10	55	54	12.8	13	0.2
SDC-1	3328	58.00	57	54	12.3	13	0.2
14B	3358	50.22	55	54	16.0	-	-
14B	3359	50.28	53	54	15.4	-	-
14B	3360	51.51	55	54	15.6	-	-

Full procedure blanks were run alongside of silicate samples and measured for B concentration to access the blank contribution on B measurements. Throughout the course of this study the full procedure blank from powdered sample to measurement on the Q ICP-MS ranged from 26 to 39 ng of B with an average value of 33 ± 2.3 ng (2SE, n = 11) (Table 2-7). Contamination tests aiming to identify the B contributions from each individual source including: 1) K_2CO_3 flux used in the alkali fusion, 2) contamination from the muffle furnace, 3) contamination from the resins during chromatography, and 4) contamination via introduction to the mass spectrometer yield that on average approximately 26 ng of B contamination originate from the furnace, 7 ng of B from the K_2CO_3 flux, < 1ng of B from the resins, and < 1 ng of B via introduction to the mass spectrometer. Since the muffle furnace was identified as the greatest contributor of B in the process, regular cleaning via long hours of baking (empty) and cleaning of any residue inside was performed regularly throughout the study. The range of B blank contributions on the geological reference materials used to test the protocol (W-2a and SDC-1) are between 4 – 5 % of the total B analyzed in each sample. Due to their lower concentrations (12 – 13 ppm), the blank contribution on these rock standards are higher than most measured samples in this study. Similar to the rock standards, bedrock and sand fraction samples also have lower B concentrations ranging from 12 – 19 ppm and 11 – 37 ppm, respectively, which represent blank

contributions between 3 – 5% (2 RSE) and 1 – 6% (2 RSE), respectively. On the contrary, clay fraction samples, which were the majority of samples measured in this study, typically have higher B concentrations (average ≈ 50 ppm) with an actual range between 19 – 61 ppm which represent blank contributions between 1 – 4% (2 RSE). In instances where B concentrations were particularly low, more than 50 mg (~60 – 65 mg) was processed through the chemistry to maintain a low blank to sample ratio. Additionally, more than 5 mL (between 5 – 15 mL) of sample supernatant was B- purified in order to obtain approximately 250 ng of B in the analyzed sample.

Dissolved load samples were also processed by ion exchange chromatography (column 2 only) and analyzed for B concentration. The blank contribution coming from ion exchange columns and chemistry reagents was assessed by running blanks alongside dissolved load samples. The B concentration of the blanks passed on the water columns vary from 1 ng – 5 ng, with the average value of 2 ± 1 ng (2SE, n = 9) (Table 2-7). The amount of B processed for dissolved load samples and seawater standards in this study is 250 ng of B per sample/standard. Hence, the B blank contribution on a dissolved load sample and standard is < 1% (2 RSE).

Table 2-7. Full procedure blank measurements processed with silicate and dissolved load (water) samples throughout the course the study

Silicates		Waters	
Blank ID	B (ng)	Blank ID	B (ng)
2048	36	3066	4.7
2200	32	3067	3.1
2448	30	3068	3.2
2546	31	3069	1.2
2604	39	3070	2.2
2681	26	3071	1.7
2682	37	3072	3.4
3166	34	3073	1.9
3361	34	3074	1.0
3605	32		
3606	30		

Silicate samples underwent alkali fusion, two steps of ion exchange chromatography, and measurement by ICP-MS. Dissolved load samples passed on the water columns only underwent one chromatography step (column 2) and measurement on the ICP-MS.

2.5.1 **Boron recovery**

The efficiency of the B chemical purification was tested by repeatedly (5x) processing a NIST SRM 951 reference solution through the entire ion exchange chromatography. The B concentration of the solutions were determined before the experiment and the effluents analyzed for B content after the second purification step. The total elution volume from the second chromatography step was 5 mL; this solution was measured in one aliquot. Results for this effort show that the B recovery from the chromatography ranged from 97% to 102% ± 2 (1SD, n = 5) with an average value of 98%. Boron recovery was also tested for the entire protocol from alkali fusion to sample elution. Individually processed aliquots of the geological reference material W-2a (USGS) were processed through the entire protocol and yield a recovery of 97% ± 3 (1SD, n = 6). Although slightly less (and more) B was measured after the entire procedure than compared to before, these results indicate a good B recovery and efficiency of the protocol. Additionally, accurate and precise B concentration measurements of geological reference materials demonstrate that an average recovery of 98% is sufficient to yield reported standard values (see below).

2.6 **Boron isotope measurements by MC ICP-MS**

Boron isotope ratios were determined by multi-collector inductively coupled plasma mass spectrometer (MC ICP-MS) on a Neptune Plus™ (Thermo Scientific, Bremen, Germany) at WIGL, using a protocol adapted from Roux et al. (2015). The MC ICP-MS offers easy and robust sample introduction, high sample throughput and mass resolution, and comparable precision to that achieved by TIMS (Albarède et al., 2004). The instrument can be divided into three parts: the ICP module, the ESA module, and the multi-collector module (Figure 2-7). The ICP module includes the inlet system where the liquid (or gas) sample is continuously fed into the nebulizer where an argon/sample aerosol is created and then passed to the quartz spray chamber that refines the aerosol by removing large droplets. The mixture is then directed into the injector of the plasma torch, which is located in the center of the load coil which couples inductive RF field into the Ar gas flow. Here, the fine sample aerosol from the inlet system is injected into the plasma with a sustained temperature of 8000°C where it is ionized. In the ESA module, ions (and other sample and gas elements) enter the mass spectrometer through the opening of the sample cone and further refined through the skimmer cone. A differential pumping system is used to pump down the

atmospheric pressure at the sample cone creating a vacuum. Inside the transfer lens, the ion beam is accelerated to kinetic ion energy. The mass analyzer controls, shapes, and focuses the

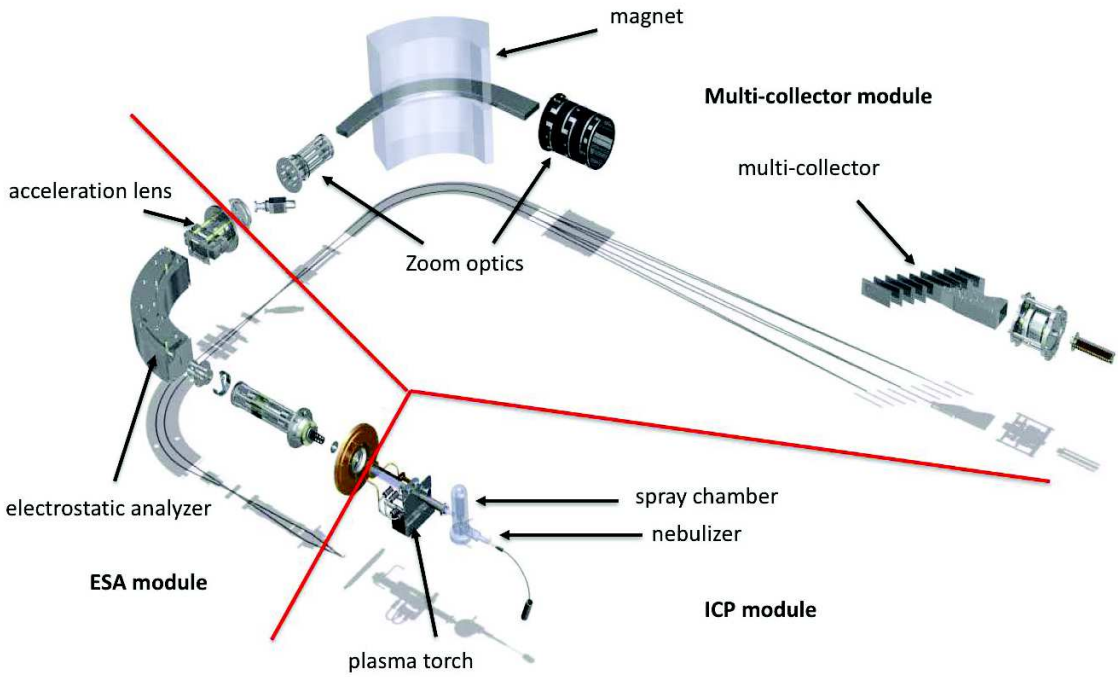

Figure 2-7. Components of the MC ICP-MS Neptune Plus (Thermo Fisher Scientific). Figure modified from Thermo Fisher Scientific (2009).

kinetic energy of the ion beam. In the multi-collector module, the ion beam is accelerated through a magnetic field, which separates ions based on their mass to charge ratio. This multi-collector is fitted with a series of Faraday cups which are connected to a current amplifier that receive the accelerated ion beams from individual masses (element isotopes) and report the resulting intensity (in Volts).

For the measurement of boron isotopes, the sample is introduced in liquid form dissolved in 0.5M HCl. The blank measurement and standard bracketing solution were all prepared with same batch of 0.5M HCl acid as that used for samples as to avoid isotopic bias induced by different acid media matrices, which was demonstrated by Roux et al. (2015). The instrument wash solution is also 0.5M HCl. The sample introduction system consists of a standard sample and skimmer cone, dual cyclonic spray chamber, and an APEX PFA nebulizer (Elemental Scientific, Omaha, USA) with a 100 µL min^{-1} flow rate (Table 2-8). Processing of all samples was automated using a CETAC ASX-112FR autosampler. H3 and L3 Faraday cups were used for collection of the ^{11}B and ^{10}B ion currents, respectively, which were each connected to 10^{-11} amplifiers. Data acquisition

was performed over 10 blocks of 10 cycles for samples and standard measurements and 5 blocks of 10 cycles for instrument blank measurements with eight seconds of integration for each measurement. An amplifier baseline and peak center were performed at the start of each analysis. Tuning was routinely performed on mass 11 using a 50 ppb NIST SRM 951 primary standard solution; this yielded an instrument sensitivity of approximately 6 – 9 V of ^{11}B per ppm of B. Figure 2-8 displays a typical peak shape after tuning. To correct for the instrumental blank contribution, a 0.5M HCl solution was measured before every sample and standard and subtracted from the sample measurement. The measured $^{11}B/^{10}B$ ratio was corrected for instrumental mass discrimination through external normalization using standard bracketing. Mass discrimination-corrected $^{11}B/^{10}B$ were expressed as $\delta^{11}B$ (unit: ‰) by normalizing the ratio of the sample to that of the NIST SRM 951 reference material:

$$\delta^{11}B\ (‰) = [(^{11}B/^{10}B)_{\text{sample}} / (^{11}B/^{10}B)_{\text{NIST-SRM 951}} - 1] \times 1000 \qquad (2\text{-}3)$$

Between sample and standard analyses, rinsing was performed for 10 min with a 0.5M HCl solution. The slope generated for this baseline correction was 0.15 mV min^{-1} corresponding to an uncertainty of approximately 0.16‰, which is deemed acceptable for this method (Roux et al., 2015).

2.6.1 **MC ICP-MS Performance**

The accuracy and precision of the $^{11}B/^{10}B$ measurements on the MC ICP-MS and overall instrument performance (tuning, signal stability, mass calibration, etc.) was assessed before and during every analytical session by measuring a 50 ppb certified B isotope standard ERM AE120 solution whose certified $\delta^{11}B = -20.2 \pm 0.6‰$ (2 SD) (Brand et al., 2014; Vogl and Rosner, 2012). The average $\delta^{11}B$ measured over the course of the study was $-20.5 \pm 0.1‰$ (2 SE, n = 34) (Figure 2-9). The grey line in Figure 2-9 is the average certified value of the standard; the grey box is the uncertainty on the certified value, the red dotted line is the average $\delta^{11}B$ value measured in this study with its associated error (1SD) in the red box. Results show that the measured $\delta^{11}B$ values in this study are slightly lower that the reported average but within range of the reported error on the reference material. Over time, no significant or systematic drift in the $^{11}B/^{10}B$ measurements of this reference solution was observed. If the measured value of the reference solution did not fall

with the error margin of the certified value, the analytical session was terminated and the instrument re-tuned.

Table 2-8. Neptune Plus MC ICP-MS measurement settings for B isotopes at WIGL

Component	**Setting**
RF power	1200 W
Ar cooling gas flow	1.050 l min^{-1}
Acceleration voltage	10 kV
Faraday cups	L3, H3
Spray chamber	Quartz dual-cyclonic
Nebulizer	APEX PFA ST-2056
Uptake time	70 sec
Uptake rate	100µL min^{-1}
No. cycles (baseline)	50
No. cycles (sample, standard)	100
Sensitivity on ^{11}B	9 V per µg g^{-1}
Primary standard	50 ng g^{-1}
NIST SRM 951	
Sample concentrations	20 – 60 ng g^{-1}

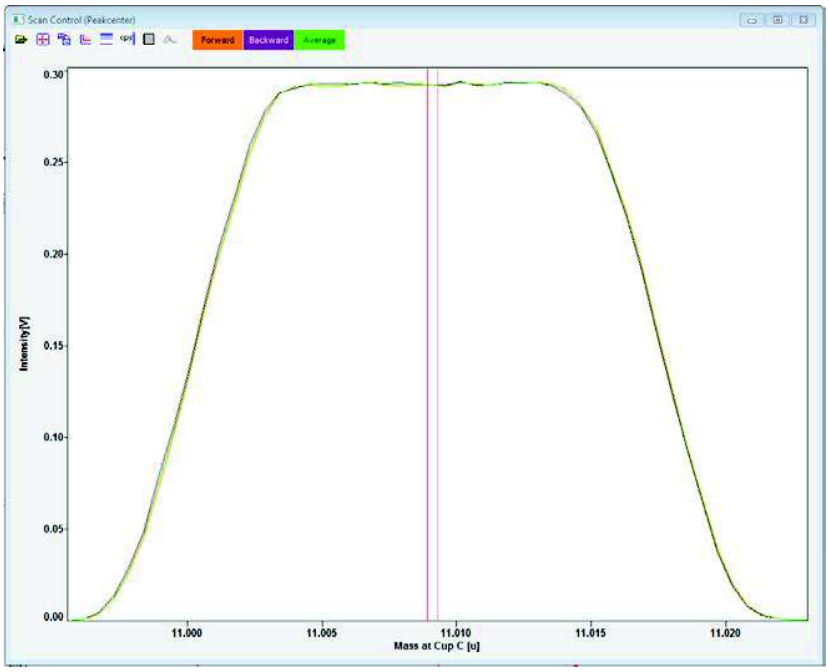

Figure 2-8. Typical peak shape measured on mass 11 after tuning in a 50 ppb NIST 951 solution during an analytical session on the Neptune Plus MC ICP-MS at WIGL, UOW

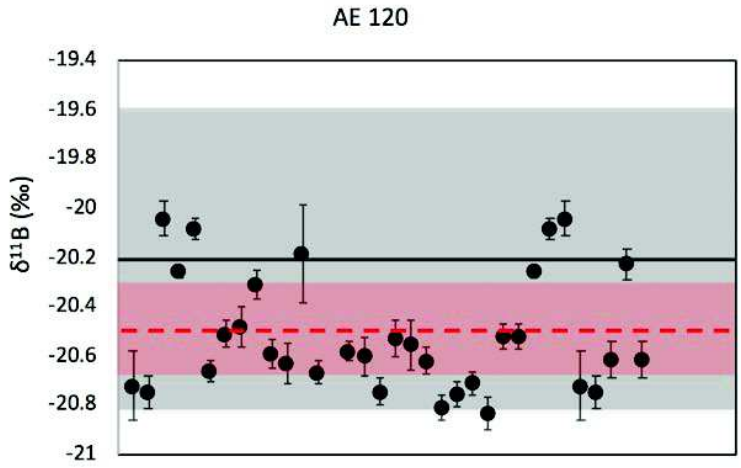

Figure 2-9. MC ICP-MS instrument performance over time assessed by measurement of the standard AE 120. The certified $\delta^{11}B = -20.2 \pm 0.6‰$ (2 SD); solid grey line is the certified standard average; grey box is the 2 SD on the certified average; and the red dashed line is the average $\delta^{11}B$ obtained throughout this course of the study, $-20.5 \pm 0.1‰$ (2 SE, n = 34). The red box represents a 1 SD error on the average measures. Data points are plotted sequentially from left to right over time.

2.6.2 **Method verification by measurement of reference materials**

Various certified geological reference materials (W-2a, diabase; BCR-2, basalt) and sample replicates (BLK 4D) were processed through the entire chemical procedure including rock dissolution, ion exchange chromatography, and measurement by MC ICP-MS to verify the precision and accuracy of the protocol. Additionally, the standard solutions ERM AE 120 and seawater were repeatedly processed via ion exchange chromatography alongside dissolved load samples and analyzed by MC ICP-MS to verify the ion exchange chromatography. All rock standard and sample aliquots were processed by alkali fusion individually. Measurement of the AE 120 standard solutions yielded $\delta^{11}B$ values ranging from $-20.1 \pm 0.2‰$ to $-20.7 \pm 0.2‰$ (Figure 2-10A; Table 2-9); BCR-2 values ranging from $-5.7 \pm 0.2‰$ to $-6.1 \pm 0.2‰$ (Figure 2-10B, Table 2-9); seawater values ranging from $39.7 \pm 0.2‰$ to $40.0 \pm 0.2‰$ (Figure 2-10C; Table 2-9); W-2a values ranging from $11.90 \pm 0.2‰$ to $12.60 \pm 0.2‰$ (Figure 2-10D, Table 2-9); and the sample replicate BLK 4D having $\delta^{11}B$ values ranging from $-11.5 \pm 0.2‰$ to $-12.14 \pm 0.2‰$ (Figure 2-10E, Table 2-9). All $\delta^{11}B$ error values are reported as 2 SE.

For AE 120 reference material, an average $\delta^{11}B$ value of $-20.4 \pm 0.2‰$ (2 SE, n = 7) is obtained, which is in good agreement with the certified $\delta^{11}B$ value of $-20.2 \pm 0.6‰$ (2SD) (Brand et al., 2014; Vogl and Rosner, 2012). The average $\delta^{11}B$ value of seawater measurements is 39.8 ±

0.2‰ (2 SE, n = 4), which is in agreement with Foster et al. (2010) who reported an average value of 39.61 ± 0.04‰ (2 SE, n = 28). However, the seawater used in this study was not the international seawater standard, but rather collected nearshore in Los Angeles, California in 2010 (reported in Roux et al., 2015). Therefore, comparisons of reported seawater measurements in this study to those of Foster et al. (2010) are only general comparisons to assess accuracy, as the same exact solution was not analyzed in both cases. These results indicate that the ion exchange chromatography used to extract and purify B has no significant effect on the measured B isotopic composition of the samples. The average $\delta^{11}B$ compositions of the geological reference materials W-2a and BCR-2 are 12.2 ± 0.2‰ (2 SE, n = 6) and –5.9 ± 0.2‰ (2 SE, n = 4), respectively. These values are very similar to measurements made by Gangjian et al. (2013) who reported $\delta^{11}B$ values for W-2a and BCR-2 of 12.2 ± 0.4‰ (2 SE, n = 3) and –5.9 ± 0.2‰ (2 SE, n = 4). These results show that the entire procedure of B extraction and purification has no significant effect on the measured B isotopic composition of the samples.

Overall, the B isotope measurements in the different reference materials demonstrate good repeatability (Figure 2-11) and are within two standard errors of reported values for all reference materials. In addition to reference materials, sample replicates were used to assess precision of B isotope measurements in natural samples. An average $\delta^{11}B$ value of –11.9 ± 0.2‰ (2 SE, n = 6) for the sample replicate BLK 4D was obtained which demonstrates good reproducibility of natural samples. The reproducibility of B isotope measurements in natural samples is therefore the same as those of BCR-2 and W-2a reference materials. Therefore, considering the external reproducibility of all silicate materials measured in this study (W-2a, BCR-2, and BLK 4D), which were processed through the entire chemical procedure including alkali fusion, the average external reproducibility on B isotope measurements is 0.4‰ (2 SD). Similarly for dissolved load samples, by considering the external reproducibility of both the ERM AE 120 and seawater solutions which passed only the ion exchange chromatography steps and measurement on the MC ICP-MS, the average external reproducibility of B isotope measurements is also 0.4‰ (2SD).

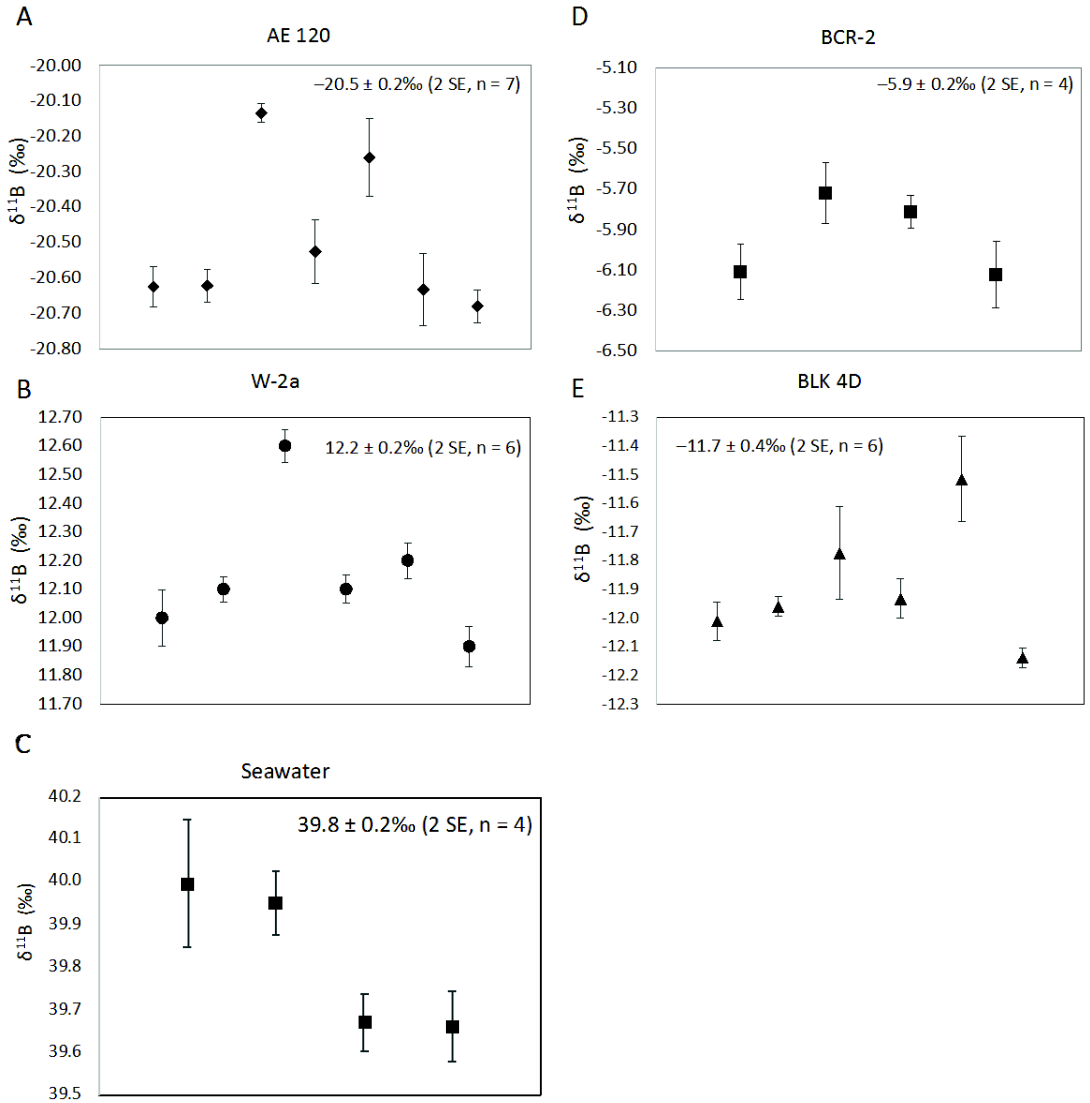

Figure 2-10. Reproducibly of $^{11}B/^{10}B$ ratio measurements (± 2SE) for A) standard solution ERM AE120 (n = 7), B) W-2a diabase (n = 6), C) seawater (n = 4), D) BCR-2 basalt (n = 4), and E) sample replicate BLK 4D (n = 6). The average measurement value and 2 SE for each standard and sample replicate is listed at the top right of each graph. The general agreement between sample and standard replicates demonstrates high reproducibility of boron isotope measurements.

Table 2-9. Boron isotope ratios of reference material processed through the entire chemical procedure

Sample	$\delta^{11}B$ (‰)	2 SE	n	Reported Value
ERM AE 120 boric acid standard	-20.5	0.2	7	–20.2 ± 0.6‰ (2SD) Vogl and Rosner (2012); Brand et al. (2014)
W-2a diabase	12.2	0.2	6	12.2 ± 0.4‰ (2 SE, n = 3) Gangjian et al. (2013)
BCR-2 basalt	-5.9	0.2	4	–5.9 ± 0.2‰ (2 SE, n = 4) Gangjian et al. (2013)
Seawater natural solution	39.8	0.2	4	–39.61 ± 0.04‰ (2 SE, n = 28) Foster et al. (2010)
BLK 4D Sample replicate	-11.9	0.2	6	

Internal analytical uncertainties are reported at 95% confidence interval. Samples were processed as individual aliquots and measured over several sessions throughout this study.
Reproducibility of B isotope ratios is assessed to be 0.4‰ (2SD).

2.7 Neodymium isotope analysis

2.7.1 Sample preparation and analyses for neodymium (Nd) isotopes

In addition to boron isotopes, many silicate samples were also measured for Nd isotopes in order to better understand sediment provenance, particularly in the paleochannel sediment deposits. Similar to B isotopes, Nd isotopes were processed at WIGL, UOW in a Class 100 cleanroom laboratory; concentrations and isotopes were measured by Q ICP-MS and MC ICP-MS, respectively. The entire protocol was then verified with geochemical reference materials.

2.7.2 Reagents, labware, and reference materials

Reagents used in sample preparation include Merck Suprapur and Ultrapur® grades: HCl (Suprapur®); HNO_3 (Ultrapur®); and HF (Ultrapur®). Deionised 18.2 MΩ-cm H_2O (Millipore) was used to prepare stock solutions and for dilution. Perfluoroalkoxy alkane (PFA) vials were used for sample digestion and to dry down solutions. Vials used for MC ICP-MS analysis were made of high-density polyethylene (HDPE), and for Q ICP-MS analysis, of polypropylene (PP). The PFA labware was washed overnight at 100°C in 7.5 M HNO_3, followed by a wash with 6 M HCl - 0.16 M HF at 100°C and rinsed with H_2O. This cleaning procedure yields Nd blanks of <0.06 pg.

HDPE and PP vials and caps were twice rinsed with 1.5 M HNO_3. Reference materials with known $^{143}Nd/^{144}Nd$ ratios were used in this study to assess accuracy of the $^{143}Nd/^{144}Nd$ ratios: BCR-2, basalt from the Bridal Veil Flow Quarry (Oregon, U.S.) (Wilson, 1997); GSP-2, granodiorite from the Silver Plume Quarry (Colorado, U.S.) (Wilson, 1998) (both USGS reference materials), and JG-2, granite from Hirukawa-mura (Japan) (GSJ reference materials) (IMAI et al., 1995).

2.7.3 **Sample digestion and ion exchange chromatography**

Approximately 100 mg of powdered geological reference material were weighed, corresponding to 2.6 µg, 2.8 µg, and 2.0 µg of Nd for BCR-2, JG-2, and GSP-2, respectively. The aliquots were then dissolved in PFA vials with 48% HF and 65% HNO_3 at 100 °C for >12 hours. The samples were then dried down and re-dissolved twice in aqua regia at 130 ºC for >12 hr to break down any fluorides. Samples were then dried down and re-dissolved in 6 mL of Ultrapur® 1.5 M HNO_3. Solutions showed no signs of undissolved residues.

The automated purification of Nd is performed using the prep*FAST*-MC™ system (ESI, Omaha, NE, USA). The prep*FAST*-MC™ is a fully-automated, low pressure (<100 psi), PFA chromatography system that performs several basic functions to isolate elements of interest, such as sample loading, cleaning and conditioning of the column, matrix wash and elution of the target fraction. Two PFA columns to perform the chromatography: the first is a 600 µL column, filled with 100 µL of 100-150 µm Prefilter resin (Eichrom Technologies, USA) under 500 µL of 100-150 µm TRU resin (Eichrom Technologies, USA); the second is a 2000 µL column which is filled with 2000 µL of 50-100 µm Ln resin (Eichrom Technologies, USA). This technique was adapted from Pin and Zalduegui (1997) and further developed (automated) at WIGL, UOW.

For the first separation, samples are loaded in 2 mL of 1.5 M HNO_3 (1/3 of the total digested sample) onto the first column. The Prefilter resin is used to prevent leakage of TRU resin during the elution. The resin is first cleaned with 6 mL of 3 M HCl, then 6 mL of 0.5 M HCl, and 6 mL of 0.1 M HCl – 0.3 M HF. The resin is then conditioned with 4 mL of 1.5 M HNO_3 and the sample is loaded in 2 mL of 1.5 M HNO_3. Following the initial sample load, 2 mL of 1.5 M HNO_3 is deposited into the sample vial to reflux any remaining sample residue and then loaded onto the column. The matrix is washed with 5 mL of 1.5 M HNO_3, and finally REE are eluted in 4.5 mL of 3 M HCl. The procedure is summarized in Table 2-10 and the elution profile is shown in Figure 2-11A. Following the first separation, the REE elution cut was dried down then refluxed in 500µL

of 0.25 M HCl. The second column is cleaned twice with 6 mL of 6 M HCl and then 4 mL of 18.2 MΩ H_2O. The column is conditioned with 4 mL of 0.25 M HCl and the sample is loaded in 0.5 mL of 0.25 M HCl. The matrix is then washed with 5 mL of 0.25 M HCl. The Nd fraction is finally eluted in two 7.5 mL steps using 0.25 M HCl. This procedure is summarized in Table 8 and the elution profile is shown in Figure 2-11B. After the chromatography, the Nd elution was dried down and refluxed in 4 mL of 0.3 M HNO_3, to achieve a concentration of 200 ppb Nd, ready for isotope ratio measurement by MC ICP-MS.

Separation of Nd from the sample matrix is achieved with the two-step chromatographic separation method described above and summarized in Table 2-10. For the first column, the elution curve determined using 9 mL of 1.5 M HNO_3 shows an almost complete matrix removal from the REE elution: Na (100%); Mg (100%); Al (100%); Fe (99.8%); and K (100%) (A). In the REE elution, 4.5 mL of 3M HCl was used to recover 100% of the Nd and 94.5% of the Sm in the solution.

Table 2-10. Ion exchange chromatography protocol for the separation of Nd from silicate materials

Column	*Step*	*Purpose*	*Volume (mL)*	*Flowrate ($\mu L\ min^{-1}$)*	*Reagent*
1[§#]	1	Clean column	6	5000	3 M HCl (UP)
	2	Clean column	6	5000	0.5 M HCl (UP)
	3	Clean column	6	5000	0.1 M HCl – 0.3 M HF (UP)
	4	Condition column	4	4000	1.5 M HNO_3 (UP)
	5	Load Sample	2	400	1.5 M HNO_3 (UP)
	6	Reflux into vial and load	2	400	1.5 M HNO_3 (UP)
	7	Elute sample matrix	5	3000	1.5 M HNO_3 (UP)
	8	Elute REE fraction	4.5	3000	3 M HCl (UP)
2[*]	1	Clean column	2 x 6	4000	6 M HCl (SP)
	2	Clean column	4	4000	H_2O (Millipore)
	3	Condition column	4	4000	0.25 M HCl (SP)
	4	Load Sample	0.5	600	0.25 M HCl (SP)
	5	Elute sample matrix	5	3000	0.25 M HCl (SP)
	6	Elute Nd fraction	2 x 7.5	3000	0.25 M HCl (SP)

[§]Prefilter Resin [100-150 µm] (Eichrom Technologies), 100µL bed volume
[#]TRU Spec resin [100-150 µm] (Eichrom Technologies), 500µL bed volume
[*]Ln Spec resin [100-150 µm] (Eichrom Technologies), 2000µL bed volume
Reagent grades: Ultrapur® (UP); Suprapur® (SP), Merck; Deionized 18.2 MΩ-cm H_2O (Millipore)

For the second column, the elution curve determined using a total of 140 mL of 0.25 M HCl shows that the Nd elution starts after 5 mL of 0.25M HCl are passed through the column, and >94% of Nd are recovered by collecting the following 15 mL (B). Following this protocol, 100%

of the Sm in solution is separated from the Nd fraction, which is eluted 20 mL after Nd elution and slowly trickles out of the column for the next 100 mL. Other REE present in the Nd elution include Pr (95% of the amount loaded), Ce (90%), Gd (83%), and La (11%) (Figure 2-11B). The presence of Pr and Gd does not interfere on the measured $^{143}Nd/^{144}Nd$ ratio, as they do not cause any relevant isobaric or spectral interferences. Both Gd isotopes (^{152}Gd and ^{154}Gd) only cause interferences on ^{152}Sm and ^{154}Sm, respectively (Yang et al., 2011), while Pr only has one stable isotope (^{141}Pr) that may only cause interference on the ^{142}Nd isotope through the molecular formation of PrH^+ (Pin et al., 1997; Braun and Ghersini, 1975). Previous studies have shown that the presence of ^{140}Ce has no effect on $^{143}Nd/^{144}Nd$ measurements (Yang et al., 2008, 2011; Gioia and Pimentel, 2000). For example, Yang et al. (2011) tested this by spiking a single element Nd solution with different amounts of Ce up to Ce/Nd = 3 (Figure 2-12). Results from this experiment confirm that the measured $^{143}Nd/^{144}Nd$ ratios are not affected by Ce/Nd ratios of ≤ 3. Note that for the geochemical reference materials analyzed in this study, the Ce/Nd ratio was always < 2. Therefore, the presence of Ce in Nd elution does not impact $^{143}Nd/^{144}Nd$ ratios. Additionally, the residual ^{139}La in the Nd elution does not cause isobaric interference on the $^{143}Nd/^{144}Nd$ ratio; the La oxide ($^{139}LaO^+$) would only cause interference on mass 155, which is not of interest.

2.7.4 **Neodymium isotope measurements**

Neodymium isotope measurements were performed on Neptune Plus MC ICP-MS at WIGL, UOW using jet sample and standard skimmer cones, a cyclonic spray chamber and a PFA nebulizer with ~100 μL min^{-1} flow rate (Elemental Scientific, Omaha, USA). The analysis was performed in static low-resolution mode via multi-collection with nine Faraday cups, monitoring masses 140, 142, 143, 144, 145, 146, 148 and 150. Data acquisition was performed over nine blocks of 10 cycles of eight seconds integration each. An amplifier baseline and peak center were performed at the start of each analysis. A routine instrumental sensitivity of ~3 V of ^{145}Nd per ppm of Nd was achieved. To correct for the instrumental blank contribution, a blank solution was measured before and after every sample and the average value was subtracted from the sample measurement. For all measured $^{143}Nd/^{144}Nd$ isotope ratios, the mean and two standard deviations from the mean (2SD) were calculated and tested for outliers. Beyond this threshold, measurements were rejected.

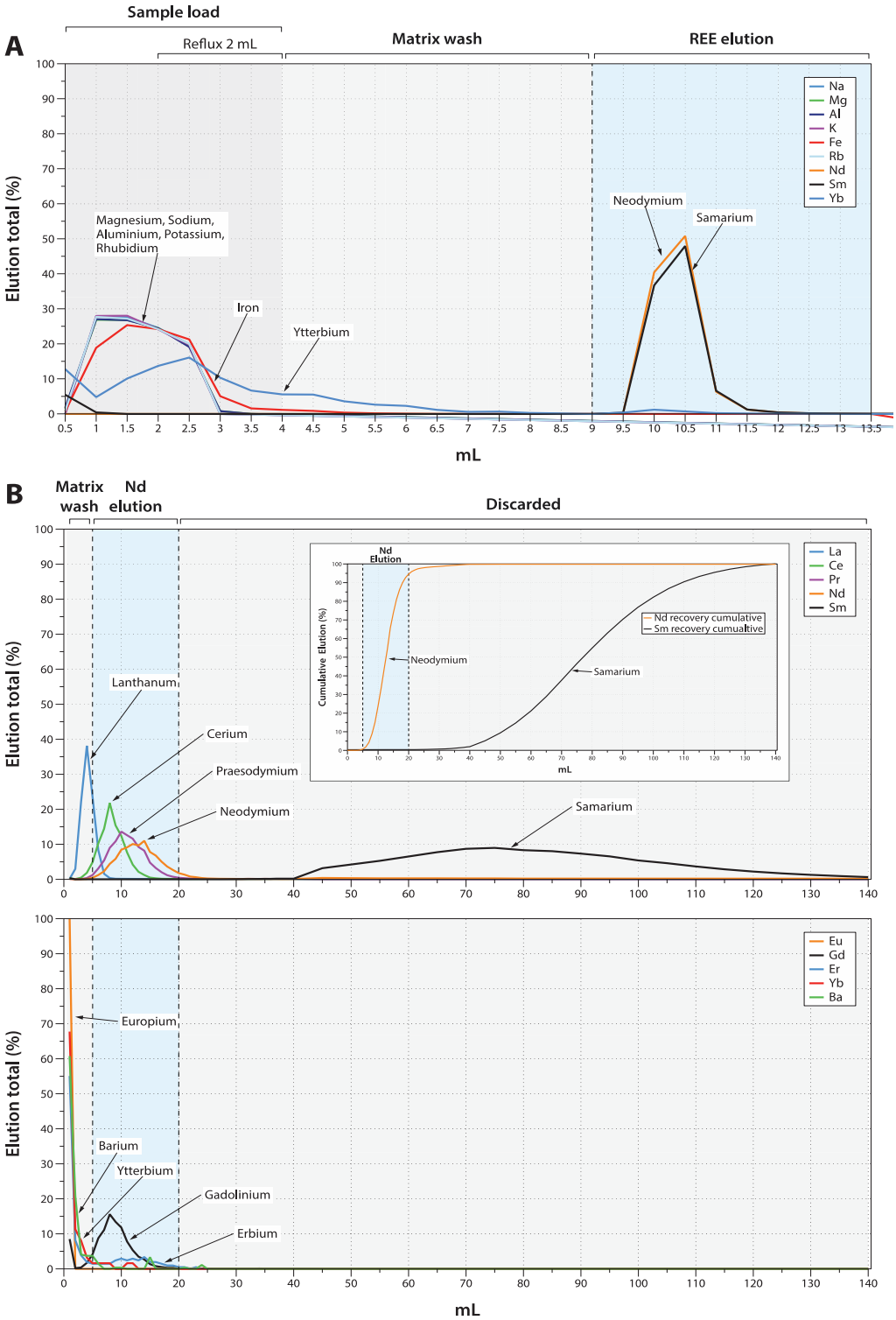

Figure 2-11. Elution profiles for Nd chromatography procedure. A) Elution curve for the first column, where REE are separated from the sample matrix (blue shaded area). B) Elution curve for the second column; Nd elution shown in blue shaded area. Neodymium and Sm are efficiently separated (inset). Concentration determination methods are explained in Section 2.3.2.

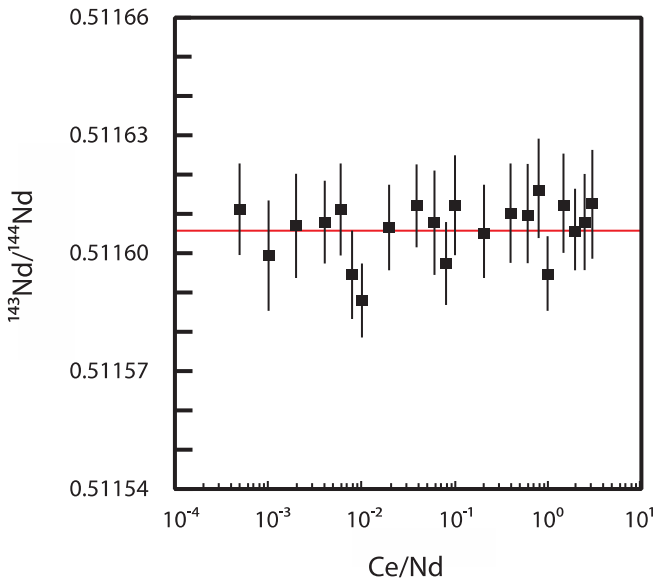

Figure 2-12. The $^{143}Nd/^{144}Nd$ isotope ratios for IGG Nd (200 μg L^{-1}) in-house standard spiked with different and increasing amounts of Ce from Ce/Nd 10^{-4} to 10^{1}. Error bars for individual measurements are 2SE. The red line represents the Mean Square of Weighted Deviates (MSWD) for all measurements. Results show that there are no spectral interferences on the mass biased corrected $^{143}Nd/^{144}Nd$ ratio for Ce/Nd up to 3 (maximum ratio found in most geological samples). The maximum Ce/Nd ratio of samples measured in our study is < 2. Modified from Yang et al. (2011).

Table 2-11. Faraday cup configuration on the MC ICP-MS

Cup	Isotope monitored	Application
L4	^{140}Ce	Indication of Ce content in sample
L3	^{142}Nd	Monitored; not used
L2	^{143}Nd	Isotope of interest
L1	^{144}Nd	Isotope of interest; used for mass bias correction
C	^{145}Nd	Used for tuning
H1	^{146}Nd	Used for mass bias correction
H2	^{147}Sm	Monitored for its interference on ^{144}Nd
H3	^{148}Nd	Monitored; not used
H4	^{150}Nd	Monitored; not used

For a radiogenic isotopes such as Sm-Nd, the use of internal normalization for mass discrimination correction is commonplace in MC ICP-MS. In this study, internal normalization of $^{143}Nd/^{144}Nd$ ratio measurements is performed using Russell's exponential law (Baxter et al., 2006) with an accepted $^{146}Nd/^{144}Nd$ ratio value of 0.7219 (Wasserburg et al., 1981). In each analytical

session, the mass fractionation coefficient (β) for the $^{146}Nd/^{144}Nd$ ratio was determined using Equations 2-4 and 2-5 (Yang et al., 2010):

$$R_t = R_m(M_2/M_1)^{\beta} \quad (2\text{-}4)$$

where R_t and R_m represent the true and measured ratios of an isotope of exact mass M_2 to an isotope with an exact mass of M_1. Therefore, β is the mass fractionation coefficient which can be expressed as:

$$\beta = ln\left(\frac{R_t}{R_m}\right)/ln\left(\frac{M_2}{M_1}\right) \quad (2\text{-}5)$$

Mass bias correction is necessary to calculate accurate $^{143}Nd/^{144}Nd$ isotope ratios. Here, relatively small variations of β (0.0298 – 0.0373) were observed within individual sessions. Interferences from ^{147}Sm were corrected by normalization to the $^{147}Sm/^{144}Nd$ ratio, applying the reported value of 4.83870 (Thermo Scientific, 2008).

2.7.5 **Blanks and Carryover**

Total procedure blanks were interspersed, processed and measured alongside rock standard aliquots. The average total procedure blank mass was 136 ± 103 pg Nd (2SE; n = 3). It affects measured $^{143}Nd/^{144}Nd$ isotope ratios by only ± 0.000003, which is less than the average analytical precision of a typical session (±0.000005). Thus, the blank contribution on the $^{143}Nd/^{144}Nd$ isotope ratio can be therefore considered negligible. The blanks observed here are comparable to those reported in other studies, ranging from 1 to 385 pg of Nd (Saji et al., 2016; Z. Chu et al., 2014; C. F. Li et al., 2007; Gioia and Pimentel, 2000).

The prep*FAST*-MC™ processes samples sequentially on a unique set of columns, thus the same resin is used for a number of samples. Therefore, the carryover from previous samples on the resin must be minimized. Chromatography blanks were processed and interspersed with samples to assess carryover effects from previous samples. The typical sample load for the geochemical reference materials used here was 800 ng of Nd. The amount of Nd carried over between samples was 102 ± 42 pg of Nd in the final Nd elution (n = 16; 2SE), or 0.01% of the total amount of processed Nd. Since the total procedure blank of the protocol is on average about 136 pg Nd, the carryover greatly contributes to the total procedure blank of the protocol (~75%).

Carryover from the total procedure was only determined after using both sets of columns, hence the contribution coming from each individual column is not known.

2.7.6 **Method verification by measurement of reference materials**

Geochemical reference materials were processed through the entire procedure including rock dissolution, ion exchange chromatography, and measurement by MC ICP-MS to verify the protocol accuracy and precision. All reference standards were processed as individually digested aliquots. Measurement of standard GSP-2 yielded $^{143}Nd/^{144}Nd$ ratio values ranging from 0.511330 ± 9 (2SE) to 0.511408 ± 13 (2SE); JG-2 values ranging from 0.512193 ± 20 (2SE) to 0.512299 ± 24 (2SE) and BCR-2 values ranging from 0.512583 ± 23 (2SE) to 0.512649 ± 84 (2SE) (Figure 2-13; Table 2-12). Samples were processed and measured in two separate sessions. For BCR-2 (n = 7), two samples were processed in the first session and five in the second; for JG-2 (n = 8), five samples in the first and three in the second; and for GSP-2 (n = 9), five in the first and four in the second. No apparent systematic drift in the isotopic ratio was found in any of the individual rock standard replicates that were processed over the entire series of experiments or within individual sessions (Figure 2-13). For geochemical reference materials GSP-2 and JG-2, average $^{143}Nd/^{144}Nd$ ratios values of 0.511364 ± 18 (2SE, n = 9) and 0.512231 ± 31 (2SE, n = 8), respectively, were obtained. These values were in good agreement with published values in most cases (Figure 2-14B and C). The average value for BCR-2 is 0.512612 ± 20 (2SE, n = 7). Although this value is within error of many other reported values, several published values were significantly different (Figure 2-14D). Here, measurements are isotopically heavier compositions compared to the literature. This could have several origins: a) isotopic heterogeneity of the reference material; b) isotopic fractionation during separation of Nd from sample matrix, [studies have shown that insufficient recovery of Nd can cause a shift in the elution curve which results in Nd isotope fractionation (Saji et al., 2016; Míková and Denková, 2007) and poor matrix separation can lead to isobaric interference and introduction of mass bias on Nd isotope measurements]; c) systematic enrichment of the eluents with carried over Nd from a previous step or sample; and d) hydride and oxide formation during sample introduction causing isobaric interference and non-linear mass dependent isotope fractionation. To reduce this occurrence, the use of the X-skimmer cone was avoided, which is known to induce additional instrumental mass fractionation compared to the standard

skimmer cone (Georg and Newman, 2015; Newman, 2012). Since an isotopic shift in measurements was only observed for BCR-2 and not with any of other geological material, it is unlikely that the shift was induced by the measurement setup and/or chromatography carryover as this should have affected all samples equally, including the JNdi-1 isotopic standard solution. Therefore, the difference of Nd isotope ratios for BCR-2 in this study compared to others is likely attributable to natural isotopic heterogeneity of the rock powder or specific matrix effects of the BCR-2 material.

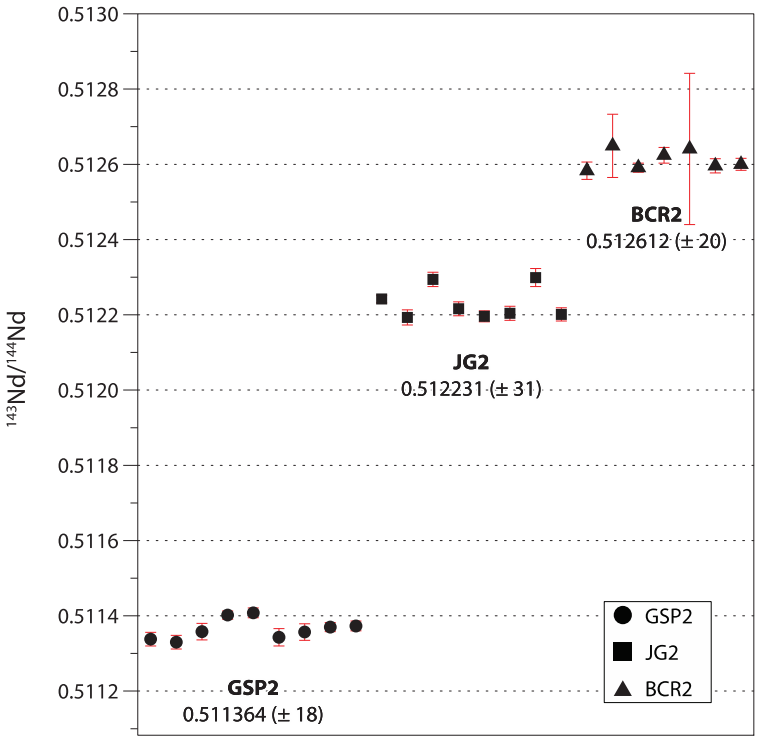

Figure 2-13. Reproducibility of $^{143}Nd/^{144}Nd$ ratio measurements (± 2SE) for geochemical reference materials GSP-2 (n = 9), JG-2 (n = 8) and BCR-2 (n = 7). The agreement between replicates demonstrates low carryover and a high degree of reproducibility.

Table 2-12. Results of $^{143}Nd/^{144}Nd$ ratio measurements of various geochemical reference materials

Sample	$^{143}Nd/^{144}Nd$	n	2SE
GSP-2 Granodiorite	0.511364	9	18
JG-2 Granite	0.512231	8	31
BCR-2 Basalt	0.512612	7	20

2.7.7 **Repeatability of Nd isotope ratios**

Overall the isotope measurements in the different rock standard types demonstrated good repeatability (Figure 2-13), with two standard errors for GSP-2 standard comparable to published values, for instance Chu et al. (2014); Chu et al. (2009) (Figure 15B). The two standard error on $^{143}Nd/^{144}Nd$ for JG-2 is larger than that of Miyazaki and Shuto (1998) (Figure 2-14C). Other published work that measured the JG-2 granite reference material did not report $^{143}Nd/^{144}Nd$ isotope ratio measurements of individual standard aliquots, therefore no external precision for this reference material can be calculated (Arakawa, 1992; Li et al., 2007; Shibata et al., 2003). Although the overall precision associated with measuring this reference material is somewhat lower than reported, all individual $^{143}Nd/^{144}Nd$ isotope ratios are within the range of published values demonstrating accuracy. The 2SE on the $^{143}Nd/^{144}Nd$ isotope ratio measurements of the BCR-2 standard is comparable to the one reported in the literature (Figure 2-14D). Despite the shift in the isotopic ratio towards lower values associated with our BCR-2 measurements, their repeatability is within an acceptable range. Additionally, the repeatability for JNdi-1 isotopic standard solution is better than that of previously published values (Aciego et al., 2009; Ali and Srinivasan, 2011; Chu et al., 2014; Chu et al., 2009; Chu et al., 2014; Crocket et al., 2014; Huang et al., 2012; Miyazaki and Shuto, 1998; Tanaka et al., 2000; Valeriano et al., 2008) (Figure 2-14). Considering geologic reference material measured in this study (BCR-2; JG-2; and GSP-2), the overall external reproducibility of the $^{143}Nd/^{144}Nd$ using this protocol is 0.000064 (2SD).

2.7.8 **Nd isotope method conclusion**

The automated chromatography method presented in this study enables the fast and reproducible separation of Nd from geological material for Nd isotope analysis. This two-step fully automated approach provides >94% Nd recovery and nearly complete separation (<5% remaining) from interfering elements such as Sm. Method verification was accomplished by processing several aliquots of the GSP-2, JG-2 and BCR-2 reference materials yielded $^{143}Nd/^{144}Nd$ ratios of 0.511364 ± 18 (2SE, n = 9), 0.512213 ± 31 (2SE, n = 8) and 0.512612 ±20 (2SE, n = 7), respectively. These values are within the range of published values. However, an observed shift to lower values was observed for BCR-2, which could result from composition heterogeneity or matrix effects of the reference material. This method has distinct advantage over previous

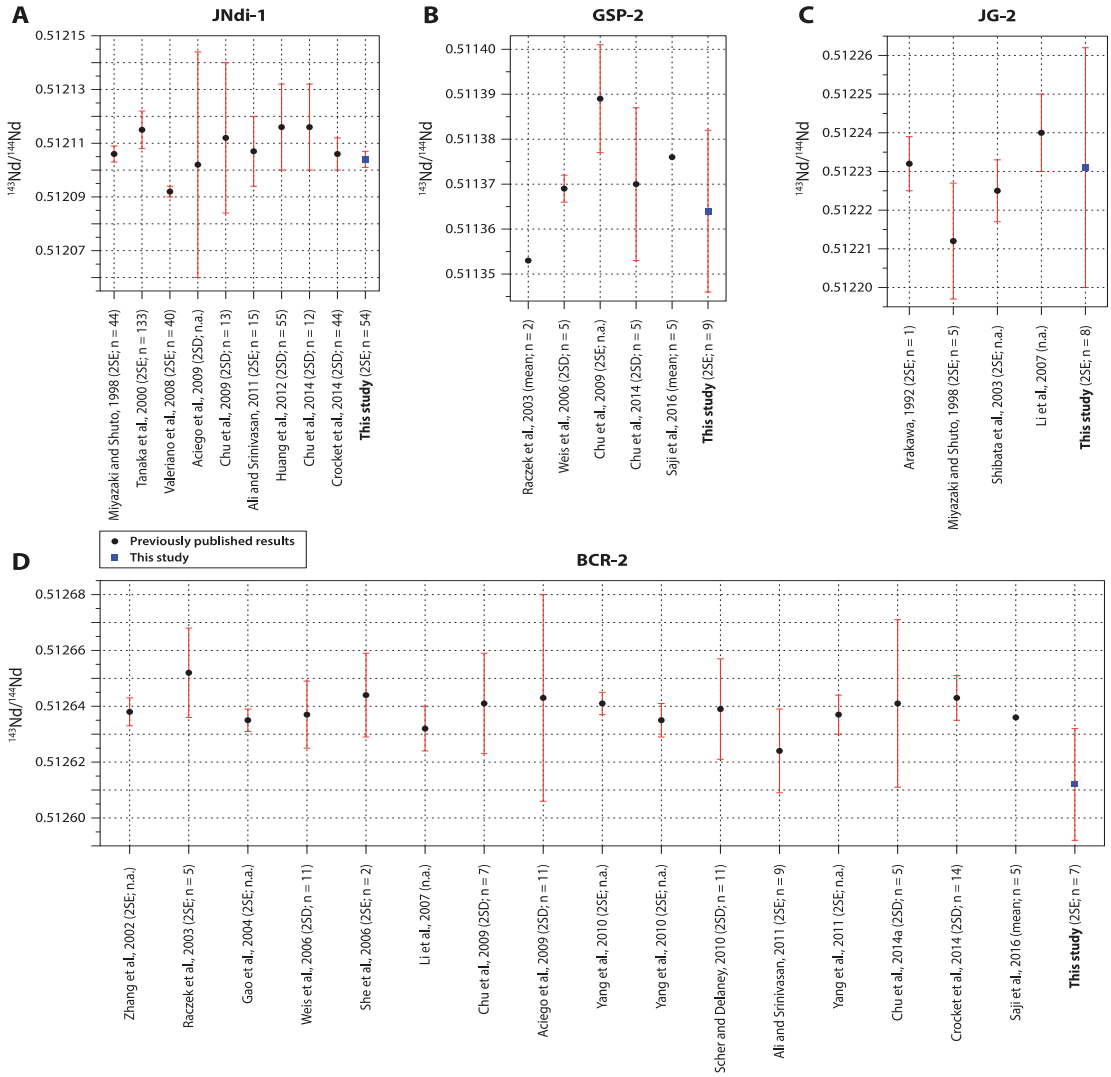

Figure 2-14. Results of $^{143}Nd/^{144}Nd$ ratio measurements in rock standards compared to previously published values: (A) JNdi-1, Nd certified isotopic standard solution, geochemical reference materials (B) GSP-2, (C) JG-2, and (D) BCR-2.

manual methods. First, it allows for the unsupervised and rapid processing of large numbers of samples. While conventional manual approaches can achieve an equally high sample throughput as the here-presented method (~90 samples per week with one set of columns), samples can be processed here unsupervised and over-night, freeing up time and resources. Secondly, it reduces the potential for human induced error to impact on the isotope ratios, and thirdly, it is characterized by low blank contribution and carryover, and ultimately allows for accurate isotope measurements with reasonable reproducibility. Since this method was adapted from an existing gravimetric protocol to fit the needs to users at WIGL, certain limitations apply. These include the incomplete

separation of ^{140}Ce and ^{142}Ce from the sample. This restricts its application to the analysis of $^{143}Nd/^{144}Nd$ isotope ratios, and precludes the accurate measurement of $^{142}Nd/^{144}Nd$ ratios. Despite the presence of Ce in the Nd elution, our results show that accurate measurement of $^{143}Nd/^{144}Nd$ ratio is achieved, with Ce/Nd ratios in the solutions of ≤ 2. Additionally, this method may not be appropriate from all sample matrixes, as shifts such as observed in the BCR-2 samples processed may be matrix dependent. With these limitations in mind, the approach is adapted for the rapid production of large datasets consisting of $^{143}Nd/^{144}Nd$ isotope ratios in sediments and rocks.

Chapter 3

MODERN RIVER SEDIMENTS

Data from this chapter contributed to the manuscript:

Insights on catchment-wide weathering regimes from boron isotopes in riverine material

C. Ercolani[1,2,*], D. Lemarchand[1], and A. Dosseto[2]

Submitted:

Accepted:

Keywords: boron isotopes, weathering regime, isotope geochemistry; Murrumbidgee River; geology

*Corresponding Author:

Christian Ercolani

Wollongong Isotope Geochronology Laboratory
School of Earth and Environmental Sciences
University of Wollongong
Wollongong, NSW, 2522
Australia
Email: cpe877@uowmail.edu.au

1. Laboratoire d'Hydrologie et de Géochimie de Strasbourg, EOST, Université de Strasbourg
1 rue Blessig, 67084 Strasbourg, France

2. Wollongong Isotope Geochronology Laboratory, School of Earth and Environmental Sciences, University of Wollongong, Wollongong NSW 2522, Australia

3.1 STUDY RATIONALE

This chapter focuses on modern river sediment of two active systems: The Gandak River in the Himalayan Mountain range (Ganges Basin) of India and Nepal, and the Murrumbidgee River in the Murray-Darling Basin in southeastern Australia. The Gandak River study was a preliminary study which investigated how mineral separates in transported river material record water-rock interactions using boron isotopes as a proxy for chemical weathering. This work was motivated by previous investigations on mineral separates in soil profiles from the Breuil-Chenue (Voinot, 2012) and Strengbach (Lemarchand et al., 2012) Forests (northeastern France), and laboratory experiments (Voinot et al., 2013) whom all reported a very similar behavior for boron isotopes in various weathering environments. Voinot (2012) and Lemarchand et al. (2012) both indicated that cogenetic primary minerals have very similar boron isotope compositions ($\delta^{11}B$), which closely resemble those of the parent bedrock. This indicates little to no B isotope fractionation during the dissociation of bedrock into primary minerals. On the contrary, phyllosilicates such as clay minerals, are subject to a variety of chemical reactions in soils that differentially involve their crystallographic sites, leading to large isotope fractionations between the clay fraction and the parent material. Neo-formed clays were reported to have similar $\delta^{11}B$ values to one another but different from coarse sand and silt-size fractions, regardless of mineralogy, likely representing the pedogenic conditions in which they were formed (i.e. the competition between dissolution and precipitation reactions). In the laboratory, Voinot et al. (2013) investigated mineral dissolution vs. transformation rates of biotite minerals by conducting flow-through experiments. Results from these experiments show that the dissolution of B isotopes in mineral separates is highly dependent on the chemistry of the reacting solution. At acidic conditions (pH 3), biotite dissolves almost stoichiometrically, while at moderate acidic conditions (pH 4.5), interlayer sites react much faster than structural sites. Voinot (2012) also hand-picked biotite and muscovite mineral separates along a soil profile developed on granite and found that during mineral weathering, B isotopes in both biotite and muscovite mineral separates become highly fractionated early in the weathering process likely in response to the preferential dissolution of the isotopically heavy interlayer sites (Figure 3-1); this makes B a good tracer of early water-rock interactions. However, during the weathering of biotite minerals, B appears to be more mobile than in the muscovite.

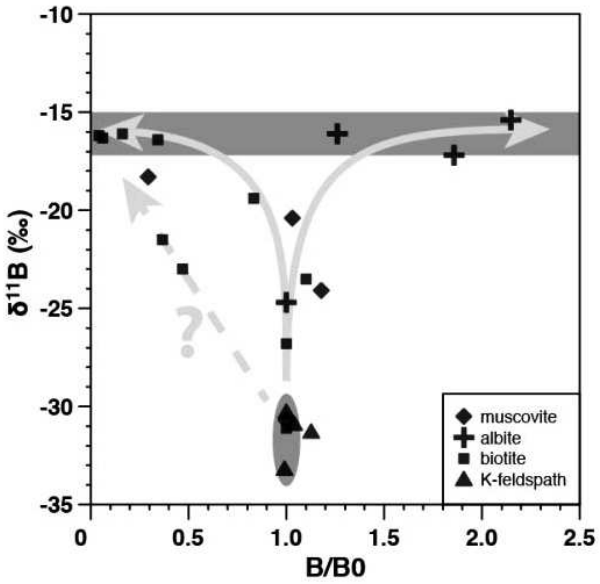

Figure 3-1. Evolution of B chemical and isotopic composition in weathered minerals. B concentrations are normalized to the corresponding unweathered samples. The grey ellipse indicates a narrow range of $\delta^{11}B$ values of difference primary minerals. The horizontal gray bar illustrates the $\delta^{11}B$ value to which all weathered minerals tend to converge. Curves with arrows illustrate two distinct weathering pathways shown by B: the left curve corresponds to micas; the right curve corresponds to albite. The dashed-line shows a binary mixing between pristine and weathered minerals, explaining some of the biotite data points.

The preliminary study of the river sediment in the Gandak River was then intended to study the parallel evolution of different grain sizes, focusing primarily on the sand and clay-sized fractions which are composed of primary and secondary minerals, respectively. Additionally, hand-picked biotite and muscovite mineral samples provide the opportunity to further explore B isotope behavior in handpicked minerals during weathering and transport, work that was started by Voinot (2012). In this study, the hypothesis that coarse sand grains trace their sources, while clay-sized fractions record weathering conditions at the location of their formation is tested. If the clay fraction is capable of keeping a record of the weathering regime (ratio between dissolution and precipitation rates) obtained during their formation when transported from the soil profile to the depositional environment on the alluvial plain, then it could be used as a proxy for paleo-weathering condition in sediment deposits. Alternatively, the clay fraction may lose its pedogenic signal, it may evolve downstream, or may record weathering conditions of the depositional environment. Since very few studies have investigated boron isotope behavior of solid phases in a

river during transport (i.e. Chetelat et al., 2009; Spivack et al., 1987), previous acquisition of the river bank and suspended load sediments taken along the course of the Gandak River provided an opportunity to further investigate B isotope behavior of mineral separates in riverine material during transport from the river headwaters to the alluvial plain.

The basic knowledge of B isotope systematics in mineral separates in soil profiles (Voinot et al., 2013; Lemarchand et al., 2012; Voinot, 2012; Muttik et al., 2011) and riverine material, which was gained from this preliminary work on Gandak River sediments, was then applied to the main study site of the Murrumbidgee River in the Murray-Darling Basin of southeastern Australia and the associated paleochannel systems (see Chapter 4). Similar to the Gandak, bedload and sand bank material was collected from the headwaters to the alluvial plain, separated by grain size into the sand (63 μm – 2 mm) and clay fraction (<2 μm), and analyzed for B isotopes and concentrations, as well as major and trace elemental composition. However, a much more comprehensive sampling approach and analyses was taken in the Murrumbidgee River watershed. Sampling in this watershed was conducted over the course of 3 field campaigns from 2015 – 2017. The Murrumbidgee River was chosen because it carries sediment from the upper catchment to its depositional environment on the alluvial plain, where a series of paleochannel systems ranging in depositional age from approximately 13 – 105 ka, lies. Channel-infill sediments of these paleochannel systems is thought to have derived from the same catchment as the modern Murrumbidgee River. It is a goal of this thesis to determine if B isotopes in these paleochannel sediment deposits could be used as a paleo-weathering proxy. A thorough understanding of how the sediment obtains its weathering signal and how that signal is transferred from source to depositional environment in the modern system must first be gained. To this end, modern sediments from the Gandak and Murrumbidgee Rivers are used to characterize B isotope behavior during pedogenesis and transport (Chapter 3). Then, with this knowledge of B isotope systematics in the modern river sediments, interpretations of paleochannel sediment deposits using B isotopes can be made (Chapter 4) with the ultimate goal of determining sediment response (paleo-weathering regime) to climate variability over the last full glacial cycle.

3.2 CHAPTER INTRODUCTION

Chemical weathering of silicate rocks shapes Earth's surface and landscapes, supplies essential nutrients to ecosystems, and is believed to be one of the main controls that regulate global climate over millennial timescales via the consumption of atmospheric CO_2 and carbonate storage in the oceans (West et al., 2005; Berner and Berner, 1997; Walker et al., 1981). Given the importance chemical weathering plays in regulating atmospheric CO_2 and maintaining a steady climate over geological timescales, a unified model of how tectonic uplift, chemical weathering, and climate interact is lacking and still a subject of debate (i.e. Berner et al., 1983; Raymo et al., 1988; Ruddiman, 1997). To better understand the climate-silicate weathering relationship, the dissolved load of both small and large rivers are often studied as they integrate information such as weathering conditions within its catchment area, which can then be extrapolated to the global scales when the river drains a large continental area such as the Amazon (i.e. Bouchez et al., 2014; Stallard and Edmond, 1983), Himalaya (i.e. Gaillardet et al., 1999; Galy and France-Lanord, 1999), and the Congo (i.e. Dupré et al., 1996). The use of solid phases such as the suspended load, bedload sediment, and clay fractions, have also been used to quantify the weathering regime (i.e. Bouchez et al., 2012; Lupker et al., 2012) although they generally received less attention.

Classical geochemical proxies used to study silicate weathering are based on major and trace elemental concentrations and ratios (Gaillardet et al., 1999; Price and Velbel, 2003). Examples of these include the chemical index of alteration, chemical index of weathering, and various chemical ratios using a mobile and immobile counterpart (Harnois, 1988; Nesbitt and Young, 1982). Although somewhat useful in determining silicate weathering rates and intensities, these proxies suffer from limitations that primarily arise from the dominant control lithology plays on the composition of the dissolved load and weathering products, often obscuring the effects of chemical weathering drivers (Bluth and Kump, 1994; Stallard and Edmond, 1983). Additionally, granulometric sorting of sediment during transport strongly controls sediment mineralogy and therefore the chemical composition of bedload sediments, leading to large inter-sample variability (e.g. Garzanti et al., 2007, 2010, 2011). The determination of sediment provenance by sampling bedload sediments, for instance, is complicated by grain-size fractionation and hydraulic processes such as physical sorting of minerals with different hydraulic behavior (e.g. concentrating heavy minerals in placer deposits or platy minerals in lower-environments) (Morton

and Hallsworth, 1999). Therefore, any provenance interpretation using the chemical or mineralogical composition of river sediment requires a thorough understanding of hydraulic control on compositional variability, which proves to be a difficult task (Garzanti et al., 2010). Unlike these chemical weathering proxies, "non-traditional" stable isotopes systems such as boron (B), lithium (Li), calcium (Ca), silicon (Si), iron (Fe), and magnesium (Mg) are an attractive new alternative because isotopic fingerprints rely on the fact that each physico-chemical process is associated with a characteristic shift in isotopic ratios of the elements involved (Bouchez et al., 2013).

Boron (B) displays physico-chemical properties that are suitable for investigating water-rock interactions, including those involving a biological component (Cividini et al., 2010; Williams, 2001). It is present in a wide range of concentrations in various natural reservoirs (ranging from low ppb levels in rivers and rainwater to hundreds of ppm in clays and thousands of ppm in some minerals like tourmaline), with moderate to high concentrations in silicate rocks (5-100 ppm). Boron has two stable isotopes, ^{10}B and ^{11}B, that undergo large isotopic fractionation during Earth surface processes, particularly during low temperature water/rock interactions (Lemarchand et al., 2002a, 2012; Muttik et al., 2011; Rose et al., 2000; Spivack and Edmond, 1987; Schwarcz et al., 1969). In natural systems, $\delta^{11}B$ values show a large range of variation from –40‰ in non-marine evaporitic and tourmaline minerals in the continental crust up to +60‰ in brines from salt lakes (Palmer and Swihart, 1996). Processes responsible for B isotope fractionation include adsorption of B onto clay and detrital particles (Lemarchand et al. 2006, 2007, 2015; Schwarcz et al., 1969; Spivack et al., 1987), precipitation of B during neoformation of secondary phases (Cividini et al., 2010; Lemarchand et al., 2012; Noireau et al., 2014; Rose et al., 2000; Williams et al., 2001a), hydrothermal alteration of clays, bedrock, and oceanic crust (Muttik et al., 2011; Williams, 2001; Spivack and Edmond, 1987) evaporation and precipitation processes during B atmospheric cycle (Rose-Koga et al., 2006; Chetelat et al., 2005; Xiao et al., 1997), and B cycling through vegetation (Noireaux et al., 2017; Roux, 2016; Cividini et al., 2010; Wieser et al., 2001; Vanderpool and Johnson, 1992)

Boron is mobile during water-rock interaction and is partitioned into the soluble and solid phases. It is released into the hydrosphere via the dissolution of primary minerals and can be incorporated into secondary phases such as clay minerals and amorphous iron oxyhydroxides. Significant isotope fractionation occurs during secondary phase neoformation whereby the lighter

isotope has a greater affinity for neo-formed solids becoming enriched in ^{10}B leaving the residual solution enriched in the heavier isotope (Lemarchand et al., 2005; Palmer et al., 1987; Schwarcz et al., 1969). A wide range of boron isotope compositions in both the solid and dissolved phases have been reported which were attributed to silicate weathering processes on the watershed scale. For instance, in the Himalaya, Rose et al. (2000) reported a 30‰ range in $\delta^{11}B$ values in the dissolved load (–6‰ to +24‰) reflecting different conditions of silicate weathering (congruent vs. incongruent silicate weathering) where large isotopic fractionations (–31‰) between the clay fraction and dissolved load is driven soil pH. Similarly, the clay fraction in soil profiles in the Strengbach catchment, France (Lemarchand et al., 2012), and at the Ries crater, Germany (Muttik et al. 2011) have $\delta^{11}B$ compositions ranging from –35 to –2‰ which are attributed to the possible hydrothermal alteration of bedrock and pedogenic processes occurring after B exchange with the surrounding ^{11}B-rich soil solution, and clay formation under different temperature and pH conditions, respectively. In the Mackenzie Basin (Canada), $\delta^{11}B$ compositions in the dissolved load of various rivers and tributaries show a range from –2 to +30‰ reflecting changes of the weathering rates of catchment shales and changes in the partition coefficient between soluble B and adsorbing surfaces (Lemarchand and Gaillardet, 2006). In the Changjiang basin (China), $\delta^{11}B$ compositions derived from silicate weathering are reported for both the dissolved and suspended loads of various rivers having values of –3 to +9‰ and –11 to –6‰, respectively (Chetelat et al., 2009). Here, they show that the isotopic compositions of both phases are controlled by the competition between boron leaching and uptake into secondary phases, where the former process causes no apparent isotopic fractionation. These studies demonstrate that B isotopes are a useful proxy in the identification and quantification of silicate weathering processes as well as broaden our understanding of the controls on B isotope fractionation at the watershed scale. However, a clear understanding of the parameters that control B isotopes during the production of secondary minerals and subsequent transport throughout the watershed is still lacking. Given the critical role secondary products play in recording water-rock interactions at present, and their potential for storing information on paleo weathering regimes in depositional environments, further research on this topic is needed.

In the following two studies, B isotope behavior of granulometrically separated riverine material is investigated during transport from the headwaters to the alluvial plain. River bank and suspended load sediments of the Gandak River in the Ganges Basin, Himalaya were collected from

the headwaters to the plain, granulometrically separated into bulk, sand (2 mm – 63 μm), and clay (< 2μm) fractions, and analyzed for B isotopes and major and trace element concentrations. Additionally, primary mica minerals (biotite and muscovite) were hand-picked from the bulk sediment in several of the river bank samples and analyzed in the same manner. In the Murrumbidgee River catchment, riverbank and bedload sediments and dissolved loads from monolithological streams, tributaries, and the main Murrumbidgee were sampled. Bedrock samples were also taken from monolithological catchment. The clay fraction (< 2 μm) of sediment samples, bedrock, and the dissolved load were analyzed for B isotopes and major and trace element concentrations. Mineral analyses by XRD was also performed on the bedrock and clay fractions.

3.3 GANDAK RIVER, HIMALAYA

3.3.1 Study Site

The Gandak River is the most important tributary of the Ganges (Ganga) river (both in terms of discharge and particle flux) and is located in central Nepal and northern India in the Himalayan Mountain range (Granet et al., 2007). It is formed by the convergence of the Kali Gandaki and Trisuli Rivers, which in turn form the Narayani River in Nepal and then the Gandak River in India (Figure 3-2). Flowing southwest into India, the river bends southeast along the state border of Uttar Pradesh–Bihar and continues for approximately 765 km across the Indo-Gangetic Plain merging with the Ganges River, and emptying into the Bay of Bengal. It is considered one of the major rivers in Nepal, along with the Kosi and Karnali Rivers, all which are running southward across the strike of the Himalayan ranges and form in transverse valleys with deep gorges. Its watershed of the Gandak River lies to the north of the river, in Tibet. The river rises to a maximum elevation of 7,620 m near its origin and has a total catchment area of 46,300 km^2 (Foster and McDonald, 2018).

The Gandak River lies within the Ganges basin; the basin drains 1,086,000 km^2 in Tibet, Nepal, India, and Bangladesh and contains the largest river system on the subcontinent. The Ganges basin is situated between the Himalayan Ranges to the north which form the Ganges-Brahmaputra divide, the Indus basin to the west, and the Vindhyas and Chota Nagpur Plateau to

the south. The Ganges River merges with the Brahmaputra and Meghna River to the east in Bangladesh via a complex system of common rivers which drain into the Bay of Bengal where

Figure 3-2. Location of the Gandak River in the Ganges-Brahmaputra-Meghna basin in the Himalayas. It originates in Nepal, flows into northern India where it merges with the Ganges River; then across the Gangetic Plain and emptying in the Bay of Bengal. Source: http://img1.wikia.nocookie.net.

it forms the Ganges Delta. Worldwide, the Ganges-Brahmaputra system has the third greatest average discharge of all the world's rivers, approximately 30,700 $m^3 s^{-1}$, of which approximately 11,000 $m^3 s^{-1}$ is supplied by the Ganges River alone (Ahmad and Lodrick, 2018). The Amazon and Congo Rivers are first and second, respectively, in terms of discharge. Combined, the Ganges-Brahmaputra-Meghna Rivers' suspended sediment load is approximately 1.84 billion tons per year, which makes it highest in the world (Holeman, 1968).

The volume of water that flows in this system is highly variable depending on region and seasonal flow. Monsoonal rains cause flooding from July to September, while Himalayan glacial and snow melt feed the river system from April to June. The basin receives nearly 1,000 mm of precipitation annually, with 84% of the annual rainfall occurring during the monsoon season. In the upper Gangetic Plain near the outlet of the Gandak River, rainfall averages approximately 760 – 1,020 mm, in the Middle Ganges Plain near Bihar from 1,020 – 1,520 mm, and in the delta

region, between 1,520 – 2,540 mm, annually. The climate in the Ganges Basin is classified as CSA (temperate mesothermal climate) by the Köppen classification system (Pravettoni, 2015). The average temperature in the Ganges Basin is 13.3°C; summers reach 31°C in June; and winters reach approximately 5°C in January (Pravettoni, 2015). The CSA classification is referred to as "hot dry summer" climate; the same climate classification as the Mediterranean under the Köppen climate classification.

The Gandak River is fed by the Kali Gandaki and Trisuli Rivers which form in alpine climate conditions at an elevation of 6,268 m in the Himalayan mountain range near the Nepal-Tibet border (Pravettoni, 2015). The Gandaki River basin, in the far north of the larger Ganges basin, is reported to contain 1025 glaciers and 338 lakes, which greatly contribute to seasonal flow of the river. These source rivers in the highlands are characterized by steep slopes and deep gorges, as the river incises the uplifting mountain. Climate in the highlands (6,268 – 4,267m) and mid elevations (3,352 – 2,133 m) is classified as CWB (subtropical highland climate) and CWA (humid subtropical climate) by the Köppen classification system, respectively (Pravettoni, 2015). Both climate regimes are monsoon-influenced, with changes in elevation significantly affecting local temperature. For instance, a temperature decrease of 6.5°C occurs with every 1000 m rise in altitude, giving rise to a variety of climates from nearly tropical at the foothills to tundra with permanent ice and snow at alpine locations (Rose et al., 2018).

The headwaters of the Gandak River (Kali Gandaki and Trisuli Rivers) drain a series of lithological formations in central Nepal. On the basis of lithology, tectonic structure, and geologic history, Nepal can be divided into 5 major zones: from north to south a) the Tibetan Tethys zone; b) the Higher Himalayan zone; c) the Lesser Himalayan zone; d) the Churia (Siwaliks) zone, and e) Terai (foreland basin) zone (Figure 3-3). Each of the zones is characterized by its own lithology and tectonics. The northernmost Tibetan-Tethys zone consists of sedimentary rocks known the Tethyan Sedimentary Series (TSS) consisting of a thick and continuous Paleozoic to lower Tertiary marine sedimentary succession. The TSS series composes the upper section of the Kali Gandaki River. The Higher Himalayan Zone is composed of a variety of gneisses that form a basement to the Tibetan-Tethys sedimentary pile such as quartzite gneisses, granitic gneiss, and garnet-kyanite gneisses (Le Fort, 1975), all which are present in the Kali Gandaki and Trisuli sections. A notable feature of the Higher Himalayan formation is the gorge carved by the Kali Gandaki river which is one of the deepest gorges in the world. The lithology of the Lesser Himalayas in central Nepal

consists of metasedimentary and crystalline rocks which are Late Precambrian-Early Paleozoic in the older sequence and Late-Carboniferous-Permian to Oligocene-Early Miocene for the younger Lesser Himalayan rocks in the western portion western Nepal. The older sequence is termed the Kali Gandaki Supergroup and is drained by the Kali Gandaki (Sakai, 1983). The Churia (Siwalik) zone forms one of largest foreland basin accumulations of Earth, consisting of Neogene to Quaternary fluvial sediment and sedimentary rocks that form in the southernmost hill range of Nepal (Upreti, 1999). It is overlain by thrusted Lesser Himalaya metasedimentary rocks, and itself, is thrusted over the Recent alluvium of the Terai zone. The sedimentary rocks of the Lower Churia Group are composed of fine-grained sediments such as mudstone, siltstone and shale with thick beds of sandstones at the base of the formation. The high abundance of biotite and light-colored quartz and feldspars gave these sandstones the nickname "salt and pepper sandstones". The Terai zone represents the northern edge of the alluvial Indo-Gangetic foreland and location of the sampling points in the study along the lower part of the Gandak River. The Terai plain consists of Pleistocene to Recent alluvium resting on rocks of the Peninsular India which are Permo-Carboniferous in age or younger (Eocene-Oligocene). Coarser Terai sediments lie closer to the mountain front forming large alluvial fans, while finer sediments are found further south (Upreti, 1999).

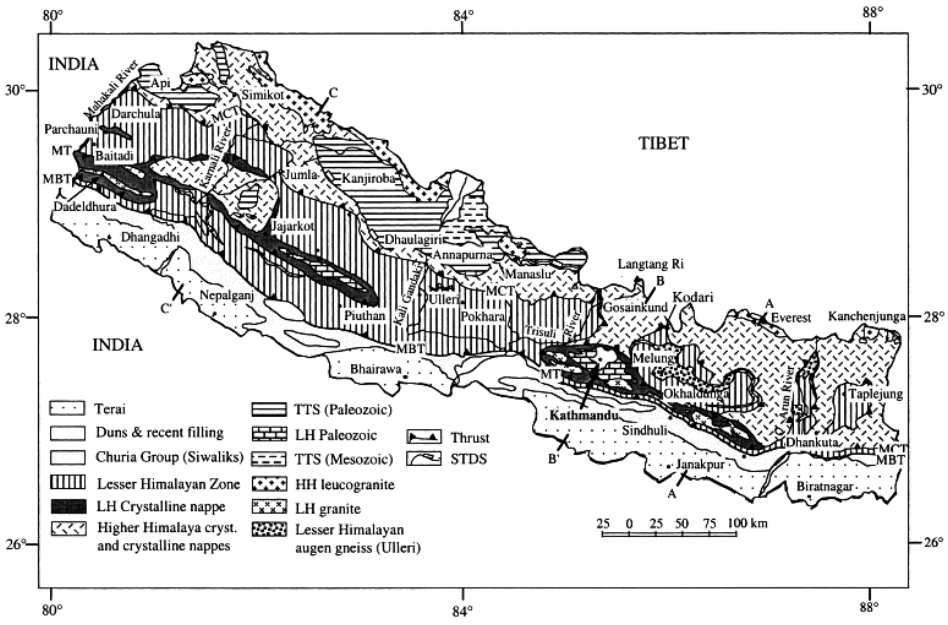

Figure 3-3. Geology of the Nepal. LH: Lesser Himalaya; HH: Higher Himalaya; TTS: Tibetan-Tethys; MBT: Main Boundary Thrust; MCT: Main Central Thrust; MT: Mahabharat Thrust; STDS: South Tibetan Detachment System. Source: Upreti (1999).

3.3.2 **Methods**

3.3.2.1 Sampling location

This study focuses on the analyses of sediments from the Gandak River, taken at 8 sampling locations along the river: one upstream in the Himalayan mountain range (Churia/Siwalik formation, Nepal) and 7 others located along the river in the alluvial plain from the mountain foothills to the confluence with the Ganges River (Figure 3-4). A total of eight bank samples (red pies) and 6 suspended load samples (yellow pies) were collected. The bank samples were collected by scooping small quantities of surface sediments at distinct points on the same river bank (~ 7 kg in total) in order to integrate a larger area (several meters squared) to obtain a representative sample of the site (Bosia et al., 2016; Chabaux et al., 2012; Granet et al., 2007). Suspended loads were collected using a 5 L PVC sampler operated from a boat situated in the center of the river (Galy et al., 2007; Granet et al., 2010). Dissolved load samples were collected and filtered through a 0.22 µm PES filter in a pressurized Teflon coated filtration unit. In this study, a total of 6 suspended load samples were collected at different depths in the water column at an upstream (#1) and a downstream (#8) location: three samples were collected from the upstream site in 2011 at 3 m, 5 m, and 8 m, depths, and three from the downstream location in 2008 at 1.5 m, 3 m, and 4.8 m depths.

The processing of these sample is described by Lupker et al. (2011). At the Laboratoire d'Hydrologie et de Geochimie de Strasbourg (LHyGeS) at the Université de Strasbourg (Strasbourg, France), bank samples were dried at 50°C in an oven, sieved at 2 mm to remove organic debris and gravels, and a representative portion of < 2 mm sample portion was obtained by quartering and labeled 'bulk'. In four of the bank samples (#1, #3, #6 and #8 in Figure 3-4), ~50 mg of biotite minerals and ~50 mg of muscovite minerals were hand-picked from the bulk sample portions using a toothpick. Quartz and other undesirable mineral species were repeatedly separated from the sample until a pure fraction was obtained. Each bank sample was then wet-sieved at 63 µm; the 63 µm – 2 mm portion was labeled 'sand fraction'; and the < 63 µm fraction was repeatedly centrifuged following the procedure of Starkey et al. (1984) to obtain the < 2 µm fraction labeled 'clay fraction'. Suspended load samples were not sieved due to lack of material; instead, they were processed as bulk samples. All wet-sieved and centrifuged sediments were then oven-dried at 50°C overnight. The bulk and sand fractions were then crushed using an agate mill

and the grain size verified by sieving the obtained powder. Suspended load and clay fraction sediments were crushed by hand using a mortar and pestle prior to chemical and isotopic analyses. To verify that the clay fraction separation protocol described by Starkey et al. (1984) is suitable for B isotopes, the clay fraction was separated from the silt fraction by centrifugation using 18.2 mΩ Milli-Q® water; both the clay fraction and water were retained and analyzed for B concentration and isotopes. Taking an aliquot of the same clay sample, the centrifugation was performed a second time and both the clay and water were analyzed again for B concentration and isotopes to ensure that the protocol does not dissolve a soluble B-bearing phase. Experimental results indicate that approximately 1% of the total B analyzed in the clay fraction dissolves in the water during the first step, while the B concentration of the water after the second centrifugation was significantly less and nearing zero. This indicates that nearly all labile B is exchanged during the first step. Boron isotope compositions of the clay fraction were –15.3‰ and –15.7‰ after the first and second centrifugation step, respectively. This results show that the separation protocol has a negligible effect on both B concentrations and isotopes in the clay fraction, making it suitable for this study.

3.3.2.2 Sample preparation for B isotope and concentration measurements

Boron was extracted and purified from powdered sediment samples via alkali fusion and ion exchange chromatography following the protocol in Chapter 2.4 of this thesis.

3.3.2.3 Major and Trace elemental analysis

Major and trace element concentrations were measured by inductively coupled plasma atomic emission spectrometer (ICP-AES) and inductively coupled plasma mass spectrometer (ICP- MS), respectively, after lithium metaborate fusion following the techniques at LHyGeS (e.g. Prunier et al., 2015). The relative analytical uncertainty (2SD) is better than 3% for major element concentrations and better than 10% for trace element concentations (e.g. Dequincey et al., 2002). Accuracy of the protocol was assessed by regular analyses of rock standards (BE-N, GS-N and AN-G) (see Prunier et al., 2015).

3.3.2.4 Boron Concentrations

Boron concentrations were measured by isotope dilution on an ICP-MS Element at LHyGeS. The procedure is described in detail by Roux et al. (2015) and is the same as described in Chapter 2.5 of this thesis. The analytical uncertainty of B concentration measurements at LHyGeS was estimated by repeated measurement of a standard solution, yielding measurement uncertainty as low as 1% (2SD) when the sample to spike ration is between 0.3 to 1.5, and 2% when ratios are vary from 0.3 to 2.0 (Roux et al., 2015). Therefore, all samples measured for B concentration in this study had sample-spike ratios between 0.3 and 2.0, producing a maximum measurement uncertainty of 2%.

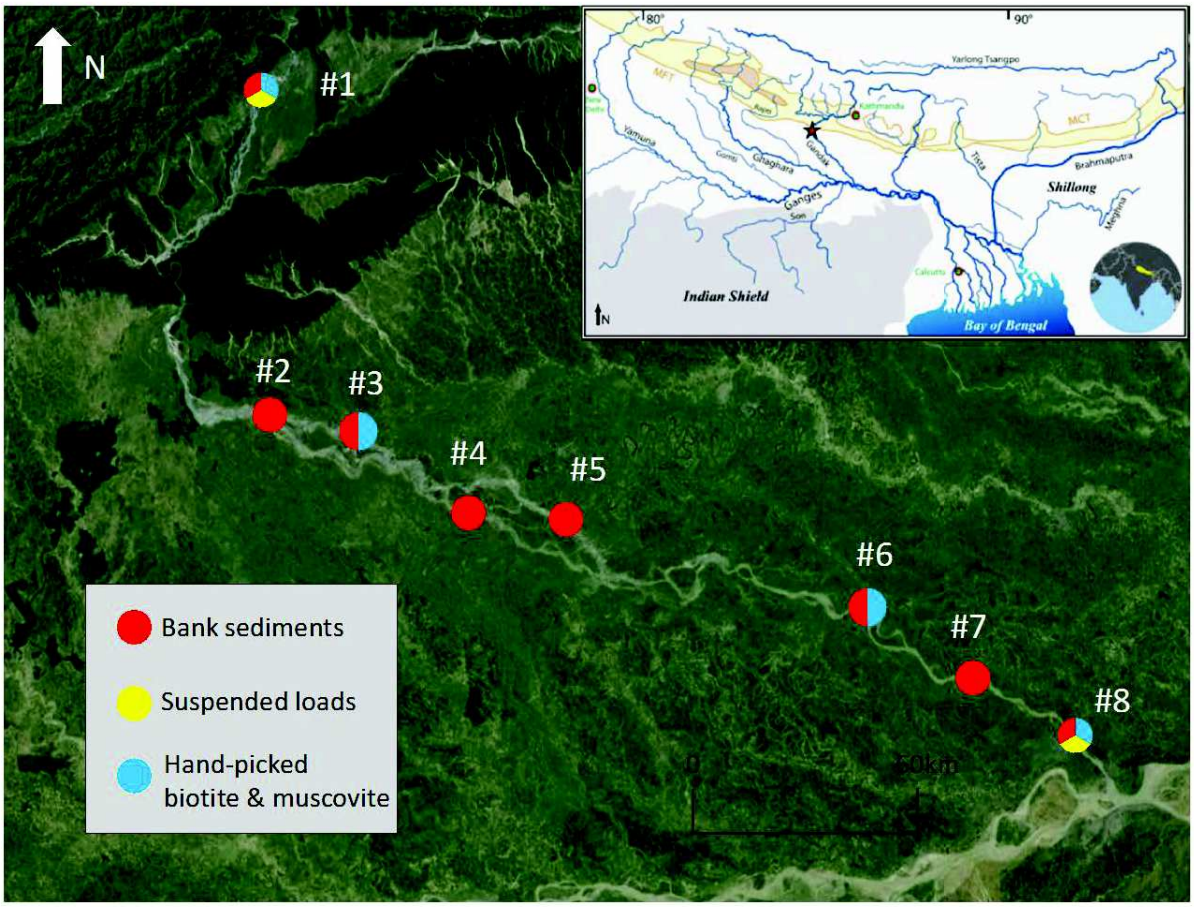

Figure 3-4. Map of the Gandak River showing sample locations #1 – #8 (numbers correspond to samples listed in Table 3-1 and Table 3-2). Map data © 2016 Google Imagery © 2016 TerrMetics). Source: re-drawn from Bosia et al. (2016). Inset map: Ganges-Brahmaputra River basin taken from Galy and France-Lanord (1999).

3.3.2.5 Boron isotope ratio measurements

Boron isotope ratios were measured by an MC ICP-MS Neptune (Thermo Scientific, Bremen, Germany) at LHyGeS. This procedure is described in detail by Roux et al. (2015) and in Chapter 2.6 of this thesis. The only difference between B isotope measurements at LHyGeS and WIGL is the wash time before baseline and sample measurements. At LHyGeS, the wash time is 20 mins to obtain the lowest baseline measurement as possible; while at WIGL, the wash time is 10 mins. Differences may be related to the maintenance or overall usage age of the instrument, as B may accumulate in the lines over a sufficient time. Precision and accuracy of B isotope ratios was assessed by routinely processing and analyzing standard solutions alongside samples. ERM AE120 and natural seawater, were used to verify the procedure and access measurement uncertainty. The average δ^{11}B values for the AE120 and seawater standards processed through the entire chemical procedure in this study is –20.16 ± 0.11 (2SE, n = 2) and 39.80 ± 0.18‰ (2SE, n = 6). Measured values are in agreement with those reported by Vogl and Rosner (2012) for ERM AE120, –20.2 ± 0.6‰ (2SE, n = 20), and with Foster et al. (2010) who reported 39.61 ± 0.04‰ (2SE, n = 28) for seawater, which demonstrates accuracy of B isotope measurements. The seawater used in this study was collected from Los Angeles, CA in 2010 and not the international standard solution used by Foster et al. (2010), therefore slight differences in isotopic composition can be expected. Overall analytical uncertainty of the B isotope measurements at LHyGeS is ±0.45‰ (2SD, n = 6)

3.3.3 Results and Discussion

3.3.3.1 Major and trace elements

Major and trace element concentrations, including boron, were measured on all grain size fractions of riverine material in this study (Major elements : Table 3-1; trace elements: Table 3-2). Following Bouchez et al. (2012) and Lupker et al. (2012), the Al/Si ratio can be used a proxy of weathering intensity and a proxy for grain size as coarse-grained, quartz-rich sediments have low Al/Si ratios and phyllosilicate-rich sediments, such as clays, have higher Al/Si ratios. Weathering indices are obtained by comparing mobile to immobile elements in all grain size fractions.

Aluminum (Al) was chosen as the immobile element as it is a major insoluble element; while Si, B, Mg, Ca, and Na are all considered mobile elements which are soluble during silicate weathering being partitioned between the dissolved and solids phases (Bouchez et al., 2012; Gaillardet et al., 1999a; Dupré et al., 1996). Because samples in the study are already sorted into grain size (suspended load – bulk fraction; bank sediment – bulk fraction; bank sediment – sand fraction; bank sediment – clay fraction) the Al/Si ratio is mainly used as a weathering intensity proxy (assuming Si is soluble during weathering reaction and Al is not) but also illustrates differences in chemical composition based on grain size. To investigate the mobility of other elements during weathering such as B, Ca, Mg, and Na, weathering indexes (X/Al ratios) are plotted for the entire set of sediment samples taken from the Gandak River as a function of the Al/Si ratio (Figure 3-5). Generally, for all sediments, B/Al, Cal/Al, and Na/Al decrease with increasing Al/Si. The bulk sediment and coarse-grained sand represent the relatively unweathered end-member displaying higher X/Al and lower Al/Si ratios, while the clay fraction represents the fine-grained fairly weathered end-member in the system displaying lower X/Al and higher Al/Si ratios. The suspended load, which was taken at several depths in the water column, appears to be a mix between the two end-member displaying both intermediate X/Al and Al/Si values. The relationship between Mg/Al and Al/Si is less clear, however in many cases Mg/Al increases as a function of increasing Al/Si when comparing all grain sizes; therefore the clay fraction generally has a higher Mg/Al than other size fractions. This classic relationship is often interpreted as being diagnostic of high temperature (>150°C) water-rock interactions resulting from the dependence of Mg hydration in solution and an inhibitor of Mg incorporation at low temperature (Schott et al., 2016; Hajash and Chandler, 1982). Data in Figure 3-5 displayed as X/Al vs. Al/Si can then be interpreted in terms of both minerals sorting/mixing between upstream and downstream locations and different degrees of weathering along the course of the river (Bouchez et al., 2012; Lupker et al., 2012). This relationship is displayed in Figure 1-8 and Figure 3-6.

3.3.3.2 B isotope measurements

Boron isotope measurements in the bulk fraction of bank sediment show indistinguishable values, ranging from –11.7 to –12.4‰ (±0.5‰, 2SD, Figure 3-7, Table 3-2); Similarly, the sand fraction of bank sediment and the bulk fraction of the suspended load B compositions also show

little variation throughout the Gandak River with compositions ranging from –11.0 to –12.4‰ and –10.5 to –12.2‰, respectively (Figure 3-7, Table 3-2). On the contrary, the clay fraction of bank sediments shows a larger range of B isotope compositions from –15.2

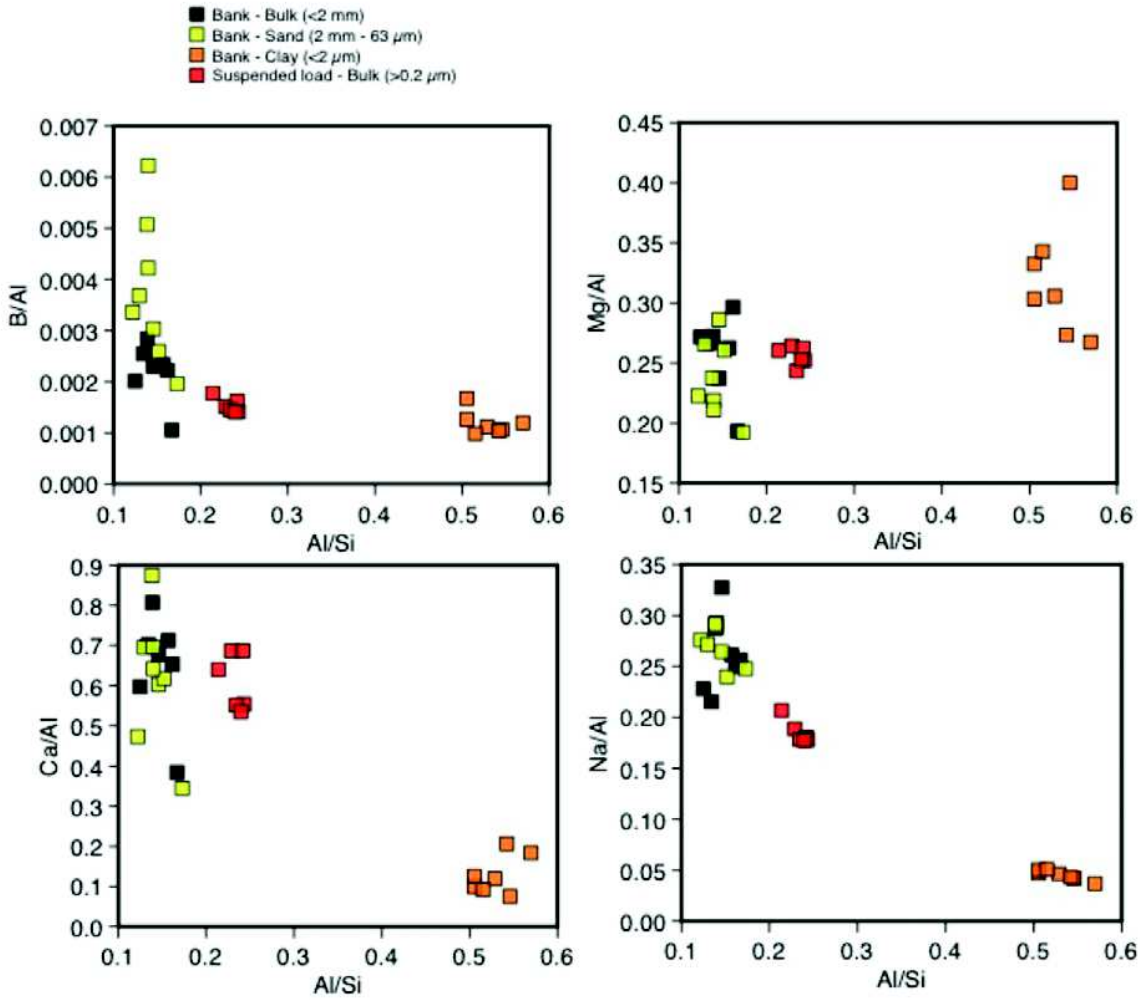

Figure 3-5. Weathering proxies B/Al, Ca/Al, Mg/Al and Na/Al as a function of the grain size proxy Al/Si for suspended load (<0.2 µm), bulk (< 2 mm), clay (<2 µm), and sand fractions (2 mm – 63 µm) in the Gandak River, Ganges Basin

to –11.9‰ which evolve towards isotopically heavier $\delta^{11}B$ values downstream (Figure 3-7, Table 3-1). This change is greatest (from –15.2 to –11.9‰) in the first 100 km of the river and then the $\delta^{11}B$ composition of the clay fraction becomes slightly lighter again but generally follows that of the suspended load, bulk, and sand fractions. Hand-picked biotite and muscovite minerals have B isotope compositions ranging from –15.4 to –7.4‰ and –15.4 to –12.6‰, respectively (Figure 3-8, Table 3-3). The B isotope composition of muscovite minerals evolves slowly and continuously

towards isotopically heavier values downstream (from –15.4 to –12.6‰), while the B isotope composition of biotite rapidly evolves towards an isotopically heavier value (from –15.4 to –7.4‰) in less than 100 km and then gradually shifts towards isotopically lighter values (as light as –9.5‰) over the next 200 km of the river. Interestingly, the $\delta^{11}B$ compositions of both the biotite and muscovite are identical in the headwater sampling location, evolve differently downstream, then seem to be converging towards a common value downstream. The magnitude of isotope shift in the biotite minerals downstream is much greater than that observed in the clay fraction.

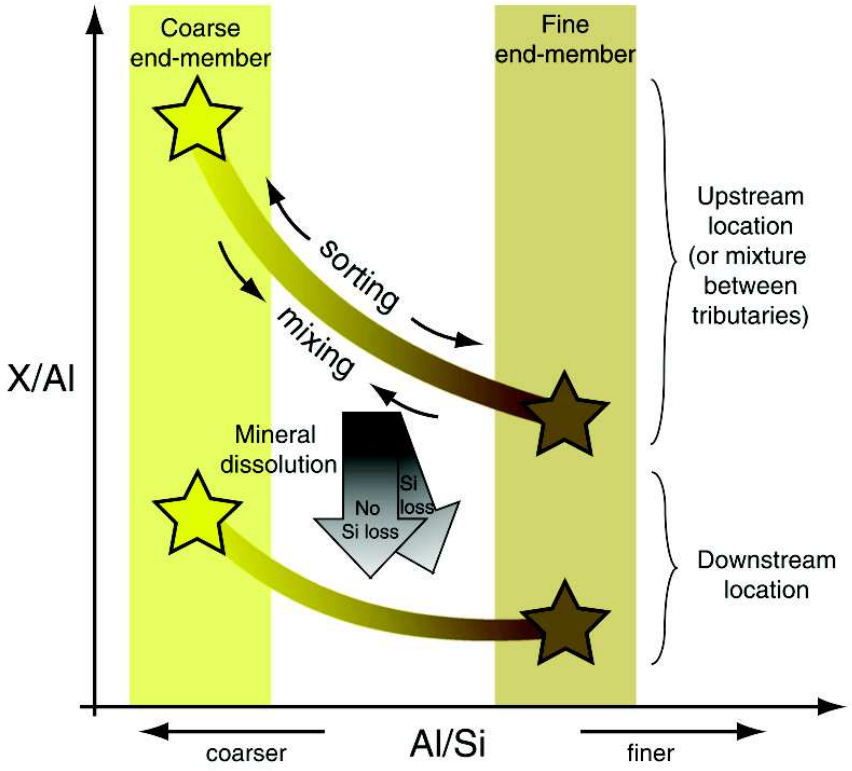

Figure 3-6. Conceptual diagram of an Al-normalized soluble element concentration (X/Al) used as a weathering index, as function of Al/Si, used as a grain size proxy. The brown star represents the fine grained end-member (channel surface) of sediment carried by the river and the yellow star is the coarse grained end-member (bottom of channel). All samples taken at intermediate depths are a mixture of each end-member that depend on sorting/mixing processes. In this example, weathering indices a changes in the X/Al ratio during transport between upstream and downstream locations; an example being that mineral dissolution would cause a decrease in the X/Al ratio. Here, Si loss due to weathering processes can be ignored. Source: Bouchez et al. (2012).

Table 3-1. Major element concentrations and B isotope compositions of Gandak River sediments

Sample	Map Position	Position Downstream (km)	Depth (m)	SiO_2 % wt	Al_2O_3 % wt	MgO % wt	CaO % wt	Fe_2O_3 % wt	MnO % wt	TiO_2 % wt	Na_2O % wt	K_2O % wt	P_2O_5 % wt	$\delta^{11}B$ (‰)
Sand Fraction														
(2 mm - 63 μm)														
CRS 248	1	0	0	71.13	8.79	1.99	5.83	2.72	0.05	0.37	1.41	2.00	0.08	-11.90
CRS 306D	2	60	0	76.86	7.97	1.40	4.15	2.09	0.04	0.27	1.34	1.83	0.06	-11.35
CRS 307	3	80	0	72.38	7.94	1.67	6.07	2.53	0.05	0.35	1.31	1.75	0.10	-11.18
CRS 305	4	125	0	69.89	9.01	1.86	6.12	3.05	0.04	0.43	1.31	2.19	0.10	-11.47
CRS 308	5	125	0	72.50	8.58	1.49	6.06	2.39	0.06	0.31	1.53	1.95	0.09	-11.77
CRS 302	6	220	0	71.74	8.49	1.42	6.50	2.50	0.06	0.35	1.49	1.88	0.10	-11.02
CRS 301B	7	245	0	69.49	8.16	1.53	7.85	2.64	0.08	0.38	1.45	1.67	0.13	-11.02
CRS BR8107	8	275	0	72.08	10.56	1.61	4.00	3.26	0.05	0.38	1.59	2.68	0.07	-12.40
Clay Fraction														
(<2 μm)														
CLY 248	1	0	0	46.62	19.98	5.25	2.18	9.57	0.09	0.88	0.58	5.24	0.12	-15.18
CLY 306D	2	60	0	45.12	20.23	4.89	2.66	10.46	0.16	0.91	0.57	4.57	0.15	-13.30
CLY 307	3	80	0	39.61	16.98	4.08	2.35	8.97	0.13	0.79	0.52	12.30	0.13	-11.96
CLY 305	4	125	0	46.71	21.63	6.84	1.81	15.56	0.19	1.23	0.56	4.68	0.15	-12.44
CLY 308	5	125	0	46.89	22.66	4.79	4.58	13.72	0.24	0.99	0.51	4.55	0.27	-12.52
CLY 302	6	220	0	41.63	19.15	4.14	4.34	10.97	0.19	0.83	0.51	4.00	0.20	-12.99
CLY 301B	7	245	0	45.11	19.71	5.35	1.99	11.92	0.17	1.01	0.61	4.43	0.15	-12.95
Bulk Fraction														
(< 2 mm)														
CA11 248	1	0	0	N/A	N/A	N/A	N/A	N/A	N/A	N/A	N/A	N/A	N/A	-11.90
CA11 306 D	2	60	0	74.30	7.87	1.69	5.17	2.63	0.04	0.30	1.09	1.72	0.07	-11.84
CA11 307	3	80	0	71.20	8.11	1.71	6.26	2.99	0.06	0.38	1.06	1.78	0.10	-11.76
CA11 305	4	125	0	67.30	9.22	2.16	6.63	3.39	0.05	0.50	1.40	2.21	0.13	-11.71
CA11 308	5	125	0	67.30	8.95	1.86	7.01	3.19	0.06	0.41	1.42	1.97	0.10	-11.70
CA11 302	6	220	0	70.60	8.74	1.64	6.52	2.90	0.06	0.36	1.74	2.10	0.10	-11.28
CA11 301 B	7	245	0	70.60	8.31	1.79	7.38	2.71	0.07	0.35	1.45	1.75	0.11	-11.90
BR 8107	8	275	0	71.09	10.07	1.54	4.25	3.22	0.05	0.38	1.57	2.55	0.07	-12.42
Suspended Load														
(>0.2 μm)														
CA11 125	1	0	3	58.93	11.43	2.39	8.63	4.30	0.06	0.53	1.31	2.85	0.17	-10.52
CA11 128	1	0	5	60.56	10.98	2.26	7.73	4.07	0.06	0.50	1.38	2.66	0.12	-12.11
CA11 126	1	0	8	57.33	11.76	2.44	8.88	4.38	0.06	0.54	1.29	2.97	0.17	-12.18
BR8103	8	275	1.5	59.75	12.32	2.46	7.50	4.49	0.06	0.56	1.33	3.01	0.13	-11.82
BR8102	8	275	3	60.59	12.04	2.32	7.30	4.27	0.06	0.54	1.31	2.95	0.12	-11.58
BR 8101	8	275	4.8	60.57	12.31	2.46	7.24	4.55	0.06	0.56	1.33	3.04	0.12	-11.81

Major element concentrations were measured by ICP-AES after an alkali fusion procedure at LHyGeS. Analytical uncertainties (2σ) are based on the external reproducibility of rock standards and are estimated between 6 – 8% for major elements; uncertainties of B isotope measurements were assessed based on external reproducibility of the seawater standard and is ±0.45‰ (2σ)

Table 3-2. Trace element concentrations of Gandak River sediments

Sample	Position (#)	Depth (m)	B	Sr	Ba	Co	Cr	Cu	Ni	Sc	V	Y	Zn	Zr	As	Rb	Nb	Mo	Cd	Sn	Sb	Cs	La	Ce	Pr	Nd	Sm	Eu	Gd	Tb	Dy	Ho	Er	Tm	Yb	Lu	Hf	Ta	W	Pb	Th	U
Bank Sediment			μg/g																																								
Sand Fraction																																											
(2 mm - 63 μm)																																											
CRS 248	1	0	56.9	127	330	5.0	38	7	16	7.0	48	20	32	124	10.6	125	7.0	0.6	0.0	3.1	3.1	5.1	27.1	53.7	6.4	23.2	4.4	0.8	3.7	0.6	3.0	0.6	1.6	0.3	1.6	0.2	3.2	0.7	2.3	15.8	11.2	2.1
CRS 306D	2	0	57.1	112	298	4.1	45	17	20	5.6	34	16	25	91	4.1	115	6.4	0.8	0.0	2.8	2.8	4.5	15.8	30.1	3.5	12.4	2.3	0.6	2.1	0.4	2.2	0.5	1.4	0.2	1.5	0.2	2.4	0.6	3.4	16.1	5.8	2.1
CRS 307	3	0	62.2	136	292	4.7	32	10	12	6.4	35	21	29	131	6.1	110	7.0	0.5	0.0	2.8	3.3	4.5	25.8	50.3	5.9	21.4	4.0	0.8	3.4	0.5	3.1	0.7	1.8	0.3	1.9	0.3	3.5	0.8	4.5	15.9	8.6	1.9
CRS 305	4	0	49.7	139	368	6.9	48	13	24	7.3	49	23	37	134	6.4	156	8.4	0.8	0.0	3.8	3.6	6.9	26.6	52.9	6.3	23.1	4.5	0.8	3.8	0.6	3.5	0.8	2.0	0.3	2.0	0.3	3.8	0.9	2.4	17.1	9.4	2.1
CRS 308	5	0	56.4	149	319	4.4	31	11	12	6.7	38	27	28	126	4.9	115	6.3	0.6	0.0	3.1	2.1	4.9	21.4	42.6	5.0	18.2	3.5	0.7	3.2	0.5	3.4	0.8	2.1	0.3	2.1	0.3	3.2	0.8	1.6	16.4	7.5	1.8
CRS 302	6	0	76.4	158	333	4.6	29	8	10	6.5	38	23	27	154	4.5	115	6.9	0.3	0.0	3.0	2.5	4.9	23.0	45.7	5.5	19.7	3.7	0.8	3.2	0.5	3.1	0.7	1.9	0.3	2.0	0.3	4.0	0.8	1.5	16.6	7.1	1.7
CRS 301B	7	0	88.2	170	285	4.2	29	10	11	7.2	37	32	29	214	4.8	101	8.1	0.4	0.0	3.1	2.4	4.4	33.8	68.0	8.0	29.1	5.7	1.0	4.9	0.8	4.5	1.0	2.8	0.4	2.8	0.4	5.6	1.0	4.5	16.8	12.3	3.2
CRS BR8107	8	0	44.1	129	449	9.8	39	6	23	7.4	52	14	45	131	10.8	182	7.1	0.3	0.0	4.2	2.2	8.3	15.8	31.7	3.7	13.5	2.6	0.6	2.2	0.3	1.9	0.4	1.1	0.2	1.1	0.2	3.4	0.7	2.0	21.8	6.1	1.4
Clay Fraction																																											
(<2 μm)																																										
CLY 248	1	0	54.0	55	829	27.9	134	50	247	19.7	154	29	149	134	48.1	275	15.8	2.8	0.0	7.9	13.6	18.6	36.7	72.0	8.5	31.0	5.8	1.0	4.9	0.8	4.4	1.0	2.6	0.4	2.8	0.4	3.9	1.6	6.9	42.9	17.9	4.7
CLY 306D	2	0	48.3	81	844	34.2	127	71	142	20.0	149	32	179	117	65.3	269	16.8	3.1	0.0	7.9	14.7	21.8	41.5	83.9	9.6	34.9	6.6	1.2	5.6	0.9	4.9	1.1	2.8	0.4	2.9	0.4	3.3	1.7	7.1	54.3	20.8	4.7
CLY 307	3	0	60.5	65	727	27.4	103	47	106	17.0	126	31	144	114	50.8	231	15.5	2.4	0.0	6.8	11.9	17.2	43.2	86.6	10.0	36.8	7.0	1.2	5.7	0.9	4.9	1.0	2.7	0.4	2.7	0.4	3.1	1.5	5.9	37.8	21.0	4.3
CLY 305	4	0	48.9	67	858	60.5	167	55	238	24.3	186	33	265	116	93.0	341	22.1	2.1	0.0	10.5	12.5	32.9	45.6	92.5	10.5	38.6	7.4	1.2	6.1	1.0	5.3	1.1	3.0	0.5	2.9	0.4	3.3	2.2	9.0	62.5	22.5	4.3
CLY 308	5	0	57.9	112	926	48.5	143	153	186	22.9	171	47	234	144	160.5	291	19.5	2.9	0.0	9.1	30.2	25.9	54.1	119.5	12.7	46.8	9.4	1.8	8.2	1.3	7.5	1.6	4.2	0.7	4.3	0.6	4.1	1.9	6.7	109.7	35.6	8.1
CLY 302	6	0	42.3	100	778	35.9	110	92	193	19.7	139	39	180	124	99.6	249	16.6	1.9	0.0	7.2	21.5	21.1	46.3	98.3	10.8	39.9	7.9	1.5	6.9	1.1	6.2	1.3	3.5	0.6	3.5	0.5	3.5	1.6	5.1	77.1	27.3	5.4
CLY 301B	7	0	41.4	67	808	42.6	136	39	197	21.1	160	30	201	115	67.4	299	19.2	1.0	0.0	8.9	11.2	27.2	39.0	80.7	9.0	33.1	6.4	1.1	5.3	0.8	4.7	1.0	2.7	0.4	2.7	0.4	3.2	1.8	5.6	46.0	19.3	3.8
Bulk Fraction																																											
(< 2 mm)																																										
CA11 306 D	2	0	33.8	125	329	6.0	31	7	15	5.7	38	17	54	126	0.0	90	6.3	0.6	0.0	2.7	0.6	6.0	19.5	38.7	4.5	16.5	3.1	0.7	2.5	0.4	2.6	0.6	1.4	0.2	1.5	0.2	3.3	0.6	1.3	13.1	6.9	1.7
CA11 307	3	0	44.0	141	324	6.0	33	0	13	6.6	41	23	56	165	0.0	91	8.4	0.5	0.0	3.3	0.7	6.3	32.5	64.9	7.5	27.6	5.2	0.9	4.2	0.7	4.0	0.8	2.2	0.4	2.2	0.3	4.4	0.8	1.4	13.2	10.9	2.5
CA11 305	4	0	43.6	152	378	8.0	40	13	17	7.5	49	30	59	294	0.0	125	12.1	0.6	0.3	4.4	1.0	9.2	45.1	90.5	10.5	38.8	7.4	1.2	6.2	1.0	5.9	1.2	3.2	0.5	3.2	0.5	9.4	1.2	5.0	15.9	17.9	4.1
CA11 308	5	0	44.6	152	365	8.0	52	6	23	7.5	48	25	41	194	1.2	100	7.7	0.3	0.3	3.9	0.7	6.3	30.4	60.9	7.0	25.3	4.9	0.9	4.4	0.8	3.7	0.8	2.3	0.4	2.3	0.3	5.0	0.9	0.6	20.5	12.5	2.6
CA11 302	6	0	42.8	162	340	7.0	65	7	15	6.8	41	23	121	169	0.0	118	9.7	0.4	0.4	4.1	0.7	8.6	36.5	72.9	8.5	31.0	6.0	1.1	4.7	0.8	4.5	0.9	2.5	0.4	2.5	0.4	5.4	0.9	2.0	16.7	12.5	2.6
CA11 301 B	7	0	50.3	175	295	6.0	85	8	11	6.8	36	28	285	156	0.0	80	8.5	0.4	0.2	3.4	0.5	5.6	32.8	65.8	7.6	27.7	5.3	0.9	4.5	0.7	4.5	1.0	2.6	0.4	2.7	0.4	4.1	0.9	2.1	13.3	10.5	2.5
BR 8107	8	0	22.6	150	491	11.5	110	22	42	0	66	26	90	228	9	154	11.3	1.1	0.3	6.0	1.2	8.9	38.8	75.5	8.1	32.7	6.5	1.1	5.4	0.8	4.6	0.9	2.5	0.4	2.5	0.4	6.1	1.3	3.0	19.0	16.3	3.5
Suspended Load																																											
(>0.2 μm)																																										
CA11 125	1	3	36.9	180	453	10.3	58	21	26	10.1	63	27	59	222	12.0	139	11.1	0.8	0.2	4.6	1.0	9.2	38.9	76.9	8.8	32.1	6.3	1.1	5.2	0.8	4.6	0.9	2.5	0.4	2.5	0.4	5.7	1.3	2.6	22.2	16.3	3.9
CA11 128	1	5	41.6	172	436	9.8	55	18	25	9.5	62	27	53	206	12.5	130	10.6	0.9	0.2	5.5	0.9	8.5	36.2	72.7	8.2	29.7	5.9	1.1	4.9	0.8	4.6	0.9	2.6	0.4	2.6	0.4	5.6	1.5	3.3	21.9	15.7	4.3
CA11 126	1	8	40.8	189	475	11.0	63	22	29	10.2	66	26	61	217	13.1	149	11.4	0.8	0.2	5.0	1.1	9.9	39.3	78.0	8.9	32.4	6.3	1.2	5.3	0.8	4.6	0.9	2.5	0.4	2.5	0.4	5.7	1.3	3.7	23.3	17.0	3.9
BR8103	8	1.5	37.1	150	569	13.0	84	27	39	0.0	76	27	87	183	12.9	177	12.3	0.9	0.2	5.6	1.6	10.4	39.7	78.1	8.5	33.2	6.5	1.2	5.4	0.8	4.8	0.9	2.6	0.4	2.7	0.4	5.1	1.4	3.5	23.9	17.2	4.0
BR8102	8	3	37.1	147	480	11.1	73	18	34	0.0	65	26	68	233	9.3	148	11.1	0.7	0.3	5.5	1.2	8.6	38.8	75.7	8.1	32.4	6.3	1.1	5.3	0.8	4.7	0.9	2.6	0.4	2.6	0.4	6.3	1.3	3.0	16.5	16.3	3.6
BR 8101	8	4.8	36.8	142	448	11.7	75	18	33	0.0	70	25	69	230	8.7	144	11.0	0.6	0.2	5.3	1.2	8.2	36.8	70.8	7.5	29.6	5.7	1.1	5.1	0.8	4.3	0.8	2.4	0.4	2.3	0.4	5.7	1.2	2.7	15.3	14.7	3.3

Trace element concentrations were measured by ICP-MS after an alkali fusion procedure ay LHyGeS. Analytical uncertainties (2σ) are based on the external reproducibility of rock standards and are 10% for trace elements. Boron concentrations were determined by ID-ICP-MS at LHyGeS. Analytical uncertainty of B concentrations is based on repeated measurement of a NIST 951 standard solution estimated to be ~1%

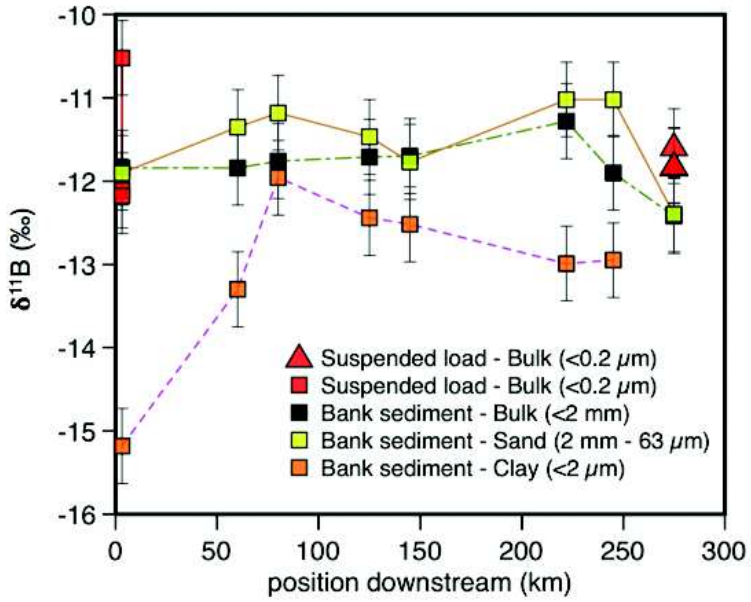

Figure 3-7. Boron isotope composition of the bulk fraction of the suspended load, and the bulk, sand, and clay fractions of bank sediment from the Gandak River as a function position downstream. Sampling positions downstream at 0 km, 60 km, 80 km, 125 km, 145 km, 220 km, 245 km, and 275 km corresponds to positions #1; #2, #3, #4, #5, #6, #7, and #8, respectively, in Figure 3-4. Dotted and solid lines are simply used to connect samples of the same category based on their position downstream.

Table 3-3. Boron isotope compositions and concentrations of hand-picked biotite and muscovite minerals from the bulk fraction of bank sediment samples

Hand-picked minerals (< 2 mm)	Map Position	Position Downstream (km)	$\delta^{11}B$ (‰)	B (ppm)
Biotite				
CA11 248	1	0	-15.35	55.79
CA11 307	3	80	-7.36	38.38
CA11 302	6	220	-8.31	66.88
BR8107	8	275	-9.46	62.83
Muscovite				
CA11 248	1	0	-15.35	81.93
CA11 307	3	80	-14.41	120.93
CA11 302	6	220	-14.96	93.95
BR8107	8	275	-12.59	67.34

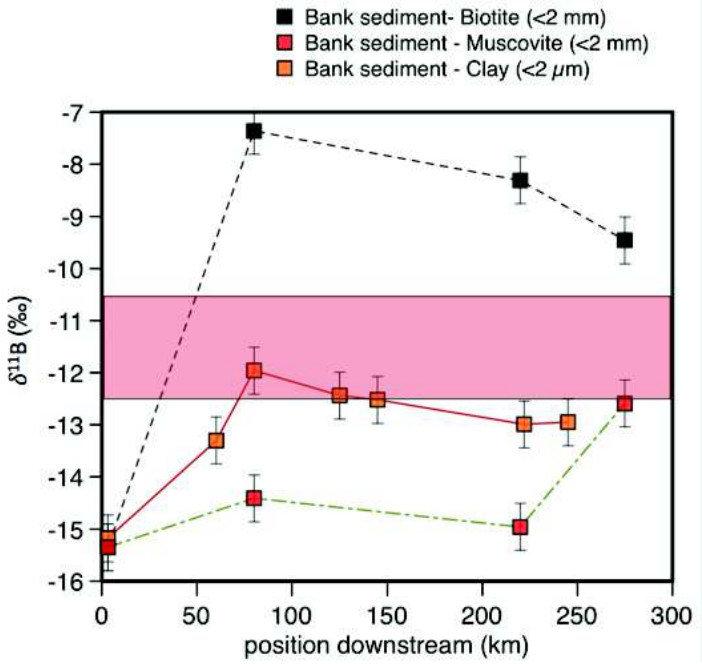

Figure 3-8. B isotope composition of hand-picked biotite and muscovite minerals from the bulk fraction of bank sediment samples from the Gandak River as function of position downstream. The dotted and solid lines connect each sample in the respective category based on position downstream. The pink bar represents the approximate variability of bulk and sand fractions of bank sediments and the bulk fraction of suspended load sediments in this study.

The B isotope compositions of the bulk sediment, sand fraction and suspended loads do not vary very significantly (±1‰) from the headwaters out to the alluvial plain. This likely indicates that the river is delivering well-mixed sediment composed of primary and secondary minerals derived from the various lithological units upstream; the B isotope composition of the bulk sediment reflects this mixture. As the B isotope composition of the suspended load (at both sites) is very similar to that of the bulk and sand fraction at those locations, it likely consists of a mixture of both secondary minerals and finely ground clay-sized primary minerals; its B isotope composition would then reflect both the source of the primary minerals, which is the bedrock, and the weathering regime associated with the secondary minerals. The exception to this is the sample taken closest to the surface (3 m depth) at headwater sampling location whose B isotope composition is –10.5‰, which is isotopically heavier than any other sample taken at that location, including the other suspended load samples at 5 m (–12.1‰) and 8 m (–12.2‰) depths. The composition of the 3 m sample may be different from the others and likely contains a larger portion of clay-sized primary minerals that are derived from an isotopically heavier source. However, clay

mineral identification was not performed on these samples; as such, this hypothesis remains speculative. The B isotope composition of the sand fraction most likely reflects only a mixture of B-carrying primary minerals derived from bedrock dissolution and therefore experiences little to no B isotope fractionation. If so, then the sand fraction would keep the memory of the bedrock and can be used as a source tracer in the catchment. This observation was also noted by Lemarchand et al. (2012) who found that the B isotope composition of the silt and sand fractions in soil profiles in the Strengbach CZO recorded the composition of the parent material.

In the absence of parent bedrock material, the $\delta^{11}B$ composition of the sand fraction in each sample can then be compared to that of the clay fraction ($\Delta^{11}B_{clay\text{-}sand} = \delta^{11}B_{clay} - \delta^{11}B_{sand}$) in order to estimate the isotope fractionation factor between weathered clay minerals and unweathered primary minerals. This assumes all mineral fractions have a common origin and therefore comparable to one another and that most of the B in the clay-size fraction is carried by the secondary minerals. The $\Delta^{11}B_{clay\text{-}sand}$ value of the headwater sample is the largest displaying an isotope fractionation of –3.3‰ (Figure 3-9A). The isotope fractionation between the two mineral separates progressively becomes smaller downstream, reaching a minimum of –0.8‰ in less than 100 km and showing a slight increase to approximately –2‰ before converging with the Ganges River. This may indicate differences in the conditions of sediment production along the course of the river with the clay fraction in the headwater sample experiencing different conditions than those on the Ganga plain.

To quantitatively determine B behavior during clay formation and investigate how this may relate to the weathering regime, the relative magnitude of the B transfer from primary minerals in the sand fraction, and by proxy the bedrock, to the neoformed clay minerals ($\varphi_{Al,B}$) can be calculated:

$$\varphi_{Al,B} = \frac{[B]_{clay}}{[B]_{sand}} \times \frac{[Al]_{sand}}{[Al]_{clay}} \quad (3\text{-}2)$$

The soluble nature of boron implies its progressive depletion in clay minerals as weathering reactions progress, leading to $\varphi_{Al,B}$ values starting from 1 in pristine materials down to 0 in totally leached weathering products. Assuming that all Al in the clay fraction comes from the dissolution of the sand fraction and no Al is lost during the reaction, then $\varphi_{Al,B}$ values greater than 1 would indicate boron incorporation from an external source. In the headwaters, large B isotope fractionation correlates with intense B leaching in the clay fraction (inferred from low $\varphi_{Al,B}$

values); on the plain, relatively small B isotope fractionation correlates with milder B loss, (inferred from higher $\varphi_{Al,B}$ values, Figure 3-9B). Low $\varphi_{Al,B}$ values in the headwaters indicate that weathering reactions are dissolution dominated, where B and other mobile elements are progressively dissolved in solution and B precipitation into the clay fraction is low. High $\varphi_{Al,B}$ values on the plain indicate that weathering reactions are either limited in intensity (slight loss of B) or precipitation-dominated which produce clay-sized fractions with a more quantitative B incorporation and hence higher $\varphi_{Al,B}$ values.

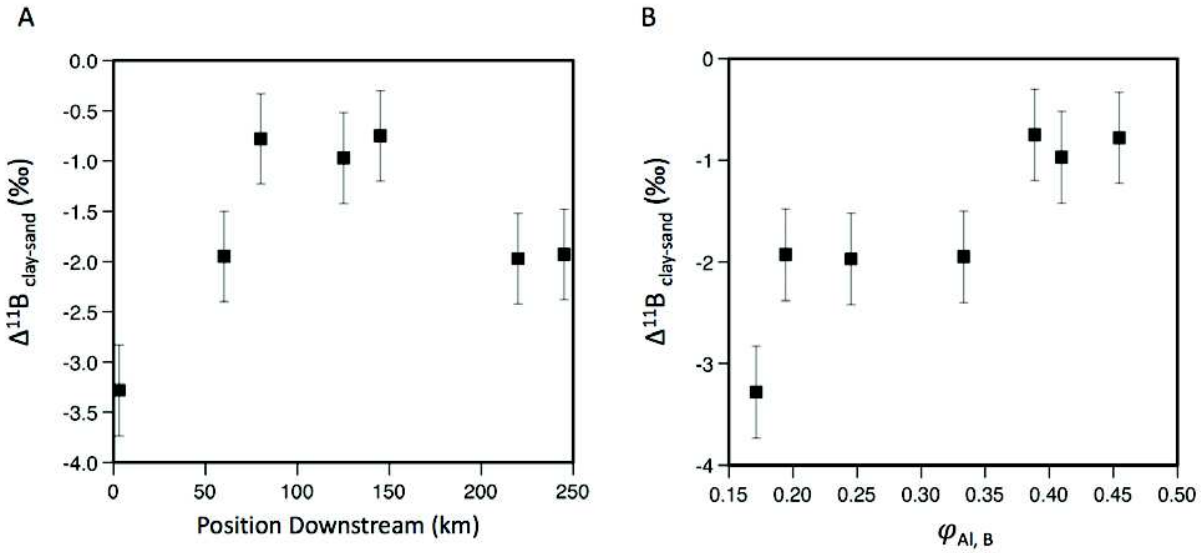

Figure 3-9. A) $\Delta^{11}B_{clay\text{-}sand}$ values as a function of downstream position of Gandak River sediments, B) $\Delta^{11}B_{clay\text{-}sand}$ values as a function of the mass transfer coefficient ($\varphi_{Al,B}$)

The use of $\varphi_{Al,B}$ as mass transfer coefficient in this case is imperfect however, and should be used with caution, as a true mass transfer from primary minerals to weathered products would involve the bulk weathered material, not only the clay fraction as calculated in Equation 3-2. Noteworthy, the $\Delta^{11}B_{clay\text{-}sand}$ values showing a relative scatter when plotted against distance downstream (Figure 3-9A) tend to organize when compared to the B depletion. This may indicate a mixing in variable proportions of clay minerals produced under different weathering regimes in tributary watersheds along the course of the Gandak.

To interpret B isotopes in terms of the weathering regime (competition between dissolution and precipitation reaction rates), a conceptual model is proposed at the end of this chapter, that will also include the results from the Murrumbidgee River.

3.3.3.3 Mineral Separates

The B isotope of hand-picked biotite and muscovite mineral separates is a complimentary and parallel approach to the analyses of the clay fraction and may provide information on the weathering regime. In particular, B isotope compositions of mica mineral separates may give insights into the stage of weathering of river sediments, as B isotope fractionation was reported to occur very early in the weathering process (Voinot, 2012). Boron mobilization in biotite was also reported to be faster than in muscovite, however the mechanism for this rapid evolution is still unknown (Voinot, 2012; Williams et al., 2001b). Possible explanations of changes in the B isotope compositions of minerals separates in these studies was attributed to a preferential release of B from interlayers sites and gradual replacement by secondary minerals such as kaolinite (mineral transformation). In the present study, the B isotope composition of hand-packed micas and their downstream evolution closely resemble that of the clay fraction, although taking slightly different paths to arrive at isotopically heavier values on the plain compared to the headwater sample (Figure 3-8). As shown by Voinot (2012) (Figure 3-1), primary minerals have very similar B isotope compositions, while all weathering minerals may evolve at different rates yet converge towards a common value that is expected to hold information on the weathering regime (i.e. the ratio between the dissolution and precipitation rates). This is a similar pattern observed in this study where minerals separates (including the clay fraction) start out with similar B isotope compositions in the headwaters, then evolve towards isotopically heavier values at different rates, and finally seem to be converging on a common value downstream. Large differences in the B isotope composition between biotite and muscovite minerals, as seen in the first two samples on the plain (taken at 75 km and 225 km, respectively) can be interpreted as weathering processes in the early stage.

Without a framework to interpret these results, however, it remains difficult to determine the mechanisms driving these patterns. When considering mineral dissolution as a possible explanation, as evoked by previously mentioned studies, it seems unlikely that mineral dissolution is the cause of the trend observed in the biotite since its isotopic signature rapidly increases in the first 100 km of the river and then decreases further downstream. Additionally, the biotite sample with the highest $\delta^{11}B$ (CA11 307; -7‰) has the lowest B concentration, indicating a preferential loss of ^{10}B, not ^{11}B expected by dissolution of isotopically heavy interfolia layers. A possible explanation for the composition of the biotite along the course of the river could be a progressive

replacement of interfolia B that is originally inherited from the conditions of the bedrock formations. Since weathering of the phyllosilicates often starts with a progressive opening of the interfolia layers, it can release B with advancement of the water front. Muscovite are more resistant to interfolia opening and therefore needs more time of water contact. Variations of $\delta^{11}B$ in micas along the course of the Gandak would therefore record mixture of micas differently affected by interactions with water. Dissolved boron in river being characterized by low concentrations (about 10-20 of $\mu g.L^{-1}$) and relatively high $\delta^{11}B$ compared to bedrock, exchange of original interfoliar B with water would tend to lower the bulk B concentration and increase the $\delta^{11}B$ value. However, without knowledge of the mineral phases of the biotite and muscovite separates and a thorough understanding of B isotope systematics during mica weathering and transformation, this study cannot clearly identify the specific mechanisms controlling B isotopes during the mineral weathering (e.g. structural breakdown of B sites or solid diffusion).

3.3.4 Conclusions

A preliminary investigation into transported riverine material in the Gandak River reveals that B isotopes in the various mineral separates transported by the river behave differently. The bulk, sand, and suspended loads all have very similar B isotope signatures that show little variation along the course of the river, likely reflecting the source of B. The sand fraction in particular may be used as a source tracer, as it does not contain a significant amount of secondary minerals and experiences with little or no isotopic fractionation during production and transport; this makes the sand fraction a good representative of the parent bedrock in the catchment. On the contrary, the clay-sized fraction that is mostly composed of secondary minerals shows an evolution towards higher $\delta^{11}B$ compositions downstream which is expected to reflect the weathering regime (competition between dissolution and precipitation reactions). The lower $\delta^{11}B$ values of the clays produced in the headwaters indicate a higher dissolution rate, where more intense bedrock dissolution produces isotopically lighter soil solutions and relatively little removal of B by production of secondary phases. Here, sediment is rapidly transported downstream which results in little clay production and therefore minimal partitioning of B between the secondary phases and the soil solution. On the alluvial plain, precipitation rates increase. This yields a higher clay production and therefore a more quantitative re-incorporation of ^{10}B into the clay fraction and a

complimentary ^{11}B enrichment of the solution. As clay formation increases and the amount of B in solution decrease, the soil solution becomes exponentially heavier; this yields neo-formed clays which also have exponentially heavier compositions (Rose et al., 2000) and bulk clay closer to that of the parent material.

To assess loss or gain of mobile elements during transport, *B/Al, *Ca/Al, *Mg/Al, and *Na/Al ratios were calculated by normalizing the ratio concentration measurements for each sediment fraction in downstream samples to the corresponding fraction of the most upstream sample. Results show that all sediment size fractions display a relatively similar behavior and show no significant evolution downstream. This indicates that the river sediment is not being weathered during transport and whose elemental composition reflects the original conditions in which the sediment was formed. This has important implications as it suggests that the composition of the sediment may reflect weathering conditions in source areas of the catchment.

The evolution of hand-picked biotite and muscovite minerals from bank sediment samples towards isotopically heavier values reveals a more complex B isotope behavior than other size fractions. Both biotite and muscovite minerals have the same B isotope composition in the headwaters, then show an evolution towards isotopically heavier values from the headwaters out to the alluvial plain, with biotite evolving faster downstream than the muscovite. This observation is in agreement with other studies that note the same behavior (Voinot et al., 2013; Voinot, 2012). Large B isotopic differences between the muscovite and biotite in upstream river samples would then indicate that mineral weathering is in the early stage, as biotite evolves faster than muscovite; inversely, their compositions seem to converge towards a similar point downstream, likely indicating more advanced weathering reactions. However, the mechanism responsible for the isotopic shift in the present study has yet to be identified and therefore warrants future research. These results suggest that a combined study of handpicked biotite and muscovite in sediments may help determine the advancement of the early reactions of weathering, before the first evidence of mineralogical evolution. From this conceptual view, similar but low $\delta^{11}B$ values in both biotite and muscovite (close to the sand value) would then indicate very early stage of water-rock interaction. With biotite evolving faster than muscovite, the isotopic shift between these two minerals first increases before decreasing again as the weathering reactions progress and $\delta^{11}B$ increases. Finally, both minerals are expected to have similar or close compositions once exchangeable B has equilibrated with water (state not reached in the present study).

Although preliminary, results from this study demonstrate the potential of B isotopes in various riverine mineral separates to record the weathering regime and therefore highlight its potential as a paleo-weathering proxy in sediment deposits. To better understand what drives the B isotope composition of biotite and muscovite mineral separates, future work on this topic should focus on these fractions in downstream sediment deposits.

3.4 MURRUMBIDGEE RIVER BASIN, SOUTHEASTERN AUSTRALIA

3.4.1 Study site

The Murrumbidgee River, located in the Murray-Darling Basin in southeastern Australia, is the major tributary of the Murray River and is Australia's third longest river (1,690 km) behind the Murray (2,530 km) and Darling River (2,740 km) (Figure 3-11). The entire basin covers an area of more 1 million km^2, roughly 14% of the Australian continent, and lies between Queensland, New South Wales, South Australia, and the Australian Capital Territory. Worldwide, the basin is the 20th largest river catchment however has the lowest rate of discharge (average annual discharge from 1885 to present: 760 $m^3 s^{-1}$) of all major river systems (Pigram, 2007). The Murray-Darling Basin is bound by the Great Dividing Range in the south and east, the central Queensland sandstone belt in the north, and the arid interior in the west. The Murray-Darling Basin is composed of 23 major river catchments (Figure 3-12) all of which ultimately flow to the Southern Ocean. In general, northern catchments drain to the Darling River and southern catchments drain to the Murray River. Watercourses generally start as fast-flowing streams in the Great Dividing Range which then flow inland across riverine plains, where channels widen and rivers meander, significantly slowing down the water flow (Murray-Darling Basin Authority, 2018). Owning to warm–hot semi-arid conditions and low-lying topography in many regions of the Basin, evaporation and transpiration rates are high (94% of the total rainfall in the Basin is transpired or evaporated). Additionally, a large portion of water in the system fills wetlands, and more recently is used to supply towns, industry, and irrigation. As a result, many lakes, creeks, and rivers are ephemeral and only reach larger rivers during the wet season or flooding events (Murray-Darling Basin Authority, 2016).

Figure 3-10. Fluvial catchment of the Murray-Darling Basin in southeastern Australia showing the location of the Darling and Murray Rivers, and the Murray's largest tributary, the Murrumbidgee River. Source: Murray-Darling Basin Authority (2015).

Climate in the basin is quite variable, reflecting its large size and diverse geography from rugged mountains to arid plains. The northern portion of the basin is sub-tropical; semi-arid in the west; and mainly temperate in the south. The eastern mountainous portion of the basin receives a high annual rainfall of 1,500 mm with several months of snowfall on the peaks of the Great Dividing Range. The western side of the basin is generally hot and dry with an average annual rainfall of < 300 mm. The average annual rainfall in the catchment is 470 mm, with potential evaotranspiration of 1,174 mm, and daily summer and winter temperatures of 25°C and 9°C, respectively (Murray-Darling Basin Authority, 2016). Many smaller catchments in the south and southeast that drain the Great Dividing Range make larger contributions to total runoff than other larger catchments.

Figure 3-11. River catchments with the Murray-Darling Basin in southeastern Australia. Source: Murray-Darling Basin Authority (2018)

The basin can be divided into major tectonic units using a framework developed by Palfreyman (1984) where rock types are grouped according to dominant lithology and broad time periods. The largest groups being the Murray Basin, Lachlan Fold Belt (LFB), Surat Basin, New England Fold Belt, Eromanga Basin, and the Barka Basin (Figure 3-13). Sediments from the Murrumbidgee River catchment (area: 84,000 km^2), located in the southeastern portion of the basin, originate from the Lachlan Fold Belt, comprising the Australian Alps (Snowy Mountains). The Lachlan Fold forms a major part of the southeastern basin, which extends from central and southeastern New South Wales (NSW) to Victoria. It is composed of three major lithotectonic assemblages (Coney, 1992): greenstone belts of Early-Middle Cambrian age, turbidite fan deposits of Ordovician-Silurian age, and the complex sedimentary, volcanic, and plutonic units of early-mid Silurian to early-Carboniferous age. The turbidite fan deposits are composed of quartz-rich sands and muds which dominate much of the LFB and appear to be sourced from Gondwanaland (Coney, 1992). Extensive orogenic granites were set in the Silurian and Devonian periods, representing a major transition towards a mature continental margin orogeny in the LFB, linked to complex sedimentary units and intense volcanism (Coney, 1992). Additional post-orogenic granites from the Carboniferous completed the development of the LFB. Plains in the Snowy Mountains northwest of Australia's highest peak, Mt. Kosciusko (2,228m). It flows north through

the Southern Highlands and then westward across the Riverine Plain before joining the Murray River (Figure 3-14). Within the drainage basin, three topographic regions can identified: the mountainous Southern Highlands east of Jugiong; the valley section westward until the town of Naranderra; and the Riverine Plain west of Naranderra. The focus of this study shown in Figure 3-14 is located predominately in the Southern Highlands, which itself can be subdivided into three distinct topographic units based on elevation. The highest part of the catchment and origin of the Murrumbidgee River is on the Kosciusko Plateau (average elevation: approximately 1375 m). Downstream of the headwaters, near town of Cooma, (average elevation: approximately 930 m) is an area of significant relief which extends just south of the capital city, Canberra. This lower sub-region (average elevation: approximately 500 m) extends westward to the town of Jugiong and is the end of the true highland region (Schumm, 1968). The river continues into the valley section westward towards Wagga Wagga progressively becoming wider until reaching the town of Narrandera (average elevation: approximately 150 m) where the valley ends and the Murrumbidgee River flows onto the Riverine Plain where it becomes highly sinuous until converging with the Murray River nearly 1,500 km from its headwaters (Wallbrink et al., 1998; Schumm, 1968). The major topographic relief on the Riverine Plain is characterized by the modern river and a series of paleochannel systems with their levee systems and associated sand dunes.

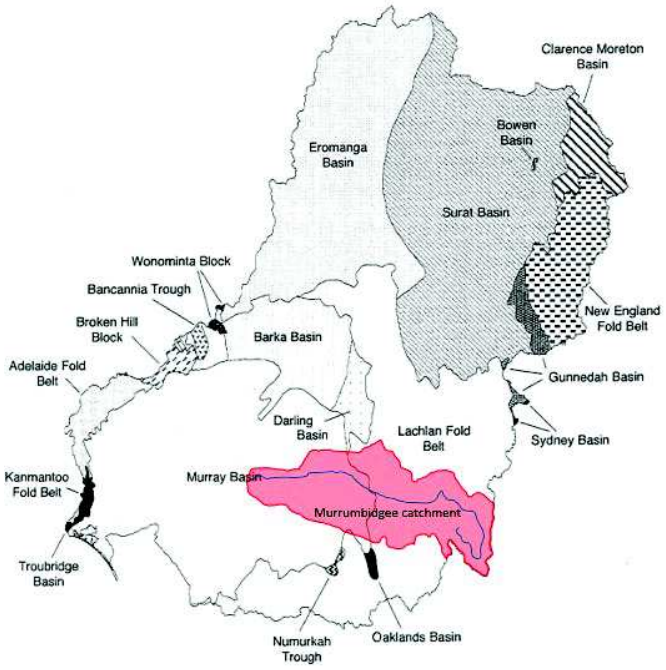

Figure 3-12. Tectonic units within the Murray-Darling Basin displaying the Murrumbidgee catchment and the Murrumbidgee River. Source: re-drawn from Kingham (1998).

Climate in the catchment is considered temperate in the Southern Highlands transitioning to semi-arid on the Riverine Plain. Climatic conditions in the Murrumbidgee River drainage basin range between two extremes characterized by cold wet winters in alpine elevations (up to 1,500 mm of average annual rainfall), and hot dry summers on the Riverine Plain (less than 300 mm of average annual rainfall) with an estimated increase of 250 mm of rainfall every 300 m rise in elevation (Murray-Darling Basin Authority, 2015). Evapotranspiration rates also increases (1,200 to 1,600 mm of potential evapotranspiration) from upper to lower elevations due to the increasing temperature gradient and decrease in precipitation, resulting in a decrease in soil moisture in lower elevations (Murray-Darling Basin Authority, 2015).

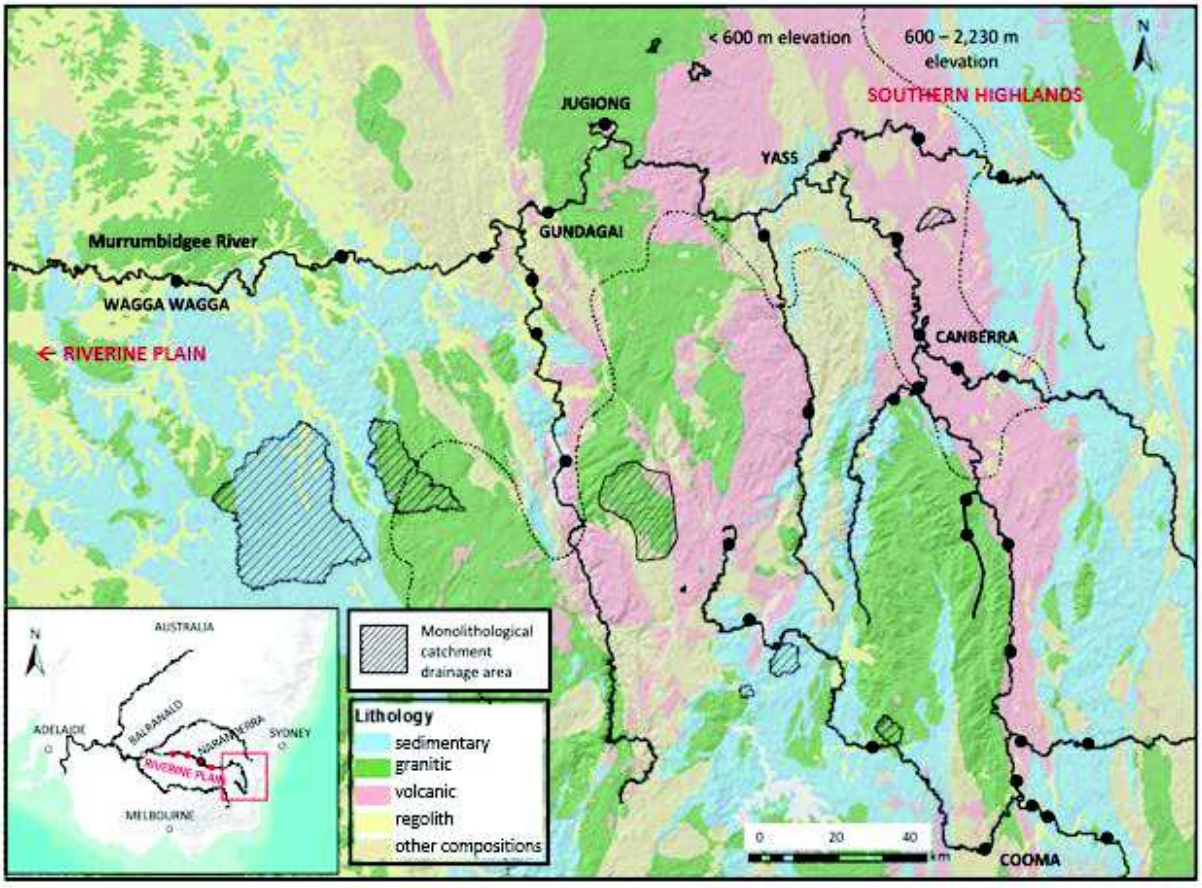

Figure 3-13. Lithology and digital elevation map (DEM) of the upper Murrumbidgee River and tributaries displaying sampling points for sediments and water (black dots) and sampling points for sediment, water, and bedrock in monolithological catchments with respective drainage catchment areas (hashed areas). The dashed line separates the upper (> 600 m elevation) and lower (< 600 m) catchments. Inset map: southeastern Australia; red rectangle shows area displayed in the main panel. Source of DEM: Geoscience Australia; source of lithology map: NSW Government; Resources and Energy; source of inset map: Esri, USGS, NOAA

The Murrumbidgee River, upstream from the town of Gundagai, drains primarily sedimentary siliciclastic rocks (sandstones, shales, and limestones), igneous intrusive rocks (predominately granite, granodiorite, and gabbro) and igneous volcanic rock compositions (Schumm, 1968). The source region of the Murrumbidgee is composed of both granite intrusives and sedimentary siliclastic rock compositions of Silurian and Middle Devonian ages, respectively (David and Browne, 1950). As it follows a southeastward course towards the town of Cooma, the catchment area drains shales, sandstones, and granites of Middle Devonian age (Figure 3-14). The river then flows north for 80 km over predominately volcanic and sedimentary rocks of the Silurian age, east of the Murrumbidgee batholith. Southeast of Yass, the river begins bending to the west and travels across north to south-oriented lithological units in the Southern Highlands. From east to west these lithologies include: sedimentary and volcanic formations of the Middle Devonian, granites of the Middle Devonian near Jugiong, shales, conglomerates, and volcanics of the Siluarian near Gundagai, and finally a mixture of limestone and sandstone of the Ordovician period near town of Wagga Wagga (Schumm, 1968). Further west, the river flows on Quaternary alluvium with small outcrops of Middle Devonian granite and clastic rocks near Narrandera. It is here where the river flows onto the alluvial plain across Quaternary fluvial sediments until joining the Murray River. A late Pliocene uplift in the eastern section of the Murrumbidgee River catchment caused a major shift in sediment type delivered to the Riverine Plain, marked by a transition from marine and lacustrine sediment deposition to fluvial sedimentation. Despite Tertiary sea-level fluctuations impacting sedimentation patterns to the west and south (Mallee Basin), the Riverine Plain has maintained continuous terrestrial environments over the last 60 Ma (Bowler, 1986).

In this study, 18 sites along the course of the Murrumbidgee River were sampled for river bank sediments and 12 sites for river water at the same locations. Additionally, eight major tributaries were sampled along their course and at their confluence with the Murrumbidgee. Using spatial data (see Methods below), monolithological catchments were identified in different parts of the Murrumbidgee River basin. Four catchments draining only granitic rocks were sampled for river sediments and bedrock, two of which were also sampled for river water. Four catchments draining only volcanic rocks were sampled for sediments, two of which were sampled for water and bedrock. Three catchments draining exclusively sedimentary rocks were sampled for sediments, two of which were also sampled for water and bedrock. For sediments collected in monolithological catchments and tributaries, only the clay-sized fraction was analyzed.

3.4.2 Methods

3.4.2.1 Spatial Analysis

A 1 arc second digital elevation model (DEM) (source: Geoscience Australia) was used in Esri ArcGIS™ 10.4 to determine catchment boundaries and average values for each catchment (elevation, rainfall, temperature). Calculated catchment boundaries were used in combination with geological spatial data (source: Geological Survey of NSW, Australia) to determine the proportions of each lithology in each catchment. Additionally, monolithological sites were identified using geological spatial data in combination with the DEM (location and type of lithological catchment shown in Figure 3-14).

3.4.2.2 Sample collection, preparation, and analysis

Bedrock samples were collected from rock outcrops in monolithological catchments (Figure 3-14) and crushed to a fine powder. Sediment samples were collected by sampling an area of approximately $1m^2$ on the river bank or sandbar and amalgamated. Sediment samples were dried at 60°C and sieved at 2 mm to remove gravels and debris. The <2 mm fraction was then wet sieved at 63 μm with DI water. Both the sand-sized (63 μm – 2 mm; termed "sand fraction" hereafter) and silt-sized (<63 μm) fractions were kept. The silt-sized fraction was further processed by centrifugation to extract the clay-sized fraction (<2 μm; termed "clay fraction" hereafter) using the protocol established in Starkey et al. (1984). River water was collected from small streams in monolithological catchments and the Murrumbidgee River. Water samples were filtered in the field using a portable water filtration system with 0.2 μm MCE membrane filters. The pH and alkalinity were determined on the <0.2 μm fraction (termed "dissolved load" hereafter) following the method of Barnes (1964). More information on bedrock, river sediment, and river water collection and sample preparation can be found in sections 2.1.1 to 2.1.3.

Bedrock and sediment clay fractions in this study were analyzed for mineralogy, major and trace element concentrations, B concentration, and B isotopes. The dissolved load was analyzed for major and trace elements, B concentration, and B isotopes. Sample preparation and analysis for mineral identification by XRD and major and trace elements by ICP-MS are described in section 2.2 and 2.3, respectively. Sample preparation for B isotope and B concentration analyses

can be found in section 2.4. Details on sample analyses for B concentration by ID-ICP-MS and B isotope measurements by MC ICP-MS can be found in sections 2.5 and 2.6, respectively.

3.4.3 **Results**

3.4.3.1 Spatial analysis

Using a geospatial lithological map and DEM (sources: Geological Survey of NSW, Australia and Geoscience Australia, respectively) monolithological catchments in both the higher (n = 5) and lower (n = 6) elevation catchments were identified (Figure 3-14). Catchments areas vary: <10 km^2, n = 4; 10 – 150 km^2, n = 5; and 500 – 1000 km^2, n = 2 (Table 3-4). In general, lower elevation catchments (LEC) are larger than higher elevation catchments (HEC). The average elevation of the Murrumbidgee HEC ranges from approximately 1415 – 1155 m, with an average elevation of 1270 m above sea level whereas those in LEC range from 433 – 595 m with have an average elevation of approximately 532 m. According to Olley and Wasson (2003), a relatively significant change in average landscape elevation occurs just south of Canberra at approximately 600 m above sea level. Mean annual temperature, mean annual rainfall, and mean catchment slope (source: Australian Government, Bureau of Meteorology) were also calculated for each of the monolithological catchments (Table 3-4). The mean annual temperatures within the five HEC and six LEC range from 6.2 – 10.0°C and 12.6 – 14.3°C with averages of 8.5°C and 13.3°C , respectively The HEC and LEC have mean annual rainfall values ranging 811 – 1259 mm and 660 – 986 mm with averages of 1143 mm and 770 mm, respectively. The average mean catchment slope in the HEC and LEC ranges from 9.8 – 13.3° and 6.7 – 10.5° with averages of 12.5° and 7.5°, respectively. Statistical analyses (one-way ANOVA, $\alpha = 0.05$) of mean annual temperature, mean annual rainfall, and mean catchment slope was performed to illustrate differences between the HEC and LEC. Results from the one-way ANOVA tests show significant differences*;* in mean annual temperature ($p < 0.001$), and mean annual rainfall ($p = 0.004$), and mean catchment slope ($p = 0.004$), between the HEC and LEC (Table 3-5).

Quantification of the proportions of lithologies drained by the Murrumbidgee River was performed at nine locations along the main channel (Figure 3-15). The proportion of felsic volcanics, hereafter referred to as ‘volcanic’, decreases from approximately 70% to between 20 and 30% downstream and felsic intrusives, hereafter referred to as ‘granitic’, proportions increase to approximately 30%. The proportion of sedimentary siliclastic, hereafter referred to as

'sedimentary', is relatively constant with proportions as low as 10%. The proportions of other compositions, mainly carbonate rocks, and regolith (alluvium) are relatively low (< 10%) and constant along the Murrumbidgee River; however its composition dominates downstream areas on the plain (not shown).

Table 3-4. Mean temperature and annual rainfall at both higher and lower locations in the Murrumbidgee River catchment

Samples	Average Catchment Elevation (m)	Catchment Area (sq. km)	Mean Annual Temperaure (°C)	Mean Annual Rainfall (mm)	Mean Catchment Slope (°)
Higher elevation catchments (HEC)					
ALAC Creek	1334	24	7.6	1125	9.8
Wares Creek	1415	4	6.2	1259	11.1
Goodmans Creek	1305	1	10	1248	13.3
Journama Creek	1145	139	9.1	1273	15.6
Back Creek	1155	17	9.4	811	12.9
Lower elevation catchments (LEC)					
Umbango Creek	433	524	13.3	843	8.3
Jugiong Creek	532	6	13.7	712	8.5
Big Hill Creek	595	17	12.6	709	4.8
Ginninderra Creek	566	1	13.5	709	6.7
Yaven Yaven Creek	595	145	12.1	986	10.5
Cunningham Creek	470	936	14.3	660	4.7

Source: Bureau of Meteorology, Australian Government

3.4.3.2 Mineralogy

Bedrock samples taken from volcanic, granitic, and sedimentary monolithological catchments consists of biotite, chlorite, quartz, muscovite, orthoclase, K-feldspar, and albite; the identification of secondary minerals in the bedrock was also performed and yielded traces of kaolinite in some samples (Figure 3-16; Table 3-6). The average composition (n = 2) of sedimentary bedrock is: biotite (7%); chlorite (5%); quartz (58%); muscovite (12%); orthoclase (7%); and K-feldspar (3%). Sedimentary bedrocks contained a small portion of secondary mineral (kaolinite: 10%) which is inevitable due to their formation. This finding is particularly important to note because this study focuses on the clay fraction of modern sediments. Hence, any residual secondary minerals in the bedrock from a previous environment would perhaps give a record of past weathering conditions and not reflect the modern weathering regime or unweathered source material, making comparisons between the compositions of the bedrock and modern sediments

less accurate. The average composition (n = 2) of volcanic bedrock is: biotite (5%); chlorite (3%); quartz (36%); muscovite (7%); orthoclase (5%), and albite (39%). Volcanic rocks were determined to be dacite, a common quartz-bearing volcanic rock in the Lachlan Fold Belt. The average composition (n = 3) of granitic bedrock is: biotite (14%); quartz (48%); muscovite had insignificant traces (2-4%) of kaolinite. Reproducibility of the quantification of biotite, chlorite, kaolinite, quartz, muscovite, orthoclase, albite, and k-feldspar in the bedrock was determined repeated analyses of a granitic bedrock sample and is 4%, 0%, 2%, 8%, 2%, 4%, 4%, and 5% (2SD, n = 2), respectively.

Table 3-5. One-way ANOVA single-factor between groups, statistical tests comparing the annual mean temperature, annual mean rainfall, and average catchment slope in the high elevation catchments (HEC) compared to the lower elevation catchments (LEC)

Annual Mean Temperature

Single-Factor Between-Subjects ANOVA (Independent Samples)					
Source	*Sum of Squares*	*df*	*Mean Square*	*F*	*p*
Between Groups	62.5748	1	62.5748	44.6007	< 0.001
Within Groups (Error)	12.627	9	1.403		
Total	75.2018	10			

Annual Mean Rainfall

Single-Factor Between-Subjects ANOVA (Independent Samples)					
Source	*Sum of Squares*	*df*	*Mean Square*	*F*	*p*
Between Groups	380189	1	380189	15.0856	0.004
Within Groups (Error)	226820	9	25202.2		
Total	607009	10			

Average Catchment Slope

Single-Factor Between-Subjects ANOVA (Independent Samples)					
Source	*Sum of Squares*	*df*	*Mean Square*	*F*	*p*
Between Groups	76.3203	1	76.3203	15.0345	0.004
Within Groups (Error)	45.687	9	5.07633		
Total	122.007	10			

Statistical significant: $\alpha = 0.05$

In all three monolithological catchments, the average mineral assemblage of the riverine clay fraction consists of kaolinite (ordered and disordered), phlogopite and lepidolite which are grouped as illite, and an illite/smectite (I/S) mixed layer. The mixed (I/S) layer clay minerals have regularly interstratified illite/smectite crystallite in a coherent stack of 2:1 layers composed of both illitic and smectitic interlayers (Veblen, 1990). Since pure smectite or montmorillonite was not detected, the mixed (I/S) layer is the best estimate of expandable (smectite) clay content in the sample; the illite interlayers are non-expandable. The average mineral composition of the clay

fraction in each of the three monolithological catchments is dominated by kaolinite (56 – 60%), with lower compositions of mixed (I/S) layer (21 – 26%) and illite (17 – 18%).

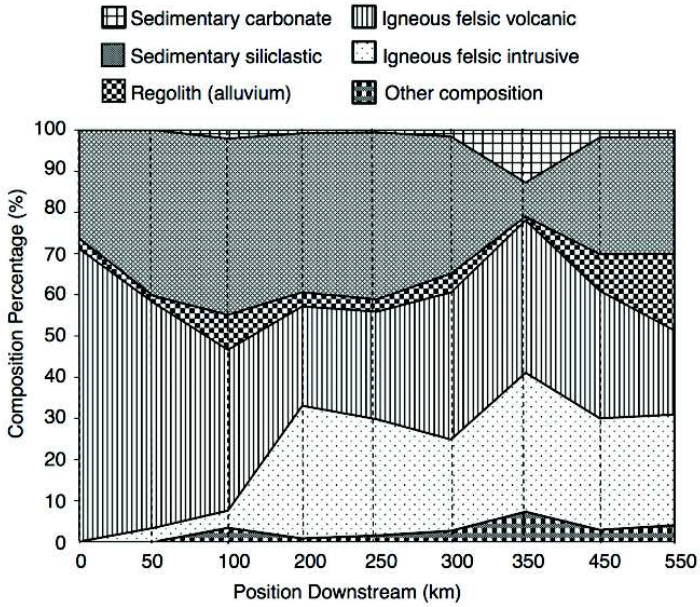

Figure 3-14. Proportions of the lithologies drained by the Murrumbidgee River catchment at different locations along the main channel. The x-axis shows the distance from the source of the river. Dashed lines represent the approximate location of sampling sites along the river.

Table 3-6. Mineral compositions of monolithological bedrock samples from the Murrumbidgee River catchment

Sample Type	Biotite (%)	Chlorite (%)	Quartz (%)	Muscovite (%)	Orthoclase (%)	Albite (%)	K- Feldspar (%)	Kaolinite (%)
Granitic								
Back Creek	9	0	41	3	7	23	15	2
Yaven Yaven Creek	19	0	45	5	10	17	0	5
Cunningham Creek	14	0	60	5	1	20	0	0
Grantic average	14	0	49	4	6	20	5	3
Sedimentary								
ALAC Creek	5	5	65	17	0	0	5	9
Sedimentary A	9	0	52	8	14	0	0	12
Sedimentary average	7	3	58	12	7	0	3	10
Volcanic								
Big Hill Creek	8	7	33	15	10	25	0	4
Goodmans Creek	2	0	40	0	0	54	0	4
Volcanic average	5	3	36	7	5	39	0	4

Quantification reproducibility based on replicate analyses of same sample yielded results with an error margin for biotite, chlorite, muscovite, orthoclase, albite, K-feldspar, and kaolinite is ±2%, 0%, 1%, 4%, 1%, 2%, 3%, and 5% respectively.

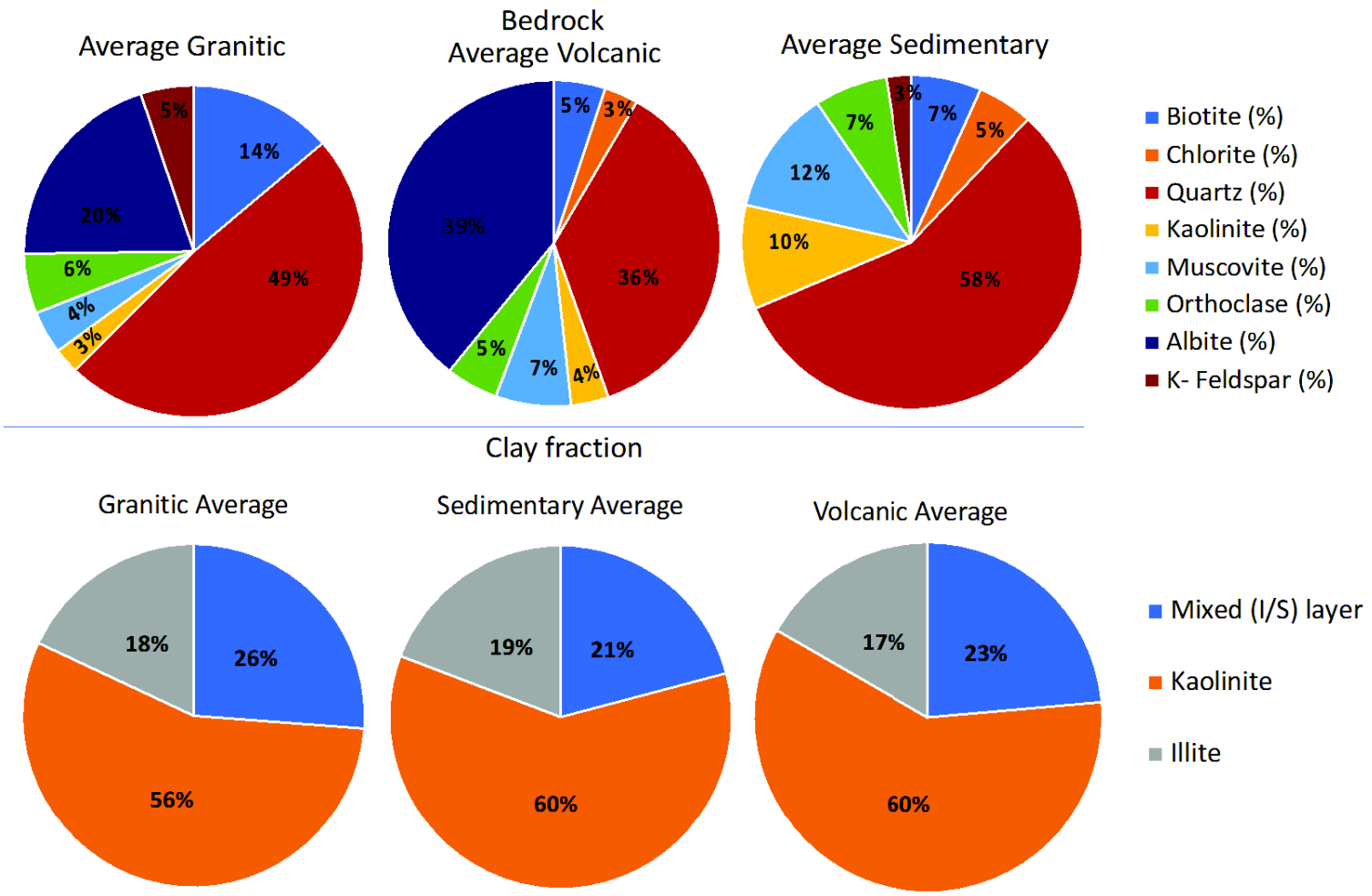

Figure 3-15. Mineral composition of the monolithological sediment and bedrock measured by XRD. Top panel: average mineral composition of granitic (n = 2), volcanic (n = 2), and sedimentary (n = 3) bedrock; Low panel: average mineral composition of the clay fraction of monolithological riverine sediments: granitic (n = 4), sedimentary (n = 6), volcanic (n = 4)

Accordingly, the average clay composition of each lithology is very similar to one another (Figure 3-16; Table 3-7). The reproducibility of the mineral quantification was performed by repeated (n = 2) analyses of same sample with mixed (I/S) layer ranging from 8 – 19; kaolinite ranging from 66 – 77; and illite ranging from 7 – 11. Based on these results of sample replicates, the reproducibility of mixed (I/S) layer, kaolinite, and illite mineral quantification is 11%, 11%, and 4% (2SD, n = 2), respectively.

Table 3-7. Mineral composition of the clay fraction of riverbank samples from creeks draining monolithological units in the Murrumbidgee River catchment

Sample Type	Mixed (I/S) layer (%)	Kaolinite (%)	Illite (%)
Granitic			
Cunningham Creek	27	56	17
Cunningham Creek	36	35	29
Back Creek	34	58	8
Yaven Yaven Creek	6	76	18
Average	**26**	**56**	**18**
Sedimentary			
Brooks Creek	2	49	49
Brooks Creek	24	70	6
Jellingro Creek	22	53	25
Jellingro Creek	19	67	15
Umbango Creek	24	69	7
Umbango Creek	36	52	13
Sed Average	**21**	**60**	**19**
Volcanic			
Ginninderra Creek	35	45	20
Ginninderra Creek	26	62	13
Jugiong Creek	14	64	23
Jugiong Creek	20	68	12
Volcanic Average	**23**	**60**	**17**

Mixed layer represents a mixed layer (illite/smectite) clay composition; kaolinite composition includes both ordered and disordered varieties; illite composition includes phlgopite and lepidolite minerals. Replicate analyses of same sample produced results with an error margin for mixed (I/S) layer, kaolinite, and illite of ±11%, 11%, and 4%, respectively

3.4.3.3 Chemical and B isotopic compositions of the bedrocks

Major elements (Al, K, Mg, Na) and both B concentrations and isotopic compositions were determined on 8 bedrock samples in monolithological catchments (Table 3-8): sedimentary (n =2); volcanic (n = 2); and granitic (n = 4). Concentrations of range from: 2.9 – 7.5% (Al); 1.0 – 4.9% (K); 0.7 – 1.4% (Mg); 1.3 – 3.2% (Na) and 15 – 36 ppm (B). Although distinctive differences between rock types are not present, we can broadly categorize volcanic bedrock as having the highest Na (3.2%) and Al (7.5%) concentrations and significant amount of quartz (~35%) indicating its dacite composition which is the common volcanic rock type in the Murrumbidgee

catchment. Granitic bedrock has the highest Mg (1.4%) and K (4.9%) concentrations and sedimentary bedrock has equivalent or lower concentrations than both the granitic and volcanic bedrocks in all measured elements excluding B, which has the highest concentration in sedimentary rocks compared to volcanic and granitic rock.

In the sedimentary catchments, B isotope compositions for the bedrock sample at higher elevation displays a slightly lower $\delta^{11}B$ composition than the sample at low average elevation: –12.5 and –10.6‰, respectively (Table 3-8). In the volcanic catchments, the higher elevation catchment sample display lower $\delta^{11}B$ composition (–10.3‰) than the low elevation one (–8.3‰). In granitic catchments, the $\delta^{11}B$ compositions of bedrock samples in higher and lower elevations catchments are –5.5 and –9.0‰; and –7.0 and –7.8‰, respectively (Figure 3-17). The $\delta^{11}B$ compositions of the granitic bedrocks displays the largest variation among lithologies. The $\delta^{11}B$ composition for volcanic and sedimentary bedrocks are for the most part lower than in granitic catchments. Considering the $\delta^{11}B$ of all bedrock samples and the proportions of different lithologies derived from spatial analysis, the average $\delta^{11}B$ of the bedrock for the Murrumbidgee River catchment at Wagga Wagga (~450 km downstream) would be –8.9 ± 4.4 ‰ (2SD, n = 8).

3.4.3.4 Boron isotopes in the sand fraction

The sand fraction of bank sediments from the Murrumbidgee River main channel show a narrow range of B isotopic composition, from –9.6 ‰ to –11.0 ‰, illustrating no significant variation as the sediment is transported downstream (Figure 3-17, Table 3-9). When comparing the average $\delta^{11}B$ value in the sand fraction of bedload sediment from the Murrumbidgee River (–10.4 ± 1.0‰, 2SD, n = 6) to the average value for the bedrock in the catchment (–8.9 ± 4.4‰,2SD, n = 8), a strong similarity is observed. This indicates that the sand fraction in the river sediment is likely a mixture of bedrock material from difference parts of the catchment and undergoes little to no isotope fractionation. To test if the B isotope composition of the sand fraction of bedload sediment reflects a mixture a unweathered source material in the catchment, simple mixing equations were performed using the proportions of drained lithology and B isotopic compositions and content of bedrock samples in the drainage area of each sand sample (see discussion below).

Table 3-8. Boron isotope compositions, B concentration, and major element concentrations of the clay fraction, dissolved load, and bedrock samples taken in monolithological catchment.

River Name	Elevation Group	δ^{11}B clay ‰	δ^{11}B rock ‰	δ^{11}B diss. ‰	B clay µg g^{-1}	Mg clay mg g^{-1}	K clay mg g^{-1}	Al clay mg g^{-1}	B rock µg g^{-1}	Mg rock mg g^{-1}	K rock mg g^{-1}	Al rock mg g^{-1}
Sedimentary												
Umbango Creek	LEC	-12.2	-10.6	30.2	33.5	29	39	240	36	12	15	30
ALAC Creek	HEC	-17.6	-12.1	31.8	56.6	-	-	-	-	-	-	-
Wares Creek	HEC	-15.2	-12.5	32.5	50.5	24	48	264	38	7	10	29
Volcanic												
Big Hill Creek	LEC	-9.7	-8.3	33.9	24.3	22	19	183	28	7	10	75
Deep Creek	HEC	-	-	40.7	15.7	24	29	211	-	-	-	-
Goodmans Creek	HEC	-13.6	-10.3	35.1	40.6	-	-	-	-	-	-	-
Jugiong Creek	LEC	-11.9	-	34.4	25.7	-	-	-	-	-	-	-
Ginninderra	LEC	-11.2	-	33.9	36.6	-	-	-	-	-	-	-
Granitic												
Cunningham	LEC	-8.5	-7.0	28.7	34.9	-	-	-	21	14	36	71
Yaven Yaven	LEC	-9.1	-7.8	32.7	51.9	19	41	255	21	14	34	74
Back Creek	HEC	-9.3	-9.0	36.2	34.1	37	31	226	16	4	49	72
Journama Creek	HEC	-5.6	-5.5	27.3	60.6	-	-	-	-	-	-	-
Carbonate												
Rock Flat Creek	HEC	-18.6	-13.1	40.7	15.68	44	10	192	15	16	10	13

Abbreviations: clay fraction (clay); dissolved load (diss.); bedrock (rock); higher elevation catchment (HEC); lower elevation catchment (LEC). Analytical uncertainty of B isotope measurements is 0.4‰ (±2SD). Analytical uncertainty for major element measurements is approximately 3% and for B is 2%.

3.4.3.5 Chemical and B isotopic compositions of the clay fraction

Chemical composition

The B concentration of the clay fraction in the main stream and tributary samples range from 16 to 60 ppm (Table 3-9). B/Al ratios decrease downstream (Figure 3-18A) and follow Mg/Al and K/Al ratios (Figure 3-18B and C, respectively). Aluminum was chosen as the reference element as it is a major insoluble element during chemical weathering and allows for B, Mg, and K concentrations in the clay fraction to be corrected for dilution by quartz (Bouchez et al., 2012). B/Al, Mg/Al and K/Al ratios in clay-size fractions sampled in downstream tributary locations (directly before the convergence with the main channel) appear undistinguishable from those sampled in the main river channel.

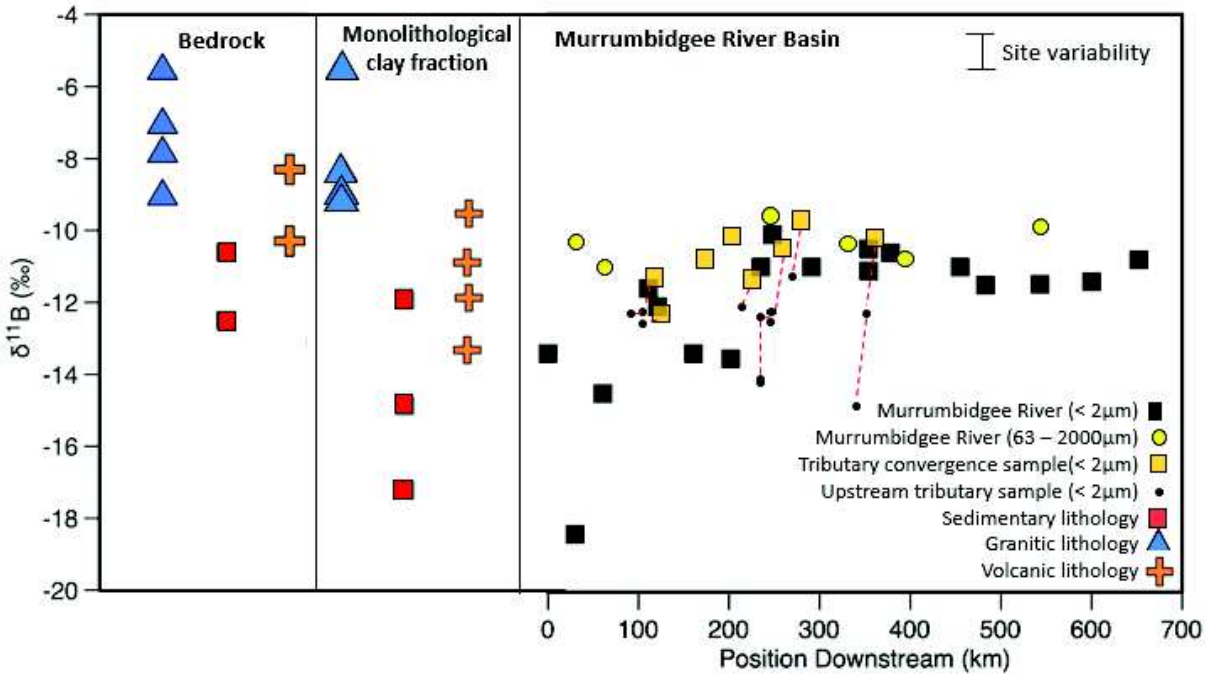

Figure 3-16. Boron isotope compositions in bedrock, the clay fraction (< 2μm) of sediments from monolithological drainage catchments, and of the clay (<2 μm) and sand fractions (63-2000 μm) from the Murrumbidgee River and its major tributaries. The x-axis in the right panel represents the distance from the source of the Murrumbidgee River. Tributary samples are plotted in regards to the convergence sample (sample taken directly before the convergence with the main river) (yellow square) being their relative position downstream and the distance between each upstream tributary sample (black dot) is subtracted from the convergence sample; individual tributaries are connected with a dotted line. Site variability was determined by taking multiple aliquots of sediment at several locations and is less than 1‰ in most cases (Table 3-10). Analytical uncertainty of all B isotope data is 0.4‰ (±2SD). The $\delta^{11}B$ composition of the clay fractions from the Murrumbidgee River significantly increases from the headwaters to the lower catchment where it levels off on the alluvial plain. Interestingly, these compositions are similar to those of clay fractions from most neighboring monolithological catchments. The $\delta^{11}B$ composition of the sand fractions from the Murrumbidgee River remains relatively constant downstream reflecting a mixture of unfractionated bedrock material.

Boron isotopes in the clay fractions from the Murrumbidgee tributaries

The B isotope composition of the clay fraction in the eight major tributaries range from –15‰ to –9.8‰ and display a slight to moderate evolution downstream characterized by isotopically lighter values in upstream locations than compared to the downstream sample taken just before the convergence with the main channel (Figure 3-17, Table 3-9). However, this

Table 3-9. Boron isotope, B concentration, and major element concentrations of the clay fraction, sand fraction, and dissolved load of Murrumbidgee River and tributaries

Sample Name	δ^{11}B clay (‰)	δ^{11}B sand (‰)	δ^{11}B diss. (‰)	B clay (µg g^{-1})	B sand (µg g^{-1})	Mg clay (mg g^{-1})	K clay (mg g^{-1})	Al clay (mg g^{-1})	B diss. (ng g^{-1})	Na diss. (ng g^{-1})	Mg diss. (ng g^{-1})
Murrumbidgee River											
MR01	-13.4	-	-	16.2	-	8	21	94	-	-	-
MR03	-18.4	-10.3	28.9	35.3	13	10	31	113	1.9	2	1.1
MR05	-14.5	-10.9	30.1	35	37	8	20	72	2.7	2.9	1.2
MR06	-	-	-	18.9	-	13	13	106	3.8	9.8	5.2
MR08	-	-	32.5	28.6	-	13	24	94	2.9	7.7	4.5
MR09	-11.6	-	-	19.7	-	8	17	82	-	14.2	6.3
MR-10	-12.1	-	26.7	31.2	-	10	27	82	4.5	14.6	7.1
MR12	-13.4	-	-	28.1	-	13	25	95	3.3	11.1	6.1
MR13	-	-	28	19	-	6	16	71	4.2	10.3	4.4
MRCTR	-13.5	-	-	31	-	11	23	130	-	-	-
MRCVN	-11	-10.2	-	22.1	17	10	20	97	-	-	-
MR20	-11	-	29.1	29	-	11	24	109	6	14.3	6.2
MR9A	-11.1	-10.6	-	36.8	11	-	-	-	6.6	-	-
MRGUND	-10.6	-	-	21.9	-	10	24	111	7.2	17.9	8.3
MRWGA	-11	-11	32.7	24.1	18	10	21	122	9.2	15.1	6.4
MRNCL	-11.5	-	-	15.6	-	8	16	97	-	-	-
MRNDR	-11.5	-	-	60.9	-	9	19	107	-	-	-
MRDAR	-11.4	-9.6	-	33.4	15	8	18	99	-	-	-
MRHAY	-10.8	-	-	31.6	-	9	25	109	-	-	-
Tributaries											
Cotter	-10.1	-	-	20.3	-	10	21	97			
Tumut 1	-10.2	-	-	15.7	-	8	15	93			
Tumut 2	-12.1	-	-	33.2	-	-	-	-			
Tumut 3	-15	-	-	33.1	-	-	-	-			
Molonglo 2	-11.3	-	-	29.1	-	7	21	92			
Molonglo 3	-11.9	-	-	25.6	-	-	-	-			
Goodradigbee	-9.8	-	-	20.7	-	7	17	98			
Goodradigbee	-11.5	-	-	56.9	-	-	-	-			
Gudgenby 1	-10.5	-	-	17.9	-	8	16	83			
Gudgenby 2	-11.5	-	-	18.6	-	-	-	-			
Bredbo 1	-12.2	-	-	25	-	8	24	94			
Bredbo 3	-12.7	-	-	29.7	-	-	-	-			
Numeralla 1	-11.3	-	-	27.2	-	11	23	94			
Numeralla 2	-12.3	-	-	21.8	-	-	-	-			
Numeralla 3	-12.3	-	-	22.8	-	-	-	-			
Yass 2	-10.6	-	-	28	-	-	-	-			
Yass 3A	-12.2	-	-	24	-	-	-	-			
Yass 3B	-12.6	-	-	41.7	-	-	-	-			
Yass 4A	-14.3	-	-	43.6	-	-	-	-			
Yass 4B	-12	-	-	31.6	-	-	-	-			
Yass 4C	-14.3	-	-	42.7	-	-	-	-			

Abbreviations: clay fraction (clay); sand fraction (sand); dissolved load (diss.) Tributary samples with labels ending in A-C refer to replicate samples taken at the same site to assess site variability.

observation can only be made for 6 of the 8 tributaries, as both the Gudgenby and Cotter Rivers were only sampled directly before the convergence due to limited field access. Similar to the concentration ratios the B isotope composition of the tributary convergence sample in most cases is nearly indistinguishable from the clay fraction taken after the convergence with the main river.

The exception to this is at approximately 200 km downstream where the lighter composition (–10.1‰) of the Cotter River does not significantly influence the composition of the main channel (–13.5‰).

At several stream and tributary locations within the watershed, multiple samples were taken at the same site to assess site variability. The difference in B isotope composition between sample replicates at a given site are nearly undistinguishable from each other when considering the analytical uncertainty (+0.45, 2SD) in most cases. The exceptions being Umbango Creek and the Yass River. The largest standard deviation from the mean observed is 1.3‰ on the Yass River, where three sample aliquots were taken. However, the two bank samples that were collected have the same B isotope composition, while the one deposit (taken several meters away from the river) has a slightly higher B isotope composition. These results generally indicate that while site specific data is observed, the B isotope composition at a given site is quite homogenous and that sampling one location at given site over another does not significantly bias the data, with the exception of the Yass River where both bank and sediment deposits were sampled. This also may indicate that sediment deposits have a slightly heavier B isotope composition than actively transported bank sediments.

Boron isotopes in the clay fractions from the Murrumbidgee main channel

In contrast with the sand fraction, clay fractions in the Murrumbidgee River show more variable $\delta^{11}B$ values and a systematic increase downstream (Figure 3-17, Table 3-9). The B isotopic composition of the clay fraction in higher elevation catchments (600 – 2,230 m elevation) range from –18.4‰ to –11.6‰. The $\delta^{11}B$ composition of the clay fractions collected in the lower catchment (< 600 m elevation) range from –12.5‰ to –10.8‰. Accordingly, the upper catchment is characterized by clay fractions with lighter B isotopic compositions that those in the lower catchment where they eventually plateau on the alluvial plain. The downstream increase in $\delta^{11}B$ values suggests that either isotopic fractionation is taking place during transport and/or the tributaries deliver sediments to the Murrumbidgee with increasingly heavy B isotope compositions. This point is discussed below.

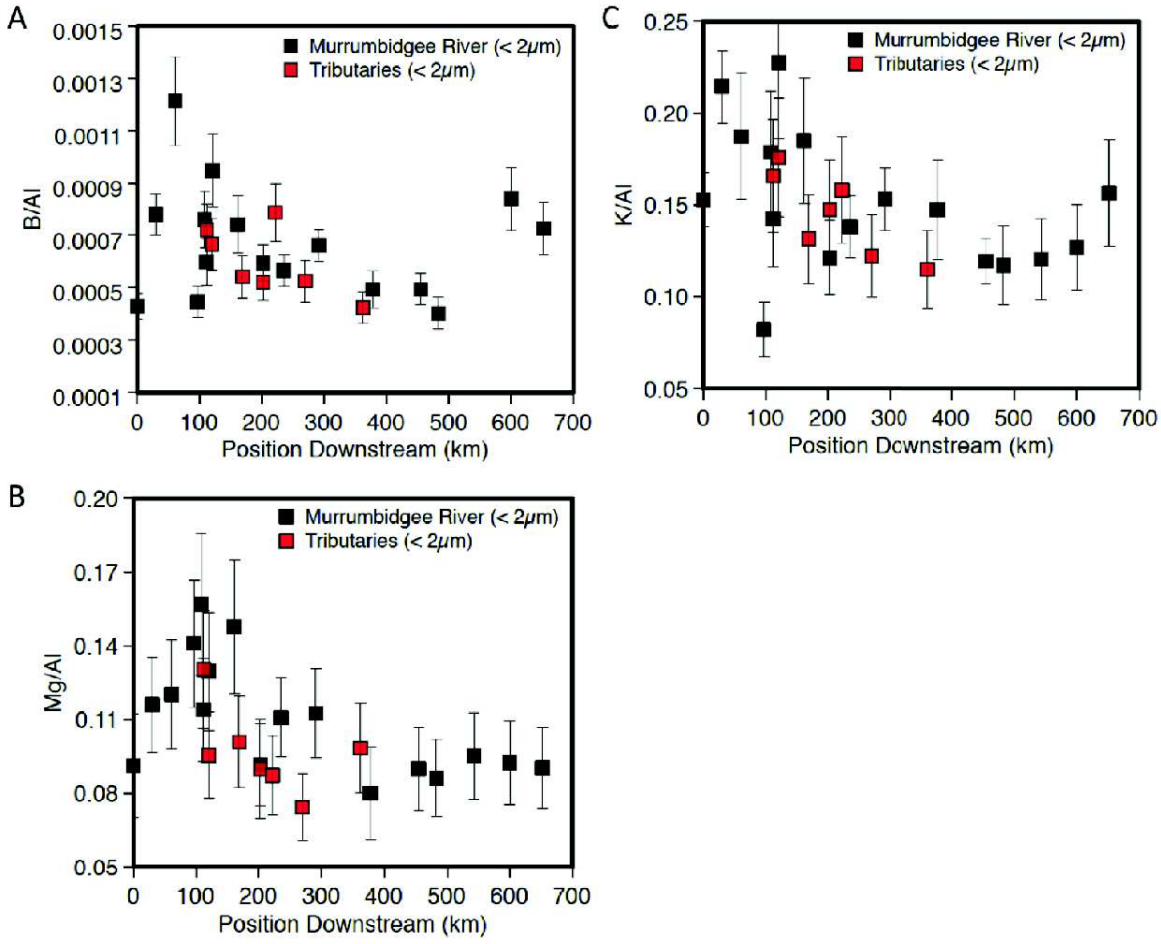

Figure 3-17. Major and trace elemental concentration ratios in clay fractions of Murrumbidgee River and main tributaries. A) an anti-correlation between the B/Al and position in the river; B and C) Mg/Al and K/Al ratios, respectively, also as a function of position downstream from the headwater sample. Major (Mg and K) and trace (B) elements are considered to be mobile elements during weathering reactions in sediments while Al is immobile in riverine clays with respect to mobile elements involved in weathering reactions. Error bars on ratio measurements are 2 SE.

3.4.3.6 Dissolved boron

Analyses of the B concentrations in the dissolved load of water samples taken along the course of the main Murrumbidgee River reveal a continuous increase (from 1 to 10 µg/L) from headwaters to the alluvial plain (Figure 3-19A, Table 3-9). After a rapid decrease upstream, B/Na and B/Mg ratios show little variation in the plain (Figure 3-19B and C). Boron isotope ratios of the dissolved load appear relatively constant (26 – 32‰) all along the Murrumbidgee River and do not show any systematic evolution downstream (Figure 3-19A). These values are high compared to other

rivers worldwide (Chetelat et al., 2009; Lemarchand and Gaillardet, 2006; Lemarchand et al., 2000; Rose et al., 2000). The $\delta^{11}B$ values of the Murrumbidgee River are significantly higher than the world average value inferred from largest rivers (+10‰) and are similar to those observed in the Niger River, Nigeria (+35‰) and the Maroni River, French Guyana (+43‰) (Lemarchand et al., 2000). In these river systems, the B geochemical cycle is thought to be heavily impacted by biological activity and atmospheric inputs.

Table 3-10. Replicates sediment samples taken at the same sites in the Murrumbidgee River catchment

Site Replicates	$\delta^{11}B$(‰)
Brooks Creek	-12.8
Brooks Creek	-12.2
Umbango Creek	-12.2
Umbango Creek	-11.3
Jellingro Creek	-11.5
Jellingro Creek	-11.6
Jugiong Creek	-11.9
Jugiong Creek	-11.9
Ginninderra Creek	-11.2
Ginninderra Creek	-11.3
Yass 3A	-12.2
Yass 3B	-12.6
Yass River 4A	-14.3
Yass River 4B	-12.0
Yass River 4C	-14.3

Samples were taken several meters apart at the same location to assess site variability. In the Yass River, samples 4A and 4C are river bank samples, while sample 4B is a river deposit collected several meters away from the river.

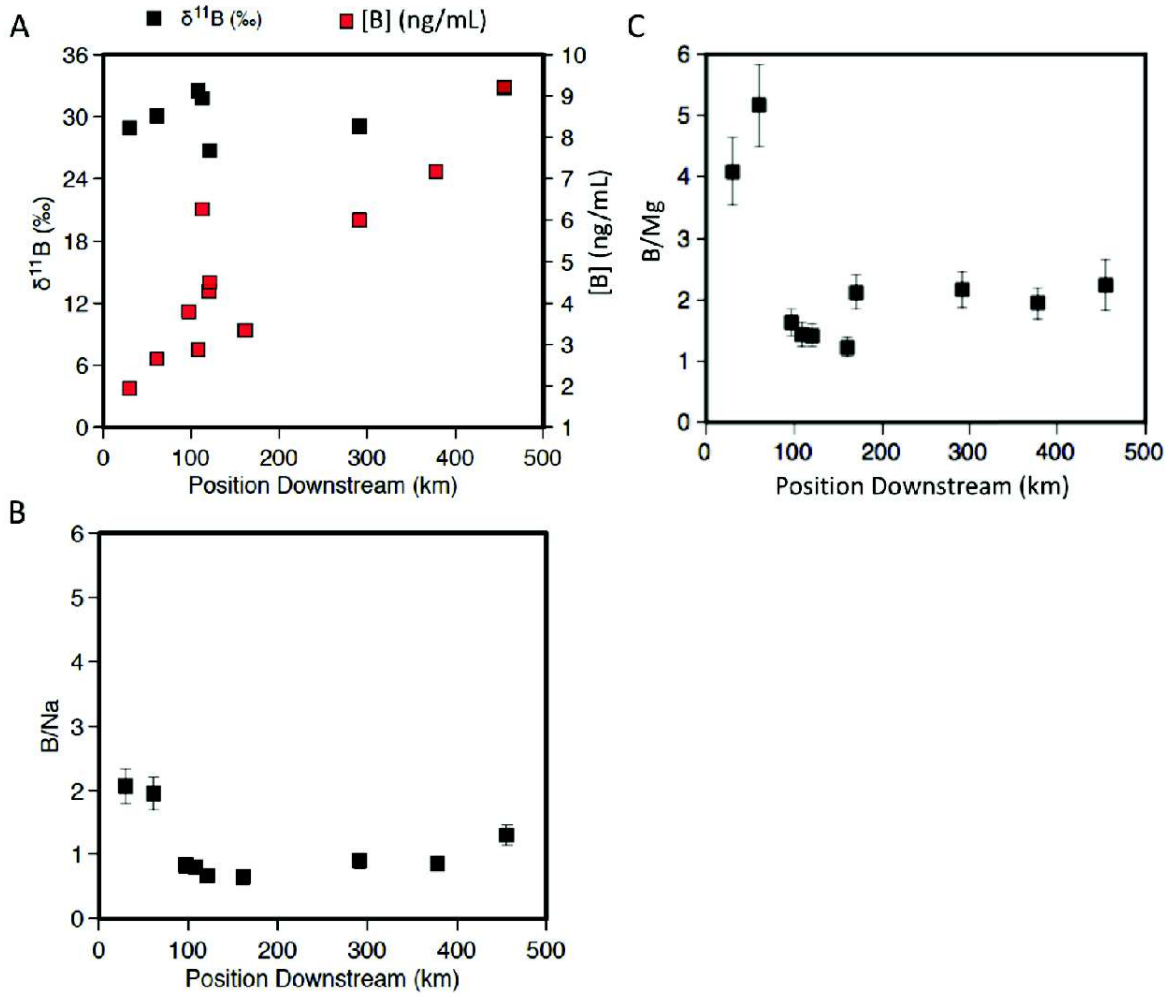

Figure 3-18. A) Boron isotopic composition and B concentration of the dissolved load showing an increasing B concentration and a relatively unchanged $\delta^{11}B$ composition as function of its position downstream; B) B/Na ratio of the dissolved load used a proxy to test for evaporation C) B/Ma ratio of the dissolved load also used as a proxy testing for evaporation. In both B and C, Na and Mg are considered conservative elements whose behavior appears similar to B in the dissolved load and also increases downstream.

3.4.4 **Discussion**

3.4.4.1 Origin of the B isotopic signal recorded by the clay-size fraction

The expandable (e.g., mixed I/S layer) or non-expandable (e.g., illite, kaolinite) nature of the clay mineral phases is a key parameter because it determines their ability to exchange cations with the surrounding solution (Mana et al., 2017). For instance, Williams et al. (2001) demonstrated

that structural B in illite minerals does not exchange readily with pore fluids and only happens when Si-O bonds are broken. This study also demonstrated that the amount of B structurally incorporated into illite clay minerals is five times greater than in smectites under experimental conditions, which agrees with Harder (1970) who reported a similar trend in nature. Bassett (1976) reported that B adsorbed on clay surfaces is easily exchangeable with aqueous fluids compared to structurally-held B. Hence, non-expandable clay minerals like illite and kaolinite retain B in their structure and may record the original conditions of their formation, while B in expandable minerals like smectite tend to exchange B with the environment and may lose record of their origin. In all the lithologies sampled in the present study, the clay-size fraction is mainly composed of kaolinite and illite (74 – 79% in total). Residual primary quartz minerals were also detected (7–10%). However, since quartz minerals are not important B carriers and are present in our samples in relative small and constant abundance, they are not expected to significantly affect the trends defined neither by B isotopes nor by concentrations in the clay-size fractions. Therefore, B in the sediment clay-size fractions is considered to be primarily bounded to the structural sites of the clay mineral and in the non-exchangeable form. Note that the procedure to separate the clay size fraction includes a prolonged contact with a large volume of water that has removed all labile B from the surface of the sediments.

3.4.4.2 Mixing or reactions during transport of sediments in the river?

The B isotopic composition of the clay fraction in the Murrumbidgee increases from the headwaters out to the alluvial plain where its composition plateaus (Figure 3-17) while B/Al, Mg/Al, and K/Al ratios systematically decrease up to approximately 300 m downstream and also plateau (Figure 3-18). Here, we quantitatively tested by mass balance if the clay fraction in the Murrumbidgee is undergoing chemical and isotopic evolution during transport or if its composition primarily reflects mixing of material supplied by the tributaries. The B isotopic compositions and B/Al, Mg/Al, and K/Al ratios in the clay fractions of the sediments collected along the Murrumbidgee main stream are compared to those calculated assuming that all lithologies drained have similar clay-size particle production rates per surface unit. The surface proportion (Figure 3-15) and chemical/isotopic signature of each lithology drained upstream of the sampling location (Figure 3-17) have been used. The mixing equations are as follows:

$$\delta^{11}B_{th} = \frac{\sum f_i [B]_i \delta^{11}B_i}{\sum f_i [B]_i} \quad (3\text{-}1)$$

$$\left.\frac{X}{Al}\right|_{th} = \frac{\sum f_i [Al]_i \left({}^{X}/_{Al}\right)_i}{\sum f_i [Al]_i} \quad (3\text{-}2)$$

where $\delta^{11}B_{th}$ and $(X/Al)_{th}$ are the theoretical B isotope composition and chemical ratio, respectively of a Murrumbidgee River sample. f_i corresponds to the surface fraction of the *i*th lithology drained (granite, volcanic or sedimentary) as calculated by ArcGIS 10.4 software in Equation 3 and the proportion of Al in each of the *i*th lithologies in Equation 4. $[B]_i$ and $[Al]_i$ are the B and Al concentrations measured for each lithology, respectively. The $\delta^{11}B_i$ and $(X/Al)_i$ correspond to the B isotope and chemical composition of the clay fraction from each lithology drained upstream of the sampling location. Proportions of drained granitic, volcanic, and sedimentary lithologies used in these calculations were normalized to 100%. The strong correlation between the observed and calculated values together with the lack of evidence of chemical evolution in the plain (Figure 3-18) indicate that the composition of the sediment clay fraction in the main channel can be explained as a simple mixing of clays derived from each of the major catchment lithologies and delivered to the Murrumbidgee River by the tributaries without significant chemical and isotopic evolution (Figure 3-20A – C). This also indicates that the clay fraction in large rivers, at least the kaolinite and illite, retains its chemical composition acquired during its formation and therefore may be interpreted as a record of the weathering regime at the location of their production.

The assumption that all major lithologies contribute equally to the clay-sized sediment load in the Murrumbidgee River is a large one, as there are many factors that contribute to sediment production and mobilization such as the type of lithology, climate, topography, and tectonics (e.g. Ludwig and Probst, 1998; Probst and Suchet, 1992; Suresh et al., 2014). In a dry climate system (such as the Murrumbidgee) Ludwig and Probst (1998) reported that climate and lithology are the key factors influencing sediment mobilization. It was reported that erodibility was greater in dry parts of the basin than compared to wet parts, a relationship that was driven by heavier

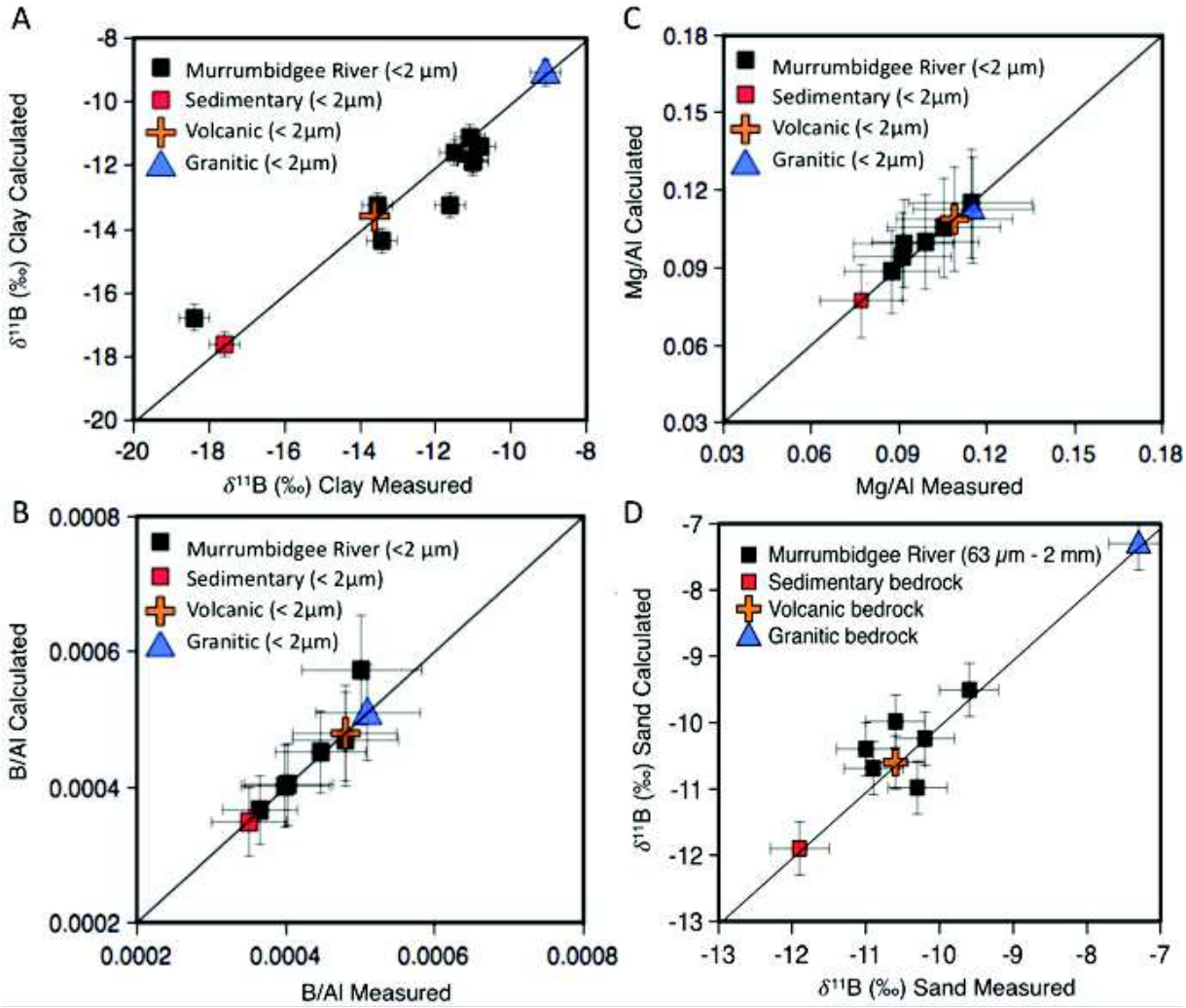

Figure 3-19. Calculated chemical and B isotopic compositions as a function of measured compositions of Murrumbidgee River sediment. Monolithological end-members used in the calculation of the $\delta^{11}B$ and X/Al are as shown as colored symbols. A) Calculated vs. measured $\delta^{11}B$ compositions of the clay fraction; B and C) calculated vs. measured B/Al and Mg/Al ratios of the clay fraction; D) calculated vs. measured $\delta^{11}B$ values of the sand fraction of Murrumbidgee River sediments. Errors on the $\delta^{11}B$ and chemical ratios are 2 SD.

vegetation cover which reduces sediment mobilization in wet areas. However, in the Murrumbidgee River catchment, vegetation in the upper (wetter) part of the catchment is not significantly different that the lower (drier) areas, indicating that differences in climate (particularly precipitation) likely do not drive differences in sediment transport within the catchment. The influence of lithology on sediment mobilization was reported by Ludwig and Probst (1998) to likely be greatest when sediment is predominately supplied by channel erosion

and to much lesser extent when sediment is delivered to the river channel by hillslope erosion. In the Murrumbidgee, Suresh et al. (2014) reported very long (~200 kyr) hillslope transport times of sediment delivered to the main channel, likely owning to the tectonic stability of the catchment. Following Ludwig and Probst (1998), this finding would then suggest that the influence of lithology type on sediment mobilization in the Murrumbidgee is likely not a key factor. In the absence of significant climatic (mainly precipitation) or lithologic control on sediment mobilization, it is then plausible that all lithologies in the catchment contribute equally to the clay-sized sediment load.

Similar to the clay fraction, the B isotope composition of the sand fraction was calculated using Equation 3-3 to assess whether its isotopic composition is representative of a mixture of unweathered parent bedrock in the catchment. A positive correlation between the measured and calculated $\delta^{11}B$ values of the sand fraction is observed, indicating that the B isotope composition of the sand fraction can adequately be explained as a mixture of bedrock material throughout the catchment (Figure 3-20D). Therefore, the sand fraction is considered to be a good estimate of the average B isotopic composition of the parent material at the catchment scale.

3.4.4.3 Boron chemical and isotopic fractionation during weathering

In order to quantitatively determine B behavior during clay formation and to investigate how this may relate to the weathering regime, the relative magnitude of the B transfer from the bedrock to the neoformed clay minerals ($\varphi_{Al,B}$) is calculated using samples from monolithological catchments:

$$\varphi_{Al,B} = \frac{[B]_{clay}}{[B]_{rock}} \times \frac{[Al]_{rock}}{[Al]_{clay}} \quad (3\text{-}3)$$

The soluble chemical character of B implies its progressive depletion in clay minerals as weathering reaction progress, with $\varphi_{Al,B}$ values starting from 1 in pristine materials down to 0 in totally leached weathering products. An intense B leaching is observed for volcanic and sedimentary catchments: $\varphi_{Al,B}$ values in lower and higher elevation sedimentary catchments are as low as 0.11 and 0.15, respectively (with caution that clay minerals may be inherited from the sedimentary bedrock and not derive from weathering reactions in the catchment); the $\varphi_{Al,B}$ value for the higher elevation volcanic catchment is 0.51 (Figure 3-20). Like observed in the Gandak, more intense leaching is associated with a larger isotopic shift towards more negative values. In

contrast, granitic catchments (at both higher and lower elevations) display $\varphi_{Al,B}$ values closer to 1 indicating a limited B loss, associated with a small isotopic shift. Similarities between the two systems likely confirm the universal character of this relationship. The apparent $\Delta^{11}B_{clay\text{-}bedrock}$ differences between lithologies demonstrates a lithological control on clay production rates throughout the catchment.

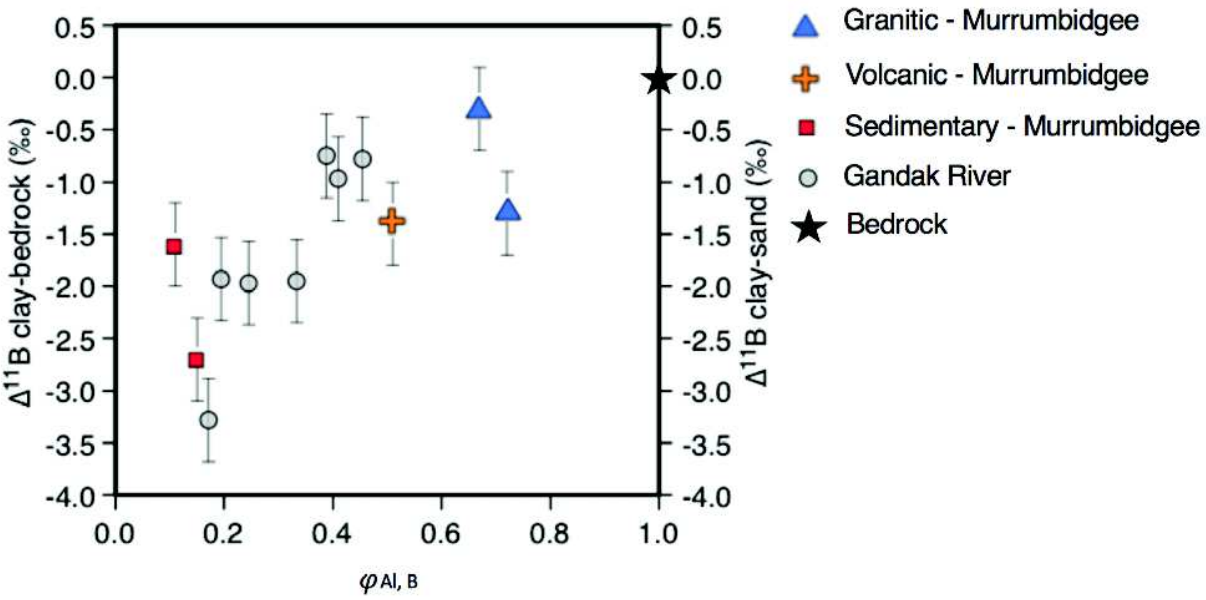

Figure 3-20. $\Delta^{11}B_{clay\text{-}bedrock}$ values in monolithological catchments observed in the Murrumbidgee River study and $\Delta^{11}B_{clay\text{-}sand}$ values from the Gandak River both as a function of the mass transfer coefficient ($\varphi_{Al,B}$). The black star (bedrock) would be equivalent to clay-sized fraction which is composed only of crushed primary minerals or alternatively has experienced a 100% reincorporation of B (considering Al to be immobile).

3.5 CONCEPTUAL FRAMEWORK TO INTERPRET B ISOTOPES IN SEDIMENTS

In both case studies, the Gandak and Murrumbidgee catchments, the B isotopic composition of the clay size fraction is slightly lower that the parent materiel (as determined by the sand fraction and bedrock). This is consistent with the general, and well documented, preferential incorporation of ^{10}B into secondary products but also rises some issues and inconsistencies with our present knowledge or assumptions on the B behavior during clay formation. To simplify, $\delta^{11}B$ values in clays are either too low compared to soil solution or too high compared to the bedrock. Following is a detailed discussion of this statement and possible explanation of the results.

3.5.1 Model of reactive transport of B and B isotopes in weathering profile

Weathering reactions occur by rock exposure to water. A classical modeling approach is to consider reactive transport of elements supplied by meteoric waters that migrate downward through the weathering profile. Working with trace elements, the basic assumptions are that they do not affect the solubility constant of the rock-forming minerals implying that their dissolution rate is independent of its concentration in solution and that its incorporation in secondary phases occurs proportionally to its concentration in solution through the partition coefficient. Here, we use the mathematical derivation for 1D reactive transport in porous media (considering only vertical water transfer) for elemental concentrations and isotopes in the percolating fluid as proposed for instance by Johnson and DePaolo (1997) or by DePaolo (2006) and many others and textbooks.

$$\rho_f \frac{\partial \phi C_f}{\partial t} = \rho_f D \frac{\partial}{\partial x}\left(\frac{\partial \phi C_f}{\partial x}\right) - v\rho_f \left(\frac{\partial \phi C_f}{\partial x}\right) + \sum_i R_{di} C_{si} - \sum_j R_{pj} K_j C_f \quad (3\text{-}4)$$

Where ρ_f and ρ_s are the density of the fluid and the solid, respectively; ϕ is the porosity; C_f is the concentration (moles/gram) of the element of interest in the fluid a, respectively; D is the diffusivity of the element of interest in water; v is the water velocity in the porous media; R_{di} is the dissolution time constant for the phase *i* (grams dissolved / unit volume / time); C_{si} is the concentration of the element of interest in the solid phase *i* (moles/gram); R_{pj} is the precipitation time constant for the phase *j* (grams precipitated / unit volume / time); and K_j is the distribution coefficient of the element of interest between the fluid and the solid phase *j*. For a porous media whose ambient conditions are stable over a time long enough to ensure steady state; where the transport of dissolved element is dominated by advection and not diffusion (water velocity >> 10 cm/yr); no spatial and temporal change in porosity occurs and considering *Rd*, *Rp,* C_r and *K* as bulk values of the mineral assemblage, then Equation (3-5) simplifies as follows:

$$v \frac{\partial C_f}{\partial x} = M\left(R_d C_r - R_p K C_f\right) \quad (3\text{-}5)$$

Where *M* is the solid/fluid mass ratio in the porous media. If parameters are constant all along the weathering profile, then the analytical solution of the C_f is of exponential form as given by Equation 3-7 (initial condition at x=0, $C_f = C_{f0}$), otherwise the solution is more complex and depends on the relation with depth each parameter takes.

$$C_f(x) = \frac{R_d C_r}{R_p K} + \left(C_{f0} - \frac{R_d C_r}{R_p K}\right) e^{-\frac{M R_p K}{v} x} \quad (3\text{-}6)$$

The concentration of the element of interest therefore starts at C_{f0}, which is controlled by atmospheric inputs including more or less contribution of the vegetation cover and then exponentially evolves to plateaus at the value given by $C_f(\infty)$ with a reaction length L, as follows:

$$C_f(\infty) = \frac{R_d C_r}{R_p K} \quad (3\text{-}7)$$

$$L = \frac{v}{M R_p K} \quad (3\text{-}8)$$

The reaction length L (expressed in m^{-1}) is equivalent to the reaction constant *k* for order 1 reaction, *dN/dt=-kN*). For $x > \sim 5L$, the concentration of the fluid no longer evolves because the budget of the element of interest is balanced between the dissolution and precipitation reactions. From Equation (3-9) it comes that the distance to reach the plateau value increases with the water velocity in the porous media and decrease with all the other parameters. This distance is therefore greatly dependent of the local hydrogeochemical conditions as well as the chemical affinity of the element of interest for the precipitating phase. For B, this distance is expected to be short because of the relatively large B chemical affinity for the clay and metal-hydroxide surfaces as well as because of its large implication in the vegetation cycle that largely consumes B from the top soil solution. In contrast, this distance is expected much larger for elements like Li or Na that are slightly involved in the vegetation cycle (Li) and those showing little chemical affinity for mineral surfaces (Na).

Following the same hypothesis, the isotopic ratio of the fluid can be modeled as follows:

$$v \frac{\partial r_f}{\partial x} = R_d M \frac{C_r}{C_f}\left(r_r - r_f\right) - R_p M K (\propto -1) r_f \quad (3\text{-}9)$$

Where r_f and r_f are the isotopic composition of the fluid and the dissolving rock, respectively and $\propto$ is the isotopic fractionation factor between the secondary phase and the fluid. At $x \gg L$, the isotopic ratio of the fluid $r_f(\infty)$ greatly simplifies when combined with Equation 3-10:

$$r_f(\infty) = \frac{r_r}{\propto} \quad (3\text{-}10)$$

Finally, because the model assumes that the neo-formed secondary phases are immobile and at chemical equilibrium with the local fluid, it comes:

$$C_w(x) = K C_f(x) \quad (3\text{-}11)$$

$$r_w(x) = \propto r_f(x) \quad (3\text{-}12)$$

Where C_w and r_w are the concentration and the isotopic ratio in the neoformed phase, respectively. Interestingly, we can note that for $x \gg L$ the concentration of the secondary phases is linked to that one of the bedrock by the ratio the dissolution and precipitation rates and that their isotopic composition is identical to the bedrock:

$$C_w(\infty) = \frac{R_d}{R_p} C_r \quad (3\text{-}13)$$

$$r_w(\infty) = r_r \quad (3\text{-}14)$$

3.5.2 Sensitivity tests for B and B isotopes in weathering profiles

This reactive transport model described above has the advantage of explaining two features of B data in clay minerals that look counterintuitive at first sight: at a distance long enough to allow chemical equilibrium of the percolating fluid with the host rock (i.e. balanced B budget between dissolution and precipitation reactions), secondary phase can be more concentrated than the primary minerals (if Rd>Rp) and their isotopic composition equals the parent material even deriving from fractionating precipitation reactions. The explanation comes from the percolating fluid that becomes highly concentrated and isotopically strongly fractionated. However, in order to test the applicability of such a reactive transport approach to model the behavior of B and B isotopes during weathering, different scenarios of dissolution and precipitation rates were tested and computationally solved the Equations 3-6 and 3-10 to evaluate how realistic such reactive transport model can be to explain the data.

Here, it is important to note that, in saprolite, water and minerals chemistry show opposite gradients: dissolved elements supplied by meteoric waters equilibrate with soil solids by dissolution/precipitation reactions during their downward migration through the saprolite, whereas minerals chemically evolve from the bottom of the saprolite (most pristine material and therefore chemically more reactive) to surface layers, which concentrate the weathering products and the residual primary minerals which are most resistant. Given these opposite trends and assuming that secondary products 1) may significantly form around the bedrock-saprolite interface as shown by typical profiles of the mass transfer coefficients (e.g. Brantley and White, 2009) and 2) keep a chemical record of the conditions of their formation (no significant exchange with the solution

once formed), then there is no reason that the water and clay chemistry should match (Figure 3-21). Moreover, the removal of top soil particles by erosion would imply that the solids are actually in movement in the soil in the opposite direction of the water. Therefore, the following numerical tests are not intended to reproduce depth profile of clay minerals in a saprolite but rather to explore the hydrogeochemical conditions that can lead to the relationship observed between $\delta^{11}B$ and B concentrations in our clay size fraction as illustrated in Figure 3-20. We consider here that the B concentrations and $\delta^{11}B$ of the clay size fraction is held by secondary phases.

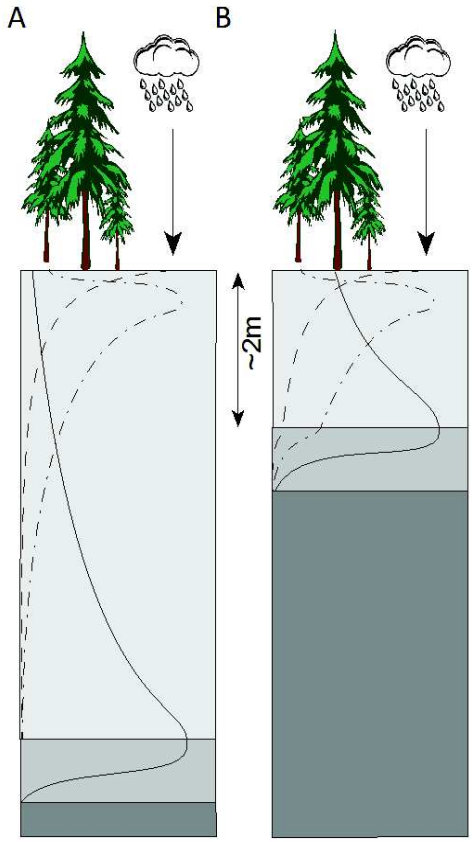

Figure 3-21. Schematic representation of the parameters controlling B isotopes in the clay fraction of soils. Dark, medium and light gray correspond to the pristine bedrock, weathered bedrock and the saprolite, respectively. The solid line corresponds to the production rate of clay minerals that is highest in the weathered bedrock and the bottom of the saprolite. Dashed line corresponds to the influence of the atmospheric inputs on the soil solution. The dash-dotted line corresponds to the influence of biologically-dominated reactions that are maximum at depth of maximum tree root density. Both atmospheric and biological imprint decrease downward as solutions migrate and interact with soil minerals. In the deep saprolite (A), clays form at a depth dominated by water-rock interactions. In the shallow saprolite (B), clays form under the control of water-rock interactions, biology, and the atmosphere. From previous work, the typical depth in which vegetation and atmospheric influence the B isotope composition of the clay fraction is approximately 2 m, however this depth is likely to be highly variable (Cividini et al., 2010).

3.5.2.1 Scenario 1: constant dissolution and precipitation rates

In this first scenario, the dissolution and precipitation are kept constant all along the weathering profile. This would imply that the changes with depth of the water chemistry and soil mineralogy do not affect the reactions of dissolution and precipitation. Despite being rather unlikely, the principal interest of such a simple scenario is to test the characteristic distance of water chemical equilibration with the solids it comes in contact with as well as the influence of the B isotopic composition of the entering solution on the pedogenic clays (or secondary phases in a large sense). Results are illustrated in Figure 3-22 with a zoom on the top 100m in Figure 3-23. Taken parameter values in the order of those classically found in the literature (see caption of the Figure 3-22), it is clearly shown that such a model mismatches our data by several orders of magnitude because it requires about 10 km of water/rock interaction to allow B concentration and $\delta^{11}B$ to be similar to that observed and are is therefore not consistent with the development of saprolite in the order of 10 m. Moreover, it would require a B concentration in the percolating solution of 12 ppm, whereas it never exceeds 10 ppb in soils and may reach 100 ppb in aquifers. Looking at the top 100 m only, the model also predicts very B-poor clays (0.01-0.6 ppm) and very low $\delta^{11}B$ (about -40‰). Finally, in the most likely case of the entering solution with $\delta^{11}B$ around +30‰ (close to the atmosphere and vegetation), then an anticorrelation is observed between the B concentration and isotope in the clay, which is contradictory with the observed data. However, erroneous values could have been taken for some of the model parameters like the actual water porous velocity or the reaction rates. The reaction rates chosen (10^{-5} yr^{-1}) are likely on the upper limit and reducing this value would increase the reaction length. For the water velocity, V=5 m yr^{-1} is the average value determined in the Strengbach watershed (Cividini et al., 2010) when actually there are average periods of rapid flush after a rain event and periods of stagnant waters between rain events during the summer. To reduce the reaction length by 3 orders of magnitude, we should take V = 5 mm yr^{-1}, leading to conditions where elements would mostly move by diffusion.

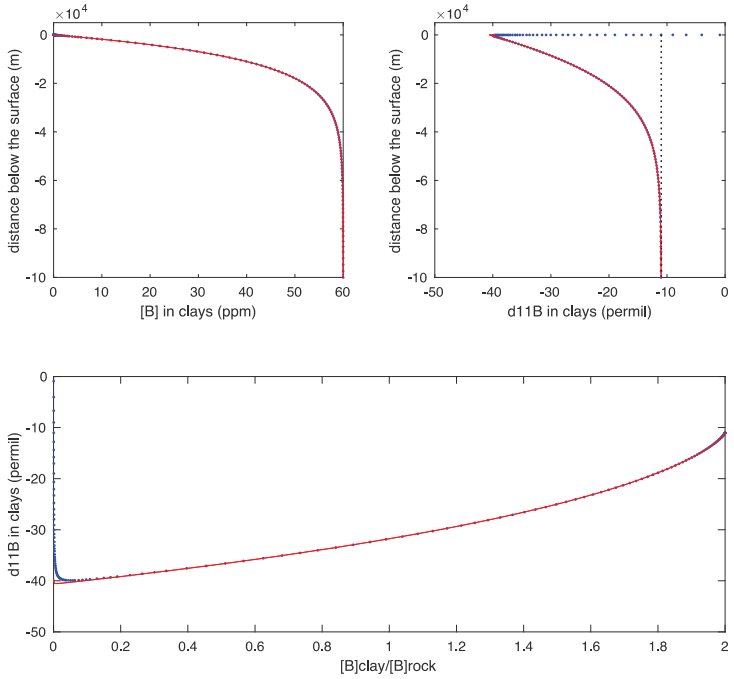

Figure 3-22. Numerical results of the transport reactive Equations (3-6) and (3-10) in the case where the dissolution and precipitation rates are kept constant. Parameters of the model are: v=5 m/yr; M=10; Rd=Rp=10^{-5} g.g^{-1}.yr^{-1}; K=5; Cs=30 ppm; r_r=-11‰; C_{f0}=0.003 ppm; rf0=30‰ (blue dots) or -11‰ (red line); ∝=0.970; K=25. The dashed black line represents the $\delta^{11}B$ of value taken for the bedrock (r_r).

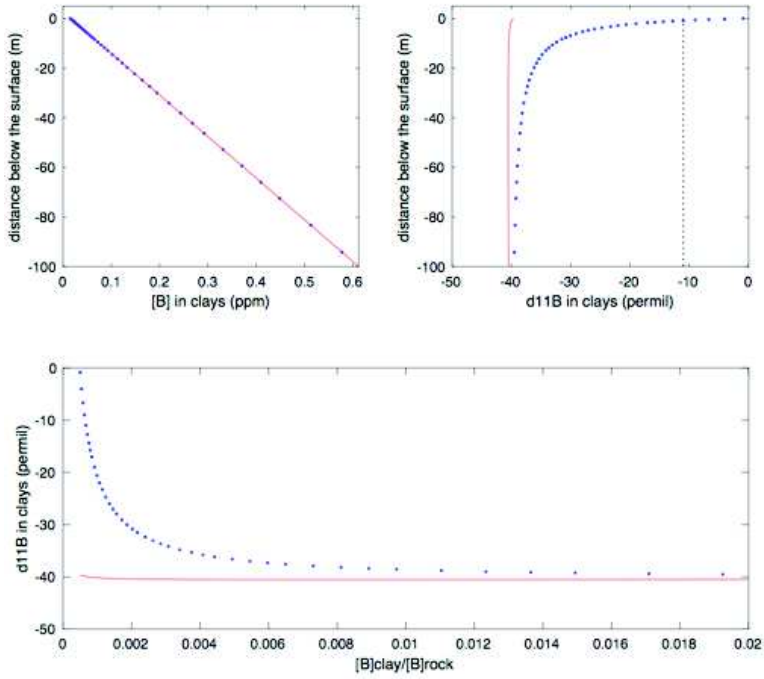

Figure 3-23. Zoom of the top 100 m along the flowpath. Parameters are identical as in Figure 3-22.

3.5.2.2 Scenario 2: hot spots of dissolution and precipitation

More realistic scenario would be to consider that the reaction rates vary with depth according to the change of water chemistry and mineralogy. A linear relationship between reaction rates and depth has been tested but gives very similar results and conclusion as taking constant ones. More likely, clays may massively form at particular depth(s), associated with strong gradients of the hydrogeochemical conditions. Two locations in the saprolite are of particular interest: 1) the top soil where meteoric water enters the soil with which it is far from chemical equilibrium, enhanced by the presence of organic compounds (acids, ligands,…) that promotes mineral dissolution, and 2) the saprolite/bedrock interface where porosity rapidly decreases and fresh minerals are exposed to water (see Figure 3-21). The hypothesis of clay minerals being massively formed at the surface can be dismissed because clays are also largely found deep in the weathering profile and because B in clays should be in equilibrium with a B-poor and high $\delta^{11}B$ solution, inconsistent with the data. We then tested the following scenario: dissolution and precipitation reactions exist all along the saprolite but at limited rate (Rd>Rp, allowing the $\delta^{11}B$ of the solution to decrease) but drastically increase (by 2 orders of magnitude at the bottom of the saprolite, Rd=Rp). Results are shown in Figure 3-24 and do not show much of a difference compared to the constant parameter scenario. The principal difference is that the reaction length is shorter; this is in line with increased precipitation and the fact that neo-formed clays have lower B concentrations due to the increased precipitation rate which reduces the B concentration of the solution.

3.5.3 Implication for weathering reactions in soils

The sensitivity tests described above indicate that the classical reactive transport modelling approach misses the B data by several orders of magnitude and hint severe contradictions on how to produce B-rich clays over a short distance, at a composition close to the bedrock, and from a diluted soil solution? Even being already mentioned in previous studies, the soil solution chemistry as determined from the samples collected with the lysimeter plates is not the one from which secondary particles form. Its diluted chemical composition driven by rapid transfer through the soil layers hinders the formation of secondary products. Instead, B data in the clay size fraction indicate that its incorporation into secondary phases must be quantitative and, since the reaction

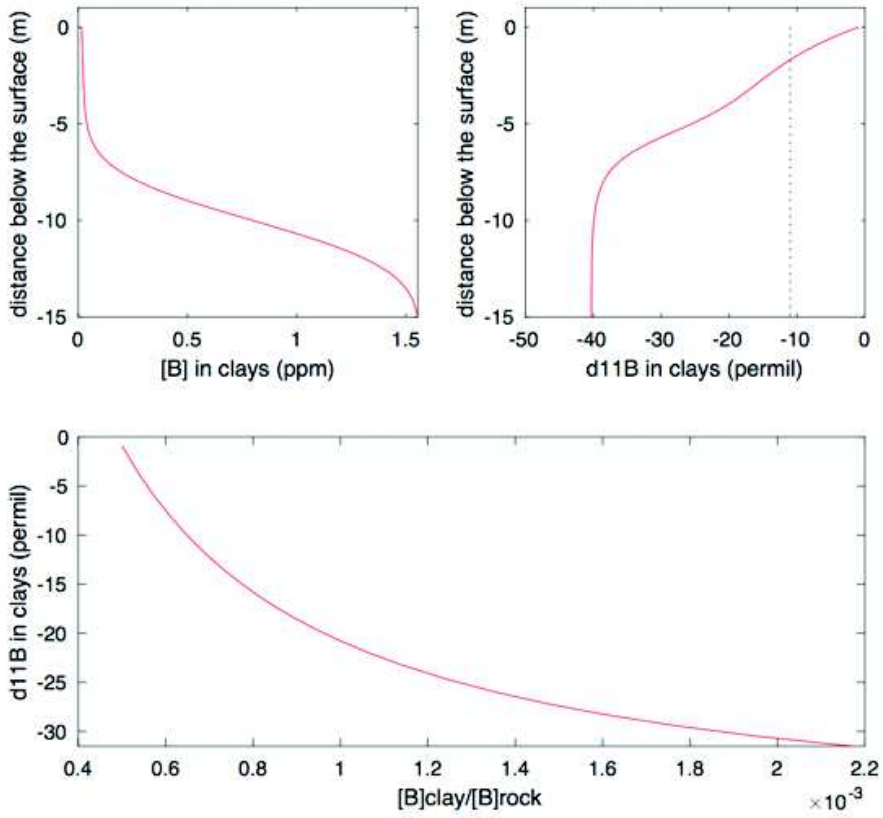

Figure 3-24. Numerical results of the transport reactive Equations (3-6) and (3-10) in the case where the dissolution and precipitation rates are increased by a factor of 100 at -10m following a gaussian distribution (σ=2m). Parameters of the model are: v=5 m/yr; M=10; background Rd=10^{-5} $g.g^{-1}.yr^{-1}$; Rp=0.5 Rd; K=5; Cs=30 ppm; r_r=-11‰; C_{f0}=0.003 ppm; rf0=30‰; $\propto$=0.970; K=25. The dashed black line represents the $\delta^{11}B$ of value taken for the bedrock (r_r).

rates are relatively low, it implies that the precipitation must take place in a confined environment. To approach the case where clays precipitate in a partially closed system, Figure 3-25 shows the results of a Rayleigh-like B chemical and isotopic evolution of a pore volume. The model predicts that the $\delta^{11}B$ of the bulk clays formed in a given pore volume approach the source value as B gets quantitatively re-incorporated. This trend appears closer to our results than the reactive transport as presented above. Here, the conceptual view for the formation of clays in soil as inferred from B concentration and isotopes is that they precipitate from partially isolated pore volumes with limited connection to the principal water flow path. Most of the soil water migrates relatively fast across the weathering profile, keeping a diluted concentration of B. At much slower rate, water and dissolved elements diffuse into small-scale pores at the mineral surface and/or grain boundaries where they interact with the host mineral and produce in-situ clay (Figure 3-26). The water

transport across these secondary pores should be slow compared to dissolution and precipitation rates to ensure a quantitative removal of B before the water replacement. Here, the main source of B is therefore the hosting mineral itself and not the soil solution. However, the initial composition of the starting solution in the Fig. 3-25 is set to +10‰, producting clays in equilibrium with this solution which are 30‰ ligher and in the range of the observed data. If boron were exclusively sourced from mineral dissolution, then the soil solution would have an isotope composition of the mineral/bedrock (approximately -10‰) as dissolution does not cause isotope fractionation. A soil solution with a composition of +10‰, as modelled in Fig. 3-25, would then indicate a B contribution from an isotopically heavy source, most likely B which has been cycled through vegetation and/or deriving from the atmosphere. In polluted environments or those near the sea, this isotopically heavy source may be from contamination or marine-derived sources such as sea spray, respectively. Regardless of the source, those secondary pore waters slowly leak to the soil solution to allow a low B concentration but a gradual isotopic imprint of the mineral dissolution.

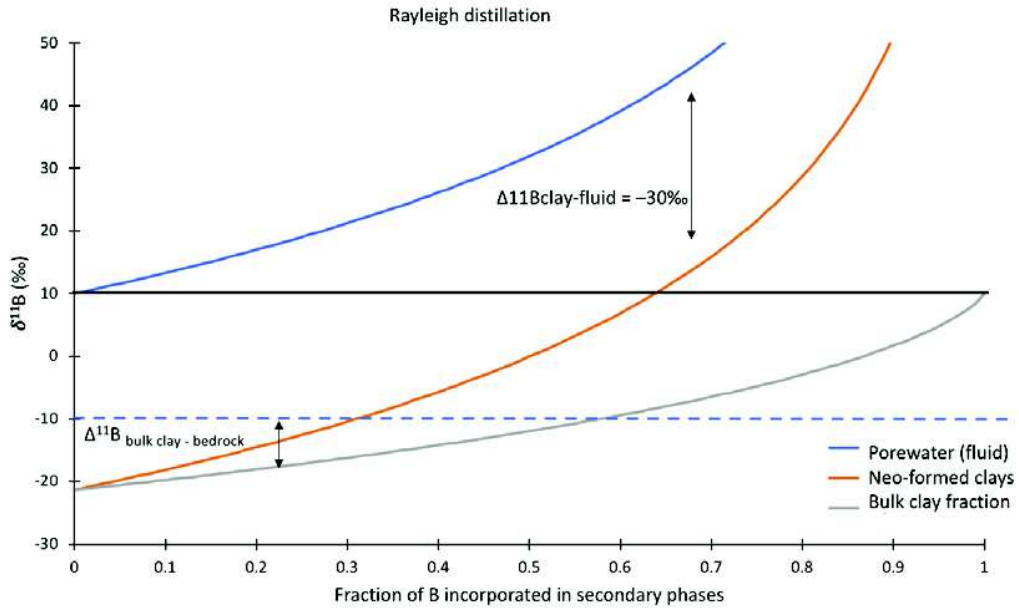

Figure 3-25. Schematic representation of B isotope systematics in a closed system where B isotopes of the soil solution and clay fraction evolve by Rayleigh distillation. This schematic can be used to describe the observed relationship between the clay fraction, porewater, and the bedrock. The average the average $\delta^{11}B$ of the bedrock was used (-10‰) as the initial composition of the porewater. The fractionation factor (α) between the adsorbed and dissolved species in this model is 0.969 which corresponds to a $\Delta^{11}B_{\text{clay – fluid}} = –30‰$ at pH 6.9 following Palmer et al. (1987).

Following this model, local hydrogeochemical conditions still have a strong influence on the B geochemical signature of clays since more aggressive weathering conditions (strong hydrological cycle, high temperature, etc.) leading to stronger chemical gradients and larger secondary pores for instance that promote dissolution reactions over the precipitation ones and therefore lead to lower B concentration and $\delta^{11}B$ in secondary products. Their numerical modeling would require to implement equations for a double porosity in reactive transport codes (e.g. DePaolo et al., 2006), beyond the scope of the present work.

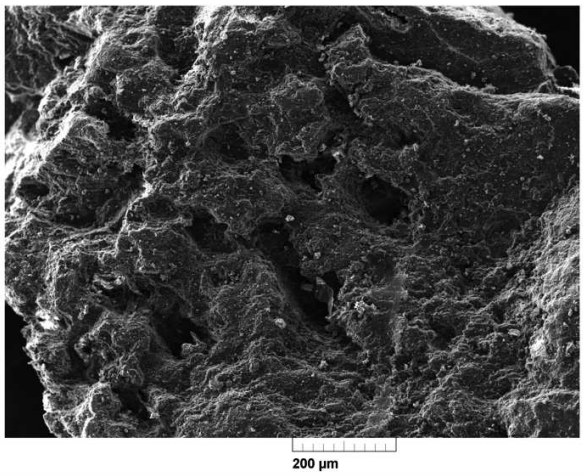

Figure 3-26. Albite mineral surface displaying a porous surface where soil solution may become trapped and evolve in a partially-closed system. Image taken by scanning electron microscopy (SEM).

3.5.4 Conclusion

This chapter comprehensively focused on how river sediments record the weathering regime and how that weathering "signal" is transported from source areas to the depositional environment using boron isotopes. Chemical and B isotope values in the Gandak and Murrumbidgee Rivers show similar behavior. Boron isotope compositions of the clay fraction in the headwaters displays large isotope fraction compared to those formed on the alluvial plain, indicating different weathering conditions in each location. The chemical composition of riverine material from the Gandak was found not to be evolving during transport. Similarly in the Murrumbidgee River, a mass balance model reveals that the chemical and B isotope composition of sediment from the main channel reflects a mixture of sediment produced in the source areas of

the catchment and drained to the main channel via the tributaries in varying proportions. To this end, no chemical or isotopic evolution of the sediment is observed during transport. This important finding implies that the chemical and B isotopic composition of river sediment can possibly be used as a proxy to reconstruct paleo-weathering conditions.

While the chemical and B isotope composition of the sand fraction keeps a record of the source of catchment material (bedrock), the clay fraction records weathering conditions at formation sites. Low $\Delta^{11}B_{clay\text{-}bedrock}$ values in monolithological samples correlate with low mass transfer coefficient values while higher $\Delta^{11}B_{clay\text{-}bedrock}$ compositions correlate with higher mass transfer coefficients. This behavior was also noted in Gandak River sediments indicating that B mobility during clay formation is controlling the B isotope composition of secondary minerals. To explain this possible global trend, a reactive transport model was used to model the composition of the percolating surface/groundwater and the clay fraction. Results show that model cannot predict B concentrations or isotopes of the soil solution and precipitating clay fraction without using unrealistic modeling parameters such as flow path distance and water velocity. This likely indicates that the clay fraction is not precipitating from the bulk soil solution. On the contrary, clays are hypothesized to be precipitating from a porewater solution that evolves in a partially-closed system best described by Rayleigh distillation. The source of B to the clay fraction comes from the mineral itself which has an isotopic composition close to that of the clay fraction. Similarly, high B concentrations in these porewaters (in the range of 10 ppm) are needed to produce clay fractions with even higher concentrations (in the range of 50 ppm), which can be explained by continual mineral dissolution in a partially-closed system. This implies a long reaction time between the secondary mineral and the porewater, likely not present in transient soil solutions.

If correct, this description has an important implication: there is no reason that B in clay minerals should be in equilibrium with dissolved B, neither in top soils nor in rivers. This is evident by the approximate -40‰ B isotopic difference between the clay fraction and the dissolved load. Clays may record only the very local conditions of their formation (possibly in a confined environment) whereas soil solutions and rivers may be fed by waters that have not substantially exchanged matter with minerals. This would imply that both the dissolved and particulate phases may record weathering information and serve as proxy. However, there is no reason to dismiss

evidence from decades of studies using mass balance made from water and particles budgets, but this research questions the direct link that exists between them.

Chapter 4

RIVERINE PALEOCHANNELS

4.1 **Chapter Introduction**

To date, few studies have investigated boron isotope behavior in silicate sediments transported by rivers (Chetelat et al., 2009; Spivack et al., 1987) or in subsequent sediment deposits such as lakes (Vengosh et al. 1991a, 1991b and Xiao et al. 1992) or paleochannels. Past studies such as Chetelat et al. (2009) and Spivack et al. (1987) have analyzed the suspended load in rivers for B isotopes to determine the modern weathering regime in the catchment. Studies using B isotope in lake sediment deposits are often investigating the geochemical evolution of the lake and have not specifically focused on the paleo-weathering information sediment deposits may contain. To evaluate chemical and isotopic variations of lake sediment Xiao et al. (1992) identified the sources of B which contribute to the composition of the lake water then calculated isotope fractionation factors between the sediment clay minerals / boron minerals and the lake water / brine to determine if changes in source or geochemical processes can explain their compositions. Results show that isotope fractionation between the brine and sediments in the salt lake is due to adsorption of ^{10}B onto clay mineral surfaces, resulting in an ^{11}B aqueous phase enrichment. Large differences in the B isotope compositions between the various B-contributing sources were also reported. Vengosh et al. (1991a) reconstructed the geochemical history of Australian salt lake brines by analyzing the chemical and B isotope composition of lake brines, groundwaters, and lake sediments over time. Similar to Xiao et al. (1992), variations in the B isotope composition of lake waters, brines, and sediments were compared to those of the B end-member sources to the lake (e.g. seawater, groundwater, mineral evaporites) and the geochemical processes within the lakes that may cause B isotope fractionation between the various components (e.g. interactions between dissolved B and clay minerals) were considered. A series of isotopic mass balance equations were also used to identify the source of the brines and chemical/geomorphological evolution of the lakes over time and to determine the marine or non-marine origin of the lakes. Results showed that in closed system maar lakes (with respect to local groundwater), ^{11}B enrichment of the lake water was caused by continual removal of ^{10}B by the sediments (enriching the water in ^{11}B) and an accumulation of ^{11}B by atmospheric inputs. In interior (terrestrial) salt lakes, higher $\delta^{11}B$ values of the lake water was interpreted to reflect a mixture of marine aerosols, internal adsorption processes within lake basins, and a mixture of terrestrial waters. This research demonstrated for the first time that B isotopes in sediment (and brine) archives can be a useful proxy in reconstructing paleo-

environmental conditions, particularly in evaporite environments, if an understanding of the B isotope systematics in the system is obtained. Boron isotopes in aeolian loess/paleosol deposits were studied by Zhao et al. (2003) and Wei et al., (2015) in China. The aim of these studies was to describe the geochemical characteristics of B isotopes during loess and paleosol weathering and to link variations in the B isotope composition of loess/paleosol deposits with paleo-environmental or paleoclimate regimes. Zhao et al. (2003) found that chemical and B isotopic signals were carried by the adsorbed phase on clay particles, with a negligible contribution of the carbonate phase within the deposit. Variations in B content and isotope values of the adsorbed phase mainly reflect a change in boron source, while those of the acid-soluble phases in the loess and paleosol layers are dominantly constrained by the intensity of weathering pedogenesis controlled by climate and environmental conditions (Figure 4-1). Specifically, higher B content and isotope ratios in the paleosols layers compared the loess

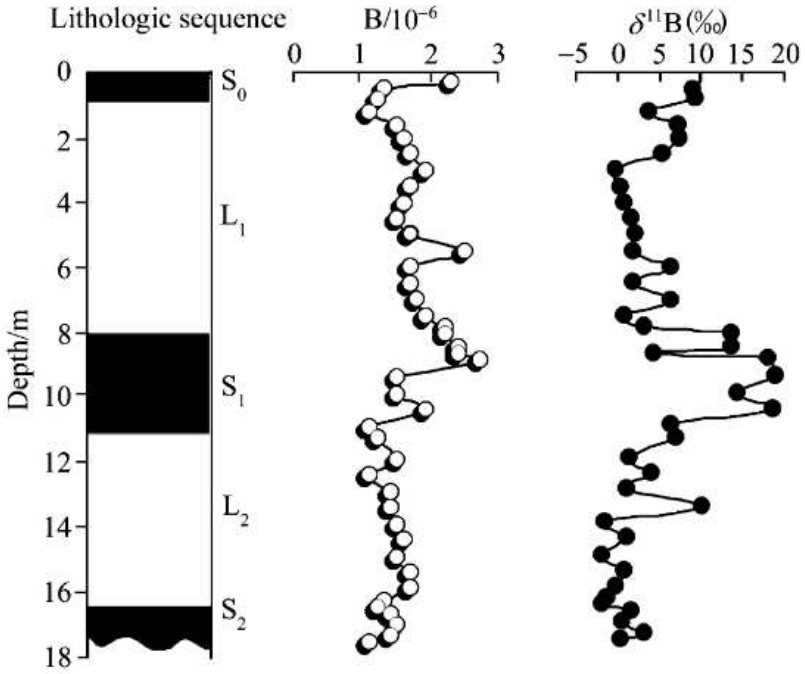

Figure 4-1. Boron content and isotope composition of the acid-soluble phases in the samples taken from the Luochuan loess section on the Chinese Loess Plateau. Source: Zhao et al. (2003).

layers occurs as a result of more intense chemical weathering during warm and moist climate regimes (paleosol layers) compared to cold-dry climates (loess layers). Increases in temperature

and precipitation lead to an intensification of low-temperature mineral alteration which increases the amount of B available for adsorption and adsorption capacity of clay minerals. Warm-moist conditions produce different weathering products, such as more clay minerals, thus changing the source of B in the water-rock system and producing variation in B isotope compositions. A similar result was found by Wei et al. (2015) who analyzed the B isotope composition of 5 loess-paleosol profiles in China. Variations in Sr and B concentrations, $\delta^{11}B$, and magnetic susceptibility (a paleo-climate proxy used to determine degree of pedogenesis) correlate well with pedogenetic intensity based on the CIW index (a weathering index using relative proportions of mobile/immobile elements, specially, aluminum, calcium, and sodium).Pedogenesis under cold climates produced low $\delta^{11}B$, lower B concentrations, higher Sr concentrations, and low magnetic susceptibility values indicating low weathering intensities; whereas warmer-humid climates show the opposite and indicate higher weathering intensities.

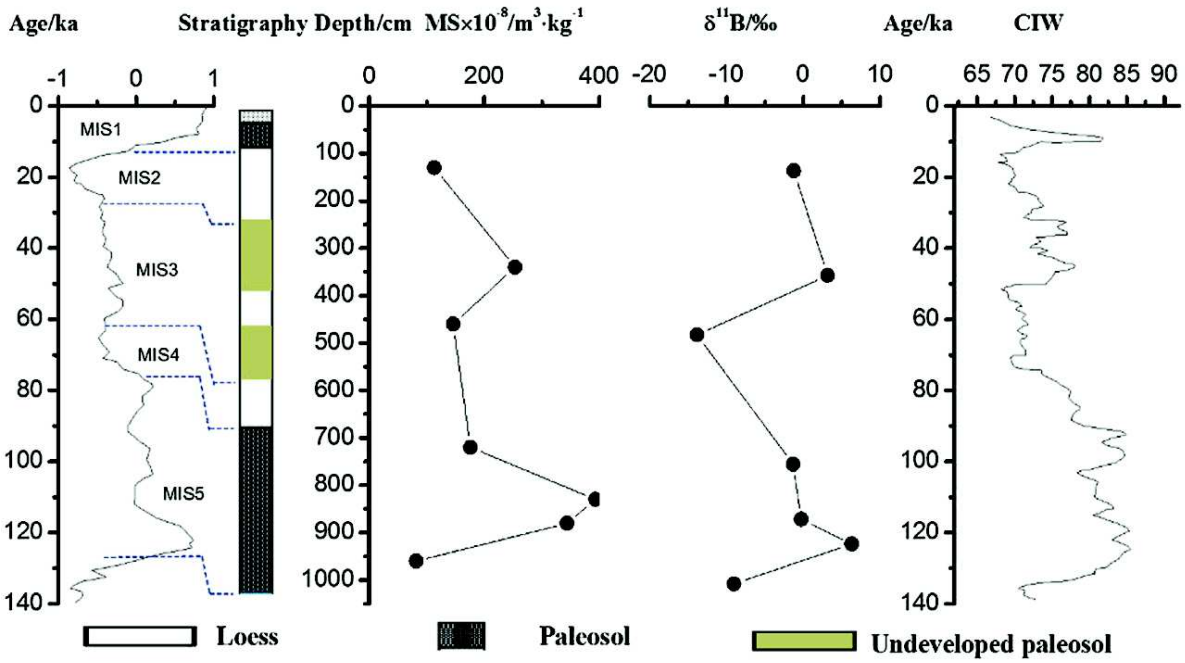

Figure 4-2. Paleoclimate reconstruction data over the last interglacial cycle compared to various proxies (magnetic susceptibility, B isotopes, and CIW index) taken from the Yangguo Reservoir Profile, China. Source: Wei et al. (2015).

Although these studies did not focus on riverine transported sediment, they employed the use of B isotopes in wind-blown soils and sediments to reconstruct paleo-environmental conditions over the last glacial-interglacial cycle with success. These pioneering studies provide evidence

supporting the use of B isotope compositions in soils and sediment as a potential geochemical proxy to reconstruct paleo-environmental changes.

In the present study, B isotope behavior in riverine sediment paleochannel deposits was investigated with the goal of reconstructing paleo-environmental and paleo-weathering conditions over the last glacial-interglacial cycle (MIS 1 – MIS 5). This study focuses on a series of well-dated and studied paleochannel deposits on the alluvial plain in the Murray-Darling Basin within the Murrumbidgee River catchment in southeast Australia (i.e. Banerjee et al., 2002; Bowler, 1986, 1967; Bulter, 1950; Dosseto et al., 2010; Page et al., 2009, 1996; Pels, 1964; Schumm, 1968). Sediment infill of these channels is thought to have derived from the headwaters of the Murrumbidgee River catchment over the last glacial cycle (Suresh et al., 2014; Page et al., 2009; Page and Nanson, 1996; Page, 1994), similar to the source of river sediment studied in Chapter 3. Because the existing study is the first to use this approach, the capability of B isotope to record paleo-weathering conditions of fluvially-transported sediments is unknown. However, one of the main conclusions in Chapter 3 (modern Murrumbidgee sediments) was a lack of chemical and B isotopic evolution in the clay fraction during transport, indicating that the B isotopic composition of clay fractions delivered to the downstream paleochannel systems are representative of those produced in source areas throughout the catchment. This finding reveals great potential for the application of this new proxy in fluvial sediment deposits with the goal of reconstructing conditions of their formation. The first study objective is to determine if the clay fractions of sediment deposits have retained their pedogenic signature or if they suffered from post-depositional alteration. If samples affected by post-depositional alteration can be identified they will be removed from the dataset before a paleo-environmental interpretation is made. The second study objective is to determine if the chemical and isotopic variation within each paleochannel system is distinct from other paleochannel systems. If so, it is necessary to determine if these variations are related to changes in sediment source or chemical weathering conditions during clay formation including weathering intensity and the influence of vegetation, both of which may be ultimately driven by climatic variability over the last glacial-interglacial period.

4.2 **Modern climate drivers and paleoclimate in temperate Australia over the last 100 ka**

In order to better understand how paleochannel formation, sediment deposition, and ultimately soil formation (pedogenesis) has responded to climate variability over the last glacial cycle in the Murrumbidgee River catchment, an understanding of modern drivers of climate variability and compilation of paleoclimate proxy records of the region is needed. The following text will discuss both, starting with the current Australian climate synoptic and drivers of modern climate then review relevant paleoclimate reconstructions of southeast Australia, including those throughout the Murray-Darling Basin, Riverine Plain, and the broader region.

4.2.1 Modern drivers of climate variability in temperate Australia

The known modern drivers that affect climate variability in terrestrial temperate Australia which include: El Niño-Southern Oscillation (ENSO), Pacific Decadal Oscillation (PDO), Southern westerly winds (SWW), the Southern Annular Mode (SAM), and the Indian Ocean Dipole (IOD) (Petherick et al., 2013). ENSO has two distinctly different phases, El Niño and La Niña, which have highly different impacts on both the spatial and temporal rainfall patterns in northern and eastern Australia (Risbey et al., 2009). Notably during an El Niño phase, the central and eastern Pacific Ocean becomes anomalously warm, with a high-pressure zone over Indonesia and northern Australia. In northern and eastern Australia, extending as far south as Tasmania, lower than average rainfall is experienced (Hill et al., 2009) which can result in major periods of drought. The opposite phase, La Niña, results in anomalously high rainfall across much of temperate Australia and can result in major flooding events, such as those observed in Lake Eyre sediment archives (Kotwicki and Allan, 1998). Operating on decadal (2 – 8 yr) timescales, ENSO was found to have increased in frequency over the Holocene until about 1,200 years ago, and then declined toward the present (Moy et al., 2002). Alternating periods of high and low ENSO activity (~2,000 years timescales) are superimposed on this long-term trend. Although ENSO variability over longer millennial timescales is poorly understood, coral records from Papua New Guinea do not indicate changes in ENSO cyclicity for the last 130 kyr (Moy et al., 2002) but rather a major change in amplitude and intensification to modern conditions (e.g. Ayliffe et al., 2004).

The Pacific Decadal Oscillation (PDO) describes an oscillation of SSTs in the North Pacific, which occurs on a decadal cycle, and has a significant influence on Australian rainfall (Mantua and Hare, 2002). The oscillations have a warm phase, which are associated with below

average rainfall in Australia, and a cool phase associated with above average rainfall in Australia. The influence of the PDO on Australian rainfall can be modulated by ENSO interactions, which can affect rainfall variability due to the combinations of both systems. This interaction extends as far south as the Murray River, where rainfall, river flow, and surface temperature correlates with PDO and ENSO interactions (Power et al., 1999).

The Southern westerly winds (SWW) are important components of Southern Hemisphere climate which have been implicated in governing precipitation in the mid to high latitudes (Garreaud et al., 2013; Garreaud, 2009). Variations in their intensity and latitudinal position are proposed to be important drivers of global climate because of their influence on deep-ocean circulation patterns (i.e. up-welling of the Southern Ocean deep water) and associated changes in atmospheric CO_2 (Rojas et al., 2009). Hesse and McTainsh (1999) suggest that SWW play an important role in Australian climate and that SWW-induced cold fronts can influence landscape dynamic through wind sediment transport and wind erosion. The Southern Annular Mode (SAM)/Antarctic Oscillation (AAO), which is the dominant inter-annual mode of the SWW, results in either a northward (negative SAM/AAO) or southward (positive SAM/AAO) shift of the SWW mean position, and therefore significantly correlated with southern temperate Australian precipitation (Hendon et al., 2007). Similar to the ENSO/PDO correlation, SAM/AAO is modulated by interactions with ENSO and amplifies climate effects of each mode when in sync.

The Indian Ocean Dipole (IOD) is a aperiodic oscillation of sea surface temperatures across the Indian Ocean involving three distinct phases: positive, neutral, and negative (Australian Government, Bureau of Meteorology, 2018). During a positive phase, westerly equatorial winds weaken, causing warm water to flow to the western part of the Indian Ocean basin (off the coast of Africa) and cool waters to upwell from the eastern basin off the coast of northwestern Australia, creating temperature differences across the Indian Ocean. In Australia, this generally produces less moisture than normal in the atmosphere and reduced rainfall. During a negative IOD phase, westerly winds intensify causing warmer water to build up near Australia and cooler than normal water in the western basin. This results in above average rainfall over Western and South Australian, as warm waters tend to supply weather systems with more atmospheric moisture. A neutral phase does not create temperature differences across the Indian Ocean basin, therefore having little influence on weather patterns in Australia.

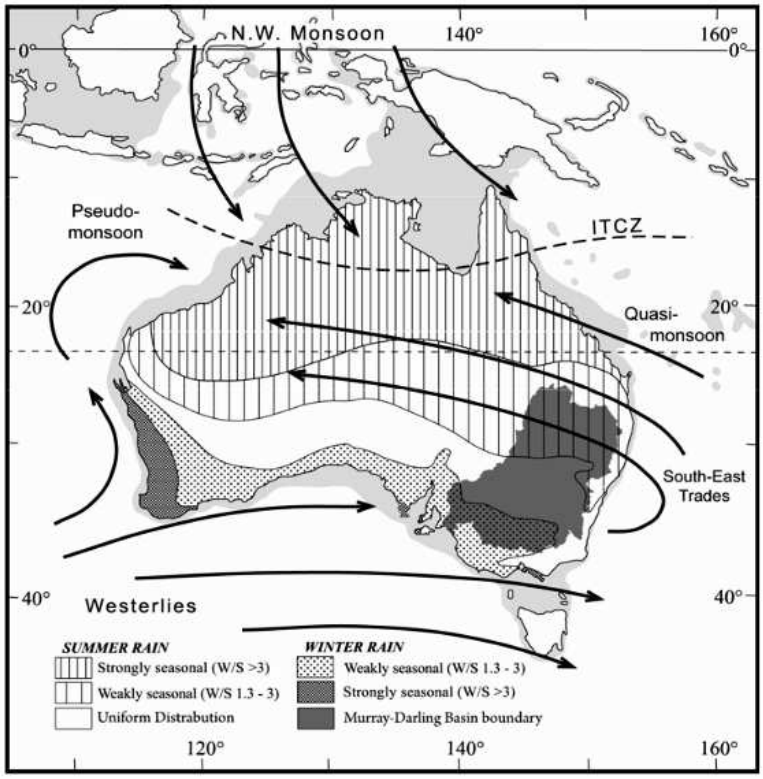

Figure 4-3. Major climatic features of Australia displaying rainfall patterns and the Murray-Darling Basin. Source: Kershaw and van der Kaars (2012)

4.2.2 Paleo-environment proxy records of the Murray-Darling Basin, Southeastern Australia, and surroundings

Despite the arid nature of much of the Australian continent, a significant amount of long, fairly continuous records of environmental change have been produced from its more humid eastern side (e.g. Mills et al., 2013; Petherick et al., 2013; Hesse et al., 2004; Page et al., 1996; Singh and Geissler, 1985; Colhoun et al., 1982). The southern portion of the Murray-Darling Basin is one of the areas most affected by climatic variability and has a high capability of recording it, including the Kosciuszko Massif in the Snowy Mountains out to the Riverine Plain (Figure 4-3). The Murray-Darling Basin (and Murrumbidgee River catchment) lies within the temperate zone in southern Australia. The zone extends from modern subtropical Queensland in the north, southward into New South Wales and Victoria, coastal South Australia, Tasmania, and southern portions of Western Australia (~20 – 45°S) (Petherick et al., 2013). The temperate zone is situated between the warm tropics in the north and the cold Southern Ocean and experiences a range of

rainfall patterns that results from different climatic drivers (Figure 4-3). The southern part of the continent (~35°S) (location of the Riverine Plain) experiences a winter dominant rainfall regime and low summer rainfall through a zone of uniformly distributed seasonal rainfall. This results from the incursion of moist westerly winds inland to southern Australia, as the subtropical dominant high pressure system shifts north in response to the Northern Hemisphere insolation maxima (Kershaw and van der Kaars, 2012). To the opposite, the northern part of the temperate zone experiences a summer dominant rainfall patterns through a zone of weakly seasonal rainfall, resulting from the poleward migration of the Inter-tropical Convergence Zone (ITCZ) and responding to the Southern Hemisphere solar maxima and rainfall brought by the southeastern trade winds. Monsoon influences are derived from the equatorial north-west and also the quasi-monsoon where moisture is derived from the Pacific Ocean.

Over long timescales (10^4 – 10^5 yr), glacial-interglacial cycles dominate climate change which are produced by solar insulation variations caused by reoccurring perturbations in Earth's orbit and rotation, known as Milankovitch Cycles(Petit et al., 1999; Raymo et al., 1998; Fischer, 1981). Additionally, a large number of complex feedback mechanisms are superimposed on these cycles including the expansion and contraction of Northern Hemisphere icesheets and the sea level fluctuations (Mills et al., 2013). Throughout the southern portion of the temperature zone and within the Murray-Darling Basin, higher temperatures during northern hemisphere interglacial periods are broadly associated with extensive woodlands in the lowland areas of the Basin compared to glacial intervals. Although vegetation (Kershaw et al., 2007) and aeolian (Twidale, 2007; Hesse et al., 2004) records within the Basin suggests increasing availability of moisture during the Holocene than compared to the LGM (20–18 kyr), other hydrological indicators suggest the opposite (Figure 4-4). For example, high lake levels (Bowler et al., 2003) and paleochannel discharges (Page and Nanson, 1996) indicate a wet LGM and a dry Holocene in the Basin. However, the complex relationships and feedbacks between these vegetation, rainfall, and runoff may explain this discrepancy. Evidence for long-term drying in eastern Australia over the last glacial cycle is evident in the hydrological records in the Murray-Darling Basin (Figure 4-4) in addition to several other sources including dust deposits in the Tasman Sea (Hesse, 1994) and decline of river activity in the Lake Eyre Basin (Maroulis et al., 2007)

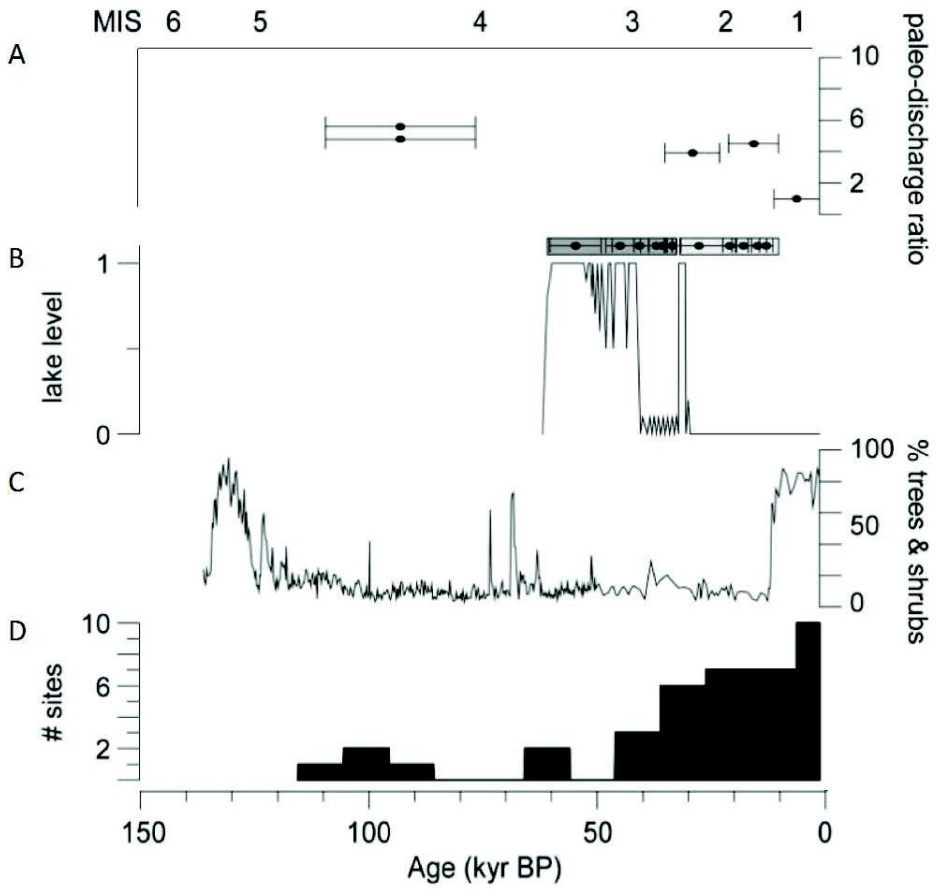

Figure 4-4. Last glacial cycle in the Murray-Darling Basin. All data are plotted as a function of depositional age before present (bottom x-axis) and Marine Isotope Stage (MIS) 1–6 (top x-axis) taken from the oxygen isotope record (not shown) from ODP Site 677 (Mix et al., 1995). A) paleo-discharge ratios from the Murrumbidgee River paleochannel systems expressed as multiples of modern river bankfull discharge (Page and Nanson, 1996); B) Lake level history of Lake Mungo based on OSL chronology (scale: 0 = dry; 1 = overflowing) (Bowler et al., 2003); C) proportion of tree and shrub pollen taken from Caledonia Fen, Victorian Highlands (Kershaw et al., 2007); D) number of investigated sites with TL-dated longitudinal sand dunes in the Murray-Darling Basin (Twidale, 2007; Hesse et al., 2004). Note that all bins are 10 ka except 0 – 5 ka where the # sites has been doubled. Source: re-drawn from Mills et al. (2013)

4.2.2.1 Temperature and Glaciation

Throughout the Quaternary Period (last 2.6 Ma), glaciation in Australia was restricted to the Tasmanian Highlands and a very small catchment in the Kosciuszko Massif (Snowy Mountains) on the eastern border of the Murray-Darling Basin, only for brief periods during glacial interval extremes (Barrows et al., 2001, 2002; Colhoun, 1985). However, periglacial soil processes may be

acted on sediment over much broader areas down to altitudes of 600 – 800 m (Barrows et al., 2002; Galloway, 1965). Accordingly, this would have affected soil formation in the headwaters of Basin rivers that supply sediment to the Riverine Plain and likely enhanced seasonal runoff. Modelling of these glacial advances indicates that large decreases in temperature and atmospheric moisture were necessary to form small ice caps (Barrows et al., 2001). Evidence of a substantial (6–10°C) decrease in temperature at sea-level in the western portion of the Basin and at Lake Eyre was reported by Miller et al. (1997) from 45 – 16 ka, however a SST reconstruction of the LGM inferred from fossil plankton assemblages (Barrows and Juggins, 2005). From the Australian margin and Indian Ocean indicate a SST change of only 5°C. More recently there have been continuous, high-resolution records of SST (Barrows et al., 2007; Calvo et al., 2007) taken off the coast of New Zealand and from the mouth of Murray River, respectively, that are in better agreement with glacial models and whose timing and degree of temperature change are more consistent with those determined by Antarctic ice cores (Petit et al., 1999) (Figure 4-5). The alkenone-derived SST record taken offshore of the Murray River in South Australia (Calvo et al., 2007) is the first

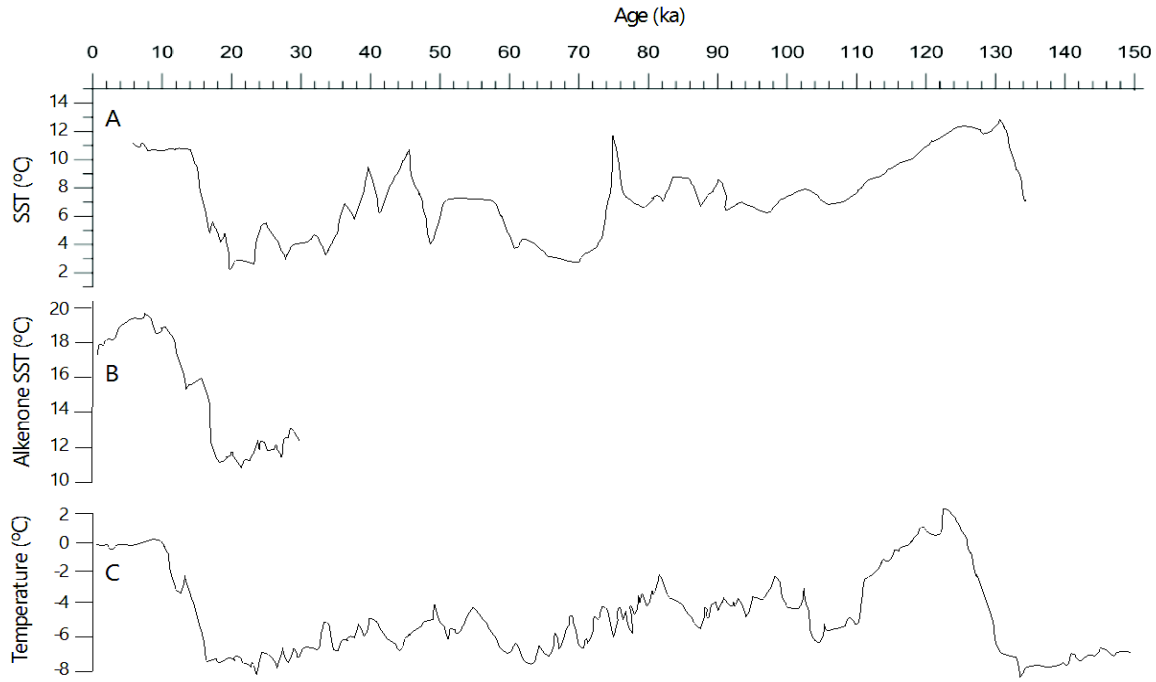

Figure 4-5. Temperature reconstruction records over the last glacial cycle. A) Estimates of SST from planktonic foraminifera at DSDP Site 594 off the east coast of New Zealand, source: re-drawn from Barrows et al. (2007); B) alkenone-derived SST record from core MD03-2611 taken from near the mouth of Murray River in South Australia, source: re-drawn from Calvo et al. (2007); C) Isotopic temperature reconstruction of the atmosphere taken from the Vostok ice core record in Antarctica, source: re-drawn from Petit et al. (1999)

continuous, high-resolution record in the Australian region, although relatively limited in duration compared to other records. The record suggests a significantly colder LGM period, with temperatures approximately 8°C lower than today (Figure 4-5B). The 150,000 year SST record inferred from planktonic foraminifera taken off of the east coast of the New Zealand's South Island (Barrows et al., 2007) offers a longer representation of climatic variability in the Southern Ocean and Southern Hemisphere in general. This record shows that rapid temperature changes occur within a few centuries in the Southern Ocean and that an approximate temperature difference of 6°C is apparent between glacial and interglacial periods. Barrows et al. (2007) reported that first-order climate change in the Southern Hemisphere (at least from the perspective of New Zealand and Australia) occurs in concert with changes in insolation of the North Hemisphere and that the glacial extent and vegetation changes (see discussion below) in New Zealand and Australia occur in tandem with SSTs, indicating a tight link between oceanic and terrestrial temperature. Taken together, the Barrows et al. (2007) and Calvo et al. (2007) records support larger changes in temperatures and moisture content, compared to today, which the glacial models require to form icecaps in temperate Australia.

4.2.2.2 Hydrological Records

As discussed earlier, our understanding of climate-driven fluvial activity in the Murray-Darling Basin is primarily based on the paleochannel work of Page et al. (1996), (1991); and Page and Nanson (1996) who used TL-dating to extend the previous chronology back to MIS 5 (105 ka). Banerjee et al. (2002) and Mueller (2017) later confirmed the TL dates of Page et al. (1996) using optimally stimulated luminescence (OSL), although Mueller (2017) dates the Yanco System to be slightly older than reported (pre-LGM) with an average age of 23 ka. Together, these studies allow an understanding of large paleochannel morphology and high bankfull discharge over a range of climate regimes including MIS 5, MIS 3, and MIS 2 (Page et al., 1996).

Few direct observations or reconstructions of climatic conditions during MIS 5 on the Riverine Plain have been made. Enhanced fluvial activity associated with the Coleambally System (Page et al., 1996) is likely the best direct evidence of paleo-environmental conditions. This record also correlates well with the fluvial activity in the Murray-Goulburn region to the south and also to a

pluvial period in northern and central Australia and coastal New South Wales (Page et al., 1991). Sea surface temperatures were about 2°C cooler than present (Figure 4-5A). Comparatively, more information is known about the timing and fluvial conditions during the Kerarbury Phases (55 – 35 ka; MIS 3). This phase correlates with Bowler's (1986) Lake Mungo lacustral phase recorded in the southern inland lakes of the Riverine Plain such as Lake Urana (Page, 1994). Schumm (1968) estimated that the bankfull discharges during MIS 3 on the Plain were between three to six times higher than the present Murrumbidgee River; the Plain experienced lower evaporation rates; and that there was a significantly larger winter snowpack in the southern Highlands. The latter likely induces a strong seasonal flow regime with high flood peaks during spring thawing. The active Gum Creek paleochannel system (35 – 25 ka) (Page et al., 1996) occurs during late MIS 3 and correlates with a high stand lake level of Lake George (Coventry, 1976), a nearby lake on the eastern side of the Snowy Mountains. The Gum Creek phase also correlates with active paleochannels of a neighboring river, the Lachlan, which also formed large channels prior to the LGM (from 34–21 ka) with peak discharges up to 16 times that of the modern river (Kemp and Rhodes, 2010). All records indicate higher energy fluvial activity around 30 ka. These records coincide with the appearance of the first glaciers since MIS 4 (Barrows et al., 2001). Large channel dimensions throughout the Plain are interpreted as reflecting high rates of lateral channel migration, driven by high sediment loads which were derived from denuded and stabilized catchments in the river headwaters. Other hydrologic records on the Riverine Plain come from lakes that were fed by large river systems, including the Willandra Lakes and Lakes Mungo and Arumpo, all which show overflowing conditions around 30 ka (Page, 1994) with oscillating lake levels persisting through the LGM (Bowler et al., 2003). Kemp and Rhodes (2010) argue that the fluvio-lacustrine activity represents increased runoff in response to increased snow melt and reduced vegetation in the catchment. Just before and right after the arid and relatively dry LGM (Kemp and Rhodes, 2010; Barrows et al., 2001, 2007; Ayliffe et al., 1998; Page and Nanson, 1996; Page, 1994; Page et al., 1991), is the Yanco paleochannel system (14 – 23 ka; MIS 2) (Mueller, 2017; Page et al., 1996). The average age for channel deposits before the LGM are about 21 – 22 ka and after is about 16 ka; there is one date associated with the Yanco System as old as 32 ka, however it is uncertain if this sample is truly part of the Yanco System or re-worked sediment from a Gum Creek paleochannel (Mueller, 2017). These periods broadly correspond to increased rates of speleothem formation in Southern Australia, suggesting increased precipitation during those

times (Ayliffe et al., 1998). Additionally, the older deposit (32 ka) of the pre-LGM phase of the Yanco System correlates with previously discussed hydrologic records in late MIS 3, similar to the Gum Creek phase. Deglaciation was nearly complete by 16 ka (Barrows et al., 2001), with SST rapidly increasing and sea ice vanishing (Calvo et al., 2007). Evidence of high fluvial activity post-LGM is shown by the large bankfull discharges of the Yanco system channels (Page and Nanson, 1996) including the migrational channels on the Murray, Goulburn, and Murrumbidgee Rivers, and shoreline and ostracod evidence suggesting high lake levels at Lake George around 14 ka and 10 ka (De Deckker, 1982). Similar increases in fluvial activity were reported in coastal rivers of New South Wales (NSW) (Nanson and Erskine, 1988). Temperature during the Holocene (12 – 0 ka) in temperature Australia is characterized as a relatively warm and wet climate by nearly all proxy records and marks the transition to modern fluvial and lacustrine environments (Petherick et al., 2013; Bowler, 1986). The shrinkage of the area subjected to periglacial activity undoubtedly reduced the amount of coarse-grained debris delivered to the river catchments, which contributed to the establishment of suspended load-dominated stream conditions (Prosser et al., 1994).

The nature of the climate forcing which caused dramatic changes in these paleochannels remains unclear. Although bankfull discharges were calculated from channel dimension (i.e. Page and Nanson, 1996) and produce evidence of fluvial activity, bankfull discharge may be a biased measure of total annual discharge or precipitation due to greater peak flows during seasonal snow melt in glacial periods, for example. Additionally, factors such as vegetation cover, soil thickness and temperature may largely impact runoff and therefore channel size (Hesse and McTainsh, 1999). Due to the complexity of factors that control catchment hydrology, there is no direct relationship between channel size and precipitation or runoff. Therefore, it is difficult to say with any certainty what the precipitation/climate regime was like during the active period of the channel based solely on channel bankfull discharge. The hydrologic record should be paired with a more direct indicator of paleo-precipitation in order to better understand the drivers of channel formation and morphology in response to climate. Ayliffe et al. (1998) provided a high-resolution 500 k.y. record of precipitation in southern Australia by $^{230}Th/^{243}U$ dating speleothems which provide a better picture of continental aridity and moisture over the last glacial cycle. However, the growth of speleothems, which reflects effective precipitation (rainfall minus precipitation), did not occur during strictly glacial or interglacial periods, but rather during interstadial intervals (short warm periods between extreme warm and cold intervals of glacial cycles). Ayliffe et al. (1998) suggested

that largest paleochannel volumes on the Riverine Plain occurred during times when the effective moisture was high. However, large river systems post-LGM do not correlate with intensive paleochannel growth on the Riverine Plain and cannot be explained by precipitation alone. Therefore, large channel systems (i.e. Yanco System) may possibly represent high seasonal discharge and flooding in an overall drier landscape (Page and Nanson, 1996).

4.2.2.3 Vegetation records

Sites suitable for paleoecological study are few due to the semi-arid climate in Australia's interior and on the Riverine Plain; sites are therefore restricted to the humid highland margins of the Murray-Darling Basin. The oldest and longest pollen and charcoal record in Australia comes from an 18 m core sample taken from Lake George that dates beyond 700 ka BP (Singh and Geissler, 1985; Singh et al., 1981). Pollen analysis indicates warm and wet interglacials with dominant Casuarinaceae forests or woodlands, while glacial periods were cool and dry denoted by extensive herbaceous vegetation cover with likely small patches of cool temperate rainforests. The charcoal record indicates that burning was largely restricted to interglacials, caused by a lack a fuel during glacial periods. The last interglacial saw the replacement of Casuarinaceae by Eucalyptus and the decline of rainforest taxa, debated to be caused by Aboriginal people and burning (Kershaw, 1986). However, the continuity of sediment deposition in the large tectonic lake system, biased pollen preservation, and limited dating all raise concerns of the integrity of this record and may explain why correlations could not be made to other long terrestrial records or the marine isotope record.

A recent pollen record taken at fairly high altitude (1300 m) in the Victorian Highlands (Kershaw et al., 2007) shows less detailed and sustained change over the last glacial cycle (Figure 4-4C). Two major periods of forest expansion to present-day levels are show in the record related to the last interglacial (MIS 5e) and the Holocene (MIS 1), with a third during an interstadial in the early part of MIS 3 dated at about 68 ka BP. Over the last glacial period, vegetation at this site was dominated by alpine steppe species typical of temperatures at least 5°C cooler than present with a local extinction of cool temperate rainforest taxa between 30 – 40 ka BP.

In Southwestern NSW (Darling Anabranch dunefields region), a 70 ka BP pollen record was recovered from playa lakes showing vegetation changes during pre-glacial, glacial, and post-

glacial periods (Cupper, 2005). This record is consistent with other records in Southeast Australia that indicate the last glacial period was cooler and drier with dominant herbaceous and shrubland species. After the LGM, a more complex vegetation structure emerged with greater diversity, however forests did not become abundant until the Holocene. This record is consistent with headwater sites in the Castlereagh catchment, Ulungra Springs (northern NSW), where trees were present during MIS 3 (until about 25 ka BP), absent during MIS 2, and then returning once again after the glacial termination during the early Holocene (Dodson and Wright, 1989).

A longer and broader record of vegetation in Southeast Australia and New Zealand can be drawn from the deep-sea core (DSDP Site 594) taken offshore of New Zealand (Barrows et al., 2007). This 150 ka BP record details the relative abundance of dominant vegetation types on nearby New Zealand, which can be broadly correlated to southeast Australia, and reflects changes in terrestrial climate (mainly precipitation and temperature). The pollen record shares common features with the SST records from the same cores (Figure 4-5A); 51% of the variation in tree and shrub pollen can be explained by variations in SST estimates, therefore variation in temperature. This demonstrates that SST is closely linked with land surface climate (Barrows et al., 2007). Over the last glacial cycle, the record shows the greatest decrease in abundances of tree pollen during MIS 2 and to lesser extent during MIS 4. The percentage of tree to shrub pollen from about 80 to 130 ka (MIS 5 – MIS 6) was slightly less (~10%) than during the Holocene and about 30% less from 40 to 60 ka (MIS 3). Similar to the Dodson and Wright (1989) record in NSW, this offshore record indicates woody species throughout much of the glacial cycle, excluding the cold and dry LGM and MIS 4. The similarities between this record and those from mainland Australia in terms of vegetation (i.e. Cupper, 2005; Dodson and Wright, 1989) and also SST (i.e. Calvo et al., 2007) make this record applicable to not only New Zealand, but also Southeast Australia (Barrows et al., 2007).

4.3 Site Description

Paleochannel systems investigated in this study are located on the Riverine Plain of the Murrumbidgee River catchment in the Murray-Darling Basin, Southeast Australia (Figure 4-6). The Riverine Plain is approximately 70,000 km^2, occupies a large portion of the eastern Murray Sedimentary Basin, and consists of coalescing floodplains of the western-flowing Murrumbidgee,

Lachlan, and Murray Rivers which originate in the Southeastern highlands of Australia. Although Tertiary sea-level fluctuations have greatly impacted sedimentation patterns in the western (Mallee) part of the Basin, the Riverine Plain has maintained terrestrial environments over the last 60 Ma (Cenozoic) and provide a superb record of episodic fluvial, lacustrine, and aeolian sedimentation (Bowler, 1986). Modern aeolian landscapes were established in the western Mallee region of the Murray Basin by about 0.5 or 0.4 Ma which coincided with the onset of semi-arid conditions in the Basin and fluvial deposition of the Shepparton Formation in the eastern Riverina region leading to the formation of the modern Riverine Plain landscape (An et al., 1986). Sediment depths are < 500 m and have accumulated under a quiescent erosion regime (David and Browne, 1950). However, despite the shift to semi-arid conditions in southeast Australia, landscape evolution in the Murray-Darling Basin and on the Riverine Plain was significantly affected by repeated global glacial-interglacial climate cycles, evidenced by fossil lakes, dune fields, and large fluvial channel systems (Bowler, 1986). The surficial features found on the Plain are impressively ancient and span more than a full glacial cycle (Page et al., 1996).

The Riverine Plain in the Murray-Darling Basin is perhaps the most intensively studied fluvial landscape in Australia, producing several classic studies in fluvial geomorphology and paleohydrological change (e.g. Bowler, 1986, 1967; Page et al., 2009; Schumm, 1968). Early interests in the Riverine Plain, i.e. Bulter (1950); Pels (1964), focused on the production of soil and ground-water maps for proposed irrigation projects and agriculture whose work systematically tries to explain the very complex geomorphologic patterns of sediment deposits, soils types, and vegetation on the landscape. Aerial photographs surveys of the Plain revealed that the distribution and pattern of soil and sediment variation were controlled to a large extent by the course of ancient river systems, not by the modern drainage patterns. The surficial geomorphology reflects a long history of fluvial activity and interaction with groundwater, fine sediments, and the episodic expansion of an arid climate, which produced a wide range of sedimentary and geomorphic archives including floodplain lakes, terraces, aeolian source-bordering dunes, and fluvial sediments (bedload, mixed load, and suspended load).

4.4 **Paleochannel Formation and Age Constraint**

4.4.1 Formation of Riverine Plain paleochannels

The most studied feature on this complex landscape are the channel deposits (e.g. Banerjee et al., 2002; Bulter, 1950; Page et al., 1996; Pels, 1964; Schumm, 1968). An example of a paleochannel system (Gum Creek) near Darlington Point on the Riverine Plain in the Murrumbidgee River catchment is shown in Figure 4-7. The paleochannel left behind visible oxbow and meander

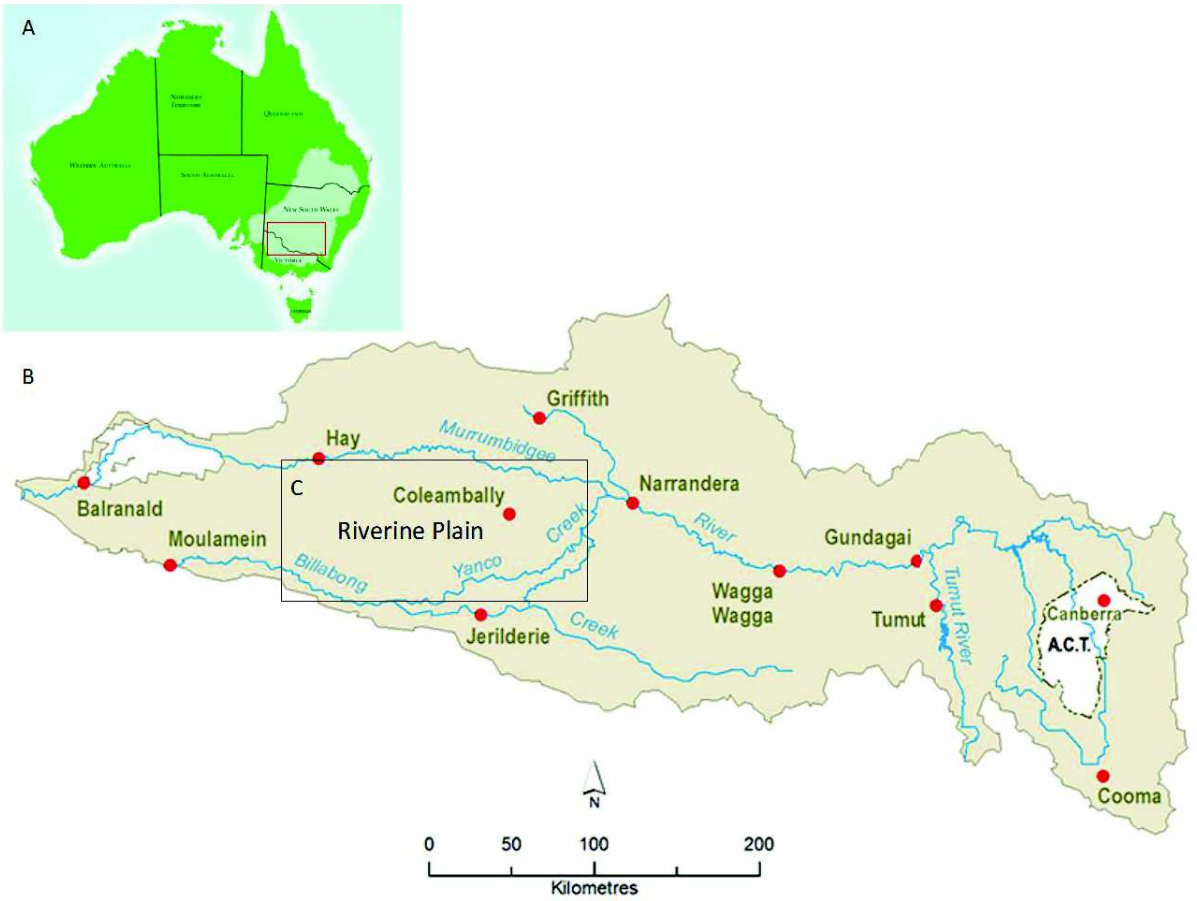

Figure 4-6. Location of the paleochannel systems investigated in this study. A) location of the Murrumbidgee River catchment (red square) within the Murray-Darling Basin (light green shading) in southeast Australia. B) The Murrumbidgee River catchment with the location of the paleochannel systems (box). C) Location of the paleochannel systems on the Riverine Plain in the Murrumbidgee River catchment approximately 550 km downstream from the headwaters of the modern Murrumbidgee River. Sources: Green left weekly, November, 2011 (inset); New South Wales State Government (main panel)

meander scars on the landscape which are much larger than those produced by the adjacent modern Murrumbidgee River. Smaller paleochannel reaches are shown branching off of the main trunk stream. Butler (1961, 1958, 1950) established in a series of papers of what he called "prior streams" which were ancient rivers that extended as a vast network of channels across the surface of the Plain. These prior streams were slightly leveed, and aggraded bedload channels with low sinuosity forming an overlapping pattern on the landscape which fade out and become less notable in the western part of the Plain. Butler argued that the phases of prior stream bedload deposition required an abundant supply of coarse-grained sediment driven by an arid and therefore vegetation-limited catchment. This was contested by Langford-Smith (1960; 1959) who responded to the argument proposed by Butler stating that on the basis of meander wavelength and discharge, that the large dimensions of the prior stream channels were associated with large discharges in wet (pluvial), rather than arid conditions. In his final rebuttal, Langford-Smith (1962) modified his previous argument and suggested that although the onset of a pluvial period, if sudden, could cause

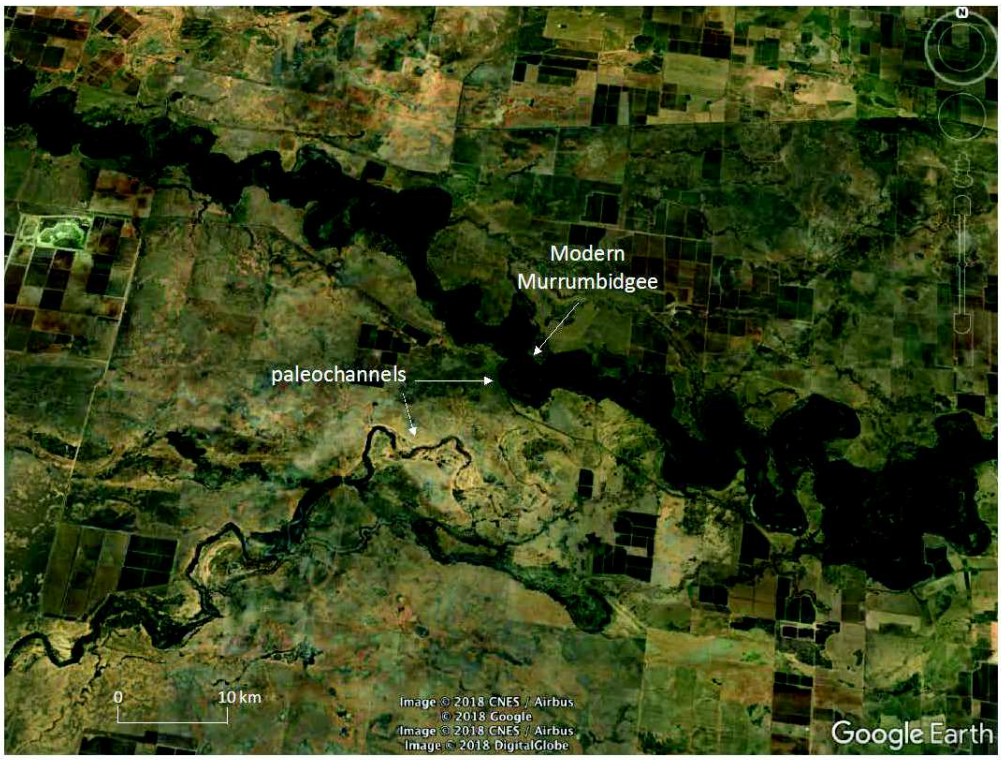

Figure 4-7. Examples of a paleochannel systems on the Riverine Plain, Murrumbidgee River catchment, near Darlington Point. Some are visible on the floodplain as oxbows and meander scars much larger than those formed by the adjacent modern Murrumbidgee River. Source: Google Earth© 2018

aggradation of the Plain, channel incision most likely resulted from increased precipitation and runoff. Langford-Smith inferred that during a waning pluvial period of climate change, progressive aggradation of prior-stream channels occurred.

The work of Pels (1964) was the next contribution to this research which argued that the differences in hypotheses between Langford-Smith and Butler stemmed from the failure to identify two distinctly different paleochannel types. Pels (1964) described in detail what he called "ancestral rivers" which were a set of paleochannels thought to post-date the prior streams and be the direct precursors of the modern drainage channels. He argued that the youngest stratigraphic unit (Coonambidgal) described by Butler (1958) was part of the ancestral river systems and more complex than first reported. According to Pels (1964) the ancestral rivers were deep, sinuous channels without levees and carried predominately suspended load sediment. Unlike the prior streams which appear to have aggraded and terminate on the Plain, the more recent ancestral rivers maintained their course across the Plain and exited as powerful rivers. In total, Pels had identified three phases of ancestral rivers, each formed by channel incision during humid periods and abandoned by aggradation during periods of waning river discharge and increased aridity (Pels, 1971). Schumm (1968) supported the prior stream–ancestral rivers paleochannel model and estimated that the ancestral river of the Murrumbidgee River had a bankfull discharge of nearly 5 times greater than the modern river. However, Bowler (1978) reported gravel and coarse-grained ancestral river sediments similar to that of the prior streams, which contradicted the finding that ancestral rivers carried mostly suspended loads, not coarse sand and gravel. The view held by Pels (1971) and Schumm (1968) was therefore rejected by Bowler (1978) who hypothesized that, in time, aggradation of ancestral channels might result in the development of prior stream characteristics. He also questioned Pels's (1971) cyclic incision-aggradation model of ancestral channel development and proposed instead a long period of high discharge and greater transport of coarse bedload sediment during the late Pleistocene, then followed by a shift to the present suspended load, lower discharge regime near the time of the Last Glacial Maximum (LGM).

Depictions of prior stream and ancestral river stratigraphy proposed by various authors in the literature are shown in Figure 4-8. The interpretations of the channel stratigraphy are however based on a limited 30 ka chronology established by the works of Bowler (1967), Butler (1958), and Pels (1964). The original model of paleochannel stratigraphy developed by Butler (1958) (Figure 4-8A) identifies lenses of gravelly sand confined to infills of incised channels. Next to the

channels are low levees and laterally tapering wedges of overbank alluvium with increasing clay content with distance from the channels. In Figure 4-8B, Schumm (1968) modifies Butler's diagram by the overbank wedges, highlights the cut and fill sequences of the channels, and notes the "shoestring" nature of the channel infills. Pels (1966) and Bowler (1978) (Figure 4-8C and 4-8D, respectively) provide cross sections of the ancestral Murray River, showing a sequence of basal gravel and sand, capped off with an approximate 3 m of medium and heavy clay. These fining-upwards deposits were approximately 2 km wide and interpreted as stream deposits whose discharge had waned in response to arid climatic conditions. Bowler (1978) challenged this interpretation by concluded that although the channels' sedimentation was thick gravel and sand beds overlain by sandy loam and clay, these were deposits of large, laterally migrating mixed-load stream. However, a better understanding of paleochannel formation, geomorphology, and sediment deposition on the Riverine Plain was not obtained until a more robust chronology of the channel deposits was established.

4.4.2 Revised formation of Riverine paleochannels

Stratigraphic profiles and boreholes of the Murrumbidgee River paleochannel systems (Page and Nanson, 1996) along with comprehensive efforts in thermo luminescence (TL) dating of paleochannel sediment throughout the Riverine Plain (Banerjee et al., 2002; Page et al., 1991, 1996) provided evidence of a new model of channel evolution, which resolved many of the discrepancies found in the literature regarding the sequential prior-ancestral model. These studies provide strong support for Bowler's (1978) doubts regarding the accepted model describing the sequential paleochannel evolution of the Riverine Plain from early 'prior streams' which were bedload-dominated, to later 'ancestral rivers' which were characterized as suspended load. Extensive TL dating of the Murray and Murrumbidgee sector paleochannels was conducted by Page et al. (1991) which revealed a 100 ka record of fluvial (paleochannel) activity on the Plain, which extended the radiocarbon-based chronology, and called into question all previous chronologic and stratigraphic interpretations of the last 40 years. Page et al. (1991)

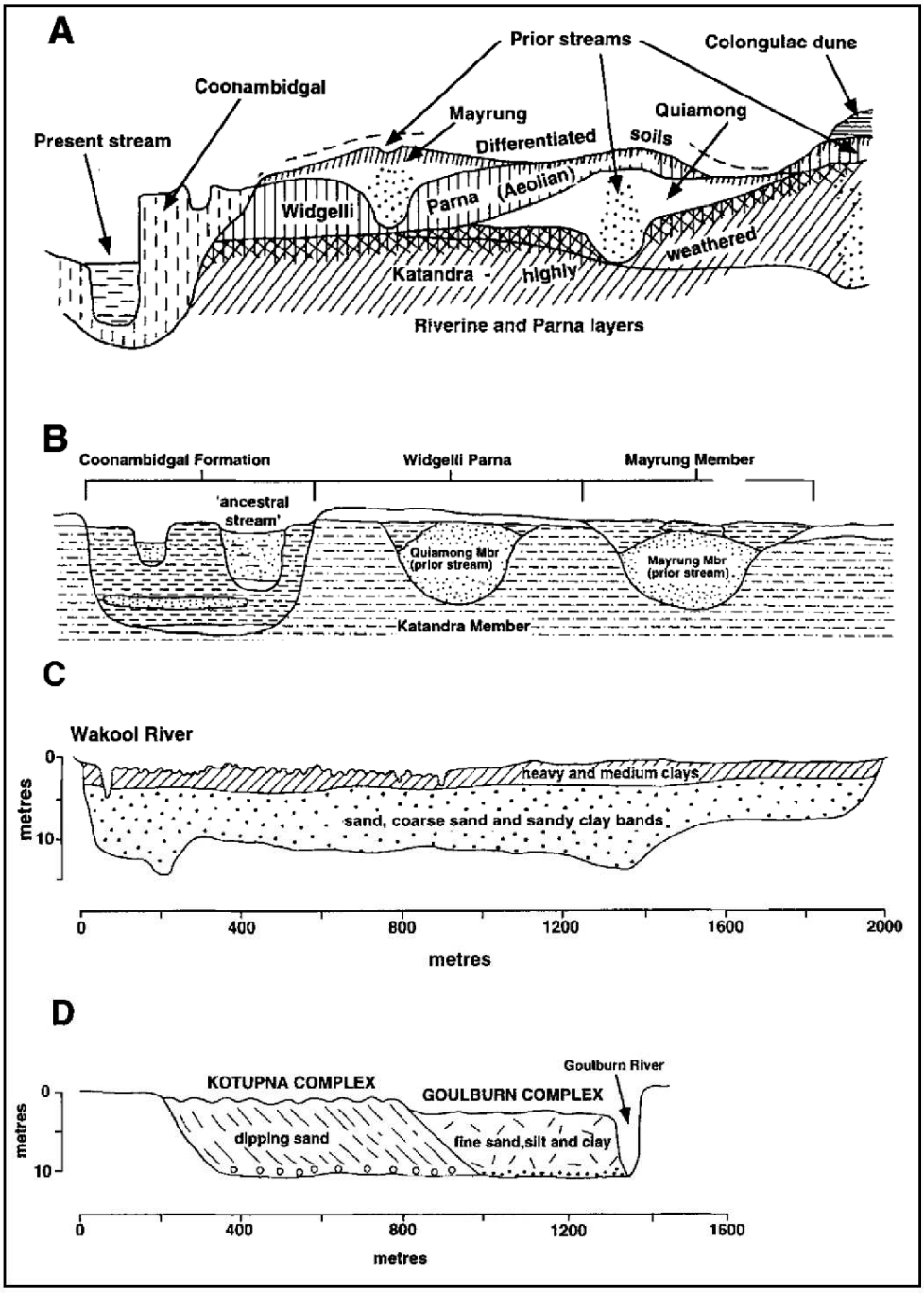

Figure 4-8. Riverine Plain paleochannel stratigraphic models. A) Butler's (1958) generalized model showing the relationship between 'prior' stream deposits, aeolian parna and younger Coonambidgal 'ancestral' deposits. B) Schumm's (1968) arroyo-style version of the Butler model. C) bore hole section across the 'ancestral' Murray showing laterally extensive fining-upwards alluvium. D) Bowler's (1979) river bank section showing lateral migration deposits of the Kotupna Complex and inset Holocene alluvium of the Goulburn River. Source: re-drawn from Page and Nanson (1996)

concluded that the simplistic model of early prior streams and later ancestral river with fundamentally different characteristics, a theory that gained significant support (e.g. Butler, 1950; Pels, 1971; Schumm, 1968), could no longer be supported. Surficial deposits in the Murray sector in the south of the Plain were originally TL-dated and although the antiquity of the paleochannels was demonstrated, tectonic movement in the region was noted to cause disruption of drainage in the vicinity of the Cadell Fault, hence complicating any interpretation of riverine response to climate variability (Page et al., 1996). The search for a better site lead to the tectonically stable Murrumbidgee sector where an equally complex system of paleochannels developed from the confined upstream valley near Narrandera.

In combination with extensive TL-dating, Page and Nanson (1996) studied many stratigraphic profiles in each of the paleochannel systems in the Murrumbidgee sector and reported that paleochannels aggraded with coarse sand and connected laterally to varying sequences of fining-upward alluvium that rest on a truncated clay basement (Figure 4-9). Paleochannel sequences are diagnostic of lateral migration by mixed-load systems and suggest that the older systems experienced alternate episodes of channel activity and occasional transitions from laterally migrating mixed-load mode to vertically aggrading bedload mode. According to Page and Nanson (1996), the complete evolution of an aggradational paleochannel consists of the following general steps: 1) establishment of a laterally migrating, sinuous, mixed load channel with occasional short-lived bedload accretion events; then 2) a shift to an aggrading bedload-dominated channel in response to a change in the sediment/water delivery ratio; and finally 3) channel avulsion and establishment of a new mixed-load sinuous system elsewhere on the alluvial plain.

The terminology used by previous studies (e.g. Butler, 1958; Pels, 1964) such as ‘prior’ and ‘ancestral’ streams was based on several inaccurate assumptions related to both channel chronology and formation. The older ‘prior stream’ which were thought to be older and characterized as laterally stable bedload-carrying streams were actually largely mixed-load streams characterized by periodic episodes of significant lateral accretion. Their termination feature, however, is a bedload-dominated phase of vertical aggradation; this is the facies sampled in most studies, including this study (described below). Page and Nanson (1996) termed

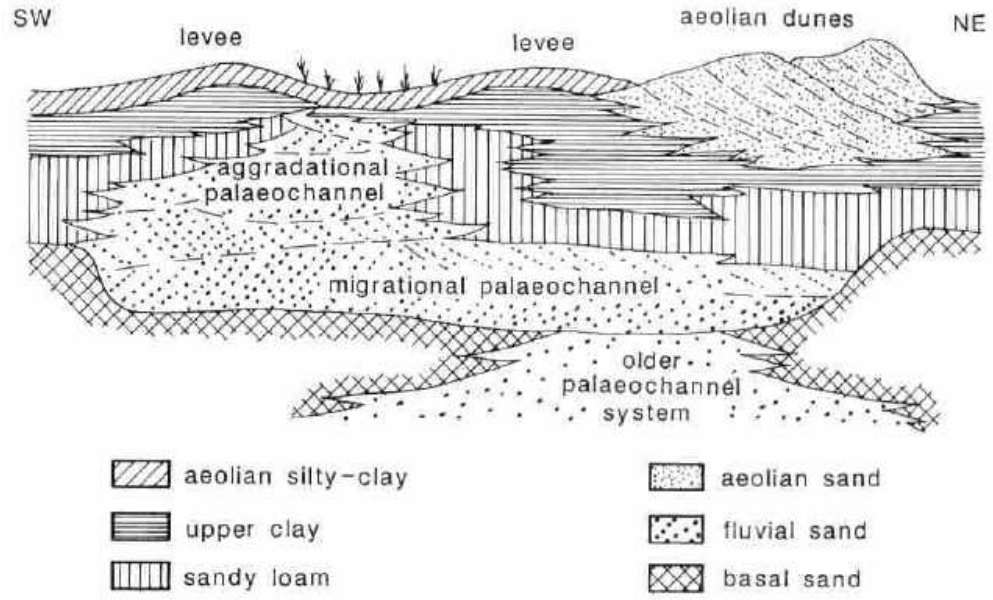

Figure 4-9. Revised model of the Riverine Plain paleochannel stratigraphy displaying sequential development of a migrational mixed-load system and an aggradational bedload system. Source: Page and Nanson (1996)

these aggradational paleochannels, which on the plain surface appear to have low sinuosity, levees, and no visible scrolls. Ancestral river is the other type of paleochannel, described as highly sinuous with visible scrolls, and thought to be much younger. We now know that these channels were created by lateral migration, similar to the early phases of the aggradational paleochannels, however did not terminate in an aggradational phase; these are termed migrational paleochannels by Page and Nanson (1996). According to the Page et al. (1996) chronology, both types of channels were coeval and therefore occurred on the Plain simultaneously, often in different reaches of the same paleochannel system and having substantially larger discharges than modern rivers on the Plain.

Through extensive TL dating of paleochannel sediments in the Murrumbidgee sector, Page et al. (1996) identified four sequential phases of paleochannel activity: the oldest being the Coleambally System (105 – 80 ka); then Kerarbury System (55 – 35 ka); Gum Creek System (35 – 25 ka); and pre- and post-LGM, Yanco System (23 – 14 ka) (Figure 4-10; Table 4-1). These dates were confirmed by Banerjee et al. (2002) and extensive OSL dating of the Gum Creek and Yanco Systems by Mueller (2017). However, there is one sample (MYA-2#4 uow 1523) dated by Mueller (2017) which dates the Yanco system at 32 ka, which is much older than all other dates

of the system. However, because the Yanco and Gum Creek paleochannel intersect at the site location, Mueller (2017) concluded that the deposit was likely part of the Gum Creek System, not the Yanco. Out of convenience, it is helpful to summarize patterns of environmental change over the last full glacial cycle in relation to the well-established deep-sea oxygen isotope record of Shackleton and Opdyke (1973), which identifies five major climatic phases (Figure 4-10). These stages correlate well with documented phases of enhanced fluvial and lacustrine activity in southern Australia and within the Murrumbidgee paleochannels (Kershaw and Nanson, 1993; Nanson et al., 1992; Bowler, 1986); particularly during Oxygen Isotope Stages 3 and 5. Estimates of paleo-bankfull discharge (Page, 1994), obtained by paleochannel cross-section reconstructions, indicate that the discharge of the channel systems exceeded that of the modern Murrumbidgee River by approximately 4 – 8 times (Table 4-2).

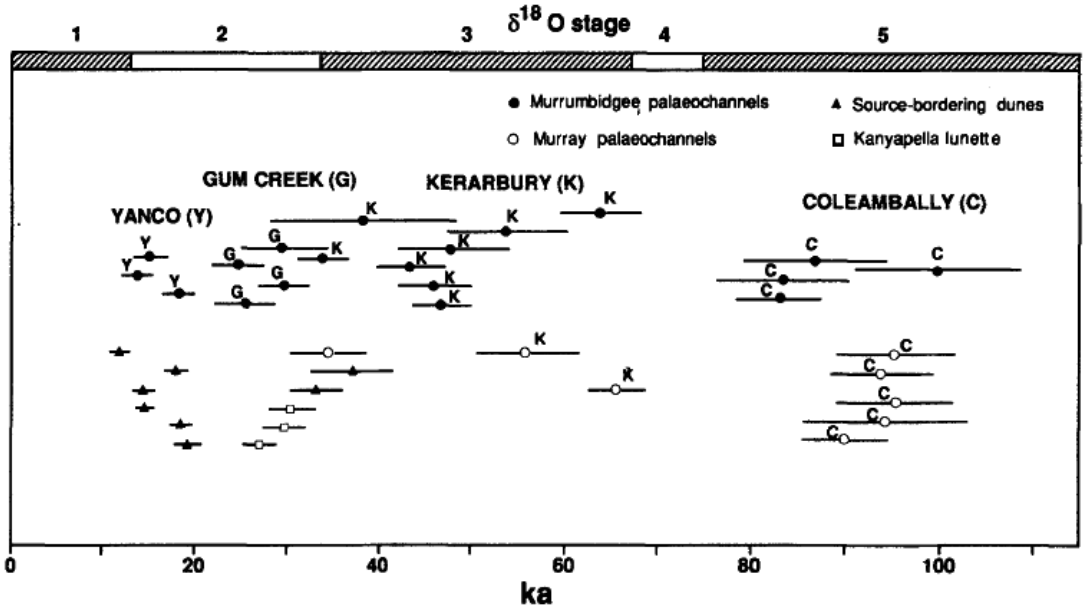

Figure 4-10. TL dates for fluvial and aeolian sediments taken from the Murrumbidgee and Murray-Goulburn sectors of the Riverine Plain. Murrumbidgee data source: Page et al. (1996); Murray-Goulburn data source: Page (1994) and Page et al. (1991); Oxygen isotope stages data source: Shackleton and Opdyke (1973); Source of figure: Page et al. (1996)

Although climatic variability is clearly implicated in the estimated higher peak discharges of each distinct channel system over the last 100 kyr, a major continental-scale climatic forcing

Table 4-1. TL dates of paleochannel sediments taken from the Murrumbidgee sector of Riverine Plain

Sample	System	Site	Age	+/-
W746	Kerarbury	Hay Pit	47	3
W906	Kerarbury	Kerarbury pit	46	3.8
W938	Kerarbury	McGrath Pit	38	10
W1360	Kerarbury	Moulamein Pit	34	2.5
W1361	Kerarbury	Booroorban Pit	54	6.6
W1362	Kerarbury	Romani Rd Pit	48	6.1
W1363	Kerarbury	Moulamein Pit	43	3.7
W1445	Kerarbury	Booroorban Pit	64	4.1
average			**47**	**9**
W745	Coleambally	Kulki Pit	87	7.5
W758	Coleambally	Gala Vale Pit	84	7.1
W904	Coleambally	Bundure Pit	100	9
W1446	Coleambally	Moul. East Pit	83	4.5
average			**88**	**8**
W995	Gum Creek	Godeldrie Scar	26	3.5
W996	Gum Creek	Old Homest Pit	30	2.9
W997	Gum Creek	Tabratong Sect	25	2.8
W998	Gum Creek	Tabratong Pit	29	4.6
MGCY-5#4 uow 1315	Gum Creek	Yarrada Lagoon West	33	1.8
MGC 4-4#5 uow 1322	Gum Creek	Yarrada Lagoon	34	0.2
MGC 4-4#4 uow 1314	Gum Creek	Yarrada Lagoon	32	1.7
MGCY 5#7 uow 1391	Gum Creek	Yarrada Lagoon West	34	2
MGC 2-1 clay uow 1306	Gum Creek	GC at Darlington Pt	37	2.1
MGC 8-3#5 uow 1390	Gum Creek	Un-named	33	1.7
MGC 8-3#5 70 uow 1389	Gum Creek	Un-named	36	1.8
average			**32**	**4**
W1557	Yanco	Thurrowa Rd Pit	15	2
W1558	Yanco	Wanganella Pit	14	1.6
W1559	Yanco	Rhyola Section	18	1.5
MYA-2#4 uow 1523	Yanco	Yanco at Bundure	32	1.7
MYA 1#6 uow 1521	Yanco	Yanco at Morundah	20	1.2
MYA 2#3 uow 1522	Yanco	Yanco at Bundure	23	1.4
MYA 1#4 uow 1520	Yanco	Yanco at Morundah	21	1.2
average			**21**	**6**

Sources: Page et al. (1996) and Mueller (2017). Errors on the average ages are 1 SD.

might not be necessary to explain the channel stratigraphy which demonstrates frequent shifts from stable laterally migrating mixed load facies to aggrading bedload facies (Page and Nanson, 1996). For example, if the shifts were caused by major climate change in the Murrumbidgee River catchment, then repeated climatic shifts within the catchment during a single oxygen isotope stage would need to have occurred to explain the higher frequency of channel shifts, which is not documented in the wider regional or global climatic records (Porter, 1989). The likely explanation for channel shifts is the channel's response to threshold exceedance, rather than major environmental or climatic change (e.g. Brizga and Finlayson, 1990; Nanson and Erskine, 1988). For instance, a modest change in channel bankfull discharge and slope (in response to reduced channel sinuosity) could greatly affect the river's morphology according to the Lane's (1957) scale which separates meandering from braiding streams; e.g. an increasing of bankfull discharge and slope by factors of 2 and 5, respectively, would change the category in which Murrumbidgee paleochannel systems are placed: from meandering to the intermediate zone between braided and meandering (Lane, 1957) and above Ferguson's (1987) transition from sandy non-braided to sandy-braided streams. In addition to Page and Nanson (1996) who propose this hypothesis to explain channel shifts, Schumm (1979) also supports the idea of stream response to threshold exceedance and suggest that streams within the zone between braided and meandering are most prone to sudden changes in river morphology. Page and Nanson (1996) also suggest that shifts from mixed load migrating to bedload aggrading were likely initiated by floods which mobilized large amounts of coarse sands from the upper catchment. After the flooding waves carried sediments onto the Plain, the combination of decreased stream slope and minimal tributary input resulted in a downstream reduction of peak flows such as that observed in the modern system. This theory is in line with modelling efforts that predict that a 50% peak reduction across the Plain compared to present values would lead to the majority of the sediment entering the eastern Plain not to reach to the outlet in the western Mallee region (Page, 1994). The excess sediment would have entered the channel and floodplain storage during a flood event and contributed to bedload aggradation, channel shoaling, levee and marginal dune formation, and finally lead to the formation of channel distributaries by avulsion (Page and Nanson, 1996). Upon the reduction of bedload input, the new channel would re-establish itself with laterally migrating, mixed load characteristics.

Table 4-2. Estimated bankfull discharges of Murrumbidgee sector paleochannel systems on the Riverine Plain based on reconstructed cross-sections.

System	Reach	Slope	Mean depth (m)	Width (m)	Mean velocity ($m\ s^{-1}$)	Bankfull discharge ($m\ s^{-1}$)	Paleo-discharge ratio
Coleambally	Bundure	0.00025	6.5	165	1.59	1740	5.6
Kerarbury	Waddi	0.00026	7	220	1.7	2610	8.3
Gum Creek	Tombullen	0.00018	5	215	1.13	1220	3.9
Yanco	Rhyola	0.0001	5.5	250	0.9	1240	4.5

Discharges were calculated using the Manning Equation and 'n' value of 0.035 at each section. Paleo-bankfull discharges on the Coleambally, Kerarbury and Gum Creek systems were compared to modern bankfull discharge of the Murrumbidgee River at Darlington Point (313 m^3s^{-1}) and on the Yanco system compared to present bankfull discharge of the Murrumbidgee River at Hay ($278m^3s^1$). Source: Page (1994).

4.4.2.1 Coleambally System

The Coleambally paleochannel system is the oldest set of paleochannel to be TL dated and is located near the Coleambally Irrigation Area. Four TL ages of the Coleambally system range from 100.0 ± 9.0 – 83.0 ± 4.5 ka (Table 4-1) and lie within Oxygen Isotope Stage 5, a time of enhanced fluvial activity in Australia's northern and inland river systems (Nanson et al., 1992). Estimated paleo-discharge for the Coleambally system is 1,740 m^3s^{-1} (Page, 1994); making it the second greatest of the four paleochannel systems (Kerarbury is the first) and 5.6 times greater than the modern system. The system consists of two main arms that correspond to the Central and Southern prior-streams (Schumm, 1968), which are the Yamma and Bundure Arms. Both arms can be traced back to a single paleochannel that emerges from the modern Yanco Creek floodplain (Figure 4-11), however the Yamma Arm can be traced downstream generally to Booroorban, nearly 100 km west of the arm formation, while the Bundure Arm heads southwest for less than half that distance. Because the Bundure Arm pre-dates 100 ka BP, its limited lateral extent is consistent with a short duration and therefore a period post-dating the last interglacial maximum of Oxygen Isotope Stage 5e (Chappell and Shackleton, 1986). The Bundure Arm extends laterally for between 1300 – 600 m and indicates alternate phases of lateral migration and vertical aggradation. However, the channel activity did not terminate with an avulsion, rather with lateral migration over a distance of 550 m (Page and Nanson, 1996). Trough and crossed-bedded coarse sand at pit exposures suggest that it was a wide, shallow channel bordered by levees and occasional aeolian dunes in the northeast section. Source-bordering dunes are present to the east and north of

the Yamma Arm, while being absent along the Bundure Arm. Page et al. (1996) suggests that this difference may indicate that the two channels were not contemporaneously active and that migration of marginal dunes across the Bundure Arm may indicate that the Bundure Arm is older. The Bundure channel intersects sands from an underlying sequence of earlier paleochannels which possibly extend more than 20 m below the present ground surface.

No TL-dated sediments yielded ages between 80 – 70 ka on the Riverine Plain and only 3 samples yielded ages between 70 – 55 ka (Page et al., 1996). Therefore, the period between the Coleambally and Kerarbury systems (approximately 80 – 55 ka) was likely one of significantly reduced fluvial activity. This period overlaps Oxygen Isotope Stage 4 which correlates with a major dust peak in the Antarctic Vostok ice core (Petit et al., 1999), suggesting widespread aridity at that time.

4.4.2.2 Kerarbury System

Kerarbury system paleochannels are the second oldest paleochannels in the Murrumbidgee River system, after the Coleambally system, and lie within Oxygen Isotope Stage 3 and border early Stage 2 (55 – 35 ka) (Page et al., 1996) (Table 4-1). This system is relatively complex, large, and forms a vast distribution of channels across the Riverine Plain. Major distributaries include the McGrath, Benerembah, Hay, and Romani Arms. It is an aggradational system that includes the northern prior-stream described by Schumm (1968) and channels southwest of Griffith mapped by Pels (1964). The estimated bankfull discharge of the Kerarbury System is 2610 m s^{-1}, making the Kerarbury System the largest of all paleochannels on the Riverine Plain in terms of discharge volume. The stream trunk can be traced from Tombullen Swamp in the northeast across the Plain to Moulamein in the southwest where it is obscured by more recent channels and floodplains of the Edward and Murray Rivers (Figure 4-11). The modern Murrumbidgee River and Gum Creek paleochannel system cut through the Kerarbury system in the northeast, both which largely post-date it. Unlike the Coleambally system, this system flowed completely across the Plain and exited as a powerful river. Near the town of Moulamein, the main Kerarbury channel is well defined, occurring as a slightly elevated sinuous depression. The spatial extent of this paleochannel system demonstrates that not all "prior" aggradational systems dissipate on the Plain. As with Coleambally, the distinct red color of the sediment is associated with pedogenesis of the sediments

which has produced red duplex profiles with abundant pisolitic carbonate (Page and Nanson, 1996). The channel infills are characterized by fining-upward sequences of coarse sand, loam and clay above the nearly horizontal clay basement. These sequences provide sufficient evidence of lateral channel migration more than 1000 m wide by a stable mixed load channel. Channel boreholes of the Mcgrath Arm reveal that the Kerarbury system is overlaying a westward flowing, deeper paleochannel system which was described by Pels et al. (1968). Sedimentation in this older system is similar to that of the Kerarbury and older Coleambally system showing a horizontal truncated clay layer at 14 – 15 m below the surface overlain by a fining upward sequence of coarse sand, loam, and clay. Alternate periods of mixed-load lateral channel migration and bedload aggradation are present, indicating that channel formed under similar hydrologic conditions as the Kerarbury and Coleambally systems and though not TL-dated, this system could have been active during the penultimate glacial cycle (before 130 ka) (Page and Nanson, 1996).

4.4.2.3 Gum Creek System

The Gum Creek system is generally composed of upstream migrational and downstream aggradational paleochannels (Page and Nanson, 1996) and corresponds to the sinuous 'ancestral' Murrumbidgee system described by Schumm (1968). Channels in the Gum Creek date from 35 to 25 ka (Page et al., 1996) coinciding with early to mid-Oxygen Isotope Stage 2. This system is distinctly different from the slightly older Kerarbury system in terms of morphology and discharge; it is estimated that the system's bankfull discharge was only 4 times larger that of the modern Murrumbidgee river, making it the smallest of the four paleo-river systems (Page, 1994) and highly sinuous and laterally-migrating in upstream regions carrying suspended load rather than bedload. It forms a complex anabranching pattern along the modern Murrumbidgee floodplain (Figure 4-11). The Gum Creek system is subdivided into three downstream reaches: Tombullen Reach (Narrandera to Yarradda); Oolambeyan and Carrathool Reaches (Yarradda Laggon to Hay); and, Uara Reach (Hay to Balranald). Upstream of the Yarradda laggon, the Tombullen Reach generally follows the modern drainage flow leaving behind remnants of large meander scars and scroll patterns on the present floodplain; this indicates it was a laterally-migrational paleochannel in this region (Page et al. 1996b). Further downstream, the Oolambeyan and Carrathool Reaches form an anabranching distributary system, with the Oolambeyan arm being superimposed by a modern

suspended load channel often carrying floodwaters and directed irrigation water. It is possible that both reaches operated simultaneously and together carried the total discharge from the Tombullen Reach upstream. The Carrathool Reach, which parallels the present floodplain for nearly 30 km, is cut by the modern Murrumbidgee and branches into three separate distributaries near Hay. Further west on the Plain, the Gum Creek continues in the Lowbidgee region in the Uara Reach.

Boreholes at the Tombullen Swamp where the Gum Creek intersects the older Kerarbury system show a heavy clay basement stratigraphy from 5 – 6 m below the surface which is overlain by 0.5 – 2.0 m of coarse sand that grades upwards to sandy clays, and finally a surficial heavy grey clay layer. The fining-upward sediment are typical of laterally migrating mixed-load streams and resemble the lateral migration facies of the older Coleambally and Kerarbury systems (Page et al., 1996a). The upstream portion of the Oolambeyan and Carrathool Reaches remains highly sinuous with auger holes revealing 2.5 – 5.0 m of fine-grained sediment overlaying 1 – 4 m of coarse sands with a maximum channel depth of 7.5 m. Further downstream, the channel becomes less sinuous and is intersected by the Murrumbidgee River at Tabratong Station (20 km east of Hay, Figure 4-11). A northern bank exposure shows fine-grained pedogenically-altered sediments with embedded carbonate pisoliths near the surface which rest on cross-bedded coarse sand infill and a clay paleosol base (Page and Nanson, 1996). The aggradational or "prior stream" characteristics of the paleochannel system and young (24.7 ± 2.8 ka) (Page et al., 1996) TL date at this location provide clear evidence that aggradational paleochannel characteristics are not limited to older channel systems and disproves the prior-ancestral theory stating that these system characteristics were chronological with aggradational/prior streams being older. In the western Uara Reach, the Gum Creek forms a branching system of aggradational arms, with some channels petering out and others modern depositional environments in the Lowbidgee region.

4.4.2.4 Yanco System

The Yanco system is the youngest of the four paleochannel systems described by Page et al. (1996) and Page and Nanson (1996), who first dated these sediment deposits and source-bordering dunes to be between 18.2 ± 1.5 to 13.6 ± 1.6 ka. However, more recent dating by Mueller (2017) reports the average age of Yanco system sediments to be 21 ± 6 ka (1 SD, n = 7) which would make the system both pre-LGM and post-LGM. Unlike the older paleochannel systems, the

Yanco system is entirely migrational (failing to terminate with bedload aggradation) and can be traced from west of Narrandera across the Plain westward to Moulamein (Figure 4-11). The system has a slightly trenched floodplain belt approximately 1 – 3 m below the surface of the Plain, with widths upstream of Murundah at their maximum of 5 km and downstream minimum widths of 2 km (Page and Nanson, 1996). The Yanco is a large system with impressive dimensions and continuity across the Plain; the estimated bankfull discharge of the Yanco system is 1240 m s^{-1} which is about 4.5 times larger than that of the modern Murrumbidgee at Hay. It has scroll-patterned floodplains, large sinuous channels, and source-bordering dunes. Sediment from pit exposures at Thurrowa Road and Wanganella Station show a thin layer of fine-grained alluvium deposits from the modern Yanco and Billabong Creeks overlying sand clays and coarse paleochannel sands of the Yanco system. In the upstream Thurrowa Road pit, there is about 2 m of fine-grained surface sediment that lies on top of approximately 4 m of yellowish-brown and grey coarse sand layers. Downstream sediments at Wanganella Pit also show a grey clay surface unit graded to brown sand clays, followed by coarse sand down to 5.4 m, with a clay basal unit at the bottom of the profile. West of Wanganella, surveying and drilling evidence reveal a well-preserved channel cross-sections 200-250 m wide which are filled with 3 m of coarse sand, capped off with a 1-m unit of light to heavy clay.

Having discussed in detail the previous work on the Murrumbidgee catchment paleochannels and the environmental and climatic conditions in southeast Australia over the last approximately 100 ka that led to their formation, I will now move on to my current study which focuses on the reconstructing the paleo-weathering regime of paleochannel sediments in each of the four paleochannel systems on the Riverine Plain in the Murrumbidgee River catchment described in the literature (Banerjee et al., 2002; Page and Nanson, 1996; Page, 1994; Page et al., 1991), using boron isotopes as my principle proxy for interpreting the sediment's response to climatic variability

4.5 **Riverine Paleochannel Study**

4.5.1 Field Sites

In this study, paleochannel sediments were collected from the 4 major fluvial phases on the Riverine Plain: Coleambally (105 – 80 ka); Kerarbury (55 – 35 ka); Gum Creek (35 – 25 ka); and Yanco (14 – 23 ka). In order to determine if the chemical and isotopic composition of paleochannel sediment is homogeneous along a single reach or if systematically evolves as it travels downstream, multiple sampling points (upstream and downstream) along a single reach was sought after. This was accomplished in all paleochannel systems besides the Coleambally, where downstream sampling locations could not be accessed. To compensate for this, several upstream locations were sampled, including different reaches of the same paleochannel system. Sampling locations in this study of the Murrumbidgee River paleochannel systems on the Riverine Plain are displayed in Figure 4-11. Channel sediment ages were obtained by TL and OSL dating from previous studies: Mueller (2017); Page et al. (1996), and (1991); and Banerjee et al. (2002). In the Yanco System, five locations were sampled, four upstream: Yanco at Morundah; Thurrowa Road; Yanco at Bundure; and Yanco A, and one downstream: Wanganella Pit. In the Coleambally System, three sites were sampled, all upstream: Gala Vale; Gala Vale South; and Bundure Pit. In the Kerarbury System, two locations were sampled, one upstream: Kerarbury Pit, and one downstream: Booroorban Pit. In the northernmost channel system, the Gum Creek, four locations were sampled, three upstream: GC at Darlington Point, Yarradda Lagoon, and Yarradda Lagoon West, and one downstream: Tabratong. Below I will describe each of the sites and profile stratigraphy on a system-by-system basis and display sampling locations. There are a number of sites from the Yanco and Gum Creek Systems that were not sampled as part of this project and therefore cannot be described in great detail. These samples were taken deep in each profile by coring with a drill rig and not collected in the same manner as other samples were in this project. The stratigraphical context of these sample are reported in Mueller (2017). Here, I report all core sample locations (Figure 4-11), depths, and OSL ages (Table 4-1), including the core samples taken by Mueller (2017) from the three upstream Gum Creek locations (GC at Darlington Point, Yarradda Lagoon, and Yarradda Lagoon West) and two upstream Yanco locations (Yanco at Morundah and Yanco at Bundure).

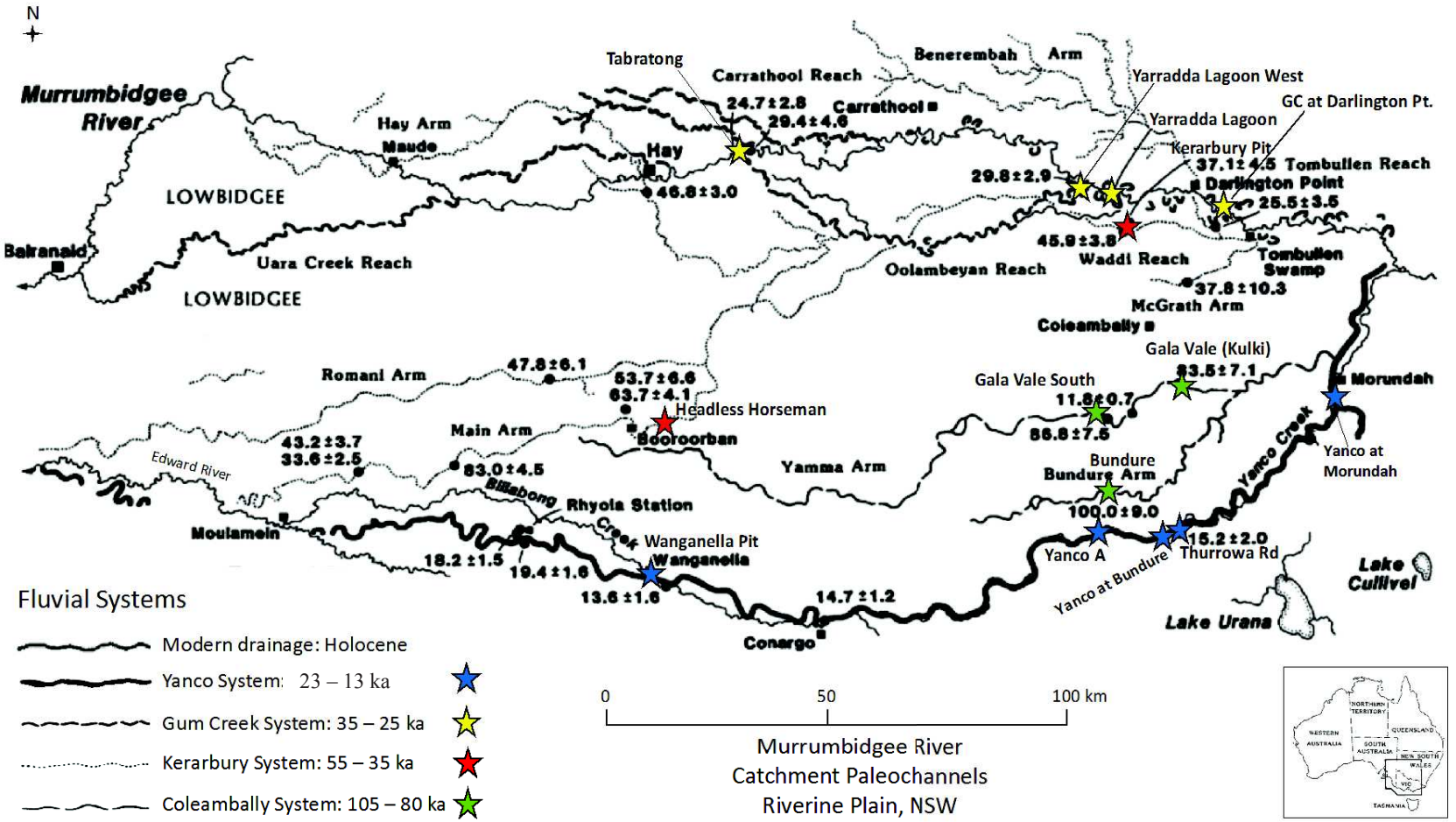

Figure 4-11. Map of Murrumbidgee River paleochannel systems on the Riverine Plain displaying sampling locations (stars) in this study and channel dates obtained by Page et al. (1996). Source of main panel and inset: re-drawn from Page and Nanson (1996)

YANCO SYSTEM (23 – 13 ka)

Yanco A
GPS: 35.1481967°S, 145.7683284°E; Elevation: 117 m

Site Description: This pit is in the middle of a flat field, near the modern Yanco River.

Profile Description: The pit shows clear stratigraphy. The outer exposed face of this wall is very brittle. The top soil layer is organic-rich and contains several imbedded greyish clay layers, which continue for approximately 1 m deep. This top layer is likely alluvial. Below this there is a series of coarse-grained paleochannel sand layers. The upper layer is a distinct light brown/white layer at 1 m depth, which is clay-rich and not as brittle as the other layers in the profile. Below this is a thick reddish layer composed of coarse-grained sand about 30 cm thick. Below this layer, again is a coarse-grained orange sand layer which transitions into a whitish coarse-grained sand layer. The entire exposed wall is approximately 3 m in thickness, however the section sampled is 2 m thick.

Notes: The pit is located about 50 m SW from where the road ends. It appears that this face has been exposed for quite some time and looks and feels dry, brittle and weathered. The face was cleaned as best as possible to avoid sampling weathered soils at depth.

Site photos and sample locations:

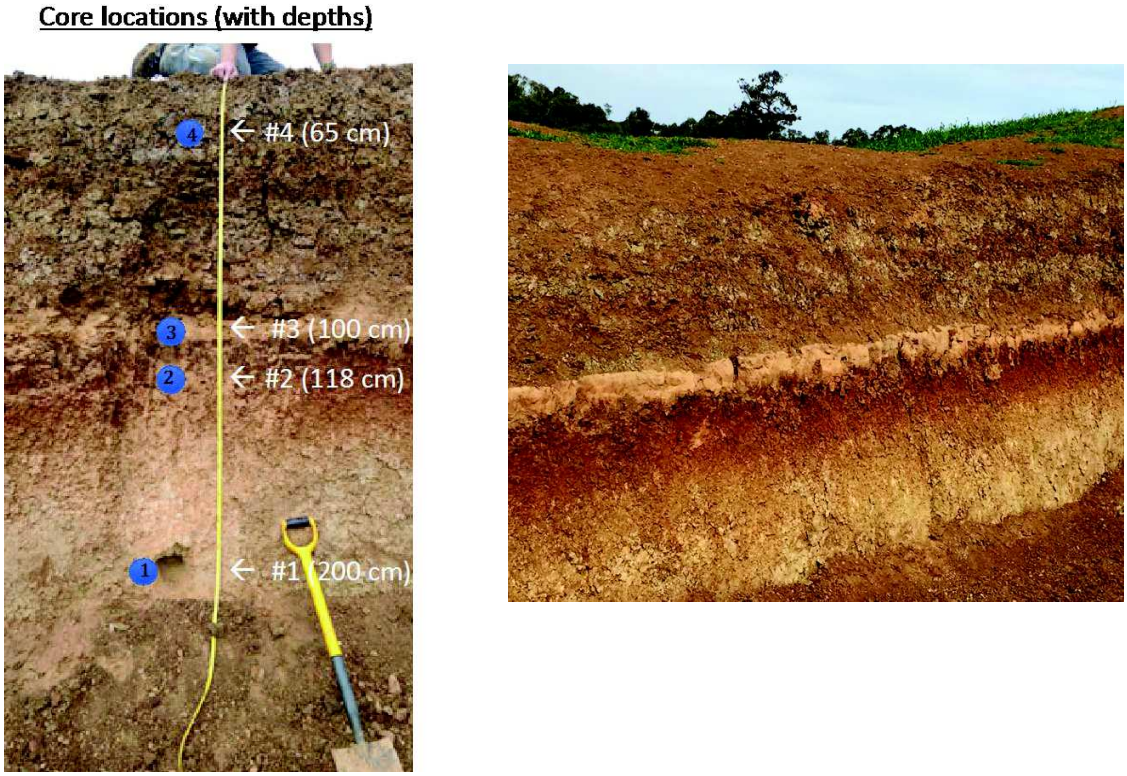

Figure 4-12. Yanco A paleochannel site, Yanco System

Thurrowa Road

GPS: 35°9’7.57”S 145°56’14.60”E

Site Description: This pit was a former mining area, likely excavated for gravel/fill material for road construction. The pit is located on the south side of Thurrowa Road.

Profile Description: The total profile thickness according to Page and Nanson (1996) is approximately 6 m; the top 370 cm of this profile was accessible and sampled. The top soil layer is quite thick, measuring 80 – 100 cm in thickness, and is a fine-grained clay-rich organic layer. Below this, lie approximately 2 m of alluvium with friable pedogenic carbonate (not pisoliths) (Page and Nanson, 1996). Below this, from about 2 – 6 m are white and orange coarse-grained sands visibly layered. A fining-upward sediment sequence is visible in some of the layers. The top white sand layer is fine-grained, overlain by the final layer orange layer of paleochannel infill. Overall, there are many changes in grain sizes throughout profile, likely indicating fluvial sorting a high energy environment.

Notes: The pit is subject to flooding and was covered in vegetation.

Site photos and sample locations:

Figure 4-13. Thurrowa Road paleochannel site, Yanco System

Wanganella Pit
GPS: 35°12’57.56”S 144°49’54.53”E

Site Description: Located south of the modern Yanco system. This pit is a former mining pit displaying a large (~250 m) cross-section of the system. Source-bordering dunes present outside the pit.

Profile Description: It appears that the top layer of this pit (alluvium), which is a white well-sorted coarse-grained sand has been eroding into the pit. The original paleochannel layers below this seem to be still intact. Below this top layer is a fine-grained white sand layer, then a reddish layer composed of a coarse-grained sand. Following down the profile, is a thin coarse sand\gravel layer about 1 cm in thickness. Below this a thick orange-red layer with imbedded white coarse sands. There is a color gradient in the profile: darker orange-red on the bottom transitioning to lighter closer towards the surface. Total profile is approximately 1 m.

Site photos and sample locations:

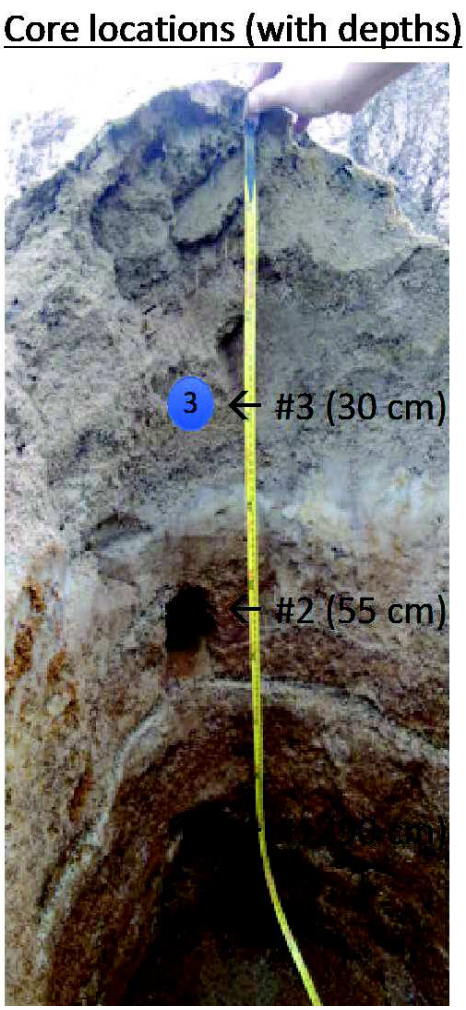

Figure 4-14. Wanganella Pit paleochannel site, Yanco System

GUM CREEK SYSTEM (35 – 25 ka)

Tabratong
GPS: 34°28.31964', 145°01.48696'

Site Description: This site is located near (about 30 m) back from the banks of modern Murrumbidgee River, approximately 20 km east of Hay. Both systems interact at this location. There are large (about 3 – 4 m) riverbanks on the modern river on both sides.

Profile Description: The entire exposed profile (north bank) is 150 cm in thickness and the base is approximately 10 m higher than the present river height The entire profile is approximately 6 m in thickness (Page and Nanson, 1996), therefore the paleochannel's true base is about 4 m higher than the modern river. There are three horizons. The top layer is a dark brown organic and clay-rich layer, about 50 cm in thickness. Below this layer is an orangish-brown sand. Both top layers appear pedogenically altered and contain $CaCO_3$ pisoliths. The bottom layer of the profile is a coarse-grained whitish sand and shows cross-beds, which evidences the aggradation character of this channel. There is a color transition from darker (modern sediments) on top to lighter (channel infill sands) down the profile.

Site photos and sample locations:

Figure 4-15. Tabratong paleochannel site, Gum Creek System

KERARBURY SYSTEM (55 – 35 ka)

Headless Horseman (Booroorban Pit)
GPS: 34°54’24.44”S 144°45’34.57”E

Site Description: This is located near the main road and is an old mining/gravel pit. The pit is approximately 5 m deep and about 150 m wide.

Profile Description: The entire profile is about 5 m in thickness; we were able to access and sample just the top meter. The top layer is a fine-grained reddish coarse-sand layer, 15 cm in thickness and appears weathered; there are roots present in this layer. Below is a coarse-grained gravel layer (channel fill) and is very hard. This layer is the largest and extends to the bottom on the profile which is 1 m in thickness. Within this white layers are many reddish coarse-grained sand laminations, occurring mostly at 70 – 80 cm. This coarse sandy channel infill continues to a depth of approximately 5 m with a basal clay layer (Page, 1994).

Site photos and sample locations:

Figure 4-16. Headless Horseman paleochannel site, Kerarbury System

Kerarbury Pit
GPS: 34°37'44.81"S 145°50'30.64"E

Site Description: Pit is located off of road A20 on the Kerarbury property, which is an orange grove. It is towards the back of the property with three exposed faces (north, south, and west). The south side appeared more weathered and penetrated by modern rainwater (Figure 4-17), so the more pristine northern face was sampled (Figure 4-18).

Profile Description: The entire profile is approximately 9 m; we were only able to access and sample the top 4 m. The top soil horizon is light brown and 15 cm in thickness with roots. From 15 – 60 cm is a truncated red-brown earth with $CaCO_3$ pisoliths. The rest of the profile displays co-sets of cross-beds in coarse and very coarse sand. The general thickness of these cross-beds is 10 – 20 cm. The sand is reddish-yellow in color with darker red laminations. These laminations are gravel-sized and show signs of sediment sorting. Some exposed faces on this side are now covered by modern muds which came from the organic, clay-rich soil layer, these were not sampled.

Notes: This was the first site visited. For each core taken, sediment was split between inside and outside, outside being 1-25cm from outer face to mid-pipe, and inside being 26-50cm mid-pipe to end of pipe. This was done to test if there might be differences in the sediment more exposed to surface processes and the sediment further in which likely has less interaction with surface weathering and therefore more pristine.

Site photos and sample locations:

Figure 4-17. Kerarbury Pit, south face (not sampled), Kerarbury System

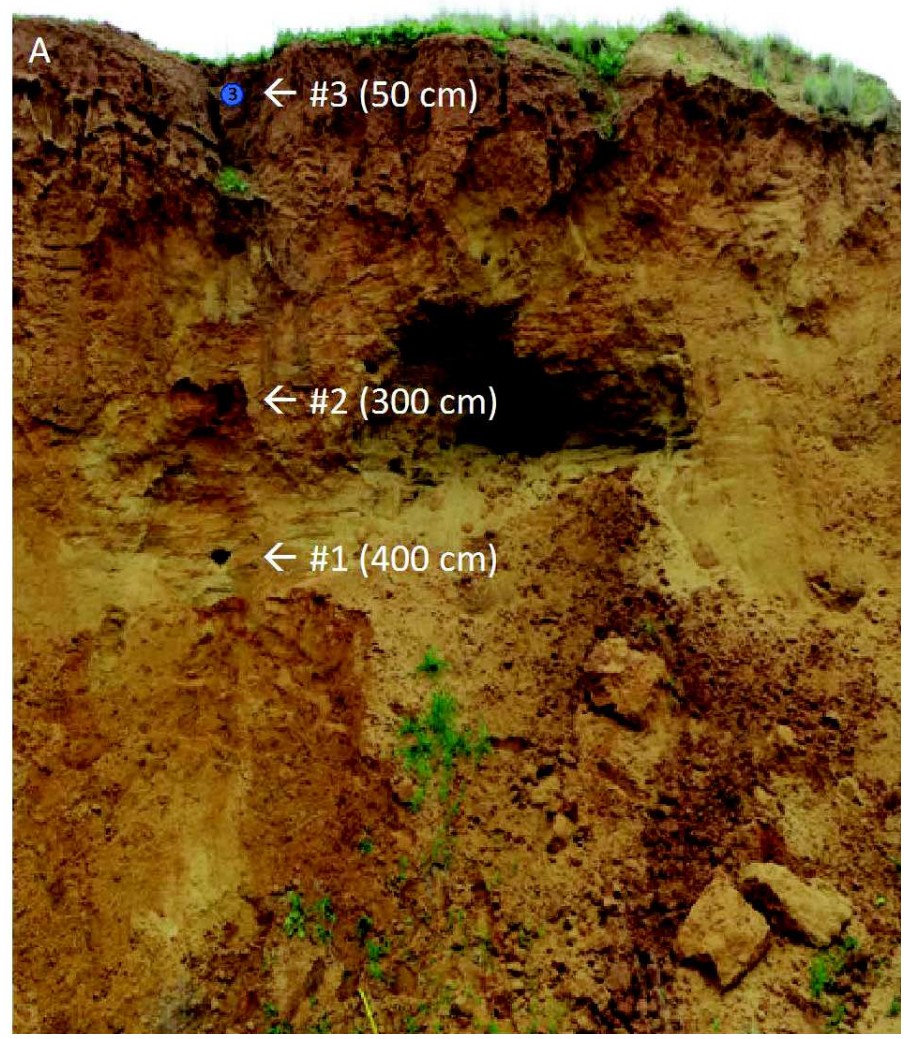

Figure 4-18. Kerarbury Pit, south face, Kerarbury System. A) Upper portion of profile (sampled); B) Surface layer showing sampling location and $CaCO_3$ pisoliths embedded in the top 60 cm of the profile

COLEAMBALLY SYSTEM (105 – 85 ka)

Gala Vale
GPS: 30°19.23392'S, 177°10.93240'E
Elevation: 125 m

Site Description: This site is a pit exposure near the side of the road main road. This site had been sampled and dated before (Page et al., 1996).

Profile Description: The entire pit exposure is approximately 130 cm in thickness. However, boreholes indicate that the channel fill extends to approximately 6 m. Stratigraphy at this site best corresponds to Page and Nanson's (1996) 'Yamma B' description (See below). Sediment within the profile is darker red on top and transitions to lighter down the profile (orange and then yellow). The top layer is 3 cm in thickness and is a hard clay layer, which prevents water from penetrating into the profile. Vegetation roots penetrated at least 80 cm though. Below the clay layer is the gravel/sand channel infill. No trough cross-beds or sediment sorting is present.

Stratigraphy of the Yamma B Arm of the Gala Vale system. Source: Page and Nanson (1996)

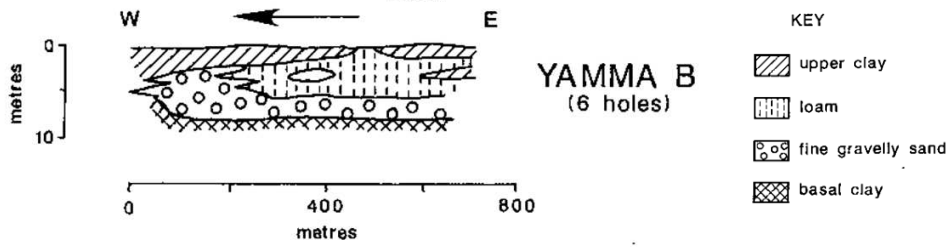

Site photos and sample locations:

Figure 4-19. Gala Vale paleochannel site, Coleambally System

Gala Vale South
GPS: 34°56.95565'S, 145°47.16573E
Elevation: 120 m

Site Description: This site was near the road on the way to the Kulki site (which was not sampled), near the town of Gala Vale.

Profile Description: The entire pit exposure is approximately 2.4 m in thickness. This site is also part of the Yamma Arm of the Coleambally system and is similar to Gala Vale. The entire paleochannel fill is about 6 m in thichness. The top layer is a thick clay-rich soil/sediment layer with roots than extends to 80 cm. Below this is a medium-grained orange-yellow sand which extends to bottom of the profile. No sediment lamination or no obvious differences in grain-size were noted throughout this sand facies; homogeneous.

Site photos and sample locations:

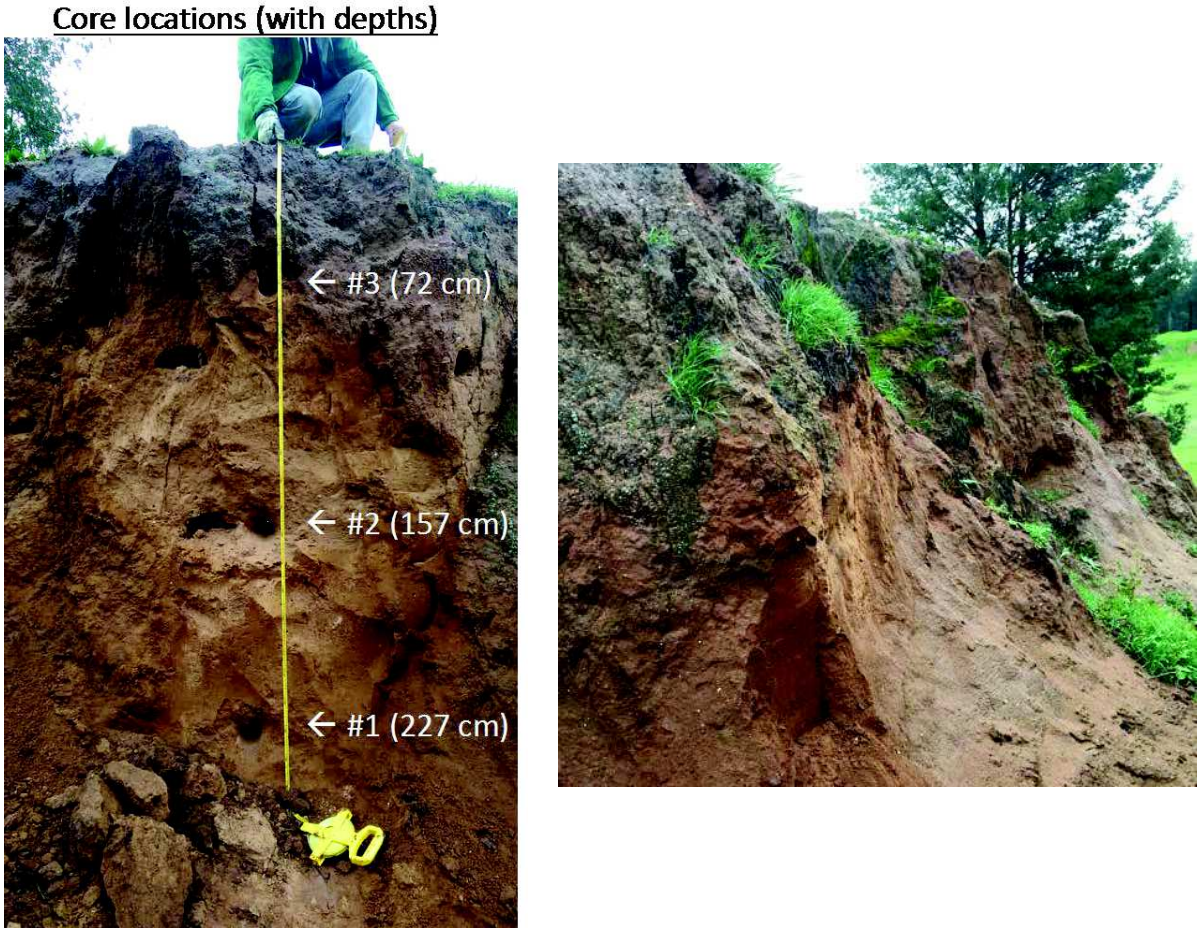

Figure 4-20. Gala Vale South paleochannel site, Coleambally System

Bundure Pit
GPS: 35°05.10345'S, 145°48.01006'E
Elevation: 109 m

Site Description: Pit located on farmland with many cows (not all alive). This exposed pit is very large. The southern face of the pit was sampled (closest to the road).

Profile Description: The pit exposure is approximate 2.5 m in thickness. However, previous boreholes were taken by Page and Nanson (1996) and indicate that the paleochannel infill is 8 – 9 m in total thickness. Two profiles were sampled because sediment was too hard to remove. The top is a very red organic-rich clay layer with coarse gravels embedded; it appears pedogenically altered. Roots and grass were present in this almost lithified pedogenic layer. Below this layer is a white coarse-grained sand/gravel layer. There was no sorting present in the sand layer. An adjacent exposure showed a loam layer between the red clay and white sand layer that showed possible signs of fluvial sorting (fining-upwards). However, this layer was not present in the profiles sampled.

Site photos and sample locations:

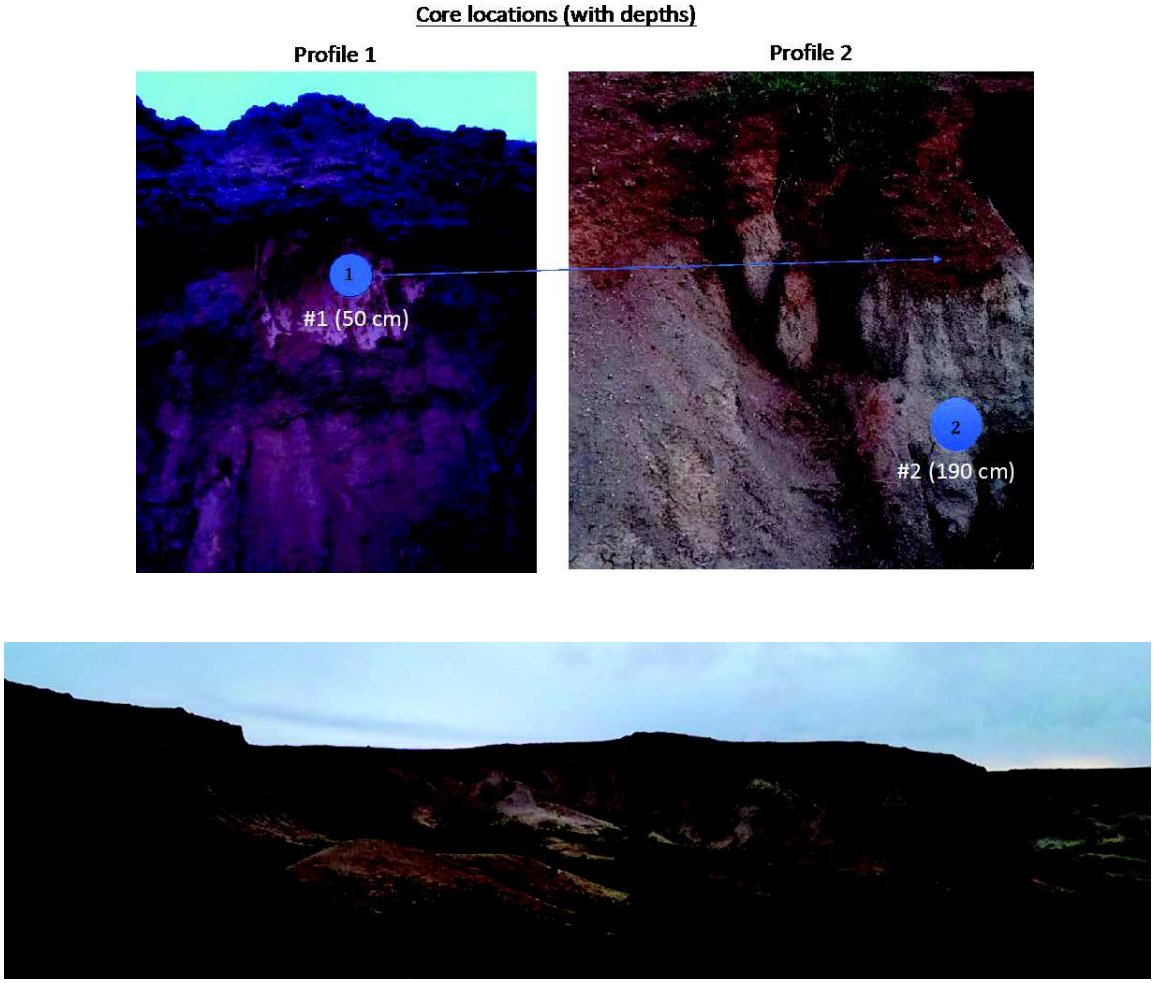

Figure 4-21. Bundure Pit paleochannel site, Coleambally System

4.5.2 Methods

4.5.2.1 Field Methods

Field collection methods for paleochannel sediments are described in Chapter 2.1.4 of this thesis. Core depths, core locations, and sediment stratigraphy descriptions are described in the previous section.

4.5.2.2 Sample preparation and analytical analysis

Paleochannel sediment clay fractions in this study were analyzed for minerology, major and trace element concentrations, B concentration, B isotopes, and Nd isotopes. The sand fraction (63 μm –2 mm) of a limited number of samples (one from each channel system) was also analyzed for B isotopes. Sample preparation and analysis for mineral identification by XRD and major and trace elements by ICP-MS are described in Chapter 2.2 and 2.3, respectively. Sample preparation for B isotopes and B concentration analyses can be found in Chapter 2.4. Details on sample analyses for B concentration by ID-ICP-MS and B isotope measurements by MC ICP-MS can be found in Chapters 2.5 and 2.6, respectively. Sample preparation for Nd isotopes by automated ion exchange chromatography and analysis by MC ICP-MS can be found in Chapter 2.7.

4.5.3 Results

4.5.3.1 Minerology

The mineral composition of the clay fraction of paleochannel sediments was determined at each site and consists of kaolinite (ordered and disordered), phlogopite and lepidolite (which are grouped in the illite category), quartz, and an illite/smectite (I/S) mixed layer (Figure 4-22; Table 4-3). To facilitate an easy comparison of the secondary clay mineral assemblages between samples, the measured abundance of quartz was removed from each sample and the remaining clay minerals were normalized to 100%. The mixed (I/S) layer clay minerals have regularly interstratified illite/smectite crystallite in a coherent stack of 2:1 layers composed of both illitic and smectitic

interlayers (Veblen, 1990). Since pure smectite or montmorillonite was not detected, the mixed layer (I/S) is the best estimate of expandable (smectite) clay content in the sample; the illite interlayers are non-expandable. Modern transported clay fractions taken from the Murrumbidgee River are primarily composed of kaolinite (ranging from 56% – 60%), then mixed (I/S) layer (ranging from 29% – 21%), and a small portion of illite (12% – 19%) (Figure 4-22A). On the contrary, clay fractions from the Yanco and Gum Creek Systems are primarily composed of the mixed (I/S) layer (49% – 65%), followed by kaolinite (23% – 41%), and illite (6% – 10%) (Figure 4-22B). Clay fractions from the Wanganella Pit are an exception to this and are similar to modern sediments with the highest composition being kaolinite (65%). Clay fractions from the Gum Creek system have kaolinite compositions ranging from 52% – 63%, followed by mixed (I/S) layer (28 – 45%), and illite (3% – 9%) (Figure 4-22C). In the Kerarbury System (Figure 4-22D), sediments at Kerarbury Pit have the highest composition of kaolinite (63%) with lower compositions of the mixed (I/S) layer (28%), and illite (9%). Sediments at the Headless Horseman site have compositions more similar to those in the Yanco and Gum Creek paleochannels with a high composition of the mixed (I/S) layer (62%), followed by kaolinite (37%), and illite (1%). The mineralogy of the clay fraction of all three Coleambally System paleochannels is quite similar to one another (Figure 4-22E), all having kaolinite-dominated compositions ranging from 66 – 72%, followed by mixed (I/S) layer (20 – 29%), and illite (4 – 8%). In general, younger Yanco and Gum Creek samples contain higher percentages of expandable mixed-layer, while older Kerarbury and Coleambally samples contain higher percentages of kaolinite. Modern sediment is most similar to older Coleambally samples with higher compositions of kaolinite.

4.5.3.2 Chemical composition of the clay fraction

Concentrations of major and trace elements in the clay fraction of paleochannel sediments are listed in Table 4-4 and Table 4-5, respectively. Similar to the modern sediments (Chapter 3), Al was used as an immobile elements in which to compared the mobile element B. Aluminum concentrations range from 8.5 – 14.2 wt.%. Boron concentrations in the clay fraction range from 21 – 78 $\mu g\ g^{-1}$. The B/Al ratios in the sample dataset range from 0.0004 – 0.0019.

Table 4-3. Mineral compositions of Murrumbidgee paleochannel clay fractions

Sample	System	Age (ka)	Mixed (I/S) layer (%)	Illite (%)	Kaolinite (%)
Granitic Ave	Modern	0	26	18	56
Volcanic Ave	Modern	0	23	17	60
Sedimentary	Modern	0	21	19	60
MR Gundagai	Modern	0	29	12	59
Yanco A	Yanco	13-23	56	6	38
Thurrowa Rd	Yanco	13-23	65	12	23
Morundah	Yanco	13-23	49	10	41
Wanganella	Yanco	13-23	28	7	65
Tabratong	Gum Creek	25-35	63	9	28
Yarradah	Gum Creek	25-35	52	3	45
H.Horseman	Kerarbury	35-55	62	1	37
Kerarbury	Kerarbury	35-55	28	9	63
Gala Vale	Coleambally	80-105	20	8	72
Gala Vale S.	Coleambally	80-105	27	7	66
Bundure	Coleambally	80-105	29	4	67

4.5.3.3 Isotopic Composition of the paleochannel sediments

Boron isotope composition of the sand fraction

In each system, the sand (63 µm – 2 mm) fraction of one sample was measured for B isotopes in order to determine the composition of relatively unweathered material which is thought to represent a mixture of bedrock (parent) material from the upper catchment. These paleochannel samples were collected on a field campaign in 2010 from the same sites that were sampled on the 2015 field campaign. In addition to the four main paleochannel systems, two modern sediment deposits were collected on the alluvial plain alongside the modern Murrumbidgee River (Eunony Bridge at Wagga Wagga; Mucklebar near Darlington Point) and the sand fraction analyzed for B isotopes. The sample at Wagga Wagga is thought to have been

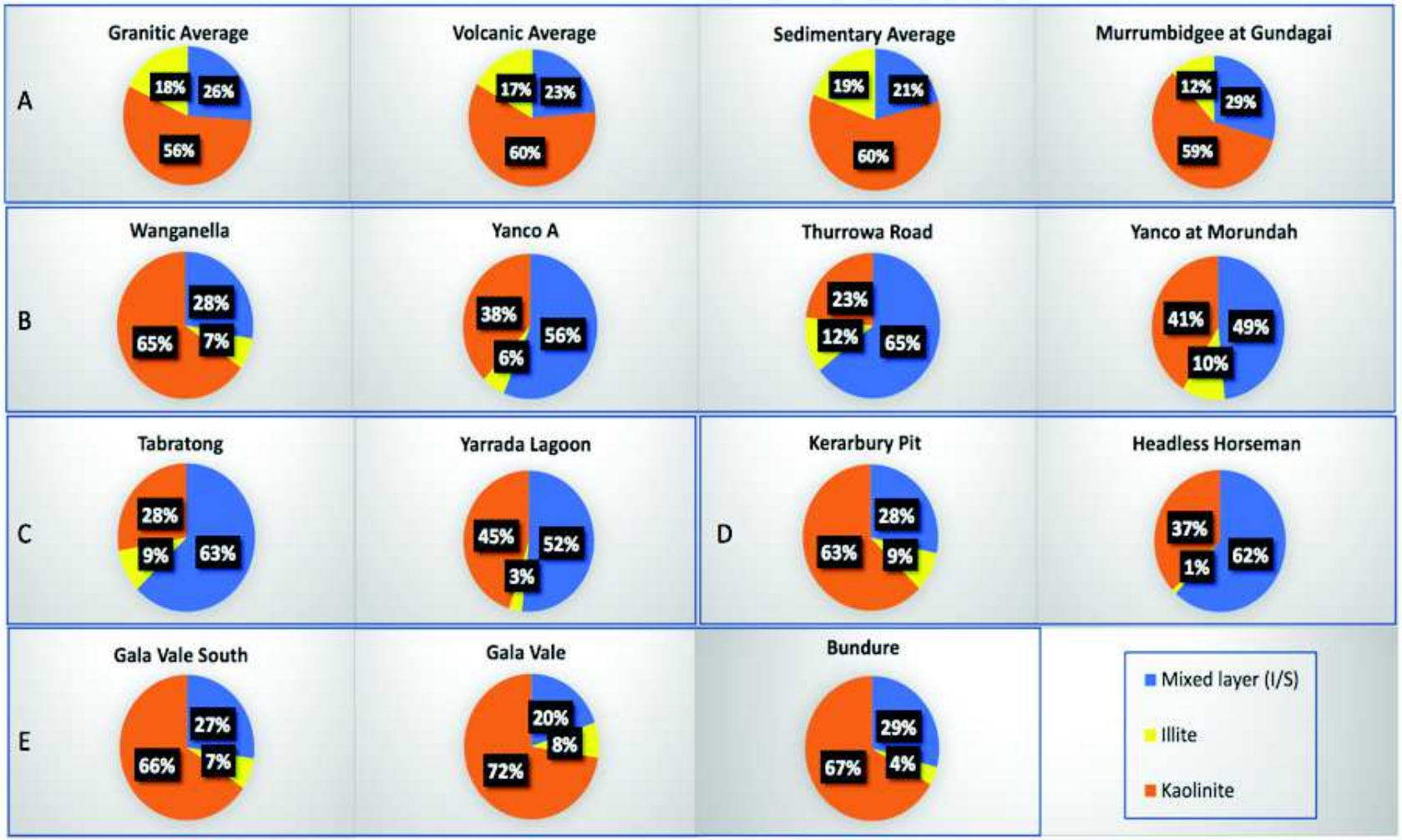

Figure 4-22. Mineralogy of the modern Murrumbidgee and paleochannel channel sediment clay fraction measured by XRD. A) Modern system (0 ka): average granitic, average volcanic, and average sedimentary compositions taken from stream sediment in monolithological catchments and the main Murrumbidgee River at Gundagai (downstream); B) Yanco System (13 – 23 ka): Wanganella Pit; Thurrowa Road; Yanco A; and Yanco at Morundah; C) Gum Creek System (25 – 35 ka): Tabratong; Yarrada Lagoon D) Kerarbury System (35 – 55 ka): Kerarbury Pit; and Headless Horseman E) Coleambally System: Bundure Pit; Gala Vale; and Gala Vale South.

deposited in that last 50 years (although not dated); while the Mucklebar sample was OSL-dated with a deposition age of approximately 3 kyr (T. Pietsch, pers. comm., see Dosseto et al., 2010). The sand fraction of both modern deposits shows very similar B isotope compositions of -9.7‰ and -10.0‰ at Wagga Wagga and Mucklebar, respectively. These values are also very similar to the average $\delta^{11}B$ of the sand fraction of bank sediments from the Murrumbidgee River measured in the modern system study (Chapter 3) which is -10.3 ± 0.4‰ (2 SE, n = 9), indicating that sediment (particularly primary minerals in the sand fraction) in downstream deposits is representative of that being carried by the modern river. At the Yanco A site, the $\delta^{11}B$ of the sand fraction is -10.1‰; at Tabratong (Gum Creek) it is -9.8‰; at Kerarbury Pit is it -8.9‰; and at the Coleambally sites of Gala Vale and Bundure they are -6.6‰ and -5.7‰, respectively, showing a steady increase in B isotope composition as a function of age (Figure 4-23). This likely indicates either an increasing contribution of granites over the last 100 ka with different mineral compositions than volcanic or sedimentary lithologies or possibly preferential mineral dissolution of isotopically lighter minerals (e.g. albite).

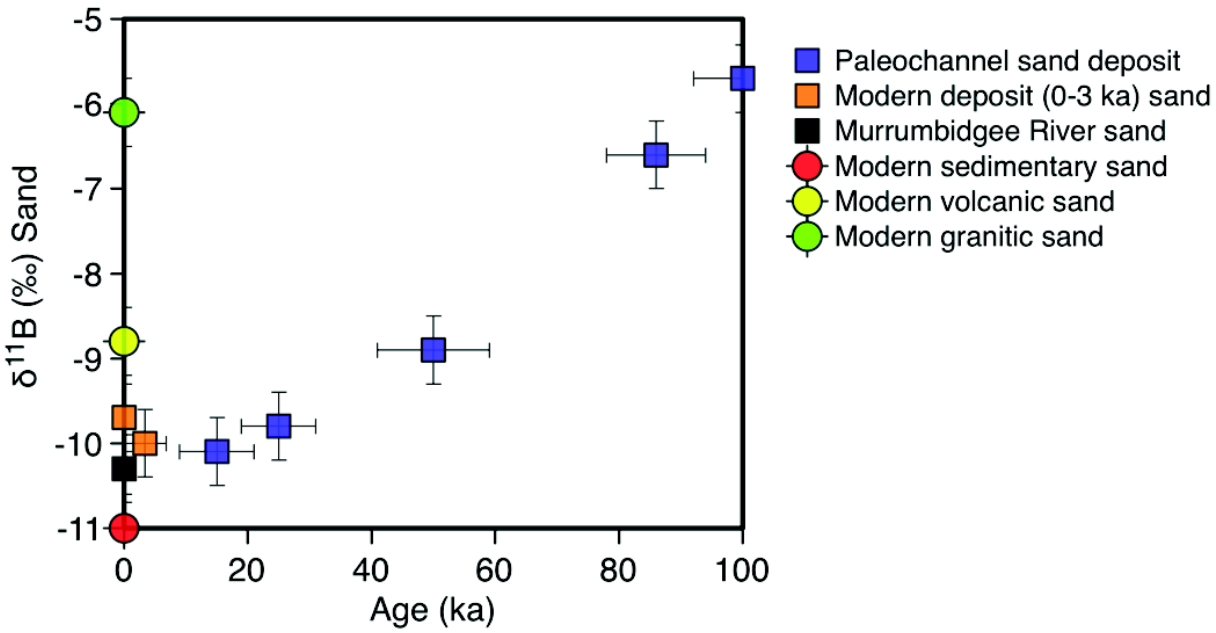

Figure 4-23. Boron isotope compositions of the sand fraction of paleochannel deposits as a function of deposition age compared to that of the modern Murrumbidgee River and modern sediment deposits from monolithological catchments.

Table 4-4. Major element and B isotope composition of paleochannel clay fractions

Sample ID	System	Site Name	Depth (cm)	Na wt %	Mg wt %	Al wt %	P wt %	K wt %	Ti wt %	Fe wt %	$\delta^{11}B$ (‰)
HH #3	Kerarbury	Headless Horseman	15	1.20	0.91	11.50	0.49	2.13	0.57	4.78	7.15
HH #1	Kerarbury	Headless Horseman	100	0.63	1.07	9.79	0.07	1.89	0.40	4.36	9.50
KER #3	Kerarbury	Kerarbury Pit	50	0.77	0.95	13.66	0.23	2.83	0.69	6.03	-5.69
KER #1 in	Kerarbury	Kerarbury Pit	400	0.71	0.90	12.99	0.17	2.36	0.53	6.68	-4.29
KER #2 out	Kerarbury	Kerarbury Pit	300	0.32	1.02	12.10	0.22	2.48	0.49	6.74	-0.68
KER #2 in	Kerarbury	Kerarbury Pit	300	0.75	0.71	11.90	0.22	2.47	0.70	5.27	-6.06
KER #1 out	Kerarbury	Kerarbury Pit	400	1.09	0.86	12.20	0.62	2.40	0.54	6.42	-7.40
GV #2 out	Coleambally	Gala Vale	80	0.66	0.60	13.83	0.42	2.51	0.46	5.76	-4.02
GV #3 in	Coleambally	Gala Vale	30	0.68	0.34	13.45	0.65	2.04	0.50	5.53	-4.18
GV #2 in	Coleambally	Gala Vale	80	0.69	0.66	13.37	0.32	2.25	0.47	5.13	-4.27
GV #1 in	Coleambally	Gala Vale	125	0.50	0.78	14.16	0.12	2.11	0.42	5.43	-1.88
GV #3 out	Coleambally	Gala Vale	30	0.47	0.49	10.29	0.26	1.78	0.41	3.97	-4.74
GV #1 out	Coleambally	Gala Vale	125	0.82	0.73	12.81	0.32	2.02	0.42	5.38	-2.76
WANG #1 out	Yanco	WanganellaPit	90	0.62	0.63	9.01	0.50	2.24	0.54	16.18	-9.97
WANG #3	Yanco	WanganellaPit	30	0.87	0.65	10.30	0.27	3.13	0.76	3.45	-9.83
WANG #2 out	Yanco	WanganellaPit	55	0.70	0.83	11.38	0.29	3.20	0.77	8.74	-11.03
WANG #2 in	Yanco	WanganellaPit	55	0.62	0.72	10.09	0.23	2.78	0.70	9.42	-10.17
WANG #1 in	Yanco	WanganellaPit	90	0.65	0.58	8.50	0.53	2.12	0.49	18.26	-8.93
WANG #2 out	Yanco	WanganellaPit	55	–	–	–	–	–	–	–	-11.03
TAB #1	Gum Creek	Tabratong	135	0.45	0.75	9.69	0.25	2.11	0.47	6.37	0.31
TAB #3	Gum Creek	Tabratong	30	–	–	–	–	–	–	–	-3.24
TAB #2	Gum Creek	Tabratong	80	0.65	1.17	11.99	0.22	2.35	0.50	7.12	1.54
GVS #3 out	Coleambally	Gala Vale South	72	0.86	1.07	12.89	0.34	2.92	0.60	6.47	-3.91
GVS #2 out	Coleambally	Gala Vale South	157	1.24	0.94	9.77	0.89	2.33	0.41	4.96	-2.23
GVS #1 in	Coleambally	Gala Vale South	227	0.84	1.04	11.63	0.32	2.81	0.53	5.46	-2.72
GVS #1 out	Coleambally	Gala Vale South	227	0.64	1.21	13.16	0.30	2.95	0.57	6.66	0.20
GVS #2 in	Coleambally	Gala Vale South	157	0.47	1.14	11.61	0.28	2.82	0.51	5.91	-0.59
GVS #3 in	Coleambally	Gala Vale South	72	0.63	0.87	12.45	0.22	2.34	0.57	6.25	-4.74
YAN A #3	Yanco	Yanco A	100	0.49	0.51	8.57	0.12	2.56	0.72	3.50	-4.73
YAN A #1	Yanco	Yanco A	200	0.88	1.21	12.16	0.16	2.63	0.49	6.12	4.43
YAN A #2	Yanco	Yanco A	118	0.93	0.87	12.97	0.43	2.52	0.59	6.49	1.46
YAN A #4	Yanco	Yanco A	65	1.15	0.94	12.17	0.33	2.81	0.63	4.81	2.66
THR #3	Yanco	Thurrowa Road	65	0.84	0.97	11.89	0.12	2.82	0.64	5.35	-8.50
THR #2	Yanco	Thurrowa Road	290	0.55	0.77	11.12	0.51	1.77	0.42	13.18	-8.93
THR #1	Yanco	Thurrowa Road	360	1.41	0.71	11.43	0.99	1.66	0.38	12.50	-9.05
BUN #2 btm	Coleambally	Bundure Pit	190	0.92	0.90	10.00	0.09	2.08	0.44	4.42	3.06
BUN #1 top	Coleambally	Bundure Pit	50	0.54	0.57	12.62	0.35	2.70	0.92	6.13	-4.75
MYA 2#3 uow 1522	Yanco	Yanco at Bundure	212	1.07	1.30	11.53	0.27	3.14	0.48	8.10	-11.90
MYA-2#4 uow 1523	Yanco	Yanco at Bundure	377	0.88	0.92	8.79	0.13	2.53	0.39	4.51	–
MYA 1#6 uow 1521	Yanco	Yanco at Morundah	672	0.95	1.04	11.28	0.24	2.66	0.37	6.40	-10.90
MYA 1#4 uow 1520	Yanco	Yanco at Morundah	424	0.46	0.72	10.72	0.12	1.69	0.44	4.52	-9.89
MGCY-5#4 uow 1315	Gum Creek	Yarrada Lagoon West	381	0.40	0.89	11.86	0.13	2.78	0.63	4.11	-8.40
MGCY 5#7 uow 1391	Gum Creek	Yarrada Lagoon West	675	0.83	0.72	11.18	0.12	2.75	0.47	3.28	-9.00
MGC 4-4#5 uow 1322	Gum Creek	Yarrada Lagoon	585	0.89	0.76	11.71	0.20	2.89	0.43	4.24	-10.20
MGC 4-4#4 uow 1314	Gum Creek	Yarrada Lagoon	405	0.79	0.73	10.34	0.12	3.18	0.52	3.07	-11.30
MGC 2-1 clay uow 1306	Gum Creek	GC at Darlington Point	455	0.58	0.57	10.50	0.15	2.28	0.63	5.03	-10.00
MGC 8-3#5 40cm TAB#4	Gum Creek	Tabratong	465	0.86	0.72	9.99	0.25	2.18	0.41	6.77	-8.40
MGC 8-3#5 70cm TAB#5	Gum Creek	Tabratong	495	0.84	0.82	9.90	0.23	2.43	0.39	8.22	-9.40

Analytical uncertainly (2 SD) on B isotope measurements is 0.4‰ and major elements (2 RSD) are approximately 10%.

Table 4-5. Trace element concentrations of paleochannel clay fractions

Sample ID	B	Li	Be	V	Cr	Ni	Co	Cu	Zn	Ga	Ge	As	Rb	Sr	Zr	Nb	Sn	Sb
HH #3	62	167	2.5	132	82	386	10.7	28	115	24	0.3	17	160	70	139	12	4.8	1.3
HH #1	77	157	2.5	120	78	411	8	29	110	24	1.3	16	158	87	117	10	4.5	0.7
KER #3	42	202	3.2	171	97	490	22	34	145	29	0.7	22	228	71	146	15	7.2	1.4
KER #1 in	31	237	3.3	149	89	532	35	41	150	28	1.1	25	196	58	121	12	5.9	1.0
KER #2 out	34	214	3.7	155	104	550	18	30	138	27	1.6	17	200	90	119	12	6.0	0.9
KER #2 in	39	203	3.0	172	94	454	15	40	120	27	1.3	19	213	89	156	16	6.6	1.2
KER #1 out	39	228	3.1	162	88	547	58	33	153	28	0.7	33	206	65	131	13	6.5	2.4
GV #2 out	47	232	4.8	149	86	493	43	39	128	27	2.0	22	159	50	118	11	5.3	1.2
GV #3 in	36	215	3.0	157	81	463	22	32	107	27	2.0	23	130	38	120	11	5.1	1.3
GV #2 in	40	208	3.7	142	77	436	29	32	106	25	0.4	20	189	51	117	10	4.9	1.1
GV #1 in	40	235	4.4	129	75	472	69	39	118	25	1.2	19	169	68	115	9	6.0	1.2
GV #3 out	37	244	3.4	180	90	486	22	34	114	29	0.8	26	213	58	130	13	5.9	1.0
GV #1 out	39	291	5.0	157	89	558	90	44	151	28	0.4	24	180	61	123	10	5.2	1.6
WANG #1 out	30	171	4.5	305	86	1334	27	84	155	23	0.4	162	209	53	134	16	5.9	2.2
WANG #3	38	146	2.4	158	82	288	11	21	104	22	0.6	19	257	67	142	21	6.2	1.6
WANG #2 out	38	178	3.9	313	105	678	22	39	140	25	0.3	49	280	65	149	20	7.0	1.9
WANG #2 in	42	174	4.3	337	92	771	24	42	137	24	0.6	60	272	63	147	20	6.6	1.8
WANG #1 in	30	135	3.8	291	71	1345	24	80	135	20	0.7	183	185	45	117	13	5.1	2.7
TAB #1	56	167	3.0	136	92	514	22	31	125	23	1.7	25	108	74	104	12	5.1	0.8
TAB #3	46	201	3.6	198	115	619	23	36	156	31	0.8	35	261	100	139	16	7.6	1.1
TAB #2	58	192	3.0	145	102	88	85	81	77	73	69.5	66	62	58	54	51	46.7	42.9
GVS #3 out	39	233	4.0	187	116	562	24	35	166	29	0.6	23	233	61	132	15	6.6	1.3
GVS #2 out	47	169	3.1	141	89	440	26	30	126	22	0.2	19	170	53	102	10	5.0	1.9
GVS #1 in	52	176	3.3	154	92	459	27	27	125	25	0.3	22	203	60	119	13	5.8	1.9
GVS #1 out	53	186	3.6	160	100	507	26	33	143	27	0.7	21	207	108	134	13	6.0	1.2
GVS #2 in	47	200	3.7	173	103	515	29	37	146	27	0.4	25	202	104	116	12	5.9	1.0
GVS #3 in	38	203	3.1	161	85	523	26	37	145	27	1.9	30	184	72	130	13	5.8	0.9
YANA #3	48	143	2.6	155	81	337	15	25	107	22	0.3	18	214	88	160	21	6.4	1.1
YANA #1	60	185	3.3	135	99	471	13	31	133	26	1.1	17	208	58	115	12	6.0	1.0
YANA #2	56	210	3.2	152	86	512	33	32	149	28	0.8	25	198	64	127	13	5.9	1.4
YANA #4	54	173	3.1	156	101	402	14	27	118	27	0.3	19	241	66	125	16	6.7	1.3
THR #3	21	169	2.8	156	105	431	18	27	126	26	0.6	16	238	58	119	17	6.6	1.0
THR #2	22	164	3.4	135	89	1001	24	36	136	25	1.2	46	200	44	107	11	5.5	0.9
THR #1	25	185	3.2	144	96	913	27	37	134	25	1.2	43	162	29	102	9	5.0	2.5
BUN #2 btm	52	174	3.3	132	101	398	12	29	148	24	0.5	13	205	37	91	12	6.0	1.0
BUN #1 top	42	165	2.9	173	91	452	25	37	128	26	0.8	16	202	87	174	21	6.3	1.1
MYA 2#3 uow 1522	45	266	5.2	273	151	788	61	68	173	35	1.0	42	266	100	154	17	8.0	1.8
MYA-2#4 uow 1523	57	297	5.7	313	192	718	62	131	211	44	0.7	48	338	84	170	22	10.0	3.9
MYA 1#6 uow 1521	29	305	6.1	263	198	772	60	72	185	39	0.9	29	273	73	150	16	8.7	1.9
MYA 1#4 uow 1520	32	318	5.2	256	174	616	28	56	189	45	3.3	23	223	86	184	22	9.1	1.3
MGCY-5#4 uow 1315	39	342	5.6	269	170	566	18	80	206	48	2.3	28	332	131	244	31	10.8	1.5
MGC 4-4#5 uow 1322	40	321	6.2	261	216	565	27	51	189	46	0.8	26	314	118	222	21	10.0	1.6
MGC 4-4#4 uow 1314	35	224	4.1	197	125	363	16	34	142	36	2.2	13	319	86	175	24	8.9	1.6
MGCY 5#7 uow 1391	25	233	4.2	172	156	319	22	49	135	32	1.0	12	222	76	157	17	7.3	1.3
MGC 2-1 clay uow 1306	49	263	4.5	212	136	528	16	52	157	38	2.9	18	147	50	179	26	9.0	1.5
MGC 8-3#5 40cm TAB#4	37	287	5.9	335	138	831	98	61	177	39	1.0	57	251	75	173	20	8.2	2.7
MGC 8-3#5 70cm TAB#5	78	250	5.5	305	131	871	94	58	162	34	1.4	80	235	62	148	17	7.4	2.2

Table 4 continued

Sample ID	Te	Cs	La	Ce	Pr	Nd	Sm	Eu	Gd	Dy	Yb	Hf	Ta	W	Pb	Th	U
HH #3	4.3	8.3	36	72	8	41	6.0	1.3	5.8	4.7	2.8	4.3	1.2	2.8	23	15	2.5
HH #1	6.2	8.0	27	51	6	30	4.7	1.0	4.4	3.7	2.3	3.9	1.0	2.3	17	14	2.1
KER #3	6.5	11.7	44	89	10	51	7.5	1.6	7.3	6.2	3.6	4.7	1.5	3.8	33	20	4.0
KER #1 in	5.2	10.2	35	93	9	50	7.2	1.5	6.8	5.2	2.8	4.0	1.2	3.3	34	18	4.1
KER #2 out	5.9	9.9	47	89	12	58	9.6	2.1	9.4	7.5	3.7	4.0	1.2	3.0	32	20	5.0
KER #2 in	5.6	10.5	44	82	11	52	8.2	1.8	8.0	6.8	4.0	4.7	1.6	3.9	33	21	3.4
KER #1 out	5.6	10.6	44	138	11	68	9.1	1.9	8.9	6.6	3.4	4.1	1.2	3.5	53	19	4.6
GV #2 out	10.7	6.5	41	91	10	54	8.4	1.9	7.6	5.8	3.1	3.8	1.1	2.8	31	15	2.9
GV #3 in	4.1	5.2	19	40	4	23	3.5	0.8	3.3	2.8	1.8	3.9	1.1	2.7	26	13	3.2
GV #2 in	4.5	8.7	33	69	8	40	6.0	1.3	5.6	4.6	2.7	3.7	1.0	2.7	31	16	3.3
GV #1 in	9.3	7.9	49	155	13	80	11.4	2.6	11.4	8.6	4.5	3.9	0.9	2.5	36	17	3.6
GV #3 out	5.1	10.2	27	51	6	29	4.5	1.0	4.2	3.7	2.4	3.8	1.2	3.2	32	16	3.6
GV #1 out	8.3	8.8	54	141	14	81	12.4	2.8	12.7	9.0	4.6	3.7	1.0	2.8	36	15	3.1
WANG #1 out	5.5	9.9	35	103	8	51	7.2	1.6	7.5	7.1	4.4	3.7	1.4	4.0	31	26	9.2
WANG #3	7.9	11.2	46	110	10	56	7.0	1.4	6.6	5.2	3.1	4.6	2.1	5.3	33	22	7.4
WANG #2 out	7.4	12.5	40	108	9	52	6.5	1.4	6.6	5.9	3.7	4.4	2.0	5.3	36	26	8.2
WANG #2 in	7.2	12.0	40	118	9	56	6.7	1.4	6.9	5.9	3.8	4.5	1.9	5.0	35	25	7.8
WANG #1 in	5.2	8.7	32	110	8	52	7.0	1.6	7.5	7.1	4.4	3.6	1.3	4.0	34	26	10.1
TAB #1	5.0	4.9	43	88	11	56	9.7	2.1	9.9	8.0	3.7	3.0	1.2	2.7	25	16	5.0
TAB #3	7.0	13.1	46	84	11	51	8.3	1.8	8.2	7.0	3.9	4.2	1.6	4.0	37	22	3.6
TAB #2	39.1	35.3	44	84	11	53	8.3	1.7	8.0	6.3	3.1	3.9	1.2	3.0	28	19	3.9
GVS #3 out	5.7	11.6	43	82	10	51	7.6	1.6	7.1	5.5	2.9	3.7	1.4	3.4	32	17	4.5
GVS #2 out	4.6	8.3	30	63	7	37	5.5	1.2	5.2	3.9	2.1	3.1	1.0	2.6	27	12	2.4
GVS #1 in	5.5	10.0	35	98	8	48	6.0	1.3	5.8	4.5	2.5	3.8	1.2	3.2	33	15	3.4
GVS #1 out	6.3	10.3	51	109	13	67	10.7	2.4	10.8	8.7	4.4	4.3	1.3	3.4	35	21	4.2
GVS #2 in	6.3	9.9	48	99	12	61	10.1	2.3	10.3	8.4	4.1	3.6	1.2	3.1	33	19	3.4
GVS #3 in	5.6	9.5	49	113	12	65	10.0	2.2	9.7	7.4	3.7	4.1	1.3	3.2	34	20	5.2
YANA #3	7.2	9.4	39	81	9	45	6.4	1.4	6.2	5.5	3.4	5.5	2.0	4.8	33	20	4.2
YANA #1	5.3	10.9	43	83	11	53	8.4	1.8	8.4	6.6	3.2	3.7	1.2	3.1	24	17	4.0
YANA #2	5.4	10.0	40	99	10	54	7.9	1.7	7.6	5.9	3.1	3.9	1.3	3.1	32	17	4.5
YANA #4	7.3	12.1	44	80	10	50	7.8	1.7	7.7	6.3	3.5	4.0	1.6	4.2	30	19	5.3
THR #3	7.6	13.2	40	68	9	43	6.7	1.4	6.3	5.3	3.1	3.8	1.7	4.3	34	19	5.7
THR #2	4.4	10.9	33	50	8	35	6.6	1.4	6.7	6.2	3.7	3.3	1.0	3.4	26	15	4.4
THR #1	3.3	8.8	30	71	7	39	6.0	1.3	6.3	5.6	3.2	3.6	0.9	2.8	27	18	4.4
BUN #2 btm	4.3	10.2	42	72	10	48	8.1	1.7	7.7	5.8	2.6	2.8	1.2	2.8	17	19	3.5
BUN #1 top	6.4	9.3	40	149	9	64	6.4	1.4	6.7	5.6	3.5	5.9	2.0	4.6	41	24	4.1
MYA 2#3 uow 1522	8.0	13.9	50	113	13	68	10.9	2.3	11.1	8.9	4.6	4.8	1.6	9.0	36	25	5.0
MYA-2#4 uow 1523	10.3	17.6	63	135	16	82	13.1	2.8	12.8	9.7	4.8	5.4	1.9	9.4	40	31	6.5
MYA 1#6 uow 1521	8.9	13.4	47	129	12	69	9.9	2.2	9.9	8.4	4.9	5.0	1.6	17.3	52	34	7.2
MYA 1#4 uow 1520	7.1	16.0	61	119	15	75	11.6	2.4	11.0	8.2	4.3	6.1	1.9	8.9	46	29	9.5
MGCY-5#4 uow 1315	11.5	17.7	104	169	25	115	18.6	3.9	17.4	13.1	6.5	7.2	2.7	14.3	69	35	9.7
MGC 4-4#5 uow 1322	11.8	15.2	62	122	14	73	11.3	2.5	12.1	10.9	6.5	6.9	2.1	17.3	69	34	8.9
MGC 4-4#4 uow 1314	11.6	15.8	44	78	10	47	7.1	1.5	6.7	5.8	3.9	5.3	2.1	18.7	40	23	6.7
MGCY 5#7 uow 1391	8.0	11.4	60	144	14	79	10.3	2.1	9.7	7.2	3.7	4.8	1.5	12.7	56	24	7.3
MGC 2-1 clay uow 1306	6.0	8.6	17	35	4	22	3.7	0.8	3.7	3.4	2.2	5.3	2.3	5.8	39	13	7.3
MGC 8-3#5 40cm TAB#4	8.1	13.7	72	200	18	105	13.9	2.9	14.0	10.5	5.5	5.4	1.7	12.9	73	29	11.3
MGC 8-3#5 70cm TAB#5	7.7	12.2	68	172	17	95	13.1	2.7	13.0	9.8	5.3	5.0	1.4	9.4	55	25	10.8

Trace element concentrations are in µg g^{-1}. Analytical uncertainty (2 RSD) for trace elements is approximately 7%.

Boron isotope composition of the clay fraction

Boron isotope compositions of all paleochannel sediments are listed in Table 4-4. When possible, core samples were split into two sections, labeled ‘inside’ and ‘outside’ referring to the presumably most pristine sediment sampled located deep inside the deposit (inside), and the more exposed sediment located closest to the sediment/atmosphere surface (outside). Sediment profiles that were too hard to core deep inside were not split into two portions. This was done to assess local variability and to test if post depositional processes affect the more exposed sediment face compared to the inner portion of the deposit. Differences in chemical composition between ‘inside’ and ‘outside’ portions may therefore represent either local variability or post deposition alteration which presumably would affect the outside portion of the sample. In the oldest system, the Coleambally, three sites were sampled: Gala Vale; Gala Vale South; and Bundure Pit. Boron isotope compositions of the six clay fractions measured at Gala Vale South range from –4.7‰ to 0.20‰; at Gale Vale the six clay fractions range from –4.3‰ to –1.9‰, and at Bundure the two clay fractions each show distinct compositions of –4.8‰ (top sample) and +3.1‰ (bottom sample) in the profile (Figure 4-24). Both samples taken at Bundure Pit would be considered ‘outside’ samples because they were taken with a shovel rather than the traditional hand-coring method as the sediment was too hard to penetrate. However, since there is no corresponding ‘inside’ portions at Bundure, samples are only labeled by site name. On the contrary, both ‘inside’ and ‘outside’ samples were taken at Gala Vale and Gala Vale South sites.

In the Kerarbury System, an upstream (Kerarbury Pit) and a downstream (Headless Horseman) site were sampled (Figure 4-25). The B isotope composition of the clay fraction of the five samples (3 inside; 2 outside) taken at the Kerarbury Pit range from –7.4‰ to –0.7‰ and the two at the Headless Horseman site range from +7.2‰ to +9.5‰. As observed, the inside portion of the all samples at the Kerarbury Pit are very consistent with depth, while the ‘outside’ samples show more variation. Additionally, samples from the Headless Horseman are significantly different from those taken at the Kerarbury Pit.

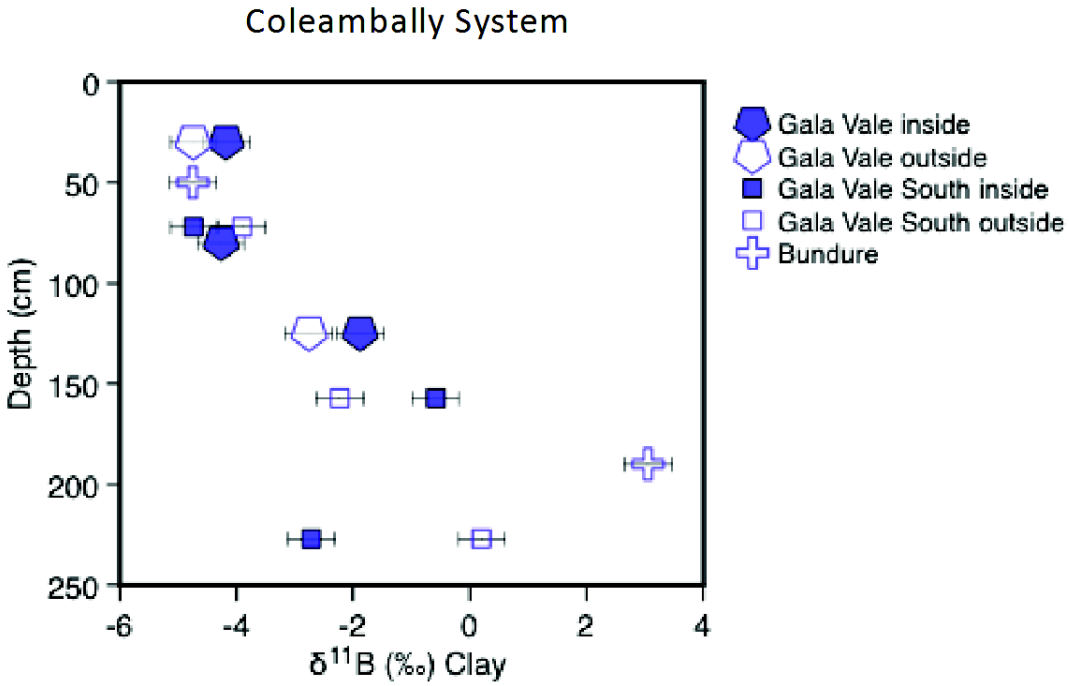

Figure 4-24. Boron isotope compositions of the clay fraction as a function depth within the Coleambally paleochannel sediment deposits taken at Gala Vale, Gala Vale South, and Bundure Pit. Inside refers to the portion of the sample located deepest within the profile; outside refers to the portion of the sample taken closest to the outer surface of the sediment deposit. Bundure Pit samples only have an outside portion.

In the Gum Creek System, three upstream sites were sampled (Figure 4-26): GC at Darlington Point, Yarrada Lagoon, and Yarrada Lagoon West and one downstream: Tabratong. At GC Darlington Point, only one deep (~450 m) core sample was taken with a $\delta^{11}B$ of the clay fraction of -10.0‰. At Yarrada Lagoon, two deep core samples were obtained with B isotopic compositions in the clay fraction of –11.3‰ (405 m) and –10.2‰ (585 m). At Yarrada Lagoon West, two deep core samples were also obtained with $\delta^{11}B$ clay fraction compositions of -8.4‰ (381 m) and -9.0‰ (675 m). At Tabratong station, five samples were collected. Three samples were taken at relatively shallow depths (< 200 cm) and two taken from deep within the profile (~465– 500 cm). The $\delta^{11}B$ compositions of the three upper and two lower samples range from –3.2‰ to +1.5‰ and from -8.4‰ to -9.4‰, respectively. The deeper clay samples show much less variation than clays located closer to the surface, suggesting that shallow sediments may be more effected by surface processes such as recent pedogenesis and/or interaction with vegetation.

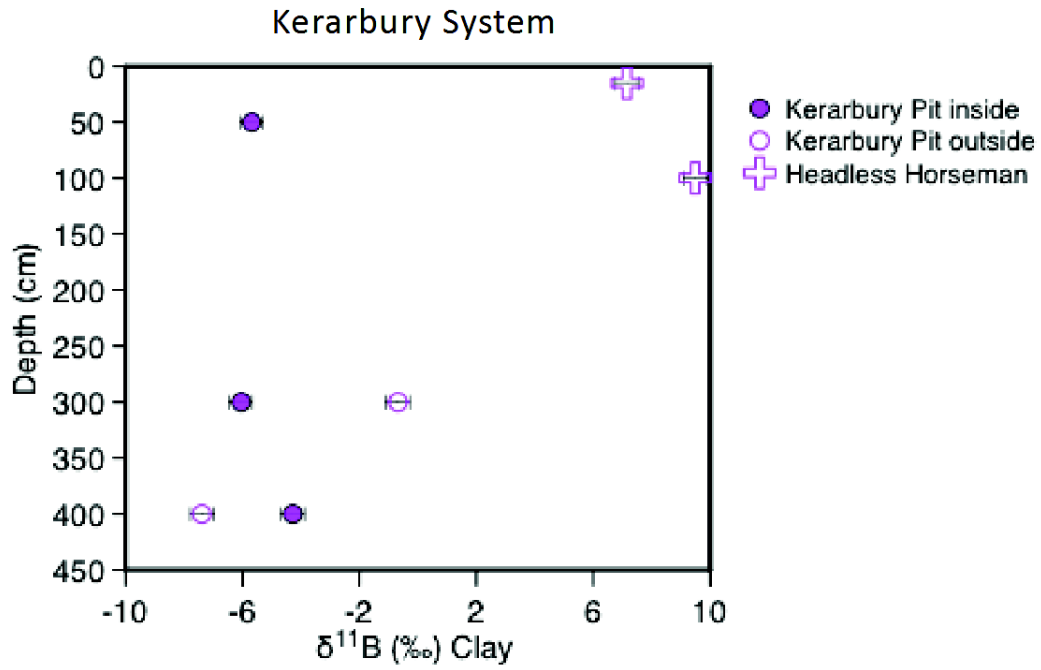

Figure 4-25. Boron isotope compositions of the clay fraction as a function depth within the Kerarbury paleochannel sediment deposits taken in the Kerarbury and the Headless Horseman Pits. Inside refers to the portion of the sample located deepest within the profile; outside refers to the portion of the sample taken closest to the outer surface of the sediment deposit. Headless Horseman samples only have an outside portion.

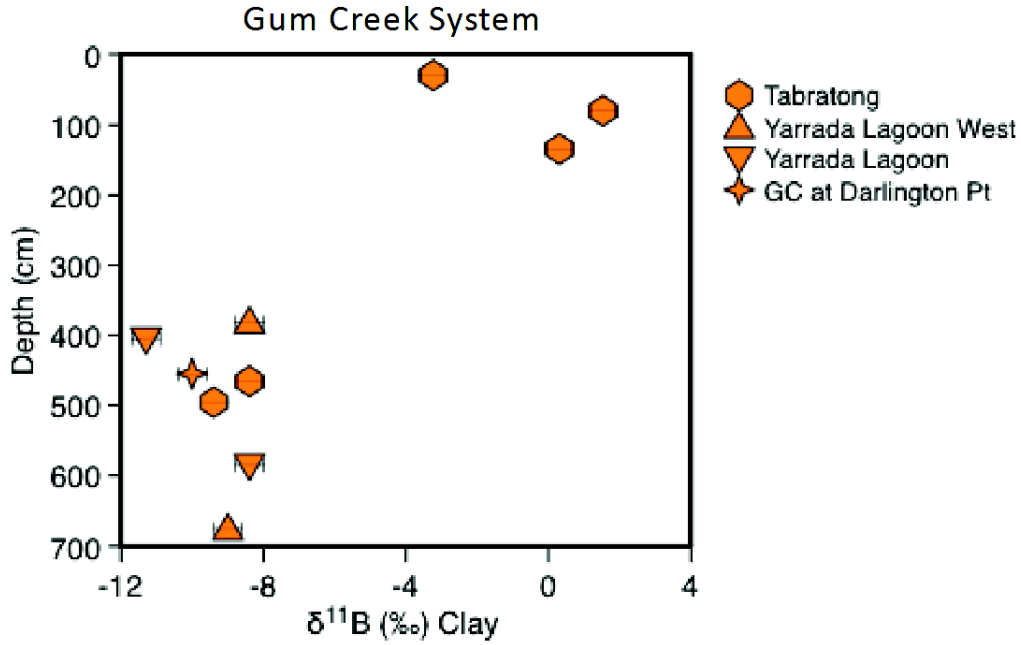

Figure 4-26. Boron isotope compositions of the clay fraction as a function depth within the Gum Creek System paleochannel sediment deposits taken Tabratong, GC at Darlington Point, Yarrada Lagoon, and Yarrada Lagoon West.

In the Yanco system, five locations along the main channel were sampled, four upstream and one downstream (Figure 4-27). At the furthest upstream site, Yanco at Morundah, two deep core samples were taken at 424 m and 672 m with B isotope clay fraction compositions of –10.9‰ and –9.9‰, respectively. Approximately 30 km downstream, the Thurrowa Road Pit exposure, which is approximately 400 m in depth, was sampled at 65 cm, 293 cm, and 360 cm. The $\delta^{11}B$ clay fraction composition of these samples range from –8.5‰ to –9.1‰, respectively, showing very little change in B isotope composition with depth. Approximately 10 km downstream, one core sample was taken at a depth of 212 m in the profile at Yanco at Bundure whose clay fraction has a $\delta^{11}B$ composition of –11.9‰. The last upstream site sampled was Yanco A which is located approximately 15 km downstream from Yanco at Bundure, where 4 samples were taken in a depth profile. Samples were taken at depths of 65 cm, 100 cm, 118 cm, and 200 cm and have $\delta^{11}B$ clay fraction compositions of 2.7‰, -4.7‰, 1.5‰, and 4.4‰, respectively. These values are very different from other Yanco System clay fraction samples showing a much larger range of values which are isotopically much heavier. Approximately 100 km downstream, 5 samples were collected at the Wanganella Pit, which is a relatively shallow pit exposure. All samples were taken within the top meter of the profile at 30 cm, 55 cm, and 90 cm depths. The bottom and middle sample have both an inside and outside portion, however the top sample does not, due to the sediment migration within the core pipe when it was extracted. The clay fraction of all samples have very similar $\delta^{11}B$ compositions ranging from –8.9‰ to –11.0‰ showing little variation with depth but slight variation between the inside the outside portion of the sample.

The B isotope clay fraction composition of all samples, including both inside and outside portions, taken in the four paleochannel systems of Murrumbidgee sector of the Riverine Plain are shown in Figure 4-28. The clay fraction of the two modern system deposits (dated between 50 and 3,000 years) are also plotted. Systems are grouped by color in the legend. There are noticeable differences in B isotope compositions of the clay fraction between most of the systems, however every system has one site that is not in agreement with other samples taken within the sample paleochannel system. The possibility of these samples being affected by post-

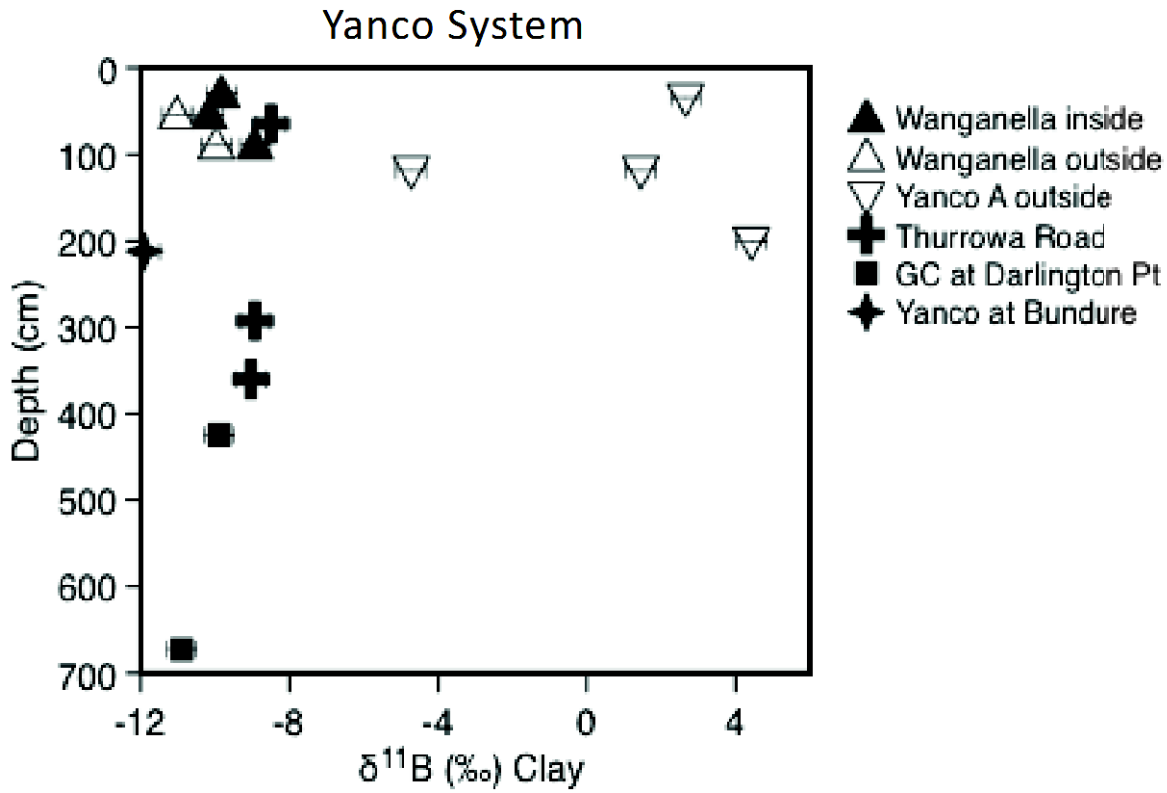

Figure 4-27. Boron isotope compositions of the clay fraction as a function depth within the Yanco System paleochannel sediment deposits taken Wanganella Pit, Thurrowa Road Pit, Yanco A, Yanco at Bundure, and Yanco at Morundah

deposition alteration will be discussed below. In general, the composition of the Yanco (orange) and Gum Creek (black) Systems completely overlap and look nearly identical, with exception of the Yanco A and Tabratong sites which may have experienced post-deposition alteration. These two systems which have formed pre- and post-LGM have $\delta^{11}B$ clay fraction compositions similar to modern transported sediment (average $\delta^{11}B$ of downstream modern Murrumbidgee River clay fractions are about –10‰, reported in Chapter 3) but slightly different from the modern Murrumbidgee River deposits (green squares) and paleochannel deposits from the Kerarbury and Coleambally systems who have isotopically heavier compositions.

Neodymium isotopes in the clay fraction

In order to determine if the source of sediment delivered to the Murrumbidgee paleochannels on the Riverine Plain has changed over the last glacial cycle, neodymium isotope

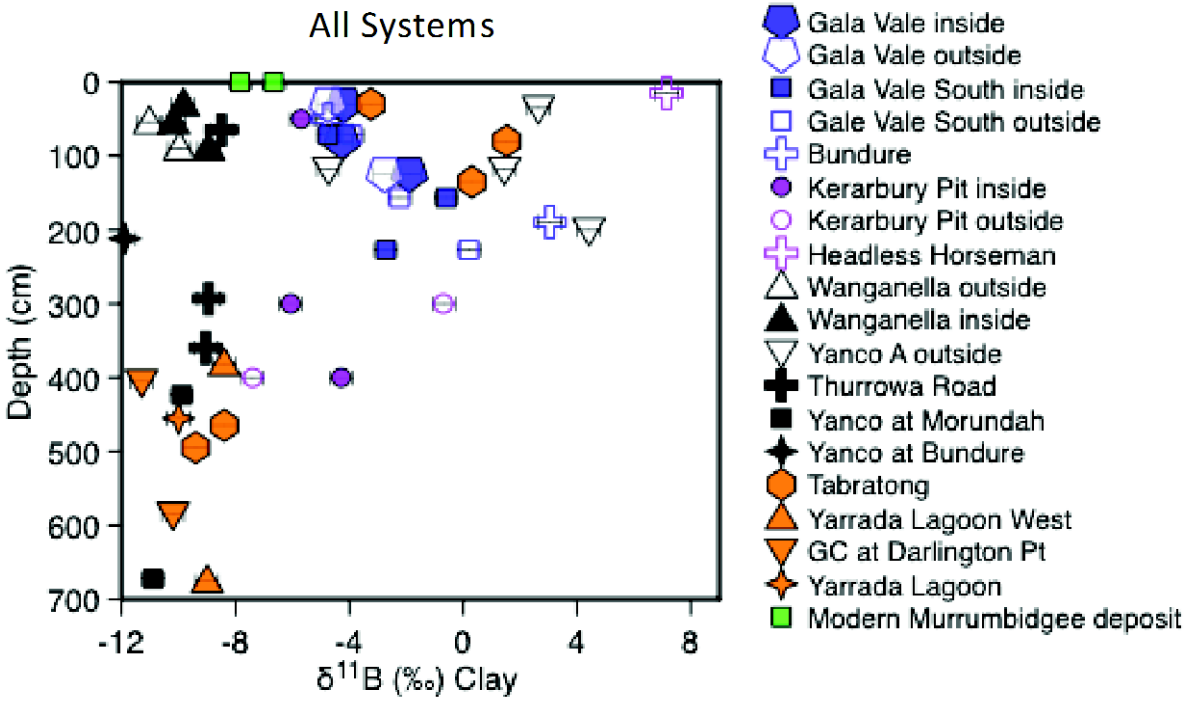

Figure 4-28. Boron isotope clay fraction compositions of all Murrumbidgee sector paleochannels (Yanco, Gum Creek, Kerarbury, and Coleambally Systems) and modern Murrumbidgee River deposits on the Riverine Plain, southeast Australia. The abbreviation 'in' and 'out' after the site name refers to 'inside' and 'outside' portions of each core sample which are the portions deepest within the sediment deposit and closest to the outside (sediment/atmosphere) portion of the deposit, respectively. Systems are listed oldest to youngest in the legend and grouped by color. Analytical errors (2 SD) on isotope measurements are 0.4‰.

($^{143}Nd/^{144}Nd$) analysis was conducted on the clay fraction of sediments from all paleochannel systems as well as bedrock samples from source areas in the upper catchment of the Murrumbidgee River and clay fractions taken along the course of the Murrumbidgee River. Measured $^{143}Nd/^{144}Nd$ ratios are expressed relative to $^{143}Nd/^{144}Nd_{CHUR}$ = 0.512638 as ε_{Nd}. Neodymium isotope compositions in the Yanco System range from –10.95 to –8.94; in the Gum Creek System they range from –7.57 to –11.11; in the Kerarbury System they range from –2.34 to –8.85; and in the Coleambally System they range from –7.24 to –12.38 (Figure 4-29; Table 4-6). Sedimentary, volcanic, and granitic bedrock samples from the upper Murrumbidgee catchment were also analyzed for Nd isotopes and yield a wide range of ε_{Nd} values of –16.18, –11.03, and –3.90, respectively. Additionally, Nd isotopes in the clay fraction of bank sediments from the modern Murrumbidgee River range from –7.3 to –13.3. When compared to catchment bedrock, the ε_{Nd} composition of paleochannel clays appear indistinguishable from that of the catchment bedrock (Figure 4-29). This comparison suggests that all sediments in each of the paleochannel systems derives from within the Murrumbidgee catchment. In order

to assess if there was a change in source of sediment over the last 100 ka which may impede on any B isotope interpretation, an ANOVA test (one-way between subjects) was performed. The test specifically checked if there were significant statistical differences in ε_{Nd} values between any of the systems, including actively transported sediment in the modern Murrumbidgee River, and the catchment bedrock. Results from the AVOVA test ($\alpha = 0.05$) reveal no significant differences between the means of all five groups with a reported *p*-value of 0.100. These test results indicate that the source of sediment has not varied significantly over the last glacial-interglacial cycle and that all samples. This interpretation, however, is limited due to the low number of samples included in the statistical test; low counting statistics and possible outliers (e.g. Kerarbury Pit, -2.43) make a change in source determination based on the available data tentative.

4.5.4 Discussion

4.5.4.1 Source of sediments in the paleochannels

Riverine paleochannel infill sediments are thought to have derived from the upper and lower portions of the Murrumbidgee River catchment and delivered to the paleochannel systems via the active river channel. This occurred over the last glacial-interglacial period during times of significant runoff which carried large amounts of coarse bedload sediments (Bowler, 1986; Kemp et al., 2017; Mueller, 2017; Page and Nanson, 1996; Suresh et al., 2014). Although all paleochannels were once migrational in character, possibly involving some degree of sediment re-working on the alluvial plain, the principle source of channel infill was coarse bedload from upstream areas which controlled the channel morphology (Page and Nanson, 1996). This is particularly evident in the Coleambally, Kerarbury, and downstream reaches of the Gum Creek Systems which aggraded with coarse sands that are connected laterally to extensive sequences of fining-upward sediments, indicating alternating episodes of channel activity which transitioned between laterally migrating mixed-load channels to vertically aggrading bedload channels. The terminal feature of these systems is bedload aggradation which resulted in channels with low sinuosity, likely triggered by high flood peaks during spring melting (Page and Nanson, 1996). Although the Yanco System, particularly after the LGM, is characterized by migrational paleochannels carrying large volumes of sand, it did not terminate in an aggradational phase, likely caused by a climatic shift which drastically reduced the supply of coarse bedload and resulted in a highly sinuous suspended-load system, similar

to the present drainage systems (Page and Nanson, 1996). Lack of an aggradational phase and presence of large dunefields along the Yanco (compared to the previous Gum Creek System which lacks similar dune fields) suggest that sediment re-working on the Riverine Plain was likely greatest during this phase.

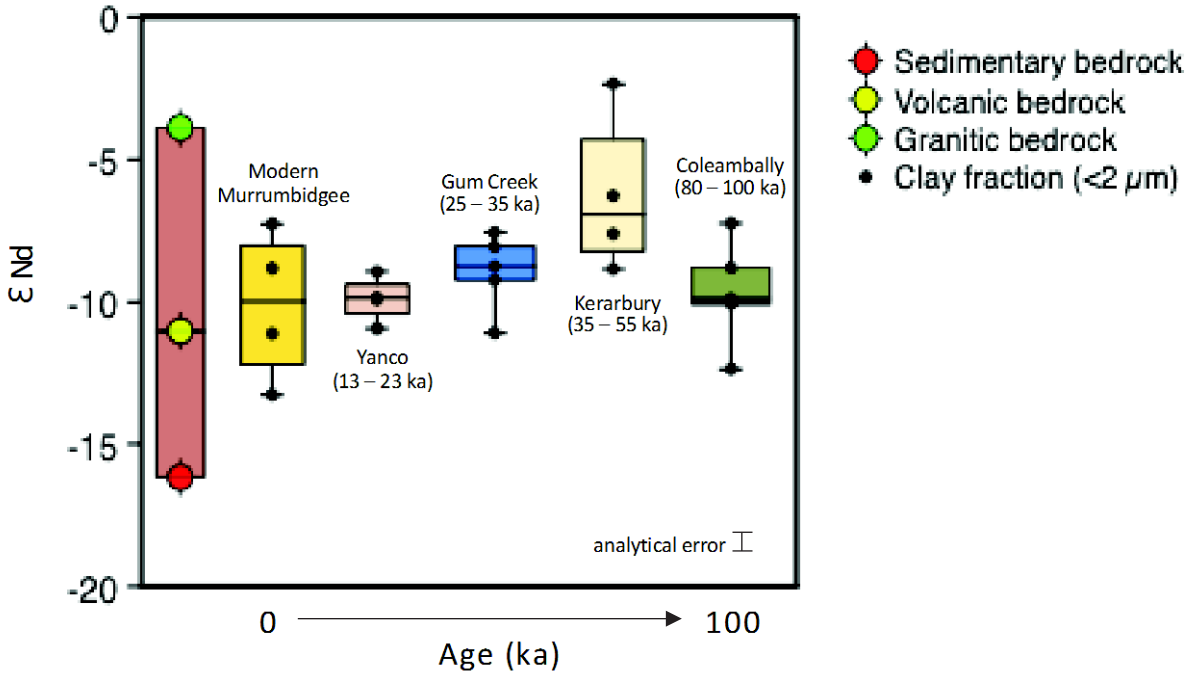

Figure 4-29. Neodymium isotope compositions of the clay fraction of paleochannel sediments and modern Murrumbidgee River catchment bedrock. Analytical uncertainly (2 SD) on ε_{Nd} ratios is 0.5.

The Nd isotope composition of paleochannel clay fractions reveals that there is no statistically significant difference in source of sediments over the last glacial-interglacial cycle and all sediments sampled can be explained as deriving from source areas within the Murrumbidgee catchment (Figure 4-29). Sedimentary, volcanic, and granitic bedrocks from the upper catchment were used for comparison, as well as clay fractions from the modern Murrumbidgee River. Neodymium isotope compositions of nearly all paleochannel clays closely resemble those of the clay fraction of bank sediment from the modern river. Since the source of sediment is confirmed not to have changed over the last glacial-interglacial cycle, changes in B isotope of the clay fraction during that period may be related to differences in paleo-weathering conditions.

The B isotope composition of sand fraction of bank sediment from the Murrumbidgee could be used a potential source tracer of paleochannel sediment. This is because B isotopes in the sand fraction is thought to experience little to isotope fractionation during weathering

Table 4-6. Neodymium isotope compositions of Murrumbidgee paleochannel systems and modern Murrumbidgee River catchment bedrock

Sample Location	System	ε_{Nd}
Wanganella Pit	Yanco	-10.95
Thurrowa Road	Yanco	-9.90
Thurrowa Road	Yanco	-9.76
Yanco A	Yanco	-8.94
Yanco at Morundah	Yanco	-9.94
Yanco at Bundure	Yanco	-9.87
Tabratong	Gum Creek	-8.76
Tabratong	Gum Creek	-7.57
Tabratong	Gum Creek	-11.11
Yarrada Lagoon West	Gum Creek	-9.25
Yarrada Laggon	Gum Creek	-8.06
Headless Horseman	Kerarbury	-6.26
Headless Horseman	Kerarbury	-7.60
Kerarbury Pit	Kerarbury	-8.85
Kerarbury Pit	Kerarbury	-2.34
Gala Vale	Coleambally	-7.24
Gala Vale	Coleambally	-12.38
Gala Vale South	Coleambally	-10.09
Gala Vale South	Coleambally	-8.80
Bundure	Coleambally	-9.90
Bundure	Coleambally	-8.67
Bedrock: Sedimentary (Umbango Ck)	Murrumbidgee	-16.18
Bedrock: Volcanic (Big Hill Ck)	Murrumbidgee	-11.03
Bedrock: Granite (Journama Creek)	Murrumbidgee	-3.90
MR13	Murrumbidgee	-13.27
MR#06	Murrumbidgee	-7.26
MR-Wagga	Murrumbidgee	-8.84
MR#12	Murrumbidgee	-11.13

ε_{Nd} values are based on the measured $^{143}Nd/^{144}Nd$ ratio and $^{143}Nd/^{144}Nd_{CHUR}$ = 0.512638. Analytical error (2 SD) on ε_{Nd} is 0.5 which is based on repeated analysis of JG-2 reference material.

and transport and therefore is a good representative of unweathered catchment bedrock (Lemarchand et al., 2012; Cividini et al., 2010; Ercolani et al. in prep., see Chapter 3). As a reliable source tracer, B isotopes in the sand fraction should then agree with Nd isotopes in the clay fraction and reveal that there is no change in the source of sediment over the last 100 ka. However, this is not the case as both proxies are not in complete agreement. Boron isotopes in the sand fraction show a shift towards isotopically heavier values over time (possibly indicating

an increasing contribution for granitic sources in older paleochannels), while Nd isotopes show that there is no significant change. Since the use of Nd as a proxy for sediment provenance is more established, and possibly more reliable than B isotopes in primary minerals, it is concluded that no significant change in sediment source occurred. The shift towards heavier B isotope compositions in the paleochannel sand fractions over time then is less clear. A possible explanation of this trend may derive from the preferential dissolution rate of isotopically lighter and more easily weathered minerals (i.e. albite for instance), particularly in older, more weathered sediments. However, without a thorough XRD analyses of these sand samples, this hypotheses is speculative and warrants further research.

4.5.4.2 Transport of sediment from source to sink

Based on an extensive study of the chemical and isotopic composition of the sand and clay fraction of bedload sediment in the modern Murrumbidgee River (Chapter 3), it was concluded that the composition of downstream sediment (both sand and clay fractions) is representative of a mixture of sediment produced throughout the catchment and experiences little or no chemical alteration during transport. This result agrees with a previous study by Suresh et al. (2014) who found no chemical evolution of Murrumbidgee River sediment along its course based on the WIS (Si-based Weathering Index). These results then suggests that the chemical and B isotopic composition of downstream paleochannel sediment is representative of the ancient weathering signal obtained in the source areas of the upper catchment. However, an understanding of B isotope behavior after active transport in the river including deposition, burial, and possible re-working is presently lacking. To address this question, the composition of modern sediment from the Murrumbidgee River (reported in Chapter 3) is compared to that of paleochannel sediment in order to assess similarities and differences. For each sample, the B isotope composition of the sand fraction is subtracted from that of the clay fraction ($\Delta^{11}B_{\text{clay-sand}}$) in order to determine the extent of isotope fractionation between weathered and non-weathered material. The $\Delta^{11}B_{\text{clay-sand}}$ term is then shown as a function of the B/Al in order to assess B isotope fractionation as a function of B mobility relative to the immobile element Al (Figure 4-30). All data points in the dataset are not shown; the 'outside' portion of core samples (when taken) was removed from this figure and only the 'inside' portion shown. This was done because the 'outside' portion, that is, the portion closest to the surface of the deposit, is likely to be affected by post-depositional processes (see discussion below). Results show that the B

isotope and B/Al compositions of most paleochannel sediments are similar to the downstream sediments actively being transported by the modern Murrumbidgee River. This is particularly true in the Gum Creek and Yanco Systems, with slightly larger differences in B isotope compositions between modern and paleochannel sediments in the Kerarbury and Coleamabally Systems; B/Al ratios between most paleochannel and modern sediments are also similar. This may indicate that the composition of the paleochannel sediment has not evolved after deposition. On the contrary, some paleochannel samples have a much heavier B/Al and/or $\Delta^{11}B_{clay\text{-}sand}$ composition than modern and other paleochannel sediments, possibly indicating a B enrichment from an isotopically heavy source after deposition.

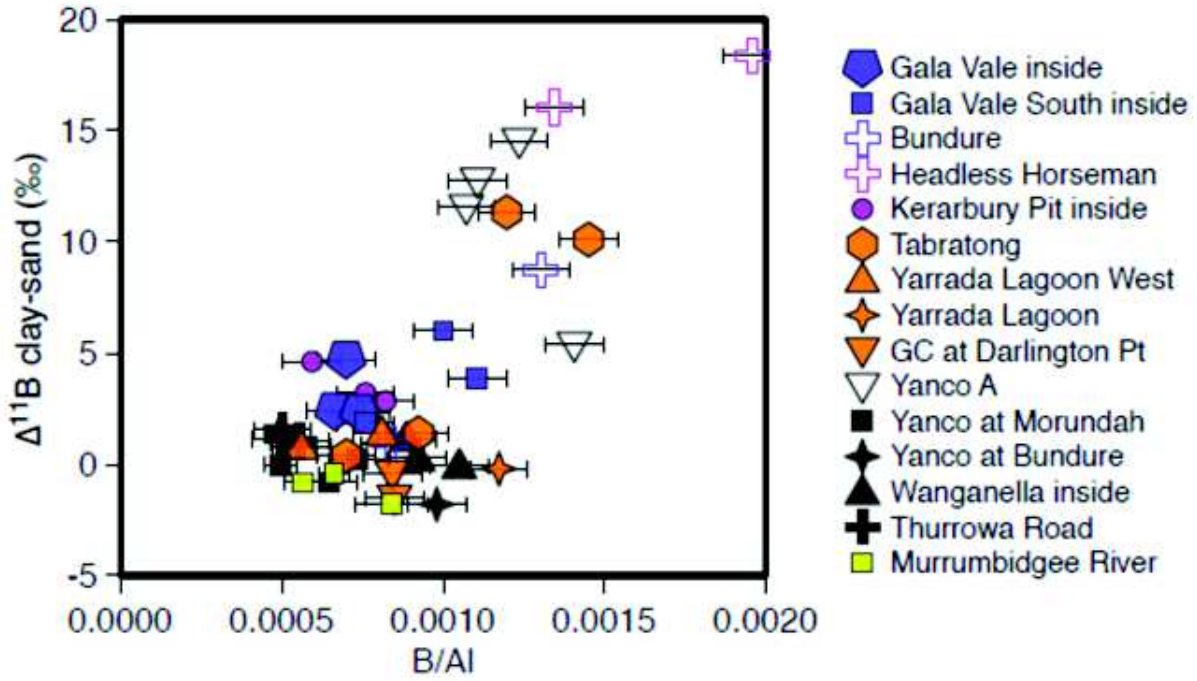

Figure 4-30. $\Delta^{11}B_{clay\text{-}sand}$ as a function of B/Al in the clay fraction in both the modern Murrumbidgee River and Riverine paleochannel sediments. The dotted line represents $\Delta^{11}B_{clay\text{-}sand} = 0$ where no isotope fractionation between the clay and sand fractions is observed. Corresponding 'outside' sample portions at Gale Vale, Gala Vale South, and Kerarbury Pit are not shown in this figure.

4.5.4.3 Effects of post-deposition alteration on the B isotope signature of the clay fraction

One of the primary goals of this chapter and thesis is to determine if the chemical and B isotope composition of transported and deposited riverine material suffers from post-depositional alteration or if the ancient weathering signal carried by the fraction is preserved over time. If the weathering signal is preserved during transport, deposition, and burial, then it may serve as a proxy to reconstruct paleo-environmental or paleo-weathering conditions (Zhao

et al., 2003; Singer, 1980). To identify post-depositional alteration, the following stragety was employed. First, several sites along the course each paleochannel system were sampled with depth to identify a weathering profile. As discussed above, samples were also split between 'outside' and 'inside' portions when possible in order to obtain the most pristine portion of the deposit. Boron isotope compositions of the clay fraction were the main proxy used to identify a weathering profile in each system. Chemical compositions (B/Al ratios) were then paired with B isotopes to investigate whether a correlation exists which can explain B isotope compositions. Finally, the depth of the depositional environement was considered which may affect the preservation of the ancient weathering signal. These points are discussed in detail in the following text.

The possible effect of post-deposition was first considered in the sampling strategy by boring horizontally into each sediment deposit and separating the core sample in two parts (when possible): the 'inside' section which is expected to be more pristine part as it located further inside the deposits; and the 'outside' section which is the section closer to the surface and therefore more likely to be affected by post-depositional alteration. By this measure, it is possible to assess the local variability of the B isotope composition of the clay fraction in each sample and possible identify post-depositional alteration. The B isotope compositions of both 'inside' and 'outside' sample portions are shown in Figures 4-24 – 27 as a function of depth within each system. In the Yanco System, samples were split between 'inside' and 'outside' at the Wanganella Pit, displaying a 1‰ shift towards isotopically lighter values in 'outside' samples taken at 55 cm and 90 cm (Figure 4-27). At the Kerarbury Pit (Kerarbury System), 'outside' samples display contradicting behavior, being both isotopically heavier (about 6‰) at 300 cm and lighter (about 3‰) at 400 cm than the corresponding 'inside' portion of the sample. Because a 6‰ shift toward isotopically heavier values in B isotope composition between 'inside' and 'outside' portions of the same sample (300 cm) is quite significant, it is likely that the 'outside' portion is being or has been influenced by "surface" processes, while the 3‰ shift towards isotopically lighter values at 400 cm likely represents site variability rather than post-deposition alteration. In the Coleambally System, 'inside' and 'outside' portions of sediment samples do not significantly vary, with a maximum $\delta^{11}B$ difference of 3‰ between 'inside' and 'outside' sample aliquots at Gala Vale South. The composition between 'inside' and 'outside' sample aliquots show inconsistencies with depth in some profiles. For example, the 'outside' portion is sometime isotopically heavier and sometimes lighter, likely representing local sample variability. It appears that the difference in B isotope

composition between ‘inside’ and ‘outside’ may be due to both local sample variability (in the case of a slight B isotope difference) and post-deposition alteration (in the case of a large B isotope difference). Although it is difficult to determine whether isotopic differences between the ‘inside’ and ‘outside’ sample portions are caused by local variability or post-depositional alteration, these variations are generally less than isotopic variations observed with depth with a given profile. Accordingly, the difference between the ‘inside’ and the ‘outside’ is negligible compared to the variation with depth. Therefore, as the ‘outside’ portion of the deposit is less likely to be intact/preserved than the ‘inside’ portion, the ‘outside’ portion was removed from the dataset. The one exception to this occurs at the Kerarbury Pit (sample taken at 300 cm), where the difference between ‘inside’ and ‘outside’ is greater than the variation with depth; however due to the significant (6‰) difference between ‘inside’ and ‘outside’ sample portions at that depth and the lack of significant difference between ‘inside’ and ‘outside’ portions of the lower (400 cm) sample, the ‘outside’ portion of the 300 cm sample is likely altered by post-depositional processes.

After removal of the ‘outside’ sample portion, the focus was on identifying ‘inside’ sample portions that were affected by post-depositional alteration by comparing differences in B isotopes with depth (Fig. 4-31). When comparing sites along a given paleochannel system with depth, a narrow variation in B isotope values exists for most sites with a given paleochannel system, with the exception of one site in each of the systems (Figure 4-31). The B isotope composition of clays fractions taken the outlier sites all have much heavier values that those than other sites within the same system, indicating a possible incorporation of B which has been cycled through vegetation after deposition. Sites/samples that appear particularly different from other sites within the same paleochannel system or samples within the same deposit include: all samples from Yanco A (Figure 4-27); the three shallow samples taken at the Tabratong site (Gum Creek System) (Figure 4-26); all samples from the Headless Horseman site (Kerarbury System) (Figure 4-25); and the lower sample (190 cm) taken at the Bundure Pit (Coleambally System) (Figure 4-24). In the Yanco System, B isotopes in the clay fraction of the Yanco A profile show a large range of values from approximately -5‰ to +5‰, with nearly all samples in that profile having compositions >2‰. These values are much heavier (> 10‰ in most cases) than the clay fractions at the four other sitesin the Yanco System, which together display a narrow range in B isotopes from approximately -12‰ to -9‰. As such, it likely that all samples from the Yanco A profile have been altered after deposition. In the Gum Creek, evidence of a weathering profile was present at the Tabratong site. The three

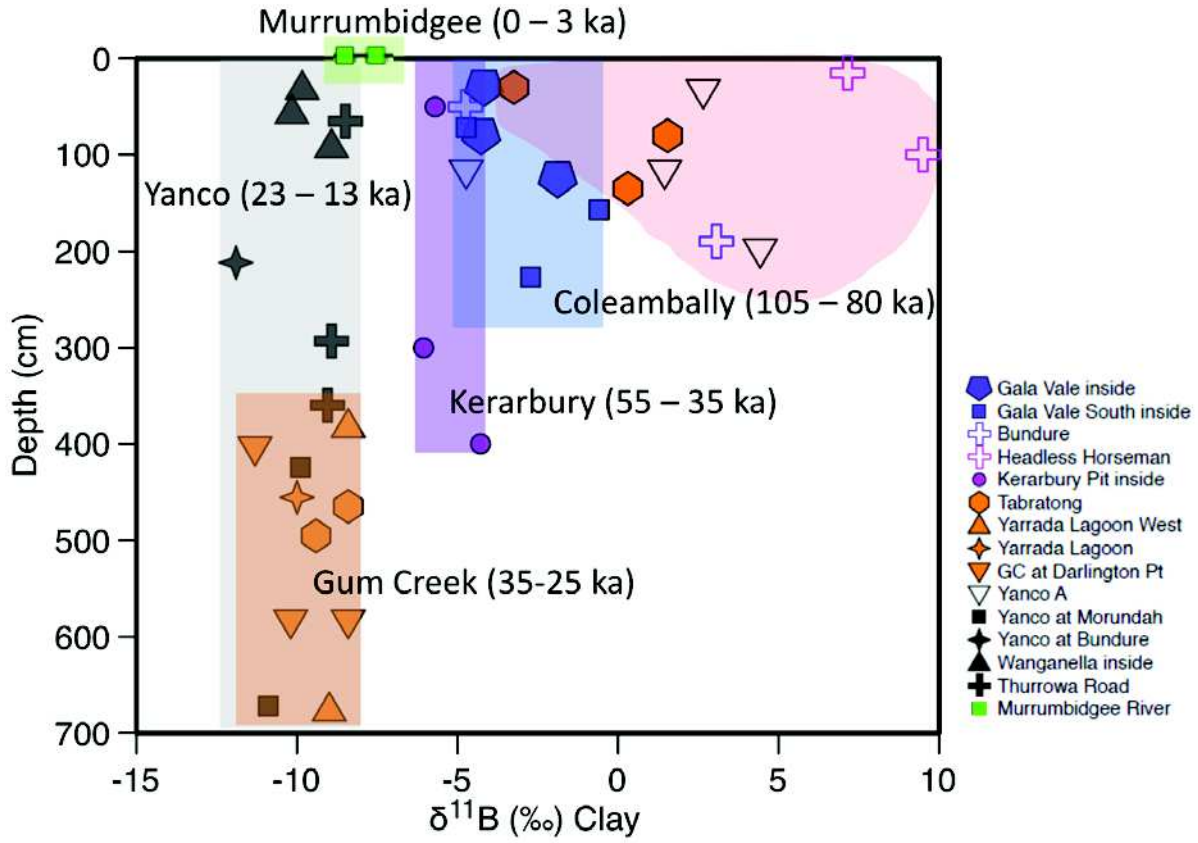

Figure 4-31. Boron isotope composition of Murrumbidgee paleochannel clay fractions as a function of depth. All sites from each system are labeled in the same color. Most sites display a narrow range of composition with depth with the exception of one site in each system which are circled in pink, displaying isotopically heavier values than other sites from the same system, possibly evidencing a weathering profile with depth.

relatively shallow samples have much heavier compositions (> 4‰) than the 2 deeper core samples taken at that site. Boron isotopes in the clay fraction of these deep cores samples have compositions which are very similar to those taken from the three upstream Gum Creek sites (also deep in the profile), likely indicating that the samples taken near to the surface at the Tabratong site have been altered after deposition. In the Kerarbury System, there were only two sites sampled (Kerarbury Pit and Headless Horseman) which have very different B isotope compositions of the clay fraction. Once 'outside' portions of samples were removed from those taken at the Kerarbury Pit, little B isotope variation (from approximately -6‰ to -4‰) exists with depth (profile is >4 m in thickness). On the contrary, shallow samples taken the Headless Horseman display B isotope compositions which are more than an 11‰ heavier than those at the Kerarbury Pit. Such a dramatic difference between sites would indicate either post-depositional alteration of samples taken from the Headless Horseman or a dramatic evolution

of the B isotope signature of the clay fraction between the two sites which are less than 100 km apart. Since results from Chapter 3 indicate that composition of the clay fraction is preserved during transport, this latter scenario does not seem likely. In the Coleambally, all sites/samples have similar B isotope compositions exclude the bottom sample taken at Bundure Pit, which is almost 8‰ heavier than other samples within this system. Additionally, the top layer sampled at the Bundure Pit consists of highly pedogenic clays and its composition would then represent modern weathering conditions (Page and Nanson, 1996). In all systems, samples which have similar B isotope compositions with depth are considered pristine, while those with isotopically heavier signatures to be possibly altered by post-depositional alteration.

Boron isotopes in paleochannel clay fractions are then compared to the B/Al ratio, an established weathering proxy, to investigate how B isotopes relate to B mobility (shown above in Fig. 4-30). As discussed above and shown in Figure 4-30, when $\Delta^{11}B_{\text{clay-sand}}$ is displayed as a function of B/Al, there are a tight cluster of samples with similar compositions to one another and to modern sediment, and a group that has much larger $\Delta^{11}B_{\text{clay-sand}}$ and/or B/Al values. Samples with heavier B isotope compositions than others in their respective systems also display higher B/Al values. Therefore, chemical evidence agrees with B isotopes and indicates an incorporation of isotopically heavy B into the clay fraction. This likely occurred after deposition and is site specific as all other sites within the same system do not have higher $\delta^{11}B$ and B/Al values and are relatively homogenous. The use of a chemical ratio such as B/Al alone to distinguish post-depositional alteration is difficult, however, by pairing B/Al ratios to B isotopes it is possible to identify post-depositional alteration. In the case of the Murrumbidee, the isotopically heavier source most likely is vegetation as the $\delta^{11}B$ of vegetation is much higher (more than 40‰) than that of the bedrock.

The depositional environment or position within the paleochannel deposit likely contributes to the preservation of the chemical and isotope composition of the clay fraction (Singer, 1980). Evidence of this is seen at several of the paleochannel sites (e.g. Kerarbury Pit, Tabratong) when comparing the B isotope clay fraction compositions of ‘inside’ vs ‘outside’ and also shallow vs deep samples. The common trend between the two types of samples is that those which are more exposed to the surface, whether higher in the profile or closer to the outside face of the deposit wall, typically have much higher B isotope compositions reflecting the incorporation of an isotopically heavy source such as B which has been cycled through vegetation and atmospheric inputs. In soil profiles from a forested ecosystem, the soil solutions

were found to be high influenced by B derived from vegetation cycling and atmospheric inputs penetrating to a depth of 60 cm with the profile (Cividini et al., 2010); below this depth, the soil solution was reported to be controlled by water-rock interactions. The B isotope composition of clays forming in this shallow zone may reflect the ^{11}B-rich soil solution as shown by Lemarchand et al. (2012). This would drive the B isotope composition of the clay fraction towards isotopically heavier values. However, our knowledge of how deep atmospherically and vegetation-cycled (^{11}B-rich) soil solution penetrates in the sediment/soil profile is limited and likely to be highly variable from site to site depended factors such as hydrology, sedimentology, porosity, etc. For instance, coarse-grained sand-rich deposits overlaid by thin layers of soil and vegetation do not have the same porosity as soil profiles. As such, one might expect the influence of ^{11}B-rich soil solution to affect or control the B isotope signature of the clay fraction to a greater depth than compared to a forested soil profile. In this case, the top meter or two might be a reasonable depth to expect an influence of atmospheric and vegetation-cycled B on the B isotope composition of the clay fraction. In addition, neo-formation of clay minerals might be expected in the upper portion of the sediment deposit where soil has developed and roots have penetrated into the sand deposit. The B isotope composition of paleochannel clay fractions might then be overprinted by modern weathering conditions and form in isotopic equilibrium with the ^{11}B-rich soil solution (Lemarchand et al., 2012).

An interesting observation between modern transported bank sediment and modern sediment deposits taken several meters away from the river was made. In bank sediment from the Murrumbidgee River (reported in Chapter 3), the clay fraction is normally isotopically lighter than the sand fraction, producing $\Delta^{11}B_{\text{clay-sand}}$ values which are less than zero. However, the two modern sediment deposits taken at Wagga Wagga and Mucklebar have $\Delta^{11}B_{\text{clay-sand}}$ values between 2 – 3‰. The reason for this difference is unknown, however, may possibly be attributed to either sampling different sediment types (e.g. bank sediment vs. bedload sediment or suspended load) or a slight shift in isotope ratio during the desiccation process. In the latter case, B exchange between the clay fractions and the porewaters within the sediment deposit may occur in response to the decrease in the water/rock ratio where a low ratio leads B to be largely in the adsorbed form in the weathering environment (Lemarchand and Gaillardet, 2006). This exchange likely occurs before or during the clay-drying process; once the clay mineral becomes dehydrated and interlayer shrinkage occurs, the cation exchange capacity (CEC) of the clay mineral will drastically decrease and therefore B exchange between the

structural network of the mineral and porewater is significantly less likely to occur (Grim, 1968). In particular, this slight exchange likely involves the smectite (exchangeable) portion of the clay sample, as it contains an expandable interlayer and has the highest CEC (compared to kaolinite which has the lowest) of all clay minerals (Ma and Eggleton, 1999). Although exchange between deposit porewaters and the kaolinite portion of the clay sample is less likely to occur, increased CEC values of kaolinites have been observed which are attributed to smectite and interstratified kaolinite/smectite impurities and also smectite layers forming on kaolinite minerals; however no structural exchange occurs within kaolinite minerals, only surficial exchanges (Ma and Eggleton, 1999). When experienced, the slight exchange between the clay fraction and porewaters within the deposit likely involves: 1) the smectite portion of the sample, 2) a rapid B exchange while the clay fraction is still wet, 3) B enrichment into the clay fraction where B is derived from an isotopically heavy source causing a shift in its isotopic composition, and finally, 4) the shrinkage and possible collapse of the mineral interlayers during wetting and drying cycles allowing little or no further exchange with the porewaters or surrounding environment after final desiccation event (Andreoli et al., 1989).

An alternative hypothesis would be that the composition of sediment deposits taken several meters away from the river may be different from that of the river bank sediments. For example, the sediment deposits were likely deposited during a flooding event in a high-energy environment, hence their displacement away from the active river. Accordingly, they may be composed of bedload and even possibly suspended load sediments which have slightly different (more positive) B isotope compositions than bank sediments, particularly in the associated clay fraction of the deposit. In the absence of suspended load measurements in the modern Murrumbidgee, this hypothesis is speculative. Since the clay fraction of paleochannel infill sediments most likely derived from a mixture of bedload, bank sediment, and suspended load (similar to modern deposits), its B isotope composition should be comparable to modern deposits. If the clay fraction experienced slight alteration due to a desiccation event, then an approximate 2‰ shift may also have occurred in paleochannel sediments. Regardless of the cause, this may have important implications to the interpretation of paleochannel sediment deposits. Unfortunately, no mineralogy, grain size, or major/trace elemental data for these modern deposits was available to aid in a more accurate interpretation. Therefore, some caution should be given to the interpretation of paleo-weathering or paleo-environmental conditions based on the current dataset. The origin of this value should be explored further in order to better determine its significance in regard to the composition of paleochannel clays.

Although post-depositional processes may have played a significant role in the chemical and B isotopic composition of some samples/sites in this study, the original signal obtained during weathering appears to be largely preserved for the majority of samples during deposition and burial. After the identification and removal of samples affected by post-deposition alteration from the data interpretation, distinctions can be made in the $\Delta^{11}B_{\text{clay-sand}}$ between paleochannel systems (Figure 4-32). Based on the analyses discussed above, the follow samples were systematically removed from the dataset: all 'outside' sample portions, all samples from Yanco A, Bundure, and Headless Horseman, and the top three samples (< 200 cm) from Tabratong; these samples are chemically and isotopically different from samples taken at different depths within the same profile and /or other sites within the same paleochannel system, possibly evidencing post-depositional alteration. Recent sediment deposits taken along the along the Murrumbidgee River (Mucklebar and Wagga Wagga), ranging in depositional ages from approximately 50 years to 3,000 years, are also plotted with paleochannel deposits in order to compare modern deposits to much older ones. The $\Delta^{11}B_{\text{clay-sand}}$ composition of sediments within the pre- and post-LGM Yanco and Gum Creek Systems are nearly identical (both ranging between about –2‰ and +2‰) and are the lowest of all systems. The $\Delta^{11}B_{\text{clay-sand}}$ composition of sediments within the Yanco and Gum Creek Systems are different from those in all other paleochannel systems, including the modern deposits. The $\Delta^{11}B_{\text{clay-sand}}$ composition of modern deposits along with those from the Kerarbury and Coleambally Systems are all quite similar, though the Kerarbury System displays with narrowest range of B isotope compositions with depth of all paleochannel systems. The Coleambally System has the widest range of B isotope compositions, however unlike other paleochannel systems, only shallow samples (0 – 2 m) could be obtained. The disadvantage of this situation is that the B isotope compositions of these samples cannot be compared to deeper samples, therefore it is more difficult to determine if these relatively shallow samples have experienced post-depositional alteration. Fortunately, three Coleambally sites were sampled and show similar isotope compositions with depth likely indicating that the channel deposits were not altered after deposition.

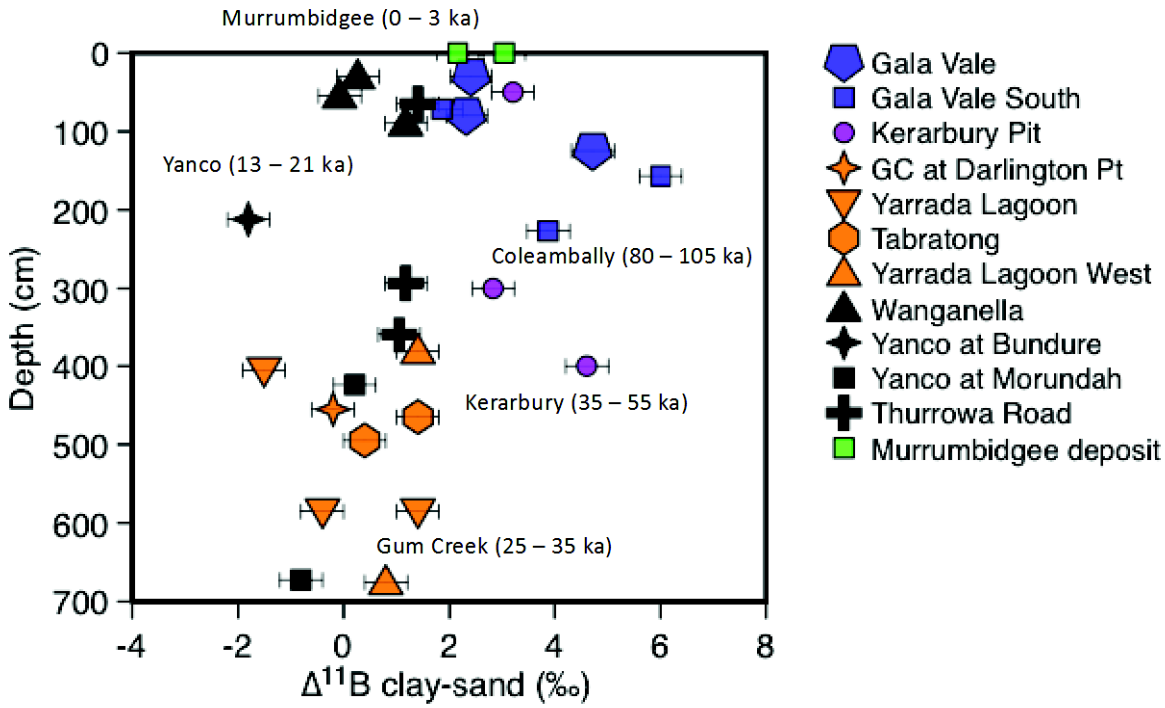

Figure 4-32. Boron isotope composition between the clay and sand fraction ($\Delta^{11}B_{\text{clay-sand}}$) as a function of depth within the Murrumbidgee paleochannel deposits on the Riverine Plain

4.5.4.4 Paleo-environmental change over the last 100 ka

The $\delta^{11}B$ of the paleochannel clay fractions which are not affected by post-depositional alteration is thought to reflect the ancient weathering regime (competition between dissolution and precipitation reactions) and the influence of vegetation cover on pedogenesis throughout the Murrumbidgee River catchment. Results from the study of modern transported sediment within the Murrumbidgee River (Chapter 3) and those from this study indicate that the clay fraction is delivered to the paleochannels with little to no bias during transport. In this case, the clay fraction of paleochannel sediment may be used as a proxy of paleo-environmental conditions and used to understand how pedogenesis has responded to climatic variability including changes in the weathering regime and the influence of vegetation on clay formation over the last glacial-interglacial cycle. The $\Delta^{11}B_{\text{clay-sand}}$ composition of all paleochannel samples not affected by post-deposition alteration are plotted as a function of deposition age alongside a faunal-based sea surface temperature reconstruction of the Southern Ocean (Figure 4-33) and a vegetation cover record for New Zealand and southern Australia (Figure 4-34). Results show co-variations between $\Delta^{11}B_{\text{clay-sand}}$ and both SST and vegetation cover over the last glacial-interglacial cycle. Both records were obtained from the same core (DSDP Site 594)

taken offshore of the South Island of New Zealand and reported in Barrows et al. (2007). As explained in Section 4.3.2, both the SST and vegetation cover records are high resolution and provide a broad picture of climatic conditions in the New Zealand and southeastern Australian regions over the last 100 ka. Although there is a more local record of SST coming from South Australia (i.e. Calvo et al., 2007) it does not cover that last 100 ka. Similarly for vegetation, the closest vegetation reconstruction to the Murrumbidgee paleochannels is at Caledonia Fen (Kershaw et al., 2007). However, this record is thought to represent a more localized site-specific reconstruction and therefore may not be representative of other areas of the Basin.

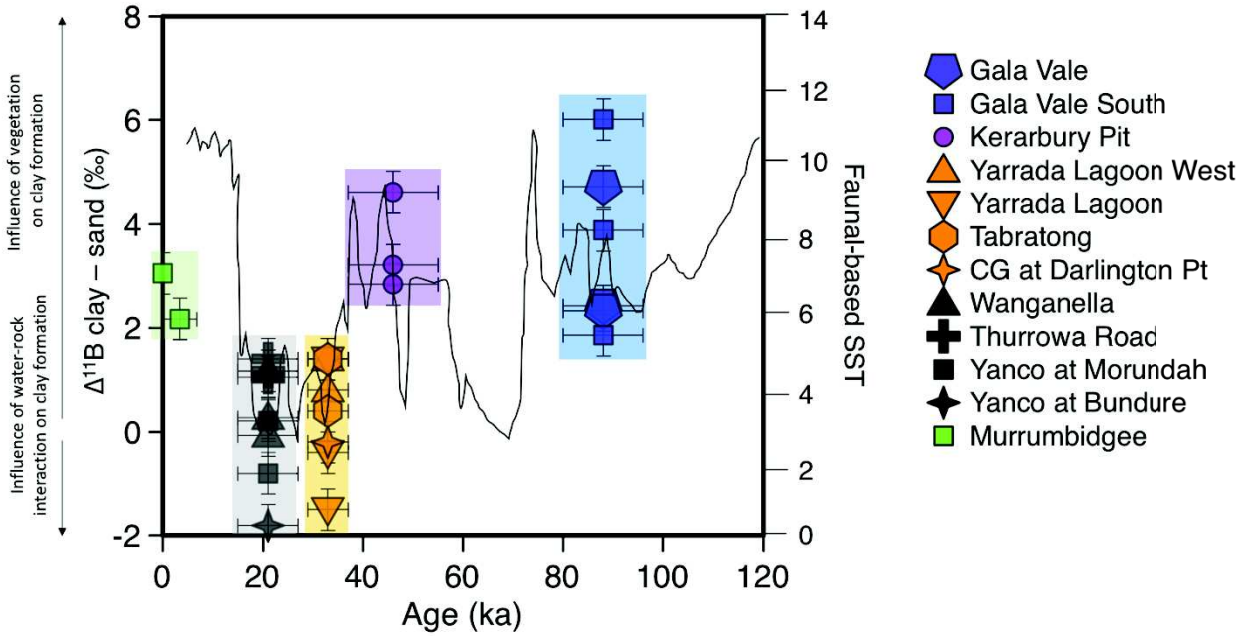

Figure 4-33. $\Delta^{11}B_{\text{clay-sand}}$ compositions of paleochannel sediment as a function of depositional age plotted with a SST reconstruction record of the Southern Ocean (Barrows et al., 2007). Co-variation between $\Delta^{11}B_{\text{clay-sand}}$ and SST may indicate that pedogenesis may respond to climatic variation.

Superposition of $\Delta^{11}B_{\text{clay-sand}}$ compositions of paleochannel sediment with SST (Figure 4-32) suggests that B isotope fractionation is closely following climate (temperature and precipitation) over the last glacial-interglacial period. Lower $\Delta^{11}B_{\text{clay-sand}}$ values occur during the coldest period of the record (during and just prior to the LGM) likely indicating that the clay fraction is primarily recording limited water-rock interactions with little influence of vegetation on pedogenesis. Since the cold and dry climate of the LGM during MIS 2 in the Murray-Darling Basin did not promote intensive chemical weathering or clay production (Barrows et al., 2001), the B isotope composition of the clay fraction is low and not significantly fractionated compared to the source, which in this case is B derived from the

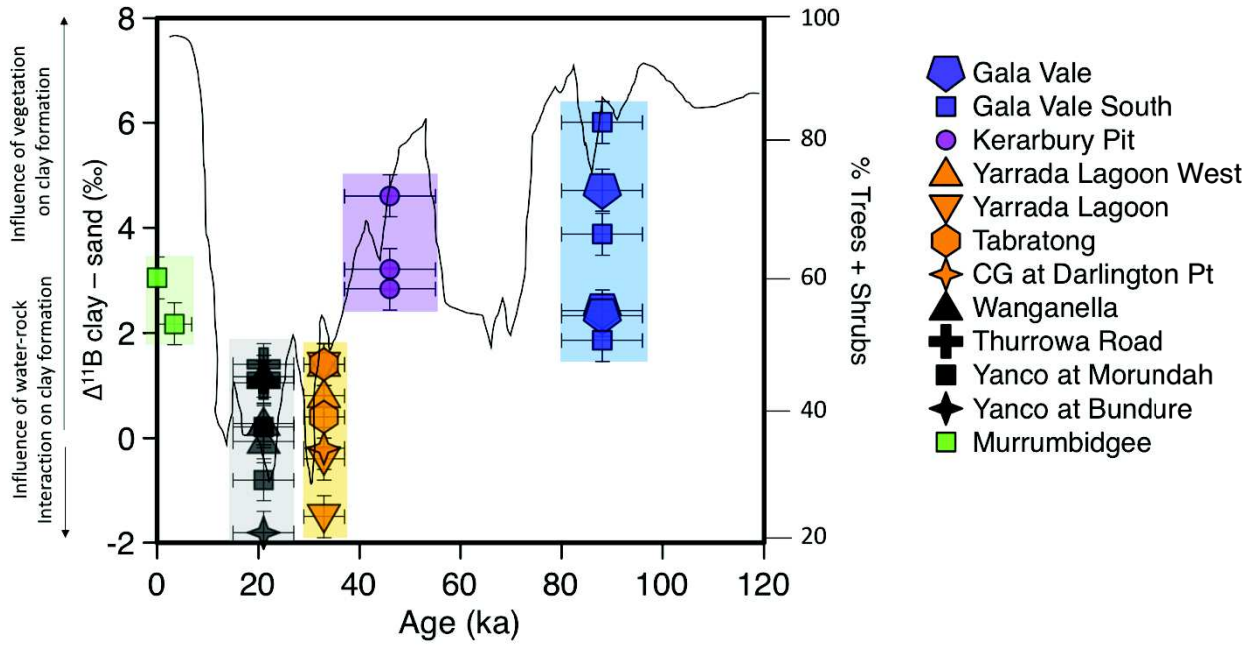

Figure 4-34. $\Delta^{11}B_{\text{clay-sand}}$ compositions of paleochannel sediment as a function of depositional age plotted with pollen-based vegetation cover reconstruction record for New Zealand and southeastern Australia (Barrows et al., 2007). Co-variation between $\Delta^{11}B_{\text{clay-sand}}$ and % Tree + Shrub indicate a variable role of vegetation on pedogenesis over the last glacial-interglacial cycle.

catchment bedrock. During the warmer and wetter inter-glacial periods (MIS 1 and 5), as well as MIS 3 which is known to be a quite active and relatively wet fluvial period (e.g. Bowler et al., 2003; Page et al., 1996), $\Delta^{11}B_{\text{clay-sand}}$ values are larger with B isotope values in the clay fractions shifting towards more positive values. This indicates that the clay fraction is interacting with an isotopically heavy B source such as atmospherically-derived B (e.g. +12‰, Wei et al., 2015) brought by increased rainfall and/or interaction with vegetation as a result of increased temperature and rainfall.

Additionally, weathering intensity during warmer/ wetter climates would expected to be greater than during colder/drier periods. In this regard, mineral identification of the clay fraction can be used to as a proxy for weathering intensity and paleo-environmental reconstruction (e.g. Mana et al., 2017; Gingele and De Deckker, 2005; Singer, 1980, 1984; Biscaye, 1965). XRD results from this study show that clay fractions in the prior and post-LGM paleochannel systems (Gum Creek and Yanco Systems) are predominately composed of mixed (I/S) layer clays, with percent abundances ranging from 49 to 65%; percent abundances of kaolinite range from 23 to 41%, with smaller percent abundances of illite (< 10%) (Figure 4-22). In modern, MIS 3, and MIS 5 sediments, mixed (I/S) layer clay compositions are much lower (ranging from 20 to 29%) while kaolinite compositions are much higher (ranging from 56 to 72%); illite compositions range from 3 to 19%. Accordingly, the presence of smectite is

indicative of early-stage low intensity weathering, climatically-interpreted as being produced in a relatively dry climate; kaolinite on the other hand, is typically produced during humid periods under more intensive weathering conditions (Singer, 1980). The clay mineral compositions measured in this study agree with this interpretation and therefore show that weathering intensity was low during the cold and dry LGM, with higher percent abundances of mixed (I/S) layer clays; during the warmer and wetter MIS 1, 3, and 5, weathering intensity is higher as clay fractions are predominately composed of kaolinite.

The co-variation of $\Delta^{11}B_{\text{clay-sand}}$ of the paleochannel sediments with the pollen record suggests that pedogenesis is responding to changes in climatic variability via the influence of vegetation on pedogenesis (Figure 4-33). Due to the cold and dry climate surrounding the LGM in southeast Australia, shrubs and herbaceous plants were dominant which are shown to have little effect on the B isotope composition of the clay fraction during pedogenesis in the headwaters of the Murrumbidgee catchment. The composition of modern deposits and those during MIS 3 (Kerarbury) and MIS 5 (Coleambally) are all very similar and display ranges of $\Delta^{11}B_{\text{clay-sand}}$ values that are notably higher than those from the MIS 2 Gum Creek and Yanco Systems. Based on a one-way (between subjects) ANOVA (α=0.05) and Bonfferoni-Dunn post-hoc tests, MIS 3 and 5 clay fractions are significantly different ($p < 0.001$) from those of MIS 2; however, MIS 1 and 2 clay fractions are not. Although, the latter result may simply be the product of low counting statistics of modern sediment deposits (n = 2). Increasing temperature and precipitation contribute to the production of more complex and woody vegetation (Barrows et al., 2001; Kershaw, 1986), which in turn have an increased capacity to cycle and heavily fractionation B isotopes (Cividini et al., 2010) compared to grassy and herbaceous species. It is then expected that a warmer and wetter climate would exert a greater influence on clay formation through the increased interaction with organic material and ^{11}B-rich soil solution. As such, the high $\Delta^{11}B_{\text{clay-sand}}$ compositions of the paleochannel deposits during MIS 1, 3, and 5 are interpreted as recording the relative influence vegetation exerts on clay formation over the last glacial-interglacial cycle. The lowest $\Delta^{11}B_{\text{clay-sand}}$ compositions during MIS 2 then suggest a minimal role of vegetation on clay formation and the increased importance of water-rock interactions on the B isotope signature of the clay fraction.

4.4.3 Conclusions

This study tests the suitability of B isotopes in sediment deposits as a potential geochemical proxy to reconstruct paleo-weathering and paleo-environmental conditions. A

thorough investigation of modern transported sediments within the Murrumbidgee catchment reveals little evidence of chemical or isotopic alteration during transport (Ercolani et al. in prep; Chapter 3). This indicates that the clay fraction retains its signature during transport and suggests that the composition of downstream paleochannel is representative of the ancient weathering signal obtained in the source areas of the catchment. However, upon deposition and burial, the behavior of B isotopes is relatively unknown. Here, we investigate B isotope behavior in paleochannel sediment deposits in the Murrumbidgee catchment (NSW, Australia) which have been deposited over the last glacial-interglacial cycle. It is hypothesize that if samples which have been affected by post-depositional alteration can be identified, then B isotopes in the clay fraction may reveal how pedogenesis has responded to climatic variability over the last 100 ka.

In this regard, samples which were suspected of being affected by post-depositional alteration have much higher B isotope compositions than other samples within the same profile or paleochannel system; higher B isotope ratios in the clay fraction are often accompanied by a shift in the B/Al ratio. This likely indicates interactions with an isotopically heavy source such as soil solution which have been cycled through vegetation. Mineral identification and characteristics of the depositional environment were also used to assess post-depositional alteration. Samples having higher B isotope and/or B/Al compositions generally have higher than average percent abundances of mixed (I/S) layer clays and/or were deposited in relatively shallow (<2 m) environments, increasing the likelihood of B exchange with the surrounding environment and therefore loss of the ancient weathering signal. In shallow profiles, the interactions between ^{11}B-rich soil solution (derived from B cycling through vegetation and atmospheric sources) and clay minerals is likely to shift the B isotope compositions of clay minerals towards heavier values. On the contrary, sediments deposited deeper within the paleochannel deposit (2 – 6 m) are less likely to be affected by surface processes and therefore have a better chance or retaining their original weathering signature. In total, clay fractions at four of the fourteen paleochannel sites were suspected of being altered by post-depositional processes and therefore removed the dataset.

After identifying and removing samples affected by post-deposition alteration from the dataset, clear distinctions in the $\Delta^{11}B_{\text{clay-sand}}$ can be made between paleochannel systems. Clay fractions from the Kerarbury and Coleambally systems deposited during MIS 3 and 5, respectively, along with two sediment deposits from the modern Murrumbidgee River have similar B isotope composition, while those from the Gum Creek and Yanco systems (pre- and

post-LGM; MIS 2) are distinctly different. The $\Delta^{11}B_{clay\text{-}sand}$ compositions of the paleochannel sediments co-vary with a SST reconstruction of the Southern Ocean (Barrows et al. 2007), indicating that pedogenesis in the Murrumbidgee catchment responds to climatic variability over the last glacial-interglacial period. In particular, higher $\Delta^{11}B_{clay\text{-}sand}$ values during MIS 1, 3, and 5 indicate an increasing influence of vegetation on clay formation, while during the cold and dry LGM (MIS 2), the influence of vegetation on clay formation is minimal and the clay fraction primarily records water-rock interactions. Weathering intensity of the clay fraction was assessed through clay mineral analyses, showing higher percent abundances of mixed (I/S) layer clays during the colder and drier LGM (Gum Creek and Yanco Systems) indicative of early-stage low intensity weathering. During warmer and wetter periods (MIS 1, 3, and 5), kaolinite was in the highest percent abundance, indicative of more intense weathering conditions. Additionally, paleochannel $\Delta^{11}B_{clay\text{-}sand}$ values co-vary with a pollen-based reconstruction of the vegetation cover for the New Zealand and southeastern Australian region (Barrows et al., 2007). This record corresponds with the SST record showing that pedogenesis responds directly to climate through the influence of vegetation, which peaks during warmer and wetter periods when more complex and woody vegetation is present on the landscape and at a minimum during the LGM when glassy and herbaceous vegetation are dominant. Since no paleochannel system was present on the Riverine Plain during the cold MIS 4, there is no data during this period.

Neodymium isotopic analyses of the Murrumbidgee sector paleochannel clay fractions reveal that the sediment delivered to the paleochannel systems derives from the upstream reaches of the Murrumbidgee River catchment and has not significantly varied over the last glacial-interglacial cycle. This has important consequences when studying B isotope compositions of paleochannel clay fractions, as a change in source can be ruled out an explanation for B isotope variations over time. Accordingly, observed variations in B isotope compositions may be interpreted in termed of the weathering regime and interactions with vegetation in the source areas of the upper catchment.

This research demonstrates the use of B isotopes in sediment deposits as a potential proxy to reconstruct paleo-weathering and paleo-environmental conditions. This is particularly possible if samples affected by post-depositional processes can be identified. Further research in this field should therefore focus on methods to identify the effects of post-depositional alteration on the clay fraction, including investigation into why the composition of modern

bank sediment is slightly different from modern sediment deposits, as this may play an important role in interpreting fluvial sediment deposits.

Chapter 5

CONCLUSION AND PERSPECTIVES

5.1 Project Conclusions

5.1.1 How do boron isotopes in modern river sediment record the weathering regime at the catchment scale?

Knowledge of B isotope fractionation during silicate weathering at the catchment scale is limited. A limited number of studies have focused on understanding the mechanisms driving weathering reactions at the catchment scale by studying the $\delta^{11}B$ composition of the dissolved load of rivers (Louvat et al., 2011, 2014; Chetelat et al., 2009; Lemarchand and Gaillardet, 2006; Lemarchand et al., 2002b; Rose et al., 2000), however very few have focused on the solid phase (Chetelat et al., 2009; Spivack et al., 1987). To date, no other study has comprehensively investigated the $\delta^{11}B$ composition of the riverine clay fraction with the goal of understanding its origin and how it records the weathering regime. Although B incorporation by precipitation or adsorption into (onto) the clay fraction during water-rock interactions in the groundwater/soil system has been invoked as the mechanism by which the dissolved load obtains its $\delta^{11}B$ signature (e.g. Chetelat et al., 2009; Lemarchand and Gaillardet, 2006; Rose et al., 2000), the original source of the $\delta^{11}B$ in the clay fraction of the river sediment remains unknown as is its relationship to the weathering regime. Consequently, no quantitative or theoretical model exists in which to explain the $\delta^{11}B$ composition of the riverine clay fraction in regards to the weathering regime. The study of modern river sediments in the Gandak and Murrumbidgee River catchments attempts to address these issues and investigate, for the first time, how river sediments record the weathering regime (competition between dissolution and precipitation reactions).

In both the Gandak and Murrumbidgee Rivers, a similar trend emerges in the B isotope composition of the sand and clay fractions along the course of each river. The $\delta^{11}B$ composition of the sand fraction remains relatively constant downstream, while the $\delta^{11}B$ of the clay fraction shows a gradual evolution towards isotopically heavier values and plateaus on the alluvial plain. Since the sand fraction is roughly representative of a mixture of unweathered bedrock in the catchment, it can be used to correct for lithological effects and compared to the clay fraction when bedrock is not available (as in the case of the Gandak River). In the Murrumbidgee, bedrock was sampled in monolithological catchments and its B isotopic composition was compared to that of the clay fraction of river bank sediments ($\Delta^{11}B_{\text{clay – bedrock}} = \delta^{11}B_{clay} - \delta^{11}B_{bedrock}$); in the Gandak, all sediments were taken from the main channel and the sand and clay fractions compared: $\Delta^{11}B_{\text{clay - sand}} = \delta^{11}B_{clay} - \delta^{11}B_{sand}$. When the isotope fractionation

factors are plotted as a function of the calculated mass transfer coefficient ($\varphi_{Al,B}$) using Al as the immobile counterpart in which to compare B mobility, both systems show a positive correlation, indicating that B mobility during clay formation is controlling the isotopic fractionation factors. In the Murrumbidgee catchment, this occurs in volcanic and sedimentary catchments at higher elevations. A more quantitative B reincorporation into the clay fraction leads to $\Delta^{11}B_{\text{clay – bedrock}}$ values towards zero in the absence of external B sources (other than the bedrock dissolution); in the Murrumbidgee, this occurs in all lithologies in the lower catchments and granitic lithologies in the upper catchment. The apparent $\Delta^{11}B_{\text{clay – bedrock}}$ differences between lithologies possibly demonstrates a lithological control on clay formation rates throughout the catchment, while differences between the upper and lower catchment demonstrate a climatic effect which is a function of catchment elevation. It is interesting to note that both systems show this trend, possibly indicating a more universal behavior of B isotopes during clay formation.

In both systems, bank sediments taken from the headwaters display larger isotope fractionations between the clay and sand fractions (in the case of the Gandak) and between the clay and bedrock in the Murrumbidgee (between 3‰ and 8‰ in the Murrumbidgee and approximately 3‰ in the Gandak) compared to those found on the alluvial plain (approximately 2‰ in the both the Murrumbidgee and the Gandak). These observations likely indicate different weathering conditions in the mountains than on the alluvial plains. In the Murrumbidgee River catchment, sediment source areas in monolithological catchments at both higher and lower elevations were identified by spatial analysis in order to determine differences in temperature, rainfall, and catchment slope that may influence weathering conditions. The upper catchment is characterized by lower temperature, higher rainfall, and steeper slopes than the lower catchment, which likely contribute to differences in clay production rates and silicate weathering intensity (Lupker et al., 2012; Millot et al., 2003). For example, in the Himalaya, Lupker et al., (2012) reported that the clay formation is more favorable in environments where the sediments have longer transfer times (in areas with less steep slopes) and in warmer and wetter conditions such as the Gangetic Plain, compared to the upper catchment where predominately erosion, rapid sediment transport, and little chemical weathering and clay formation occur. Lupker et al. (2012) also reported increased proportions of smectites and other expandable clays from the Himalaya front downstream to the Gangetic Plain, and increased H_2O^+/Al and δD compositions which reflect a larger incorporation of clay minerals in equilibrium with floodplain surface waters. Both Lupker et al. (2012) and Millot et al. (2003)

(Mackenzie Basin, Canada) report that silicate weathering on the floodplain is predominant over weathering in the mountain, a finding that contradicts the "Raymo Hypothesis" (Raymo and Ruddiman, 1992; Ruddiman et al., 1988). Gandak River sediments do not show a systematic decrease in mobile elements downstream (indicative of higher weathering intensity) as reported by Lupker et al. (2012) for other Himalayan rivers. When applied to the Murrumbidgee, lower temperatures, higher rainfall, and steeper slopes would not favor clay formation or intense chemical weathering, but rather physical erosion and rapid sediment transport to the lower catchment. On the contrary, warmer temperatures and longer sediment transport times at lower elevations would promote clay formation and increased weathering rates and intensities.

The development of a conceptual model for the clay-porewater system capable of describing the B isotopic composition between the clay fraction and bedrock in terms of the weathering regime (competition between dissolution and precipitation reactions) is a significant advancement in this field which has not previously been undertaken. The need for a framework to interpret B isotope data in transported river sediment is increasing as more studies focusing on the solid phase. For instance, several recent studies, (e.g. Noireaux et al., 2014; and Lemarchand et al., 2012; Ercolani et al. in prep) investigated B isotope behavior during weathering reactions in soil profiles that would benefit from such a model and aid in the interpretation of B isotopes in the clay fraction.

To model the chemical and B isotopic composition of the percolating surface/groundwater and clay fraction, a reactive transport model was used, which describes an ^{11}B enriched surface water (derived from atmospheric inputs and vegetation) which has percolated through the soil profile on its downward migration. With depth, the B isotope composition of this solution progressively becomes isotopically lighter (as does the precipitated clay fraction; in equilibrium with dissolution/precipitation ratio. Cividini et al. (2010) and Noireaux et al. (2017) confirm this hypothesis in forested ecosystems, where the porewaters within the upper soil layers (particularly the top 60 cm) are observed being enriched in ^{11} and that this heavy B isotope signature is progressively lost in deeper porewaters. However, results show that model cannot predict B concentrations or isotopes of the soil solution and observed clay fraction values without using unrealistic modeling parameters such as flow path distance and water velocity. This likely indicates that the clay fraction is not precipitating from the bulk soil solution. On the contrary, clays are hypothesized to be precipitating from a porewater solution that evolves in a partially-closed system best described by Rayleigh distillation. An example of such a porewater may be inside a primary mineral (similar to secondary mineral

replacement). The source of B to the clay fraction comes from the mineral itself which has an isotopic composition close to that of the clay fraction. Similarly, high B concentrations in these pore spaces (in the range of 10 ppm) are needed to produce clay fractions with even higher concentrations (in the range of 50 ppm), which can be explained by continual mineral dissolution in a partially-closed system. This implies a long reaction time between the secondary mineral and the porewater, likely not present in transient soil solutions.

In the case of the Murrumbidgee, the average B isotope composition of the dissolved load is approximately +31‰ while the average B isotope composition of clay fraction is –12‰, which is more than a 40‰ difference between the two components. If the B isotope composition of the dissolved load was controlled by B exchange between clay particles and porewaters as proposed by many studies (Chetelat et al., 2009; Lemarchand and Gaillardet, 2006; Lemarchand et al., 2000; Rose et al., 2000), then the B isotope fractionation between the two components, if in equilibrium, would be approximately -30‰ and a function of pH (Rose et al., 2000; Palmer et al., 1987; Spivack et al., 1987). However, the average difference of ~40‰ between clay fraction and the dissolved load makes this possibility very unlikely. This indicates that the chemical and B isotope compositions of the dissolved load and clay fraction are not in equilibrium and thereofere the clay fraction did not precipitate from a solution with characteristics of the dissolve. This apparent disconnection in B isotopic composition between the dissolved load and transported sediment likely derives from the fact that river waters integrate all surface to underground processes including reactive transport processes, active biogeochemical cycles, and incorporate vegetation and atmospheric sources. This produces higher boron isotope compositions in soil solution (and dissolve load) with low B concentrations while the signature of the clay is obtained from a porewater solution that has a low B isotope composition and a relatively high B concentration (at least in the case of the Murrumbidgee). This interpretation of B isotopes can likely apply to Noireaux et al. (2014) who also reported B isotope compositions of the soil (where B is carried by the fine fraction) which are lower than the bedrock by 1%. Lemarchand et al. (2012) on the other hand reported an isotopically heavier B isotope composition of the clay fraction than the bedrock (up to 7%), indicating that the pedogenic clays (formed in the top meter of the profile) are forming in contact with an isotopically heavy soil solution which was attributed to B derived from vegetation cycling and the atmosphere. If correct, this description has an important implication: there is no reason that B in clay minerals should be in equilibrium with dissolved B, neither in top soils nor in rivers. This is evident by the approximate -40‰ B isotopic difference between the clay fraction and the dissolved load. Clays may record only the very local conditions of

their formation (possibly in a confined environment) whereas soil solutions and rivers may be fed by waters that have not substantially exchanged matter with minerals. This would imply that both the dissolved and particulate phases may record weathering information and serve as proxy.

5.1.2 What is the behavior of B isotope in river sediment during transport from sediment source areas to the depositional environment?

No study to date has investigated how the clay fraction in river sediments obtain their $\delta^{11}B$ signature or how that signature is transported from upstream sediment source areas to the downstream deposition environment. This study therefore constitutes the beginning of our understanding of these important topics which will be necessary in order to address the third research question: whether B isotopes in sediment deposits can be used a proxy to reconstruct paleo-weathering and paleo-environmental conditions. In a previous study of Murrumbidgee River sediment (Suresh et al., 2014), bank and sand bar sediment were collected along the course of the river and major and trace elemental analyses was performed. A Chemical Index of Weathering (CIW) calculation revealed that no significant chemical weathering occurs during transport, a result that was confirmed by the present study using both major and trace elements, and boron isotopes. Here it was tested whether the chemical and B isotopic composition of the clay fraction can be explained as a mixture of sources throughout the catchment or if they are evolving downstream. Theoretical $\delta^{11}B$, B/Al, and Mg/Al compositions of the clay fraction at 10 points along the Murrumbidgee River were calculated using a mass balance model. The clay composition of stream bank sediment in monolithological catchments (see discussion above) was used as mixing endmembers along with surface proportions of drained lithologies to the various points along the Murrumbidgee River. Results show that the compositions of the calculated values are all within error of measured values, indicating that their $\delta^{11}B$, B/Al, K/Al, and Mg/Al compositions are the result of a mixture of clays produced throughout the catchment drained to the main channel in different proportions by the tributaries with little or no alteration during transport. Using the bedrock in monolithological catchments as mixing end-members, the theoretical $\delta^{11}B$ sand values were also calculated in the same manner. Results also show that the composition of the sand fraction can adequately be explained as a mixture of catchment bedrock.

This result, shown for the first time, is significant as it suggests that B isotopes in the clay fraction of riverine sediment deposits may be used as a paleo-weathering proxy due to the fact

that it retains its original chemical and isotopic signature during transport. In terms of the paleochannel deposits in the Murrumbidgee, the chemical and B isotopic composition of the clay fractions delivered to the channels is expected to reflect weathering conditions in the source areas of the catchment, with little to no bias during transport.

The $\Delta^{11}B_{clay-sand}$ composition of actively transported bank sediment collected from the downstream reaches of the modern Murrumbidgee was compared to modern sediment deposits (deposited several meters away from the banks of the modern Murrumbidgee River) to check for similarities or differences as this may reveal B isotope behavior after deposit and burial. This comparison shows that modern bank sediment has a $\Delta^{11}B_{clay-sand}$ composition of approximately 0‰ while modern sediment deposits have values of approximately 2‰. While the reason for this apparent difference is not known (due to lack of chemical, mineralogy, or grain-size data of modern deposits), it is hypothesized that a grain size / mineral sorting between actively transported bank sediment and a sediment deposit might be the cause. Alternatively, the B isotope composition of the sediment deposit may not have been preserved after deposition. However, the B isotope composition of the modern sediment deposits are very similar to other paleochannel deposits which show no evidence of a weather profile or post-depositional alteration (see discussion below). Therefore, these differences are more likely to be caused by a sorting effect or even the result of local site variability. Regardless of this possible shift, the composition of modern deposits and most paleochannel deposits are very similar indicating that the B isotope composition of paleochannel sediments is largely preserved after deposition and burial.

5.1.1 Can boron isotopes in sediment deposits be used as a proxy for the paleo-weathering and paleo-environmental reconstruction and reveal how pedogenesis has responded to climate variability over the last glacial-interglacial cycle?

The investigation of B isotopes in fluvial sediment deposits has not been undertaken prior to this study. As with the behavior of B isotopes in sediments during fluvial transport, our knowledge of B isotope behavior and its use in fluvial sediment deposits as a paleo-weathering proxy is limited to this study. Results from this work constitute a significant advancement in the field of B isotope geochemistry and provide the first example of how B isotopes in fluvial sediment deposits can be used as a geochemical proxy for paleo-weathering and paleo-environmental reconstruction. As mentioned earlier in this chapter, B isotopes in loess-paleosol

sequences in China (Wei et al., 2015; Zhao et al., 2003) are the only other works that utilize B isotopes to reconstruct paleo-weathering conditions over a similar timescale (last glacial-interglacial cycle). The successful application of B isotopes in loess-paleosol profiles and the promising results from the study of B isotopes in modern sediments in the Murrumbidgee River catchment (Chapter 3; Ercolani et al., in prep) indicating the retention of the weathering signal carried by the clay fraction during transport, provide an indication that this approach may be successful and applicable to other depositional settings.

In the absence of post-depositional alteration, the composition of the clay fraction is expected to reflect the ancient weathering signal from the source area. Therefore, the identification of samples which have been altered after deposition is critical if the aim is to determine changes of past weathering regimes because their signature no longer reflects the original weathering conditions. This was first considered by splitting the core sample into 2 portions: a more pristine 'inside' portion and a more exposed (closer to the surface) 'outside' portion. Boron isotope analyses on both sample aliquots indicates contradicting behavior, showing that the 'outside' portion can be isotopically heavier or lighter depending on the site. This may be attributed to either post-depositional alteration or local sample variability. Regardless of the cause, the 'outside' portion of the samples was removed from the dataset as the variation in B isotope composition in the clay fraction with depth was generally greater than variation between the inner and outer portion of the sample. Boron isotope compositions in the clay fraction at each site were compared with other samples/site within the same system as a function of depth in order to identify a possible weathering profile. Within each system there was one site where the B isotope clay fraction compositions were much heavier than other samples/site within that system. These high B isotope compositions were often accompanied by an increase in the B/Al ratio which together indicate interaction with an isotopically heavy source such as ^{11}B-rich soil solution that has been cycled through vegetation. Additionally, these samples were deposited in relatively shallow environments (< 2 m in depth) which would facilitate greater B exchange with the environment and therefore loss of their original weathering signal. The chemical and B isotopic composition of samples/sites that do not show visible evidence of a weathering profile nor display exceptionally higher δ^{11}B values are therefore considered to be pristine and reflect the original weathering conditions; this was the case for the majority of paleochannel samples.

To determine whether variations in the B isotope composition of the paleochannel clay fraction are the result of the paleo-weathering regime, or due to changes in sediment

provenance over the last 100 ka, the source of the sediment was determined using Nd isotopes. The Nd isotope composition of paleochannel clay fractions was also compared to that of the modern Murrumbidgee River and granitic, volcanic, and sedimentary bedrock. Results show that the εNd composition of paleochannel clays can be explained as a mixture of sediment from within the Murrumbidgee River catchment with no significant change in sediment source over the last glacial-interglacial cycle detected. Without a major change in the source of sediment delivered to the Riverine Plain over the last 100 ka, variations in the $\delta^{11}B$ of the clay fractions between channel systems can be interpreted as reflecting processes that affect their B isotope compositions such as variations in the weathering regime or changes in environmental conditions.

Finally, after the removal of samples affected by post-depositional alteration and determination that changes in sediment source are not responsible for the B isotope variation in the clay fraction of paleochannel sediments; variations in the B isotope composition of the clay fraction can be compared to overall drivers of the weathering regime such as climate and change in the paleo-environments such as vegetation cover. When the $\Delta^{11}B_{clay-sand}$ composition of paleochannel sediment is plotted as a function of depth, clear differences between systems can be recognized; both LGM systems, the Yanco (21 – 13 ka) and Gum Creek, have very similar $\Delta^{11}B_{clay-sand}$ compositions which are distinct from the Kerarbury and Coleambally Systems. Although an ANOVA test reveals the composition of modern sediment deposits are not significantly different from those in the Yanco and Gum Creek systems, this result is likely caused by poor counting statistics (n = 2) for modern deposits. Nevertheless, clay fraction deposited during the LGM have lower B isotope compositions than modern deposits and those deposited during the Kerarbury (MIS 3) and Coleambally (MIS 5) phases.

Plotted as a function of age (0 – 100 ka), $\Delta^{11}B_{clay-sand}$ compositions of paleochannel sediment co-vary with a SST reconstruction of the Southern Ocean (Barrows et al., 2007) and a vegetation record of southeast Australia and New Zealand (Barrows et al., 2007). The co-variation of B isotopes in the clay fraction with SST and vegetation indicate that pedogenesis has responded to variations in climate over the last glacial-interglacial cycle. Increases in temperature and precipitation should produce more complex vegetation on the landscape which have the potential to increase chemical weathering rates and intensities (e.g. Gíslason et al., 1996), while amplification of the hydrologic cycle should directly increase weathering fluxes (Maher and Chamberlain, 2014; Gaillardet et al., 1999a).

During the cold period of the LGM (MIS 2) corresponding to the Yanco and Gum Creek systems, little B isotope fractionation is observed between the sand and clay fractions, indicating that during cold, dry periods clay production is minimal and B is mainly sourced from the dissolution of bedrock. During warmer periods such as the Holocene (MIS 1), MIS 3, and MIS 5, $\Delta^{11}B_{clay-sand}$ compositions are larger (up to +6‰) and the clay fraction is always isotopically heavier than the sand fraction, indicating an active weathering regime of increased precipitation with a significant part of B in the clay fraction coming from an isotopically heavy source such as vegetation or atmosphere. XRD analysis of the paleochannel clay fractions agree with this interpretation, showing the composition of the clay fractions during warmer climates is predominantly kaolinite (~75%) which is indicative of clays in a more advanced weathering stage produced by higher leaching rates of water in soil profiles (Ma and Eggleton, 1999; Singer, 1980). During colder periods, the clay fraction has a much larger percentage of mixed (I/S) layer clays which are formed in the first phase of clay production indicating a less advanced weathering state in drier conditions (Singer, 1980). This result agrees with Wei et al. (2015) who reported that pedogenic intensity correlates with climate variability over the last glacial-interglacial cycle using B isotopes in the acid-soluble phase of several loess-paleosol sequences; cold climates are characterized by lower $\delta^{11}B$ values and less intense pedogenesis while warmer climate are characterized by higher $\delta^{11}B$ values and more intense pedogenesis. Higher $\delta^{11}B$ values in loess-paleosol sequence were attributed to increased atmospheric inputs during summer monsoon circulation. In the current study $\Delta^{11}B_{clay-sand}$ compositions of paleochannel sediments strongly correlate with vegetation cover in southeast Australia. This indicates that higher $\Delta^{11}B_{clay-sand}$ compositions reflect an increasing role of vegetation on pedogenesis during the warmer and wetter climates (MIS 1, 3, and 5) and less of a role during colder, drier climates (MIS 2 and 4).

Specifically, boron isotope compositions in the clay fractions of paleochannel deposits reflect climate variability (precipitation and temperature) which produce different vegetation covers and influence pedogenesis to different degrees. In particular, during colder and drier periods, less precipitation and lower temperatures produce grassy and herbaceous species which have less of an influence on pedogenesis. Boron isotope compositions in the clay fraction remain low and reflect water-rock interactions. On the contrary, during warmer and wetter periods, increased precipitation and temperature produce a more complex vegetation cover which have a greater influence on pedogenesis. Boron isotope compositions in the clay

fraction are higher and reflect the increased flux of boron which has been cycled through vegetation.

5.2 Perspective and future research

In the study of the Gandak River in the Himalayas, sediment samples were limited. Only one sample was obtained from the true headwaters of the Gandak River and no samples were taken after the convergence with the Ganges River further downstream on the Gangetic Plain. Obtaining additional headwater sediment samples would be particularly important as it appears that the weathering regime controlling the B isotope composition of the clay fraction in the headwaters is different from that on the plain, though, this hypothesis is only based on one point. A similar trend in the $\delta^{11}B$ composition of hand-picked biotite and muscovite minerals and the clay fraction of bank sediment was observed (all showing isotopically lighter values in the headwaters which gradually increase downstream), which is difficult to explain and therefore warrants further investigation. At the moment, it appears that the primary minerals may be incorporating secondary phases into their structures and therefore evolve downstream in response to changes in weathering conditions along the river, similar to the clay fraction. It is possible, however, the source of the minerals may be different and therefore their B isotope composition can only be used as a source tracer and not used to trace weathering reactions. Additional downstream samples would be useful for a more detailed investigation. Finally, the Gandak River was the only Himalayan River sampled, therefore results may be localized as not apply to the entire system. As many Himalayan rivers have been studied for various purposes and sediment samples have already been collected by others, it would be prudent to conduct a similar study in a different Himalayan river, thereby verifying the generality of the conclusions of this study. However, conclusions from the Murrumbidgee study are in agreement with those from the Gandak River study, providing support for a more global interpretation of the B isotope behavior in river sediment during transport.

In the Murrumbidgee study the sampling strategy was more thorough than the Gandak. The study focused on the clay fraction which is particularly difficult to obtain in most bank river samples (sometime sieving more than 1 kg of sediment to obtain 50 – 100 mg of clay) and quite heterogeneous in its chemical and isotopic composition, therefore, more clay should have been sieved at the beginning of the study for each sample. It became particularly obvious more clay was needed for each sample when the number of chemical and isotopic analyses was realized which included 100 mg of clay for major and trace elements, 50 mg of clay for B

isotopes, 10 mg of clay for XRD, and 100 mg of clay for Nd isotopes. Consequently, more clay needed to be sieved from the bulk sediment of numerous samples which may have had a slightly different chemical and isotopic compositions than the previous aliquot of sieved clays. Regarding the relationship between $\Delta^{11}B_{clay-bedrock}$ and the weathering regime at the catchment scale, additional studies should be conducted to confirm the results of the preliminary Murrumbidgee study because rivers draining different lithologies (e.g. carbonates) and under different geologic and climatic settings may not record the weathering regime in the same manner (e.g. in tectonically active area with high erosion and high weathering rates, or in tropical environments where the B isotopes in clay fraction might be controlled by vegetation inputs).

Boron isotope compositions in sediment deposits show great potential as a new geochemical proxy for paleo-weathering and paleo-environmental reconstruction. This is evidenced by the ability of B isotopes in the clay fraction of paleochannel sediment to record the influence of climate and vegetation cover on pedogenesis over the last glacial-interglacial period and also by previous studies using B isotopes in loess-paleosol sequences (Wei et al., 2015; Zhao et al., 2003) which demonstrate its usefulness in determining paleo-weathering intensity in relation to climatic variability. However, the applicability of this proxy in other environments or sites is relatively unknown as the development of this proxy is still in the very early stages. The ability to use this proxy ultimately depends on the preservation of the B isotope composition of the sample which is likely affected by factors such as mineralogy (e.g. expandable vs. non-expandable clays), depositional environment (e.g. shallow vs. deep depths in the profile), and climate conditions of modern environment (e.g. heavily vegetated, humid vs. dry environment). Additionally, the ability to identify and remove samples that have been possibly altered by post-depositional processes is essential to obtain a more pristine record of paleo-environmental change. Therefore, further research should focus more closely on different sampling techniques and analytical methods to identify post-depositional alteration and applying this proxy to different depoostional environments. In the Murrumbidgee catchment, paleochannel deposits were obtained at both shallow (< 2 m) and deep (> 2 m) depths in all systems (Yanco, Gum Creek, and Kerarbury) but the Coleambally in order to assess chemical and isotopic variation with depth which may be related to post-depositional alteration. Deeper samples in the Coleambally system were not obtained because pit exposures at all Coleambally sites were relatively shallow, therefore it was not possible to obtain deeper samples without using a drill rig (which was not used in this field campaign). At the Kerarbury

Pit, the surface exposure was quite deep (~6 m) so obtaining deeper samples was possible. In the Yanco and Gum Creek systems, deeper samples in the profile were taken with a drill rig by colleagues at UOW and donated to this project. However, in the Coleambally system, neither of these options were available, so a comparison between deeper (presumably more pristine) and more shallow channel deposits was not possible. Without this comparison, some doubt remains if shallow samples collected from the Coleambally system have been altered by post-depositional processes, although similar B isotope clay fraction compositions in two of the three sites (excluding Bundure) suggests that post-depositional alteration has not occurred. To better address this issue and strengthen the interpretation of the last 50 ka for the record, samples deeper in the sediment profile should be obtained using a drill rig to verify the B isotope composition of the clay fraction in shallow samples is similar to those of deeper samples at the same sites.

Appendix 1

RÉSUMÉ

A.1 Introduction du projet

L'altération chimique couplée à la précipitation carbonatée dans l'océan est responsable d'une grande partie de la séquestration du CO_2 atmosphérique qui équilibre les apports de CO_2 dans l'atmosphère du dégazage planétaire et des éruptions volcaniques et régule donc le climat global sur l'échelle géologique (Ruddiman et al., 1988; Berner et al., 1983; Walker et al., 1981). Malgré l'importance de l'altération chimique pour redistribuer les éléments chimiques entre les réservoirs de surface et maintenir des conditions habitables à la surface de la Terre (White and Blum, 1995), la quantification de l'altération chimique passée et présente reste difficile en raison de la complexité des facteurs d'interaction. Les régimes d'altération modernes (taux, intensités, etc.) sont classiquement déduits des flux de solutés des rivières (e.g. West et al., 2005; Gaillardet et al., 1999b) en utilisant des concentrations d'éléments mobiles et immobiles. Cependant, cette approche est imparfaite en raison du contrôle lithologique sur la charge dissoute (Gaillardet et al., 1999b; Dupré et al., 1996). L'autre approche est d'analyser les concentrations d'éléments majeurs et traces dans les solides formés au cours d'altération (e.g. Lupker et al., 2012; Gaillardet et al., 1999a; France-Lanord and Derry, 1997). Cependant, la lithologie a un impact sur la composition des phases solides (Gaillardet et al., 1999a; Vital et al., 1999) et il est difficile d'intégrer la variabilité des sédiments détritiques dans le temps et dans l'espace, ce qui représente encore un défi pour cette approche (Bouchez et al., 2011; Lupker et al., 2011). Contrairement à ces traceurs chimiques de l'altération des silicates, les isotopes stables 'non-traditionnels' tels que le bore (B), le lithium (Li) et le calcium (Ca) constituent une alternative intéressante car les processus d'altération engendrent des fractionnements isotopiques entre les phases solides et dissoutes que l'on peut ensuite interpréter en terme de bilans des réactions mises en jeu (Bouchez et al., 2013).

En particulier, B présente des propriétés physico-chimiques propres à l'étude des interactions eau-roche, y compris celles impliquant une composante biologique (Noireaux et

al., 2017; Cividini et al., 2010; Lemarchand et al., 2000). Les processus responsables du fractionnement isotopique B sont l'adsorption de B sur les particules argileuses et détritiques (Spivack et al., 1987; Schwarcz et al., 1969), la précipitation de B dans les phases secondaires (Williams, 2001; Williams et al., 2001a), l'altération de la roche-mère continentale ou océanique (Muttik et al., 2011; Williams, 2001; Spivack et al., 1987), l'évaporation et la dissolution durant le cycle atmosphérique du B (Chetelat et al., 2005; Rose-Koga et al., 2006; Roux et al., 2017; Xiao et al., 1997), et le recyclage par la végétation (Noireaux et al., 2017; Roux et al., 2017; Cividini et al., 2010; Wieser et al., 2001; Vanderpool and Johnson, 1992). Alors que plusieurs études ont utilisé les isotopes B comme traceurs pour quantifier et suivre les réactions chimiques d'altération dans la charge dissoute des fleuves (Chetelat et al., 2005, 2009; Lemarchand and Gaillardet, 2006; Lemarchand et al., 2002b; Rose et al., 2000; Spivack et al., 1987), peu ont étudié la composition isotopique du B dans des sédiments (Chetelat et al., 2009; Spivack et al., 1987). Dans les deux études qui se concentrent sur les sédiments des rivières, les auteurs ont analysé les isotopes B dans la charge suspendue et négligé la charge de fond et les sédiments détritiques (argileux). Spivack et al. (1987) and Chetelat et al. (2009) montrent que les charges suspendues et dissoutes des rivières ont des valeurs $\delta^{11}B$ nettement différentes et que la charge en suspension a une composition isotopique du bore proche de celle de la croûte continentale (-7 ‰). Dans la rivière Chiangjiang, Chetelat et al. (2009) ont montré également que B/Al, un indicateur de la mobilité B durant l'altération chimique, est positivement corrélé avec le facteur de fractionnement isotopique entre la charge dissoute et la charge suspendue, suggérant que la réincorporation de B dans les minéraux secondaires contrôle la composition isotopique B de la charge dissoute. En dehors de l'exploration limitée de la composition isotopique du B de la charge suspendue, la connaissance du comportement des isotopes du B dans les sédiments fluviaux pendant le transport et sa capacité à enregistrer les interactions eau-roche à l'échelle du bassin manquent sévèrement. De plus, comme suggéré

par Chaussidon and Albarède (1992), l'utilisation des isotopes du B dans les dépôts de sédiments comme traceurs de paléo-altération ou paléo-environnement a du potentiel et devraient être dévelopée, comme le montrent les quelques séquences de loess-paléosol chinois (Wei et al., 2015; Zhao et al., 2003) et des dépôts lacustres (Xiao et al., 1992; Vengosh et al., 1991a). A travers l'identification des sources B dans les lacs et les processus géochimiques qui affectent les isotopes du B (principalement l'adsorption B sur les minéraux argileux entraînant un enrichissement en ^{10}B dans la fraction argileuse et un enrichissement en ^{11}B dans la charge dissolvante) Xiao et al. (1992) et Vengosh et al. (1991) ont reconstruit l'histoire géochimique et géomorphologique des lacs salés qui sont indicatifs des conditions paléo-environnementales. Dans les séquences de loess-paléosol, Zhao et al. (2003) ont trouvé que le signal chimique et isotopique du B était porté par la phase adsorbée sur les particules d'argile, avec une contribution négligeable de la phase carbonatée dans le dépôt. Les variations de la teneur de B et des isotopes B de la phase adsorbée reflètent principalement un changement de la source de bore, tandis que celles des phases acide-solubles dans les couches de loess et de paléosol sont contrôlées par l'intensité de l'altération qui est contrôlée par les conditions climatiques et environnementales. Spécifiquement, une teneur plus élevée de B dans les phases acide-solubles résulte d'une altération chimique plus intense pendant les régimes climatiques chauds et humides. Un résultat similaire a été trouvé par Wei et al. (2015) qui ont analysé la composition isotopique B de 5 profils loess-paléosol en Chine. Ici, les variations de [Sr], [B], $\delta^{11}B$, et la susceptibilité magnétique (un proxy paléo-climatique utilisé pour déterminer le degré de pédogenèse) corrèlent bien avec l'intensité pédogénétique déterminée par l'indice CIW (dans trois des cinq profils) où la pédogenèse pendent des climats froids a produit de faibles $\delta^{11}B$, des concentrations basses en B mais élevées en Sr ainsi que de faibles valeurs de susceptibilité magnétique indiquant des intensités d'altération faibles ; alors que les climats plus chauds et humides montrent le contraire et indiquent des intensités d'altération plus élevées. Bien que

l'utilisation des isotopes B dans les sédiments comme traceurs des conditions paléo-climatiques et paléo-environnementales ait été limitée à quelques études, ces résultats préliminaires démontrent son grand potentiel.

La motivation de ce projet a été fondée sur le manque apparent de connaissance du comportement des isotopes B pendant la pédogenèse et le transport, ainsi que sur la promesse d'utiliser les isotopes B dans les dépôts de sédiments comme indicateur de la paléo-altération et de la reconstruction paléo-environnementale. Dans cette thèse, il a été supposé que si la connaissance des isotopes B pendant la production et le transport des sédiments peut être acquise (Chapitre 3), les isotopes du B dans les sédiments de paléochenaux (en particulier la fraction argileuse) peuvent être utilisés pour reconstituer les conditions des paléo-altérations et paléo-environnementales et de mieux comprendre comment l'altération des continents répond à la variabilité environnementale/climatique (Chapitre 4). Comme indiqué dans l'introduction de cette thèse (Chapitre 1), cette recherche aborde trois aspects clés du comportement des isotopes B dans la zone d'altération qui sont actuellement sous-étudiés avec les objectifs suivants :

1. Mieux comprendre comment les isotopes du bore dans les sédiments fluviaux modernes enregistrent le régime d'altération à l'échelle du bassin versant.
2. Mieux comprendre comment le signal d'altération porté par les sédiments fluviaux est transféré des zones sources vers l'environnement de dépôt.
3. Déterminer si les isotopes du B dans les dépôts sédimentaires (paléo-canaux) peuvent être utilisés pour reconstituer les conditions paléo-climatiques et paléo-environnementales et ainsi révéler comment l'altération continentale au sens large (production et transport de sédiments) a réagi à la variabilité climatique au cours du dernier cycle glaciaire-interglaciaire (derniers 100 ka).

A.2 **Méthodes de projet**

Les deux premiers objectifs ont été abordés en étudiant le comportement isotopique du B des minéraux séparés par des fleuves activement transportés dans deux systèmes fluviaux très différents : la rivière Gandak dans le bassin du Gange dans l'Himalaya; et la rivière Murrumbidgee dans le bassin Murray-Darling du sud-est de l'Australie. L'étude du fleuve Gandak a été menée en premier lieu sur le comportement isotopique B des sédiments minéraux transportés (les fractions totale, sable (63 μm - 2 mm), argileuse (<2 μm), charge suspendue, et les minéraux sépares biotite et muscovite cueillies à la main). Des échantillons de sédiments de berge ont été collectés le long du cours de la rivière Gandak environ tous les 20 km et tamisés et centrifugés pour obtenir les fractions sableuse et argileuses. Des échantillons de charge en suspension ont été collectés à différentes profondeurs dans la colonne d'eau à un site amont (cours supérieur de la rivière) et à un site en aval avant la convergence avec le Gange. Des minéraux de biotite et de muscovite ont été sélectionnés dans quatre des échantillons de sédiments prélevés le long de la rivière. Toutes les fractions séparées ont été prélevées le long de la rivière afin de vérifier si le sédiment évolue chimiquement ou isotopiquement pendant le transport, ce qui peut être attribué aux changements dans la source de sédiments, au régime d'altération (réactions de dissolution et de précipitation) le long du cours de la rivière, ou peut-être d'altération chimique pendant le transport. Tous les échantillons de cette étude ont été analysés pour les isotopes B par le spectromètre de masse à plasma inductif multi-collecteur (MC ICP-MS), la concentration B par dilution isotopique sur l'ICP-MS (ID-ICP-MS), et les concentrations d'éléments majeurs par spectroscopie d'émission atomique à plasma couplé par induction (ICP-AES) et concentrations d'éléments traces par ICP-MS à LHyGeS, Université de Strasbourg. La quantification de la mobilité B pendant la formation d'argile est calculée par l'intermédiaire du coefficient de transfert de masse ($\varphi_{Al,B}$) entre les fractions d'argileuse et sable, en utilisant Al comme un élément immobile pour comparer B, un élément mobile durant

l'altération chimique. Étant donné que la fraction de sable est composée principalement de minéraux primaires et qu'elle subit peu ou pas de fractionnement isotopique B au cours de l'altération chimique, elle est considérée comme une bonne estimation de la matière non altérée dans le bassin versant. En conséquence, la composition isotopique du B de la fraction sableuse est également utilisée pour corriger l'effet de la lithologie sur la composition isotopique du B dans la fraction argileuse, exprimée en $\Delta^{11}B_{clay\text{-}sand} = \delta^{11}B_{clay} - \delta^{11}B_{sand}$. Les comparaisons entre $\Delta^{11}B_{clay\text{-}sand}$ et $\varphi_{Al,\ B}$ sont ensuite utilisées pour décrire le comportement des isotopes B et la mobilité de B pendant la formation d'argile. La composition isotopique du B des minéraux biotite et muscovite prélevés à la main donne des informations sur l'évolution des minéraux primaires qui portent le B pendant le transport.

L'étude du bassin versant de la rivière Murrumbidgee a également porté sur les deux premiers objectifs de recherche: 1) comprendre comment les isotopes du B dans les fractions de sédiments de cours d'eau modernes enregistrent le régime d'altération à l'échelle du bassin versant; et 2) déterminer comment le signal d'altération dans les minéraux séparés est transporté des zones sources dans les sédiments à l'environnement de dépôt, qui dans le cas du bassin versant Murrumbidgee a été des systèmes de paléochenaux dans la plaine alluviale au cours des derniers 100 ka. Dans l'étude de la rivière Murrumbidgee, une stratégie d'échantillonnage plus approfondie a été utilisée que dans l'étude de la rivière Gandak, y compris l'analyse des sédiments de berge du fleuve principal, des principaux affluents, et des cours d'eau dans les bassins monolithologiques ; la roche-mère du bassin et la charge dissoute de petits cours d'eau dans des bassins monolithologiques ont été échantillonnés également. Les échantillons de charge dissoute de la rivière Murrumbidgee ont été échantillonnés le long de son cours environ tous les 50 km des eaux d'amont vers la plaine alluviale (jusqu'à Wagga Wagga) pour évaluer les changements dans la chimie de l'eau et la composition isotopique B. Des échantillons de sédiments ont été prélevés dans la rivière Murrumbidgee environ tous les 20 à 50 km depuis

les têtes de bassin jusqu'à la plaine alluviale (~650 km au totale) et tous les 10 à 20 km le long de chacun des huit principaux affluents. Les sédiments de fond et de berge ont été tamisés à 2 mm et 63 μm et la fraction inférieure à 63 μm a été centrifugée pour obtenir la fraction de taille argileuse (< 2 μm). Parce que la composition isotopique B de la fraction de sable dans l'étude du fleuve Gandak n'a révélé aucune évolution chimique ou isotopique B par rapport à la fraction argileuse, la fraction de sable n'a été analysée que pour la concentration de B et les isotopes B dans quelques échantillons représentatifs de la rivière Murrumbidgee. La fraction argileuse et la roche-mère ont été analysées pour la minéralogie, la concentration en B, les concentrations en éléments majeurs et en traces, les isotopes Nd et les isotopes B. La charge dissoute a été analysée pour la concentration en B, les concentrations en éléments majeurs et en traces et les isotopes B. La minéralogie de l'échantillon a été déterminée par XRD; les concentrations de B par ID-ICP-MS; éléments majeurs et traces par ICP-MS; et les isotopes du B par MC ICP-MS. Toutes les mesures d'échantillons dans cette étude ont été analysées à WIGL, Université de Wollongong.

Dans le bassin versant de Murrumbidgee, les bassins de drainage monolithologiques ont été identifiés grâce à une analyse spatiale (logiciel Esri™ ArcGIS 10.4) du Modèle d'Elévation Numérique (DEM), recouverte d'une carte lithologique de bassin versant du Murrumbidgee. Au total, 11 bassins versants monolithologiques ont été identifiés dans les bassins versants d'altitude supérieure et inférieure ; les charges dissoutes, les sédiments de fond des petits cours d'eau et les rocheux-mères ont été échantillonnés. Les compositions chimiques et isotopiques du B des sédiments et des échantillons de charge dissoute des bassins hydrographiques monolithologiques devraient refléter celles des roches mères et de leurs régimes d'altération. Cette approche permet d'identifier le signal d'altération porté par la fraction d'argile sédimentaire et la charge dissoute dans chaque lithologie majeure du bassin versant. Similaire à l'étude de la rivière Gandak, la mobilité du B pendant la formation d'argile est calculée par le

coefficient de transfert de masse $\varphi_{Al,\ B,}$ et été comparée à la composition isotopique du B entre la fraction argileuse et la roche mère ($\Delta^{11}B_{clay\text{-}bedrock} = \delta^{11}B_{clay} - \delta^{11}B_{bedrock}$).

Afin de tester si la composition en fraction argileuse des sédiments de berge accumulés le long de la rivière principale est le résultat d'un mélange de sédiments produits dans les différentes zones du bassin versant ou si leur composition indique l'altération durant le transport (objectif 2), la composition chimique et isotopique du B de la fraction argileuse dans le Murrumbidgee a été calculée quantitativement par bilan de masse. Les compositions chimique (B/Al, K/Al, Mg/Al) et isotopique du B des fractions argileuses qui ont été produites dans les bassins monolithologiques ont été utilisées pour calculer les proportions de drainage de surface de chaque lithologie majeure à divers points le long de la rivière principale (calculées par le logiciel ArcGIS 10.4). Si la composition chimique isotopique et la composition isotopique du B des fractions argileuses de la rivière Murrumbidgee sont dans l'erreur analytique de celles mesurées le long de la rivière, donc la composition de la fraction argileuse riveraine peut être expliquée comme un mélange de sources de sédiments dans tout le bassin. Si ce n'est pas le cas, leur évolution chimique et / ou isotopique peut être attribuée aux actions d'altération qui se produisent pendant le transport dans la rivière.

Enfin, la relation entre l'altération chimique et la composition isotopique du sédiment fluvial transporté est mieux comprise (objectif 1) et la connaissance de la façon dont le signal d'altération isotopique du B porté par les sédiments fluviatiles est transférée des zones sources à l'environnement de dépôt.), le troisième objectif de recherche peut être étudié: tester si les isotopes du B dans les dépôts de sédiments peuvent servir de proxy pour reconstruire les conditions paléo-environnementales (i.e. végétation) et de paléo-altération du dernier cycle glaciaire-interglaciaire. Cet objectif de recherche a été examiné en échantillonnant quatre systèmes bien datés (Mueller, 2017, Banerjee et al., 2002, Page et al., 1996) et stratigraphiquement décrits (Page et Nanson, 1996) (Yanco Phase: 13 - 21 ka; Gum Creek

Phase: 25 - 35 ka; Kerarbury Phase: 35 - 55 ka; Coleambally Phase: 80 - 105 ka) sur la Riverine Plain du bassin de la rivière Murrumbidgee (Murray-Darling Basin), sud-est de l'Australie. Tous les sites paléo-chenaux ont été échantillonnés par carottage à la main horizontalement dans la face des expositions sur puits le long d'un profil de profondeur ; plusieurs sites (en amont et en aval) ont été échantillonnés à la portée de chaque paléo-canal quand c'était possible. Les échantillons ont été tamisés pour obtenir la fraction de sable et ensuite centrifugés pour obtenir la fraction d'argile. L'étude s'est concentrée sur la fraction argileuse, qui a été analysée pour la minéralogie par XRD, les compositions majeurs et traces par ICP-MS, les concentrations B par ID-ICP-MS, et les isotopes des B et Nd par MC ICP-MS à WIGL, Université de Wollongong. La concentration du bore et les isotopes du B de la fraction de sable n'ont été mesurés que sur un échantillon dans chaque paléo-canal. En échantillonnant le long des profils de profondeur à chaque site et à plusieurs sites le long d'un seul paléo-chenal, il est possible de déterminer si une évolution chimique et / ou isotopique du B de la fraction argileuse existe avec la profondeur et le long d'un paléo-canal qui peut être liée à une modification post-dépôt ou aux réactions d'altération pendant le transport, respectivement. L'identification des échantillons affectés par l'altération post-dépôt a été accomplie par plusieurs méthodes différentes qui incluent : la comparaison de la composition chimique et isotopique du B des portions d'échantillon ''intérieur' et 'extérieur' (qui se réfèrent à la partie la plus l'intérieur et à la plus l'extérieur de dépôt de sédiment, respectivement) ; comparaison de la composition chimique et isotopique du B à d'autres échantillons dans le même profil de profondeur et dans le même système paléo-canal ; comparaisons minéralogiques entre échantillons du même profil et système ; prise en compte de l'environnement de dépôt avec une attention particulière sur la présence de végétation et profondeur de dépôt dans le profil ; et aussi comparaisons de la composition chimique et isotopique du B des sédiments paléo-canaux à ceux des sédiments modernes qui sont transportés par la rivière Murrumbidgee. Après l'identification et

l'élimination des échantillons qui ont été modifiés après le dépôt, les compositions minéralogiques, chimiques et isotopiques (B et Nd) des fractions d'argile ont été comparées entre les systèmes paléo-canaux, y compris deux dépôts modernes, dans le but de déterminer si les variations des compositions minéralogiques, chimiques et isotopiques des fractions argileuses entre chaque système paléo-canal sont liées aux changements dans la source des sédiments ou aux changements des conditions d'altération, y compris l'influence de la végétation sur la formation d'argile, qui peut être déterminé par la variabilité climatique du dernier cycle glaciaire-interglaciaire.

A.3 **Résultats, discussion et conclusions**

A.3.1 **Comment les isotopes de bore dans les sédiments fluviaux modernes enregistrent-ils le régime d'altération à l'échelle du bassin versant ?**

La connaissance du fractionnement des isotopes du B pendant l'altération du silicate à l'échelle du bassin versant est assez limitée. Quelques études se sont concentrées sur la compréhension des mécanismes qui controlent l'altération à l'échelle du bassin versant en analysant la composition isotopique du B de la charge dissoute des rivières (Louvat et al., 2011, 2014; Chetelat et al., 2009; Lemarchand and Gaillardet, 2006; Lemarchand et al., 2002b; Rose et al., 2000), mais très peu se sont concentrées sur la phase solide (Chetelat et al., 2009; Spivack et al., 1987). À ce jour, aucune autre étude n'a étudié de manière exhaustive la composition en $\delta^{11}B$ de la fraction d'argile des sédiments de la rivière dans le but de comprendre son origine et la façon dont elle enregistre le régime d'altération. Bien que l'incorporation de B (précipitation ou adsorption) dans la fraction argileuse pendant les interactions eau-roche dans le système eau souterraine / sol ait été invoquée comme mécanisme par lequel la charge dissoute obtient sa signature $\delta^{11}B$ (e.g. Chetelat et al., 2009; Lemarchand et Gaillardet, 2006; Rose et al., 2000)

(en plus de la contribution du $\delta^{11}B$ de diverses sources), la source originale du $\delta^{11}B$ dans la fraction argileuse du sédiment fluvial reste inconnue, et aussi sa relation avec l'altération régime. L'étude des sédiments fluviaux modernes dans les bassins des rivières Gandak et Murrumbidgee tente d'aborder ces problèmes et d'étudier, pour la première fois, comment les sédiments fluviaux enregistrent le régime d'altération (compétition entre les réactions de dissolution et de précipitation).

Dans les rivières Gandak et Murrumbidgee, une tendance similaire se dégage dans la composition isotopique du B des fractions de sable et d'argile le long du cours de la rivière. La composition en $\delta^{11}B$ de la fraction de sable reste relativement constante en aval, tandis que le $\delta^{11}B$ de la fraction argileuse montre une évolution progressive vers des valeurs isotopiquement plus lourdes qui se stabilisent dans la plaine alluviale. Comme la fraction de sable est grossièrement représentative d'un mélange de roches-mères pas modifié isotopiquement dans le bassin versant, elle peut être utilisée pour corriger les effets lithologiques et comparée à la fraction argileuse quand la roche-mère n'est pas disponible (comme dans le cas de la rivière Gandak). Dans le Murrumbidgee, la roche-mère a été échantillonnée dans des bassins monolithologiques et sa composition isotopique du B a été comparée à la fraction argileuse de sédiments de cours d'eau monolithologiques ($\Delta^{11}B_{\text{clay – bedrock}} = \delta^{11}B_{\text{clay}} - \delta^{11}B_{\text{bedrock}}$); dans le Gandak, tous les sédiments ont été prélevés dans le chenal principal et les fractions sable et argile ont été comparées : $\Delta^{11}B_{\text{clay - sand}} = \delta^{11}B_{\text{clay}} - \delta^{11}B_{\text{sand}}$. Lorsque les facteurs de fractionnement isotopique sont tracés en fonction du coefficient de transfert de masse calculé ($\varphi_{Al,B}$) en utilisant Al comme contrepartie immobile pour comparer la mobilité de B, les deux systèmes montrent une corrélation positive, indiquant que la mobilité de B pendant la formation d'argile est contrôler les facteurs de fractionnement isotopique. Dans le bassin versant de Murrumbidgee, ceci se produit dans les lithologies volcaniques et sédimentaires à des altitudes plus élevées. Une réincorporation plus quantitative de B conduit des facteurs de fractionnement

isotopique entre la fraction argileuse et la roche-mère tendant vers zéro en l'absence de sources externes de B (autres que la dissolution du roche-mère); dans le Murrumbidgee, ceci se produit dans toutes les lithologies des bassins versants inférieurs et des lithologies granitiques dans le bassin supérieur. Les différences apparentes des valeurs de $\Delta^{11}B_{\text{argile}-\text{roche}}$ entre les lithologies démontrent probablement un contrôle lithologique sur les taux de formation d'argile dans tout le bassin versant, tandis que les différences entre les bassins versant supérieur et inférieur démontrent un effet climatique fonction de l'altitude du bassin versant. Il est intéressant de noter que les deux systèmes montrent cette tendance, indiquant possiblement un comportement commun des isotopes B pendant la formation de l'argile.

Dans les deux systèmes, les sédiments de berge montrent un grand fractionnement entre les fractions argileuse et sableuse (entre 3 ‰ et 8 ‰ dans le Murrumbidgee et environ 3 ‰ dans le Gandak, respectivement) par rapport à celles trouvées dans la plaine alluviale (environ 2 ‰ dans le Murrumbidgee et le Gandak). Ces observations indiquent probablement différentes conditions d'altération dans les montagnes que dans les plaines alluviales. Dans le bassin versant de la rivière Murrumbidgee, les zones de source de sédiments dans les bassins versants monolithologiques à des altitudes plus élevées et plus basses ont été identifiées par analyse spatiale afin de déterminer les différences de température, de précipitations et de pente de captage. Le bassin supérieur est caractérisé par des températures plus basses, des précipitations plus élevées et des pentes plus abruptes que le bassin inférieur, caractéristiques qui contribuent probablement aux différences de taux de production d'argile et des intensités d'altération au silicate (Lupker et al., 2012; Millot et al., 2003). Par exemple, dans l'Himalaya, Lupker et al. (2012) ont signalé que la formation d'argile est plus favorable dans les environnements où les sédiments ont des temps de transfert plus longs (dans les zones moins pentues) et dans des conditions plus chaudes et plus humides comme la plaine du Gange, comparée au bassin supérieur où l'érosion prédomine, le transport rapide des sédiments, et peu d'altération

chimique et de formation d'argile. Lupker et al. (2012) ont également signalé des proportions accrues de smectites et d'autres argiles expansibles du front de l'Himalaya en aval de la plaine du Gange, et des compositions δD plus élevées reflétant une plus grande incorporation de minéraux argileux en équilibre avec les eaux de surface de plaine d'inondation. Lupker et al. (2012) et Millot et al. (2003) (Mackenzie Basin, Canada) signalent que l'altération du silicate dans la plaine inondable prédomine plus de l'altération dans la montagne, une conclusion qui contredit l'hypothèse de Raymo (Raymo and Ruddiman, 1992, Ruddiman et al., 1988). Les sédiments de la Gandak ne montrent pas de diminution systématique des éléments mobiles en aval, tel que rapporté par Lupker et al. (2012) pour les autres rivières himalayennes. Les températures plus basses, les précipitations plus élevées et les pentes plus raides ne favorisent pas la formation d'argile ou l'altération chimique intense, mais plutôt l'érosion physique et le transport rapide des sédiments vers le bassin versant inférieur. Au contraire, des températures plus élevées et des temps de transport des sédiments plus longs à des altitudes plus basses favoriseraient la formation d'argiles et augmenteraient l'intensité de l'altération.

Le développement d'un modèle de bilan massique du système argile-eaux interstitielles, capable de décrire la composition isotopique B apparente entre la fraction argileuse et la roche-mère en termes de régime d'altération (compétition entre dissolution et réactions de précipitation) serait un grand progrès dans ce domaine. La nécessité d'un cadre permettant d'interpréter les données isotopiques du B dans les sédiments transportés par les rivières augmente alors que plusieurs études sont se concentrent maintenant davantage sur la phase solide plutôt que dissoute transportée par les fleuves. Par exemple, il y a eu plusieurs études récentes, y compris la présente étude (chapitre 3, Ercolani et al., in prep), telles que Noireaux et al. (2014) et Lemarchand et al. (2012) qui étudient le comportement des isotopes du B au cours des réactions d'altération dans les profils de sol qui pourraient bénéficier d'un tel modèle et aider à l'interprétation des isotopes du B dans la fraction argileuse.

Un modèle de transport réactif a été utilisé pour modéliser la composition chimique et isotopique du B de la fraction percolant surface/eau souterraine et argile, qui décrit une eau de surface enrichie en ^{11}B (dérivée des apports atmosphériques et de la végétation) percolée à travers le sol. Avec la profondeur, la composition isotopique du B de cette solution devient progressivement plus légère (tout comme la fraction argileuse précipitée) en réponse à une augmentation de la contribution des reactions de dissolution des minéraux primaires. Cividini et al. (2010) et Noireaux et al (2017) confirment cette hypothèse dans les écosystèmes forestiers, où les eaux interstitielles dans les couches supérieures du sol (en particulier les 60 cm supérieurs) sont enrichies en ^{11}B à cause des apports de B par l'atmosphère et la végétation et que cette signature isotopique du B est progressivement perdue dans les eaux interstitielles plus profondes. Les résultats montrent que le modèle ne peut prédire les concentrations B ou les isotopes de la solution du sol et les valeurs de la fraction argileuse observée sans utiliser des paramètres de modélisation irréalistes tels que la distance du trajet d'écoulement et la vitesse de l'eau. Cela indique probablement que la fraction d'argile ne précipite pas à partir de la solution de sol, telle que celle échantillonnée par les plaques lysimétriques. Au contraire, les argiles sont supposées précipiter à partir d'une solution d'eau interstitielle qui évolue dans un système partiellement fermé mieux décrit par la distillation de Rayleigh. Un exemple d'un tel espace poreux serait à l'intérieur d'un minéral primaire (similaire au remplacement minéral secondaire) ou à des joints de grain. La source de B dans la fraction argileuse provient du minéral lui-même qui a une composition isotopique proche de celle de la fraction argileuse. De même, des concentrations élevées de B dans ces espaces interstitiels (de l'ordre de 10 ppm) sont nécessaires pour produire des fractions argileuses avec des concentrations encore plus élevées (de l'ordre de 50 ppm) expliquées par une dissolution minérale continue dans un système partiellement fermé. Ceci implique un long temps de réaction entre le minéral

secondaire et l'eau interstitielle, probablement incohérent avec l'hypothèse d'une précipitation à partir des solutions de sol.

Dans le cas du Murrumbidgee, la composition isotopique du B moyenne de la charge dissoute est d'environ +31‰ alors que la composition isotopique B moyenne de la fraction argileuse est de –12‰, ce qui représente plus de 40 ‰ de différence entre les deux composants. Si la composition isotopique du B de la charge dissoute était contrôlée par échange de bore entre les particules d'argile et les eaux interstitielles comme proposé par de nombreuses études (Lemarchand et al., 2009, Lemarchand et al., 2000, Rose et al. 2000), donc le fractionnement isotopique du B entre les deux composants, s'ils sont en équilibre, serait d'environ –30‰ et serait fonction du pH (Rose et al., 2000, Palmer et al., 1987, Spivack et al., 1987). Cependant, la différence moyenne de –40‰ entre les deux rend cette possibilité très improbable. Ceci indique que les compositions chimiques et isotopiques du bore de la charge dissoute et de la fraction argileuse ne sont pas en équilibre et la fraction argileuse ne précipite pas d'une solution présentant les caractéristiques de la charge dissoute. Cette déconnexion apparente de la composition isotopique du B entre la charge dissoute et les sédiments transportés pourrait dériver du fait que les eaux fluviales intègrent tous les processus de surface et souterrains, y compris les processus de transport réactif, les cycles biogéochimiques actifs, incorporent la végétation et les sources atmosphériques. Cela produit des compositions isotopiques de bore plus élevées dans la solution du sol (et la charge dissolvante) avec de faibles concentrations de B tandis que la signature de l'argile est obtenue à partir d'une solution d'eau interstitielle à forte teneur en B (au moins dans le cas de le Murrumbidgee). Cette interprétation des isotopes du B s'applique probablement au Gandak et à Noireaux et al. (2014) qui ont également rapporté des compositions isotopiques de B du sol (où B est porté par la fraction fine) qui sont inférieures de 1‰ à la roche-mère. Lemarchand et al. (2012) ont rapporté une composition des isotopes du B isotopiquement plus lourds de la fraction argileuse que la roche mère (jusqu'à +7‰),

indiquant que les argiles pédogéniques (formées dans le mètre supérieur du profil) se forment en équilibre isotopique avec un solution de sol isotopiquement lourde qui a été attribuée au B dérivé du cycle de la végétation et de l'atmosphère. Si correcte, cette interprétation a une implication importante: il n'y a aucune raison que la teneur et les isotopes du bore dans les minéraux argileux soient en équilibre avec le bore dissous des rivières. Ceci est évident par la différence isotopique du bore d'environ -40‰ entre la fraction d'argile et la charge dissoute. Les argiles peuvent enregistrer uniquement les conditions très locales de leur formation (éventuellement dans un environnement confiné), tandis que les solutions du sol et les rivières peuvent être alimentées par des eaux n'ayant pas substantiellement échangé de matières avec des minéraux.

A.3.2 Quel est le comportement de les isotopes du B dans les sédiments des cours d'eau durant le transport entre les zones sources de sédiments et l'environnement de dépôt?

Aucune étude à ce jour n'a étudié la façon dont la fraction argileuse dans les sédiments fluviaux obtient sa signature $\delta^{11}B$ ou la façon dont cette signature est transportée des zones sources de sédiments en amont à l'environnement de dépôt en aval. Cette étude constitue donc le début de notre compréhension de ces sujets importants qui seront nécessaires pour répondre à la troisième question de savoir si les isotopes du B dans les sédiments peuvent servir de traceurs pour reconstruire les conditions paléo-climatiques et paléo-environnementales. Dans une étude précédente sur les sédiments de la rivière Murrumbidgee (Suresh et al., 2014), des sédiments de berge ont été échantillonnés le long de la rivière et des analyses en éléments majeurs and traces ont été effectuées. Le Chemical Index of Weathering (CIW) a révélé qu'il n'y a pas d'altération chimique significative au cours du transport, résultat confirmé par la présente étude utilisant à la fois des éléments majeurs et traces et des isotopes du bore. Ici, il a

été testé si la composition chimique et isotopique du B de la fraction argileuse peut être expliquée comme un mélange de sources dans tout le bassin ou si elle évolue en aval. Les compositions théoriques $\delta^{11}B$, B/Al, et Mg/Al de la fraction argileuse à 10 points le long de la rivière Murrumbidgee ont été calculées en utilisant un modèle de bilan de masse. Les résultats montrent que les valeurs calculées sont toutes similaires à celles mesurées, indiquant que leurs compositions $\delta^{11}B$, B/Al, et Mg/Al sont le résultat d'un mélange d'argiles produites dans tout le bassin versant drainé vers le chenal principal. En utilisant la composition de la roche-mère dans des bassins monolithologiques comme composant du mélange, les valeurs théoriques de $\delta^{11}B$ de sable ont également été calculées de la même manière. Les résultats montrent également que la composition de la fraction de sable peut être expliquée comme un mélange de substrat rocheux. Ce résultat, montré pour la première fois, est significatif car il suggère que les isotopes du B dans la fraction argileuse des sédiments de rivière conservent leur signature chimique et isotopique d'origine et donc peuvent être utilisés comme traceurs du régime d'altération. Dans ce cas, la composition chimique et isotopique B des fractions d'argile dans les dépôts de paléo-chenaux du Murrumbidgee devraient refléter les conditions d'altération dans les zones sources du bassin versant, avec peu ou pas de biais durant le transport.

La composition de $\Delta^{11}B_{\text{argile – sable}}$ des sédiments de berge transportés activement dans la rivière Murrumbidgee a été comparée aux sédiments modernes (déposés à plusieurs mètres des berges de la rivière Murrumbidgee moderne) pour vérifier s'il existe des similitudes ou des différences qui peuvent révéler un comportement isotopique du bore après le dépôt et l'enfouissement. Cette comparaison montre que les sédiments des berges modernes ont une composition de $\Delta^{11}B_{\text{ argile – sable}}$ d'environ 0‰, tandis que les sédiments modernes ont des valeurs d'environ 2‰. Bien que la raison de cette différence apparente ne soit pas connue (en raison du manque de données chimiques, minéralogiques ou granulométriques des dépôts modernes), l'hypothèse est que la taille des grains et le tri minéral entre les sédiments de la berge transportés

activement et un dépôt de sédiments pourrait être la cause. Alternativement, la composition isotopique du B du dépôt de sédiments peut ne pas avoir été conservée après le dépôt. Cependant, la composition isotopique du B des dépôts de sédiments modernes est très semblable à celle des autres dépôts de paléochenaux qui ne montrent aucun signe de profil d'altération ou d'altération après dépôt (voir la discussion ci-dessous). Ces différences sont plus susceptibles d'être causées par un effet de triage ou peut-être le résultat de la variabilité locale du site. Indépendamment de ce biais possible, la composition des dépôts modernes et de la plupart des sédiments paléochenaux est très similaire, ce qui indique que la composition isotope du B des sédiments de paléochenaux est préservée après le dépôt et l'enfouissement.

A.3.3 Les isotopes du bore présents dans les sédiments peuvent-ils être utilisés comme un traceur de la paléo-altération et paléo-environnementale au cours du dernier cycle glaciaire-interglaciaire?

Comme pour le comportement des isotopes du B dans les sédiments pendant le transport fluvial, notre connaissance du comportement des isotopes du B et de son utilisation dans les dépôts de sédiments fluviatiles comme un traceur de paléo-altération est limitée à cette étude. Les résultats de ce travail représentent un avancement significatif dans le domaine de la géochimie des isotopes du B et fournissent le premier exemple de la façon dont les isotopes du B peuvent être utilisés et interprétés dans les sédiments fluviaux comme un nouveau traceur géochimique pour la reconstruction paléo-altération et paléo-environnemental. Comme mentionné précédemment, les isotopes du B dans les séquences de loess-paléosol en Chine (Wei et al., 2015, Zhao et al., 2003) sont les seuls autres travaux utilisant les isotopes du B pour reconstruire les conditions de paléo-altération sur une échelle de temps similaire (dernier cycle glaciaire-interglaciaire). L'application des isotopes du B dans les profils loess-paléosol et les résultats prometteurs de l'étude isotopique du B dans les sédiments modernes du bassin versant

de la rivière Murrumbidgee (Chapitre 3, Ercolani et al., in prep) indiquent la conservation du signal d'altération original du sédiment pendent le transport fournit une indication que cette approche peut être efficace et applicable à d'autres milieux de dépôt.

En l'absence d'altération post-dépôt, la composition de la fraction argileuse devrait refléter le signal d'altération d'origine provenant de la zone source. Par conséquent, l'identification des échantillons qui ont été modifiés après leurs dépôt est essentielle si l'objectif est de déterminer les changements des régimes d'altération passés. Cela a été considéré en divisant l'échantillon en deux moitiés (si possible) : une partie «intérieure» plus vierge et une partie «extérieure» plus exposée (plus près de la surface). Les analyses d'isotopes de bore sur les deux aliquotes d'échantillon indiquent un comportement contradictoire, montrant que la partie «extérieure» peut être isotopiquement plus lourde ou plus légère selon le site. Ceci peut être attribué à une modification après dépot ou variabilité locale du site. Indépendamment de la cause, la partie «extérieure» des échantillons a été retirée de l'ensemble de données car la variation de la composition isotopique du bore dans la fraction argileuse avec la profondeur était généralement supérieure à la variation entre la partie «intérieure» et «extérieure» de l'échantillon. Les compositions isotopiques du bore dans la fraction argileuse de chaque site ont été comparées à d'autres échantillons / sites dans le même système en fonction de la profondeur afin de vérifier l'absence de profil d'altération marqué. Dans chaque système, il existe un site où la composition isotopique du bore de la fraction argileuse est beaucoup plus lourde que les autres sites. Ces compositions d'isotopes du bore élevées étaient souvent accompagnées par une augmentation du rapport B/Al qui, ensemble, indique une interaction avec une source isotopiquement lourde telle qu'une solution de sol riche en ^{11}B qui a été recyclée à travers la végétation. De plus, ces échantillons étaient déposés dans des environnements relativement peu profonds (<2 m de profondeur) qui faciliteraient l'échange de bore avec l'environnement et donc la perte de leur signal d'altération d'origine. La composition chimique et isotopique du bore des

échantillons/sites qui ne présentent pas de traces visibles d'un profil d'altération sont par conséquent considérées vierges et reflètent les conditions d'altération d'origine; c'était le cas pour la majorité des échantillons de paléochenaux.

Pour déterminer si les variations de la composition isotopique du bore de la fraction d'argile dans les paléochenaux sont le résultat du régime de paléo-altération, ou en raison des changements de provenance des sédiments au cours des 100 derniers ka, la source du sédiment a été déterminée à l'aide d'isotopes de Nd. Aussi, la composition isotopique de Nd des fractions d'argile a été comparée à celle de la rivière Murrumbidgee moderne et des roches granitiques, volcaniques et sédimentaires. Les résultats montrent que la composition de εNd des argiles dans les paléochenaux peut être expliquée comme un mélange de sédiments à l'intérieur du bassin versant de Murrumbidgee, sans changement significatif de la source de sédiments au cours du dernier cycle glaciaire-interglaciaire. Sans modification majeure de la source de sédiments apportée à la Riverine Plain au cours des dernières 100 ka, les variations de la composition isotopique du bore de la fraction argileuse entre les systèmes de paleochenaux peuvent être interprétées comme reflétant des processus affectant leurs compositions isotopiques du B comme les variations de le régime d'altération ou des changements dans les conditions environnementales.

Enfin, après l'élimination des échantillons affectés par l'altération post-dépôt et la vérification que les variations de la source de sédiments ne sont pas responsables de la variation isotopique B dans la fraction argileuse des sédiments paléo-canaux, on peut comparer directement les variations de la composition isotopique du B aux paramètres environnementaux qui controlent le régime d'altération tels que le climat et les changements dans les conditions de paléo-environnement tels que le couvert végétal. Lorsque la composition $\Delta^{11}B_{\text{clay – sand}}$ des sédiments paléo-canaux est représentée en fonction de la profondeur, des différences claires entre les systèmes peuvent être reconnues : les deux systèmes formés près du dernier maximum

glaciaire, le Yanco (21 - 13 ka) et le Gum Creek (35 – 25 ka), ont des compositions $\Delta^{11}B_{\text{argile – sable}}$ très similaires qui sont distinctes des systèmes de Kerarbury et de Coleambally. Bien qu'un test ANOVA révèle que la composition des sédiments sédimentaires modernes ne diffère pas significativement de celle des systèmes Yanco et Gum Creek, ce résultat est probablement dû à de mauvaises statistiques de comptage (n = 2) pour les dépôts modernes. Néanmoins, la fraction argileuse déposée pendant le dernier maximum glaciaire présente des compositions isotopiques du B plus faibles que les dépôts modernes et ceux déposés lors des phases Kerarbury (MIS 3) et Coleambally (MIS 5).

Représentées en fonction de l'âge (0-100 ka), les compositions de $\Delta^{11}B_{\text{argile – sable}}$ des sédiments paléochenaux co-varient avec une reconstruction de température de surface de la mer de l'océan Austral (Barrows et al., 2007) et une reconstruction de la végétation du sud-est de l'Australie et de Nouvelle-Zélande (Barrows et al., 2007). La co-variation des isotopes B dans la fraction argileuse avec la température de surface de la mer et la végétation indique que la pédogenèse a répondu aux variations du climat au cours du dernier cycle glaciaire-interglaciaire. L'augmentation de la température et des précipitations devrait produire une végétation plus complexe dans le paysage qui pourrait augmenter les taux et les intensités chimiques (par exemple Gíslason et al., 1996), tandis que l'amplification du cycle hydrologique devrait directement augmenter les flux d'altération (Maher et Chamberlain, 2014, Gaillardet et al., 1999a).

Au cours du dernier maximum glaciaire (MIS 2) correspondant aux systèmes Yanco et Gum Creek, un petit fractionnement isotopique B est observé entre les fractions de sable et d'argile, indiquant que pendant les périodes froides et sèches la production d'argile est minime et le bore est dérivé principalement de la dissolution du roche-mère. Pendant les périodes plus chaudes telles que Holocène (MIS 1), MIS 3 et 5, les compositions de $\Delta^{11}B_{\text{argile – sable}}$ sont plus grandes (jusqu'à + 6 ‰) et la fraction argileuse est toujours isotopiquement plus lourde que la

fraction de sable, indiquant un régime d'altération actif de précipitation avec une partie significative de bore dans la fraction argileuse dérivant d'une source isotopiquement lourde telle que la végétation ou l'atmosphère. L'analyse de diffraction des rayons X fractions d'argile est en accord avec cette interprétation, montrant que la composition de la fraction argileuse durant les climats chauds est principalement la kaolinite (~ 75%), ce qui est indicatif des argiles dans un stade d'altération plus avancé produit par des taux plus élevés de lixiviation de l'eau dans les profils de sol (Ma et Eggleton, 1999; Singer, 1980). Pendant les périodes les plus froides, la fraction argileuse a un pourcentage beaucoup plus élevé d'argiles interstratifiées (I/S) qui sont formées dans la première phase de production d'argiles indiquant un état d'altération moins avancé dans les conditions sèches (Singer, 1980). Ce résultat est en accord avec Wei et al. (2015) qui ont rapporté que l'intensité pédogénétique est corrélée avec la variabilité climatique au cours du dernier cycle glaciaire-interglaciaire utilisant les isotopes du B dans la phase soluble dans l'acide de plusieurs séquences loess-paléosol ; les climats froids sont caractérisés par des valeurs de $\delta^{11}B$ plus basses et une pédogenèse moins intense tandis que des climats plus chauds sont caractérisés par des valeurs de $\delta^{11}B$ plus élevées et une pédogenèse plus intense. Des valeurs élevées de $\delta^{11}B$ dans la séquence loess-paléosol ont été attribuées à l'augmentation des apports atmosphériques pendant la circulation d'été de la mousson. Cependant, dans la présente étude, les compositions de $\Delta^{11}B_{\text{argile – sable}}$ des sédiments paléo-canal sont fortement corrélées avec la couverture végétale dans le sud-est de l'Australie. Ceci indique que des compositions plus élevées de $\Delta^{11}B_{\text{argile – sable}}$ reflètent un rôle croissant de la végétation sur la pédogenèse durant les climats plus chauds et humides (MIS 1, 3 et 5) et moins dans les climats plus froids et secs (MIS 2 et 4). Les compositions de $\Delta^{11}B_{\text{argile – sable}}$ isotopiquement plus élevées sont ensuite attribuées à l 'incorporation de B isotopiquement lourd dans la fraction argileuse qui a été recyclée de la végétation. De cette manière, les compositions isotopiques du bore dans les fractions argileuses des dépôts de paléochenaux

réagissent directement au climat par les précipitations et la température qui produisent différentes couvertures végétales et influencent la pédogenèse à différents degrés. En particulier, pendant les périodes plus froides et plus sèches, moins de précipitations et des températures plus basses produisent des espèces herbacées ; par conséquent, l'influence de la végétation sur la pédogenèse est moindre sous un climat plus froid et plus sec. Les compositions isotopiques du bore dans la fraction argileuse restent faibles et reflètent les interactions eau-roche. Au contraire, pendant les périodes plus chaudes et plus humides, l'augmentation des précipitations et de la température produit un couvert végétal plus dense ; par conséquent, l'influence de la végétation sur la pédogenèse est plus grande sous un climat plus humide et plus chaud. Les compositions isotopiques du bore dans la fraction argileuse sont plus élevées et reflètent le flux accru de bore qui a été recyclé à travers la végétation.

A.4 **Perspective et recherche future**

Dans l'étude de la rivière Gandak dans l'Himalaya, les échantillons de sédiments étaient limités. Un seul échantillon a été prélevé dans les vraies sources de la rivière Gandak et aucun échantillon n'a été prélevé après la convergence avec le Gange, plus en aval dans la plaine du Gange. Il serait particulièrement interessant d'obtenir des échantillons de sédiments en amont supplémentaires car il semble que l'altération contrôle la composition isotopique de la fraction d'argile dans les eaux d'amont est différente de celle de la plaine. Cependant, cette hypothèse n'est basée que sur un point. Une tendance similaire a été observée dans la composition en $\delta^{11}B$ des biotites et des muscovites ramassés à la main et de la fraction argileuse des sédiments riverains (tous montrant des valeurs isotopiquement plus faibles dans les eaux d'amont qui augmentent progressivement en aval). Au contraire, la source des minéraux peut être différente et, par conséquent, leur composition isotopique B peut seulement être utilisée comme traceur de source et non utilisée pour tracer les réactions d'altération. Des échantillons supplémentaires

en aval seraient utiles pour une étude plus détaillée. Enfin, la rivière Gandak était la seule rivière Himalayenne échantillonnée, par conséquent les résultats peuvent être localisés et ne pas s'appliquer à l'ensemble du système. Comme de nombreux cours d'eau himalayens ont été étudiés à des fins diverses et que des échantillons de sédiments ont déjà été recueillis par d'autres, il serait prudent de mener une étude similaire dans une rivière Himalaya différente, vérifiant ainsi la généralité des conclusions de cette étude. Cependant, les conclusions de l'étude de Murrumbidgee sont en bon accord avec celles de l'étude de la rivière Gandak, fournissant un support pour une interprétation plus globale du comportement des isotopes du bore dans les sédiments fluviaux pendant la formation et le transport.

Dans l'étude de Murrumbidgee, la stratégie d'échantillonnage était plus approfondie et toutes les données nécessaires ont été recueillies. Cependant, parce que l'étude a porté sur la fraction argileuse particulièrement difficile à obtenir dans la plupart des échantillons de rivières de fond (tamisage de plus de 1 kg de sédiments pour obtenir 50-100 mg d'argile) et hétérogène dans sa composition chimique et isotopique, plus l'argile devrait avoir été tamisée au début de l'étude pour chaque échantillon. Il devenait particulièrement évident que plus d'argile était nécessaire pour chaque échantillon lorsque le nombre d'analyses chimiques et isotopiques comprenait 100 mg d'argile pour les éléments majeurs et traces, 50 mg d'argile pour les isotopes du B, 10 mg d'argile pour DRX et 100 mg d'argile pour les isotopes du Nd. Par conséquent, plus d'argile devait être tamisée pour de nombreux échantillons qui pouvaient avoir des compositions chimiques et isotopiques légèrement différentes de celles de l'aliquote précédente des argiles tamisées. En ce qui concerne la relation entre $\Delta^{11}B_{clay-bedrock}$ et le régime d'altération à l'échelle du bassin versant, des études supplémentaires devraient être menées pour confirmer les résultats de l'étude préliminaire de Murrumbidgee, car les rivières drainant différentes lithologies (par exemple les carbonates) peuvent varier selon les conditions géologiques et climatiques ne pas enregistrer le régime d'altération de la même manière (par exemple dans

une zone tectoniquement active avec une forte érosion et des taux d'altération élevés, ou dans des environnements tropicaux où les isotopes du B dans la fraction argileuse pourraient être contrôlés par des intrants végétaux). Cependant, des tendances de $\Delta^{11}B_{argile\ -\ sable}$ vs. $\varphi_{Al,\ B}$ similaires ont été observées dans les rivières Murrumbidgee et Gandak, indiquant probablement une tendance plus globale où un fractionnement isotopique élevé est corrélé avec une précipitation B faible dans la fraction argileuse et vice versa.

Les compositions d'isotopes du bore dans les sédiments présentent un grand potentiel en tant que nouvelle variable géochimique pour la reconstitution des paléo-altérations et des paléo-environnements. Ceci est démontré par la capacité des isotopes du B dans la fraction argileuse des sédiments paléo-canaux à enregistrer l'influence du climat et de la couverture végétale sur la pédogenèse durant la dernière période glaciaire-interglaciaire et aussi par des études antérieures utilisant des isotopes du B dans les séquences loess-paléosol (Wei et al., 2015; Zhao et al., 2003) qui démontrent son utilité pour déterminer l'intensité des paléo-altérations par rapport à la variabilité climatique. Cependant, l'applicabilité de cette approximation dans d'autres environnements ou sites est relativement inconnue car le développement de cette approximation n'en est qu'à ses débuts. La capacité à utiliser ce traceur dépend finalement de la préservation de la composition isotopique B de l'échantillon qui est probablement affectée par des facteurs tels que la minéralogie (e.g. argiles expansibles ou non expansibles), l'environnement de dépôt (profondeur faible ou profonde dans le profil), et les conditions climatiques de l'environnement moderne (e.g. environnement fortement végétalisé, environnements humides vs. secs). De plus, la capacité d'identifier et d'enlever des échantillons qui ont été altérés par des processus post-dépôt est essentielle pour obtenir un enregistrement plus vierge du changement paléo-environnemental. Par conséquent, les recherches à venir devraient se concentrer davantage sur différentes techniques d'échantillonnage et méthodes analytiques pour identifier l'altération post-dépôt et appliquer ce traceur à différents

environnements de dépôt. Dans le bassin versant de Murrumbidgee, des dépôts de paléo-canaux ont été obtenus à des profondeurs peu profondes (<2 m) et plus profondes (> 2 m) dans tous les systèmes (Yanco, Gum Creek et Kerarbury) sauf dans le système Coleambally afin d'évaluer la variation chimique et isotopique qui peut être liée à une modification après dépôt. Des échantillons plus profonds dans le système Coleambally n'ont pas été obtenus parce que tous les sites de Coleambally étaient relativement peu profonds et qu'il n'était donc pas possible d'obtenir des échantillons plus profonds sans utiliser une foreuse (qui n'a pas été utilisée dans cette campagne). À Kerarbury Pit, l'exposition de surface était assez profonde (~6 m), ce qui a permis d'obtenir des échantillons plus profonds. Dans les systèmes de Yanco et de Gum Creek, des échantillons plus profonds du profil ont été prélevés avec une foreuse par des collègues de l'UOW et donnés à ce projet. Cependant, dans le système Coleambally, aucune de ces options n'était disponible, donc une comparaison entre des dépôts plus profonds (vraisemblablement plus vierges) et plus profonds n'était pas possible. Sans cette comparaison, certains doutes subsistent si les processus post-dépôt modifient les échantillons peu profonds recueillis dans le système Coleambally, bien que des compositions similaires de fractions d'isotopes B dans deux des trois sites (à l'exclusion de Bundure) suggèrent qu'une altération post-dépôt n'a pas eu lieu. Pour mieux répondre à ce problème et renforcer l'interprétation des derniers 50 ka du record, des échantillons plus profonds dans le profil des sédiments devraient être obtenus à l'aide d'une foreuse pour vérifier que la composition isotopique du B de la fraction argileuse est similaire à celle des échantillons profonds sur les mêmes sites.

REFERENCES

Aciego, S.M., Bourdon, B., Lupker, M., Rickli, J., 2009. A new procedure for separating and measuring radiogenic isotopes (U, Th, Pa, Ra, Sr, Nd, Hf) in ice cores. Chem. Geol. 266, 203–213.

Ackerer, J., Chabaux, F., Van der Woerd, J., Viville, D., Pelt, E., Kali, E., Lerouge, C., Ackerer, P., di Chiara Roupert, R., Négrel, P., 2016. Regolith evolution on the millennial timescale from combined U–Th–Ra isotopes and in situ cosmogenic10Be analysis in a weathering profile (Strengbach catchment, France). Earth Planet. Sci. Lett. 453, 33–43.

Ahmad, N., Lodrick, D.O., 2018. Ganges River. Encycl. Br.

Albarède, F., Telouk, P., Blichert-Toft, J., Boyet, M., Agranier, A., Nelson, B., 2004. Precise and accurate isotopic measurements using multiple-collector ICPMS. Geochim. Cosmochim. Acta 68, 2725–2744.

Ali, A., Srinivasan, G., 2011. Precise thermal ionization mass spectrometric measurements of 142Nd/144Nd and 143Nd/144Nd isotopic ratios of Nd separated from geological standards by chromatographic methods. Int. J. Mass Spectrom. 299, 27–34.

Alloway, B., 2008. Micronutrient Deficiencies in Global Crop Production. Springer.

An, Z., Bowler, J.M., Opdyke, N.D., Macumber, P.G., Firman, J.B., 1986. Palaeomagnetic stratigraphy of Lake Bungunnia: Plio-pleistocene precursor of aridity in the murray basin, Southeastern Australia. Palaeogeogr. Palaeoclimatol. Palaeoecol. 54, 219–239.

Andersen, K.K., Azuma, N., Barnola, J.M., Bigler, M., Biscaye, P., Caillon, N., Chappellaz, J., Clausen, H.B., Dahl-Jensen, D., Fischer, H., Flückiger, J., Fritzsche, D., Fujii, Y., Goto-Azuma, K., Grønvold, K., Gundestrup, N.S., Hansson, M., Huber, C., Hvidberg, C.S., Johnsen, S.J., Jonsell, U., Jouzel, J., Kipfstuhl, S., Landais, A., Leuenberger, M., Lorrain, R., Masson-Delmotte, V., Miller, H., Motoyama, H., Narita, H., Popp, T., Rasmussen, S.O., Raynaud, D., Rothlisberger, R., Ruth, U., Samyn, D., Schwander, J., Shoji, H., Siggard-Andersen, M.L., Steffensen, J.P., Stocker, T., Sveinbjörnsdóttir, A.E., Svensson, A., Takata, M., Tison, J.L., Thorsteinsson, T., Watanabe, O., Wilhelms, F., White, J.W.C., 2004. High-resolution record of Northern Hemisphere climate extending into the last interglacial period. Nature 431, 147–151.

Anderson, R.S., Repka, J.L., Dick, G.S., 1996. Explicit treatment of inheritance in dating depositional surfaces using in situ 10Be and 26Al. Geology.

Andreoli, C.Y., Robert, M., Pons, C.H., 1989. First steps of smectite-illite transformation with humectation and desiccation cycles. Appl. Clay Sci. 4, 423–435.

April, R., Newton, R., Coles, L.T., 1986. Chemical weathering in two Adirondack watersheds: past and present-day rates. Geol. Soc. Am. Bull. 97, 1232–1238.

Arakawa, Y., 1992. 143Nd/144Nd ratios of twelve GSJ rock reference samples and reproducibility of the data. Geochem. J. 26, 105–109.

Augustin, L., Barbante, C., Barnes, P.R.F., Barnola, J.M., Bigler, M., Castellano, E., Cattani, O., Chappellaz, J., Dahl-Jensen, D., Delmonte, B., Dreyfus, G., Durand, G., Falourd, S., Fischer, H., Flückiger, J., Hansson, M.E., Huybrechts, P., Jugie, G., Johnsen, S.J.,

Jouzel, J., Kaufmann, P., Kipfstuhl, J., Lambert, F., Lipenkov, V.Y., Littot, G.C., Longinelli, A., Lorrain, R., Maggi, V., Masson-Delmotte, V., Miller, H., Mulvaney, R., Oerlemans, J., Oerter, H., Orombelli, G., Parrenin, F., Peel, D.A., Petit, J.R., Raynaud, D., Ritz, C., Ruth, U., Schwander, J., Siegenthaler, U., Souchez, R., Stauffer, B., Steffensen, J.P., Stenni, B., Stocker, T.F., Tabacco, I.E., Udisti, R., van de Wal, R.S.W., van den Broeke, M., Weiss, J., Wilhelms, F., Winther, J.G., Wolff, E.W., Zucchelli, M., 2004. Eight glacial cycles from an Antarctic ice core. Nature 429, 623–628.

Ayliffe, L.K., Bird, M.I., Gagan, M.K., Isdale, P.J., Scott-gagan, H., Parker, B., Griffin, D., Nongkas, M., Mcculloch, M.T., 2004. Geochemistry of coral from Papua New Guinea as a proxy for ENSO ocean – atmosphere interactions in the Pacific Warm Pool. Cont. Shelf Res. 24, 2343–2356.

Ayliffe, L.K., Marianelli, P.C., Moriarty, K.C., Wells, R.T., McCulloch, M.T., Mortimer, G.E., Hellstrom, J.C., 1998. 500 ka precipitation record from southeastern Australia: Evidence for interglacial relative aridity. Geology 26, 147–150.

Bain, D.C., Mellor, A., Robertson-Rintoul, M.S.E., Buckland, S.T., 1993. Variations in weathering processes and rates with time in a chronosequence of soils from Glen Feshie, Scotland. Geoderma 57, 275–293.

Banerjee, D., Page, K.J., Lepper, K., 2002. Optical dating of palaeochannel deposits in the Riverine Plain, southeastern Australia: testing the reliability of existing thermoluminescence dates. Radiat. Prot. Dosimetry 101, 327–332.

Barnes, I., 1964. Field measurement of alkalinity and pH. USGS Water Supply Pap. 1535–H.

Barrows, T.T., Juggins, S., 2005. Sea-surface temperatures around the Australian margin and Indian Ocean during the Last Glacial Maximum. Quat. Sci. Rev. 24, 1017–1047.

Barrows, T.T., Juggins, S., De Deckker, P., Calvo, E., Pelejero, C., 2007. Long-term sea surface temperature and climate change in the Australian-New Zealand region. Paleoceanography 22, 1–17.

Barrows, T.T., Stone, J.O., Fifield, L.K., Cresswell, R.G., 2001. Late pleistocene glaciation of the kosciouszko massif, snowy mountains, Australia. Quat. Res. 55, 179–189.

Barrows, T.T., Stone, J.O., Fifield, L.K., Cresswell, R.G., 2002. The timing of the last glacial maximum in Australia. Quat. Sci. Rev. 21, 159–173.

Bassett, R.L., 1976. THE GEOCHEMISTRY OF BORON IN THERMAL WATERS. Standford University.

Bastian, L., Revel, M., Bayon, G., Dufour, A., Vigier, N., 2017. Abrupt response of chemical weathering to Late Quaternary hydroclimate changes in northeast Africa. Sci. Rep. 7, 44231.

Bauer, A., Berger, G., 1998. Kaolinite and smectite dissolution rate in high molar KOH solutions at 35°and 80°C. Appl. Geochemistry 13, 905–916.

Baxter, D.C., Rodushkin, I., Engström, E., Malinovsky, D., 2006. Revised exponential model for mass bias correction using an internal standard for isotope abundance ratio measurements by multi-collector inductively coupled plasma mass spectrometry. J. Anal. At. Spectrom. 21, 427.

Beaulieu, E., Goddéris, Y., Donnadieu, Y., Labat, D., Roelandt, C., 2012. High sensitivity of the continental-weathering carbon dioxide sink to future climate change. Nat. Clim. Chang. 2, 346–349.

Berger, A., 1978. Long-Term Variations of Daily Insolation and Quaternary Climatic Changes. J. Atmos. Sci. 35, 2362–2367.

Berner, R.A., 1978. Rate control of mineral dissolution under Earth surface conditions. Am. J. Sci. 278, 1235–1252.

Berner, R.A., 2003. The long-term carbon cycle, fossil fuels and atmospheric composition. Nature.

Berner, R.A., 1992. Weathering, plants, and the long-term carbon cycle. Geochim. Cosmochim. Acta 56, 3225–3231.

Berner, R.A., Berner, E.K., 1997. Silicate Weathering and Climate, in: Tectonic Uplift and Climate Change. Springer US, Boston, MA, pp. 353–365.

Berner, R.A., Caldeira, K., 1997. Geology The need for mass balance and feedback in the geochemical carbon cycle The need for mass balance and feedback in the geochemical carbon cycle. Geology 25, 955–956.

Berner, R.A., Kothavala, Z., 1994. GEOCARB II; a revised model of atmospheric CO 2 over Phanerozoic time. Am. J. Sci. 294, 56–91.

Berner, R.A., Lasaga, A.C., Garrels, R.M., 1983. The carbonate-silicate geochemical cycle and its effect on atmospheric carbon dioxide over the past 100 million years. Am. J. Sci. 283, 641–683.

Biscaye, P.E., 1965. Mineralogy and Sedimentation of Recent Deep-Sea Clay in Atlantic Ocean and Adjacent Seas and Oceans. Geol. Soc. Am. Bull. 76, 803-.

Blevins, D.G., Lukaszewski, K.M., 1998. BORON IN PLANT STRUCTURE AND FUNCTION. Annu. Rev. Plant Physiol. Plant Mol. Biol. 49, 481–500.

Blum, A.E., Stillings, L.L., 1995. Feldspar dissolution kinetics. Rev. Mineral. Geochemistry 31, 291–351.

Bluth, G.J.S., Kump, L.R., 1994. Lithologic and climatologic controls of river chemistry. Geochim. Cosmochim. Acta 58, 2341–2359.

Bosia, C., Chabaux, F., Pelt, E., France-Lanord, C., Morin, G., Lavé, J., Stille, P., 2016. U–Th–Ra variations in Himalayan river sediments (Gandak river, India): Weathering fractionation and/or grain-size sorting? Geochim. Cosmochim. Acta 193, 176–196.

Bouchez, J., Blanckenburg, V., Schuessler, J.A., 2013. MODELING NOVEL STABLE ISOTOPE RATIOS IN THE WEATHERING ZONE. - Am. J. Sci. Am. J. Sci. 313, 267–308.

Bouchez, J., Gaillardet, J., Lupker, M., Louvat, P., France-Lanord, C., Maurice, L., Armijos, E., Moquet, J.-S., 2012. Floodplains of large rivers: Weathering reactors or simple silos? Chem. Geol. 332–333, 166–184.

Bouchez, J., Gaillardet, J., von Blanckenburg, F., 2014. Weathering Intensity in Lowland River Basins: From the Andes to the Amazon Mouth. Procedia Earth Planet. Sci. 10, 280–286.

Bouchez, J., Métivier, F., Lupker, M., Maurice, L., Perez, M., Gaillardet, J., France-Lanord, C., 2011. Prediction of depth-integrated fluxes of suspended sediment in the Amazon River: particle aggregation as a complicating factor. Hydrol. Process. 25, 778–794.

Bowler, J.M., 1967. Quaternary chronology of goulburn valley sediments and their correlation in southeastern australia. J. Geol. Soc. Aust. 14, 287–292.

Bowler, J.M., 1986. Quaternary landform evolution. Nat. Environ. Aust. - A Geogr. Vol 1.

Bowler, J.M., 1978. Quaternary climate and tectonics in the evolution of the Riverine Plain, southeastern Australia, Landform evolution in Australasia.

Bowler, J.M., Johnston, H., Olley, J.M., Prescott, J.R., Roberts, R.G., Shawcross, W., Spooner, N.A., 2003. New ages for human occupation and climatic change at Lake Mungo, Australia. Nature 421, 837–840.

Brady, P. V, Carroll, S.A., 1994. Direct effects of CO2 and temperature on silicate weathering: Possible implications for climate control. Geochim. Cosmochim. Acta 58, 1853–1856.

Brand, W.A., Coplen, T.B., Vogl, J., Rosner, M., Prohaska, T., 2014. Assessment of international reference materials for isotope-ratio analysis (IUPAC technical report), in: Pure and Applied Chemistry. De Gruyter, pp. 425–467.

Brantley, S.L., Chen, Y., 1995. Chemical weathering rates of pyroxenes and amphiboles. Rev. Mineral. Geochemistry 31, 119–172.

Brantley, S.L., Olsen, A.A., 2013. Reaction Kinetics of Primary Rock-Forming Minerals under Ambient Conditions, in: Treatise on Geochemistry: Second Edition. Elsevier, pp. 69–113.

Brantley, S.L., White, A.F., 2009. Approaches to Modeling Weathered Regolith. Rev. Mineral. Geochemistry 70, 435–484.

Braucher, R., Brown, E.T., Bourlès, D.L., Colin, F., 2003. In situ produced10Be measurements at great depths: Implications for production rates by fast muons. Earth Planet. Sci. Lett. 211, 251–258.

Braun, J.J., Descloitres, M., Riotte, J., Fleury, S., Barbiéro, L., Boeglin, J.L., Violette, A., Lacarce, E., Ruiz, L., Sekhar, M., Mohan Kumar, M.S., Subramanian, S., Dupré, B., 2009. Regolith mass balance inferred from combined mineralogical, geochemical and geophysical studies: Mule Hole gneissic watershed, South India. Geochim. Cosmochim. Acta 73, 935–961.

Braun, T., Ghersini, G., 1975. Extraction Chromatography, in: Braun, T., Ghersini, G. (Eds.), Extraction Chromatography. Elsevier Scientific Publishing Company, p. 226.

Brimhall Jr., G.H., Dietrich, W.E., 1987. Constitutive relationships between chemical composition, volume, density, porosity, and strain in metasomatic hydrothermal systems. Geochim. Cosmochim. Acta 51, 567–587.

Brizga, S.O., Finlayson, B.L., 1990. Channel avulsion and river metamorphosis: The case of the Thomson River, Victoria, Australia. Earth Surf. Process. Landforms 15, 391–404.

Broecker, W.S., Sanyal, A., 1998. Does atmospheric CO2 police the rate of chemical weathering? Global Biogeochem. Cycles 12, 403–408.

Brown, E.T., Edmond, J.M., Raisbeck, G.M., Yiou, F., Kurz, M.D., Brook, E.J., 1991. Examination of surface exposure ages of Antarctic moraines using in situ produced10Be and26Al. Geochim. Cosmochim. Acta 55, 2269–2283.

Brown, E.T., Stallard, R.F., Larsen, M.C., Raisbeck, G.M., Yiou, F., 1995. Denudation rates determined from the accumulation of in situ-produced 10Be in the luquillo experimental forest, Puerto Rico. Earth Planet. Sci. Lett. 129, 193–202.

Brown, L., Pavich, M.J., Hickman, R.E., Klein, J., Middleton, R., 1988. Erosion of the

eastern United States observed with 10Be. Earth Surf. Process. Landforms 13, 441–457.

Budyko, M.I., 1969. The effect of solar radiation variations of the climate of the Earth. Tellus XXI, 611–619.

Burns, D.A., McDonnell, J.J., Hooper, R.P., Peters, N.E., Freer, J.E., Kendall, C., Beven, K., 2001. Quantifying contributions to storm runoff through end-member mixing analysis and hydrologic measurements at the Panola Mountain research watershed (Georgia, USA). Hydrol. Process. 15, 1903–1924.

Butler, B.E., 1950. A theory of prior streams as a causal factor of soil research in the Riverine Plain of south-eastern Australia. Aust. J. Agriculatural Res. 1, 231–252.

Butler, B.E., 1958. Depositional systems of the Riverine Plain in relation to soils.

Butler, B.E., 1961. Ground surfaces and the history of the Riverine Plain. Aust. J. Sci.

Caldeira, K., Kasting, J.F., 1992. Susceptibility of the early Earth to irreversible glaciation caused by carbon dioxide clouds. Nature 359, 226–228.

Calvo, E., Pelejero, C., De Deckker, P., Logan, G.A., 2007. Antarctic deglacial pattern in a 30 kyr record of sea surface temperature offshore South Australia. Geophys. Res. Lett. 34, n/a-n/a.

Carroll, D., 1970. Chemical Weathering. Rock Weather. 89–115.

Catanzaro, E.J., 1970. Boric Acid: Isotopic and Assay Standard Reference Materials - Google Books. U.S. Department of Commerce.

Chabaux, F., 2003. U-Th-Ra Fractionation During Weathering and River Transport. Rev. Mineral. Geochemistry 52, 533–576.

Chabaux, F., Blaes, E., Granet, M., Roupert, R. di C., Stille, P., 2012. Determination of transfer time for sediments in alluvial plains using238U-234U-230Th disequilibria: The case of the Ganges river system. Comptes Rendus - Geosci.

Chappell, J., Shackleton, N.J., 1986. Oxygen isotopes and sea level. Nature 324, 137–140.

Chaussidon, M., Albarède, F., 1992. Secular boron isotope variations in the continental crust: an ion microprobe study. Earth Planet. Sci. Lett. 108, 229–241.

Chetelat, B., Gaillardet, J., 2005. Boron Isotopes in the Seine River , France : A Probe of Anthropogenic Contamination Boron Isotopes in the Seine River, France : A Probe of Anthropogenic Contamination. Environ. Sci. Technol. 39, 2486–2493.

Chetelat, B., Gaillardet, J., Freydier, R., Négrel, P., 2005. Boron isotopes in precipitation: Experimental constraints and field evidence from French Guiana. Earth Planet. Sci. Lett. 235, 16–30.

Chetelat, B., Liu, C.-Q., Gaillardet, J., Wang, Q.L., Zhao, Z.Q., Liang, C.S., Xiao, Y.K., 2009. Boron isotopes geochemistry of the Changjiang basin rivers. Geochim. Cosmochim. Acta 73, 6084–6097.

Christie-Blick, N., 1982. Pre-Pleistocene glaciation on Earth: Implications for climatic history of Mars. Icarus 50, 423–443.

Chu, Z.-Y.Y., Li, C.-F.F., Hegner, E., Chen, Z., Yan, Y., Guo, J.-H.H., 2014. High-precision 143ND/144ND ratios from NDO+ data corrected with in-run measured oxygen isotope ratios. Anal. Chem. 86, 11141–11150.

Chu, Z., Chen, F., Yang, Y., Guo, J., 2009. Precise determination of Sm, Nd concentrations

and Nd isotopic compositions at the nanogram level in geological samples by thermal ionization mass spectrometry. J. Anal. At. Spectrom. 24, 1534–1544.

Chu, Z., Guo, J., Yang, Y., Qi, L., Li, C., 2014. Precise Determination of Sm and Nd Concentrations and Nd Isotopic Compositions in Highly Depleted Ultramafic Reference Materials. Geostand. Geoanalytical Res. 38, 61–72.

Cividini, D., Lemarchand, D., Chabaux, F., Boutin, R., Pierret, M.C., 2010. From biological to lithological control of the B geochemical cycle in a forest watershed (Strengbach, Vosges). Geochim. Cosmochim. Acta 74, 3143–3163.

Clement, A.C., Peterson, L.C., 2008. Mechanisms of abrupt climate change of the last glacial period. Rev. Geophys.

Colhoun, E.A., 1985. Glaciations of the West Coast Range, Tasmania. Quat. Res. 24, 39–59.

Colhoun, E.A., van de Geer, G., Mook, W.G., 1982. Stratigraphy, Pollen Analysis, and Paleoclimatic Interpretation of Pulbeena Swamp, Northwestern Tasmania. Quat. Res. 18, 108–126.

Coney, P.J., 1992. The Lachlan belt of eastern Australian and Circum-Pacific tectonic evolution. Tectonophysics 214, 1–25.

Coventry, R.J., 1976. Abandoned shorelines and the late quaternary history of lake george, New South Wales. J. Geol. Soc. Aust. 23, 249–273.

Crocket, K.C., Lambelet, M., van de Flierdt, T., Rehkämper, M., Robinson, L.F., 2014. Measurement of fossil deep-sea coral Nd isotopic compositions and concentrations by TIMS as NdO+, with evaluation of cleaning protocols. Chem. Geol. 374–375, 128–140.

Cupper, M.L., 2005. Last glacial to Holocene evolution of semi-arid rangelands in southeastern Australia. The Holocene 15, 541–553.

Curry, J. a., Schramm, J.L., Ebert, E.E., 1995. Sea-Ice Albedo Climate Feedback Mechanism. J. Clim. 8, 240–247.

Curtis, C.D., 1990. Aspects of climatic influence on the clay mineralogy and geochemistry of soils, palaeosols and clastic sedimentary rocks. J. Geol. Soc. London. 147, 351–357.

David, T., Browne, W., 1950. The geology of the Commonwealth of Australia.

De Deckker, P., 1982. Late Quaternary ostracods from Lake George, New South Wales. Alcheringa 6, 305–318.

Dellinger, M., Bouchez, J., Gaillardet, J., Faure, L., Moureau, J., 2017. Tracing weathering regimes using the lithium isotope composition of detrital sediments. Geology 45, 411–414.

Dellinger, M., Gaillardet, J., Bouchez, J., Calmels, D., Galy, V., Hilton, R.G., Louvat, P., France-Lanord, C., 2014. Lithium isotopes in large rivers reveal the cannibalistic nature of modern continental weathering and erosion. Earth Planet. Sci. Lett. 401, 359–372.

DePaolo, D.J., 2006. Isotopic effects in fracture-dominated reactive fluid-rock systems. Geochim. Cosmochim. Acta 70, 1077–1096.

DePaolo, D.J., Maher, K., Christensen, J.N., McManus, J., 2006. Sediment transport time measured with U-series isotopes: Results from ODP North Atlantic drift site 984. Earth Planet. Sci. Lett. 248, 379–395.

Dequincey, O., Chabaux, F., Clauer, N., Sigmarsson, O., Liewig, N., Leprun, J.C., 2002.

Chemical mobilizations in laterites: Evidence from trace elements and 238U-234U-230Th disequilibria. Geochim. Cosmochim. Acta 66, 1197–1210.

Derry, L.A., France-Lanord, C., 1996. Neogene Himalayan weathering history and river87Sr86Sr: impact on the marine Sr record. Earth Planet. Sci. Lett. 142, 59–74.

Dessert, C., Dupré, B., Gaillardet, J., François, L.M., Allègre, C.J., 2003. Basalt weathering laws and the impact of basalt weathering on the global carbon cycle. Chem. Geol. 202, 257–273.

Dodson, J.R., Wright, R.V.S., 1989. Humid to arid to subhumid vegetation shift on Pilliga Sandstone, Ulungra Springs, New South Wales. Quat. Res. 32, 182–192.

Dorn, R.I., Brady, P. V, 1995. Rock-based measurement of temperature-dependent plagioclase weathering. Geochim. Cosmochim. Acta.

Dosseto, A., Buss, H.L., Chabaux, F., 2014. Age and weathering rate of sediments in small catchments: The role of hillslope erosion. Geochim. Cosmochim. Acta 132, 238–258.

Dosseto, A., Hesse, P.P., Maher, K., Fryirs, K., Turner, S., 2010. Climatic and vegetation control on sediment dynamics during the last glacial cycle. Geology 38, 395–398.

Dosseto, A., Turner, S.P., Chappell, J., 2008. The evolution of weathering profiles through time: New insights from uranium-series isotopes. Earth Planet. Sci. Lett. 274, 359–371.

Dosseto, A., Vigier, N., Joannes-Boyau, R., Moffat, I., Singh, T., Srivastava, P., 2015. Rapid response of silicate weathering rates to climate change in the Himalaya. Geochemical Perspect. Lett. 1, 10–19.

Dove, P.M., 1995. Kinetic and thermodynamic controls on silica reactivity in weathering environments. Rev. Mineral. Geochemistry 31, 235–290.

Dupré, B., Gaillardet, J., Rousseau, D., Allègre, C.J., 1996. Major and trace elements of river-borne material: The Congo Basin. Geochim. Cosmochim. Acta 60, 1301–1321.

Edmond, J.M., Palmer, M.R., Measures, C.I., Grant, B., Stallard, R.F., 1995. The fluvial geochemistry and denudation rate of the Guayana Shield in Venezuela, Colombia, and Brazil. Geochim. Cosmochim. Acta 59, 3301–3325.

Emiliani, C., 1955. Pleistocene Temperatures. J. Geol. 63, 538–578.

Fedo, C.M., Nesbitt, H.W., Young, G.M., 1995. Unravelling the effects of potassium metasomatism in sedimentary rocks and paleosols, with implications for paleoweathering conditions and provenance. Geology 23, 921–924.

Ferguson, R.I., 1987. Accuracy and precision of methods for estimating river loads. Earth Surf. Process. Landforms 12, 95–104.

Ferrier, K.L., Kirchner, J.W., 2008. Effects of physical erosion on chemical denudation rates: A numerical modeling study of soil-mantled hillslopes. Earth Planet. Sci. Lett. 272, 591–599.

Fischer, A.G., 1981. Climatic oscillations in the biosphere. Biot. Cris. Ecol. Evol. time 103–131.

Foster, G.L., Pogge Von Strandmann, P.A.E., Rae, J.W.B., 2010. Boron and magnesium isotopic composition of seawater. Geochemistry, Geophys. Geosystems 11, n/a-n/a.

Foster, G.L., Vance, D., 2006. Negligible glacial-interglacial variation in continental chemical weathering rates. Nature 444, 918–921.

Foster, S., McDonald, B.K., 2018. Kiribati | Culture, History, & People | Britannica.com [WWW Document]. Encycl. Br.

Fournier, F., 1960. Climat et érosion: la relation entre l'érosion du sol par l'eau et les précipitations atmosphériques. Presses universitaires de France,.

France-Lanord, C., Derry, L.A., 1997. Organic-carbon burial forcing of the carbon cycle from Himalyan erosion. Nature 390, 65–67.

Gaillardet, J., Allègre, C.J., 1995. Boron isotopic compositions of corals: Seawater or diagenesis record? Earth Planet. Sci. Lett. 136, 665–676.

Gaillardet, J., Dupré, B., Allègre, C.J., 1999a. Geochemistry of large river suspended sediments: silicate weathering or recycling tracer? Geochim. Cosmochim. Acta 63, 4037–4051.

Gaillardet, J., Dupré, B., Allègre, C.J., 1995. A global geochemical mass budget applied to the Congo basin rivers: Erosion rates and continental crust composition. Geochim. Cosmochim. Acta 59, 3469–3485.

Gaillardet, J., Dupré, B., Louvat, P., Allègre, C.J., 1999b. Global silicate weathering and CO2consumption rates deduced from the chemistry of large rivers. Chem. Geol. 159, 3–30.

Gaillardet, J., Lemarchand, D., 2017. Boron in the weathering environment, in: Boron Isotopes. pp. 1–50.

Gaillardet, J., Lemarchand, D., Göpel, C., Manhès, G., 2001. Evaporation and sublimation of boric acid: Application for boron purification from organic rich solutions. Geostand. Newsl. 25, 67–75.

Galloway, R.W., 1965. Late Quaternary Climates in Australia. J. Geol. 73, 603–618.

Galy, A., France-Lanord, C., 1999. Weathering processes in the Ganges-Brahmaputra basin and the riverine alkalinity budget. Chem. Geol. 159, 31–60.

Galy, A., France-Lanord, C., 2001. Higher erosion rates in the Himalaya: Geochemical constraints on riverine fluxes. Geology 29, 23–26.

Galy, V., Bouchez, J., France-Lanord, C., 2007. Determination of total organic carbon content and δ13C in carbonate-rich detrital sediments. Geostand. Geoanalytical Res. 31, 199–207.

Gangjian, W., Jingxian, W., Ying, L., Ting, K., Zhongyuan, R., Jinlong, M., Yigang, X., 2013. Measurement on high-precision boron isotope of silicate materials by a single column purification method and MC-ICP-MS. J. Anal. At. Spectrom. 28, 606.

Ganopolski, A., Rahmstorf, S., 2001. Rapid changes of glacial climate simulated in a couples climate model. Nature 409, 153–158.

Gao, S., Rudnick, R.L., Yuan, H., Liu, X.-M., Liu, Y., Xu, W., Ling, W., Ayers, J., Wang, X.-C., Wang, Q.-H., 2004. Recycling lower continental crust in the North China craton. Nature 432, 892–897.

Garreaud, R., Lopez, P., Minvielle, M., Rojas, M., 2013. Large-scale control on the Patagonian climate. J. Clim. 26, 215–230.

Garreaud, R.D., 2009. The Andes climate and weather. Adv. Geosci 22, 3–11.

Garrels, R.M., 1988. Sediment Cycling During Earth History, in: Physical and Chemical

Weathering in Geochemical Cycles. Springer Netherlands, Dordrecht, pp. 341–355.

Garrels, R.M., Mackenzie, F.T., 1971. Gregor's Denudation of the Continents. Nature 231, 382–383.

GARRELS, R.M., MACKENZIE, F.T., 1967. Origin of the Chemical Compositions of Some Springs and Lakes. pp. 222–242.

Garzanti, E., Andó, S., France-Lanord, C., Censi, P., Vignola, P., Galy, V., Lupker, M., 2011. Mineralogical and chemical variability of fluvial sediments 2. Suspended-load silt (Ganga-Brahmaputra, Bangladesh). Earth Planet. Sci. Lett. 302, 107–120.

Garzanti, E., Andò, S., France-Lanord, C., Vezzoli, G., Censi, P., Galy, V., Najman, Y., 2010. Mineralogical and chemical variability of fluvial sediments1. Bedload sand (Ganga–Brahmaputra, Bangladesh). Earth Planet. Sci. Lett. 299, 368–381.

Garzanti, E., Vezzoli, G., Andò, S., Lavé, J., Attal, M., France-Lanord, C., DeCelles, P., 2007. Quantifying sand provenance and erosion (Marsyandi River, Nepal Himalaya). Earth Planet. Sci. Lett. 258, 500–515.

Georg, R.B., Newman, K., 2015. The effect of hydride formation on instrumental mass discrimination in MC-ICP-MS: a case study of mercury (Hg) and thallium (Tl) isotopes. J. Anal. At. Spectrom. 30, 1935–1944.

Gingele, F.X., De Deckker, P., 2005. Clay mineral, geochemical and Sr/Nd isotopic fingerprinting of sediments in the Murray-Darling fluvial system, southeast Australia. Aust. J. Earth Sci. 52, 965–974.

Gioia, S.M.C.L., Pimentel, M.M., 2000. The Sm-Nd isotopic method in the Geochronology Laboratory of the University of Brasilia. An. Acad. Bras. Cienc. 72, 218–245.

Gíslason, S.D.S.R., Arnórsson, S., Ármannsson, H., 1996. Chemical weathering of basalt in Southwest Iceland: Effects of runoff, age of rocks and vegetative/glacial cover. Am. J. Sci. 296, 837–907.

Gislason, S.R., Oelkers, E.H., Eiriksdottir, E.S., Kardjilov, M.I., Gisladottir, G., Sigfusson, B., Snorrason, A., Elefsen, S., Hardardottir, J., Torssander, P., Oskarsson, N., 2009. Direct evidence of the feedback between climate and weathering. Earth Planet. Sci. Lett. 277, 213–222.

Gislason, S.R., Oelkers, E.H., Snorrason, Á., 2006. Role of river-suspended material in the global carbon cycle. Geology 34, 49–52.

Goddéris, Y., François, L.M., 1996. Balancing the Cenozoic carbon and alkalinity cycles: Constraints from isotopic records. Geophys. Res. Lett. 23, 3743–3746.

Goldberg, S., 1997. Reactions of boron with soils. Plant Soil 193, 35–48.

Goldberg, S., Forster, H.S., 1991. Boron sorption on calcareous soils and reference calcites. Soil Sci. 152, 304–310.

Gough, D.O., 1981. Solar interior structure and luminosity variations. Sol. Phys. 74, 21–34.

Govindaraju, K., 1994. 1994 COMPILATION OF WORKING VALUES AND SAMPLE DESCRIPTION FOR 383 GEOSTANDARDS. Geostand. Geoanalytical Res. 18, 1–158.

Granet, M., Chabaux, F., Stille, P., Dosseto, A., France-Lanord, C., Blaes, E., 2010. U-series disequilibria in suspended river sediments and implication for sediment transfer time in alluvial plains: The case of the Himalayan rivers. Geochim. Cosmochim. Acta 74, 2851–2865.

Granet, M., Chabaux, F., Stille, P., France-Lanord, C., Pelt, E., 2007. Time-scales of sedimentary transfer and weathering processes from U-series nuclides: Clues from the Himalayan rivers. Earth Planet. Sci. Lett. 261, 389–406.

Grim, R.E., 1968. Clay mineralogy. McGraw Hill.

Hajash, A., Chandler, G.W., 1982. An experimental investigation of high-temperature interactions between seawater and rhyolite, andesite, basalt and peridotite. Contrib. to Mineral. Petrol. 78, 240–254.

Hambrey, M.J., Harland, W.B., 1981. Earth's pre-Pleistocene Glacial Record, Cambridge earth science series. Cambridge University Press.

Handley, H.K., Turner, S., Afonso, J.C., Dosseto, A., Cohen, T., 2013. Sediment residence times constrained by uranium-series isotopes: A critical appraisal of the comminution approach. Geochim. Cosmochim. Acta 103, 245–262.

Harder, H., 1970. Boron content of sediments as a tool in facies analysis. Sediment. Geol. 4, 153–175.

Harland, W.B., 1981. Chronology of Earth's glacial and tectonic record. J. Geol. Soc. London 138, 197–203.

Harnois, L., 1988. THE CIW INDEX: A NEW CHEMICAL INDEX OF WEATHERING *. Sediment. Geol. 55, 319–322.

Hay, W.W., Sloan Ii, J.L., Wold, C.N., 1988. Mass/Age Distribution and Composition of Sediments on the Ocean Floor and the Global Rate of Sediment Subduction. J. Geophys. Res. 93940, 933–14.

Heimsath, A.M., Chappell, J., Dietrich, W.E., Nishiizumi, K., Finkel, R.C., 2000. Soil production on a retreating escarpment in southeastern Australia. Geology 28, 787–790.

Hemming, N.G., Hanson, G.N., 1992. Boron isotopic composition and concentration in modern marine carbonates. Geochim. Cosmochim. Acta 56, 537–543.

Hemming, N.G., Reeder, R.J., Hanson, G.N., 1995. Mineral-fluid partitioning and isotopic fractionation of boron in synthetic calcium carbonate. Geochim. Cosmochim. Acta 59, 371–379.

Henderson, G.M., Martel, D.J., O'Nions, R.K., Shackleton, N.J., 1994. Evolution of seawater87Sr86Sr over the last 400 ka: the absence of glacial/interglacial cycles. Earth Planet. Sci. Lett. 128, 643–651.

Hendon, H.H., Thompson, D.W.J., Wheeler, M.C., 2007. Australian rainfall and surface temperature variations associated with the Southern Hemisphere annular mode. J. Clim. 20, 2452–2467.

Hershey, J.P., Fernandez, M., Milne, P.J., Millero, F.J., 1986. The ionization of boric acid in NaCl, Na- Ca-Cl and Na- Mg- Cl solutions at 25° C. Geochim. Cosmochim. Actat Cosmochim. Acta 50, 143–148.

Hervig, R.L., Moore, G.M., Williams, L.B., Peacock, S.M., Holloway, J.R., Roggensack, K., 2002. Isotopic and elemental partitioning of boron between hydrous fluid and silicate melt. Am. Mineral. 87, 769–774.

Hesse, P.P., 1994. The record of continental dust from Australia in Tasman Sea Sediments. Quat. Sci. Rev. 13, 257–272.

Hesse, P.P., Magee, J.W., van der Kaars, S., 2004. Late Quaternary climates of the Australian

arid zone: A review. Quat. Int. 118–119, 87–102.

Hesse, P.P., McTainsh, G.H., 1999. Last glacial maximum to early Holocene wind strength in the mid-latitudes of the Southern Hemisphere from Aeolian Dust in the Tasman Sea. Quat. Res. 52, 343–349.

Hill, K.J., Santoso, A., England, M.H., 2009. Interannual Tasmanian rainfall variability associated with large-scale climate modes. J. Clim. 22, 4383–4397.

Hilley, G.E., Chamberlain, C.P., Moon, S., Porder, S., Willett, S.D., 2010. Competition between erosion and reaction kinetics in controlling silicate-weathering rates. Earth Planet. Sci. Lett. 293, 191–199.

Hilley, G.E., Porder, S., 2008. A framework for predicting global silicate weathering and CO2 drawdown rates over geologic time-scales. Proc. Natl. Acad. Sci. U. S. A. 105, 16855–9.

Hogan, J.F., Blum, J.D., 2003. Boron and lithium isotopes as groundwater tracers: a study at the Fresh Kills Landfill, Staten Island, New York, USA. Appl. Geochemistry 18, 615–627.

Holeman, J.N., 1968. The Sediment Yield of Major Rivers of the World. Water Resour. Res. 4, 737–747.

Holland, H.D., 1978. The chemistry of the atmosphere and oceans-(v. 1). New York, N.Y. (USA) Wiley-Interscience.

Hu, Z., Gao, S., 2008. Upper crustal abundances of trace elements: A revision and update. Chem. Geol. 253, 205–221.

Huang, K.-F., Blusztajn, J., Oppo, D.W., Curry, W.B., Peucker-Ehrenbrink, B., 2012. High-precision and accurate determinations of neodymium isotopic compositions at nanogram levels in natural materials by MC-ICP-MS. J. Anal. At. Spectrom. 27, 1560.

Huh, Y., Tsoi, M.Y., Zaitsev, A., Edmond, J.M., 1998. The fluvial geochemistry of the rivers of eastern Siberia: I. Tributaries of the Lena River draining the sedimentary platform of the Siberian Craton. Geochim. Cosmochim. Acta 62, 1657–1676.

IMAI, N., TERASHIMA, S., ITOH, S., ANDO, A., 1995. 1994 COMPILATION OF ANALYTICAL DATA FOR MINOR AND TRACE ELEMENTS IN SEVENTEEN GSJ GEOCHEMICAL REFERENCE SAMPLES, ???IGNEOUS ROCK SERIES??? Geostand. Newsl. 19, 135–213.

Jackson, T.A., 1975. Humic matter in natural waters and sediments. Soil Sci. 119.

Jenny, H., 1941. Factors of soil formation. A system of quantitative pedology, Geoderma.

Johnson, T.M., DePaolo, D.J., 1997. Rapid exchange effects on isotope ratios in groundwater systems 1. Development of a transport-dissolution-exchange model. Water Resour. Res. 33, 187–195.

Julius Dasch, E., 1969. Strontium isotopes in weathering profiles, deep-seas sediments, and sedimentary rocks. Geochim. Cosmochim. Acta 33, 1521–1552.

Kakihana, H., Kotaka, M., 1977. Equilibrium constants for boron isotope-exchange reactions. Bull. Res. Lab. Nucl. React. (Tokyo Inst. Technol.

Kakihana, H., Kotaka, M., Satoh, S., Nomura, M., Okamoto, M., 1977. Fundamental Studies on the Ion-Exchange Separation of Boron Isotopes. Bull. Chem. Soc. Jpn. 50, 158–163.

Kasting, J.F., 1993. Earth's Early Atmosphere. Science (80-.). 259, 920–925.

Kemp, J., Pietsch, T., Gontz, A., Olley, J., 2017. Lacustrine-fluvial interactions in Australia's Riverine Plains. Quat. Sci. Rev. 166, 352–362.

Kemp, J., Rhodes, E.J., 2010. Episodic fluvial activity of inland rivers in southeastern Australia: Palaeochannel systems and terraces of the Lachlan River. Quat. Sci. Rev. 29, 732–752.

Keren, R., Mezuman, U., 1981. BORON ADSORPTION BY CLAY MINERALS USING A PHENOMENOLOGICAL EQUATION I. Clays Clay Miner. 29, 198–204.

Kershaw, A.P., 1986. Climatic change and aboriginal burning in north-east Australia during the last two glacial/interglacial cycles. Nature 322, 47–49.

Kershaw, A.P., McKenzie, G.M., Porch, N., Roberts, R.G., Brown, J., Heijnis, H., Orr, M.L., Jacobsen, G., Newall, P.R., 2007. A high-resolution record of vegetation and climate through the last glacial cycle from Caledonia Fen, southeastern highlands of Australia. J. Quat. Sci. 22, 481–500.

Kershaw, P., Nanson, G.C., 1993. The last full glacial cycle in the Australian region. Glob. Planet. Change 7, 1–9.

Kershaw, P., van der Kaars, S., 2012. Australia and the Southwest Pacific, in: Quaternary Environmental Change in the Tropics. John Wiley & Sons, Ltd, Chichester, UK, pp. 236–262.

Kingham, R., 1998. Geology of the Murray-Darling Basin — Simplified Lithostratigraphic Groupings. Aust. Geol. Surv. Organ. Dep. Promary Ind. energy.

Korotev, R.L., 1996. A self-consistent compilation of elemental concentration data for 93 geochemical reference samples. Geostand. Newsl. 20, 217–245.

Kotwicki, V., Allan, R., 1998. La Nina de Australia - Contemporary and palaeo-hydrology of Lake Eyre. Palaeogeogr. Palaeoclimatol. Palaeoecol. 144, 265–280.

Kronberg, B.I., Nesbitt, H.W., Fyfe, W.S., 1987. Mobilities of alkalis, alkaline earths and halogens during weathering. Chem. Geol. 60, 41–49.

Kump, L.R., Brantley, S.L., Arthur, M.A., 2000. CHEMICAL WEATHERING, ATMOSPHERIC CO 2 , AND CLIMATE. Annu. Rev. Earth Planet. Sci 28, 611–67.

Lal, D., 1991. Cosmic ray labeling of erosion surfaces: in situ nuclide production rates and erosion models. Earth Planet. Sci. Lett. 104, 424–439.

Lane, E.W., 1957. A study of the shape of channels formed by natural streams flowing in erodible material.

Langford-Smith, T., 1959. Deposition on the Riverine Plain of southeastern Australia. Aust. J. Sci.

Langford-Smith, T., 1960. The Dead River Systems of the Murrumbidgee. Geogr. Rev. 50, 368.

Langford-Smith, T., 1962. Riverine plains geochronology. Aust. J. Sci. 25, 96.

Lasaga, A.C., Berner, R.A., Garrels, R.M., 1985. An Improved Geochemical Model of Atmospheric CO2 Fluctuations Over the Past 100 Million Years, in: The Carbon Cycle and Atmospheric CO2: Natural Variations Archean to Present. American Geophysical Union, pp. 397–411.

Lasaga, A.C., Soler, J.M., Ganor, J., Burch, T.E., Nagy, K.L., 1994. Chemical weathering rate laws and global geochemical cycles. Geochim. Cosmochim. Acta 58, 2361–2386.

Le Fort, P., 1975. Himalayas: the collided range. present knowledge of the continental arc. Am. J. Sci.

Leeman, W.P., Tonarini, S., Chan, L.H., Borg, L.E., 2004. Boron and lithium isotopic variations in a hot subduction zone - The southern Washington Cascades. Chem. Geol. 212, 101–124.

Lehto, T., Ruuhola, T., Dell, B., 2010. Boron in forest trees and forest ecosystems. For. Ecol. Manage. 260, 2053–2069.

Lemarchand, D., 2001. Géochimie isotopique du bore: érosion continentale: bilan océanique et Paléo-pH. Université Denie Diderot.

Lemarchand, D., Cividini, D., Turpault, M.P., Chabaux, F., 2012. Boron isotopes in different grain size fractions: Exploring past and present water–rock interactions from two soil profiles (Strengbach, Vosges Mountains). Geochim. Cosmochim. Acta 98, 78–93.

Lemarchand, D., Gaillardet, J., 2006. Transient features of the erosion of shales in the Mackenzie basin (Canada), evidences from boron isotopes. Earth Planet. Sci. Lett. 245, 174–189.

Lemarchand, D., Gaillardet, J., Göpel, C., Manhès, G., 2002a. An optimized procedure for boron separation and mass spectrometry analysis for river samples. Chem. Geol. 182, 323–334.

Lemarchand, D., Gaillardet, J., Lewin, E., Allegre, C.J., 2002b. Boron isotope systematics in large rivers:implications for the marine boron budgret and paleo-pH reconstriction over the Cenozoic. Chem. Geol. 190, 123–140.

Lemarchand, D., Gaillardet, J., Lewin, E., Allegre, C.J., 2000. The influence of rivers on marine boron isotopes and implications for reconstructing past ocean pH. Nature 408, 951–954.

Lemarchand, D., Jacobson, A.D., Cividini, D., Chabaux, F., 2015. The major ion, 87Sr/86Sr, and δ11B geochemistry of groundwater in the Wyodak-Anderson coal bed aquifer (Powder River Basin, Wyoming, USA). Comptes Rendus Geosci. 347, 348–357.

Lemarchand, E., Schott, J., Gaillardet, J., 2007. How surface complexes impact boron isotope fractionation: Evidence from Fe and Mn oxides sorption experiments. Earth Planet. Sci. Lett. 260, 277–296.

Lemarchand, E., Schott, J., Gaillardet, J., 2005. Boron isotopic fractionation related to boron sorption on humic acid and the structure of surface complexes formed. Geochim. Cosmochim. Acta 69, 3519–3533.

Leslie, D., Berry Lyons, W., Warner, N., Vengosh, A., Olesik, J., Welch, K., Deuerling, K., 2014. Boron isotopic geochemistry of the McMurdo Dry Valley lakes, Antarctica. Chem. Geol. 386, 152–164.

Li, C.-F., Chen, F., Li, X.-H., 2007. Precise isotopic measurements of sub-nanogram Nd of standard reference material by thermal ionization mass spectrometry using the NdO+ technique. Int. J. Mass Spectrom. 266, 34–41.

Li, C., Yang, S., 2010. Is chemical index of alteration (cia) a reliable proxy for chemical weathering in global drainage basins? Am. J. Sci. 310, 111–127.

Li, C.F., Chen, F., Li, X.H., 2007. Precise isotopic measurements of sub-nanogram Nd of standard reference material by thermal ionization mass spectrometry using the NdO+ technique. Int. J. Mass Spectrom. 266, 34–41.

Liu, Y.-C., You, C.-F., Huang, K.-F., Wang, R.-M., Chung, C.-H., Liu, H.-C., 2012. Boron sources and transport mechanisms in river waters collected from southwestern Taiwan: Isotopic evidence.

Livingstone, D.A., 1972. GARRELS, R. M., AND F. T. MACKENZIE. 1971. Evolution of sedimentary rocks. W. W. Norton & Co., New York. xvi + 397 p. $11.50. Limnol. Oceanogr. 17, 165–166.

Louvat, P., Allègre, C.J., 1997. Present denudation rates on the island of Réunion determined by river geochemistry: Basalt weathering and mass budget between chemical and mechanical erosions. Geochim. Cosmochim. Acta 61, 3645–3669.

Louvat, P., Gaillardet, J., Paris, G., Dessert, C., 2011. Boron isotope ratios of surface waters in Guadeloupe, Lesser Antilles. Appl. Geochemistry 26, S76–S79.

Louvat, P., Gayer, E., Gaillardet, J., 2014. Boron Behavior in the Rivers of Réunion Island, Inferred from Boron Isotope Ratios and Concentrations of Major and Trace Elements. Procedia Earth Planet. Sci. 10, 231–237.

Ludwig, W., Probst, J.L., 1998. River sediment discharge to the oceans: Present-day controls and global budgets. Am. J. Sci. 298, 265–295.

Lupker, M., France-Lanord, C., Galy, V., Lavé, J., Gaillardet, J., Gajurel, A.P., Guilmette, C., Rahman, M., Singh, S.K., Sinha, R., 2012. Predominant floodplain over mountain weathering of Himalayan sediments (Ganga basin). Geochim. Cosmochim. Acta 84, 410–432.

Lupker, M., France-Lanord, C., Lavé, J., Bouchez, J., Galy, V., Métivier, F., Gaillardet, J., Lartiges, B., Mugnier, J.L., 2011. A Rouse-based method to integrate the chemical composition of river sediments: Application to the Ganga basin. J. Geophys. Res. Earth Surf. 116, F04012.

Ma, C., Eggleton, R.A., 1999. Cation exchange capacity of kaolinite. Clays Clay Miner. 47, 174–180.

Ma, L., Chabaux, F., Pelt, E., Blaes, E., Jin, L., Brantley, S., 2010. Regolith production rates calculated with uranium-series isotopes at Susquehanna/Shale Hills Critical Zone Observatory. Earth Planet. Sci. Lett. 297, 211–225.

Macaire, J.J., Bossuet, G., Choquier, A., Cocirta, C., De Luca, P., Dupis, A., Gay, I., Mathey, E., Guenet, P., 1997. Sediment yield during Late Glacial and Holocene periods in the Lac Chambon watershed, massif central, France. Earth Surf. Process. Landforms 22, 473–489.

Maher, K., Chamberlain, C.P., 2014. Hydrologic Regulation of Chemical Weathering and the Geologic Carbon Cycle. Science (80-.). 343, 1502–1504.

Mana, S.C.A., Hanafiah, M.M., Chowdhury, A.J.K., 2017. Environmental characteristics of clay and clay-based minerals 1, 155–161.

Mantua, N.J., Hare, S.R., 2002. The Pacific Decadal Oscillation. J. Oceanogr. 58, 35–44.

Maroulis, J.C., Nanson, G.C., Price, D.M., Pietsch, T., 2007. Aeolian-fluvial interaction and climate change: source-bordering dune development over the past ~100 ka on Cooper Creek, central Australia. Quat. Sci. Rev. 26, 386–404.

Matoh, T., 1997. Boron in plant cell walls. Plant Soil 193, 59–70.

Mavromatis, V., Montouillout, V., Noireaux, J., Gaillardet, J., Schott, J., 2015. Characterization of boron incorporation and speciation in calcite and aragonite from co-precipitation experiments under controlled pH, temperature and precipitation rate. Geochim. Cosmochim. Acta 150, 299–313.

McKean, J.A., Dietrich, W.E., Finkel, R.C., Southon, J.R., Caffee, M.W., 1993. Quantification of soil production and downslope creep rates from cosmogenic 10Be accumulations on a hillslope profile. Geology.

McLennan, S.M., 1993. Weathering and Global Denudation. J. Geol. 101, 295–303.

Meade, R.H., Weibezhan, F.H., Lewis Jr., W.M., Hernandez, D.P., 1990. Suspended-sediment budget for the Orinoco River, in: The Orinoco River as an Ecosystem. pp. 55–79.

Menard, G., Vlastélic, I., Ionov, D.A., Rose-Koga, E.F., Piro, J.L., Pin, C., 2013. Precise and accurate determination of boron concentration in silicate rocks by direct isotope dilution ICP-MS: Insights into the B budget of the mantle and B behavior in magmatic systems. Chem. Geol. 354, 139–149.

Meybeck, M., 1987. Global chemical weathering of surficial rocks estimated from river dissolved loads. Am. J. Sci. 287, 401–428.

Míková, J., Denková, P., 2007. Modified chromatographic separation scheme for Sr and Nd isotope analysis in geological silicate samples. J. Geosci. 52, 221–226.

Miller, G.H., Magee, J.W., Jull, A.J.T., 1997. Low-latitude glacial cooling in the southern hemisphere from amino-acid racemization in emu eggshells. Nature 385, 241–244.

Millot, R., Gaillardet, J., Dupré, B., Allégre, C.J., 2003. Northern latitude chemical weathering rates: Clues from the Mackenzie River Basin, Canada. Geochim. Cosmochim. Acta 67, 1305–1329.

Millot, R., Gaillardet, J., Dupré, B., Allègre, C.J., 2002. The global control of silicate weathering rates and the coupling with physical erosion: New insights from rivers of the Canadian Shield. Earth Planet. Sci. Lett. 196, 83–98.

Millot, R., Négrel, P., 2007. Multi-isotopic tracing (δ7Li, δ11B,87Sr/86Sr) and chemical geothermometry: evidence from hydro-geothermal systems in France. Chem. Geol. 244, 664–678.

Millot, R., Petelet-Giraud, E., Guerrot, C., Négrel, P., 2010. Multi-isotopic composition (δ7Li–δ11B–δD–δ18O) of rainwaters in France: Origin and spatio-temporal characterization. Appl. Geochemistry 25, 1510–1524.

Mills, K., Gell, P., Hesse, P.P., Jones, R., Kershaw, P., Drysdale, R., McDonald, J., 2013. Paleoclimate studies and natural-resource management in the Murray-Darling Basin I: past, present and future climates. Aust. J. Earth Sci. 60, 547–560.

Mix, A.C., Pisias, N.G., Rugh, W., Wilson, J., Morey, A., Hagelberg, T.K., 1995. Benthic Foraminifer Stable Isotope Record from Site 849 (0-5 Ma): Local and Global Climate Changes. Proc. Ocean Drill. Program, 138 Sci. Results 138.

Miyazaki, T., Shuto, K., 1998. Sr and Nd isotope ratios of twelve GSJ rock reference samples. Geochem. J. 32, 345–350.

Molnar, P., England, P., 1990. Late Cenozoic uplift of mountain ranges and global climate

change: chicken or egg? Nature 346, 29–34.

Moon, S., Chamberlain, C.P., Hilley, G.E., 2014. New estimates of silicate weathering rates and their uncertainties in global rivers. Geochim. Cosmochim. Acta 134, 257–274.

Moquet, J.S., Crave, A., Viers, J., Seyler, P., Armijos, E., Bourrel, L., Chavarri, E., Lagane, C., Laraque, A., Casimiro, W.S.L., Pombosa, R., Noriega, L., Vera, A., Guyot, J.L., 2011. Chemical weathering and atmospheric/soil CO2uptake in the Andean and Foreland Amazon basins. Chem. Geol. 287, 1–26.

Morton, A.C., Hallsworth, C.R., 1999. Processes controlling the composition of heavy mineral assemblages in sandstones. Sediment. Geol. 124, 3–29.

Moy, C.M., Seltzer, G.O., Rodbell, D.T., Anderson, D.M., 2002. Variability of El Niño/Southern Oscillation activity at millennial timescales during the Holocene epoch. Nature 420, 162–165.

Mueller, D., 2017. Rivers of the Last Glacial Maximum: a southeast Australian perspective. Univ. Wollongong Thesis Collect.

Murray-Darling Basin Authority, 2018. Landscape | Murray-Darling Basin Authority [WWW Document].

Murray-Darling Basin Authority, 2016. Murray-Darling Basin Authority annual report 2016-2017.

Muttik, N., Kirsimäe, K., Newsom, H.E., Williams, L.B., 2011. Boron isotope composition of secondary smectite in suevites at the Ries crater, Germany: Boron fractionation in weathering and hydrothermal processes. Earth Planet. Sci. Lett. 310, 244–251.

Nanson, C.G., Price, D.M., Short, S. a, 1992. Wetting and drying of Australia over the past 300,000 years. Geology 20, 791–794.

Nanson, G.C., Erskine, W.D., 1988. Episodic changes of channels and floodplains on coastal rivers in New South Wales. Fluv. Geomorphol. Aust. 201–221.

Négrel, P., Allègre, C.J., Dupré, B., Lewin, E., 1993. Erosion sources determined by inversion of major and trace element ratios and strontium isotopic ratios in river: The Congo Basin case. Earth Planet. Sci. Lett. 120, 59–76.

Nesbit, H.W., Wilson, R.E., 1992. Recent chemical weathering of basalts. Am. J. Sci.

Nesbitt, H.W., Young, G.M., 1982. Early proterozoic climates and plate motions inferred from major element chemistry of lutites. Nature 299, 715–717.

Newman, K., 2012. Effects of the sampling interface in MC-ICP-MS: Relative elemental sensitivities and non-linear mass dependent fractionation of Nd isotopes. J. Anal. At. Spectrom. 27, 63–70.

Noireaux, J., Gaillardet, J., Sullivan, P.L., Brantley, S.L., 2014a. Boron Isotope Fractionation in Soils at Shale Hills CZO. Procedia Earth Planet. Sci. 10, 218–222.

Noireaux, J., Gaillardet, J., Sullivan, P.L., Brantley, S.L., Noireaux J, A, G.J., Sullivan P L, Brantley S L, 2014b. Boron Isotope Fractionation in Soils at Shale Hills CZO. Procedia Earth Planet. Sci. 10, 218–222.

Noireaux, J., Mavromatis, V., Gaillardet, J., Schott, J., Montouillout, V., Louvat, P., Rollion-Bard, C., Neuville, D.R., 2015. Crystallographic control on the boron isotope paleo-pH proxy. Earth Planet. Sci. Lett. 430, 398–407.

Noireaux, J., Riotte, J., Gaillardet, J., Louvat, P., Bouchez, J., Sekkar, M., Kumar, M., Candaudap, F., Braun, J.J., 2017. Vegetation cycling and chemical weathering in a tropical catchment: constraints from boron isotope geochemistry. Geochim. Cosmochim. Acta.

O'Neill, M.A., Eberhard, S., Albersheim, P., Darvill, A.G., 2001. Requirement of borate cross-linking of cell wall rhamnogalacturonan II for Arabidopsis growth. Science (80-.). 294, 846–849.

Olley, J.M., Wasson, R.J., 2003. Changes in the flux of sediment in the Upper Murrumbidgee catchment, Southeastern Australia, since European settlement. Hydrol. Process. 17, 3307–3320.

Page, K.J., 1994. Late quaternary chronology of the riverine plain of Southeastern Australia.

Page, K.J., Kemp, J., Nanson, G.C., 2009. Late Quaternary evolution of Riverine Plain paleochannels, southeastern Australia. Aust. J. Earth Sci. 56, S19–S33.

Page, K.J., Nanson, G.C., 1996. Stratigraphic architecture resulting from Late Quaternary evolution of the Riverine Plain, south-eastern Australia. Sedimentology 43, 927–945.

Page, K.J., Nanson, G.C., Price, D., 1996. Chronology of Murrumbidgee River palaeochannels on the Riverine Plain, southeastern Australia. J. Quat. Sci. 11, 311–326.

Page, K.J., Nanson, G.C., Price, D.M., 1991. Thermoluminescence chronology of late quaternary deposition on the riverine plain of south-eastern Australia. Aust. Geogr. 22, 14–23.

Palfreyman, W.D., 1984. Guide to the Geology of Australia. Bur. Miner. Resour. Aust. 181, 222.

Palmer, M.R., Pearson, P.N., Cobb, S.J., 1998. Reconstructing Past Ocean pH-Depth Profiles. Science (80-.). 282, 1468–1471.

Palmer, M.R., Spivack, A.J., Edmond, J.M., 1987. Temperature and pH controls over isotopic fractionation during adsorption of boron on marine clay. Geochim. Cosmochim. Acta 51, 2319–2323.

Palmer, M.R., Swihart, G.H., 1996. Boron isotope geochemistry; an overview. Rev. Mineral. Geochemistry 33.

Parker, A., 1970. An Index of Weathering for Silicate Rocks. Geol. Mag. 107, 501–504.

Pels, S., 1971. River systems and climatic changes in southeastern Australia, Aboriginal men and Environment in Australia. Australian National University Press, Canberra.

Pels, S., 1964. The present and ancestral Murray River system. Geogr. Res. 2, 111–119.

Pels, S., 1966. Late quaternary chronology of the riverine plain of Southeastern Australia. J. Geol. Soc. Aust. 13, 27–40.

Pels, S., Stannard, M.E., Talsma, T., 1968. Environmental studies of the Coleambally Irrigation Area and surrounding districts. Water Conserv. Areas Irrig. Comm. Bull. 2.

Petelet-Giraud, E., Klaver, G., Negrel, P., 2009. Natural versus anthropogenic sources in the surface- and groundwater dissolved load of the Dommel river (Meuse basin): Constraints by boron and strontium isotopes and gadolinium anomaly. J. Hydrol. 369, 336–349.

Peters, N.E., 1982. Evaluation of Environmental Factors Affecting Yields of Major Dissolved

Ions of Streams in the United States, United States Geological Survey.

Petherick, L., Bostock, H., Cohen, T.J., Fitzsimmons, K., Tibby, J., 2013. Climatic records over the past 30 ka from temperate Australia - a synthesis from the Oz- INTIMATE workgroup. Quat. Sci. Rev. 74, 58–77.

Petit, J.R., Jouzel, J., Raynaud, D., Barkov, N.I., Barnola, J.M., Basile, I., Bender, M., Chappellaz, J., Davis, M., Delaygue, G., Delmotte, M., Kotiyakov, V.M., Legrand, M., Lipenkov, V.Y., Lorius, C., Pépin, L., Ritz, C., Saltzman, E., Stievenard, M., 1999. Climate and atmospheric history of the past 420,000 years from the Vostok ice core, Antarctica. Nature.

Pigram, J.J.J., 2007. Australia's water resources : from use to management. CSIRO Pub.

Pin, C., Zalduegui, J.F.S., Santos Zalduegui, J.F., 1997. Sequential separation of light rare-earth elements, thorium and uranium by miniaturized extraction chromatography: Application to isotopic analyses of silicate rocks. Anal. Chim. Acta 339, 79–89.

Pizer, R., Selzer, R., 1984. The Boric Acid/Lactic Acid System. Equilibria and Reaction Mechanism1. Inorg. Chem. 23, 3023–3026.

Porter, S.C., 1989. Some Geological Implications of Average Quaternary Glacial Conditions. Quat. Res. 32, 245–261.

Power, S., Casey, T., Folland, C., Colman, A., Mehta, V., 1999. Inter-decadal modulation of the impact of ENSO on Australia. Clim. Dyn. 15, 319–324.

Pravettoni, R., 2015. Ganges basin climate indicators – Rainfall & Temperature | GRID-Arendal [WWW Document]. Himal. Clim. Water Altas.

Price, J.R., Velbel, M.A., 2003. Chemical weathering indices applied to weathering profiles developed on heterogeneous felsic metamorphic parent rocks. Chem. Geol. 202, 397–416.

Probst, J.L., Suchet, P.A., 1992. Fluvial suspended sediment transport and mechanical erosionin the maghreb (north africa). Hydrol. Sci. J. 37, 621–637.

Prosser, I.P., Chappell, J., Gillespie, R., 1994. Holocene valley aggradation and gully erosion in headwater catchments, south-eastern highlands of Australia. Earth Surf. Process. Landforms 19, 465–480.

Prunier, J., Chabaux, F., Stille, P., Gangloff, S., Pierret, M.C., Viville, D., Aubert, A., 2015. Geochemical and isotopic (Sr, U) monitoring of soil solutions from the Strengbach catchment (Vosges mountains, France): Evidence for recent weathering evolution. Chem. Geol. 417, 289–305.

Raczek, I., Stoll, B., Hofmann, A.W., Jochum, K.P., 2001. High-precision trace element data for the USGS reference materials BCR-1, BCR-2, BHVO-1, BHVO-2, AGV-1, AGV-2, DTS-1, DTS-2, GSP-1 and GSP-2 by ID-TIMS and MIC-SSMS. Geostand. Newsl.

Rasmussen, S.O., Bigler, M., Blockley, S.P., Blunier, T., Buchardt, S.L., Clausen, H.B., Cvijanovic, I., Dahl-Jensen, D., Johnsen, S.J., Fischer, H., Gkinis, V., Guillevic, M., Hoek, W.Z., Lowe, J.J., Pedro, J.B., Popp, T., Seierstad, I.K., Steffensen, J.P., Svensson, A.M., Vallelonga, P., Vinther, B.M., Walker, M.J.C., Wheatley, J.J., Winstrup, M., 2014. A stratigraphic framework for abrupt climatic changes during the Last Glacial period based on three synchronized Greenland ice-core records: Refining and extending the INTIMATE event stratigraphy. Quat. Sci. Rev. 106, 14–28.

Raymo, M.E., Ganley, K., Carter, S., Oppo, D.W., McManus, J., 1998. Millennial-scale

climate instability during the early Pleistocene epoch. Nature 392, 699–702.

Raymo, M.E., Ruddiman, W.F., Froelich, P.N., 1988. Influence of late Cenozoic mountain building on ocean geochemical cycles. Geology 16, 649–653.

Raymo, W.E., Ruddiman, W.F., 1992. Tectonic Forcing of Late Cenozoic Climate. Nature 359, 117.

Retallack, G.J., 1986. The fossil record of soils, in: Wright, P. V. (Ed.), Paleosols: Their Recognition and Interpretation. Blackwell Scientific Publications: Oxford.

Riebe, C.S., Kirchner, J.W., Finkel, R.C., 2003. Long-term rates of chemical weathering and physical erosion from cosmogenic nuclides and geochemical mass balance. Geochim. Cosmochim. Acta 67, 4411–4427.

Risbey, J.S., Pook, M.J., McIntosh, P.C., Wheeler, M.C., Hendon, H.H., 2009. On the Remote Drivers of Rainfall Variability in Australia. Mon. Weather Rev. 137, 3233–3253.

Rojas, M., Moreno, P., Kageyama, M., Crucifix, M., Hewitt, C., Abe-Ouchi, A., Ohgaito, R., Brady, E.C., Hope, P., 2009. The Southern Westerlies during the last glacial maximum in PMIP2 simulations. Clim. Dyn. 32, 525–548.

Rose-Koga, E.F., Sheppard, S.M.F., Chaussidon, M., Carignan, J., 2006. Boron isotopic composition of atmospheric precipitations and liquid–vapour fractionations. Geochim. Cosmochim. Acta 70, 1603–1615.

Rose, E.F., Chaussidon, M., France-Lanord, C., 2000. Fractionation of boron isotopes during erosion processes: The example of Himalayan rivers. Geochim. Cosmochim. Acta 64, 397–408.

Rose, L.E., Karan, P.P., Proud, R.R., Zuberi, M., 2018. Nepal. Encycl. Br.

Rothacker, L., Dosseto, A., Francke, A., Chivas, A.R., Vigier, N., Kotarba-Morley, A.M., Menozzi, D., 2018. Impact of climate change and human activity on soil landscapes over the past 12,300 years. Sci. Rep. 8, 247.

Roux, P., 2016. Cycle biogéochimique du bore dans un écosystème forestier: étude de la hêtraie du site de Montiers.

Roux, P., Lemarchand, D., Hughes, H.J., Turpault, M.-P., 2015. A Rapid Method for Determining Boron Concentration (ID-ICP-MS) and δ 11 B (MC-ICP-MS) in Vegetation Samples after Microwave Digestion and Cation Exchange Chemical Purification. Geostand. Geoanalytical Res. 39, 453–466.

Roux, P., Turpault, M.P., Kirchen, G., Redon, P.O., Lemarchand, D., 2017. Boron Dissolved and Particulate Atmospheric Inputs to a Forest Ecosystem (Northeastern France). Environ. Sci. Technol. 51, 14038–14046.

Ruddiman, W.F., 1997. Tectonic Uplift and Climate Change, 1997 Spring Science+Business Media New York.

Ruddiman, W.F., Raymo, M.E., Lamb, H.H., Andrews, J.T., 1988. Northern Hemisphere Climate Regimes During the Past 3 Ma: Possible Tectonic Connections [and Discussion]. Philos. Trans. R. Soc. B Biol. Sci. 318, 411–430.

Ruiz, J.M., Baghour, M., Bretones, G., Belakbir, A., Romero, L., 1998. Nitrogen Metabolism in Tobacco Plants (Nicotiana tabacum L.): Role of Boron as a Possible Regulatory Factor. Int. J. Plant Sci. 159, 121.

Sagan, C., Mullen, G., 1972. Earth and Mars: Evolution of Atmospheres and Surface Temperatures. Science (80-.). 177, 52–56.

Saji, N.S., Wielandt, D., Paton, C., Bizzarro, M., 2016. Ultra-high-precision Nd-isotope measurements of geological materials by MC-ICPMS. J. Anal. At. Spectrom. 31, 1490–1504.

Sakai, H., 1983. Geology of the Tansen Group of the Lesser Himalaya in Nepal. Mem. Fac. Sci. Kyushu Univ. XXV, 27–74.

Saleem, M., Khanif, Y.M., Ishak, F., Samsuri, A.W., Hafeez, B., 2013. International Research Journal of Agriculture and Soil Science. Int. Res. J. Agric. Soil Sci. 3, 293–300.

Sayyed, M.R.G., 2014. Lithological control on the mobility of elements during chemical weathering. Comun. Geol. t. 101 101, 63–69.

Schaller, M., Von Blanckenburg, F., Veldkamp, A., Tebbens, L.A., Hovius, N., Kubik, P.W., 2002. A 30 000 yr record of erosion rates from cosmogenic 10Be in Middle European river terraces. Earth Planet. Sci. Lett. 204, 307–320.

Schmitt, A.D., Vigier, N., Lemarchand, D., Millot, R., Stille, P., Chabaux, F., 2012. Processes controlling the stable isotope compositions of Li, B, Mg and Ca in plants, soils and waters: A review. Comptes Rendus - Geosci. 344, 704–722.

Schnoor, J.L., 1990. Kinetics of chemical waethering: A comparison of laboratory and field weathering rates. Aquat. Chem. Kinet. 475–504.

Schott, J., Mavromatis, V., Fujii, T., Pearce, C.R., Oelkers, E.H., 2016. The control of carbonate mineral Mg isotope composition by aqueous speciation: Theoretical and experimental modeling. Chem. Geol. 445, 120–134.

Schumm, S.A., 1968. River Adjustment to Altered Hydrologic Regimen- Murrumbidgee River and Paleochannels, Australia. Geol. Surv. Proffesional Pap. 598 1–74.

Schumm, S.A., 1979. Geomorphic Thresholds: The Concept and Its Applications. Trans. Inst. Br. Geogr. 4, 485.

Schwarcz, H.P., Agyei, E.K., McMullen, C.C., 1969. Boron isotopic fractionation during clay adsorption from sea-water. Earth Planet. Sci. Lett. 6, 1–5.

Sellers, W.D., 1969. A Global Climatic Model Based on the Energy Balance of the Earth-Atmosphere System. J. Appl. Meteorol. 8, 392–400.

Shackleton, N.J., Opdyke, N.D., 1973. Oxygen isotope and palaeomagnetic stratigraphy of Equatorial Pacific core V28-238: Oxygen isotope temperatures and ice volumes on a 105year and 106year scale. Quat. Res. 3, 39–55.

Shibata, T., Yoshikawa, M., Tatsumi, Y., 2003. An analytical method for determining precise Sr and Nd isotopic compositions and results for thirteen rock standard materials. Front. Res. Earth Evol. 1, 363–367.

Siever, R., 1968. Sedimentogical consquences of a stready-state ocean-atmosphere. Sedimentology 11, 5–29.

Singer, A., 1980. The paleoclimatic interpretation of clay minerals in soils and weathering profiles. Earth Sci. Rev. 15, 303–326.

Singer, A., 1984. The paleoclimatic interpretation of clay minerals in sediments - a review. Earth Sci. Rev. 21, 251–293.

Singh, G., Geissler, E. a., 1985. Late Cainozoic History of Vegetation, Fire, Lake Levels and Climate, at Lake George, New South Wales, Australia. Philos. Trans. R. Soc. B Biol. Sci. 311, 379–447.

Singh, G., Opdyke, N.D., Bowler, J.M., 1981. Late Cainozoic stratigraphy, palaeomagnetic chronology and vegetational history from Lake George, N.S.W. J. Geol. Soc. Aust. 28, 435–452.

Small, E.E., Anderson, R.S., Hancock, G.S., 1999. Estimates of the rate of regolith production using 10Be and 26Al from an alpine hillslope. Geomorphology 27, 131–150.

Spivack, A.., Edmond, J.., 1987. Boron isotope exchange between seawater and the oceanic crust. Geochim. Cosmochim. Acta 51, 1033–1043.

Spivack, A., Palmer, M.., Edmond, J.., 1987. The sedimentary cycle of the boron isotopes. Geochim. Cosmochim. Acta 51, 1939–1949.

Spivack, A.J., Berndt, M.E., Seyfried, W.E., 1990. Boron isotope fractionation during supercritical phase separation. Geochim. Cosmochim. Acta 54, 2337–2339.

Stallard, R.F., Edmond, J.M., 1983. Geochemistry of the Amazon Basin 2. The influence of geology and weathering environment on the dissolved load. J. Geophys. Res. 88, 9671–9688.

Starkey, H.C., Blackmon, P.D., Pevear, D.R., 1984. Sample preparation procedures for the analysis of clay minerals by X-ray diffraction.

Suresh, P.O., Dosseto, A., Hesse, P.P., Handley, H.K., 2014. Very long hillslope transport timescales determined from uranium-series isotopes in river sediments from a large, tectonically stable catchment. Geochim. Cosmochim. Acta 142, 442–457.

Sutton, S.J., Maynard, J.B., 1992. Multiple alteration events in the history of a sub-Huronian regolith at Lauzon Bay, Ontario. Can. J. Earth Sci. 29, 432–445.

Tanaka, T., Togashi, S., Kamioka, H., Amakawa, H., Kagami, H., Hamamoto, T., Yuhara, M., Orihashi, Y., Yoneda, S., Shimizu, H., Kunimaru, T., Takahashi, K., Yanagi, T., Nakano, T., Fujimaki, H., Shinjo, R., Asahara, Y., Tanimizu, M., Dragusanu, C., 2000. JNdi-1: A neodymium isotopic reference in consistency with LaJolla neodymium. Chem. Geol. 168, 279–281.

Taylor, A., Blum, J.D., 1995. Relation between soil age and silicate weathering rates determined from the chemical evolution of a glacial chronosequence. Geology.

The Basin Plan annual report 2014-15, 2015.

Thermo Fisher Scientic, 2012. iCAP Q Operating Manual.

Thermo Fisher Scientific, 2009. NEPTUNE Hardware Manual.

Thermo Scientific, 2008. Interference Corrections in Isotope Ratio Measurements Using MC-ICP-MS : Examples for Nd-Sm, Application Note.

Tonarini, S., Pennisi, M., Leeman, W.P., 1997. Precise boron isotopic analysis of complex silicate (rock) samples using alkali carbonate fusion and ion-exchange separation. Chem. Geol. 142, 129–137.

Twidale, C.R., 2007. Ancient Australian Landscapes. Rosenberg Publishing.

Upreti, B.. N., 1999. An overview of the stratigraphy and tectonics of the Nepal Himalaya. J. Asian Earth Sci. 17, 577–606.

Vail, P.R., Mitchum, R.M., Thompson, S., 1977. Seismic Stratigraphy--Applications to Hydrocarbon Exploration, AAPG Special Volumes. AAPG Special Volumes.

Valeriano, C.M., Vaz, G.S., Medeiros, S.R., Neto, C.C.., Ragatky, C.D., Geraldes, M.C., 2008. THE NEODYMIUM ISOTOPE COMPOSITION OF THE JNdi-1 OXIDE REFERENCE MATERIAL : RESULTS FROM THE LAGIR LABORATORY , RIO DE JANEIRO, in: VI South American Symposium on Isotope Geology. San Carlos de Bariloche, Argentina, pp. 1–3.

Vance, D., Teagle, D.A.H., Foster, G.L., 2009. Variable Quaternary chemical weathering fluxes and imbalances in marine geochemical budgets. Nature 458, 493–496.

Vanderpool, R.A., Johnson, P.E., 1992. Boron isotope ratios in commercial produce and boron-10 foliar and hydroponic enriched plants. J. Agric. Food Chem. 40, 462–466.

Veblen, D.R., 1990. High-Resolution Transmission Electron Microscopy and Electron Diffraction of Mixed-Layer Illite/Smectite: Experimental Results. Clays Clay Miner. 38, 1–13.

Velbel, M.A., 1993a. Constancy of silicate-mineral weathering-rate ratios between natural and experimental weathering: implications for hydrologic control of differences in absolute rates. Chem. Geol. 105, 89–99.

Velbel, M.A., 1993b. Temperature-dependence of silicate weathering in nature - how strong a negatvie feedback on long-term accumulation of atmospheric CO2 and global greenhouse warming. Geology 21, 1059–1062.

Vengosh, A., Chivas, A.R., McCulloch, M.T., Starinsky, A., Kolodny, Y., 1991a. Boron isotope geochemistry of Australian salt lakes. Geochim. Cosmochim. Acta 55, 2591–2606.

Vengosh, A., Chivas, A.R., Starinsky, A., Kolodny, Y., Baozhen, Z., Pengxi, Z., 1995. Chemical and boron isotope compositions of non-marine brines from the Qaidam Basin, Qinghai, China. Chem. Geol. 120, 135–154.

Vengosh, A., Kolodny, Y., Starinsky, A., Chivas, A.R., McCulloch, M.T., 1991b. Coprecipitation and isotopic fractionation of boron in modern biogenic carbonates. Geochim. Cosmochim. Acta 55, 2901–2910.

Vengosh, A., Starinsky, A., Kolodny, Y., Chivas, A.R., Raab, M., 1992. Boron isotope variations during fractional evaporation of sea water: New constraints on the marine vs. nonmarine debate. Geology 20, 799.

Vital, H., Stattegger, K., 2000. Major and trace elements of stream sediments from the lowermost Amazon River. Chem. Geol. 168, 151–168.

Vital, H., Stattegger, K., Garbe-Schoenberg, C.-D., 1999. Composition and trace-element geochemistry of detrital clay and heavy-mineral suites of the lowermost Amazon River; a provenance study. J. Sediment. Res. 69, 563–575.

Vogl, J., Rosner, M., 2012. Production and Certification of a Unique Set of Isotope and Delta Reference Materials for Boron Isotope Determination in Geochemical, Environmental and Industrial Materials. Geostand. Geoanalytical Res. 36, 161–175.

Voinot, A., 2012. Contribution des isotopes du bore à l'étude des mécanismes et bilans d'altération des minéraux des sols. Université de Strasbourg.

Voinot, A., Lemarchand, D., Collignon, C., Granet, M., Chabaux, F., Turpault, M.-P.P., 2013. Experimental dissolution vs. transformation of micas under acidic soil conditions:

Clues from boron isotopes. Geochim. Cosmochim. Acta 117, 144–160.

Walker, J.C.G., Hays, P.B., Kasting, J.F., 1981. A negative feedback mechanism for the long-term stabilization of Earth's surface temperature. J. Geophys. Res. 86, 9776.

Wallbrink, P.J., Murray, A.S., Olley, J.M., Olive, L.J., 1998. Determining sources and transit times of suspended sediment in the Murrumbidgee River, New South Wales, Australia, using fallout 137 Cs and 210 Pb. Water Resour. Res. 34, 879–887.

Wasserburg, G.., Jacousen, S.., DePaolo, D.., McCulloch, M.., Wen, T., 1981. Precise determination of ratios, Sm and Nd isotopic abundances in standard solutions. Geochim. Cosmochim. Acta 45, 2311–2323.

Wedepohl, H., 1986. Chapter 5: The Composition of the Continental Crust. Int. Geophys. 34, 213–241.

Wei, H.Z., Lei, F., Jiang, S.Y., Lu, H.Y., Xiao, Y.K., Zhang, H.Z., Sun, X.F., 2015. Implication of boron isotope geochemistry for the pedogenic environments in loess and paleosol sequences of central China. Quat. Res. (United States) 83, 243–255.

West, A.J., Galy, A., Bickle, M., 2005. Tectonic and climatic controls on silicate weathering. Earth Planet. Sci. Lett. 235, 211–228.

White, A.F., Blum, A.E., 1995. Effects of climate on chemical_ weathering in watersheds. Geochim. Cosmochim. Acta 59, 1729–1747.

White, A.F., Blum, A.E., Bullen, T.D., Vivit, D. V, Schulz, M., Fitzpatrick, J., 1999. The effect of temperature on experimental and natural chemical weathering rates of granitoid rocks. Geochim. Cosmochim. Acta 63, 3277–3291.

White, A.F., Brantley, S.L., 1995. Chemical weathering rates of silicate minerals, Reviews in Mineralogy and Geochemistry. Mineralogical Society of America.

White, A.F., Hochella, M.F., 1992. Surface chemistry associated with the cooling and subaerial weathering of recent basalt flows. Geochim. Cosmochim. Acta 56, 3711–3721.

Wieser, M.E., Iyer, S.S.S., Krouse, H.R.R., Cantagallo, M.I.I., 2001. Variations in the boron isotope composition of Coffea arabica beans. Appl. Geochemistry 16, 317–322.

Willenbring, J.K., von Blanckenburg, F., 2010. Long-term stability of global erosion rates and weathering during late-Cenozoic cooling. Nature 465, 211–214.

Williams, L., 2001. The influence of organic matter on the boron isotope geochemistry of the gulf coast sedimentary basin, USA. Chem. Geol. 174, 445–461.

Williams, L.B., Hervig, R.L., 2005. Lithium and boron isotopes in illite-smectite: The importance of crystal size. Geochim. Cosmochim. Acta 69, 5705–5716.

Williams, L.B., Hervig, R.L., Holloway, J.R., Hutcheon, I., 2001a. Boron isotope geochemistry during diagenesis. Part I. Experimental determination of fractionation during illitization of smectite. Geochim. Cosmochim. Acta 65, 1769–1782.

Williams, L.B., Hervig, R.L., Holloway, J.R., Hutcheon, I., 2001b. Boron isotope geochemistry during diagenesis. Part I. Experimental determination of fractionation during illitization of smectite. Geochim. Cosmochim. Acta 65, 1769–1782.

Williams, L.B., Hervig, R.L., Hutcheon, I., 2001c. Boron isotope geochemistry during diagenesis. Part II. Applications to organic-rich sediments. Geochim. Cosmochim. Acta 65, 1783–1794.

Wilson, L., 1973. Variations in mean annual sediment yield as a function of mean annual precipitation. Am. J. Sci. 273, 335–349.

Wilson, S.A., 1997. The collection, preparation and testing of USGS reference material BRC-1, Columbia River, U.S. Geological Survey Open Report 98-00x.

Wilson, S.A., 1998. Data compilation for USGS reference material GSP-SS, Granodiorite, Silver Plume, Colorado, U.S. Geological Survey Open Report xxxxx.

Xiao, J., Xiao, Y.K., Jin, Z.D., He, M.Y., Liu, C.Q., 2013. Boron isotope variations and its geochemical application in nature. Aust. J. Earth Sci. 60, 431–447.

Xiao, Y., Dapeng, S., Yunhui, W., Hairing, Q., Lin, J., 1992. Boron isotopic compositions of brine, sediments, and source water in Da Qaidam Lake, Qinghai, China. Geochim. Cosmochim. Acta 56, 1561–1568.

Xiao, Y., Swihart, G.H., Xiao, Y., Vocke, R.D., 2001. A preliminary experimental study of the boron concentration in vapor and the isotopic fractionation of boron between seawater and vapor during evaporation of seawater. Sci. China Ser. B Chem. 44, 540–551.

Xiao, Y.K., Vocke, R.D., Swihart, G.H., Xiao, Y., 1997. Boron Volatilization and Its Isotope Fractionation during Evaporation of Boron Solution. Anal. Chem. 69, 5203–5207.

Yang, Y.-H., Chu, Z.-Y., Wu, F.-Y., Xie, L.-W., Yang, J.-H., 2011. Precise and accurate determination of Sm, Nd concentrations and Nd isotopic compositions in geological samples by MC-ICP-MS. J. Anal. At. Spectrom. 26, 1237.

Yang, Y., Wu, F., Xie, L., Zhang, Y., 2010. High-Precision Measurements of the 143Nd/144Nd Isotope Ratio in Certified Reference Materials without Nd and Sm Separation by Multiple Collector Inductively Coupled Plasma Mass Spectrometry. Anal. Lett. 43, 142–150.

Yang, Y., Zhang, H., Xie, L., Wu, F., 2008. Accurate measurement of neodymium isotopic composition using Neptune MC-ICP-MS. Front. Chem. China 3, 94–98.

Zhao, M., Running, S.W., 2010. Drought-induced reduction in global terrestrial net primary production from 2000 through 2009. Science (80-.). 329, 940–943.

Zhao, Z., Liu, C., Xiao, Y., Lang, Y., 2003. Geochemical study of boron isotopes in the process of loess weathering. Sci. China Ser. D Earth Sci. 46, 106–116.